2021–2022 COMPREHENSIVE EMERGENCY DROUGHT BARRIER

Effectiveness Report

Prepared by
California Department of Water Resources

June 2024

2021–2022 COMPREHENSIVE EMERGENCY DROUGHT BARRIER

Effectiveness Report

Prepared by
California Department of Water Resources
Contact: Jacob McQuirk, Manager
Water Initiatives Planning and Management Branch
Division of Operations and Maintenance
jacob.mcquirk@water.ca.gov
Office: 916-902-9905

June 2024

ACKNOWLEDGMENTS

The following individuals, agencies, and organizations contributed to the 2021–2022 Comprehensive Emergency Drought Barrier Effectiveness Report.

Key Report Authors

California Department of Water Resources

Eli Ateljevich, W.R., PE, Senior Engineer
Raul Barba, W.R., PE, Senior Engineer
James Campbell, PLS, Geomatics Engineer
Kevin Clark, M.S., Environmental Program Manager I
Nathan Evenson, W.R., Engineer
Jared Frantzich, Senior Environmental Scientist Supervisor
Lesley Hamamoto, Program Manager I
Rosemary Hartman, PhD, Environmental Program Manager
Tracy Hinojosa, W.R., PE, Supervising Engineer
Dave Huston, W.R., PE, Senior Engineer
Kenneth Karcher, W.R., PE, Senior Engineer
Kate Le, W.R., P.E., Senior Engineer
Tyler Salman, Environmental Scientist
Patrick Tami, PLS, Geomatics Branch Manager
Robert Trang, W.R., PE, Supervising Engineer
Veronica Wunderlich, Senior Environmental Scientist, Specialist

ICFESA Joint Venture

Paul Bergman, ESA, Senior Scientist
Andrew Kalmbach, ICF, Senior Biologist

Additional Acknowledgments

This project team would also like to acknowledge with special thanks all the **U.S. Geological Survey–California Water Science Center** technical contributors who provided valuable technical input on the project study plan, field/lab support, data analysis, report review, and document production. The individuals and organizations listed below along with numerous additional staff from the California Department of Water Resources, U.S. Geological Survey, and ICFESA Joint Venture made this report possible.

U.S. Geological Survey–California Water Science Center, Biogeochemistry Group

Keith Bouma-Gregson, Research Biologist
Brian Bergamaschi, Research Chemist
Jacob Brinkman, Physical Scientist
Katrina Cone, Physical Scientist
Andrea Jaegge, Biologist
Tamara Kraus, Research Soil Scientist
Katy O'Donnell, Hydrologist
Emily Richardson, Physical Scientist
Crystal Sturgeon, Ecologist

U.S. Geological Survey–California Water Science Center, Hydrodynamics Group

Jon Burau, Supervisory Hydrologist
Anna Conlen, Hydrologic Technician
Eli Duber, Hydrologic Technician
Lawrence Fujiwara, Hydrologic Technician
Brittany Griffiths, Hydrologic Technician
Joseph Hatfield, Hydrologic Technician
Mark Inc, Hydrologic Technician
Ryan Johnson, Hydrologic Technician
Tara Morgan-King, Hydrologist
Catherine Ruhl, Supervisory Hydrologist
Norman Soeder, Hydrologic Technician
Paul Stumpner, Hydrologist
Norbert Vanden Branden, Hydrologic Technician
Trevor Violette, Hydrologic Technician

ICFESA Joint Venture

Julie Nichols, Senior Technical Editor
Kristine Olsen, Senior Publications Specialist

TABLE OF CONTENTS

2021–2022 Comprehensive Emergency Drought Barrier Effectiveness Report

Page

Figures

Page

Page

Page

Page

Page

Page

Page

Page

Page

Page

Page

Tables

Page

Appendices

ACRONYMS AND OTHER ABBREVIATIONS

Abbreviation	Definition
°C	degrees Celsius
δP	source water isotopes
δR	rainwater isotopes
µg/L	micrograms per liter
µm	micron(s)
µM	micromole(s)
µS/cm	microsiemens per centimeter
ρ_p	plate reflectance
ρ_s	non-dimensional surface reflectance
2D	two-dimensional
3D	three-dimensional
2021–2022 EDB	2021–2022 West False River Emergency Drought Salinity Barrier
ADCP	acoustic Doppler current profiler
AIC	Akaike information criterion
BAC	Bacon Island station
barrier	2021–2022 West False River Emergency Drought Salinity Barrier
Bay-Delta	San Francisco Bay/Sacramento–San Joaquin Delta
BET	Bethel Island at Piper Slough station
BLP	San Joaquin River at Blind Point station
CART	Constituent oriented Age and Residence Time
CCH41	Cache Slough above Ryer Island Ferry near Rio Vista station
CDE	continuous detection event
CDFW	California Department of Fish and Wildlife
CEQA	California Environmental Quality Act
cfs	cubic feet per second
chl *a*	chlorophyll *a*
cfs	cubic feet per second
CI	Cyanobacterial Index
CVP	Central Valley Project
CyAN	Cyanobacterial Assessment Network
cyanoHAB	cyanobacterial harmful algal bloom
D4	Sacramento River above Point Sacramento station
D11A	Sacramento River near Sherman Island station
D16	San Joaquin River at Twitchell Island station

Abbreviation	Definition
D19	Franks Tract near Russo's Landing station
D22	Sacramento River at Emmaton station
D26	San Joaquin River at Potato Point station
DCC	Delta Cross Channel
Delta	Sacramento–San Joaquin Delta
DIN	dissolved inorganic nitrogen
DIN:DIP	ratio of dissolved inorganic nitrogen to dissolved inorganic phosphorus
DIP	dissolved inorganic phosphorus
DO	dissolved oxygen
DOC	dissolved organic carbon
DSJ	Dutch Slough at Jersey Island station
DWR	California Department of Water Resources
E:I	ratio of evaporation to inflow
EC	electrical conductivity
EDB	emergency drought barrier
EDBPS	Emergency Drought Barrier Predation Study
EMP	Environmental Monitoring Program
EPA	U.S. Environmental Protection Agency
ETM	Estuarine Turbidity Maximum
Et_O	evapotranspiration
FAL	False River near Oakley station
fCHL	chlorophyll fluorescence
FCT	Fisherman's Cut station
fDOM	fluorescent dissolved organic matter
FNU	formazin nephelometric units
FRK	Franks Tract Mid Tract station
ft/s	feet per second
GPS	Global Positioning System
H:V	ratio of horizontal units to vertical units
HAB	harmful algal bloom
HLL	Holland Cut station
HLT	Middle River near Holt station
HOL	Holland Cut near Bethel Island station
HOOD	Sacramento River at Hood station
IDW	inverse distance weighting
IMU	Inertial Measurement Unit
JER	San Joaquin River at Jersey Point station
JSATS	Juvenile Salmonid Acoustic Telemetry System
Kt	kilotons

Abbreviation	Definition
LE ratio	Lagrangian/Eulerian ratio
LIB	Cache Slough at South Liberty Island near Rio Vista station
LS1	Delta Rmp Yolo-003 station
m/s	meters per second
m^2	square meter(s)
m^3	cubic meters
MB-ADCP	moving boat acoustic Doppler current profiler
MBP	maximum blanking period
MDM	Middle River at Middle River station
MERIS	Medium Resolution Imaging Spectrometer
mg-C/L	milligrams carbon per liter
mg-N/L	milligrams nitrogen per liter
mg-P/L	milligrams phosphorus per liter
mg/L	milligrams per liter
mL	milliliter(s)
mm	millimeter(s)
MS1	Miner Slough at Holland Road near Paintersville station
MS2	Miner Slough at Highway 84 near Walker Landing station
NASA	National Aeronautics and Space Administration
NAVD88	North American Vertical Datum of 1988
NCCOS	National Center for Coastal Observing Science (National Oceanic and Atmospheric Administration)
NH_4	ammonium
nm	nanometer(s)
NO_3	nitrate
$NO_3 + NO_2$	nitrate and nitrite
NTU	nephelometric turbidity units
NZ068	Sacramento River near Rio Vista station
OBI	Old River at Bacon Island station
OH4	Old River at Highway 4 station
OLCI	Ocean Land Color Instrument
ORQ	Old River at Quimby Island station
OSJ	Old River at Franks Tract near Terminous station
PER	predation-event recorder
PERMANOVA	permutational multivariate analysis of variance
PO_4	soluble reactive phosphorus
QA/QC	quality assurance/quality control
Rho_s	non-dimensional surface reflectance
R_{rs}	remote sensing reflectance
RSIL	Reston Stable Isotope Laboratory (U.S. Geological Survey)

Abbreviation	Definition
RVB	Sacramento River at Rio Vista Bridge station
SAL	Mokelumne River at San Andreas
SAV	submerged aquatic vegetation
SCHISM	Semi-implicit Cross-Scale Hydroscience Integrated System Model
SJJ	San Joaquin River at Jersey Point station
SL-ADCP	side-looking acoustic Doppler current profiler
SR&D	Sacramento River and distributaries
SRP	soluble reactive phosphorus
SS	Liberty Island at Upper Stair Step near Five Points station
SSB	Shag Slough at Liberty Island near Courtland station
SSI	Sacramento River near Sherman Island station
State Water Board	State Water Resources Control Board
SUNA	Submersible Underwater Nitrate Analyzer
SVC	Spectra Vista Corporation
SWP	State Water Project
SXS	Steamboat Slough near Isleton station
TDN	total dissolved nitrogen
Timberline	Timberline Instruments
TIV	Time in Vicinity at the visit scale
TN	total nitrogen
TN:TP	ratio of total nitrogen to total phosphorus
TP	total phosphorus
TPCN	total particulate carbon and nitrogen
TSL	Threemile Slough at San Joaquin River station
TSS	total suspended solids
TTIV	Total Time in Vicinity at the individual scale
TWI	San Joaquin River at Twitchell Island station
USGS	U.S. Geological Survey
V-ADCP	vertical acoustic Doppler current profiler
VCU	Victoria Canal near Byron station
VMT	Velocity Mapping Toolbox
WGA	Sacramento River above Delta Cross Channel station
WGC	Sacramento River Mile 28 near Walnut Grove station
WY	Water Year
YSI	Yellow Springs Instruments

CHAPTER 1
Construction and Compliance

1.1 Introduction and Purpose

This report summarizes the construction, monitoring, effectiveness, and impacts of the 2021–2022 West False River Emergency Drought Salinity Barrier (2021–2022 EDB). The purpose of this report is to meet the reporting requirements in the State Water Resources Control Board's (State Water Board) May 2021 Water Quality Certification (Section 8.0, Condition 1: Monitoring, Analysis, and Reporting) and the commitment detailed in the California Department of Water Resources' (DWR) Monitoring Plan (updated in January 2022).

In spring 2021, DWR requested emergency authorization to install the 2021–2022 EDB in accordance with Governor Gavin Newsom's emergency proclamations issued on April 21 and May 10, 2021 (Newsom 2021). To manage the critically low 2021 water supply for beneficial uses, DWR installed the temporary emergency drought barrier (EDB) on West False River in the Sacramento–San Joaquin Delta (Delta), approximately 5 miles south of Rio Vista in Contra Costa County, California. The 2021–2022 EDB was installed in the same location where DWR had installed a drought salinity barrier in 2015 (California Department of Water Resources 2019). The installation proceeded in compliance with all regulatory permits and authorizations as expeditiously as possible after the May 10, 2021, Governor's drought proclamation, and was completed in June 2021.

The factors used to evaluate the need for the EDB included forecasted drought conditions in multiple consecutive years, low levels of reservoir water storage, the high risk of exceeding water quality objectives, and the results of drought modeling and monitoring. The West False River location was selected based on the results of hydrodynamic modeling of salinity patterns in the Delta. This location optimizes salinity management through the installation of a single barrier, and the 2015 drought salinity barrier proved to be effective in the complex Delta channel system (California Department of Water Resources 2019; Kimmerer et al. 2019).

Construction of a temporary drought salinity barrier in West False River was needed in response to the drought condition that California was experiencing. The 2021–2022 EDB was a temporary physical rock fill barrier

that reduced the intrusion of high-salinity water into the Central Delta. The 2021–2022 EDB was very similar in terms of location, size, and design to the drought salinity barrier that was permitted and installed in May 2015 and removed in October 2015. However, the 2021–2022 EDB was kept in place through November 2022 instead of being removed in fall 2021, the same year in which it was installed.

1.2 Hydrologic Background

1.2.1 Hydrologic Conditions

Water Year (WY) 2020 (October 1, 2019, through September 30, 2020) was mostly dry in Northern California, while parts of Southern California experienced above-average precipitation. Overall, the water year ended with a Sacramento Valley Water Year Hydrologic Classification Index of "Dry" (California Data Exchange Center 2021), and precipitation in the state as a whole was below average.

WY 2020 was characterized by a lack of precipitation that resulted in a snowpack of just 50 percent of average on April 1, 2020. California's major reservoirs received about one-third as much water runoff from precipitation and snowmelt as during the same period in the previous year. DWR's eight-station precipitation index, which tracks conditions in the Sacramento River Basin, ended the year at 62 percent of average. The five-station San Joaquin precipitation index and six-station Tulare Basin index wrapped up the year at 62 percent and 65 percent of average, respectively (California Department of Water Resources 2020).

California experienced a second consecutive drought year in WY 2021 (October 1, 2020, through September 30, 2021). Reduced runoff from rain and snowpack led to further reductions in reservoir storage. On April 21, 2021, Governor Newsom proclaimed a state of emergency in select counties because of drought conditions and directed State agencies to take immediate action to bolster drought resilience. On May 10, 2021, Governor Newsom extended the state of emergency to include 41 counties in the Klamath River, Delta, and Tulare Lake watersheds because warm temperatures and extremely dry soils resulted in a historic depletion of runoff from the Sierra Nevada snowpack (Newsom 2021).

Drought conditions continued to worsen after the May 10 drought proclamation. For example, Lake Oroville and Shasta Lake, the principal reservoirs for the State Water Project (SWP) and Central Valley Project (CVP), respectively, were at 41 percent and 48 percent of storage capacity as of May 10. By September 30, 2021, the end of the water year, storage capacity in Lake Oroville and Shasta Lake had decreased to 22 percent and 24 percent, respectively, with Lake Oroville reaching its lowest storage ever since its

initial filling. Storage levels at California's major reservoirs remained well below average at the end of WY 2021 (**Figure 1.2.1-1**), which was recorded as the second driest year on record, following the fifth driest year in WY 2020.

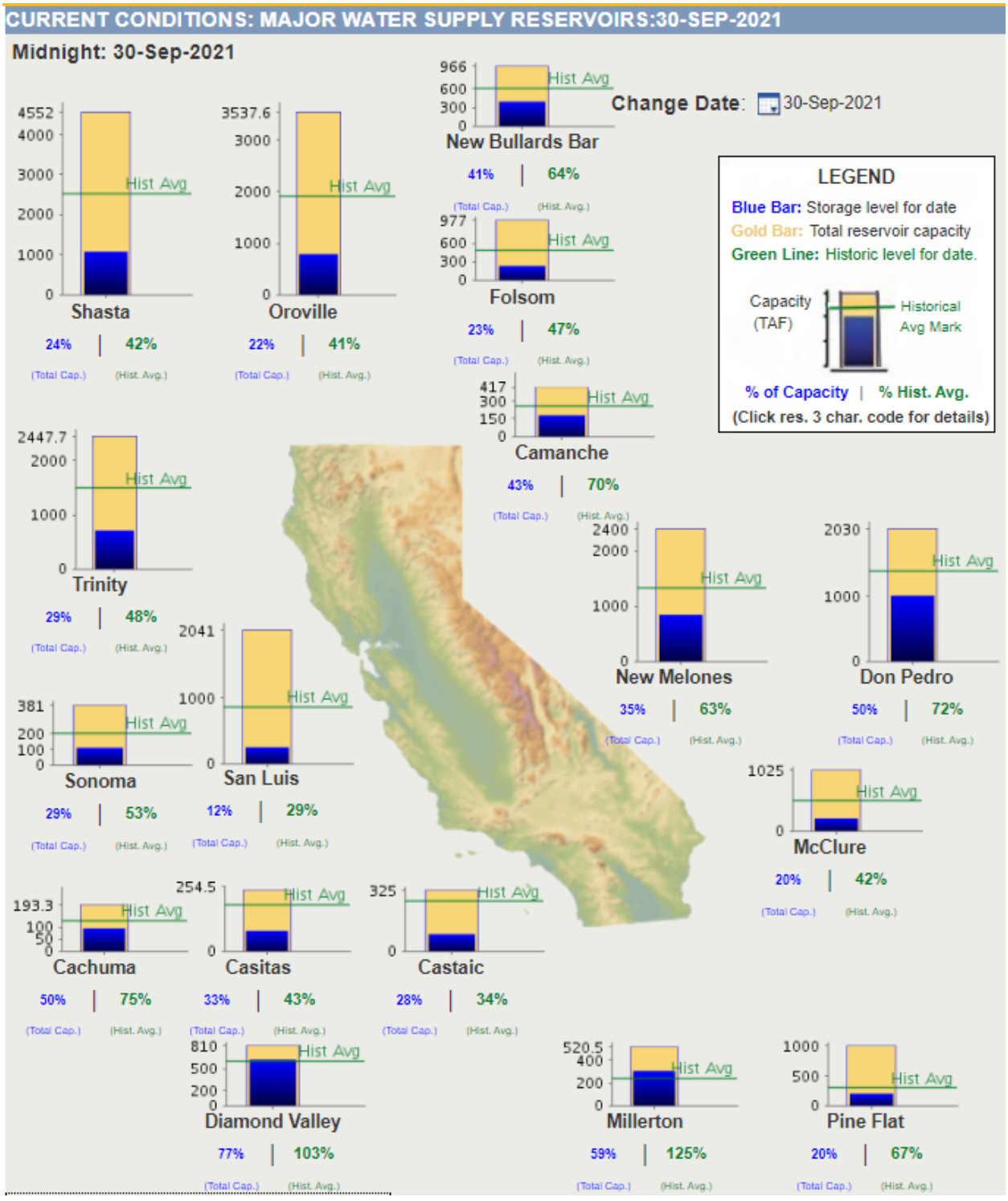

Figure 1.2.1-1 Conditions at major California reservoirs, September 20, 2021.

WY 2022 (October 1, 2021, to September 30, 2022) was a third dry year as the drought continued. To that effect, on October 5, 2021, the Governor's state of emergency expanded prior drought emergency proclamations to cover all 58 California counties. The water year was characterized by extreme swings between record-breaking storms and dry conditions driven by climate change. For example, in October 2021, parts of Northern California experienced the highest single-day rain totals ever, which were followed by a dry November and then a record snowfall in parts of the Sierra Nevada in December. Conditions took a turn again in early 2022, with the driest January, February, and March in more than 100 years. WY 2022 ended with statewide precipitation at 76 percent of average. Statewide reservoir storage was 69 percent of average for the end of September (**Figure 1.2.2-1**).

Overall, the drought from 2020 to 2022 was California's driest three-year period on record, breaking the old record set by the 2013–2015 drought.

1.2.2 Goals and Objectives of the Barrier

The Delta is influenced by tides from San Francisco Bay, with flood tides pushing ocean water upstream. However, if saltwater were to intrude too far inland and enter the Central Delta, freshwater supplies would be compromised. Intrusion of saltwater into the Central Delta would affect Delta agriculture, local municipal supplies, and the natural environment. It also would threaten California's primary water delivery system, which supplies water to 27 million Californians and supports the world's fifth largest economy.

Generally, the SWP and CVP manage Delta outflow to keep saltwater out of the Central Delta. However, during severe droughts, storage in upstream reservoirs may be depleted and natural inflows may be insufficient to prevent ocean water from moving upstream through the Delta. This scenario presents a difficult water management challenge, requiring certain measures like installation of the EDB at West False River to minimize saltwater intrusion.

The EDB is a physical obstacle constructed to accomplish the following goals:

- Help prevent saltwater intrusion and protect the beneficial uses of Central Delta water during persistent drought conditions.
- Protect water quality and prevent contamination of water supplies for Delta agriculture and municipal supplies.
- Reduce the amount of water released from reservoirs upstream to keep ocean water out of the Central Delta.

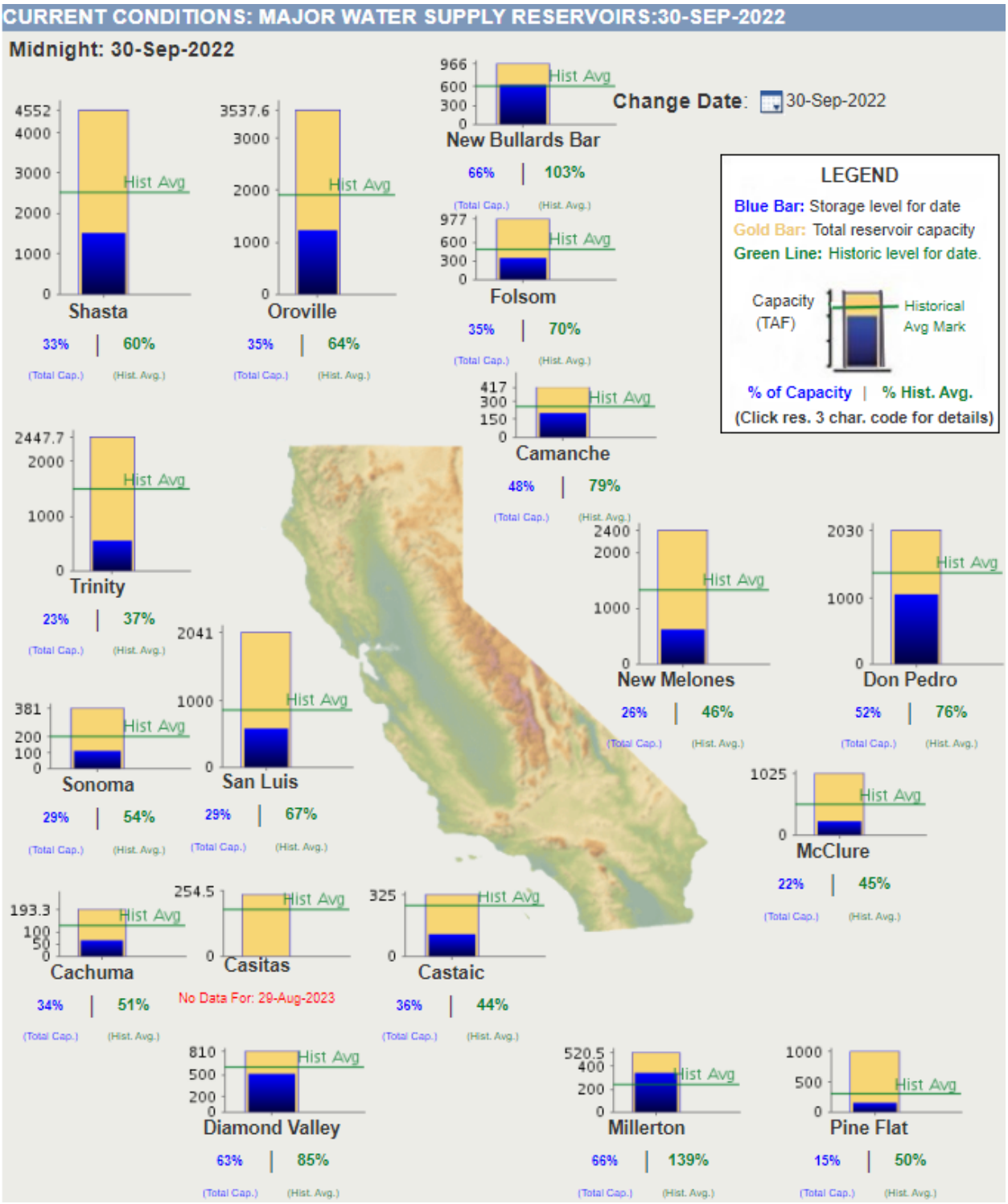

Figure 1.2.2-1 Conditions at major California reservoirs, September 30, 2022.

1.2.3 Barrier Design

The temporary EDB was constructed across West False River in the Delta in June 2021. The approximately 800-foot-long temporary barrier consisted of nearly 110,000 tons of 24-inch-minus riprap rock. The base of the barrier was roughly 200 feet wide along the bottom of the channel and 12 feet wide along its crest. The barrier sloped down to the riverbed from its crest at a rate of 2 horizontal units to 1 vertical unit (2H:1V). **Figure 1.2.3-1** shows a typical cross-section through the EDB.

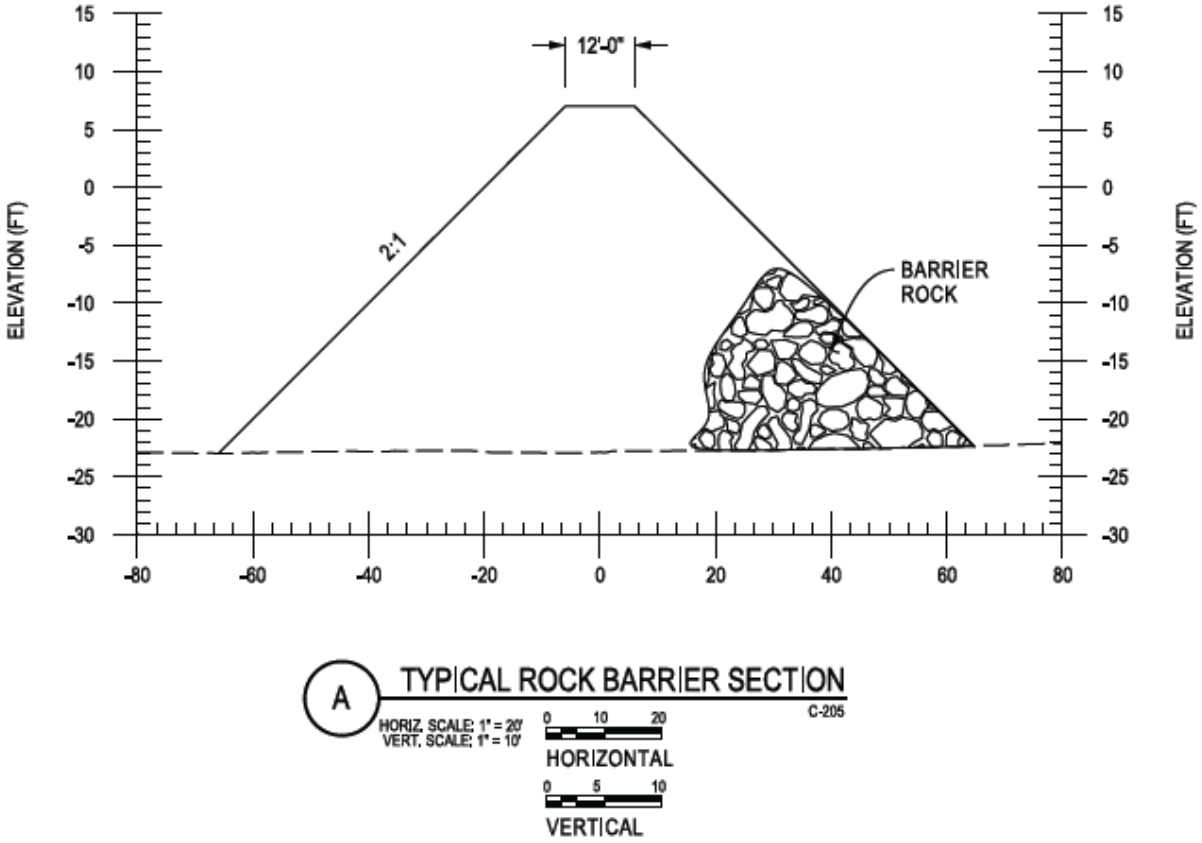

Figure 1.2.3-1 Typical drought barrier cross-section.

Additionally, DWR constructed a temporary 442-foot-wide, 19-foot-deep notch in the center of the barrier from January 2022 to March 2022. The notch was sloped at a rate of 3H:1V to an invert elevation of -12 feet North American Vertical Datum of 1988 (NAVD88) to facilitate fish and boat passage (**Figure 1.2.3-2**).

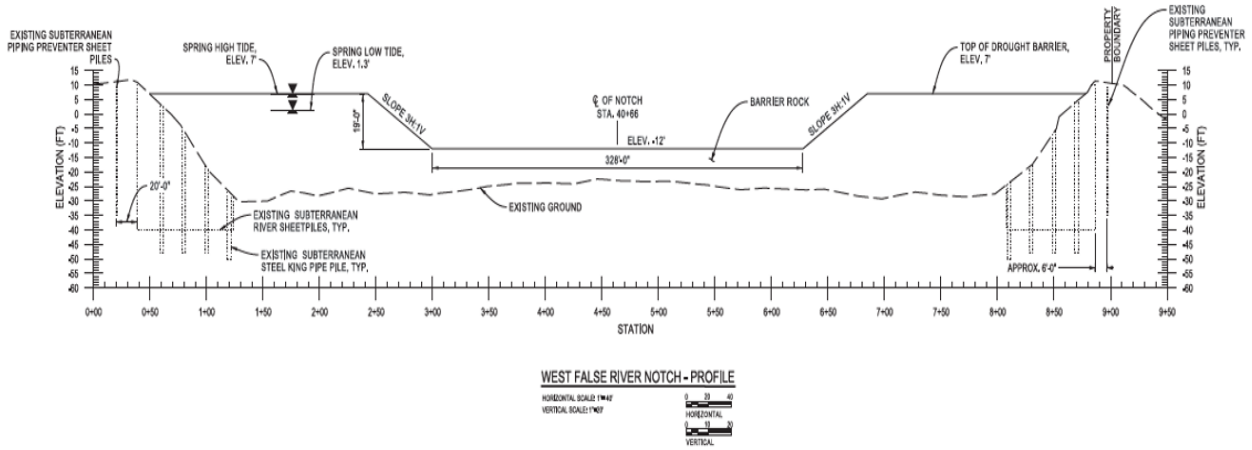

Figure 1.2.3-2 West False River drought salinity barrier notch—profile view.

1.3 Construction Summary

The EDB was built mostly by excavators mounted on a barge. Construction began on the Jersey Island embankment of False River, then transitioned to the Bradford Island embankment to hydraulically close the barrier at the middle. Approximately 110,000 tons of 24-inch-minus riprap rock were placed in a trapezoidal configuration perpendicular to the West False River channel. EDB construction started on June 3, 2021; working 24 hours per day, contractors achieved hydraulic closure of the barrier on June 18 and completed the barrier on June 24, 2021 (**Table 1.3-1**). **Figure 1.3-1** shows the progression of rock placement for installation of the temporary EDB in West False River.

TABLE 1.3-1
CONSTRUCTION MILESTONES FOR THE TEMPORARY EMERGENCY DROUGHT BARRIER

Date	Action
June 3, 2021	In-water construction initiated.
June 18, 2021	Barrier hydraulically closed.
June 24, 2021	In-water construction completed.
January 4, 2022	Notch construction initiated.
January 7, 2022	Barrier hydraulically breached.
January 18, 2022	Notch construction completed.
April 1, 2022	Notch filling initiated.
April 13, 2022	Barrier hydraulically closed.
October 15, 2022	Barrier removal initiated.
November 1, 2022	Barrier hydraulically breached.
November 23, 2022	In-water barrier removal work completed.

SOURCE: Data compiled by California Department of Water Resources in 2023

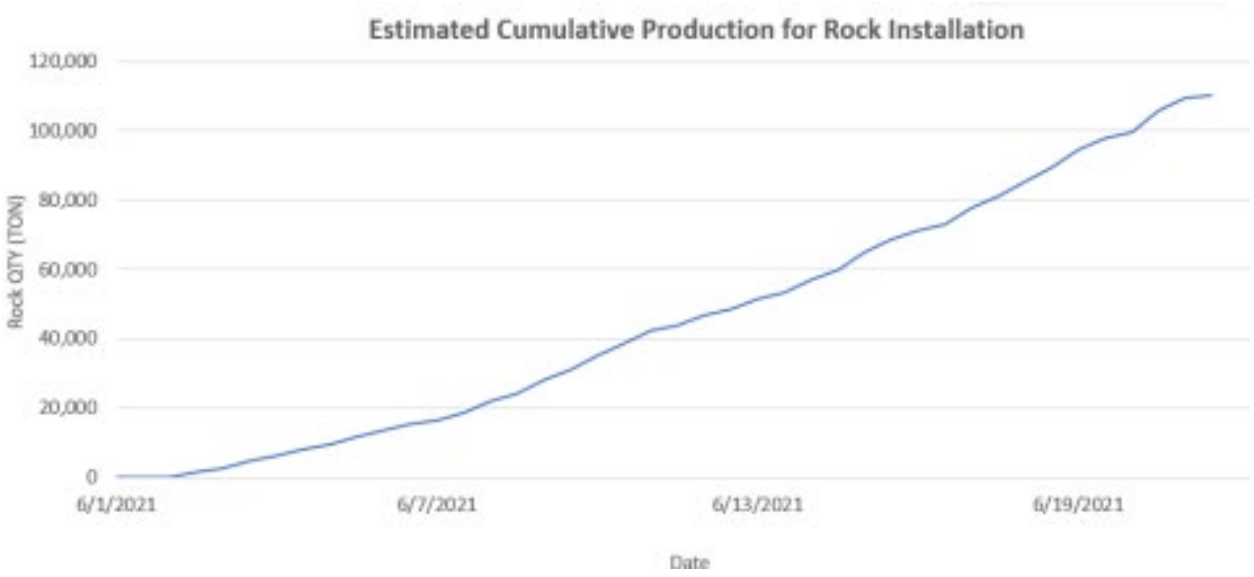

Figure 1.3-1 Emergency drought barrier—estimated cumulative production for rock installation.

The existing barrier design remained in place until January 4, 2022, when the contractor began removing embankment rock from the center of the barrier, creating a notch to allow fish and boat passage. This partial removal of the barrier was completed on January 18, 2022, with the hydraulic breach achieved on January 7. DWR hydraulically re-closed the barrier on April 13, restoring the barrier to its original design. The barrier continued to provide salinity protection until the barrier was hydraulically breached on November 1, 2022 (**Figure 1.3-1**). Full barrier removal was completed on November 23, 2022.

1.3.1 Biological Monitoring during Construction

Approved biologists conducted biological monitoring at the 2021–2022 EDB site and the Weber Rock Yard for all construction activities that had the potential to adversely affect special-status species. Construction activities were conducted at four discrete times: during barrier construction, barrier notching, barrier notch filling, and barrier removal. Monitoring during each of these activities is summarized below.

Figure 1.3-1 Removal of the temporary emergency drought barrier in West False River.

1.3.1.1 2021 Barrier Construction

For 2021 barrier construction at the 2021–2022 EDB site, biological monitoring of preconstruction activities and equipment staging began on May 29, 2021. Barrier construction began on June 2, with monitors initially scheduled for 24 hours per day, split into two 12-hour shifts. On June 19, after rock placement on the Bradford Island and Jersey Island levees was complete, monitoring shifts were adjusted to cover the hours from sunrise to sunset, with the day shift present from 6 a.m. until 2 p.m. and the evening shift from 2 p.m. until 9 p.m. Monitors generally walked the entire site, inspecting the giant garter snake (*Thamnophis gigas*) exclusion fence for damage. They ensured that vehicles and equipment were located within designated staging areas and that workers were complying with all avoidance and mitigation measures, and then monitored activities throughout the remainder of their shifts.

An approved biologist conducted weekly surveys for Swainson's hawk (*Buteo swainsoni*) on June 10, 13, and 22, 2021, using binoculars and a spotting

scope to scan trees and the surrounding areas from both the Jersey Island and Bradford Island levees. During the surveys, Swainson's hawks and other raptor species were observed foraging, and landing in several trees, but no nests were identified. The birds observed did not show any signs of disturbance during the surveys or during other sightings throughout the barrier installation period.

Though not required by permit conditions, biological monitoring was also conducted at the Weber Rock Yard to ensure that no take of protected species would occur. Biological monitoring at the Weber Rock Yard began on May 28, 2021. Monitors remained on site during all work conducted, which included staging of equipment and installation of an exclusion fence along the waterside. On June 1, rock loading onto barges began and monitors were scheduled for 24 hours per day, split into two 12-hour shifts.

On June 4, 2021, after three days of continuous monitoring during active rock loading, the lead biologists determined that overnight monitoring was no longer warranted at the Weber Rock Yard, given the nature of the work and the lack of sensitive-species encounters in the exclusion area. As a result, monitoring was reduced to 8 a.m. to 5 p.m. daily. Monitors walked the giant garter snake exclusion fence and inspected it for damage at the beginning of each shift; they then remained on site, monitoring activities during the remainder of the shift. Daily monitoring continued until work at the Weber Rock Yard concluded on June 23, 2021.

During the 2021 barrier construction period, no sensitive species were encountered or found to be adversely affected in the action area.

1.3.1.2 2022 Barrier Notching

For 2022 barrier notching at the 2021–2022 EDB site, biological monitoring of pre-work activities and staging began on January 4, 2022. Beginning on January 5, monitors were scheduled for 12-hour shifts that covered roughly the hours from sunrise to sunset. Monitoring continued until January 19, 2022. Monitors would generally walk the entire site, inspecting the giant garter snake exclusion fence for damage. They ensured that all vehicles and equipment were located within designated staging areas and that construction work was complying with all avoidance and mitigation measures, and then monitored activities throughout the remainder of their shifts. Monitors were able to travel between Bradford Island and Jersey Island on a small boat as needed to ensure that all activities with the potential to adversely affect special-status species could be monitored, and that areas to be affected could be cleared before the start of work.

During the 2022 barrier notching period, no sensitive species were encountered or found to be adversely affected in the action area.

1.3.1.3 2022 Barrier Notch Filling

For 2022 barrier notch filling at the 2021–2022 EDB site, biological monitoring of pre-work activities and staging began on the afternoon of March 30, 2022, and continued until April 15. Beginning on March 31, monitors were scheduled for 12-hour shifts that covered roughly the hours from sunrise to sunset. Monitors would generally walk the entire site, inspecting the giant garter snake exclusion fence for damage. They ensured that vehicles and equipment were located within designated staging areas and that construction work was complying with all avoidance and mitigation measures, and then monitored all activities throughout the remainder of their shifts. Monitors were able to travel between Bradford Island and Jersey Island on a small boat as needed to ensure that all activities with the potential to adversely affect special-status species could be monitored, and that areas to be affected could be cleared before the start of work.

A red-tailed hawk nest was identified during the weekly monitoring before the onset of construction activities and was confirmed during the preconstruction surveys. During the daily construction monitoring, the nest was monitored for evidence of disturbance and was found to be not adversely affected. During the 2022 barrier notch filling period, no other sensitive species were encountered or found to be adversely affected within the action area.

1.3.1.4 2022 Barrier Removal

For 2022 barrier removal at the 2021–2022 EDB site, biological monitoring began on the afternoon of October 13, 2022, and continued until November 28. Beginning on October 15, monitors were scheduled for 12-hour shifts that covered roughly the hours from sunrise to sunset. Monitors would generally walk the entire site, inspecting the giant garter snake exclusion fence for damage. They ensured that vehicles and equipment were located within designated staging areas and that construction work was complying with all avoidance and mitigation measures, and then monitored activities throughout the remainder of their shifts. Monitors traveled between Bradford Island and Jersey Island on a small boat as needed to ensure that all activities with the potential to adversely affect special-status species could be monitored, and that affected areas could be cleared before the start of work.

At 1 p.m. on November 28, 2022, a single basking giant garter snake was encountered on the downslope portion of the land side of the levee, outside of the exclusion fence, as crews prepared to remove the fencing during demobilization. The monitor immediately reported the encounter to the designated biologist via cell phone. Fence removal was halted until the snake was no longer in the vicinity. The snake was not handled or harassed and was allowed to leave the area of its own volition. The snake was monitored

for approximately 35 minutes, at which time it moved down the land side of the levee slope and entered a burrow located beneath vegetation. The burrow was marked with flagging and monitored while the crew removed the exclusion fence to ensure that the snake would not emerge during the activity. Once all demobilization activities were completed, the flagging was removed. The snake's basking location and burrow were recorded using a Global Positioning System, ground and air temperatures were measured, and the approximate length of the snake was estimated. Appropriate agency notifications were made on November 28, 2022, and a California Natural Diversity Database submission was filed on December 1, 2022.

During the 2022 barrier removal period, no other sensitive species were encountered or found to be adversely affected within the action area.

1.3.2 Environmental Compliance

Construction of the 2021–2022 EDB began on June 3, 2021, after the required permit authorizations had been received from the U.S. Army Corps of Engineers (Regional General Permit 8 SPK-2014-00187 for Section 10 of the Rivers and Harbors Act of 1899 and Section 404 of the Clean Water Act), the State Water Board (Section 401 of the Clean Water Act Individual Water Quality Certification for Federal Permit or License), and CDFW (Final Lake and Streambed Alteration Agreement EPIMS-CCA-19852-R3 and Incidental Take Permit 2081-2021-041-03). The barrier was hydraulically closed on June 18, 2021.

In advance of the barrier removal planned to occur November 30, 2021, DWR requested and received authorization to leave the barrier in place until November 30, 2022, with notching and notch re-closure taking place in January and April 2022, respectively. These approvals included a reauthorization under U.S. Army Corps of Engineers Regional General Permit 8; a consistency clarification from the State Water Board stating that the previously issued water quality certification was valid to cover the requested activities and barrier duration; and amendments to the Lake and Streambed Alteration Agreement and Incidental Take Permit from CDFW.

Subsequently, barrier notch construction began on January 4, 2022, and was completed on January 18. Site mobilization began on March 30, with rock placement and notch refilling efforts commencing the following day. The barrier was hydraulically closed on April 13, 2022, and in-water work was completed on April 15, with demobilization from the site on April 19. The permit conditions required that the barrier be completely removed from West False River by November 30, 2022. Accordingly, preparation for barrier removal activities was initiated on October 13, 2022; barrier removal began on October 15 and was completed on November 23. Site demobilization was completed on November 28, 2022.

All barrier construction activities and subsequent monitoring were completed in accordance with the authorizations identified above.

1.3.3 Turbidity Monitoring during Construction

During planned in-water work, dewatering activities, or the installation or removal of the temporary water diversion, any discharge(s) to waters of the State were required to conform to the water quality standards, sample collection protocols, and data management requirements listed below.

In-Water Work

a. Samples of turbidity and settleable solids will be taken, at a minimum, every three hours during in-water work (approximately 9 a.m., 12 noon, and 3 p.m.). Samples shall be taken from shore or boat 300 feet upstream and downstream of construction activities. 2100Q (turbidity) and Imhoff cone testing (settleable solids) equivalent equipment or better shall be used as the data collection tools.

b. Waters shall not contain oils, greases, waxes, or other materials in concentrations that cause a nuisance, result in a visible film or coating on the surface of the water, or otherwise adversely affect beneficial use.

Reporting Limits for Dissolved Oxygen, Turbidity, and Other Pollutants

a. Activities shall not cause settleable solids in surface water to exceed the following limits:

    i. Where natural turbidity is less than 1 nephelometric turbidity unit (NTU), controllable factors shall not cause downstream turbidity to exceed 2 NTU.

    ii. Where natural turbidity is between 1 and 5 NTU, increases shall not exceed 1 NTU.

    iii. Where natural turbidity is between 5 and 50 NTU, increases shall not exceed 20 percent.

    iv. Where natural turbidity is between 50 and 100 NTU, increases shall not exceed 10 NTU.

    v. Where natural turbidity is greater than 100 NTU, increases shall not exceed 10 percent.

In determining compliance with the above limits, appropriate averaging periods may be applied, provided that beneficial uses will be fully protected. Averaging periods may be used only with prior permission of the Central Valley Water Board's Executive Officer.

For Delta waters, the general objectives for turbidity apply subject to the following: Except for periods of stormwater runoff, the turbidity of Central Delta waters shall not exceed 50 NTU and 150 NTU in other Delta waters.

b. Activity shall not cause settleable solids to be more than 0.1 milliliter per liter.

Protocols for Sample Collection

Sampling during in-water work or throughout temporary water diversions shall be conducted on site, in person, in accordance with the sampling parameters shown in **Table 1.3.3-1**. The sampling identified in Table 1.3.3-1 shall be conducted upstream out of the influence of the project and approximately 300 feet downstream and downstream of the work area. Sampling shall be conducted when staff is present at the work area during construction activities for the installation or removal of the temporary barrier.

TABLE 1.3.3-1
SAMPLE TYPE AND FREQUENCY REQUIREMENTS DURING BARRIER INSTALLATION AND REMOVAL

Parameter	Unit of Measurement	Type of Sample	Minimum Frequency
Turbidity	NTU	Grab	Every 3 hours
Settleable solids	mL/L	Grab	Every 3 hours
Visible construction-related pollutants	Observations	Visual inspections	Continuous throughout the construction period

NOTES: mL/L = milliliters per liter; NTU = nephelometric turbidity units

SOURCE: Data compiled by California Department of Water Resources in 2023

Discrete samples will be collected and tested on site with the Hach 2100Q portable turbidimeter and Yellow Springs Instruments (YSI) PRO DSS water quality sonde. Data will be collected and recorded. Sampling data collection will be monitored to assure that the data are within the allowed reporting limits as listed under "Reporting Limits for Dissolved Oxygen, Turbidity, and Other Pollutants."

If no sampling is required, the Permittee shall submit a written statement stating "No sampling required" within two weeks of the initiation of in-water construction, and every two weeks thereafter.

Data Management

All equipment will be calibrated to required specifications before deployment. Final data that have completed the quality assurance/quality control (QA/QC) process shall be submitted within two weeks upon completion of in-water construction. The data will be displayed in tabular form so that the sampling locations, date, constituents, and concentrations are discernable. Surface water sampling results, visual observations, and identification of the turbidity results can be found in **Appendix A**, "Monitoring Results for Turbidity and Settleable Solids."

1.3.4 Subsidence Monitoring

Subsidence monitoring was conducted by a contractor during installation of the temporary EDB in West False River. The Geomatics Branch of DWR's Division of Engineering received a survey monitoring report for this construction project from the contractor, which collected survey monitor measurement data throughout barrier construction. No subsidence was noted in this report. A copy of the contractor's subsidence monitoring report is included in **Appendix B**.

This page intentionally left blank

CHAPTER 2
Effectiveness and Impacts

2.1 Goals and Objectives of Effectiveness Monitoring

2.1.1 Goal 1: Reduce Salinity Entering the Central Delta

The major goal of the 2021–2022 EDB was to protect water quality in the Central Delta while allowing reduced Delta outflow. Therefore, monitoring was conducted primarily for salinity, to assess the barrier's effectiveness in meeting the end goal of preserving water quality. Flow was also monitored to assess the function of the barrier in rerouting saline water away from the South Delta.

2.1.2 Goal 2: Prevent Negative Impacts on the Ecosystem and Other Beneficial Uses

DWR used the 2021–2022 EDB to preserve water quality for human use but was also committed to reducing negative impacts on other beneficial uses. In particular, the impact of the barrier on the following parameters was assessed:

- Bathymetry and channel bed elevation.
- Salinity, nutrients, and turbidity.
- Phytoplankton and zooplankton.
- Harmful algal blooms (HABs).
- Aquatic weeds.
- Fish community.
- Fish predation.
- Salvage of at-risk fishes.

Each of these metrics is described in detail below.

2.2 Effectiveness

2.2.1 Time Series Plots

Time series plots help to put the magnitudes in the salinity difference maps into perspective. **Figure 2.2.1-1** shows the difference in (tidally filtered) specific conductance between modeled scenarios with and without the EDB at several stations that often influence flow management: Bethel Island at Piper Slough, Old River at Bacon Island, and Clifton Court.

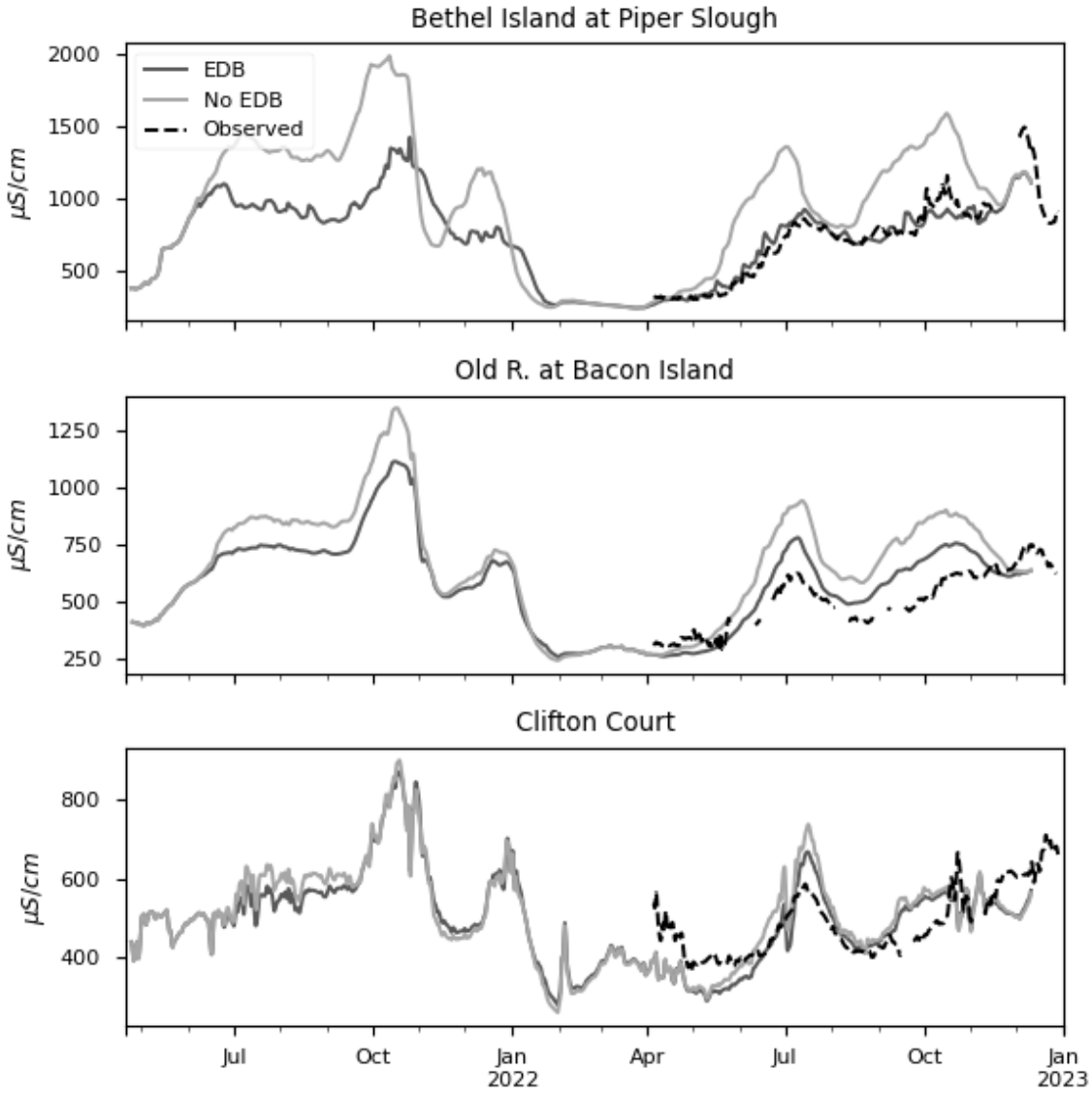

NOTES: µS/cm = microsiemens per centimeter; EDB = emergency drought barrier; OBS = observation

Figure 2.2.1-1 Salinity time series over calendar year 2021 at three stations on the salinity intrusion pathway.

As shown by the time series at Bethel Island at Piper Slough, the 2021–2022 EDB was very effective at preventing the migration of salinity from Jersey Point into Franks Tract. The Old River at Bacon Island time series shows smaller reductions, but the reductions there are still meaningful given the significance of this station as an indicator. Note that this station has more model bias than the others. The effect of the EDB at Clifton Court seems to be considerably smaller: Clifton Court is affected by other sources of salinity such as Middle River and the South Delta.

2.2.1.1 Modeled Conditions with and without the Barrier

To assess the effectiveness of the 2021–2022 EDB at reducing salinity intrusion, simulations were carried out using the San Francisco Bay/ Sacramento–San Joaquin Delta (Bay-Delta) SCHISM, a three-dimensional (3D) circulation model (Ateljevich et al. 2014). Bay-Delta SCHISM is an application of the Semi-implicit Cross-Scale Hydroscience Integrated System Model (Zhang and Baptista 2008; Zhang et al. 2016). The results shown here focus on the historical period of June 1, 2021–December 31, 2022.

To determine the effect of the barrier, salinity difference maps were generated comparing salinity from historical operations and geometry (the EDB case) to a hypothetical case with no drought barrier (the No EDB case). Field data were used for flow boundary conditions, the Delta Cross Channel (DCC) gates, the Net Delta Outflow Index, and exports through the end of the calendar year. **Figure 2.2.1-2** shows the summer and early-fall hydrology, **Figure 2.2.1-3** shows the hydrology for late fall 2021 through spring 2022 (Water Year [WY] 2022), and **Figure 2.2.1-4** shows May–December 2022 hydrology. Note that the scales of the plots differ.

Figure 2.2.1-5 through **Figure 2.2.1-7** are the salinity change maps, showing the EDB case minus the No EDB case for the first 14 days of each month in the study period, given units of specific conductance. Each month represents a different operational context, hydrology, or salinity management challenge. **Table 2.2.1-1** describes some of the salient details.

With the exception of the November 2021 map—map (d) in Figure 2.2.1-5—the model's change maps indicate water quality improvements attributable to the 2021–2022 EDB in Franks Tract and at locations on Old River immediately south of Franks Tract. The degree of improvement shown decreases upstream along Old River, caused in part by exchanges with Middle River and by additional salinity influences in the South Delta such as Old River and the Grant Line Canal. According to the model, salinity above San Andreas Landing on the San Joaquin River and in Middle River increased during all periods with the barrier in place. Under its current calibration, the model tends to overestimate salt in this region of the San Joaquin River, but a change in relative salinity is observed.

TABLE 2.2.1-1
SUMMARY OF OPERATIONAL CONDITIONS BY MONTH

Period	Notes
August 1–14, 2021	The Threemile Slough standard in State Water Resources Control Board D-1641 limits operations.
September 2021	Outflow is controlled; salinity is lower than in August.
October 1–14, 2021	Salinity/flow is controlled; seasonal peak salinity occurs. The Delta Cross Channel is toggled.
November 1–14, 2021	A large storm occurs; Jersey Point is fresh and the barrier limits freshening.
December 1–14, 2021	The salinity field revives between storms.
January–May 2022	The barrier is notched; salinity is controlled downstream.
June–August 15, 2022	Operated to D-1641 Ag requirements and no urgency change order was enforced after June 2022.
August 15–December 2022	Operated to Central Delta salinity requirements.

NOTES: D-1641 = Water Right Decision 1641; Delta = Sacramento–San Joaquin Delta

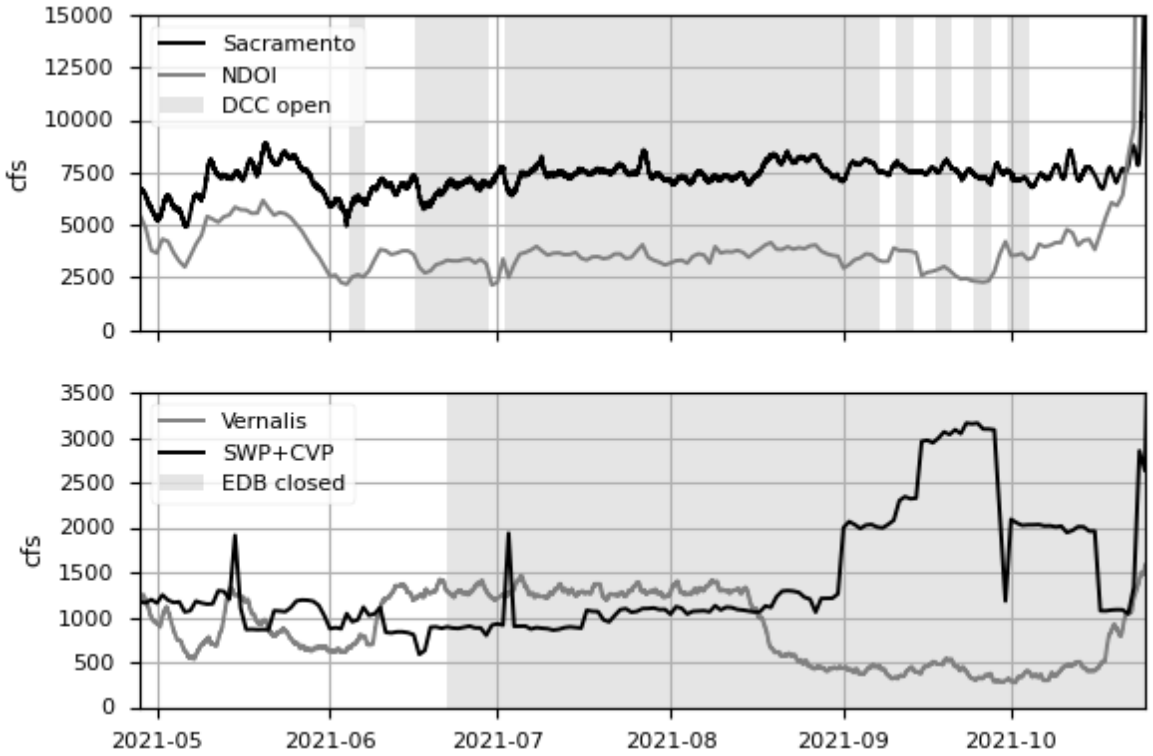

NOTES: cfs = cubic feet per second; CVP = Central Valley Project; DCC = Delta Cross Channel; EDB = emergency drought barrier; NDOI = Net Delta Outflow Index; SWP = State Water Project

Figure 2.2.1-2 Hydrologic and Delta Cross Channel conditions, summer and early fall 2021 (observed).

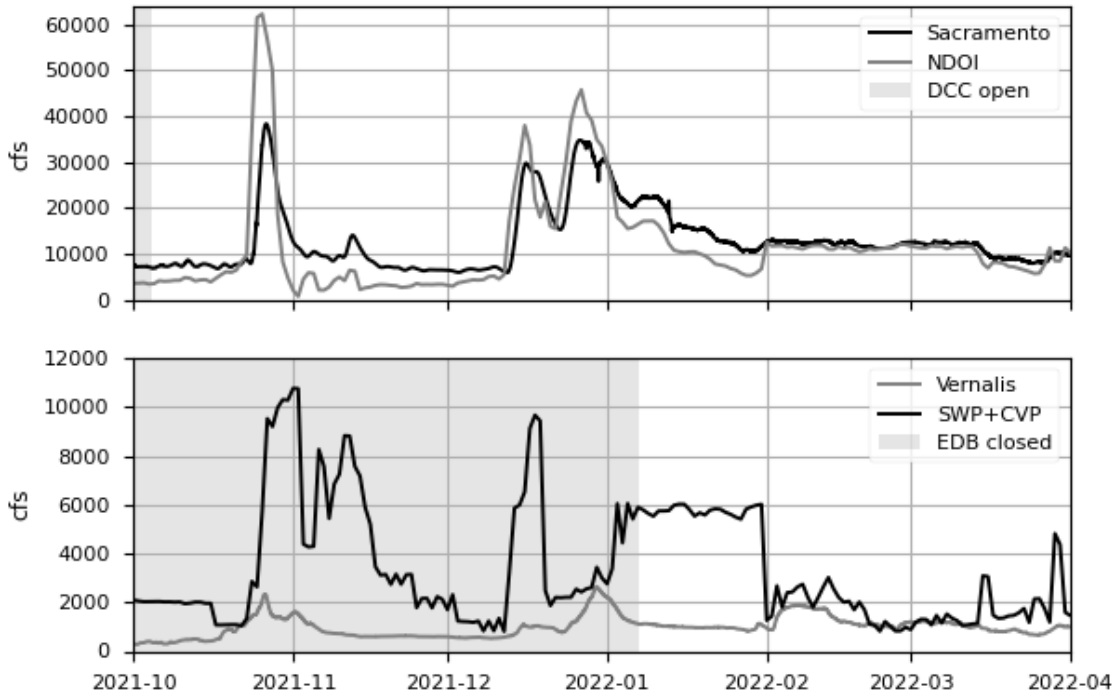

NOTES: cfs = cubic feet per second; CVP = Central Valley Project; DCC = Delta Cross Channel; EDB = emergency drought barrier; NDOI = Net Delta Outflow Index; SWP = State Water Project

Figure 2.2.1-3 Hydrologic and Delta Cross Channel conditions, October 2021 to April 2022 (observed).

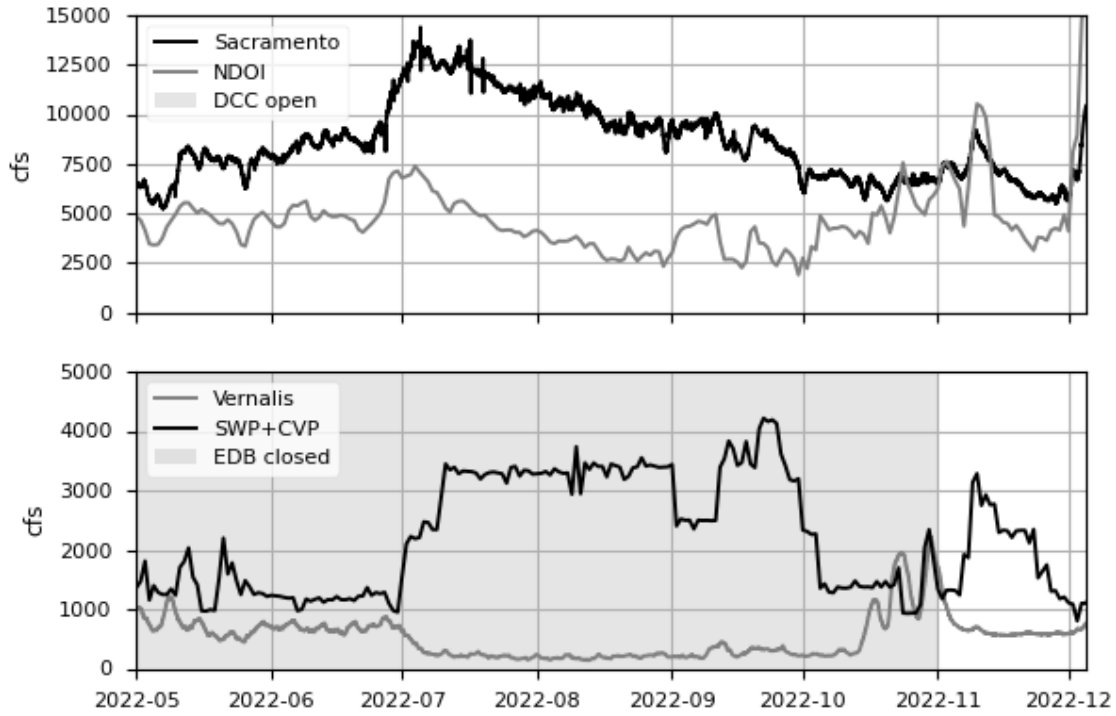

NOTES: cfs = cubic feet per second; CVP = Central Valley Project; DCC = Delta Cross Channel; EDB = emergency drought barrier; NDOI = Net Delta Outflow Index; SWP = State Water Project

Figure 2.2.1-4 Hydrologic and Delta Cross Channel conditions, May–December 2022 (observed).

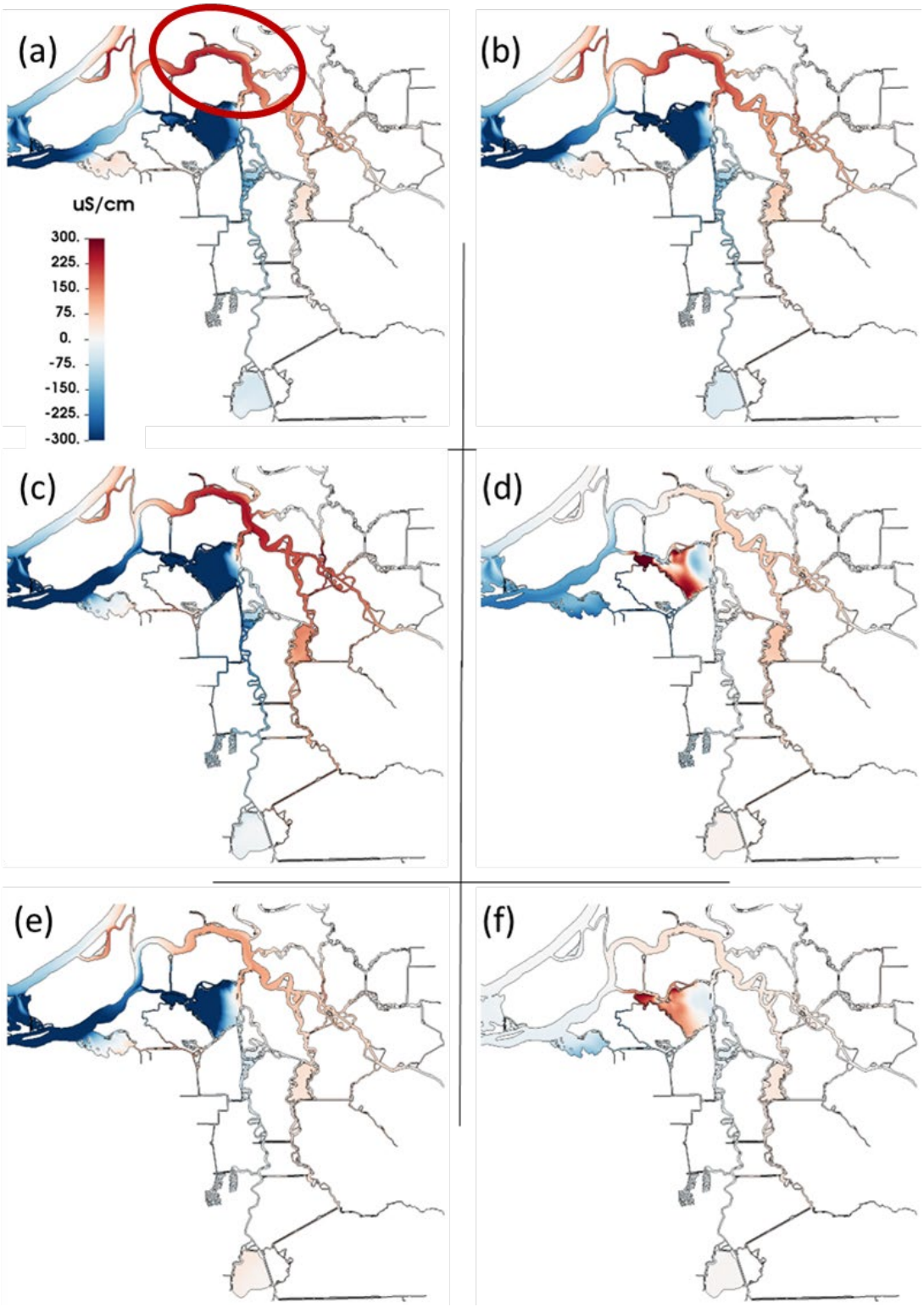

NOTES: (a) August 1–14, 2021; (b) September 1–14, 2021; (c) October 1–14, 2021; (d) November 1–15, 2021; (e) December 1–14, 2021; (f) January 1–14, 2022.
µs/cm = microsiemens per centimeter. Blue = regions where the emergency drought barrier reduced the salinity level. The circled region in map (a) includes the mouth of the Mokelumne River, where most Delta Cross Channel water enters the Central Delta.

Figure 2.2.1-5 Differences in salinity between scenarios with and without the emergency drought barrier, 2021 and January 2022.

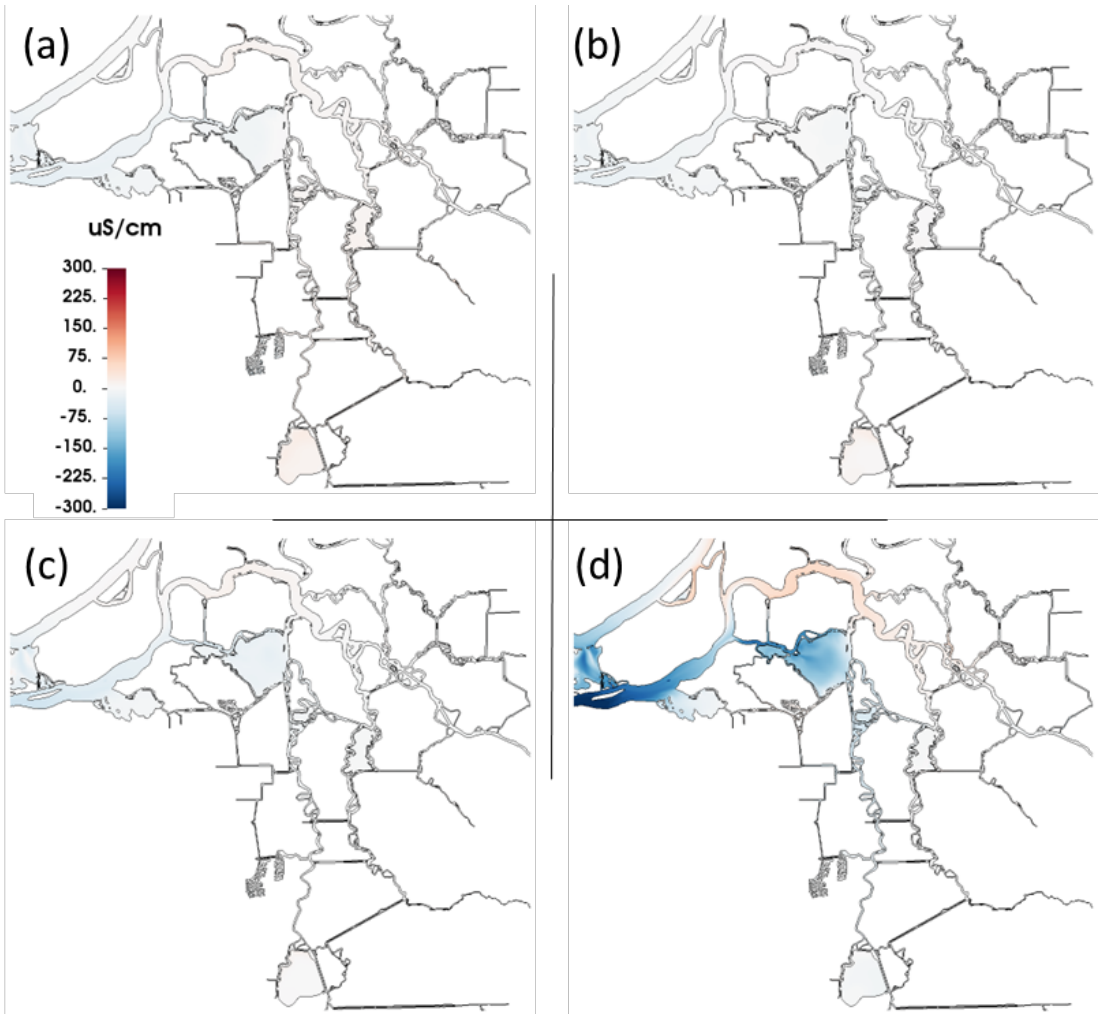

NOTES: (a) February 1–14, 2022; (b) March 1–14, 2022; (c) April 1–14, 2022; (d) May 1–15, 2022.
µs/cm = microsiemens per centimeter. Note that the maps mostly indicate zero or small differences.

Figure 2.2.1-6 Differences in salinity between scenarios with the notched emergency drought barrier and without the barrier, spring 2022.

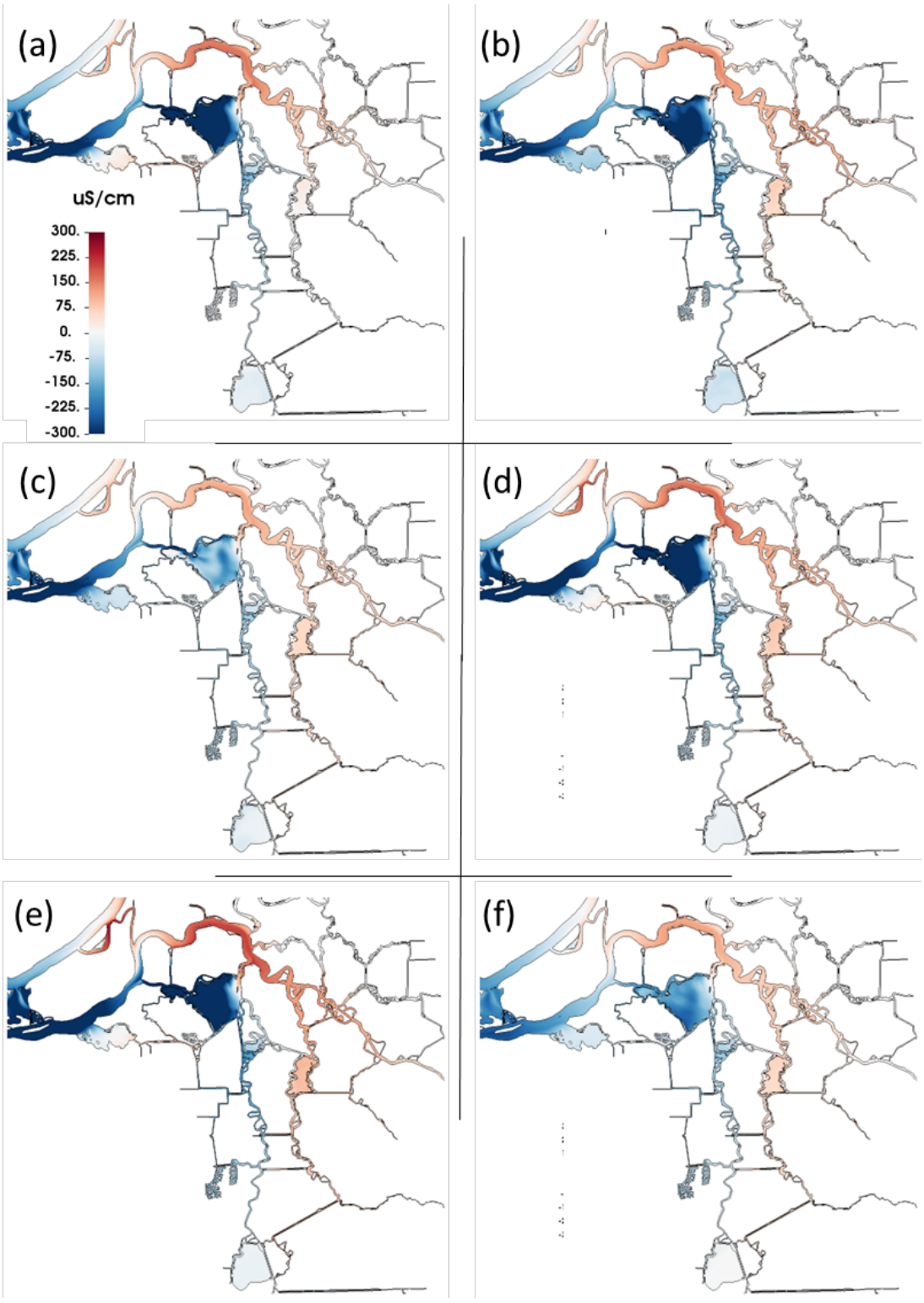

NOTES: (a) June 1–14, 2022; (b) July 1–14, 2022; (c) August 1–14, 2022; (d) September 1–15, 2022; (e) October 1–15, 2022; (f) November 1–15, 2022. µs/cm = microsiemens per centimeter.

Figure 2.2.1-7 Differences in salinity between scenarios with and without the emergency drought barrier, June–November 2022.

Because of the greater relative influence of Old River at the export locations during health-and-safety levels of pumping, the beneficial effect generally prevails in this area. Based on the salinity change maps, the EDB appears to have significantly simplified the compliance onus in the Central Delta and protected part of the freshwater corridor, but to have improved salinity at the SWP and CVP export locations to only a modest degree.

November 2021 Freshet

As noted previously, the November 2021 change map—map (d) in Figure 2.2.1-5—is an exception in the map series because it shows patches of degradation in western Franks Tract, rather than freshening. This map is timed to the aftermath of late-October storms that produced outflow as high as 61,600 cubic feet per second (cfs) and reduced salinity at Jersey Point to levels fresher than the water at adjoining Bethel Island.

Under these circumstances, the tidal pumping at False River and Franks Tract—which produces salinity intrusion in summer and which the EDB is designed to shut down—would have been beneficial. The monitoring team speculated that because this mechanism was blocked, there might be circumstances under which the barrier could even delay widespread freshening (which would have been offset by the January notch), but it appears that 2021 was not such a case. In December 2021 and January 2022, freshening of Franks Tract and the Central Delta from Old River in the east was nearly complete by the time Jersey Point salinity became low enough to be a source of freshening.

Notch, January–April 2022

During the January–April 2022 notching period, the EDB was effectively open to tidal flow and regional salinity was low, so no salinity improvements occurred. Figure 2.2.1-6 shows modeled salinity for the first 14 days of each of these months. The plots indicate no significant difference between the with-barrier and without-barrier cases.

2.2.1.2 Delta Cross Channel

The salinity difference maps for August through October show an area of water quality degradation around San Andreas Landing, the Mokelumne River, and the mouth of Old River that develops as a result of the barrier. In Figure 2.2.1-5A, the area under discussion is circled in red, and the tendency recurs in other months such as September and October in nearly the same location. This area northeast of Franks Tract is a critical region when the EDB is installed: It represents not only the influx of tributary water from the DCC, but also the location of enhanced exchange between the San Joaquin River and Franks Tract through Old River when the barrier is in place.

In fall 2021, the DCC gates (Figure 2.2.1-2) were toggled open and closed to balance water quality concerns in the Delta with Rio Vista flow requirements. During most of October, for instance, operations followed a pattern of three days open, four days closed. Although there was not necessarily any latitude to increase the use of the cross channel, it is natural to inquire whether a synergy exists between DCC operations and the 2021–2022 EDB.

To investigate this question, additional hypothetical/sensitivity simulations were performed by modeling water quality under enhanced operation of the DCC gates. The enhancement was to add two tidal days (50 hours) at the beginning of each weekly open/close cycle in September and October. This was purely a sensitivity experiment; additional use of the DCC probably would not have been feasible, given the gate closures needed to meet Rio Vista flow standards.

Figure 2.2.1-8 shows the results of this sensitivity experiment. The dotted lines show salinity under these enhanced DCC gate operations at the same locations as in Figure 2.2.1-5. At Bethel Island at Piper Slough [BET], the added DCC gate operations made only a little difference; the effect of the EDB was far larger than that of the cross channel. At Clifton Court, the opposite was true: Differences were small overall and the DCC was more influential. At Old River at Bacon Island, enhanced DCC gate operations and the EDB induced change at approximately equal magnitudes.

The sensitivity experiment found only a very weak synergy. In the first approximation, the combined DCC and EDB actions provided benefits equal to the sum of the benefits of the individual actions; in reaches where the EDB was estimated to increase salinity, the DCC enhancement was still beneficial. This occurred mostly on the Middle River corridor.

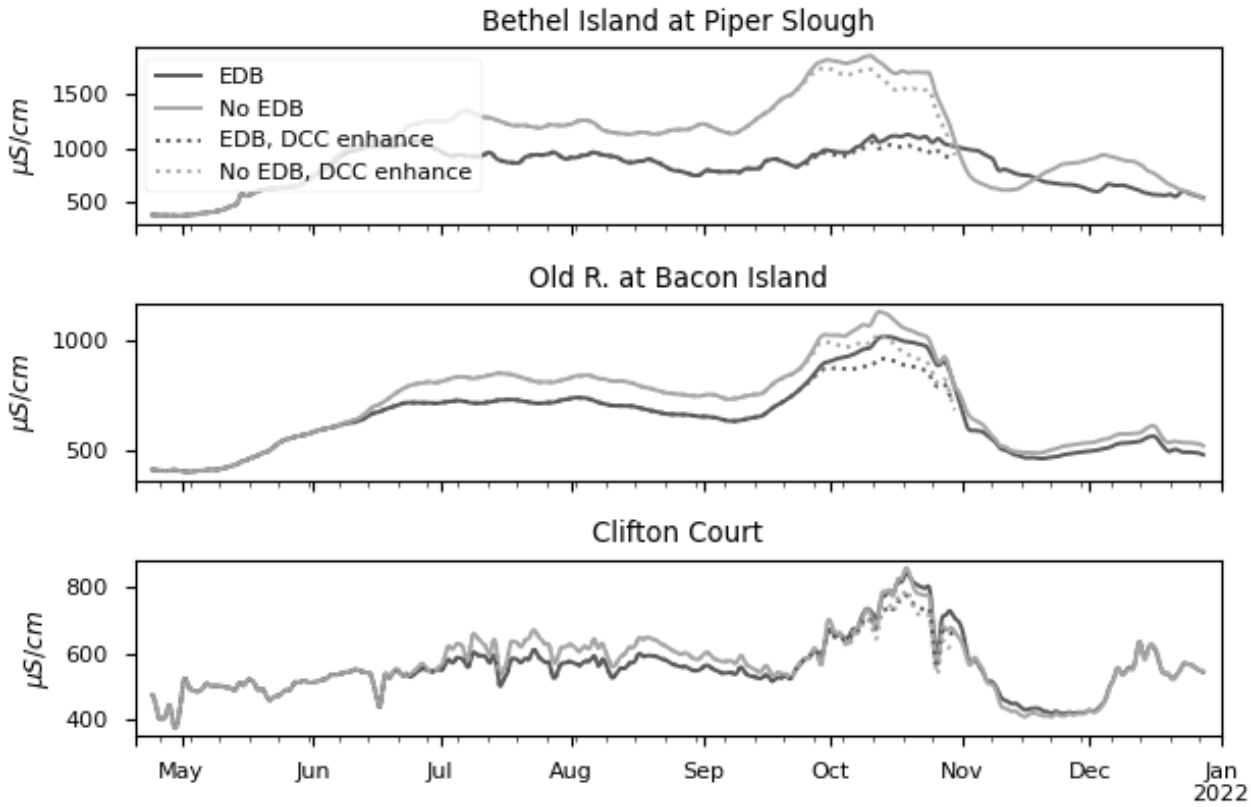

NOTES: µS/cm = microsiemens per centimeter; DCC = Delta Cross Channel; EDB = emergency drought barrier

Figure 2.2.1-8 Effect of two additional tidal days of Delta Cross Channel gate operation on the EDB and No EDB scenarios.

2.2.2 Effect of the Emergency Drought Barrier on Hydrodynamics and Salt Transport

2.2.2.1 Introduction and Caveats

As described in the previous sections, the primary objective of the 2021–2022 EDB was to eliminate salinity intrusion (salt transport) into the Central and South Delta through False River during extreme droughts—periods when water supplies in upstream reservoirs are inadequate to achieve this objective.

This section describes the effect the EDB had on hydrodynamics—velocities and discharges—that drive transport processes in the Central Delta. Except for increases in net flows from Middle River to Old River through Railroad Cut and the Woodward Canal, the Central Delta is, remarkably, the only region directly affected by the EDB. "Transport" is the movement from place to place of whatever is present in the water (e.g., salinity, suspended sediment, chlorophyll *a* [chl *a*], small organisms, fish).

There are two primary transport mechanisms in the Delta: "horizontal dispersion," driven by tidal currents, and "net advection," driven by tidally

averaged or net flows (**Figure 2.2.2-1** and Equation 5 in Section 2.2.2.2, "Approach and Methods"). Conceptual models of dispersive mixing processes are presented in **Appendix C** for reference.

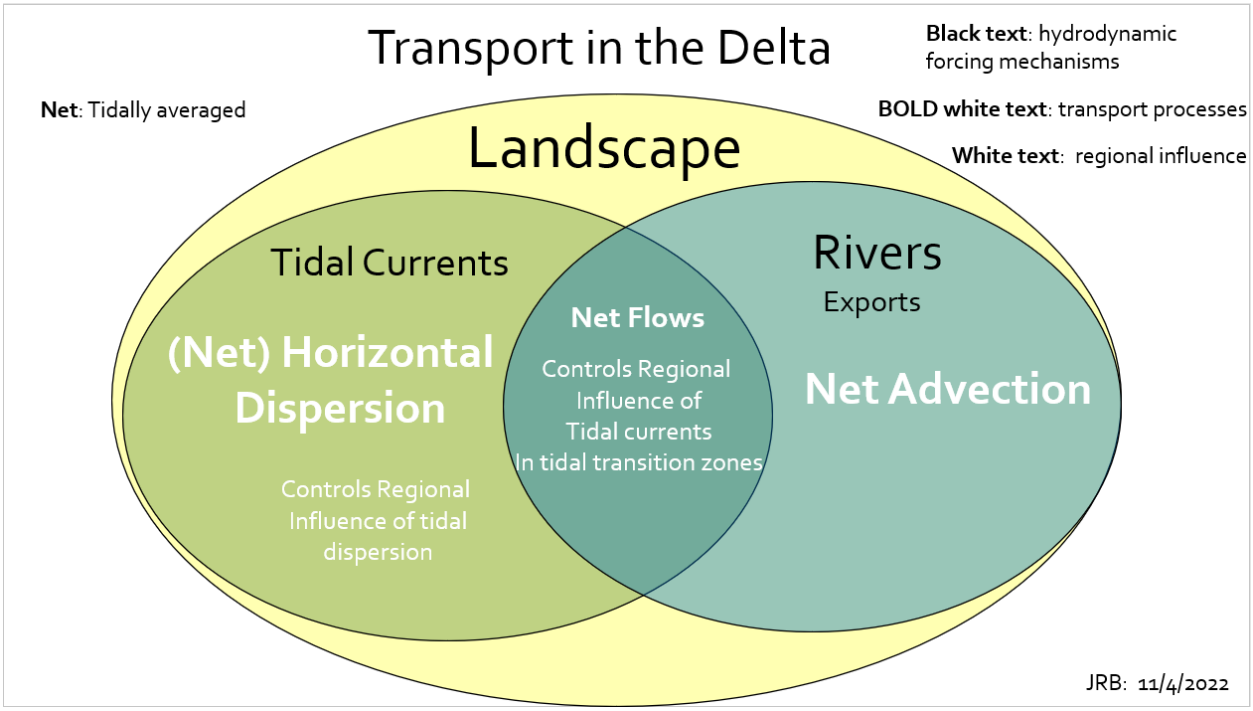

NOTE: A conceptual model of transport in the non-brackish portion of the estuary (e.g., landward of the low-salinity zone) involves two interacting hydrodynamic forcing mechanisms, shown in black text. The boldfaced white text identifies the type of transport derived from each of these processes, and the non-boldfaced white text identifies the regional influence of each. The landscape strongly mediates the interaction between all of these processes, through a combination of planform and bathymetry. Transport via the horizontal salinity gradient occurs only in the brackish portion of the estuary and therefore does not play a role in the Delta.

Figure 2.2.2-1 Illustration of modes of net transport in the Sacramento–San Joaquin Delta.

The direction and the magnitude of transport via horizontal dispersive mixing depend on the spatial gradient, from higher to lower concentration, of whatever is present in the water. Therefore, transport via dispersion can be in opposition to the movement of the water (net flow). This is the case for salinity in most estuaries because the salinity gradient is from the estuary mouth, where the water is salty, to the rivers, where the water is fresh.

Salinity intrusion via horizontal dispersion into the Delta is *the* reason the EDB is needed during droughts: The water project operators simply do not have sufficient water in upstream reservoirs to keep salinity from intruding into Franks Tract through False River. Thus, quantifying the interplay between transport via horizontal dispersion and advection (net flows) in regulating the movements of the salt field is central to understanding the effect of the EDB on the hydrodynamics, and thus the transport processes, of the Central Delta. This interplay ultimately drives the efficacy of the EDB in controlling salinity intrusion into the Central and South Delta.

Summary of Changes Caused by the Barrier

The EDB's most consequential change to the Central Delta's hydrodynamics—and thus its most consequential effect on salt transport—was the elimination of tidal discharges (flows) and velocities that normally exchange into Franks Tract through False River, peaking at approximately 56,000 cfs (**Figure 2.2.2-2**). For maps depicting the areas affected, see **Figure 2.2.2-3** and **Figure 2.2.2-4**.

The elimination of these tidal flows by the EDB caused the redistribution of roughly 20 percent of the approximately 300,000 cfs in total tidal discharge that enters the Delta past Chipps Island twice a day, every day. This was an extraordinary change to the hydrodynamic processes that drive the transport of not only salinity, but of whatever else is present in the water in the Central Delta.

Once the EDB was hydraulically closed in June 2021, flows began leaking through the rock barrier in False River at levels of up to 2,100 cfs, or approximately 3 percent of the peak tidal discharge, as verified by check flow measurements conducted in July 2021 during the peak of a spring tide.

The 2021–2022 EDB remained in place for nearly the entire year, although it was notched for about three months, with the goal of allowing outmigrant fish passage.

Installation of the EDB eliminated salinity intrusion into Franks Tract through False River, and thus achieved its intended purpose.

However, the barrier likely increased rates of salinity intrusion via dispersive mixing in the San Andreas Shoal Reach, in Fisherman's Cut (FCT), and in Old River at Franks Tract near Terminous (OSJ), simply because tidal currents increased in these channels (e.g., horizontal dispersion scales with the velocity [Fischer et al. 1979]). Meanwhile, salinity intrusion at Holland Cut near Bethel Island (HOL) and at Old River at Quimby Island (ORQ) likely decreased because tidal currents decreased in these channels, but only if salinity was present (see "Effects of the Emergency Drought Barrier on Dispersive Mixing [Potential]" in Section 2.2.2.3, "Results").

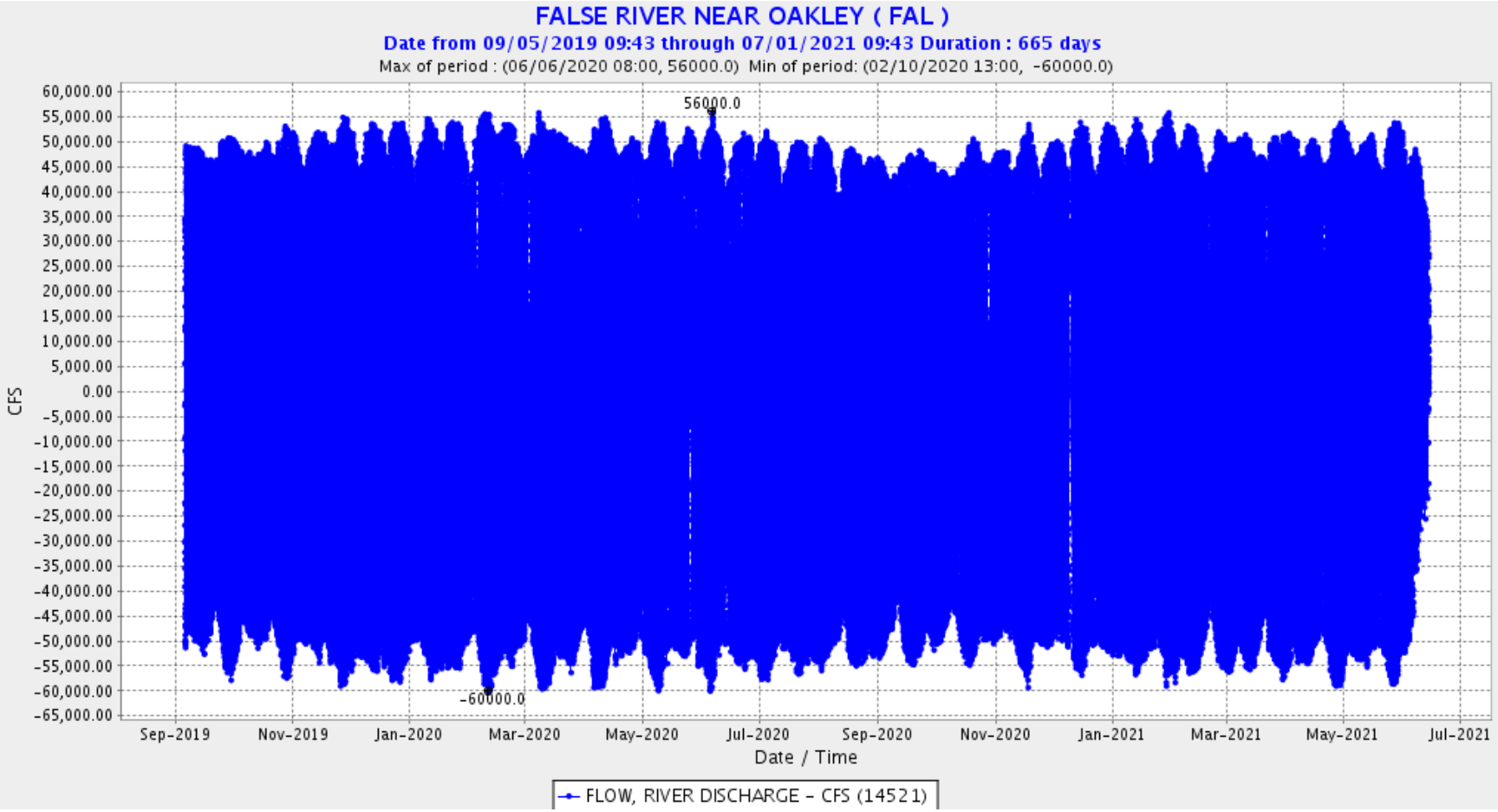

NOTE: As shown, the results of the roughly 1.5-year investigation indicate that peak tidal discharges in False River were approximately 56,000 cubic feet per second (cfs). The 14-day periodic patterns in the outer envelopes of the ebb (positive) and flood (negative) tidal discharges are caused by the spring/neap cycle.

Figure 2.2.2-2 Discharges in False River, September 5, 2019, to July 1, 2021.

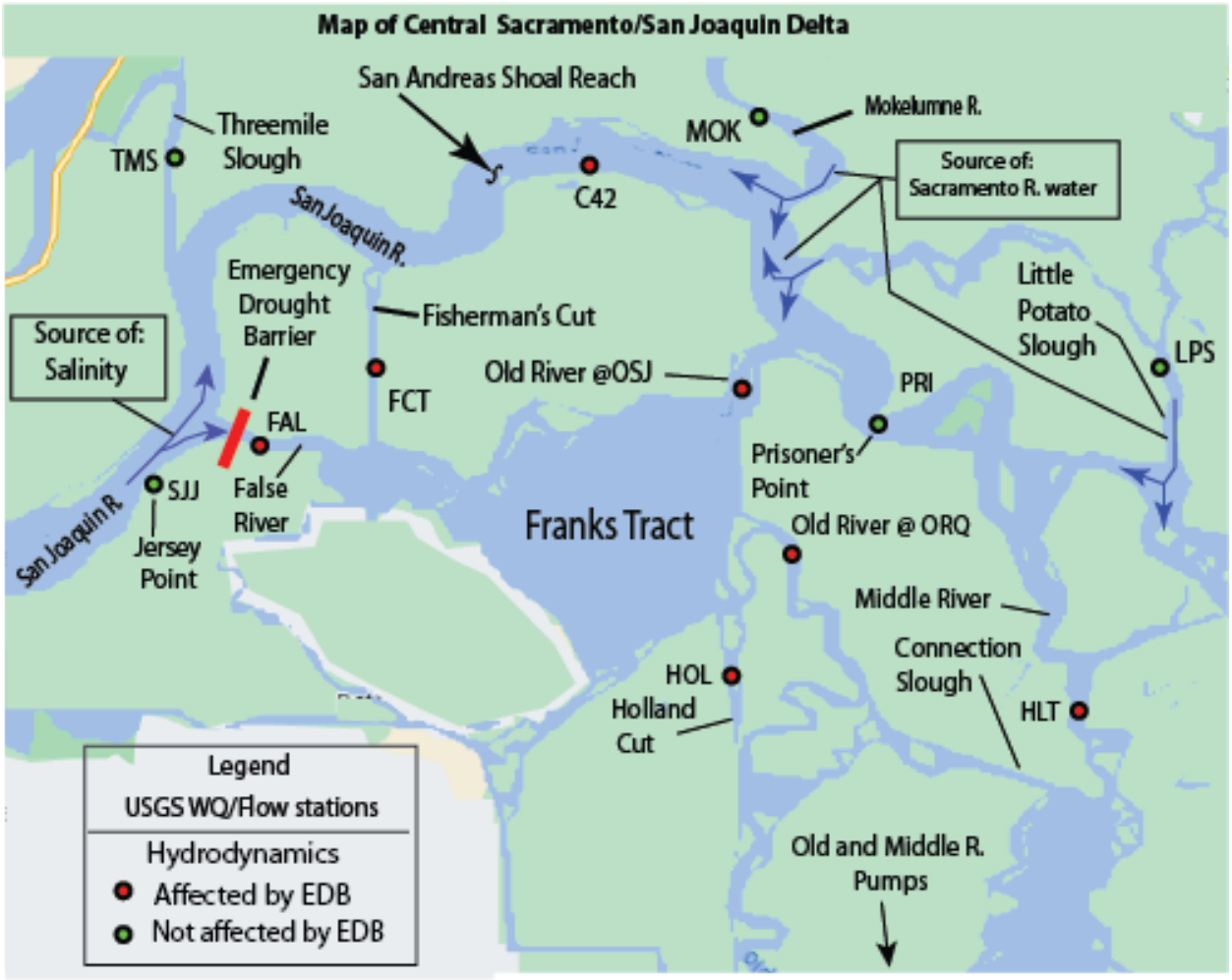

NOTES: EDB = emergency drought barrier; USGS WQ = U.S. Geological Survey water quality. False and Old rivers and Fisherman's and Holland cuts exchange with Franks Tract.
Red dots show the locations and California Data Exchange Center station names of monitoring stations where the EDB affected hydrodynamics. Green dots show stations that were not affected by the EDB.

Figure 2.2.2-3 Emergency drought barrier, monitoring stations, channels exchanging with Franks Tract, and pathways for salinity and Sacramento River water to enter the Central and South Delta.

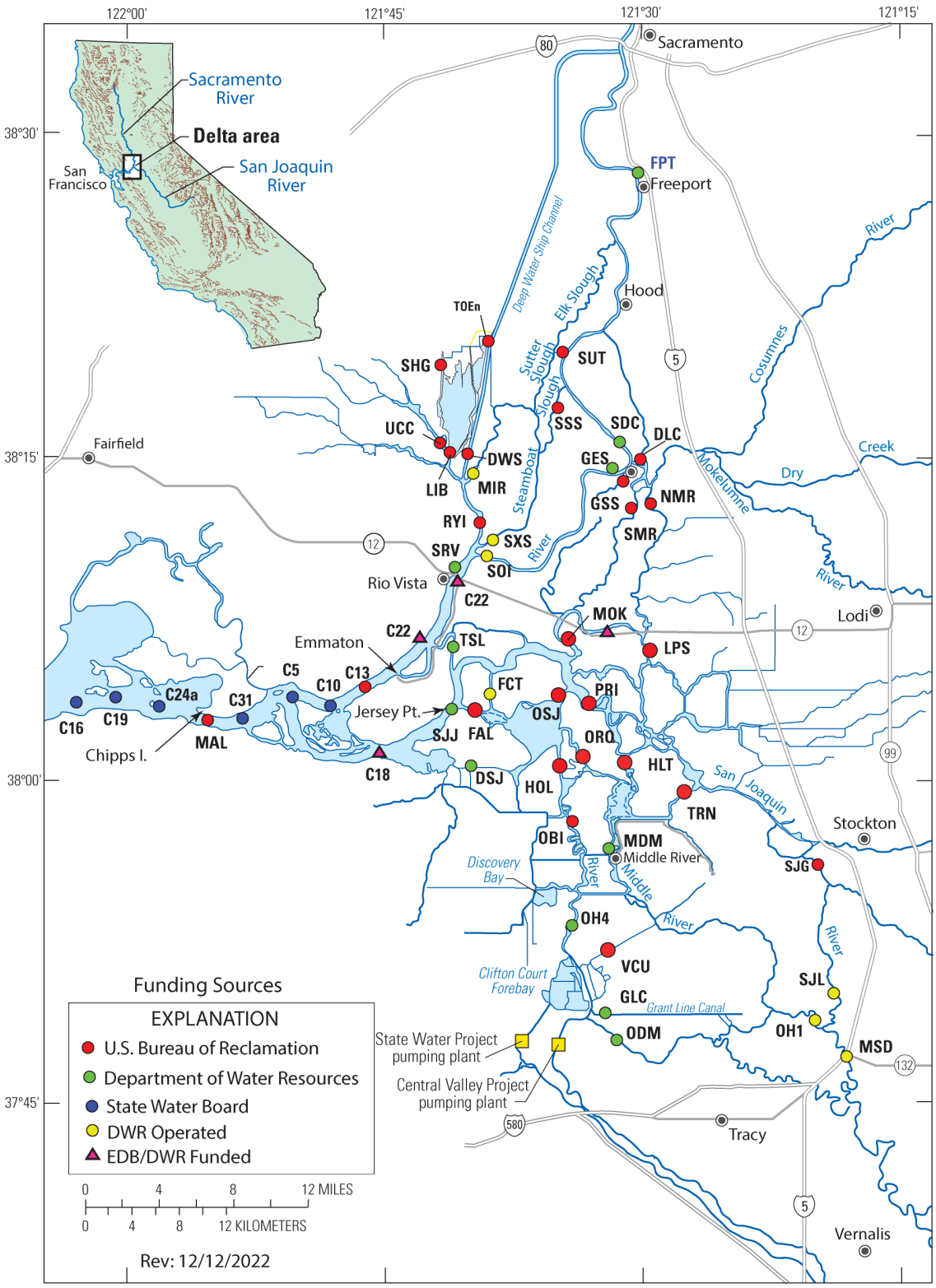

NOTES: DWR = California Department of Water Resources; EDB = emergency drought barrier; State Water Board = State Water Resources Control Board.
Colored dots indicate funding sources for the U.S. Geological Survey and those stations operated by DWR.

Figure 2.2.2-4 Map of the Delta showing flow and water quality monitoring locations.

Data Analysis Caveats

Horizontal Dispersion Estimates

The term "likely" is used here because the SWP and CVP operators allowed very little salinity to intrude into these reaches while the EDB was installed (**Figure 2.2.2-5**C), which prevents a direct assessment of dispersive mixing under conditions when salt is farther into the system. Such conditions could occur during a more severe drought in the future.

Salinity levels in the Central Delta were generally low while the EDB was present. Therefore, this analysis uses a ratio of the tidal excursion to the characteristic channel length (or basin dimension)—the so-called "LE ratio" (Stumpner et al. 2020)—to quantify changes in dispersive mixing potential attributable to the EDB. The "tidal excursion" is the distance traveled by a water parcel on any given flood or ebb tide. Tidal excursions used in this analysis are based on the (spring tide) peaks in the tidal current magnitudes at a given location. The LE ratio is discussed further at the end of Section 2.2.2.2, "Approach and Methods."

Net Flow Estimates

Net flows are always a small fraction of tidal flows in the Central Delta, but they are especially small during droughts when river flows and exports from the Delta are at their minimum (**Figure 2.2.2-6**B). These conditions create a classic signal-to-noise (net flow to tidal flow) problem.

This signal-to-noise problem worsens as net flows approach zero because the "noise" created by the tides becomes progressively greater relative to net flows. Particularly problematic is a bias in either the velocity measurements or the flow calibrations, both of which can lead to spurious data. However, Simpson and Bland (2000) found no bias in the velocity measurements obtained from the acoustic Doppler current profilers (ADCPs) used in the flow calculations. Consequently, if there is no inherent bias in either the velocity measurements or the flow calibrations, the absolute value of the tidal average of flow and velocity data may be inaccurate, but the variability about the tidal average is likely viable for analysis. Therefore, in evaluating the effect of the 2021–2022 EDB on net flows, this report calls out only obvious shifts in the net flows that correspond to changes in barrier state, river inputs, export rates, etc., but does not reference the absolute values.

Still, the larger scale changes in net flows in False River toward the pumps pre-barrier (mid-November 2019 to late December 2020, early April to late October 2020) correspond well to broad-scale changes in export rates (**Figure 2.2.2-7**C).

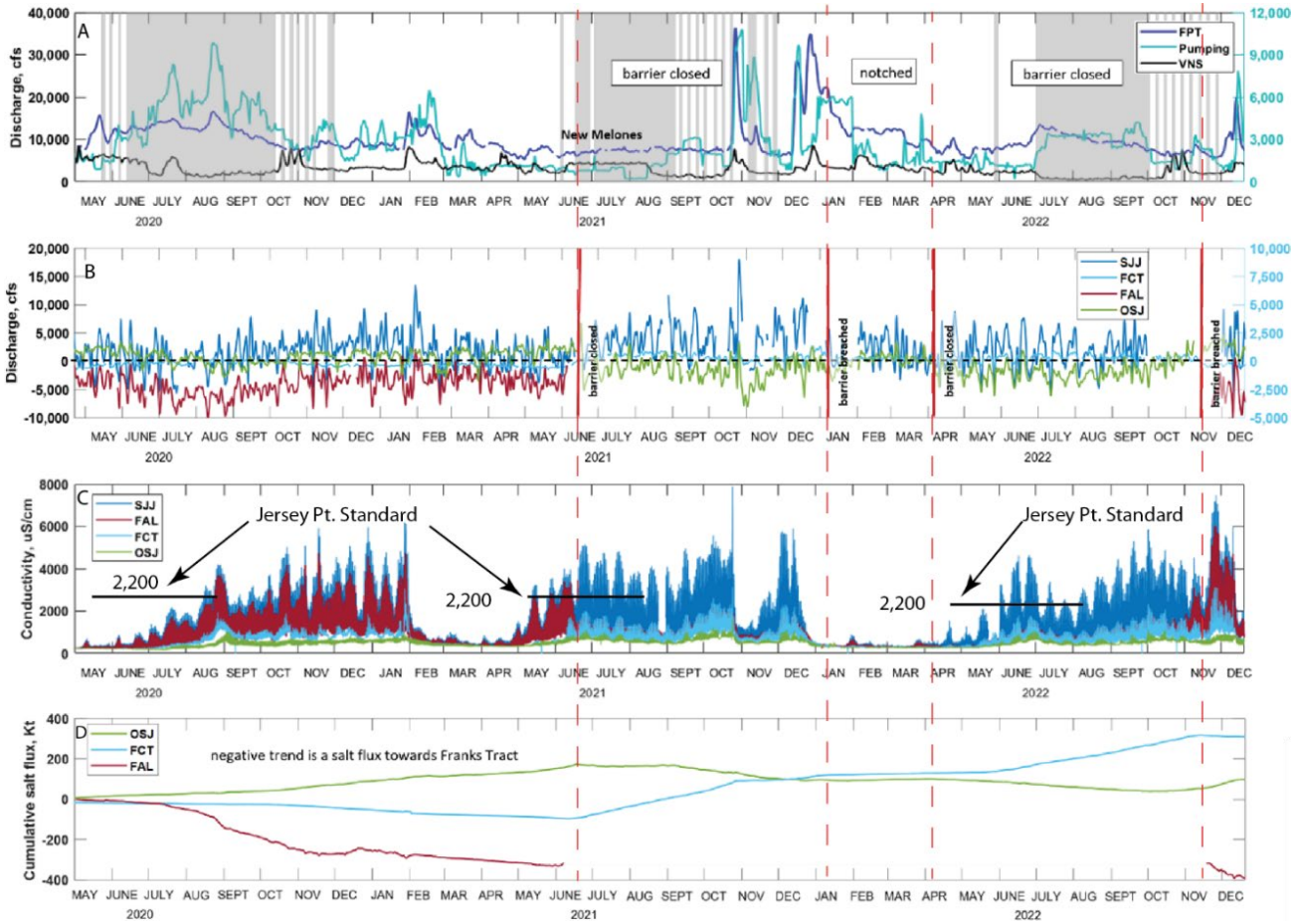

NOTES:

(A) Sacramento River inflows at Freeport (FPT), San Joaquin River inflow at Vernalis (VNS) (positive into the Delta), and exports (positive out of the Delta) (cubic feet per second [cfs].

(B) Net discharges (cfs) at Jersey Point (SJJ) (positive toward the bay), Fisherman's Cut (FCT) (negative toward Franks Tract), False River (FAL) (negative toward Franks Tract), and Old River at OSJ (negative toward Franks Tract).

(C) Conductivity (microsiemens per centimeter [µS/cm]) at Jersey Point (SJJ), False River (FAL), Fisherman's Cut (FCT), and Old River at OSJ.

(D) Cumulative salt flux (kilotons [Kt]) for False River (FAL), Fisherman's Cut (FCT), and Old River at OSJ.

This figure reflects all water project operations at FPT and VNS, exports, and Delta Cross Channel (DCC) gate operations (with gray shading indicating DCC-open conditions), because all these factors can affect net flows (B) and salinity in the channels that connect to Franks Tract (C). The effects of net flows on flow toward the bay (positive) at SJJ are somewhat muted, partly because net flows are a small fraction of tidal discharges. However, there is a noticeable response to high Freeport flows in October and December 2021. In contrast, net flows at FAL toward Franks Tract (negative) closely follow pumping (positive out of the Delta). The most noticeable change in net flows in the channels is an increase in net flows in OSJ and in FCT toward Franks Tract (hard to see in the plot; see "Summary of Changes Caused by the Barrier") when the barrier was in place compared to both no-barrier and notched-barrier conditions.

Figure 2.2.2-5 Time series plots comparing pre-barrier, barrier-closed, and barrier-notched conditions, May 2020–December 2022.

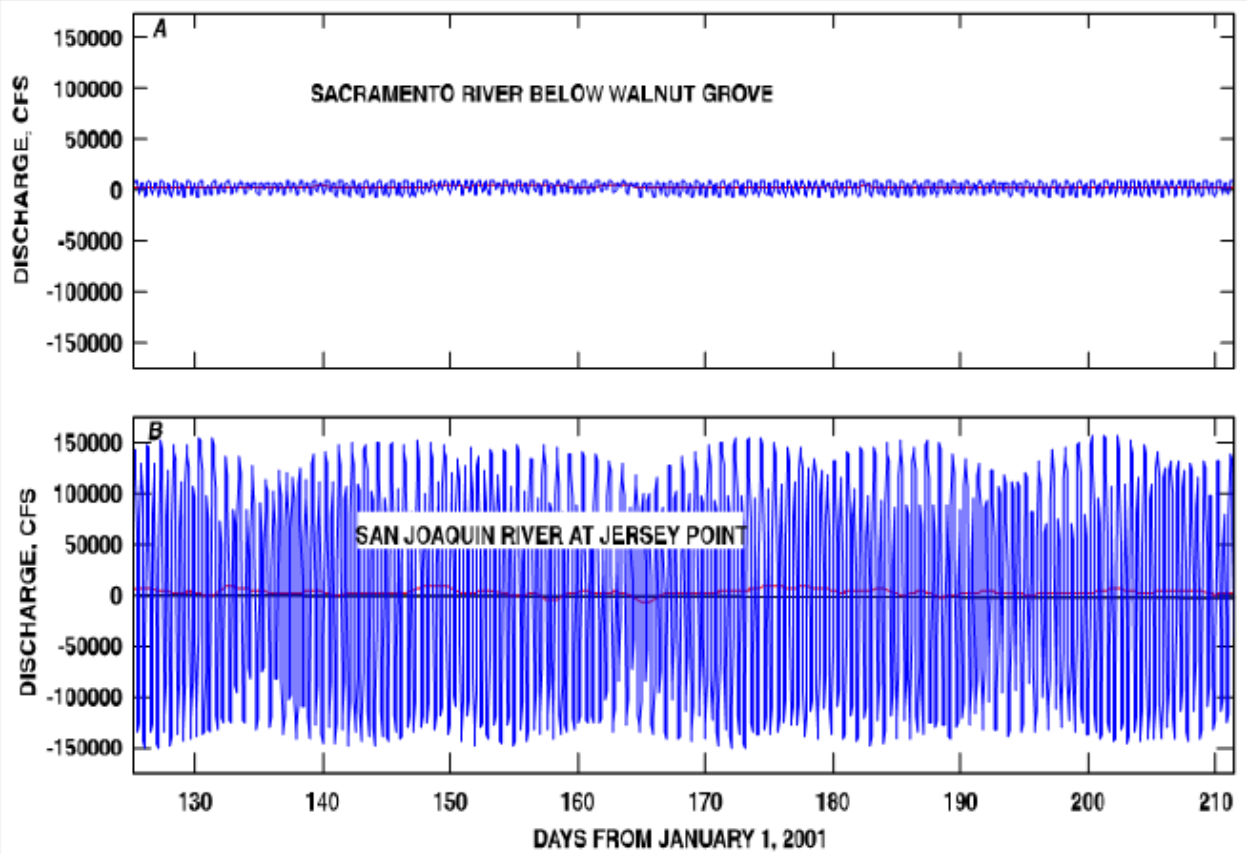

NOTES: cfs = cubic feet per second.
Blue line = tidal discharges; red line = tidally averaged or net flow.

Figure 2.2.2-6 Time series plots of discharges in (A) Sacramento River below Walnut Grove and (B) San Joaquin River at Jersey Point.

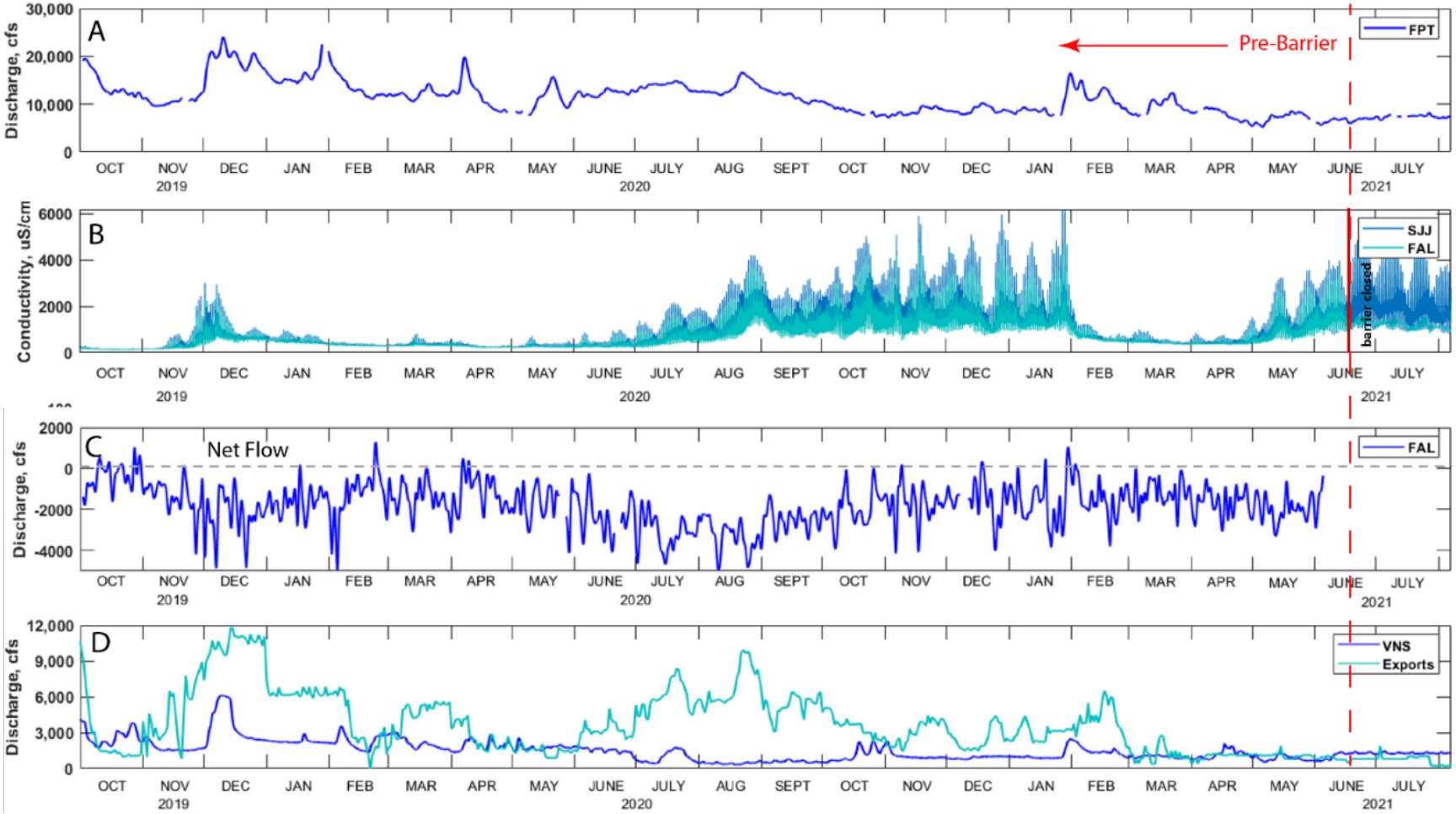

NOTES: (A) Sacramento River discharge at Freeport (FPT) (cubic feet per second [cfs]); (B) conductivity at Jersey Point (SJJ) and False River (FAL) (microsiemens per centimeter [µS/cm]; (C) net discharge (flow) in False River (cfs) (negative is toward the pumps); and (D) San Joaquin River inflow at Vernalis (VNS) (positive into the Delta) and exports (positive out of the Delta) (cfs).

This figure reflects all water project operations at FPT and VNS and exports, except Delta Cross Channel gate operations, because all of these factors can affect net flows in False River (C), which can affect salinity intrusion. In this case, the primary driver of increases in net flow in False River and consequent increases in salinity (B) (July–October 2020) is related to high exports (positive out of the Delta), which are correlated with large net (negative) flows into Franks Tract. For example, in December 2019, net flows in False River into Franks Tract were weaker even though exports were higher because of high inflows from the San Joaquin River.

Figure 2.2.2-7 Time series plots of pre-barrier conditions, October 2019–June 2021.

Salinity Measurements and Salt Flux Estimates

Inaccuracies in the true position and movement of the salt field within the Delta can occur because measurements are almost always made near the channel bank at the data collection locations shown in Figure 2.2.2-4. These monitoring stations do not account for lateral variability across the channel of salinity and other constituents.

Lateral variability can be particularly problematic in wide channels because the tidal currents across the channel can turn at different times, given the difference in momentum between the center of the channel, which is deeper, and the banks, where salinity data are typically collected. Moreover, cross-channel salinities can vary considerably down-current of junctions where the entrance channels have different salinities. Stations near the banks do not measure this variability. In the study region, exchanges between the San Andreas Shoal Reach, Threemile Slough, and the Mokelumne River system represent known examples where significant lateral variability is present.

Lateral variability can introduce an unknown bias into calculations of salt flux, especially if there is a flood/ebb asymmetry in lateral variability. For example, a bias in the salt flux can occur when one phase of the tide always maintains significant lateral variability (when salt is present) while the other tidal phase is laterally well mixed.

In contrast, narrow channels are generally well mixed, where lateral variability is not an issue.

However, the Delta has the advantage of supporting a dense network of monitoring stations (Figure 2.2.2-4), and conclusions made at a single station can be corroborated by data from nearby stations. Moreover, comparisons between parameters collected at the same station can be used to corroborate conclusions based on a single parameter. Several examples of this approach are provided in this analysis.

2.2.2.2 Approach and Methods

This analysis uses flow, velocity, and salinity time series data from fixed monitoring stations (Figure 2.2.2-4) to quantify the effect of the 2021–2022 EDB on the hydrodynamics (flows and velocities) that drive salinity intrusion (salt transport).

It is obvious why salinity data are useful in assessing the EDB's efficacy in mitigating or eliminating salinity intrusion into the Central and South Delta. Less obvious, however, is the role of hydrodynamic processes, represented by flow and velocity data, in combination with salinity data. For example, calculating the product of flow and salinity data quantifies the amount of salt passing a given sampling location in the same way that discharge or flow

quantifies the amount of water passing a given sampling location. This product provides the rate of salinity intrusion (salt per unit time)—the so-called "salt flux"—at any of the station locations shown in Figure 2.2.2-4.

Furthermore, the salt flux can be decomposed into the principal physical process that governs salt transport at each location: either horizontal dispersion or net advection (Figure 2.2.2-1). Temporal and spatial variability in velocity governs both processes: (1) Horizontal dispersion (in all its forms presented in **Appendix C**) scales with the magnitude of the tidal currents; and (2) net velocities (created mostly by river inputs and exports) govern net advection. In general, the faster the currents and the greater their spatial variability, the farther water parcels move with the tides, which leads to greater transport via horizontal dispersion.

The approach and methods used in the analyses of flow, velocity, and salinity time series data are presented below.

This section first describes the decomposition of flow, velocity, and salinity time series data into tidal and tidally averaged components. Next is a discussion of the analytical methods used on flow data and on the product of flow and salinity to compute salt fluxes, salt flux decompositions, and cumulative salt fluxes. This is followed by a description of the importance of the tidal and net velocities in creating transports associated with net horizontal dispersion and net advection (Figure 2.2.2-1), respectively. Finally, this section presents the methodology associated with the LE ratio, as a possible predictor of dispersive mixing potential in the near-absence of salinity in the Central and South Delta while the EDB was installed.

Decomposition of Time Series Data into Tidal and Tidally Averaged (Net) Components

One of the most important analytical tools (Fischer et al. 1979; Walters and Gartner 1985) used in understanding transport processes in tidally dominated systems like the Delta is the decomposition of temporal variability in time series data into tidal and tidally averaged, or net, components.

For example, the decomposition of flow, velocity, and salinity time series is simply:

$$Q(t) = \langle Q(t) \rangle + Q'(t) \qquad (1)$$

$$U(t) = \langle U(t) \rangle + U'(t) \qquad (2)$$

$$S(t) = \langle S(t) \rangle + S'(t) \qquad (3)$$

where *Q(t)*, *U(t)*, and *S(t)* are the measured flow, velocity, and salinity time series, respectively; "< >" represents a tidal average (or net), computed using a tidal filter (Godin 1972; Walters and Heston 1982); and the ` (prime)

represents the tidal deviations from the net (computed as, for example, Q'(t) = Q(t) -<Q(t)>).

This decomposition is useful (and technically justifiable) because most of the temporal variability in discharge (e.g., the blue line in Figure 2.2.2-6B), velocity, and salinity time series is not spread over a broad spectrum. Rather, most temporal variability in discharge occurs in distinct clusters or groupings, at tidal periods of approximately 12 and approximately 24 hours (shown in **Figure 2.2.2-8**) and at fortnightly and longer frequencies (not shown).

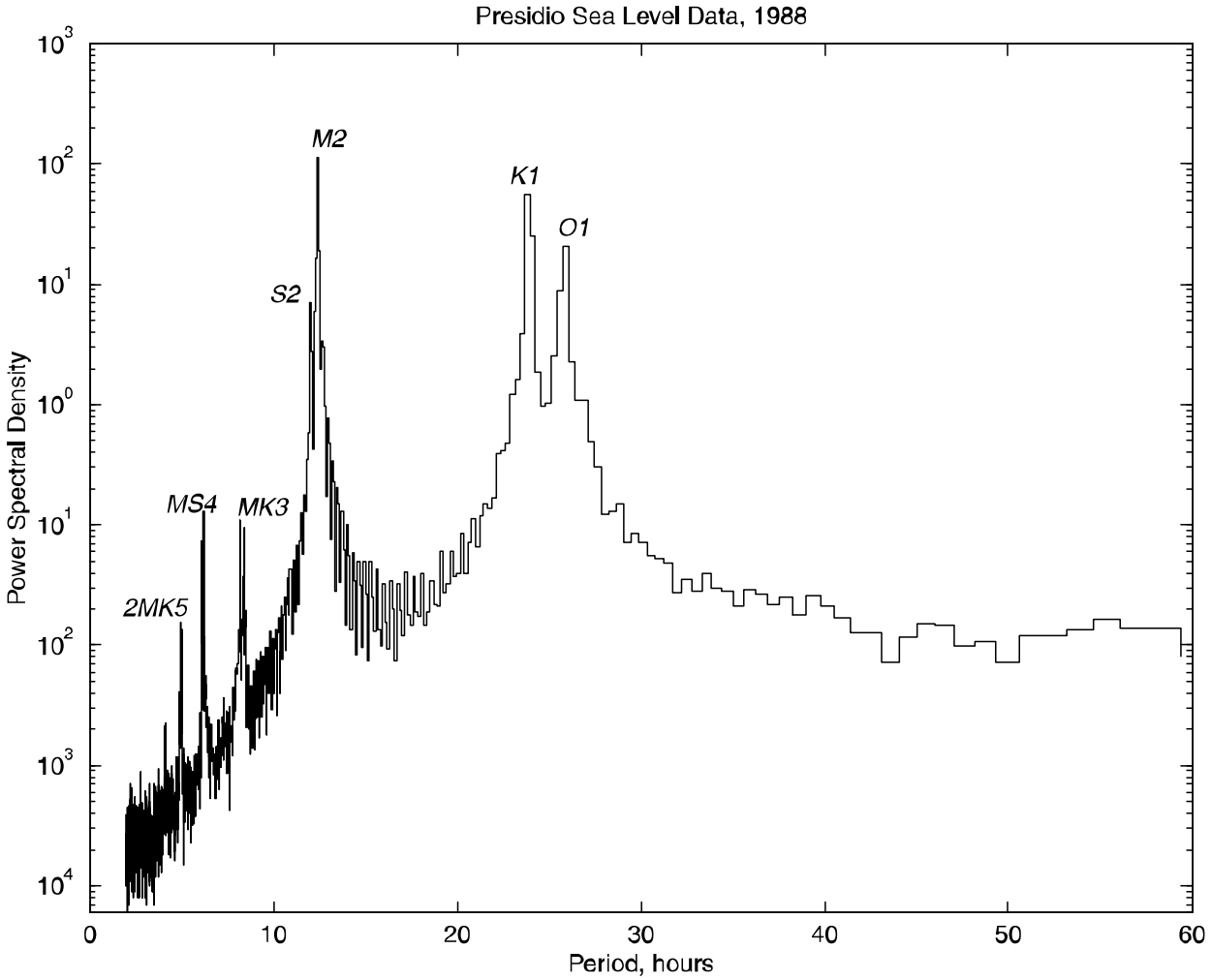

SOURCE: Data courtesy of National Oceanic and Atmospheric Administration, https://tidesandcurrents.noaa.gov/map/index.html?id=9414290.

Figure 2.2.2-8 Power spectrum of sea level data collected at the Presidio near the Golden Gate Bridge, 1988 calendar year.

Tidal filters essentially produce two time series, shown on the right-hand side of Equations 1–3. All the power spectral density at periods less than 30 hours is included in the primed time series representing the tidal

fluctuations, while everything at periods greater than 30 hours is included in the tidal averaged time series, "< >."

Flow Data

In the case of the EDB, flow is important as a measure of the redistribution volume of water (called the "tidal prism") that exchanges through False River at tidal and net flow timescales (see "Effects of the Emergency Drought Barrier on Flows" in Section 2.2.2.3, "Results"). Flow data are also used to calculate the salt flux and cumulative salt flux (see "Effects of the Emergency Drought Barrier on Salt [Fluxes] Transport" in Section 2.2.2.3, "Results").

Salt Flux and Salt Flux Decomposition

By calculating the salt flux, one can determine whether salt is intruding into the Delta or retreating from it, and at what rate. By convention, positive flows, velocities, and salt fluxes are directed seaward, while negative values are directed landward.

The salt flux quantifies the amount of salt that passes a given location per unit of time, just as the discharge is the quantity of water that flows past a given location per unit of time. Fluxes are used to understand (and model) salt transport because the quantity of salt passing a given location depends not only on the concentration, but also on the flow (see Equation 4 below). For example, the transport of a lower salt concentration into the Delta by stronger tidal currents (or net flows) can introduce the same salt flux as the transport of a high salt concentration by weaker tidal currents (or flows).

Finally, the salt flux can be decomposed into tidally averaged dispersive (tidally driven) and advective (river and export–driven) components to determine the fundamental mechanisms that lead the salt field to move into, out of, and through the Delta. These mechanisms can be identified by computing salt fluxes at the relevant monitoring stations shown in Figure 2.2.2-4.

The total salt flux (both tidal and tidally averaged components) is:

$$\text{Total Salt Flux} = Q(t)*S(t) \qquad (4)$$

The total salt flux calculated in Equation 4 can be split into advective and dispersive components by plugging Equations 1 and 3 into Equation 4, and by ignoring the cross terms, which are generally small (Fischer et al. 1979):

$$\langle Q(t)S(t)\rangle = \langle Q(t)\rangle\langle S(t)\rangle + \langle Q'(t)S'(t)\rangle \qquad (5)$$

This decomposition is useful because the tidal average of the product of the primed terms (tidal timescale terms), $\langle Q'(t)S'(t)\rangle$, drives salinity intrusion

via dispersive mixing (left side of Figure 2.2.2-1), while the product of the tidally averaged terms, the "< >" terms, drives advective transport (right side of Figure 2.2.2-1; red line in Figure 2.2.2-6B).

Advective transports are driven by river inputs, DCC gate operations, and export rates—factors that the SWP and CVP operators marginally control in the Central Delta. The illustration in **Figure 2.2.2-9**, based on 2002 data from False River, shows that dispersive flux—driven by the tides, which cannot be directly controlled—can be on the order of advective flux in False River. The magnitude of dispersive flux, the uncontrollable component of salinity intrusion, is the reason the EDB is needed in droughts.

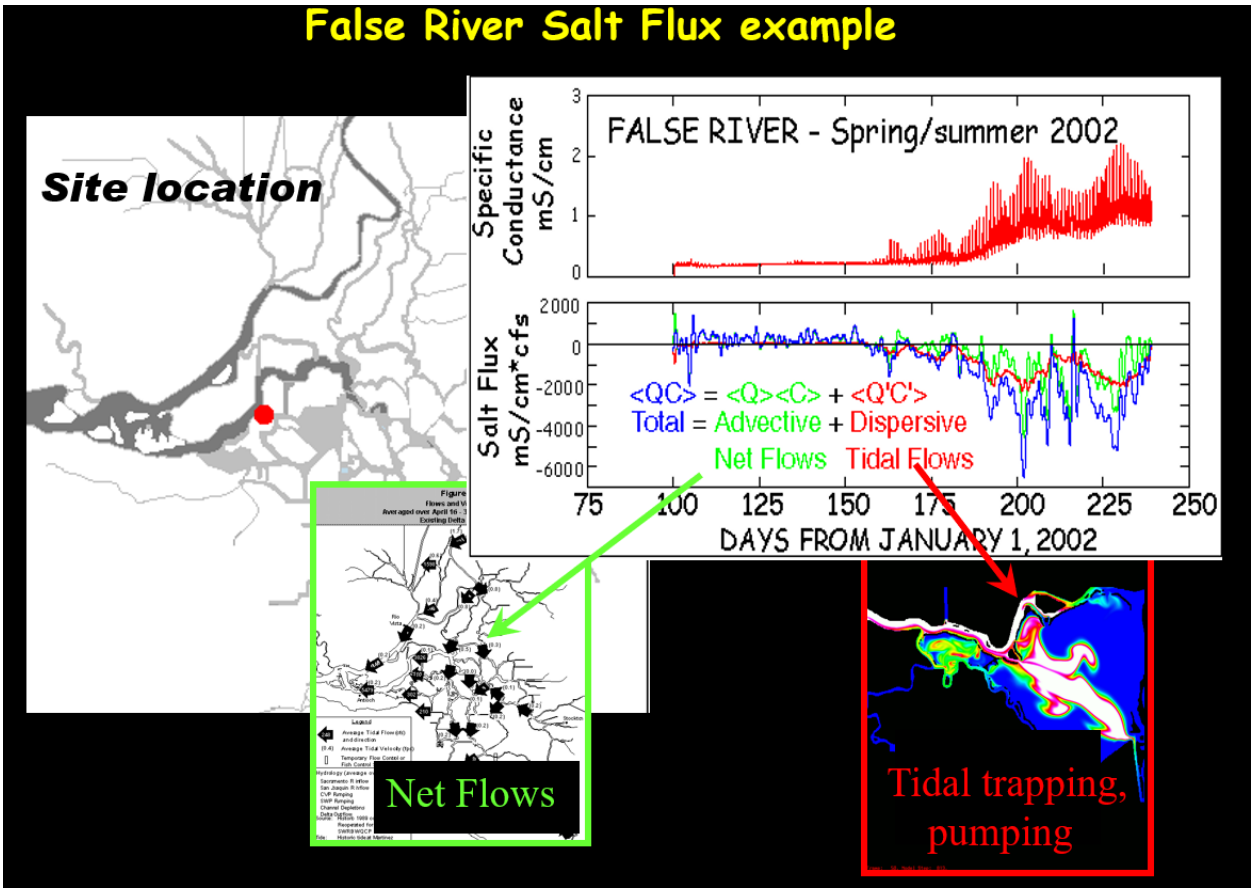

NOTE: This illustration shows the total flux (blue) and partitions the salt flux between advective (green) and dispersive (red). The decomposition in the contemporary Delta is likely significantly different than in 2002 given the bathymetry, the size of the breaches, and the introduction of *Egeria* in Franks Tract.

Figure 2.2.2-9 Illustration of flux decomposition in False River without the barrier.

Cumulative Salt Flux

Another tool used to understand changes in constituent fluxes is the "cumulative constituent flux," which is the moving average of the sum of the total salt flux, $<Q(t)S(t)>$ (left side of Equation 5).

In plots of cumulative constituent flux, changes in the slope indicate changes in the flux, where the direction of the slope determines whether the salt flux is increasing or decreasing: A positive slope indicates an increase in the flux for the assumed positive direction of *Q(t)*, a negative slope a decrease in the flux. No slope—a flat line—indicates zero change in the flux.

The cumulative constituent flux is useful because it can be difficult to discern long-term trends when the fluxes are small and/or steady, as they were during the period studied in this report (see Figure 2.2.2-5D for an example).

Velocity Data

Velocities are fundamentally important in driving salt transport, while the product of the flow and salinity quantifies where salt is going at fixed locations and at what rate, as described above.

Salt transport is mechanistically complex; it evolves from the interaction between temporal and spatial variability in the velocity and salinity fields, mediated by variability in the Delta's planform (bends) and bathymetric variability (channels with shoals). For conceptual models of these processes, see Appendix C.

Conceptually, in terms of dispersive mixing, the discharge, velocity, and salinity time series data collected at fixed sites encapsulate the detailed mixing processes (e.g., shear flow dispersion, tidal straining [Appendix C]) that occur within a tidal excursion of sampling locations. Thus, the detailed dispersive mixing processes that occur within a tidal excursion (shear and straining) and the distance over which this integration occurs (e.g., the tidal excursion) both change when there are significant changes in the velocity. As discussed later in this section, the EDB significantly changed the velocities and tidal excursions in all the channels that directly connect to Franks Tract, representing the most significant effect of the EDB on hydrodynamics in the Central Delta.

These observations led to the development of the LE ratio, the ratio of the tidal excursion to channel length. As discussed below, the 2021–2022 EDB significantly changed the velocities (shear, straining) and tidal excursions in the channels that connect to Franks Tract and in Middle River near Holt (HLT), which effectively changed dispersive mixing processes at these locations. This finding is encapsulated, in an integrated way, in the data collected at the fixed sampling locations.

Thus, velocity enters this analysis in two ways. First, dispersive mixing scales with velocity (Fischer et al. 1979). When velocities increase in a given reach—for example, because the EDB redistributes the tidal flows—dispersive mixing increases. When velocities decrease, dispersive mixing

decreases. The change in dispersive mixing depends on the dispersive mechanism involved, which is mediated by channel geometry. The faster the velocity, the greater the potential for horizontal mixing, and the farther water parcels move over the landscape and relative to each other. For conceptual models of dispersive mixing, see Appendix C.

Tidal Excursion Estimates

Velocity is also important to salt transport in terms of the distance water parcels travel over the landscape, the so-called "tidal excursion."

Although tidal excursions are a fundamentally Lagrangian quantity (observing the water by drifting along with it like a particle), they can be estimated using:

$$L_{ex} \text{ (miles)} = 2.6969 * U(\text{ft/s}) \qquad (6)$$

where L_{ex}, the tidal excursion in miles, equals 2.6969 times the velocity amplitude, U, in feet per second (ft/s) based on fixed site velocity data (Stumpner et al. 2020).

Tidal excursion estimates based on monitoring data from fixed sites (Eulerian, i.e., observing the water from sampling stations) are easy to calculate and are reasonably good first-order estimates in the Delta's prismatic channels. They are less accurate if there are significant changes in geomorphology along the tidal excursion path, such as shoals, channel junctions, and transitions between channels and open-water habitats.

LE Ratio

The length of tidal excursions relative to bathymetric and planform variability can be important in controlling net horizontal dispersion of salinity (Fischer et al. 1979). This discussion includes "planform variability" to explicitly recognize the importance of two factors in creating horizontal dispersion:

(1) Secondary circulation in bends (Appendix C, Figure C-3): Visualize water corkscrewing as it travels through a river bend, scouring out the outer portion of the bend and depositing sediment in the inner portion of the bend).

(2) Large open water features.

For example, tidal trapping and pumping of salt associated with the spatial variability in Franks Tract is the reason an EDB is required in False River when storage in upstream reservoirs is insufficient to prevent salinity from entering the Central and South Delta through False River (bottom panels in **Figure 2.2.2-10**). Exchange through a narrow prismatic channel—Threemile Slough, in the example shown in the top panels in Figure 2.2.2-10—into a

larger channel with highly variable bathymetry (the San Andreas Shoal Reach [**Figure 2.2.2-11**]) can also create large transports via tidal dispersion. In both cases, if the tidal excursion were significantly less, or if the planform and bathymetry were less spatially variable than it is now, tidal dispersion would be less than it is now. As an extreme hypothetical example, if the tidal excursion in Threemile Slough were less than 3 miles, or if the tidal excursion in False River were less than the distance to Franks Tract (5.2 miles), dispersive mixing would be limited to relatively weak velocity shear and tidal straining (see Appendix C) in these nearly prismatic channels.

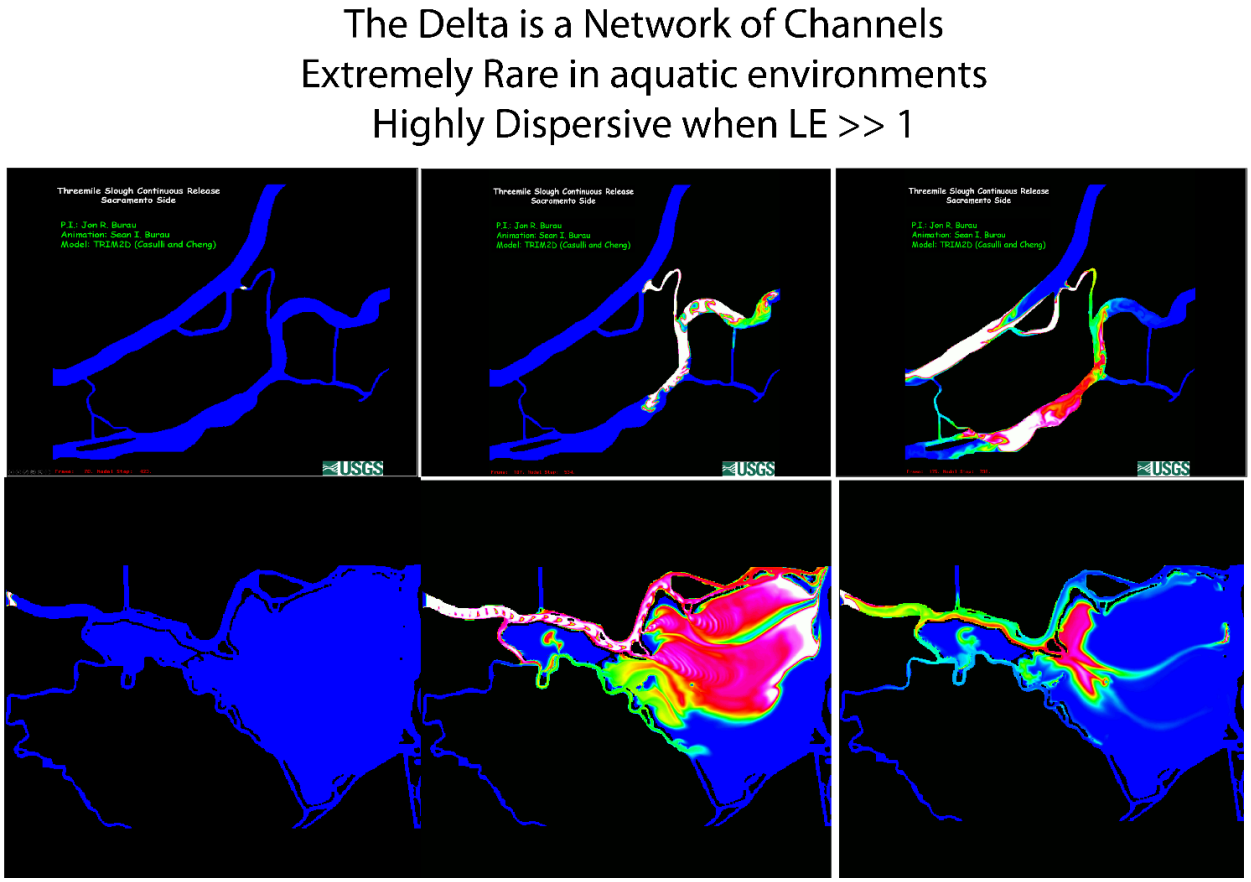

NOTE: *Top panels:* The highly dispersive channel system at Threemile Slough/San Joaquin River. Top left—release of dye at the Sacramento River/Threemile Slough junction at the beginning of an ebb tide. Top middle—dye after a complete tidal cycle. Top right—dye after several tidal cycles, exhibiting a large amount of dispersive mixing. *Bottom panels:* The highly dispersive channel/ open water system at False River/Franks Tract. These panels depict the same sequence as shown above, where the dye is released instead in the entrance to False River, with a similar large dispersive mixing outcome.

Figure 2.2.2-10 Examples of a highly dispersive channel system (Threemile Slough/San Joaquin River) and a highly dispersive channel/ open water system (False River/Franks Tract) based on a numerical model simulation.

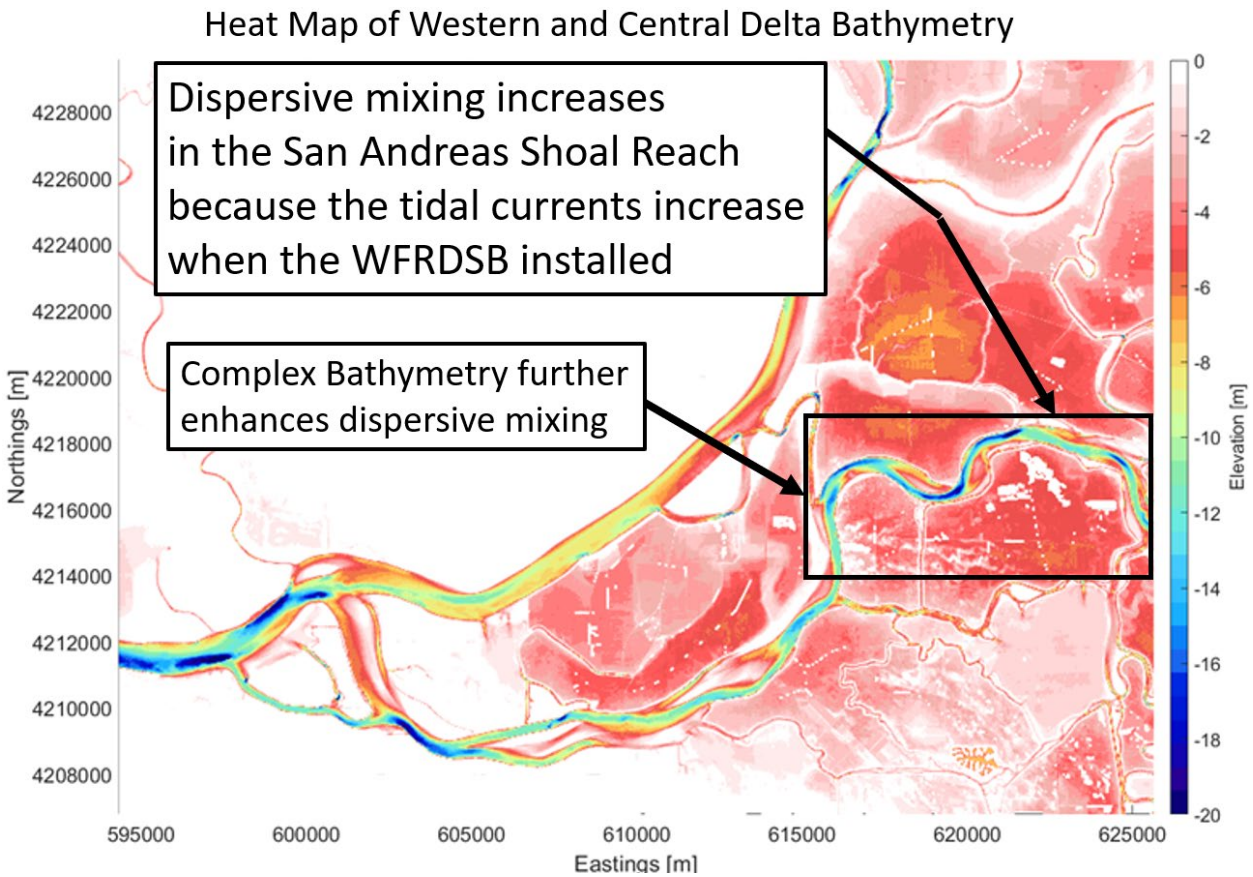

Figure 2.2.2-11 Complex bathymetry of the San Andreas Shoal Reach.

The primary motivation for the LE ratio in the context of the EDB is that two other channels—Fisherman's Cut (FCT) and Old River at Franks Tract (OSJ)—can also be significant conduits of salinity into the Central and South Delta, and both channels can maintain the same tidal trapping and pumping dispersive potential as False River. Unfortunately, the potential for dispersive mixing in these channels increases when the EDB is installed because of increased tidal excursions driven by the large increase in velocities into Franks Tract, which increases the amount of tidal trapping and pumping into Franks Tract. Thus, if salt significantly intrudes into Fisherman's Cut and Old River at Franks Tract (creating the required local spatial gradient in salinity), increased salinity intrusion into Franks Tract will occur as a result of the EDB. This will be followed in short order by the entry of salinity into the South Delta toward the pumps, for the same reason that salinity passes through Franks Tract when the EDB is not installed.

The tidal excursion is used as a measure of dispersive mixing potential because the longer the tidal excursion, the greater the dispersive mixing, which is modulated by bathymetric and planform variability. For example, as shown in the bottom panels of Figure 2.2.2-10, the longer the distance dye intrudes into Franks Tract (as a surrogate for salinity), the greater the

mixing of the dye within Franks Tract. The result: Less dye leaves Franks Tract on ebb than enters on flood, which in the end creates tidally driven dispersive transport into Franks Tract. Similarly, the one-way tidal exchange of dye released in the north end of Threemile Slough into the San Joaquin River (Figure 2.2.2-10, top panels) increases because of an increase in mixing in the San Andreas Shoal Reach when the tidal excursion into the San Joaquin River is longer. This increased mixing is created by shear flow dispersion in the shoals and secondary circulation (Appendix C, Figure C-3) in the bends in this reach.

In summary, an increase or decrease in dispersive mixing potential depends on both the amount of the increase or decrease in the length of the tidal excursion caused by the EDB and the bathymetric or planform variability over the increase or decrease in tidal excursion. In cases where the bathymetric variability occurs at the end of the tidal excursion, as it does in False River (FAL), Fisherman's Cut (FCT), Old River at Franks Tract (OSJ), Holland Cut near Bethel Island (HOL), and Old River at Quimby Island (ORQ), a change in tidal excursion length can have an outsized influence on dispersive transports.

The LE ratio is the tidal excursion, L_{ex}, divided by the channel length, E: (**Figure 2.2.2-12**):

$$LE = \frac{L_{ex}}{E} = \frac{Tidal\ excursion}{Channel\ Length\ or\ basin\ dimension} \qquad (7)$$

following the nomenclature introduced by Stumpner et al. (2020), who introduced the LE ratio in the context of a terminal (dead-end) channel system, like the Cache Slough Complex.

The tidal excursion can vary significantly over the course of a tidal day with diurnal inequality and over the 14-day spring/neap cycle. E is the Eulerian, fixed-in-space length scale that is useful in identifying regions where significant changes in system morphology that may lead to significant changes in dispersive mixing.

Figure 2.2.2-12 provides a schematic of three different channel configurations in which the LE ratio is useful. Sketch 1 is the only one applicable to this discussion but highlights the general applicability of this ratio. This figure illustrates a channel network with both an LE ratio less than 1 (LE<1, green arrow) and an LE ratio greater than 1 (LE>1, red arrow). A channel network in which LE<1 generally creates very little dispersive transport; by contrast, in a channel network where LE>1, dispersive mixing can be large, especially if the channel empties into a large channel (the Threemile Slough example in the top panels in Figure 2.2.2-10) or into an open waterbody such as Franks Tract (bottom panels in Figure 2.2.2-10).

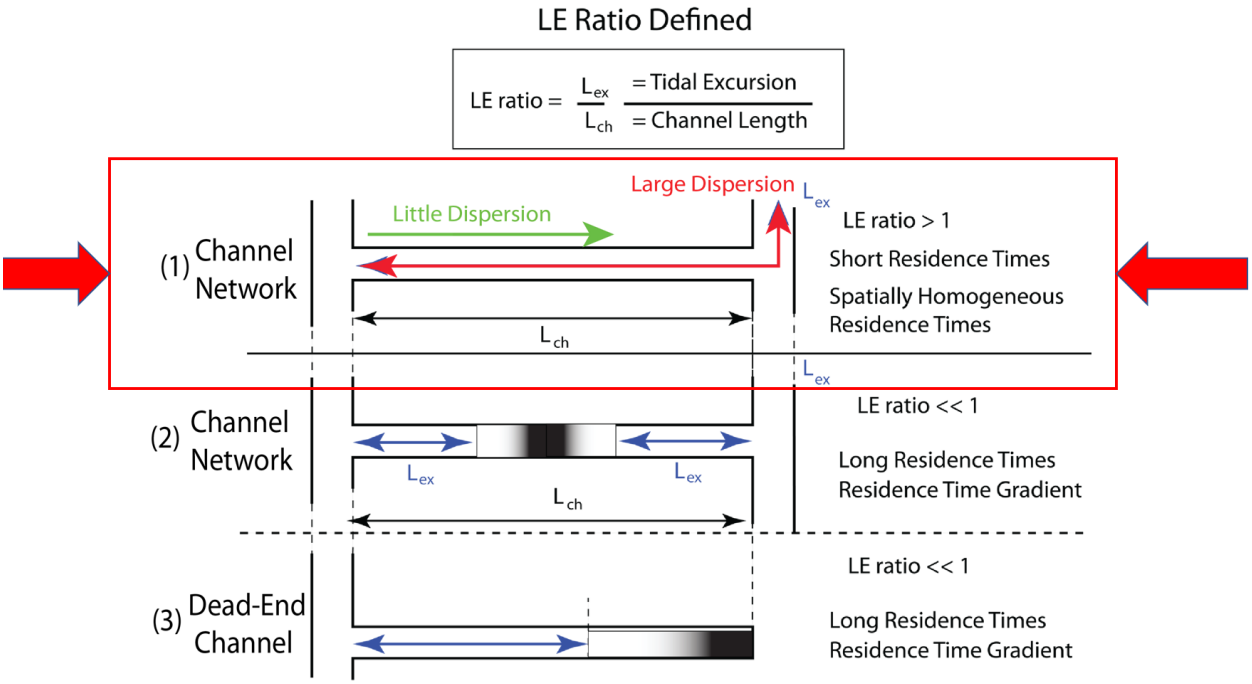

NOTE: Lagrangian/Eulerian (LE) ratio = ratio of the length of the tidal excursion to channel length. These sketches show the following channel systems:
(1) Channel network where the tidal excursion is longer than the channel length and the LE ratio is greater than 1 (typical of the Central and South Delta).
(2) Channel network with two openings whose total length is longer than the tidal excursions from both connection channels, and where the LE ratio is much less than 1. (*Examples:* Montezuma and Connection sloughs in Suisun Marsh.)
(3) Dead-end channel system, where the tidal excursion is less than the channel length and the LE ratio is much less than 1.

Figure 2.2.2-12 Definition sketches of the Lagrangian/Eulerian ratio for three different channel systems.

Figure 2.2.2-13 provides a simple example of how the LE ratio (Equation 7) is computed. In this case, channel length is measured using Google Earth and tidal excursion is estimated using Equation 6, where the tidal excursion transitions through a significant change in bathymetry: a prismatic channel (False River) into a large shallow water tidal oscillation basin (Franks Tract).

Dispersive mixing potential can increase greatly at a given location (usually measured from a channel junction, as shown in Figure 2.2.2-12) when significant changes in bathymetry occur within a tidal excursion. Examples of significant changes include rapid expansions or contractions of a channel, significant natural geomorphology (e.g., sinuosity, bends, bars, shoals—see the San Andreas Shoal Reach [Figure 2.2.2-11]), transiting of a junction (e.g., Threemile Slough, Railroad Cut, Old River at OSJ), or exchange between channels and open water areas such as Franks Tract (Figure 2.2.2-13).

In summary, dispersive transports can occur wherever there is a spatial constituent gradient across the length of channels that have LE ratios greater than 1. The amount of transport (flux) of a constituent depends on

the strength of the gradient, the distance the water parcels travel in the receiving waterbody, the degree of mixing within the receiving waterbody, and the spring/neap cycle. Moreover, the greater tidal currents that occur during spring tides increase the overall potential for dispersive transport by increasing both the LE ratio and dispersion from lateral (cross-channel) shear within all water bodies (see Appendix C).

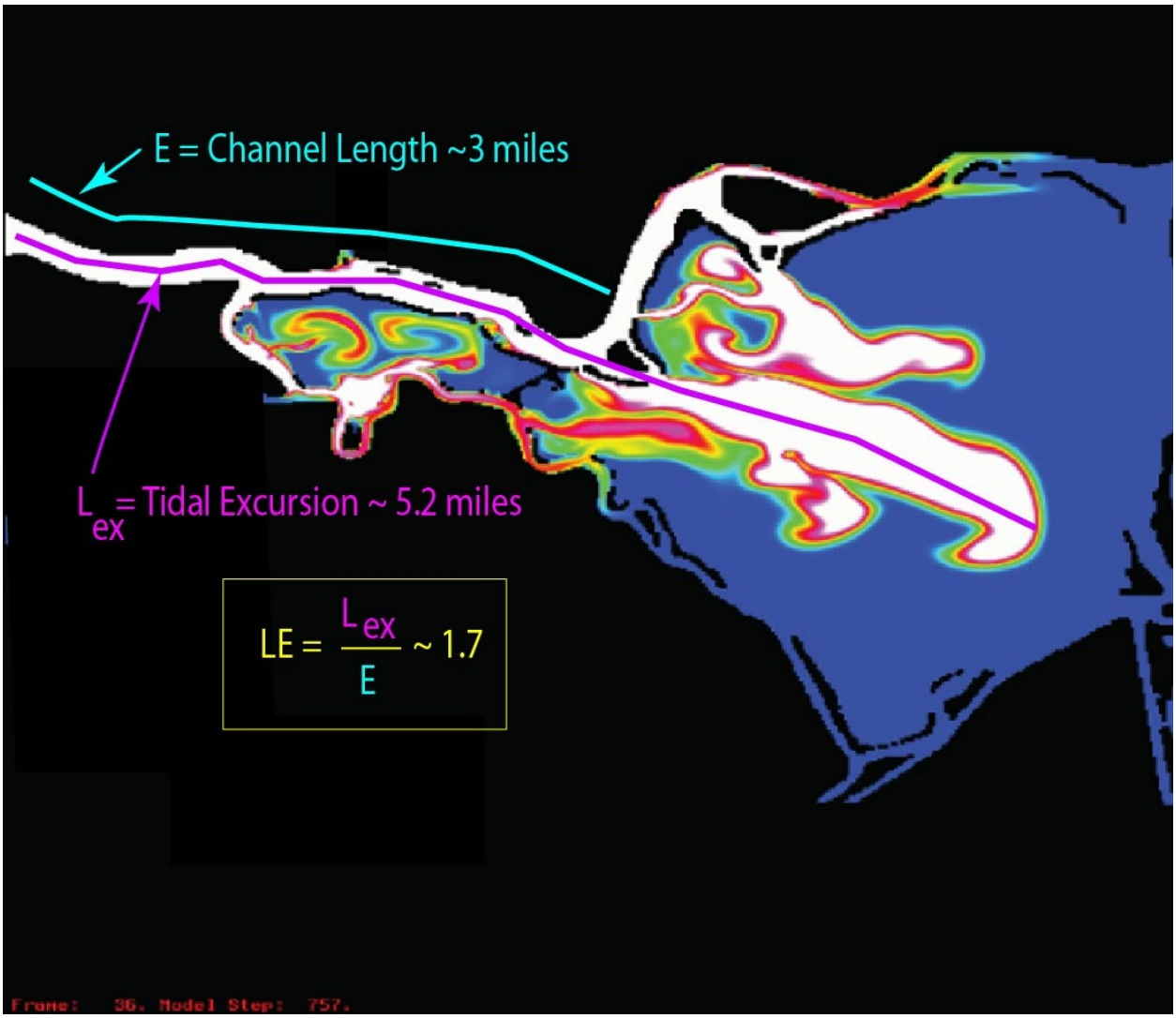

NOTE: The warmer colors represent the tidal excursion of the release of a dye in the entrance of False River in a numerical experiment after a complete flood (incoming) tide.

Figure 2.2.2-13 Physical illustration of channel length, *E*, and tidal excursion, L_{ex}, in Franks Tract.

An LE ratio that significantly exceeds unity (LE>1) does not guarantee increased dispersive mixing. Nonetheless, dispersive mixing clearly increases with the combination of an LE ratio much greater than 1 and a tidal excursion path that traverses bathymetric or planform complexity (Figure 2.2.2-10, Figure 2.2.2-11).

2.2.2.3 Results

The following discussion first describes the effect of the EDB on hydrodynamics in the Central Delta, beginning with changes in flows. This discussion recognizes that flows are often used as a proxy for temporal and spatial variability in velocities (e.g., not flow), the actual driver of transport via both dispersion and advection (Figure 2.2.2-1).

The effect of the EDB on velocities is discussed next, followed by the EDB's effect on salt transport, which quantifies the rate of salinity intrusion, or salt flux, past the sampling locations. These analyses are then used to describe the tidally averaged movements of the salt field.

Finally, the effect of the EDB on dispersive mixing potential is discussed, followed by the analysis of transport between Old and Middle rivers through Railroad Cut and the Woodward Canal.

Effects of the Emergency Drought Barrier on Flows

This section discusses effects of the EDB on net flows and tidal flows separately because the forcing mechanisms are different and there is a large difference in their orders of magnitude. Accordingly, the analysis in this and subsequent sections makes heavy use of a temporal decomposition of the measured flows, velocities, and salinities into net and tidal flows. For example, net flows in the Central Delta are created mostly by the combined influence of Sacramento River inputs, DCC gate operations, and exports, where the combined effects of these assets are (somewhat) controllable by humans but are generally small relative to the effect of the tides—in the case of Figure 2.2.2-6B, less than a couple of percent. Nevertheless, both net flows and tidal dispersion contribute to salinity intrusion into, within, and out of Franks Tract: Both dispersive mixing by the tidal currents (with the salinity gradient moving from the bay toward the pumps) and net flows (driven mostly by exports) are generally directed toward the pumps.

Tidal Flows

Introduction and Overview

Dispersive mixing into Franks Tract through False River is the primary transport mechanism the EDB was intended to eliminate in order to keep salinity from intruding into Franks Tract, then into the South Delta toward the pumps. Accordingly, this section focuses on the changes in tidal flows that create transport via dispersion.

Figure 2.2.2-14 presents time series plots of flows from a relatively broad region in the Delta. These flows were measured at data collection locations where the EDB had little to no effect. This approach was followed to document the EDB's sphere of influence on hydrodynamics.

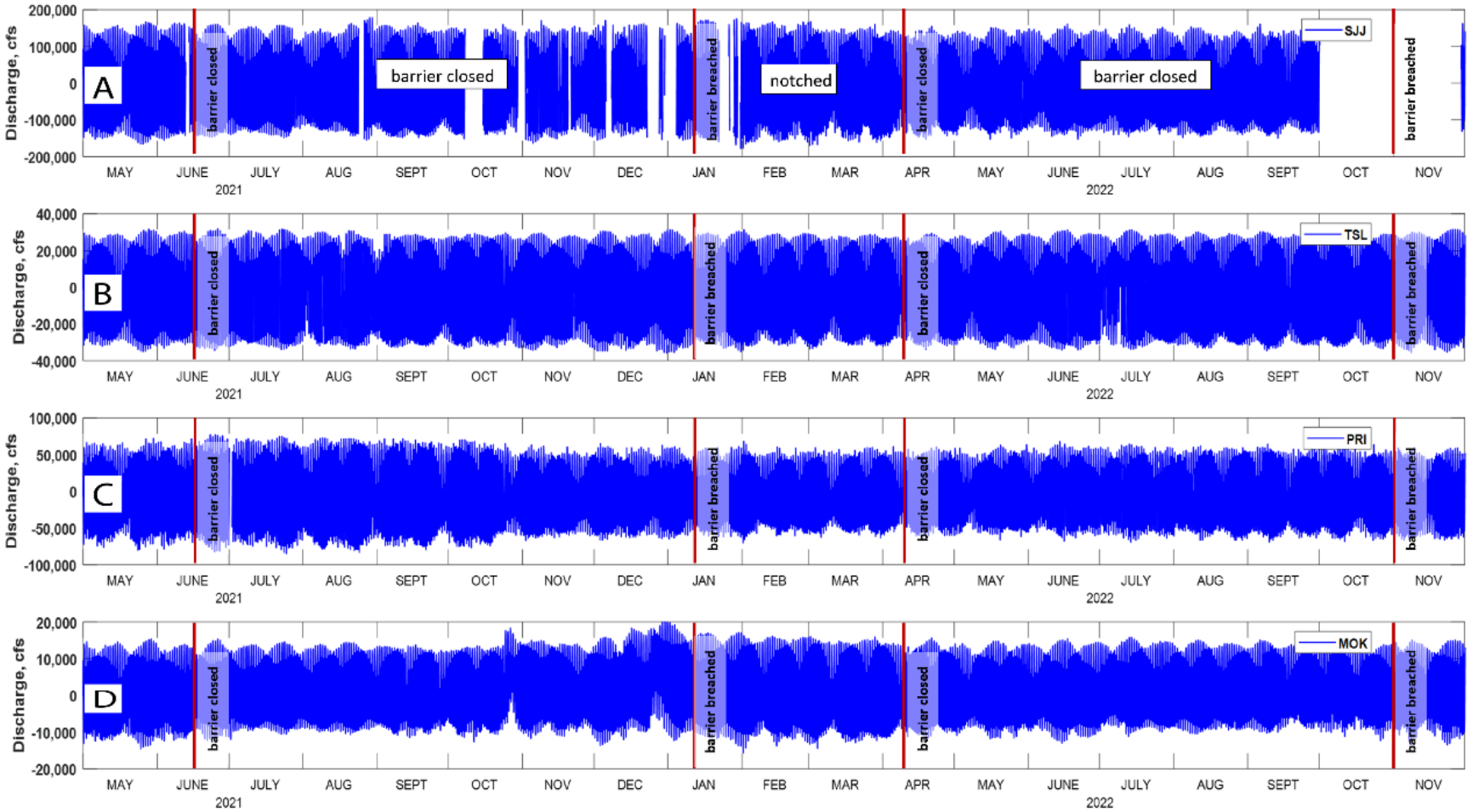

NOTES: cfs = cubic feet per second; MOK = Mokelumne River; PRI = San Joaquin River at Prisoner's Point; SJJ = San Joaquin River at Jersey Point; TSL = Threemile Slough at San Joaquin River.

Figure 2.2.2-14 Time series plots of measured discharge: (A) San Joaquin River at Jersey Point, (B) Threemile Slough, (C) San Joaquin River at Prisoner's Point, (D) Mokelumne River.

The time series plots shown in Figure 2.2.2-14 are presented without discussion, except to show that the effect of the EDB on hydrodynamics was limited to Middle River and the channels that directly connect to Franks Tract, as discussed below.

Elimination of the strong tidal flows—and by association, the velocities—in False River resulted in a redistribution (**Figure 2.2.2-15**, **Table 2.2.2-1**) of tidal flows in Middle River and the channels that directly connect to Franks Tract. The order-of-magnitude changes in tidal flows identified in Figure 2.2.2-15 and Table 2.2.2-1 were estimated from time series plots shown in **Figure 2.2.2-16**.

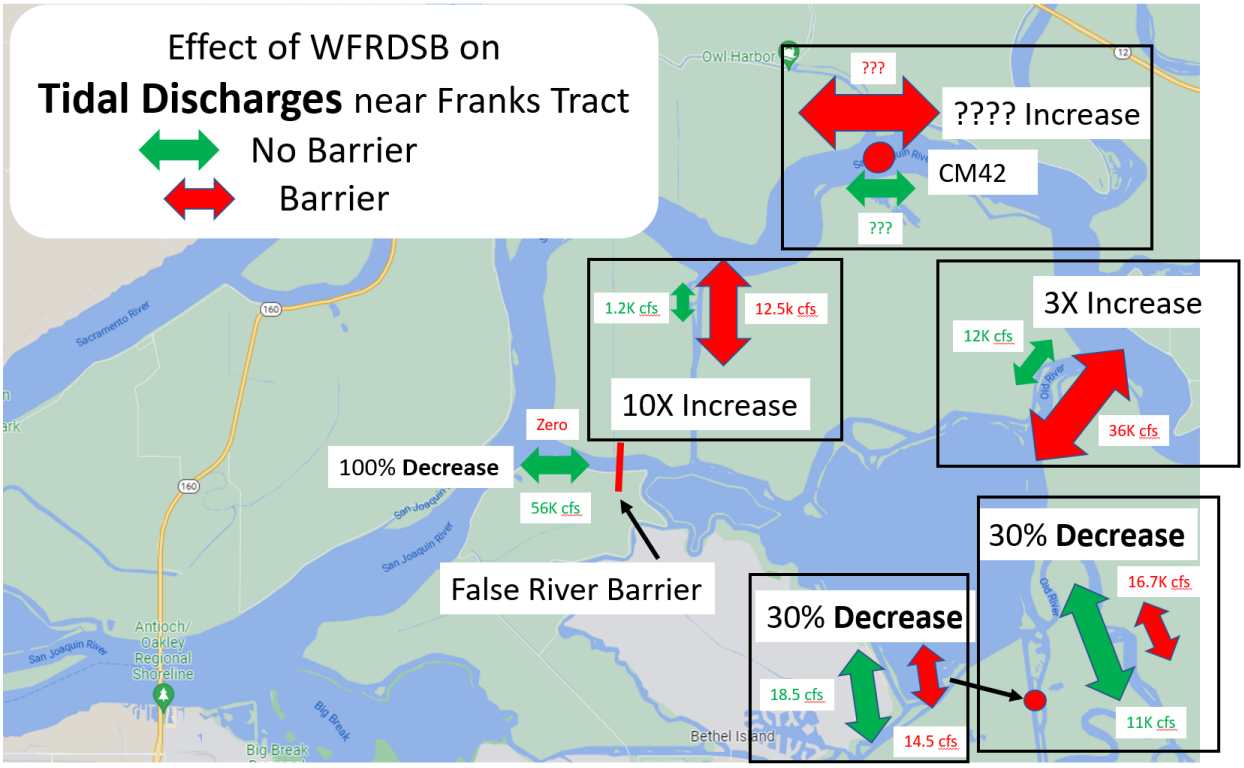

NOTE: The scale of the arrows represents the amplitude of tidal discharges: Green arrows = without the barrier; red arrows = with the barrier installed.

Figure 2.2.2-15 Conceptual illustration of the effect of the West False River drought salinity barrier on tidal discharges.

Given that roughly 20 percent of the total tidal discharge entering the Delta passes through False River into Franks Tract, it is surprising that the effect of the EDB was limited to the channels that directly exchange with Franks Tract, the San Andreas Shoal Reach, and Middle River near Holt (HLT). These channels are represented by the red dots on the map in Figure 2.2.2-3 and the time series are shown in **Figure 2.2.2-17** and **Figure 2.2.2-18**.

TABLE 2.2.2-1
HYDRODYNAMIC CONDITIONS WITH AND WITHOUT THE WEST FALSE RIVER DROUGHT SALINITY BARRIER INSTALLED AND CHANGES FOR THE CHANNELS IN THE FRANKS TRACT REGION

	Station ID	Channel Length Lch (mi)	Discharge Amplitude, Q (cfs)			Velocity Amplitude, V (ft/s)			Tidal Excursion, Lex (mi)			Lagrangian/Eulerian Ratio (LE Ratio)		
			No Barrier	Barrier Installed	Change	No Barrier	Barrier Installed	Change	No Barrier	Barrier Installed	Change	No Barrier	Barrier Installed	Change
	TSL	3.3	31,000	31,000	None	2.2	2.2	1 X	9.2	9.2	None	2.8	2.8	None
Inputs into Franks Tract	FAL	3.0	56,000	0	NA	2.6	0.0	NA	5.2	0.0	NA	1.7	NA	NA
	FCT	1.8	1,200	12,500	10.4 X	0.5	2.3	4.6 X	1.4	6.2	4.6 X	0.8	3.4	4.3 X
	OSJ	1.1	12,000	36,000	3 X	1.0	2.4	2.4 X	2.7	5.9	2.4 X	2.5	5.4	2.2 X
Output from Franks Tract	HOL	1.6	18,500	14,500	0.7 X	1.3	1.2	0.92 X	3.50	3.24	0.92 X	2.2	2.0	0.9 X
	ORQ	2.8	16,700	11,000	0.7 X	1.2	0.8	0.67 X	3.24	2.16	0.67 X	1.2	0.8	0.7 X

NOTES: Increase | Decrease | Dispersive | Non-dispersive

cfs = cubic feet per second; FAL = False River; FCT = Fisherman's Cut; ft/s = feet per second; HOL = Holland Cut near Bethel Island; ID = identification; mi = miles; NA = not applicable; ORQ = Old River at Quimby Island; OSJ = Old River at Franks Tract near Terminous; TSL = Threemile Slough at San Joaquin River.

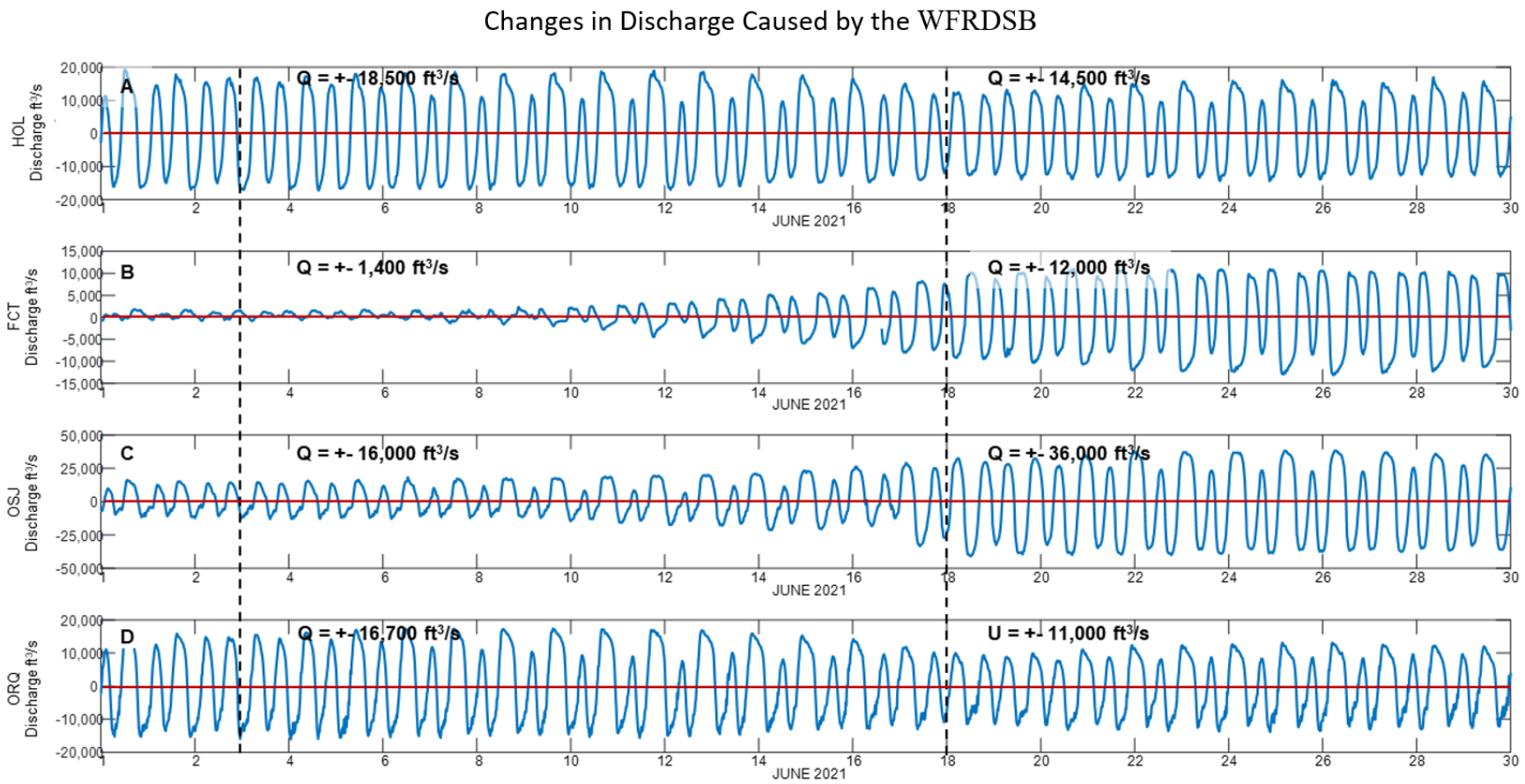

NOTES: FCT = Fisherman's Cut; ft^3/s = cubic feet per second, cfs; HOL = Holland Cut; ORQ = Old River at Quimby Island; OSJ = Old River at Franks Tract.
The dashed vertical lines on June 3 and June 18, 2021, indicate the start and the completion of barrier installation, respectively.

Figure 2.2.2-16 Time series plots of as-measured discharge before barrier installation and after completion of barrier installation: (A) Holland Cut, (B) Fisherman's Cut, (C) Old River at Franks Tract, (D) Old River at Quimby Island.

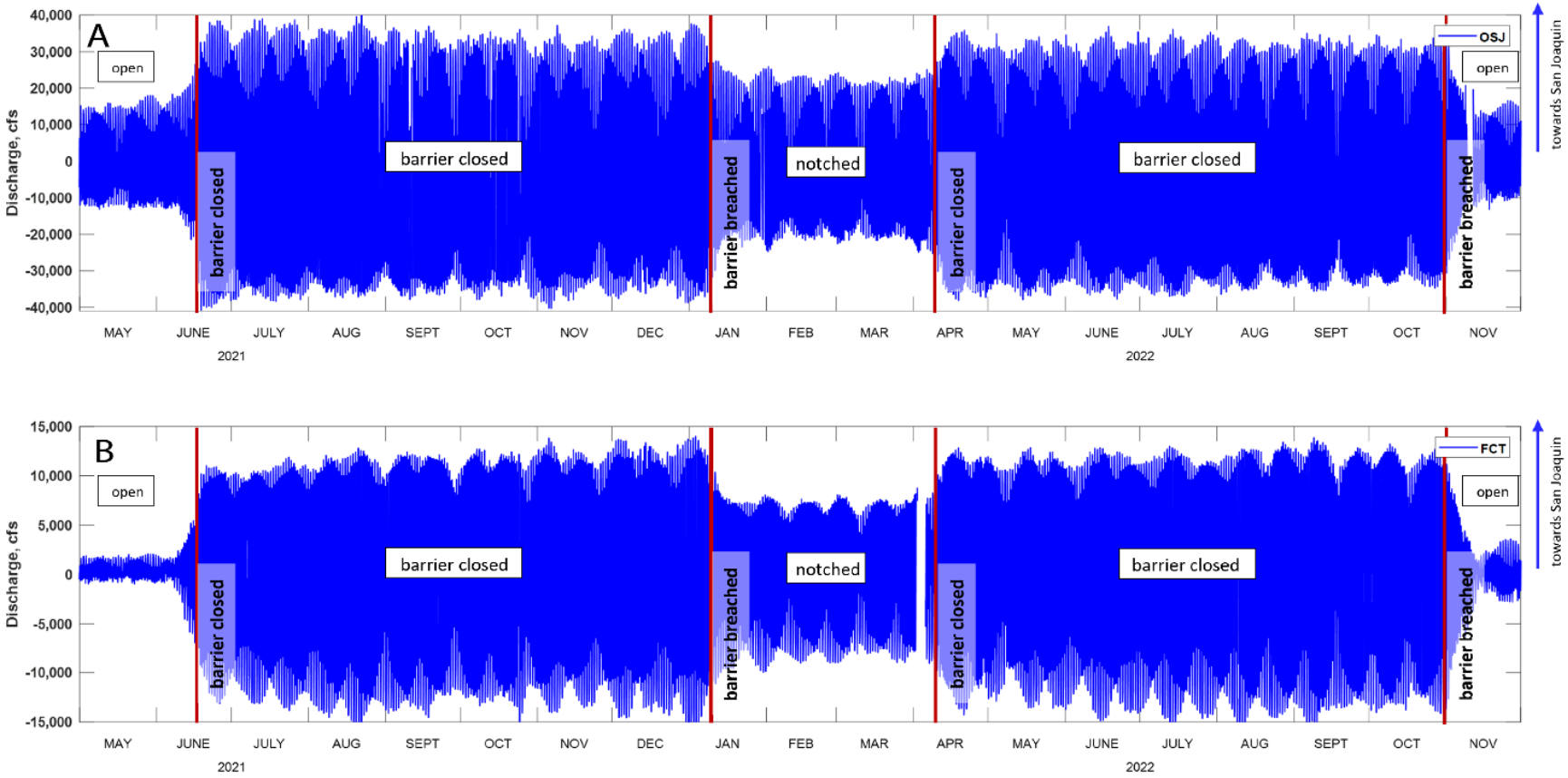

NOTES: cfs = cubic feet per second; FCT = Fisherman's Cut; OSJ = Old River at Franks Tract.

Figure 2.2.2-17 Time series plots of measured discharge: (A) Old River at Franks Tract, (B) Fisherman's Cut.

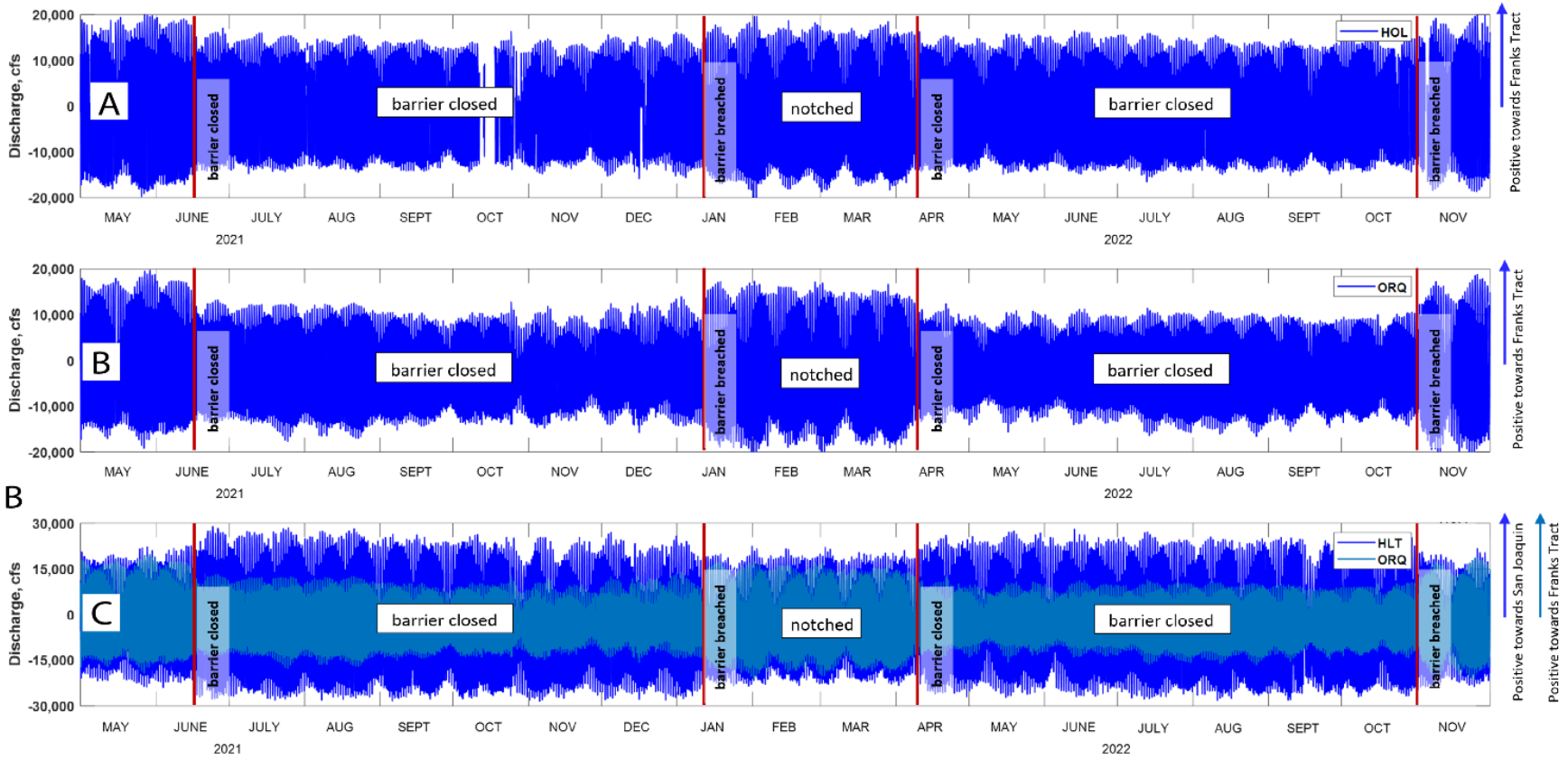

NOTES: cfs = cubic feet per second; HLT = Middle River near Holt; HOL = Holland Cut; ORQ = Old River at Quimby Island.

Figure 2.2.2-18 Time series plots of measured discharge: (A) Holland Cut, (B) Old River at Quimby Island, (C) Middle River near Holt.

The channels that are the next most proximate to Franks Tract, represented by the green dots in Figure 2.2.2-3, show little to no effect from the EDB (Figure 2.2.2-14). These monitoring stations include San Joaquin River at Jersey Point (SJJ) (Figure 2.2.2-14A), Threemile Slough at San Joaquin River (TSL) (Figure 2.2.2-14B), San Joaquin River at Prisoner's Point (PRI) (Figure 2.2.2-14C), the Mokelumne River (MOK) (Figure 2.2.2-14D), and Little Potato Slough (not shown).

When the EDB was installed, tidal flows increased in the San Andreas Shoal Reach of the San Joaquin River (not shown, inferred from mass conservation), OSJ (Figure 2.2.2-17A), FCT (Figure 2.2.2-17B), Dutch Slough (not shown), and HLT (Figure 2.2.2-18C), and decreased at HOL (Figure 2.2.2-18A) and ORQ (Figure 2.2.2-18B).

The channels most affected by the EDB were the "input" channels north of Franks Tract, OSJ and FCT (Figure 2.2.2-17); the "output" channels southeast of Franks Tract, HOL and ORQ (Figure 2.2.2-18A and Figure 2.2.2-18B); and Middle River near Holt (HLT) (Figure 2.2.2-18C).

Details

The EDB affected tidal discharges at the following locations (see also Table 2.2.2-1):

- **Old River at Franks Tract near Terminous (OSJ)** (Figure 2.2.2-17A). When the EDB was installed, tidal discharge levels at OSJ increased dramatically, from ±12,000 cfs to ±35,000 cfs. Tidal discharges declined from ±35,000 cfs to ±20,000 cfs when the barrier was notched, and pre-barrier values of ±12,000 cfs resumed after the EDB was removed.
- **Fisherman's Cut (FCT)** (Figure 2.2.2-17B). Effects of the barrier at FCT were twofold:
  - As at OSJ, tidal discharge levels at FCT increased dramatically—from ±2,000 cfs to ±12,000 cfs—when the EDB was installed. Tidal discharges declined from ±12,000 cfs to ±6,500 cfs when the barrier was notched, then decreased to ±4,000 cfs after the notch was filled, representing an increase of ±2,000 cfs from the pre-barrier condition after the EDB was removed. The change from ±2,000 cfs pre-barrier to ±4,000 cfs post-barrier was likely caused by scour associated with the increase in velocity in this channel that increased channel capacity in FCT.
  - The barrier effectively reversed the direction of the tidal currents in Fisherman's Cut relative to the tidal current direction in the San Joaquin River. This occurred because the EDB alters the tidal phase difference between the San Joaquin River and False River at their

junctions with Fisherman's Cut. All surface water flows are water surface slope driven—water flows downhill, or from a higher to a lower water surface elevation—and the tides are no different. In the Delta's narrower, shorter, usually human-made channels (**Figure 2.2.2-19**) that connect larger channels, the tidal phase differences between the larger channels create water surface slopes that drive the direction and amount of the exchanges within the connection channels, rather than tide wave propagation.

The EDB changes this tidal-phase-difference relationship: When the EDB is in place, the tide mostly propagates into Franks Tract through Old River at OSJ and then into False River, instead of propagating directly into Franks Tract, as occurs when the barrier is not installed. Without the barrier, water in Fisherman's Cut during a San Joaquin River ebb tide (positive velocities by convention) travels from the San Joaquin River south into False River, then northward back into the San Joaquin River on San Joaquin River flood tides. This reversal has the effect of freshening salty water exiting Franks Tract into the San Joaquin River (if it is salty in Franks Tract).

- **Holland Cut near Bethel Island (HOL)** (Figure 2.2.2-18A). When the EDB was installed, tidal discharge at HOL decreased from ±20,000 cfs to ±12,000 cfs. Tidal discharges showed no appreciable change from pre-barrier conditions when the barrier was notched, and pre-barrier values of ±20,000 cfs resumed after the EDB was removed.
- **Old River at Quimby Island (ORQ)** (Figure 2.2.2-18B). When the EDB was installed, tidal discharge at ORQ decreased from ±18,000 cfs to ±12,000 cfs. Tidal discharges showed no appreciable change from pre-barrier conditions when the barrier was notched, and pre-barrier values of ±18,000 cfs resumed after the EDB was removed.
- **Middle River near Holt (HLT)** (Figure 2.2.2-18C). Similar to OSJ and FCT, tidal discharge at HLT increased when the EDB was installed, from ±16,000 cfs to ±28,000 cfs. Installation of the notch did not appreciably change the discharges from their pre-barrier levels, and tidal discharges were reduced to ±12,000 cfs after the EDB was removed.

In summary, the EDB had a localized, Franks Tract–centric effect on tidal flows. This effect was mostly limited to the stations directly connected to Franks Tract, but the EDB also affected Middle River near Holt (HLT). Tidal discharges increased salinity intrusion into Franks Tract, while increased dispersive mixing of fresh water from Middle River into Old River from Connection Slough was observed at HLT.

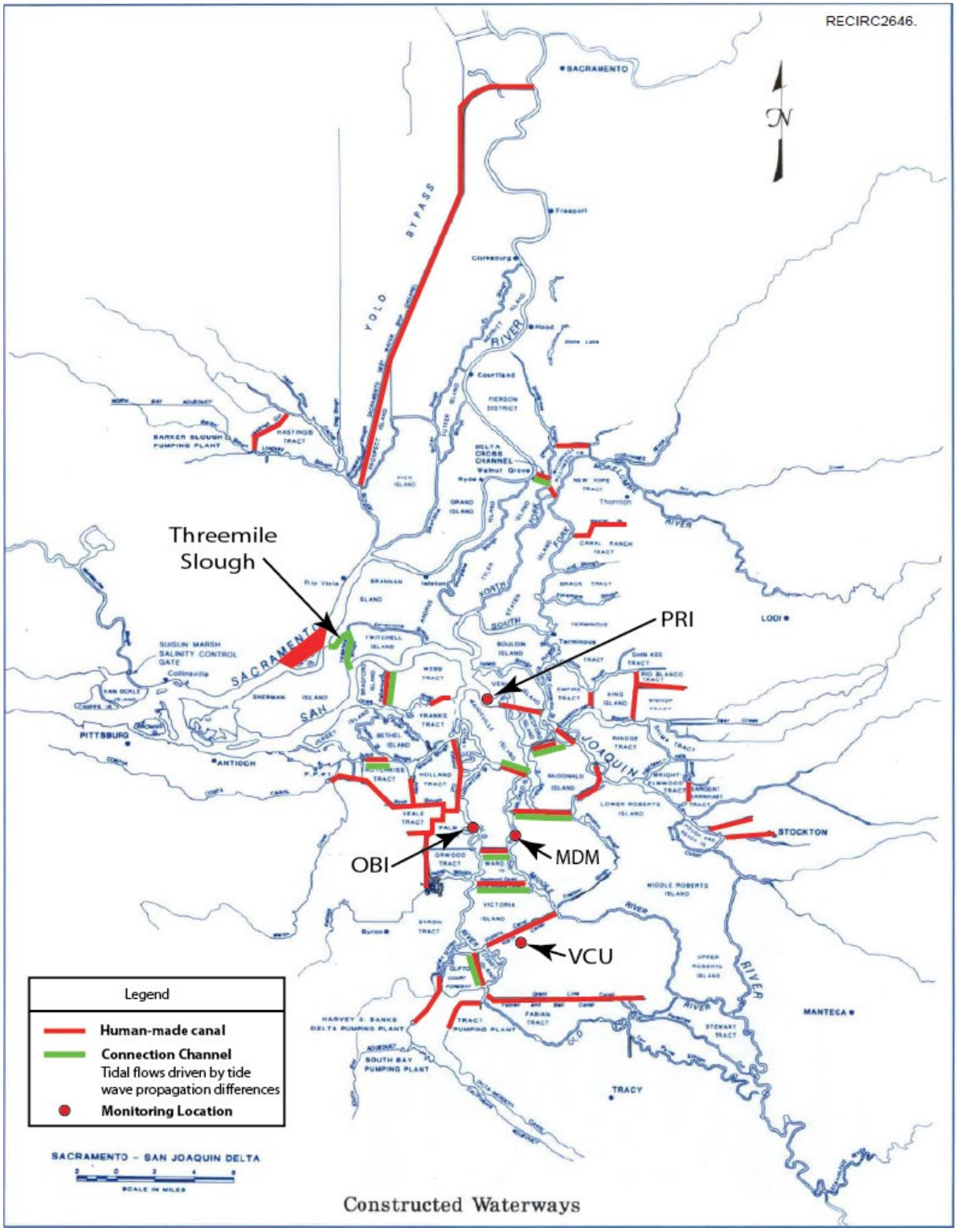

NOTES: MDM = Middle River at Middle River; OBI = Old River at Bacon Island; PRI = San Joaquin River at Prisoner's Point; VCU = Victoria Canal near Byron.
Base map from *Sacramento–San Joaquin Delta Atlas* (California Department of Water Resources 1995).

Figure 2.2.2-19 Human-made and connection channels in the Delta and flow and water quality stations at Old River at Bacon Island, Victoria Canal near Byron, and San Joaquin River at Prisoner's Point.

Tidal discharges in both "input channels" (OSJ and FCT) increased significantly with the EDB installed, while tidal discharges in the "output channels" (HOL and ORQ) decreased slightly. Overall, the general responses of HOL and ORQ to the barrier were similar: At these stations, tidal discharges decreased with the EDB installed, but the notch appeared to have a negligible effect on tidal discharges over non-EDB conditions.

Finally, under non-EDB conditions, most of the tidal exchange into the South Delta occurred at HOL+ORQ (approximately 38,000 cfs), compared to approximately 16,000 cfs at HLT. In contrast, during EDB conditions, HOL+ORQ tidal discharges were reduced to approximately 24,000 cfs while HLT tidal discharges increased to approximately 28,000 cfs.

Effect of the Notched Emergency Drought Barrier on Tidal Flows

Given the width and depth of the invert, the effect of the notch on tidal flows (Figure 2.2.2-14 through Figure 2.2.2-18) was surprisingly minimal, with changes on the order of 10 percent over no-barrier conditions. Consequently, with the notched barrier, conditions in all the channels discussed above were roughly the same as non-barrier conditions. However, the effect of notching the EDB on near-field hydrodynamics was extraordinary: the greatest peak velocities ever measured in the Delta of 7–9 ft/s, whereas typical peak velocity in the Delta is on the order of 1.5 to 2 ft/s.

Net Flows

Background

Even though net flows are generally small in the Central Delta relative to tidal flows (Figure 2.2.2-6B), they remain important in transporting salt—the reason that exports are curtailed during the summer and during droughts.

Like tidal flows, net flows were redistributed throughout the Central Delta by the EDB. For example, while tidal flows in False River are around 56,000 cfs (Table 2.2.2-1), net flows can be about 3,000 cfs (or nearly 5 percent of tidal flows). Figure 2.2.2-7C shows that net flows in False River are closely associated with increases in exports that occurred before barrier installation. This at least partially verifies that the net flows are not completely wrong, and most often their temporal variability closely follows the forcing variables one would expect—in this case, temporal variability in exports and in the tidally averaged salinities. The redistribution of net flows is particularly relevant in contributing to the "freshening" of Middle River, as discussed below under "Effects of the Emergency Drought Barrier on Tidally Averaged Salinity Distributions."

Net Flows Contributing to Dispersive Transports

Net flows into Franks Tract can contribute to additional dispersive mixing via tidal trapping and pumping because net flows increase net velocities, thus

increasing tidal excursions into Franks Tract while simultaneously reducing tidal excursions out of Franks Tract. Together the differences in the incoming and outgoing tidal excursions contribute to the trapping of salt in Franks Tract in proportion to the strength of the net current. (The net flows increase the amount of salt that enters Franks Tract while reducing the amount that leaves it.) The importance of net flow–driven asymmetric tidal excursions on dispersive transports is an underappreciated consequence of net flows that shows up as a dispersive flux in the flux decompositions (last term in Equation 5) in the tidal deviations in salinity data.

Finally, the "freshening" of Middle River was observed in the salinity data when the EDB was installed (**Figure 2.2.2-20**B, light blue and red lines), which is supported by a change in the direction of the net flows. This observation suggests that the flow data are, at a minimum, in the right direction. Thus, fortunately, installation of the EDB likely contributed to the freshening of Middle River (Figure 2.2.2-20B), which reduced the overall salt loads in the export facilities.

Net flows into Franks Tract are strongly influenced by Sacramento River inflows and DCC gate operations in the northern portion of the Central Delta, which give way to increasing influences of exports and San Joaquin River inputs in the south. Water project operations in both the north and south can have a significant influence on transport into and through Franks Tract, even with the large volume of water that enters and exits Franks Tract twice a day, every day. Thus, Franks Tract acts as a hydrodynamic transition between the effects of SWP and CVP operations in the north and in the south. All the while, items (5) through (8) listed below create high-frequency "noise" (e.g., with periods < 24 hours) while the tides create fortnightly and longer period variability, which can be observed in the net discharges and salt flux decomposition time series shown in the following sections.

The effects of the EDB on net flows are examined by placing them in the context of all the other factors that can affect net flows. These other factors include, in approximate order of importance:

(1) Sacramento River inflows at Freeport (FPT) (Figure 2.2.2-5A).

(2) DCC gate operations. (Gray bars in Figure 2.2.2-5A indicate periods when the DCC gates are open.)

(3) San Joaquin River inflows at Vernalis (VNS).

(4) Export rates.

(5) Net flows through the Golden Gate.

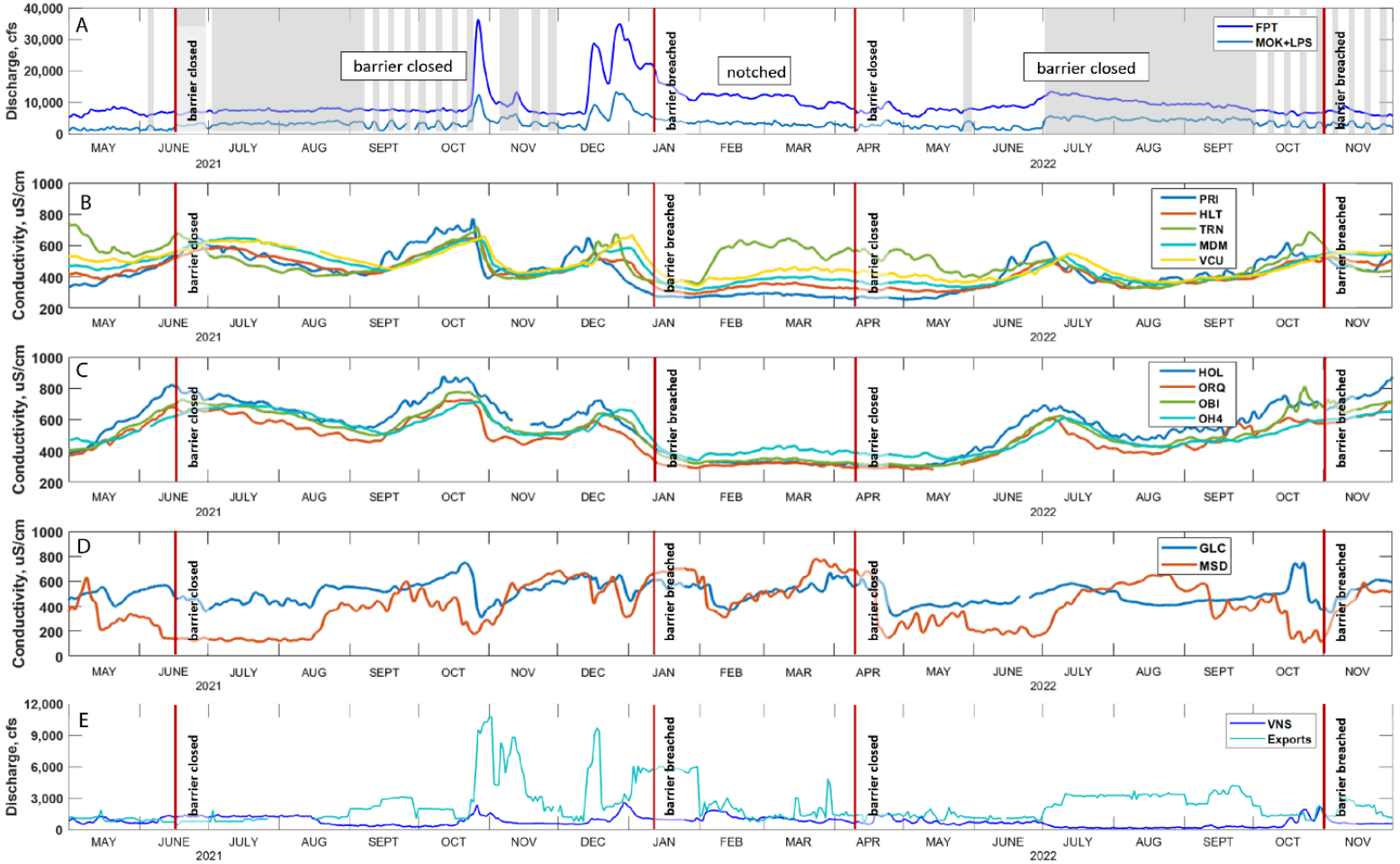

NOTES: µS/cm = microsiemens per centimeter; cfs = cubic feet per second; FPT = Sacramento River at Freeport; HLT = Middle River near Holt; HOL = Holland Cut; LPS = Little Potato Slough; MDM = Middle River at Middle River; MOK = Mokelumne River; OBI = Old River at Bacon Island; OH4 = Old River at Highway 4; ORQ = Old River at Quimby Island; PRI = San Joaquin River at Prisoner's Point; TRN = Turner Cut; VCU = Victoria Canal near Byron; VNS = San Joaquin River at Vernalis

Figure 2.2.2-20 Time series plots: (A) Measured discharge in the Sacramento River at Freeport and sum of tidally averaged discharge at Mokelumne River and Little Potato Slough; (B) conductivity in the San Joaquin River at Prisoner's Point, Middle River near Holt, Turner Cut, Middle River at Middle River, and Victoria Canal near Byron; (C) conductivity at Holland Cut, Old River at Quimby Island, Old River at Bacon Island, and Old River at Highway 4; (D) discharge entering the Delta from San Joaquin River at Vernalis and exports.

(6) Net flows in the Delta. Net flows both through the Golden Gate and in the Delta are due to non-linearities in the equations of motion, where both contribute to the "filling and draining" of the Delta (Monismith 2016).

(7) Atmospheric pressure changes (important mostly in the spring and fall during the transitions between the summer's high-pressure conditions and the winter's low-pressure conditions).

(8) Persistent and strong winds (blowing at more than 20 miles per hour for more than a day or so) that occur mostly during prolonged, multi-day winter storm events.

The effect of the EDB is examined in the context of items (1) through (4) above; items (5) through (8) are beyond the scope of this report.

Exchange of Sacramento and Mokelumne River Water into the Central Delta

A portion of the Sacramento River inflows (FPT) enters the Central Delta from the Mokelumne River (MOK) and Little Potato Slough (LPS), having traversed either Georgiana Slough when the DCC gates are closed or both Georgiana Slough and the DCC when the gates are open. More Sacramento River water enters the Central Delta when the DCC gates are open, the reason that the DCC was constructed.

Figure 2.2.2-21 shows flows entering the Central Delta from the Mokelumne River system, the spatial and temporal distribution between MOK and LPS flows, and the effect of the status of the DCC gates. The percentages of flows (Figure 2.2.2-21C) entering the San Joaquin River at MOK and LPS are highly variable, depending on the DCC gate status and the Sacramento River flow rate. Overall, a greater percentage of Sacramento River water that passes through the Mokelumne River system enters the San Joaquin River when Sacramento River flows are low and the DCC gates are open; this is the reason that the gates are maintained in an open position as often as possible. Under all conditions, a higher percentage of net flow enters the San Joaquin River at station MOK, providing most of the water needed to repel salinity intrusion in the San Joaquin River and most of the water exported from the Delta. The percentage of water entering the San Joaquin River from MOK is reduced (by approximately 25 percent) as more water enters the San Joaquin River at LPS.

Under normal summertime Sacramento River inflows (FPT flows of approximately >12,000 cfs), exports and San Joaquin River flows have very little influence on the quantity of water that enters the Central Delta from the Mokelumne River system when the DCC gates are closed. However, exports may have an influence when the gates are open.

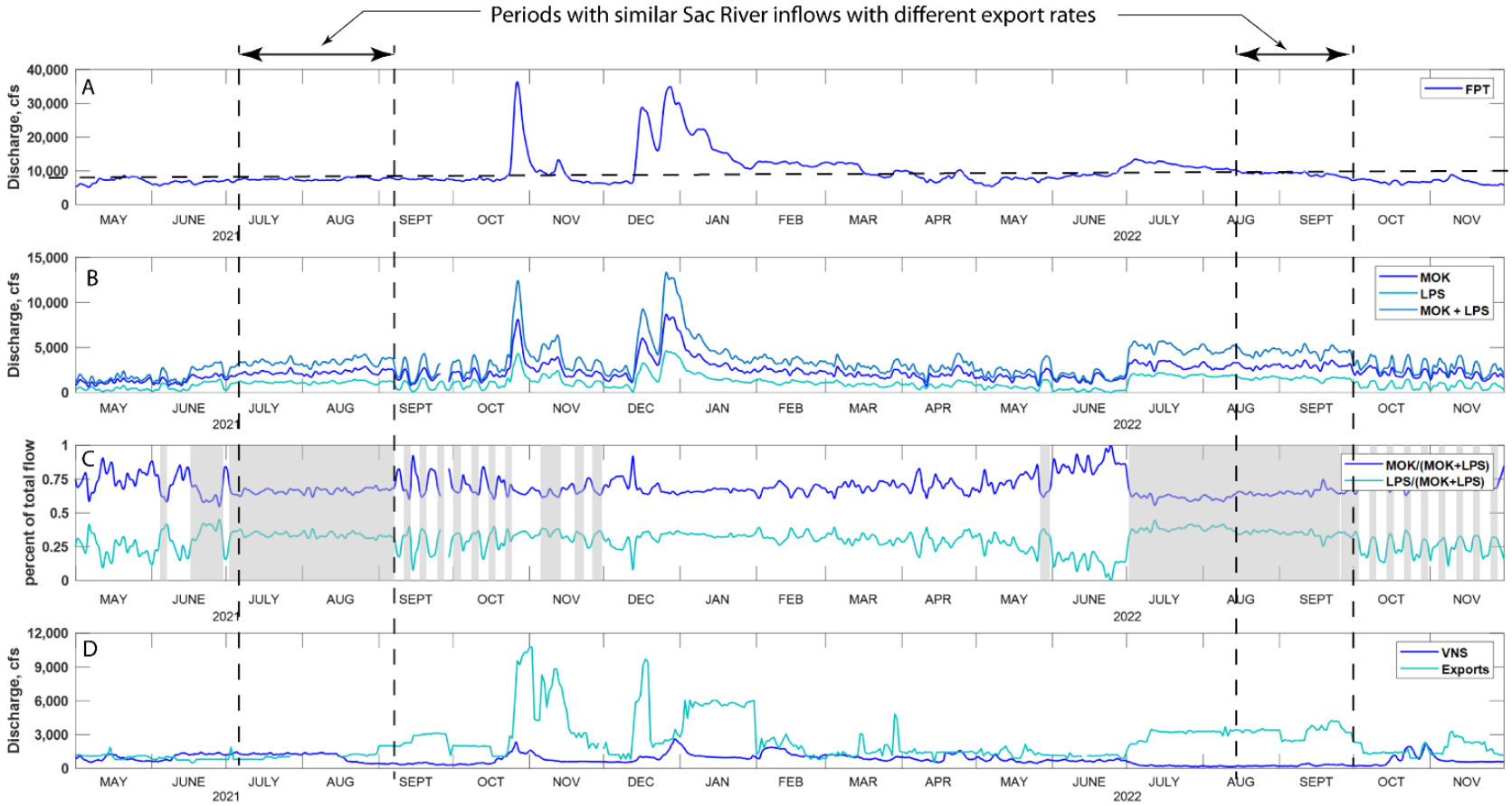

NOTES: cfs = cubic feet per second; FPT = Sacramento River at Freeport; LPS = Little Potato Slough; MOK = Mokelumne River; VNS = San Joaquin River at Vernalis. Shading in panel C represents periods when the Delta Cross Channel gates are open.

Figure 2.2.2-21 Time series plots: Measured discharge at (A) Sacramento River at Freeport and (B) Mokelumne River, Little Potato Slough, and MOK+LPS; (C) percentages of flow from Mokelumne River system as a whole (MOK+LPS) and from Little Potato Slough, LPS/(MOK+LPS); (D) discharge entering the Delta from San Joaquin River at Vernalis and exports.

This influence can be seen by comparing periods of low exports (mid-June through early September 2021) and high exports (in this case, approximately 3,000 cfs in mid-August through September 2022), shown on the graphs between the black, dashed vertical lines in Figure 2.2.2-21. The combined inflow from the Mokelumne River system into the Central Delta was roughly twice as high during periods when the FPT flows were similar. It is unclear from this dataset whether the EDB had an influence on this observation, because the EDB was installed during both of these time periods.

Net Flows in the Input Channels to Franks Tract

The input channels, FCT and ORQ, mostly respond to Sacramento River flows that reach the Central Delta via the Mokelumne River system and DCC gate operations, as described above. As with tidal flows, net flows in these channels were the most affected by the EDB; however, both changed in magnitude and direction with changes in barrier state (**Figure 2.2.2-22**).

At Old River (OSJ) (Figure 2.2.2-22B), net discharge changed from toward the San Joaquin River pre- and post-EDB, then flipped to flowing into Franks Tract when the EDB was installed. Net flow at OSJ was essentially zero when the EDB was notched.

At Fisherman's Cut (FCT) (Figure 2.2.2-22C), net discharge changed from toward Franks Tract pre- and post-EDB, then flipped to flowing into the San Joaquin River when the EDB was installed. (The same thing occurred with the tidal flows discussed above.) And, as at OSJ, net flow at FCT was essentially zero when the EDB was notched. The notch may have acted like a weir, creating a hydraulic control on the tidally averaged water surface slope across the notch.

In summary, the net flow inputs into and out of Franks Tract are clearly coupled (as mass balance would dictate). For example, when the EDB is not installed, net flows entering Franks Tract flow toward the San Joaquin River at OSJ and into Franks Tract at FCT. In contrast, when the EDB is installed, net flows from the Mokelumne River system enter Franks Tract through OSJ and flow out of FCT into the San Joaquin River, and into Holland Cut at HOL and Old River at ORQ.

This observation (see **Figure 2.2.2-23**) reveals a problematic scenario. Such a scenario would arise if salinity were to significantly reach OSJ when net flows entering the San Joaquin River from the Mokelumne River system become too weak to repel salinity intrusion in the San Andreas Shoal Reach during an extreme drought (e.g., after barriers are installed in False River and in Sutter and Steamboat sloughs):

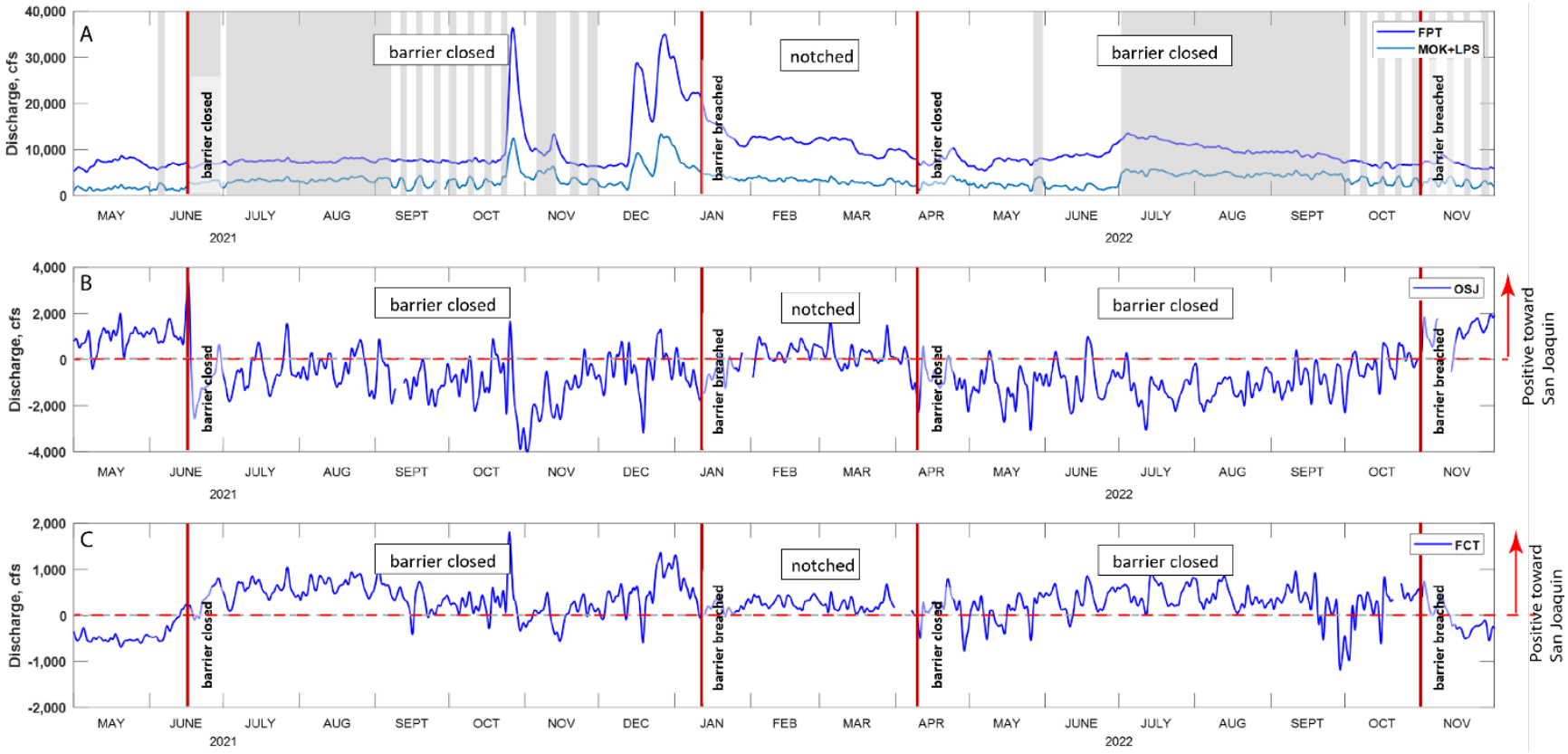

NOTES: cfs = cubic feet per second; FCT = Fisherman's Cut; FPT = Sacramento River at Freeport; LPS = Little Potato Slough; MOK = Mokelumne River; OSJ = Old River at Franks Tract. Horizontal red dashed lines represent a change in direction where the positive direction is indicated in the right margin.

Figure 2.2.2-22 Time series plots: (A) Measured discharge in the Sacramento River at Freeport and sum of tidally averaged discharge at Mokelumne River and Little Potato Slough; (B) tidally averaged discharge at Old River at Franks Tract; (C) tidally averaged discharge at Fisherman's Cut.

(1) Net flows from MOK would begin to fill both Franks Tract (through OSJ) and eventually Old River south of Franks Tract (via the net flows in HOL and ORQ) with salt.

(2) At the same time, dispersive mixing through OSJ would increase salt concentrations in Franks Tract if a significant spatial salinity gradient were created between the San Joaquin River and Franks Tract at OSJ. (See "Effects of the Emergency Drought Barrier on Dispersive Mixing [Potential]" section below.)

This scenario would accelerate a full stoppage of exports because both the net flows and dispersive mixing would increase salinity in Franks Tract. At best, this situation would create a transitory burst of salt into Old River from both advection from the net flows and dispersive mixing, making it nearly impossible for the SWP and CVP operators to continue pumping (which creates the net flows in HOL and ORQ) without exceeding municipal and industrial standards at the export facilities.

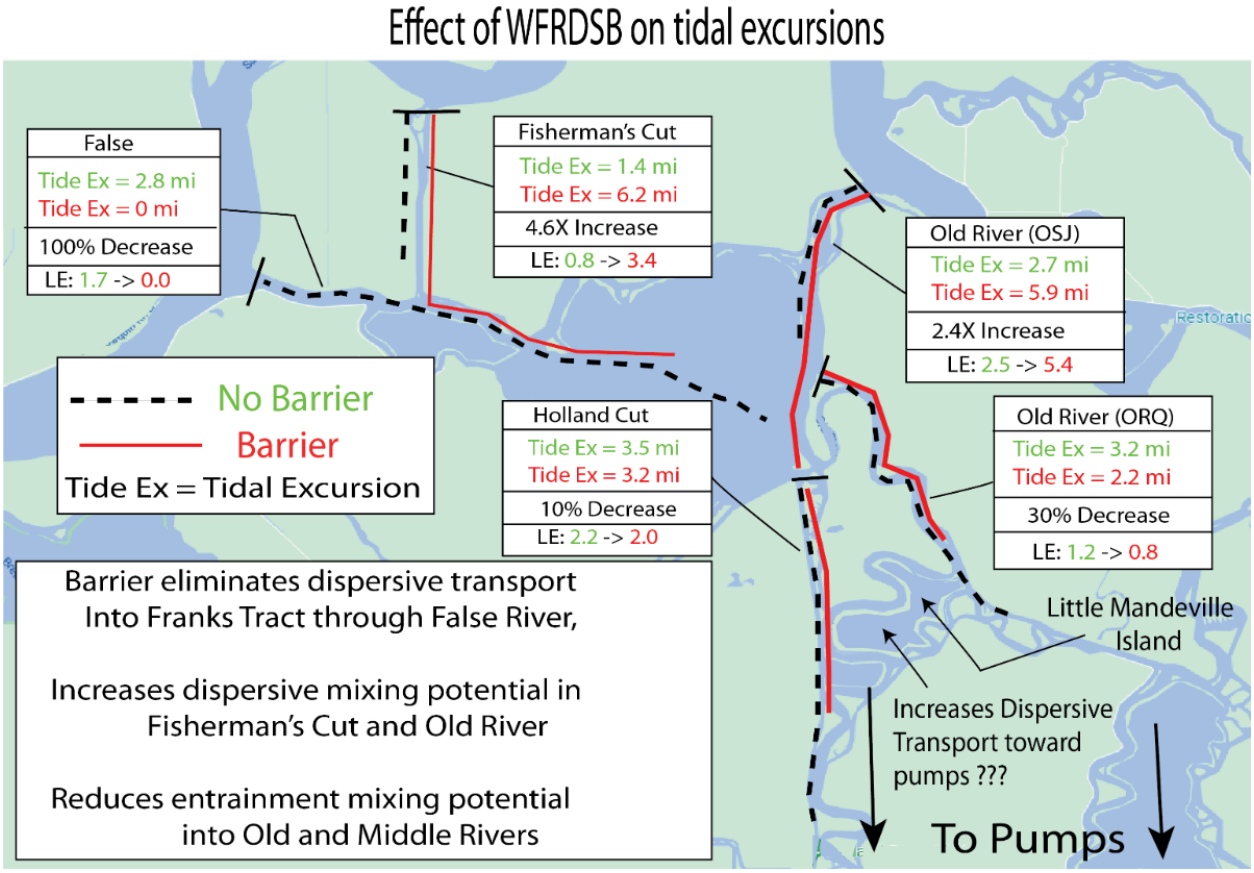

NOTES: LE = ratio of the tidal excursion to the characteristic channel length (or basin dimension); WFRDSB = West False River drought salinity barrier (emergency drought barrier).
The lengths of the lines illustrate the tidal excursions and LE ratios identified in red and green text: Dashed line and green text = without the barrier; red line and red text = with the barrier.

Figure 2.2.2-23 Conceptual illustration of the effect of the West False River drought salinity barrier on tidal excursions.

Net Flows in the Output Channels to Franks Tract and Middle River

Net flows in the output channels from Franks Tract and in Middle River were less affected by the EDB than the input channels described above, yet they are both strongly affected by both Sacramento River inflows and export rates. See the net-flow time series in Old and Middle rivers plotted in **Figure 2.2.2-24**; the discharge (Y-axis) scales in time series plots B, C, and D were varied to emphasize the coherence in the temporal response between these channels.

Of the channels that supply water to the pumps, Holland Cut near Bethel Island (HOL) (Figure 2.2.2-24B) contributes the least to the net flow entering the Old and Middle River corridor during low Sacramento River inflows and export rates, but net flows increase when both the inflows and export rates are high. The direction of the net flow in HOL and at ORQ shifted, from flowing into Franks Tract before installation of the EDB to flowing into the Old and Middle River corridor when the EDB was installed.

Middle River (HLT) and Old River (ORQ) (Figure 2.2.2-24C) provide the lion's share of the tidally averaged flow and were more strongly influenced by the EDB. Tidally averaged flow toward the pumps increased when the DCC gates were open (June–September 2021 and July–October 1, 2022) and when the EDB was installed; the flow decreased when the EDB was notched but remained toward the pumps after the barrier was removed.

Middle River is the main conduit of net flows toward the pumps. Accordingly, Middle River near Holt (HLT) (Figure 2.2.2-24D) responds strongly to Sacramento River inflows, export rates, and DCC gate operations. HLT responded less to the EDB than did either HOL or ORQ, apparently because Middle River is not directly connected to Franks Tract.

Fortunately for SWP and CVP operations, the water in Middle River is the freshest in the Central Delta. This is the reason that numerical modeling showed that restoring levees along the so-called "emergency pathway"—essentially Middle River and the Victoria Canal—was the quickest way the South Delta could be restored after multiple levee failures caused by an earthquake. Thus, one possible way of increasing the amount of fresh water available to the pumps in the aftermath of numerous levee failures in the Central and South Delta would be to place a barrier in False River.

Summary

Middle River (HLT) conveys most of the net discharge toward the pumps, followed by Old River (ORQ), and Holland Cut near Bethel Island (HOL) is the least responsive to the DCC and EDB. In most cases, HLT conveys more water toward the pumps than HOL and ORQ combined. ORQ is second in its contribution to the net flow toward the pumps and, of the output channels, responds most strongly to the status of the EDB.

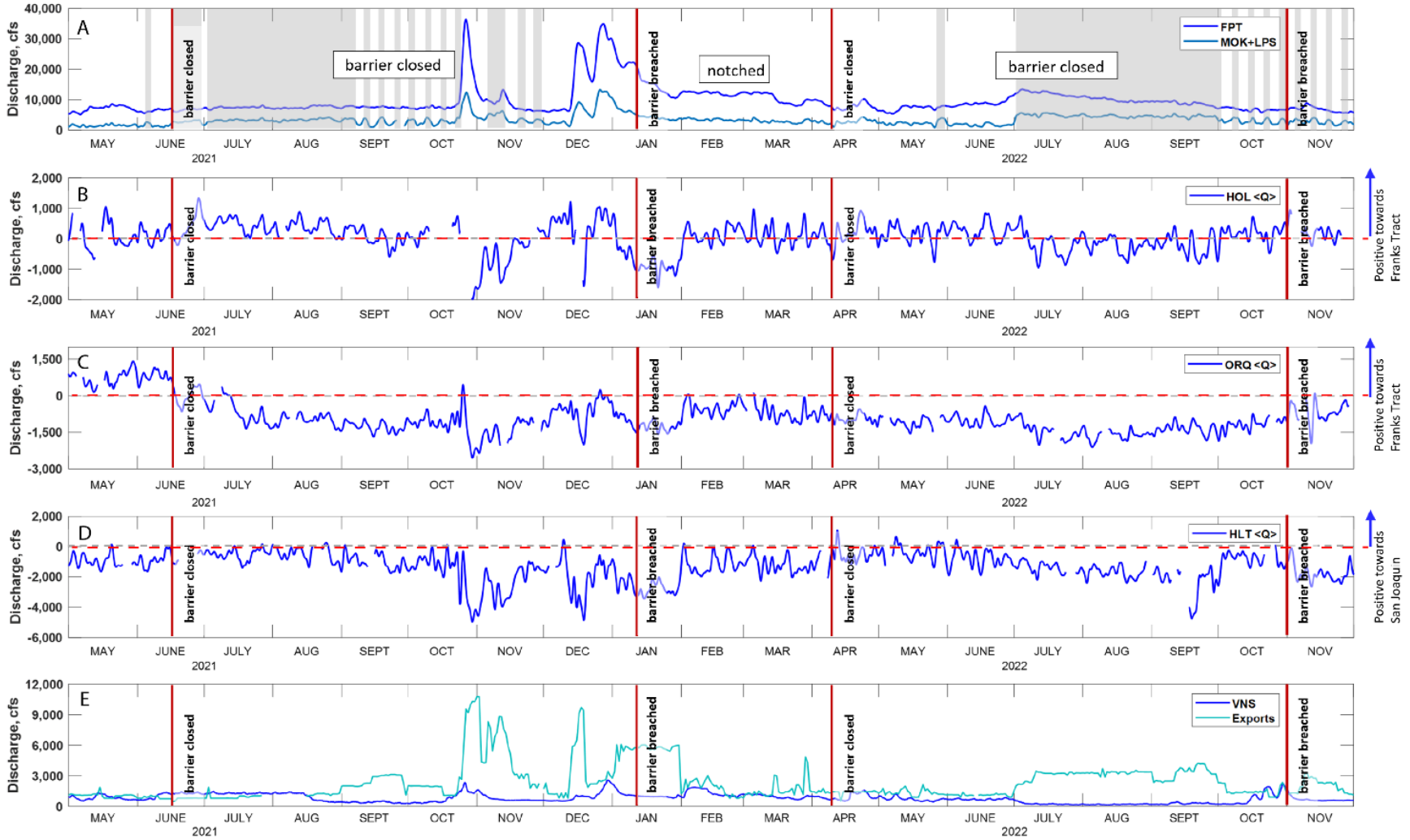

NOTES: cfs = cubic feet per second; FPT = Sacramento River at Freeport; HCT = Holland Cut; HLT = Middle River near Holt; LPS = Little Potato Slough; MOK = Mokelumne River; ORQ = Old River at Quimby Island; VNS = San Joaquin River at Vernalis. Horizontal red dashed lines represent a change in direction where the positive direction is indicated in the right margin.

Figure 2.2.2-24 Time series plots: (A) Measured discharge in the Sacramento River at Freeport and sum of tidally averaged discharge (net flow) at Mokelumne River and Little Potato Slough; (B) net flow at Holland Cut; (C) net flow at Old River at Quimby Island; (D) net flow at Middle River near Holt; (E) discharge entering the Delta from the San Joaquin River at Vernalis and exports.

The fact that ORQ provides the lion's share of the tidally averaged flow out of Franks Tract and was the most strongly influenced by the EDB is a problem for exports. For example, if salt were to reach Old River at Franks Tract near Terminous (OSJ), this would expedite the cessation of pumping from the Delta, because salt would be transported into Franks Tract by the tidally averaged flow at OSJ (Figure 2.2.2-24D), and possibly would be transported dispersively (Figure 2.2.2-17A). Finally, the net flows switched directions when the EDB was installed (Figure 2.2.2-24B through Figure 2.2.2-24D).

Effects of the Emergency Drought Barrier on Velocities

Net flows are often considered the sole control on transport in the Delta, because the SWP and CVP operators use manipulations of the net flows as their only tool to control salinity intrusion (e.g., State Water Board Decision 1460) or to move the salt field landward in accordance with the so-called "X2 standard" (the U.S. Fish and Wildlife Service Delta Smelt Biological Opinion Fall X2 Action).

Measurements of net flows are important; however, because they are used in combination with salinity measurements to quantify the magnitude and direction of salt transport (e.g., the salt flux), it is the interaction between the velocity and salt fields between stations that mechanistically controls both advective and dispersive transports in this system, as shown conceptually in Figure 2.2.2-1.

Net Velocities

Changes in net velocities either repel salinity intrusion, when directed seaward, or they increase it, when directed inland. For example, the SWP and CVP operators maintain seaward net velocities through reservoir releases (flows) and/or through changes in pumping to maintain salinity standards at key locations, such as Jersey Point and Emmaton (Figure 2.2.2-4).

Discharge and velocity are clearly correlated as discharge $Q=VA$, where V is the cross-sectionally averaged velocity and A is the cross-sectional area. Yet it is important to recognize that net velocities do the work of moving the salt field around. Accordingly, net velocities are not plotted in this report, following the standard practice of using changes in net flow as a surrogate for changes in net velocities.

Tidal Velocities

Tidal velocities are the driver of net horizontal dispersion, which evolves from the interaction between tidal velocities and salinity distributions within a tidal excursion of a monitoring location. As a generalization, bathymetric and planform variability within channels and in open water create spatial

variability in velocities, which in turn creates spatial variability in the salt field at tidal timescales. This combination of spatially variable velocities and salinity distributions creates net horizontal dispersion (see Appendix C for a description of conceptual dispersion models). **Figure 2.2.2-25** and Table 2.2.2-1 summarize the effect of the EDB on tidal velocities based on the time series data shown in **Figure 2.2.2-26**.

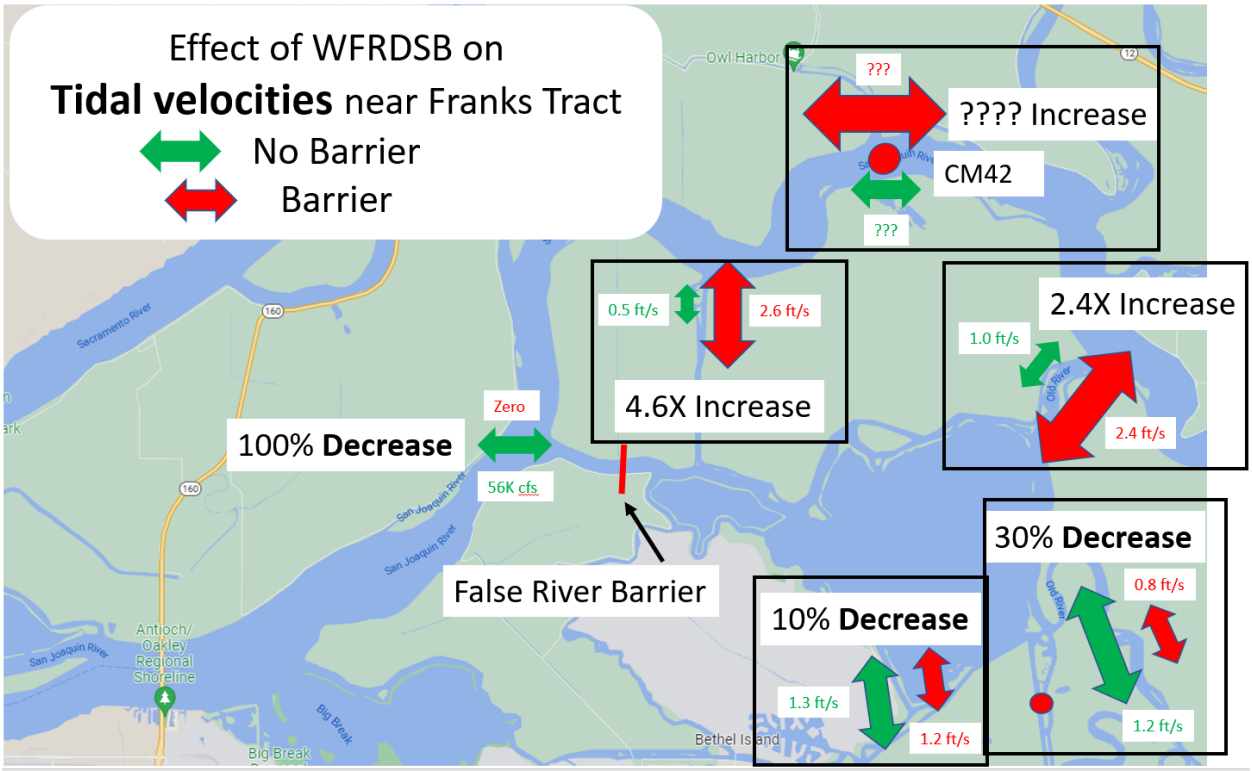

NOTES: WFRDSB = West False River drought salinity barrier (emergency drought barrier). The scale of the arrows represents the amplitude of tidal velocities: Green arrows = without the barrier; red arrows = with the barrier installed.

Figure 2.2.2-25 Conceptual illustration of the effect of the emergency drought barrier on tidal velocities.

Effects of the Emergency Drought Barrier on Salt (Fluxes) Transport

This section discusses changes in salt transport attributable to the EDB. As discussed previously, to maintain regulatory mandates in the Sacramento River, the SWP and CVP operators did not allow salinity to intrude very far past Jersey Point during the study period. Nevertheless, there is sufficient salinity in the Central and South Delta to use as a conservative tracer in this report to investigate the effect of the EDB on net advection of salt into and through Franks Tract. Thus, this section explores the impact of the EDB on the distribution of Sacramento River inputs, DCC gate operations, and exports on salt transport in the Central Delta.

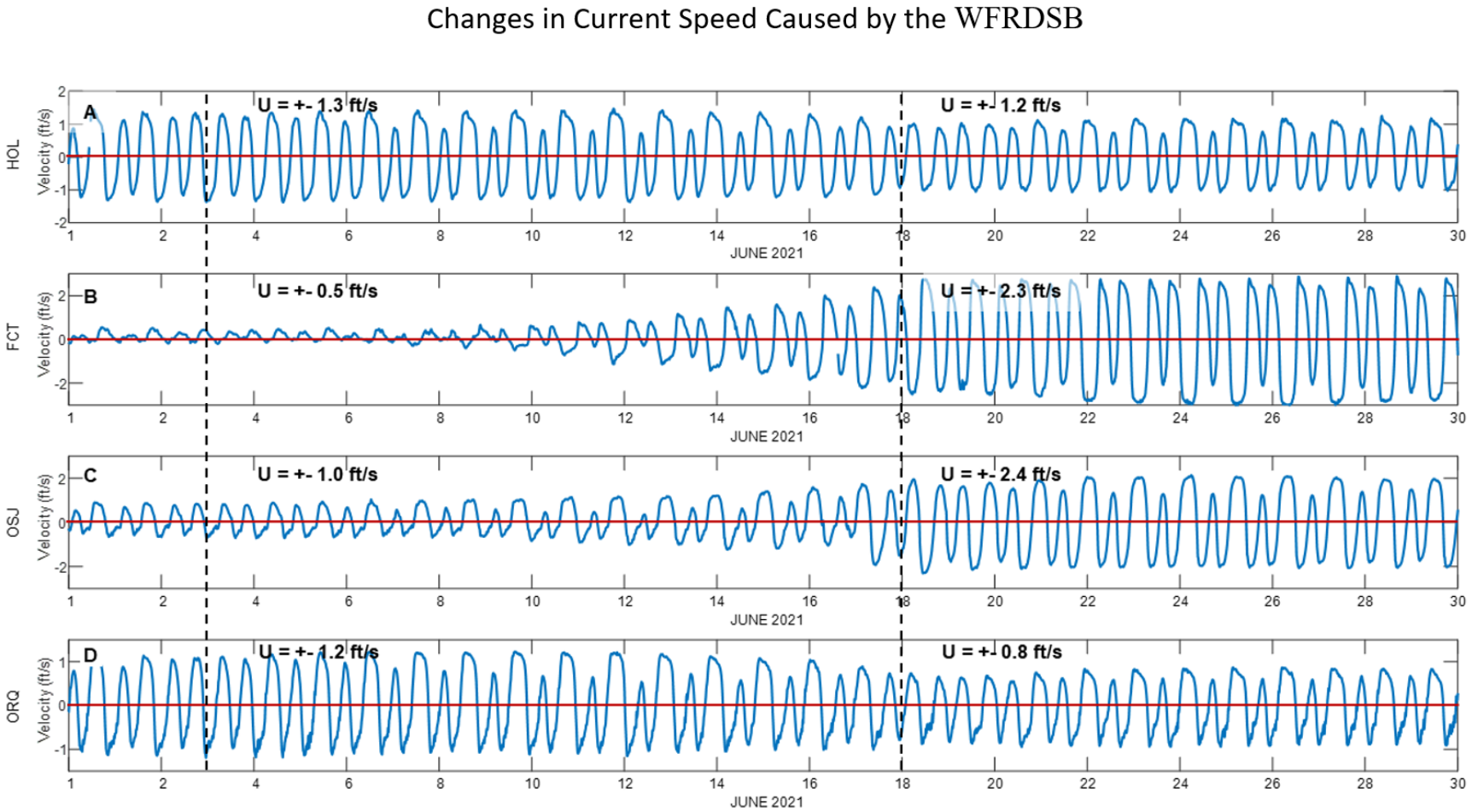

NOTES: ft/s = feet per second; HOL = Holland Cut; ORQ = Old River at Quimby Island; OSJ = Old River at Franks Tract; WFRDSB = West False River drought salinity barrier (emergency drought barrier).
Horizontal red dashed lines represent a change in direction where the positive direction is indicated in the right margin. The dashed vertical lines on June 3 and June 18, 2021, indicate the start and the completion of barrier installation.

Figure 2.2.2-26 Time series plots of as-measured velocity at the start of barrier installation and after the completion of barrier installation, at (A) Holland Cut, (B) Fisherman's Cut, (C) Old River at Franks Tract, and (D) Old River at Quimby Island.

This section uses salt flux decompositions to investigate the mechanisms behind the transport of salinity. In all but Fisherman's Cut (FCT), the horizontal salinity gradient was insufficient to drive dispersive transports, because salinity was mostly seaward of Fisherman's Cut (Figure 2.2.2-4). The total salt flux was driven almost completely by the advective flux (net flows) in most of the channels investigated in this report.

The salient feature in these time series plots is the cumulative salt flux. This is an important reminder that total salt load (cumulative salt flux over a prescribed period) past a point, or into the export facilities, is not necessarily governed by the channel with the highest salinity, but by the tidal average, < >, of the product of the discharge *Q* and the salt concentration *S*, or <QS> (Equation 4).

The cumulative salt flux time series are plotted in this report based on the total salt flux (<*Q(t)*S(t)*> in Equation 4) because the dispersive salt fluxes were zero at all stations except FCT.

As a reminder, increases and decreases in salt flux are associated with changes in the slope of the cumulative salt flux. A positive slope in the cumulative salt flux is associated with an increase in total salt flux (in this case, advective) in the assumed positive flow direction, whereas a negative slope is associated with total salt flux in the assumed negative flow direction. No change in slope is indicative of zero to minimal total salt flux.

Pre-barrier Conditions—Salt Flux through False River into Franks Tract

This section describes how salt transport works in Franks Tract in the absence of the EDB, for a comparison to conditions when the barrier was installed.

Figure 2.2.2-27 presents time series plots from a roughly two-year period (October 2019–July 2021) to provide a reasonable snapshot of how transport works in False River during droughts. As shown, Sacramento River flows (Figure 2.2.2-27A) were generally very low during this period, at roughly 10,000 cfs, with a few peaks of approximately 20,000 cfs. Discharge over this period was far lower than during either a "typical" average water year or an above-average water year. Salt intruded weakly into False River from mid-November to mid-December 2019 (Figure 2.2.2-27B), and two significant salinity intrusion events occurred: one from early July 2020 to January 1, 2021, and the other from May 2021 forward.

The increase in salinity that began November 28, 2019 (red vertical line [1] in Figure 2.2.2-27) was clearly a result of exports, which can be seen in the net discharge (Figure 2.2.2-27E). However, the salinity intrusion event was short-lived because Sacramento River flow increased shortly after the increase in exports.

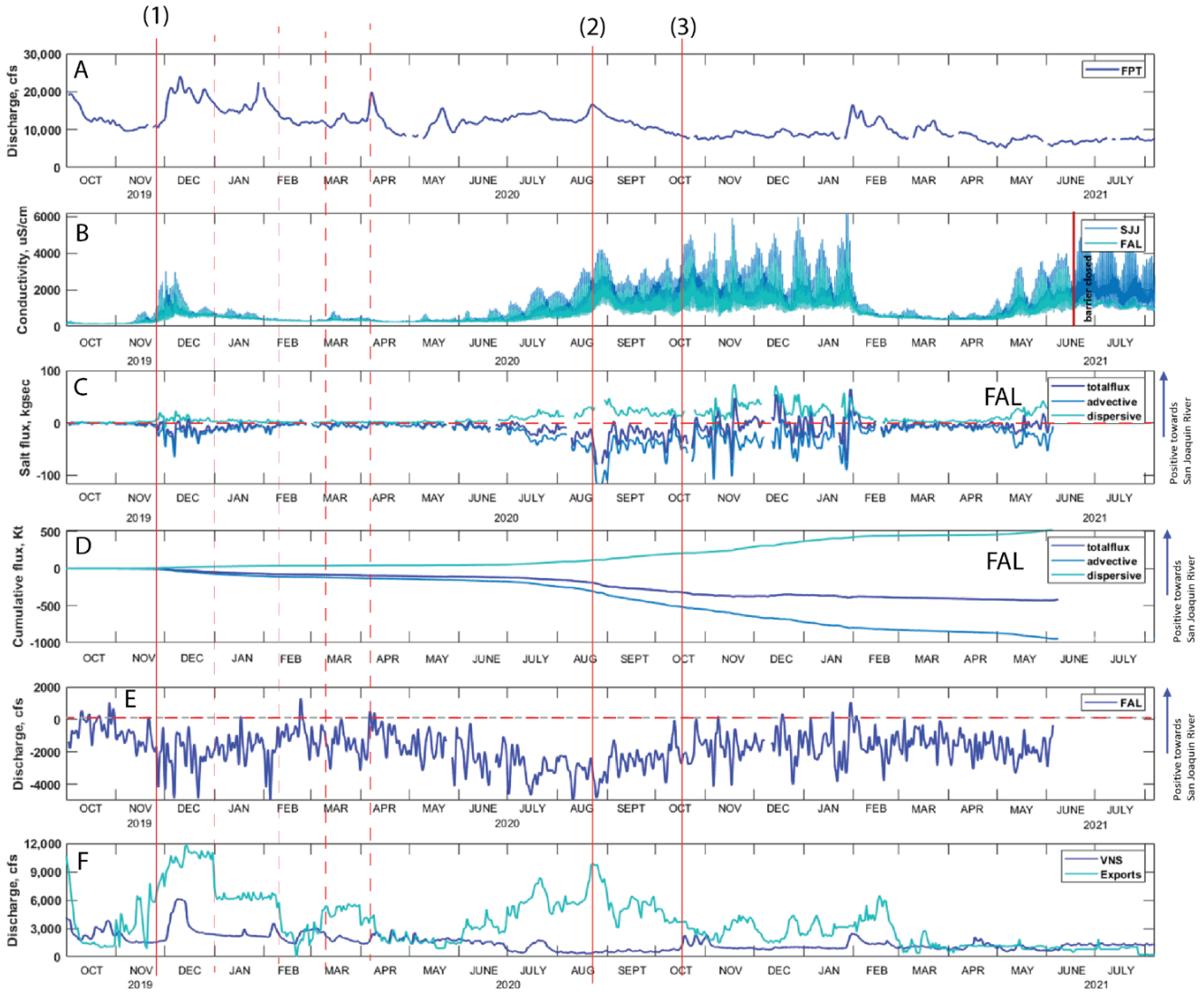

NOTES: µS/cm = microsiemens per centimeter; cfs = cubic feet per second; FAL = False River; FPT = Sacramento River at Freeport; kg/sec = kilograms per second; Kt = kilotons; SJJ = Jersey Point; VNS = San Joaquin River at Vernalis.
Horizontal red dashed lines represent a change in direction where the positive direction is indicated in the right margin. Vertical dashed red lines indicate noteworthy events.

Figure 2.2.2-27 Time series plots: (A) Sacramento River discharge at Freeport; (B) conductivity at Jersey Point and False River; (C) salt flux decomposition at False River; (D) cumulative salt flux decomposition at False River; (E) net discharge in False River; (F) discharge in the San Joaquin River at Vernalis.

There is a lack of high-frequency response at False River to abrupt changes in exports (see the dashed red vertical lines in Figure 2.2.2-27) because of a combination of Franks Tract's large volume and its distance from the export facilities. Nevertheless, the trend is for increases in negative net flows toward the pumps to generally follow changes in exports. For example, the increase in exports from mid-June to mid-October 2020 generally shows an increase in negative flows (toward the pumps) and a decrease in net flows after mid-October after exports were reduced.

Unexpectedly, the salt flux decomposition (Figure 2.2.2-27C) shows that advection caused by negative net flows (toward the pumps) drives advective transport toward the South Delta, but with a significant dispersive flux (roughly half the advective flux) out of Franks Tract back into the San Joaquin River. This was especially the case during the prolonged salinity intrusion event that began in early July 2020. Over the period of record (October 2019–July 2021), roughly half the salt load that entered Franks Tract via advection through False River (-1,000 kilotons [Kt])—500 Kt—was transported dispersively out of Franks Tract back into the San Joaquin River.

Pre-barrier Advective Transports

In Water Year (WY) 2020, net flows (Figure 2.2.2-27E) were driven primarily by exports (Figure 2.2.2-27F). Net flows in WY 2020 were unusually high (November–December 2019, July–September 2020) because the salt field was mostly seaward of Jersey Point (SJJ) (Figure 2.2.3-4), to move as much water south as possible after 10 years of drought. This condition created net flows in False River (Figure 2.2.2-27E) of approximately 3,000 cfs with peaks of approximately 4,000 cfs, or 5–7 percent of the tidal discharge of 56,000 cfs. This is not huge but is important, especially considering the duration and the low level of flows (mostly less than 3,000 cfs) from the San Joaquin River measured at Vernalis (VNS) (blue line in Figure 2.2.2-27F).

Relationship between the Emergency Drought Barrier, Franks Tract, and Water Project Operations

Transport of salt in the San Andreas Shoal Reach is critically important because salinity intrusion through this reach could cause exports to cease if salt begins to significantly dispersively mix into Franks Tract through Old River at OSJ (Figure 2.2.2-3). If this dispersive mixing occurs, Old River at OSJ will begin to act in a manner like False River. Salt significantly entering Franks Tract through Old River at OSJ could limit SWP and CVP water deliveries and lead to a salinity pattern that is difficult to flush from Franks Tract.

Dispersive Transport in the San Andreas Shoal Reach

Based on Equation 6 in Section 2.2.2.2, "Approach and Methods," above, the tidal excursion in the San Joaquin River landward from Jersey Point is 7.2 miles, using a maximum velocity at Jersey Point (SJJ) of 2.7 feet per second.

This tidal excursion is roughly 80 percent of the distance on the San Joaquin River from False River to the Mokelumne River (8.7 miles), the source of fresh Sacramento River water that is keeping salt at bay. However, the tidal excursion increases in this reach because the tidal prism that typically exchanges through False River into Franks Tract is redirected into the San Andreas Shoal Reach when it is eliminated by the EDB.

Measurements of the increase in tidal discharge or velocity in this reach are not available; however, this additional approximately 56,000 cfs tidal discharge that would have entered Franks Tract through False River was diverted into Fisherman's Cut (approximately 11,000 cfs), leaving an approximately 45,000 cfs increase in tidal discharge in the San Andreas Shoal Reach with the EDB installed. This increase in tidal discharge increased velocities in the San Andreas Shoal Reach, which in turn increased dispersive mixing caused by velocity shear and tidal time-scale straining of the salt field in this reach (Appendix C).

Moreover, this reach is one of the few in the Delta that has somewhat natural river geomorphology. A couple of significant bends create dispersive mixing caused by secondary circulation; shoals create lateral shear, which in turn creates large lateral constituent distributions (often seen as fronts on the water surface) that mix during slack water periods, which also increases dispersive mixing. The greater the velocity, the greater the secondary circulation and shear adjacent to shoals, which, in combination, increases dispersive transport in this reach when the EDB is in place.

Effects of the Emergency Drought Barrier on Salt Fluxes

Figure 2.2.2-28 through Figure 2.2.2-32 present time series plots from May 2022 through November 2022 to show the effect of the EDB on salt fluxes in all channels significantly affected by the barrier. These effects are summarized below.

- **Fisherman's Cut (FCT)** (Figure 2.2.2-28)—As mentioned previously, FCT is the only station where a dispersive flux occurred. Nevertheless, net flows (advective flux) overwhelmed the dispersive flux. The advective flux dominated salt transport in this channel. Because salt flux was negative (toward Franks Tract) before installation of the EDB (Figure 2.2.2-28C), the slope of the cumulative salt flux was negative at that time (Figure 2.2.2-28D). However, once the barrier was installed—though not *because* it was installed—salt flux was out of Franks Tract into the San Joaquin River, as a result of the increased tidally averaged flow into Franks Tract from OSJ (Figure 2.2.2-22B). While the EDB was notched, salt flux was zero because salinity was downstream of FCT. Finally, once salinity returned to FCT, total salt flux was once again out of Franks Tract into the San Joaquin River. Total salt load out of Franks Tract into the San

Joaquin River through FCT was approximately 100 Kt for the period of record shown.

- **Old River (OSJ)** (Figure 2.2.2-29)—Salt flux at OSJ was out of Franks Tract into the San Joaquin River before installation of the EDB because of the net flow entering Franks Tract through False River (Figure 2.2.2-29C). After the EDB was installed, salt flux at OSJ was negligible while the DCC gates were open, then into Franks Tract while DCC gate operations cycled between open and closed. While the EDB was notched, salinity was seaward of OSJ and salt flux was zero. Once salinity returned to the region with the EDB intact, salt flux began to intrude into Franks Tract. Finally, after the EDB was removed, salt flux was toward the San Joaquin River. Total salt load through OSJ was into Franks Tract at approximately 50 Kt for the period of record shown (Figure 2.2.3-28D).
- **Holland Cut near Bethel Island (HOL)** (Figure 2.2.2-30)—Total salt load into and out of Franks Tract at HOL was relatively insignificant, owing to the relatively weak net flows. Salt flux was slightly out of Franks Tract before the EDB was installed, weakly into Franks Tract after the barrier was installed, then out again after the atmospheric river that arrived at the end of October 2022 (Figure 2.2.2-30D). No salt flux occurred (no salt was present) when the barrier was notched. Salt flux began out of Franks Tract early in July 2022, associated with an increase in Sacramento River flow and an opening of the DCC gates. Total salt load through HOL was out of Franks Tract at approximately 50 Kt for the period of record shown.
- **Old River at Quimby Island (ORQ)** (Figure 2.2.2-31)—ORQ had the second largest salt load toward the export facilities during the period of record shown. Ironically, this location had the lowest conductivity in Old River between Franks Tract and the pumps, because of dispersive mixing of fresh water into ORQ, as explained above. However, because the net flow was greater at HOL (Figure 2.2.2-24B), the salt flux was greater at ORQ even though the conductivity was lower than at HOL and second to salt flux at HLT (Figure 2.2.2-32D). HLT had the largest salt flux toward the pumps because of its greater net flow and had the lowest conductivity, as described below. Total salt load through HOL was out of Franks Tract at approximately 300 Kt for the period of record shown.
- **Middle River near Holt (HLT)** (Figure 2.2.2-32)—Salt flux at HLT increased until the EDB was installed. Salt flux at HLT provided the largest salt load to the pumping facilities over the period studied—approximately 275 Kt—despite the generally lower conductivities at HLT than in Old River (Figure 2.2.2-31B and Figure 2.2.2-31C), because HLT maintained the largest net flow in the region (Figure 2.2.2-24D).

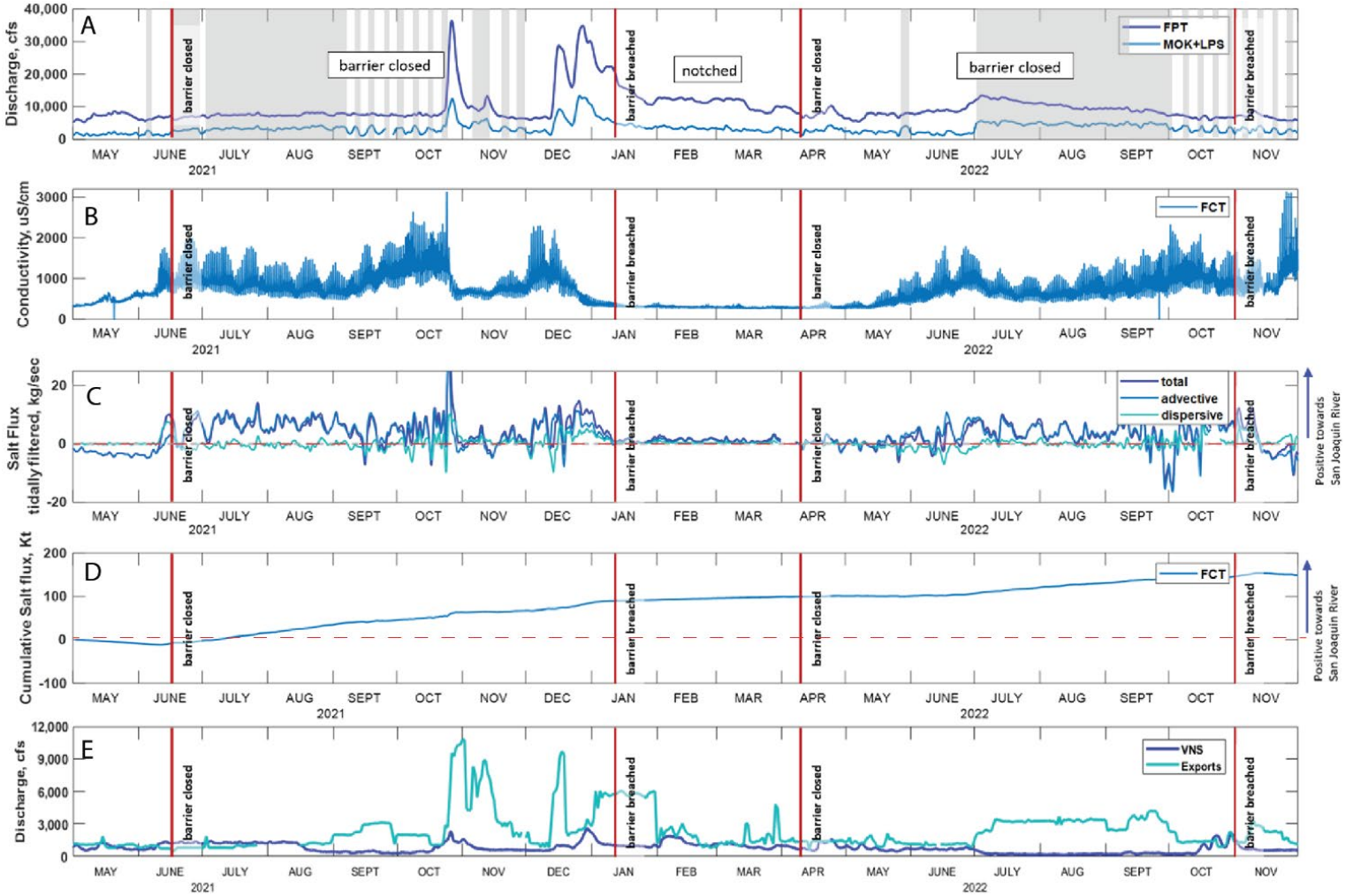

NOTES: µS/cm = microsiemens per centimeter; cfs = cubic feet per second; FCT = Fisherman's Cut; FPT = Sacramento River at Freeport; kg/sec = kilograms per second; Kt = kilotons; LPS = Little Potato Slough; MOK = Mokelumne River; VNS = San Joaquin River at Vernalis.
Horizontal red dashed lines represent a change in direction where the positive direction is indicated in the right margin.

Figure 2.2.2-28 Time series plots: (A) Measured discharge in the Sacramento River at Freeport and sum of tidally averaged discharge at Mokelumne River and Little Potato Slough, and at Fisherman's Cut; (B) conductivity and (C) salt flux decomposition: total flux and advective and dispersive components; (D) cumulative flux; (E) discharge entering the Delta from the San Joaquin River at Vernalis and exports.

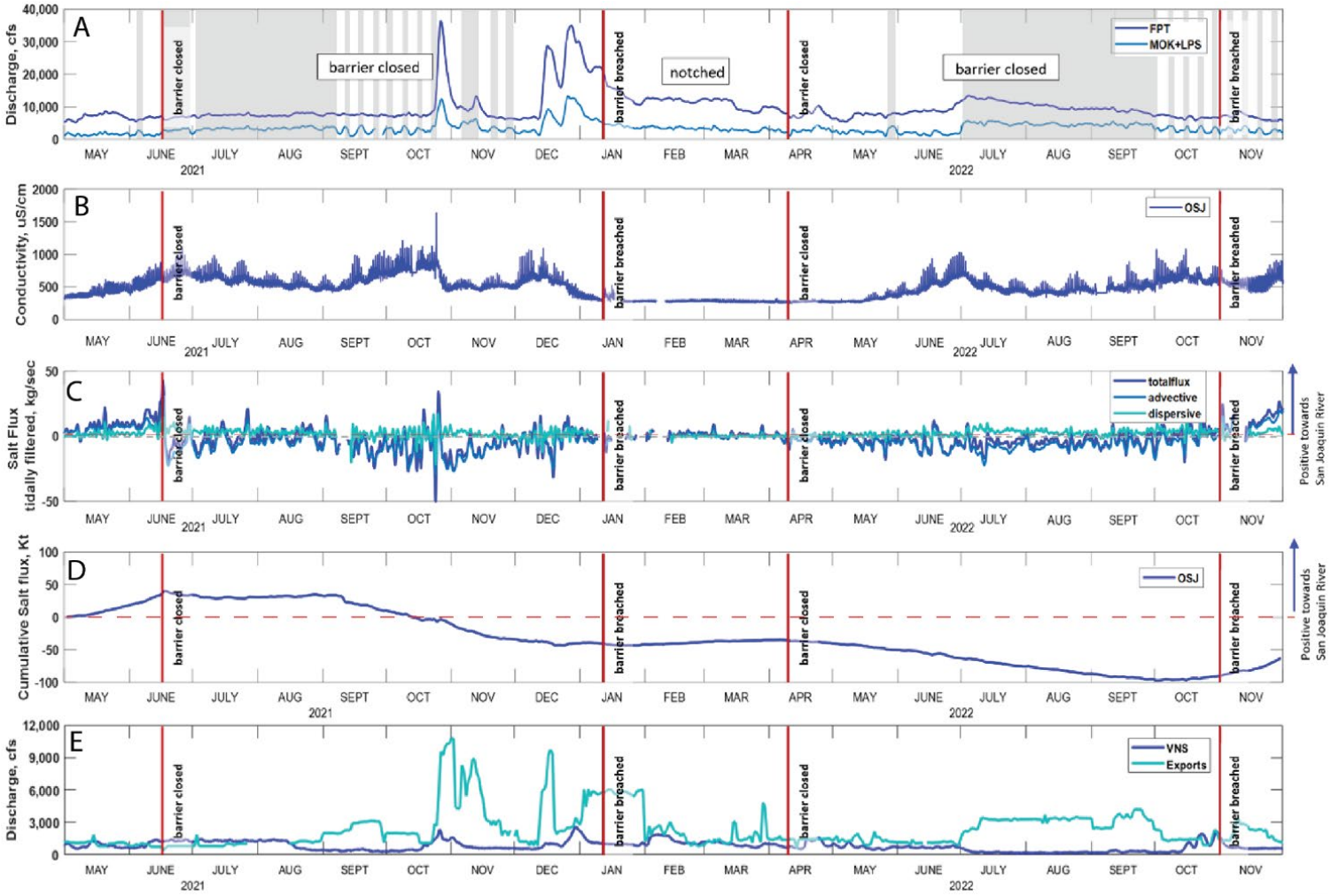

NOTES: µS/cm = microsiemens per centimeter; cfs = cubic feet per second; FPT = Sacramento River at Freeport; kg/sec = kilograms per second; Kt = kilotons; LPS = Little Potato Slough; MOK = Mokelumne River; OSJ = Old River at Franks Tract; VNS = San Joaquin River at Vernalis.
Horizontal red dashed lines represent a change in direction where the positive direction is indicated in the right margin.

Figure 2.2.2-29 Time series plots: (A) Measured discharge in the Sacramento River at Freeport and sum of tidally averaged discharge at Mokelumne River and Little Potato Slough, and at Old River at Franks Tract; (B) conductivity and (C) salt flux decomposition: total flux and advective and dispersive components; (D) cumulative flux; and (E) discharge entering the Delta from the San Joaquin River at Vernalis and exports.

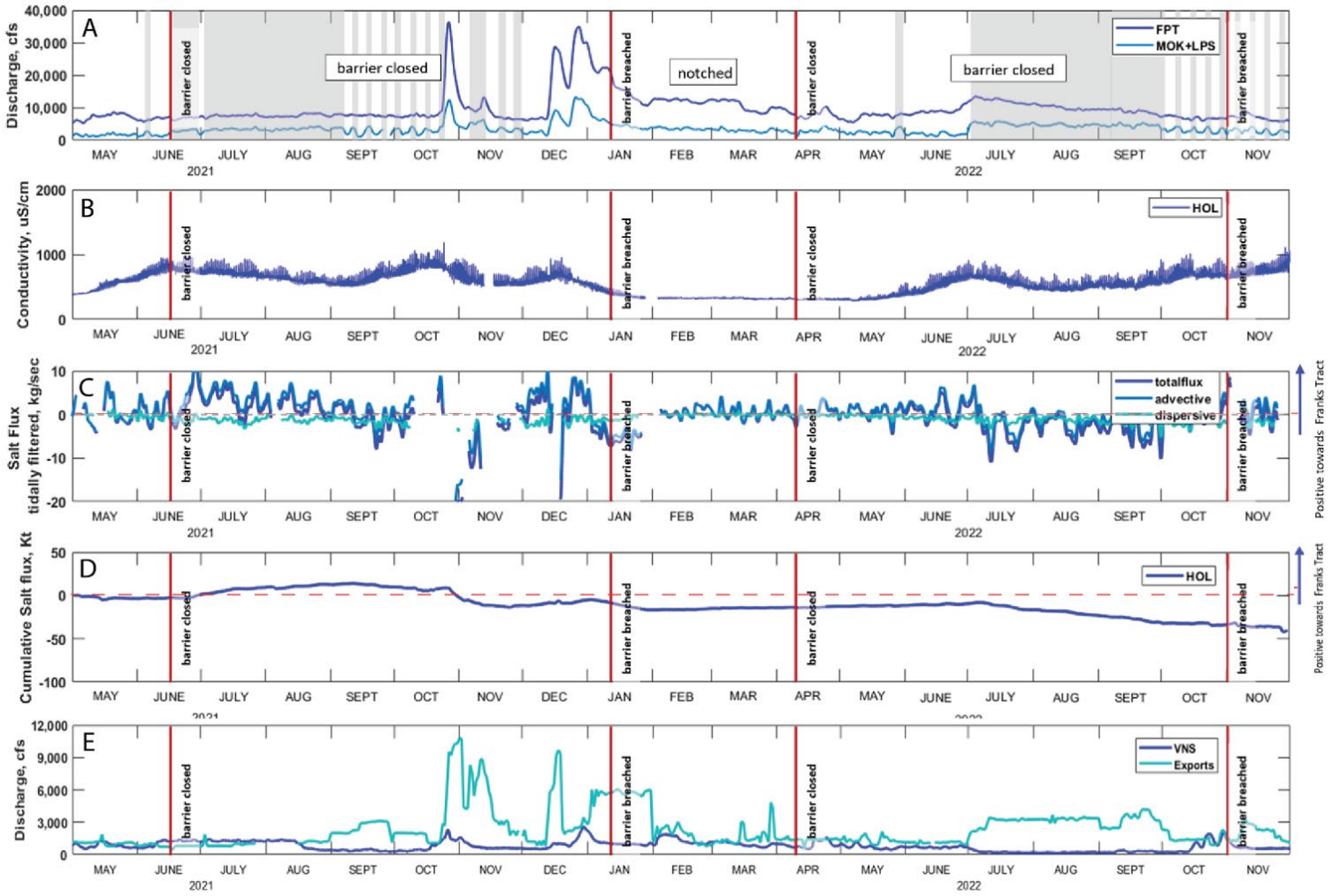

NOTES: µS/cm = microsiemens per centimeter; cfs = cubic feet per second; FPT = Sacramento River at Freeport; HOL = Holland Cut; kg/sec = kilograms per second; Kt = kilotons; LPS = Little Potato Slough; MOK = Mokelumne River; VNS = San Joaquin River at Vernalis.
Horizontal red dashed lines represent a change in direction where the positive direction is indicated in the right margin.

Figure 2.2.2-30 Time series plots: (A) Measured discharge in the Sacramento River at Freeport and sum of tidally averaged discharge at Mokelumne River and Little Potato Slough, and at Holland Cut; (B) conductivity and (C) salt flux decomposition: total flux and advective and dispersive components; (D) cumulative flux; (E) discharge entering the Delta from the San Joaquin River at Vernalis and exports.

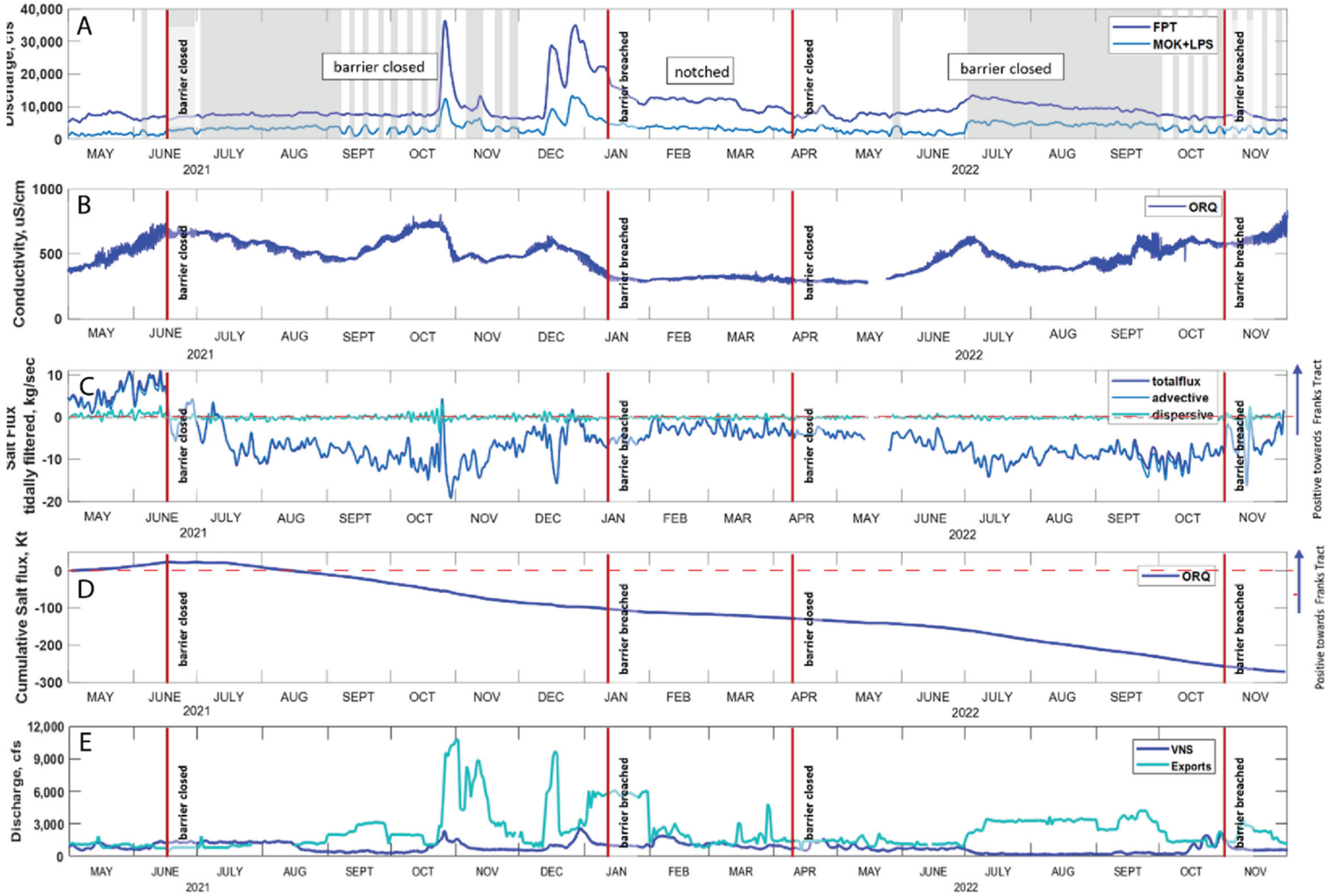

NOTE: µS/cm = microsiemens per centimeter; cfs = cubic feet per second; FPT = Sacramento River at Freeport; kg/sec = kilograms per second; Kt = kilotons; LPS = Little Potato Slough; MOK = Mokelumne River; ORQ = Old River at Quimby Island; VNS = San Joaquin River at Vernalis.
Horizontal red dashed lines represent a change in direction where the positive direction is indicated in the right margin.

Figure 2.2.2-31 Time series plots: (A) Measured discharge in the Sacramento River at Freeport and sum of tidally averaged discharge at Mokelumne River and Little Potato Slough, and at Old River at Quimby Island; (B) conductivity and (C) salt flux decomposition: total flux and advective and dispersive components; (D) cumulative flux; (E) discharge entering the Delta from the San Joaquin River at Vernalis and exports.

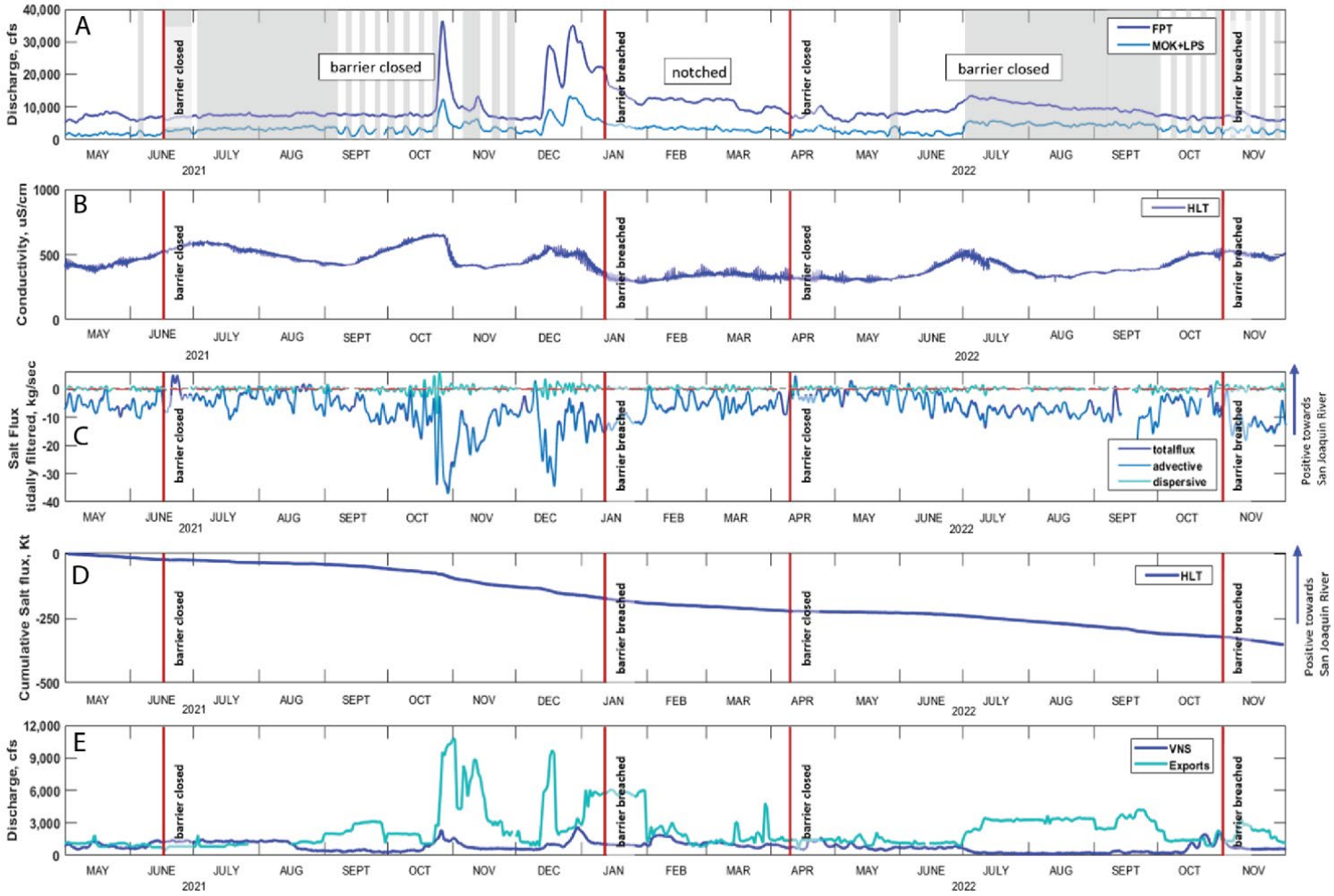

NOTES: µS/cm = microsiemens per centimeter; cfs = cubic feet per second; FPT = Sacramento River at Freeport; HLT = Middle River near Holt; kg/sec = kilograms per second; Kt = kilotons; LPS = Little Potato Slough; MOK = Mokelumne River; VNS = San Joaquin River at Vernalis.
Horizontal red dashed lines represent a change in direction where the positive direction is indicated in the right margin.

Figure 2.2.2-32 Time series plots: (A) Measured discharge in the Sacramento River at Freeport and sum of tidally averaged discharge at Mokelumne River and Little Potato Slough, and at Middle River near Holt; (B) conductivity and (C) salt flux decomposition: total flux and advective and dispersive components; (D) cumulative flux; (E) discharge entering the Delta from the San Joaquin River at Vernalis and exports.

In summary, during the period studied, most of the salt flux from Franks Tract into Old and Middle rivers—and eventually into the export facilities—was from HLT (approximately 275 Kt), followed by ORQ (200 Kt). This was the case even though HOL and ORQ had higher concentrations because the net flow was higher in HLT and in ORQ, because the total tidally averaged salt flux is the tidal average, < >, the product of the discharge, *Q*, and the salt concentration, C (e.g., Equation 5).

Old River at Quimby Island (ORQ) was the likely the largest contributor to the salt load in Old River at Bacon Island (OBI) (Figure 2.2.2-20C) and at Middle River near Holt (HLT) (Figure 2.2.2-32D). The salt could not have come from anywhere else: Net flow in the San Joaquin River at Prisoner's Point (PRI) was near zero (**Figure 2.2.2-33**C) and salinity there was not high, except for a brief blip from mid-June to mid-July 2022 (**Figure 2.2.2-34**B) (e.g., <*QC*> was small), and the salt load in HOL was also low, at approximately 50 Kt.

Effects of the Emergency Drought Barrier on Tidally Averaged Salinity Distributions

This section discusses the spatial and temporal evolution of the salt field in the Central and South Delta, including the effect of the hydrodynamics discussed in the previous sections on the horizontal (or along channel) salinity gradient in Old and Middle rivers between Franks Tract and the export facilities.

Along Old River

One of the most surprising features of the salinity gradient in Old River (Figure 2.2.2-34C) is that the largest gradient occurs between HOL, generally the saltiest station, and ORQ, the freshest station. These stations are located very close to each other (approximately 1.5 miles apart), and both connect to Franks Tract on its southern border and essentially draw water from the same location. Yet the water at ORQ is fresh (Figure 2.2.2-34C) even though the net flow is out of Franks Tract toward the pumps at HOL and ORQ (Figure 2.2.2-24B and Figure 2.2.2-24C). The reason for this is the dispersive mixing of fresh water into ORQ from Middle River through Connection Slough: yet another reason for the freshening of this region.

Along Middle River

There are two features of the salinity gradient in Middle River (Figure 2.2.2-34B). The first feature is the concerningly high salinity level at San Joaquin River at Prisoner's Point (PRI) that began in mid-September 2021 and abruptly ended at the end of October with the arrival of one of many atmospheric rivers. This observation is particularly concerning because salt entering the heart of the Central Delta is problematic, as discussed previously.

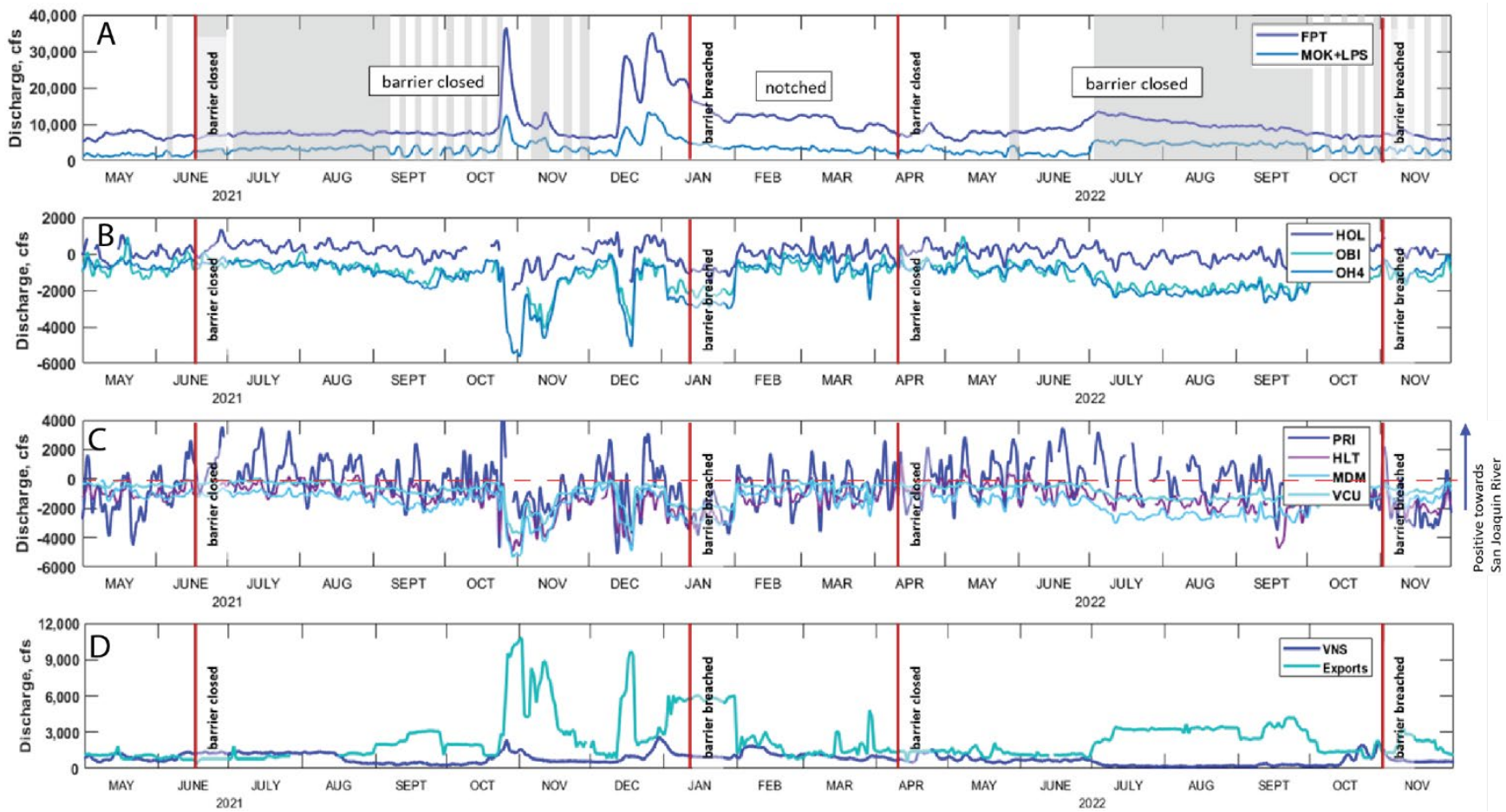

NOTES: µS/cm = microsiemens per centimeter; cfs = cubic feet per second; FPT = Sacramento River at Freeport; HLT = Middle River near Holt; HOL = Holland Cut; kg/sec = kilograms per second; Kt = kilotons; LPS = Little Potato Slough; MDM = Middle River at Middle River; MOK = Mokelumne River; OBI = Old River at Bacon Island; OH4 = Old River at Highway 4; PRI = San Joaquin River at Prisoner's Point; VCU = Victoria Canal near Byron; VNS = San Joaquin River at Vernalis.
Horizontal red dashed lines represent a change in direction where the positive direction is indicated in the right margin.

Figure 2.2.2-33 Time series plots: (A) Measured discharge in the Sacramento River at Freeport and sum of tidally averaged discharge at Mokelumne River and Little Potato Slough; tidally averaged discharge (B) at Holland Cut, Old River at Bacon Island, and Old River at Highway 4; (C) in the San Joaquin River at Prisoner's Point and at Middle River near Holt, Middle River at Middle River, and Victoria Canal near Byron; (D) discharge entering the Delta from the San Joaquin River at Vernalis and exports.

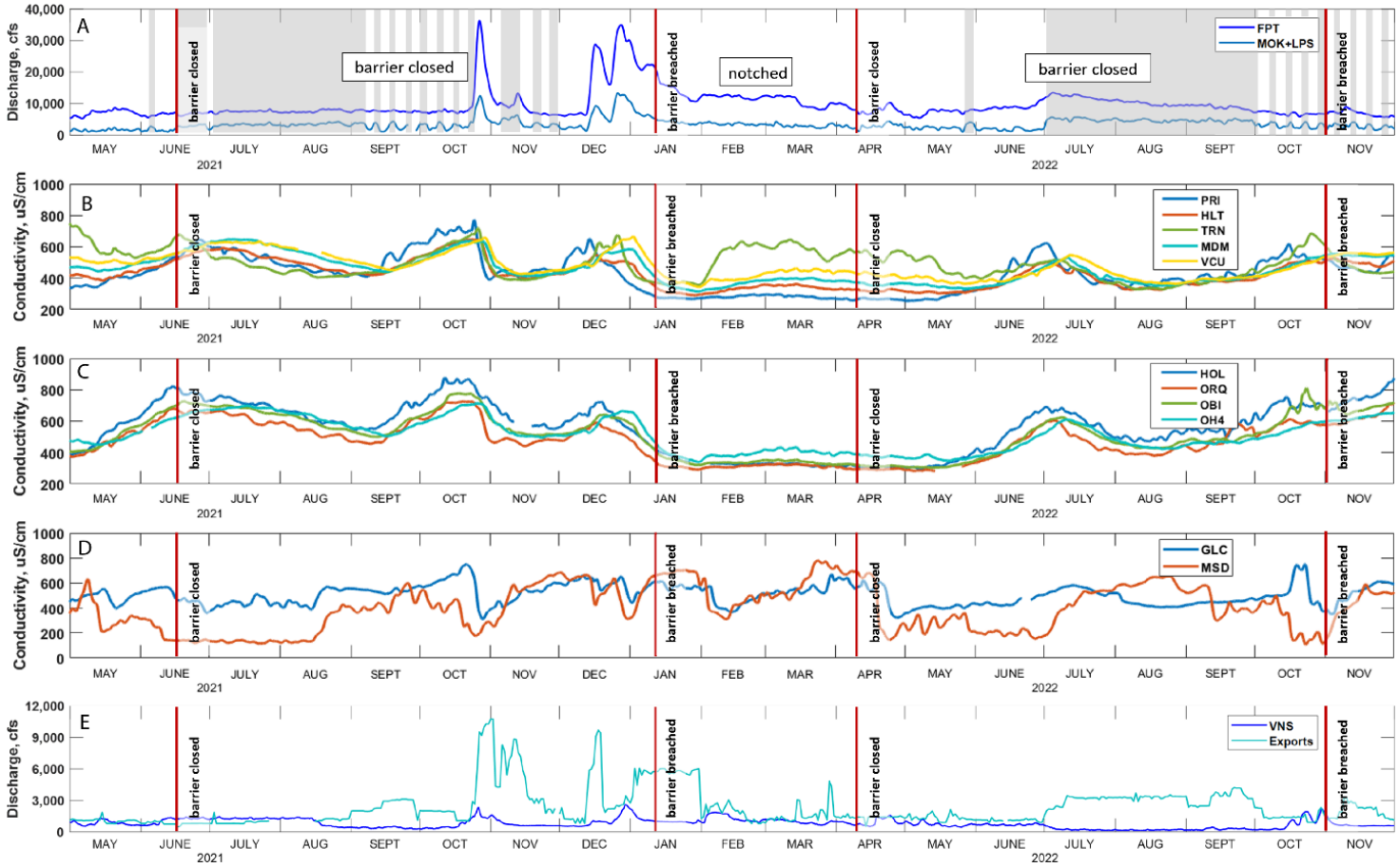

NOTES: µS/cm = microsiemens per centimeter; cfs = cubic feet per second; FPT = Sacramento River at Freeport; GLC = Grant Line Canal; HLT = Middle River near Holt; HOL = Holland Cut; kg/sec = kilograms per second; Kt = kilotons; LPS = Little Potato Slough; MDM = Middle River at Middle River; MOK = Mokelumne River; MSD = Mossdale; OBI = Old River at Bacon Island; OH4 = Old River at Highway 4; ORQ = Old River at Quimby Island; PRI = San Joaquin River at Prisoner's Point; TRN = Turner Cut; VCU = Victoria Canal near Byron; VNS = San Joaquin River at Vernalis.

Figure 2.2.2-34 Time series plots: (A) Measured discharge in the Sacramento River at Freeport and sum of tidally averaged discharge at Mokelumne River and Little Potato Sough; (B) conductivity in the San Joaquin River at Prisoner's Point, Middle River near Holt, Turner Cut, Middle River at Middle River, and Victoria Canal near Byron; (C) conductivity at Holland Cut, Old River at Quimby Island, Old River at Bacon Island, and Old River at Highway 4; (D) conductivity at Grant Line Canal and Mossdale; (E) discharge entering the Delta from the San Joaquin River at Vernalis and exports.

Salinity entering Middle River at PRI is concerning because the greater net flow in Middle River toward the pumps will allow salinity to rapidly intrude into the South Delta, which could lead to a shutdown of exports from the South Delta.

The second feature of Middle River's salinity gradient is the elevated salinity that began February 1, 2022, and continued until June 1, 2022.

High conductivities from the San Joaquin River at Mossdale (MSD) (Figure 2.2.2-34D) may have intruded in the San Joaquin River all the way to Turner Cut (TRN) (Figure 2.2.2-34B).

This is a reminder that salinity intrusion into the Delta from the San Joaquin River can also be problematic during droughts.

Freshening of Middle River

One of the most intriguing hydrodynamic effects of the EDB is the freshening of Middle River. Most of the increase in net flow at Middle River near Holt (HLT) appears to have been water flowing in from Little Potato Slough (LPS) (Figure 2.2.2-21C) during times when Sacramento River flows were low and the DCC gates were open and when the percentage of the Sacramento River flow entering the San Joaquin River at LPS increased by about 25 percent. Between July 1 and October 1, 2022—a period when Sacramento River inputs were low, exports were elevated, and the DCC gates were open—net flow in the San Joaquin River at Prisoner's Point (PRI) was extremely noisy (e.g., having a lot of high-frequency "wiggles"; Figure 2.2.2-33C) and on average, slightly positive (seaward), while net flows at HLT and station Middle River at Middle River (MDM) were toward the pumps.

Taken together, these observations suggest that the net flow did not pass PRI, but rather came from Little Potato Slough when the DCC gates were open (Figure 2.2.2-21C). Thus, it is likely that LPS also increases the net flow at MDM. However, the net flow from LPS may also be increasing the flow at MDM from Turner Cut, particularly when the DCC gates are open and San Joaquin River inflows are low and exceeded by exports.

Finally, under non-EDB conditions, most of the tidal exchange into the South Delta occurred in Holland Cut and Old River (HOL+ORQ), at approximately 38,000 cfs, compared to approximately 16,000 cfs in Middle River (HLT). In contrast, during EDB conditions, HOL+ORQ tidal discharges were reduced to approximately 24,000 cfs while HLT tidal discharges increased to approximately 28,000 cfs (Figure 2.2.2-16 and Table 2.2.2-1).

Therefore, the reduction in tidal exchange in Holland Cut and Old River (HOL+ORQ) combined with the increase in Middle River (MDM) is another explanation for a freshening in Old River southeast of Franks Tract and at

OSJ. Fortunately, this tidal flow switch would reduce the dispersion of saltier water from HOL and ORQ into Old River and would increase the dispersion of fresher water into Old River from HLT in a significantly worse drought. In fact, overall, ORQ is fresher than HOL (Figure 2.2.2-34C) because of the dispersive mixing of fresher water toward Franks Tract created by the increase in the net flow of fresher water from HLT. (See Figure 2.2.2-24D; note the change in the Y-axis scale: HOL = -2,000 cfs, ORQ = -3,000 cfs, and HLT = -6,000 cfs.)

Overall, Little Potato Slough (LPS) plays a large role in setting up conditions for a fresher South Delta, and the EDB enhances this freshening effect.

Effects of the Emergency Drought Barrier on Dispersive Mixing (Potential)

As discussed previously, to maintain regulatory mandates in the Sacramento River, the SWP and CVP operators did not allow salinity to intrude very far past Jersey Point during the study period. Thus, salt did not disperse into and through Franks Tract in the manner in which it would have if salt had been allowed to transit farther into the Delta, creating the horizontal salinity gradient that would have driven dispersive transports into and through Franks Tract.

LE Ratio Approach

This observation inspired the development of the generally useful idea of dispersive mixing potential based on the LE ratio (Stumpner et al. 2020).

Because the horizontal salinity gradient was insufficient to drive dispersive transports, this analysis uses the LE ratio in all but Fisherman's Cut (FCT) to estimate the potential for horizontal dispersion attributable to the large increases in tidal velocities at stations FCT and ORQ and the reduction in tidal velocities at HOL and ORQ.

Estimates of tidal excursion can serve as a surrogate for the potential for dispersion that can occur when tidal excursions traverse a change in channel geometry. Such a scenario can occur in multiple locations:

- A channel that is connected to a large area of shallow water (e.g., all channels that connect to Franks Tract [Figure 2.2.2-3]).
- A channel junction where the capacities of the converging channels are greatly dissimilar (e.g., the junction of Threemile Slough and the San Joaquin River [Figure 2.2.2-3]).
- A location where the tidal excursion traverses complex bathymetry (e.g., the San Andreas Shoal Reach [Figure 2.2.2-11]).

In all cases, the longer the tidal excursion, the greater the horizontal dispersion, in all its forms (see Appendix C). The amount of the increase in horizontal dispersion depends on the overall length of the tidal excursion relative to the length scales of the changes in bathymetry or change in planform (e.g., when the bathymetric or planform change is large relative to the tidal excursion).

For example, tidal trapping of salt into Franks Tract through False River is the primary mechanistic reason that the EDB is required when water storage in upstream reservoirs is insufficient to prevent salinity from entering the Central and South Delta. However, Fisherman's Cut and Old River at OSJ, each of which maintains the same dispersive mixing potential as False River, can also provide a conduit for salt to enter the South Delta. Unfortunately, the potential for dispersive mixing in these channels increases significantly when the EDB is installed.

In summary, dispersive mixing potential in Fisherman's Cut and in Old River at OSJ increased significantly while the EDB was installed and fully intact (not notched), while tidal exchange from Franks Tract into the Old and Middle River corridor decreased slightly.

Because salinity was mostly seaward of FCT (Figure 2.2.2-5C), almost no data were collected during the period of record studied in this report that had a spatial salinity gradient sufficient to drive dispersive mixing. Nevertheless, the following discussion uses the gradients that did exist during this study to address the relative importance of advective and dispersive mixing to provide insights into what would happen if salinity were to intrude into the Central Delta in an extreme drought. The LE ratio concept and the conceptual models of dispersive mixing discussed in Appendix C were used to infer the "potential" for dispersive mixing, based purely on the strength of the tidal currents and the geomorphology along a tidal excursion in a given location within the Delta.

Dispersive mixing is relevant in the Central Delta because it has a trifecta of dispersive mixing geomorphologies:

- A wide channel with geomorphic complexity—the San Andreas Shoal Reach.
- A flooded island/channel exchange that creates dispersion through a tidal trapping and pumping mechanism in Franks Tract through three channels—False River, Old River at OSJ, and Fisherman's Cut.
- Network dispersion south of Franks Tract in Holland Cut and Old River at ORQ and in Connection Slough.

This section examines the potential for the EDB to directly create large changes in dispersive salt transport in the channels that exchange with Franks Tract. "Potential" is used here because unlike transport via net flow, which simply depends on the direction of the flow, dispersive transport past a given location depends on a spatial salinity gradient in constituent concentration (or organism abundance) within a tidal excursion at a given location.

The analysis found that the EDB has the following effects, discussed below:

- Eliminates the exchange of salt into Franks Tract through False River.
- Significantly increases tidal discharges, velocities, and dispersive mixing potential in Fisherman's Cut and in Old River at OSJ while reducing these same quantities in Holland Cut (HOL) and Old River at ORQ.

Elimination of Salt Exchange into Franks Tract through False River

The LE ratio through False River into Franks Tract is one of the largest in the Delta (1.7) because False River's channel length, approximately 3 miles, is short compared to a tidal excursion of approximately 5.2 miles (Figure 2.2.2-13). The farther the tidal excursion transits Franks Tract and the greater the spatial salinity gradient between the San Joaquin River and Franks Tract through False River, the greater the salinity intrusion. (This is the classic tidal pumping/trapping mechanism described by Fischer et al. [1979].)

For example, relatively large horizontal salinity gradients occurred at Jersey Point (SJJ) in the San Joaquin River (e.g., October 2020–January 2021, June–October 2021, and September–December 2022) and in False River (FAL) before closure of the barrier (Figure 2.2.2-5C; see also Figure 2.2.2-4). Large tidal-timescale fluctuations in salinity in these figures indicate the presence of large horizontal salinity gradients within a tidal excursion of a given (station) location (e.g., a gradient in the salt field sloshing back and forth past the monitoring station). If the salinity gradient were to increase significantly between the San Joaquin River at its junction with False River and Franks Tract, with its LE ratio of 1.7 without the EDB, the SWP and CVP operators would have difficulty controlling the dispersive transport of salt into Franks Tract through False River. This is the mechanistic explanation for the installation of the EDB.

Effects on Tidal Discharges, Velocities, and Dispersive Mixing Potential in Fisherman's Cut and Old River at OSJ

As identified above, installation of the EDB causes tidal flows (Figure 2.2.2-15 through Figure 2.2.2-17), velocities (Figure 2.2.2-25 and Figure 2.2.2-26), and tidal excursions in Fisherman's Cut and in Old River at OSJ to increase significantly (Figure 2.2.2-23). All these details are summarized in Table 2.2.2-1.

During the study period, these increases led to a significant increase in dispersive mixing potential in Franks Tract through Fisherman's Cut and past Old River at OSJ because the LE ratio is much greater than 1 in both cases. Therefore, when a salinity gradient exists between the San Joaquin River and Franks Tract at these locations, salinity will intrude into Franks Tract via a dispersive mixing mechanism at a greater rate. Notably, Fisherman's Cut went from non-dispersive to significantly dispersive with the installation of the EDB.

In summary, the San Andreas Shoal Reach's planform and bathymetric complexity will likely lead to increased transport via dispersive mixing because of the increase in tidal currents (shear flow dispersion, tidal straining [Appendix C]). At the same time, dispersive mixing caused by tidal trapping and pumping (conceptual tidal trapping and pumping; see Appendix C) will mostly increase in Fisherman's Cut (FCT) and Old River at Franks Tract (OSJ) and will decrease at Old River at Quimby Island (ORQ) and in Holland Cut near Bethel Island (HOL). (Shear flow dispersion will occur in these channels because they are too narrow to support tidal straining, given that they are usually laterally well mixed because near-bank velocity shear takes up a significant fraction of the cross-section in narrow channels.)

Dispersive mixing potential is relevant in the context of the EDB in False River because redistribution of False River's discharge alters tidal velocities and the tidal excursion relative to the planform (bends) and bathymetric variability (channels with shoals) in the Central Delta. This change either increases or decreases dispersive mixing locally when salt is present. Finally, the magnitude and the direction of salt transport at any given time depend on the sum of the magnitude and direction of both the advective and dispersive transport components (see Equation 4 in Section 2.2.2.2, "Approach and Methods," above).

Most often, dispersive transports are directed upstream (e.g., resulting in salinity intrusion) because salinities are higher seaward; meanwhile, advective transports follow net flows, which generally are directed toward San Francisco Bay in the North Delta, throughout the Sacramento River, and in the San Joaquin River seaward of the Mokelumne River confluence, by regulatory mandate. However, at False River, Fisherman's Cut, and Old River at OSJ (without the barrier), both advective and dispersive transport are almost always toward the pumps, especially when exports are high relative to San Joaquin River flows. This change to hydrodynamics in this region is another reason that the EDB is needed during droughts.

Transport between Old and Middle Rivers through Railroad Cut and the Woodward Canal

Relevance and Purpose

The exchange of salinity from Franks Tract toward the export facilities through Old and Middle rivers is of great interest not only to the agencies that provide water south of the Delta, but also to the fisheries agencies. The same hydrodynamics processes that transport salinity into Franks Tract (e.g., advection and dispersion) through False River also transport and trap in Franks Tract anything else in the water, such as suspended solids, organic carbon, and nutrients; non-motile (phytoplankton) and feeble-swimming organisms (zooplankton and larval fish); and small fish such as delta smelt and juvenile salmon. Thus, both advection by net flows and dispersion by the tides also entrain and trap delta smelt and juvenile salmon in Franks Tract, likely exposing them to increased far-field mortality and—if they are subsequently entrained into the Old and Middle River corridor—direct salvage at the pumps.

Moreover, the distribution of water quality constituents in the Central and South Delta, such as salinity and turbidity, can constrain exports from the Delta. For example, water cannot be pumped from the Delta when electrical conductivity (EC) exceeds municipal and industrial standards. Moreover, pumping must be reduced when the three-day running-average turbidity at three monitoring stations—Prisoner's Point (PRI), Old River at Bacon Island (OBI), and Victoria Canal near Byron (VCU) (Figure 2.2.2-4)—exceeds 12 nephelometric turbidity units (NTU). Finally, far-field mortality of fishes in the South Delta and their salvage at the export facilities can constrain exports, posing an additional concern for SWP and CVP operations.

However, no data exist on the transport (Figure 2.2.2-1) of water and water quality constituents between Old River and Middle River through Railroad Cut and the Woodward Canal (**Figure 2.2.2-35**). In addition, data have not been collected on transport processes such as discharge, salinity, and velocity, either during a drought or when the EDB is installed—even though salinity intrusion and harmful algal blooms that pass through or originate in Franks Tract during these respective periods can reduce exports.

This section documents discharge and salt flux between Old and Middle rivers through Railroad Cut and the Woodward Canal, data that are useful for the calibration and validation of numerical models in this critical region of the Delta.

The objective of these measurements is to understand the relative roles of tidal and advective transport (Figure 2.2.2-1; Equation 5 in Section 2.2.2.2, "Approach and Methods," above) between Old River and Middle River, the two most important channels that supply water for export.

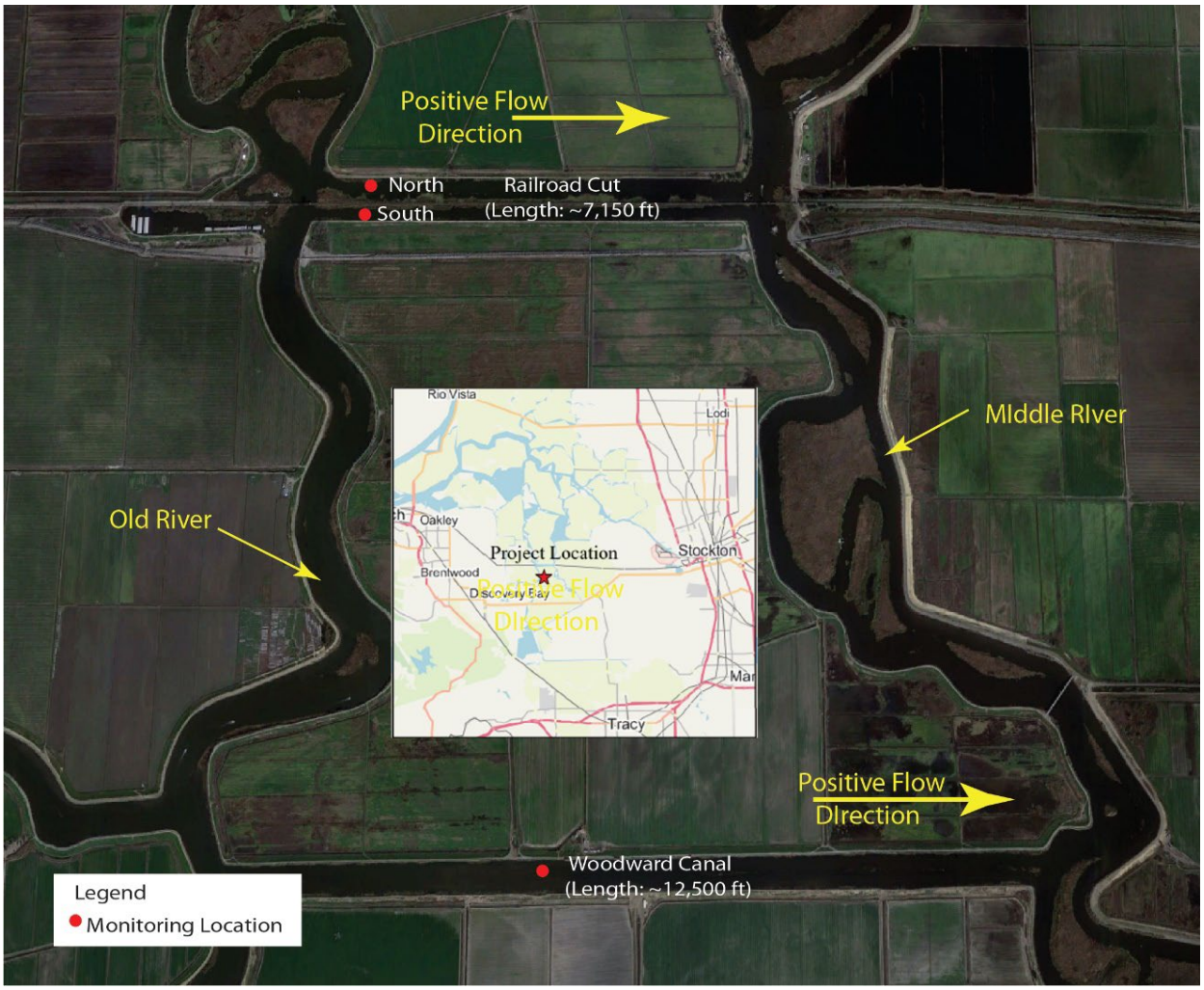

NOTE: Red circles designate the locations of acoustic Doppler current profilers. Salinity sensors were also deployed at the North Railroad Cut and Woodward Canal monitoring stations. Positive flow direction convention is from west to east, or toward Middle River.

Figure 2.2.2-35 Locations of Railroad Cut and Woodward Canal flow and salinity monitoring stations in the Sacramento–San Joaquin Delta.

Approach

Time series data for stage, velocity, discharge, and salinity (derived from temperature and specific conductance) were measured from September 17, 2021, to February 3, 2022. The data were measured using two vertical acoustic Doppler current profilers, or ADCPs, in Railroad Cut—one each in the north and south channels—and a single vertical ADCP in the Woodward Canal. Single salinity sensors were deployed in Railroad Cut and the Woodward Canal (Figure 2.2.2-35).

Methods

Measurements of Stage, Velocity, Salinity, and Discharge Estimates

Stage data (in this case, measured at station Middle River at Middle River [MDM], shown in **Figure 2.2.2-36**) and cross-sectionally averaged (index)

velocity were collected at the locations indicated by red dots in Figure 2.2.2-35. Total discharge time series were estimated using the index-velocity method with boat-measured discharge data (see Ruhl and Simpson 2005).

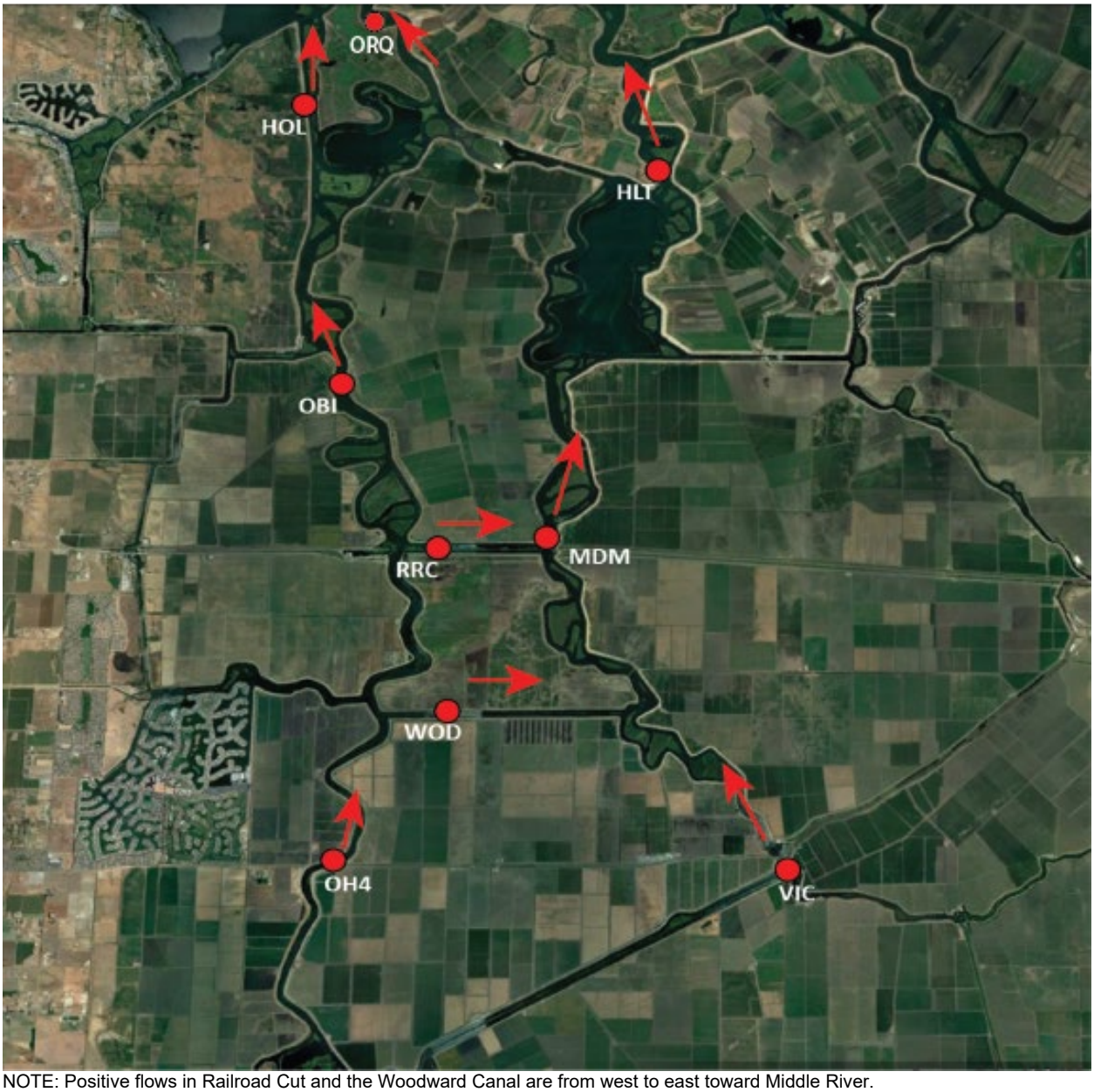

NOTE: Positive flows in Railroad Cut and the Woodward Canal are from west to east toward Middle River.

Figure 2.2.2-36 Direction of positive (ebb) flow across various DWR and U.S. Geological Survey monitoring stations.

As mentioned above, salinity was measured at stations in North Railroad Cut and the Woodward Canal; each measurement was completed at a single point in the water column, using a Yellow Springs Instrument (YSI) EXO1 sonde (Figure 2.2.2-35). As is typical in the Delta, single point measurements are assumed to represent the cross-sectional average. This is a reasonable

assumption for most of the narrow Delta channels, like Railroad Cut and the Woodward Canal, because sidewall boundary layers extend laterally from each bank into a significant fraction of the total cross-section, creating turbulence that accomplishes near-complete lateral mixing.

Analytical Approach

Constituent (salt) flux decompositions and the LE ratio (Equation 5 and Equation 7, respectively, in Section 2.2.2.2, "Approach and Methods," above) are the analytical approaches used in this section.

Results

Hydrodynamics

Background and Overview

Like all surface water flows, tidal and net (tidally averaged) velocities and discharges in Railroad Cut and the Woodward Canal are driven by water surface gradients (slopes), where water moves from higher to lower water surface elevations.

Tidal velocities and discharges in Railroad Cut and the Woodward Canal are forced by differences in tidal propagation between Old River and Middle River, rather than being directly forced by tide wave propagation, which is typical of many of the connection channels in the Delta (Figure 2.2.2-19).

Thus, differences between Old River and Middle River at the times when the tide waves arrive at the junctions with Railroad Cut and the Woodward Canal determine the differences in the respective channels' tidal water surface elevations, which drives the tidal flows through these channels. The differences between Old River and Middle River in tide wave arrival times at Railroad Cut and the Woodward Canal are driven by differences in channel depth (the deeper the water, the faster the tide wave propagates) or channel length, or both.

Tidal flows in Railroad Cut and the Woodward Canal that are out of phase with Old River and Middle River flows represent an example of how all the connection channels shown in Figure 2.2.2-19 work in the Delta. This is important because exchanges through all the connection channels are out of phase with the main channels to which they are connected. Together these connection channels increase overall dispersion within the Delta's network as a whole.

In contrast, net flows in Railroad Cut and the Woodward Canal are driven by the difference in the tidally averaged water surface elevations at their junctions with Old River and Middle River, which are created mostly by the difference between exports and San Joaquin River inputs. The differences in the net flows in Railroad Cut and the Woodward Canal are controlled by a

combination of the differences in conveyance between Railroad Cut and the Woodward Canal and within Old and Middle rivers. However, during droughts—the period analyzed here—this water level difference is driven mostly by exports because San Joaquin River flows were low.

In Railroad Cut and the Woodward Canal, advection of fresh water via the net flow is toward Old River, in opposition to the dispersive transport of salt toward Middle River, from higher salinity in Old River toward the fresher water in Middle River. Ultimately, Railroad Cut and the Woodward Canal transport fresher water from Middle River to Old River, because Old River is almost always saltier than Middle River, given dispersive transport of salt through Franks Tract and Middle River's affiliation with the fresher water exiting the Mokelumne River system.

Importantly, "flood" (incoming tides) and "ebb" (outgoing tides flowing toward the ocean) have little meaning in the context of tidal velocities driven by differences in tidal propagation between adjacent channels. Nevertheless, for this analysis, the authors chose positive flow in Railroad Cut and the Woodward Canal to be toward Middle River (west to east) (Figure 2.2.2-35) by convention, to be consistent with the negative tidal and net flows in Old and Middle rivers toward the pumps (flood tides). Therefore, the following analysis uses "ebb" and "flood" when describing what is happening in Old and Middle rivers. To be more intuitive about the direction of the salt flux, this analysis uses simply "toward Middle River" (positive), which occurs on ebb tides in Old and Middle rivers, and "toward Old River" (negative), which occurs during flood tides.

Measured Velocities and Discharges

Measured velocities in Railroad Cut for September 17, 2021, to February 3, 2022, ranged from nearly -1.0 ft/s to 0.8 ft/s (**Figure 2.2.2-37**A). These velocities were slightly higher than those in the Woodward Canal, which ranged from roughly -0.8 ft/s to 0.5 ft/s (Figure 2.2.2-37B). Measured discharge in Railroad Cut ranged from roughly 1,500 cfs to -1,500 cfs, while flow in the Woodward Canal ranged from -2,200 cfs to 2,000 cfs (not shown). Figure 2.2.2-36 shows the positive flow (velocity) convention for all the channels in the Railroad Cut/Woodward Canal region.

Net Velocities and Discharges

Net velocities and discharges in Old and Middle rivers and in Railroad Cut and the Woodward Canal are driven mostly by exports, which can be moderated by San Joaquin River inputs, depending on the magnitude of exports relative to San Joaquin River flows.

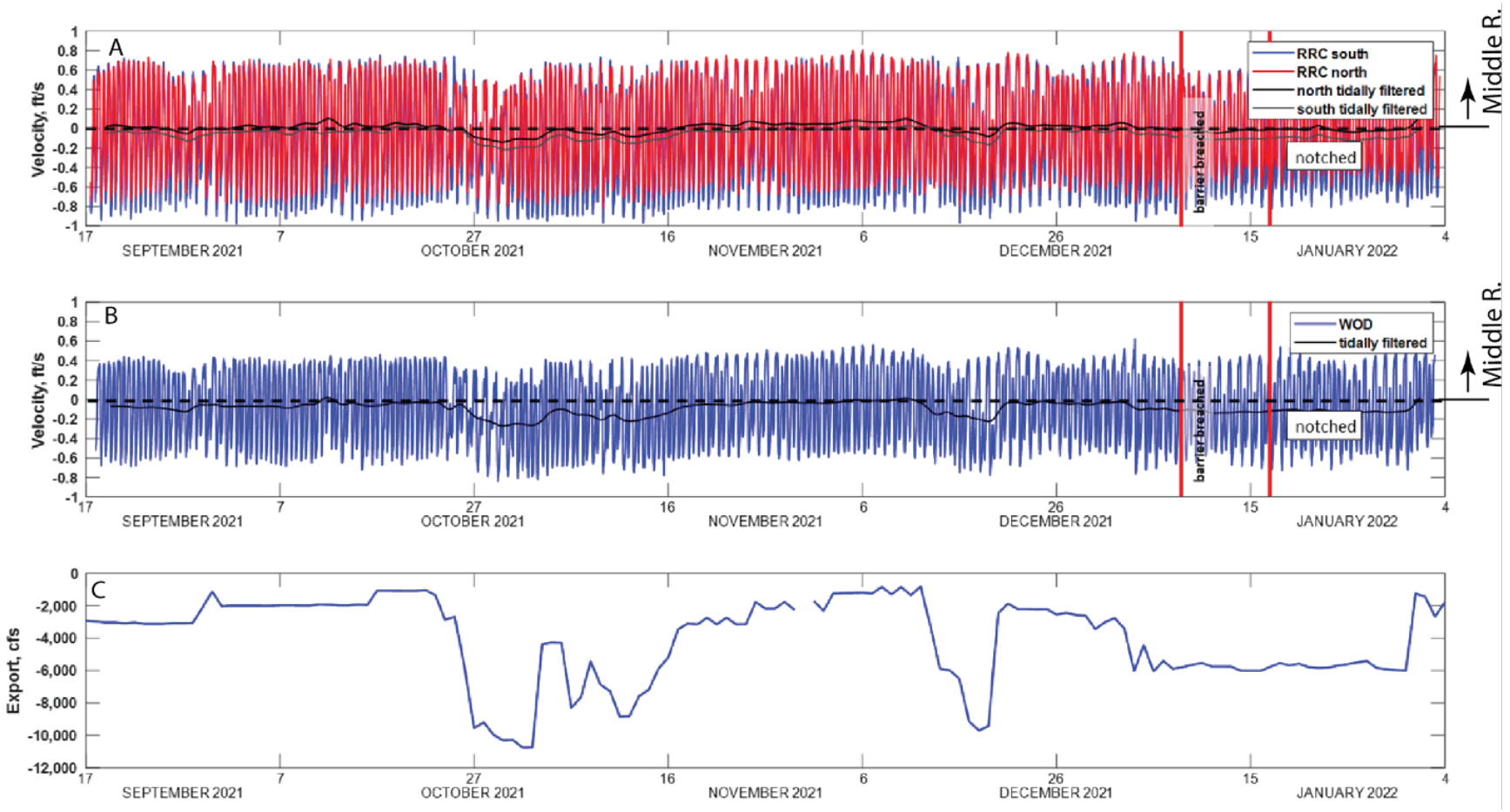

NOTES: Tidal velocities, in feet per second, in (A) Railroad Cut (RRC) and (B) the Woodward Canal (WOD); and (C) exports from the South Delta pumping facilities, in cubic feet per second. The vertical red lines delineate the approximate dates when the barrier was breached and when the notch was fully open. Positive is toward Middle River and negative is toward Old River and the pumps.

Figure 2.2.2-37 Tidal velocities in Railroad Cut and the Woodward Canal and exports from the South Delta pumping facilities.

The pumps do not "suck" water out of the South Delta. Rather, they create a local depression in the water surface that causes water from the surrounding channels to flow toward this depression, where the distribution of net discharge and velocities between Old and Middle rivers, Railroad Cut, and the Woodward Canal is determined by the difference in conveyance between these channels. "Conveyance" refers to the amount of discharge a channel can carry for a given water surface slope based on frictional controls on the discharge, such as the shape of the cross-sections and the roughness of the channel bed (and bank, in narrow channels).

Net velocities in Railroad Cut for September 17, 2021, to February 3, 2022, ranged from nearly -0.2 ft/s to 0.1 ft/s (see the gray and black time series in Figure 2.2.2-37A). These net velocities were slightly less than those in the Woodward Canal, which ranged from roughly 0.3 ft/s to 0.0 ft/s (Figure 2.2.2-37B). Net flows in Railroad Cut and the Woodward Canal were predominantly negative (toward Old River), with peaks of -700 cfs and -1,000 cfs and average discharges of 197 cfs and -360 cfs, respectively (**Figure 2.2.2-38**B and **Figure 2.2.2-39**B).

Constituent Transport

Dispersive Mixing Potential: Measured Tidal Excursion Estimates and LE Ratios

The effect of net velocities on the tidal excursion, and thus on dispersive mixing potential in the Central Delta, was ignored because net velocities in the channels that exchange with Franks Tract are most often negligible compared to tidal velocities.

However, dispersive mixing potential can be dependent on measured velocity when the net velocity is a significant fraction of tidal velocity, which is the case in both Railroad Cut and the Woodward Canal (Figure 2.2.2-35) when exports are high or in the North Delta when river inputs are high. The contribution of the net velocity can significantly lengthen the tidal excursion in the direction of the net currents, and can reduce it when the net and tidal currents are in opposition. Thus, transport of constituents and organisms via dispersive mixing potential increases in the direction of the net currents, especially if the complexity of the bathymetry or planform increases along the tidal excursion's measured trajectory (tidal plus net velocity) in the direction of the net velocity. Similarly, if the net currents are in opposition to the dispersive mixing potential, net dispersion will be less because the tidal excursion will be shorter.

During most ebb tides, Railroad Cut had an LE ratio of 1.3. In this case, the tidal excursion (**Figure 2.2.2-40**A) is greater than the channel length (**Figure 2.2.2-41**), which suggests that salt can be transported from Old River to Middle River through Railroad Cut via network dispersion (Appendix C).

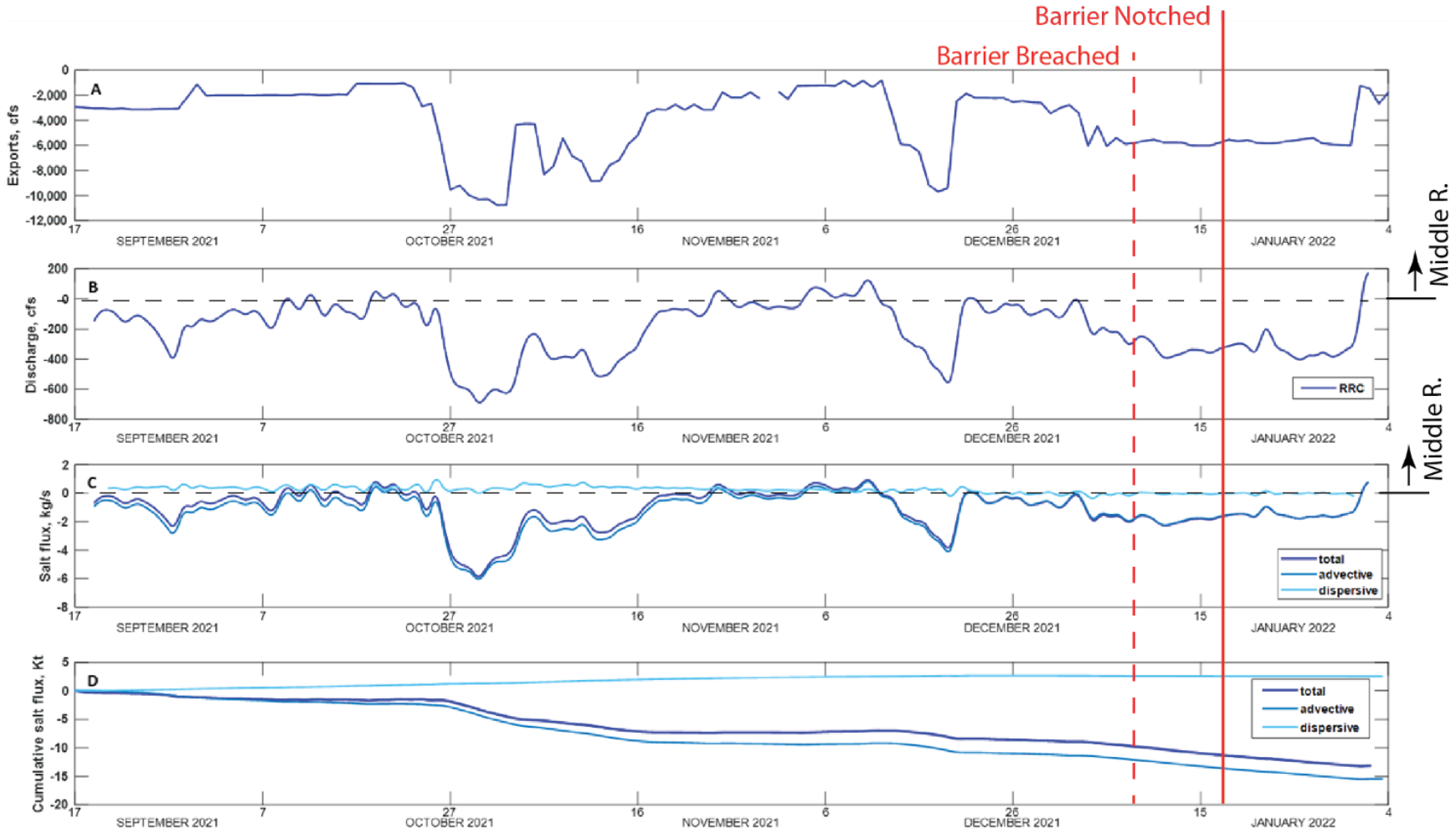

NOTES: cfs = cubic feet per second; kg/s = kilograms per second; Kt = kilotons; RRC = Railroad Cut.
Data collection period: September 2021–January 2022.

Figure 2.2.2-38 Time series plots: (A) Exports from the South Delta; (B) tide-filtered discharge (Godin filter) at Railroad Cut; (C) total, advective, and dispersive salt flux at Railroad Cut; and (D) cumulative advective, dispersive, and total salt flux at Railroad Cut.

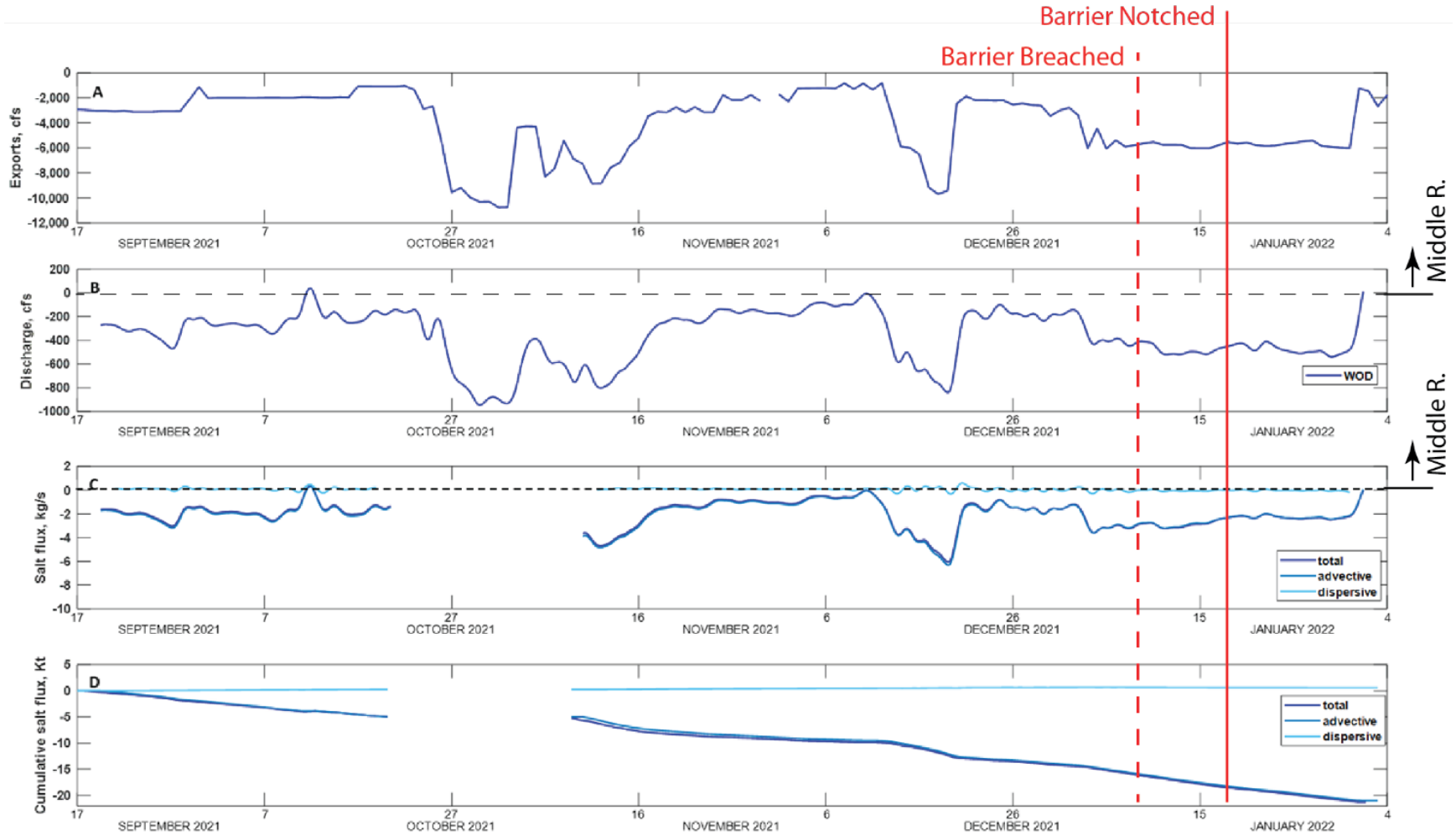

NOTES: cfs = cubic feet per second; kg/s = kilograms per second; Kt = kilotons; WOD = Woodward Canal.
Data collection period: September 2021–January 2022.

Figure 2.2.2-39 Time series plots: (A) Daily exports from the South Delta; (B) tide-filtered discharge (Godin filter) at the Woodward Canal; (C) tide-filtered total, advective, and dispersive salt flux at the Woodward Canal; and (D) cumulative total, advective, and dispersive salt flux at the Woodward Canal.

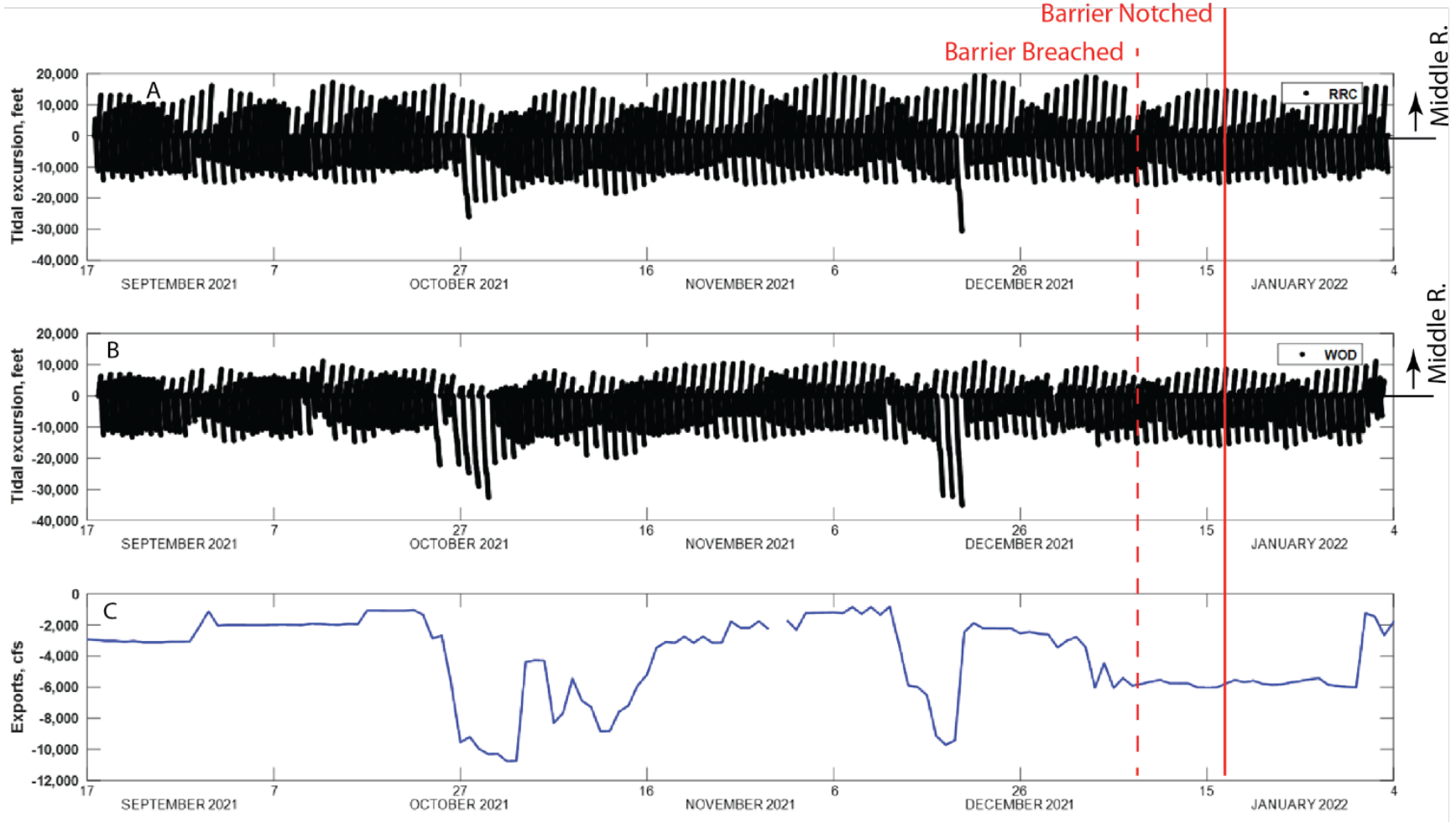

NOTES: cfs = cubic feet per second; RRC = Railroad Cut; WOD = Woodward Canal

Figure 2.2.2-40 Time series plots of tidal excursions for each flood (negative) and ebb (positive) tide (A) at Railroad Cut and (B) at the Woodward Canal, and (C) water exports from the South Delta.

Dispersive Transport Potential

Railroad Cut (Dispersive)
Channel Length = 7,150 ft
Ebb Tides
Ave. Velocity: 0.4 ft/s
Tidal Excursion: 9,500 ft
LE ratio = 1.3
Flood Tides
Ave. Velocity: 0.5 ft/s
Tidal Excursion: 12,000 ft
LE ratio = 1.7

Woodward Canal (Non-Dispersive)
Channel Length = 12,500 ft
Ebb Tides
Ave. Velocity: 0.2 ft/s
Tidal Excursion: 2,300 – 10,000
LE ratio = 0.2 – 0.8
Flood Tides
Ave. Velocity: 0.4 ft/s
Tidal Excursion: 8,150
LE ratio = 0.7

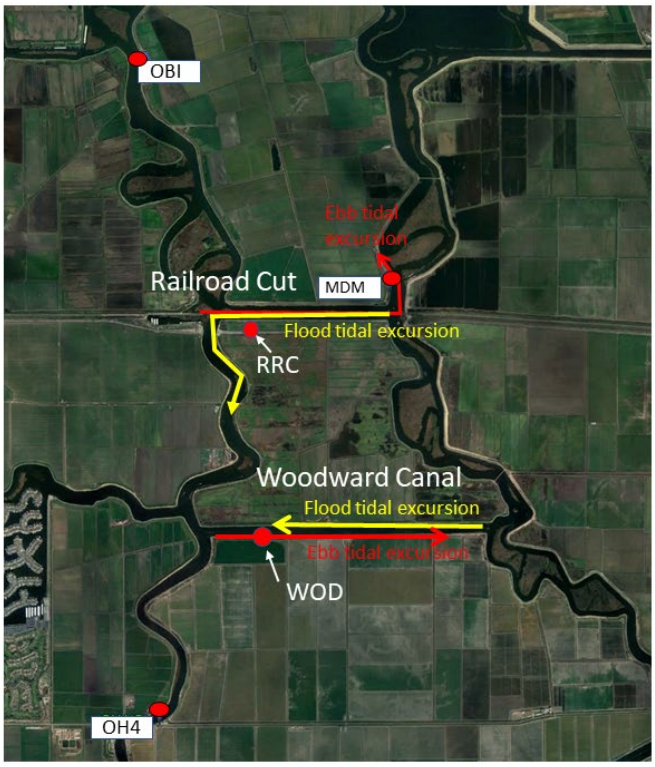

Figure 2.2.2-41 Statistics for dispersive transport potential for Railroad Cut and the Woodward Canal and direction of the ebb and flood tidal excursions.

This is shown to occur in the latter part of the ebb tide at monitoring station MDM (**Figure 2.2.2-42**A). However, most of this saltier water likely flows back into Railroad Cut and is ultimately advected back into Old River.

On flood tides, Railroad Cut had an LE ratio of 1.7 and a tidal excursion toward Old River of 12,000 feet, with fresher water from Middle River flowing roughly 4,700 feet in Old River toward the pumps on the tidal currents. This scenario shows significant exchange of lower salinity water from Middle River through Railroad Cut into Old River, both via dispersive mixing and as a result of the net flow, which is observed at the end of the flood tide at monitoring station Old River at Highway 4 (OH4) (Figure 2.2.2-38A).

Middle River generally has lower conductivity than Old River (Figure 2.2.2-42B) because Middle River is a greater distance from San Francisco Bay and has a direct connection with fresh water exiting monitoring stations Mokelumne River at San Joaquin River (MOK) and Little Potato Slough at Terminous (LPS). Therefore, during flood tides, fresher water from Middle River is transported both dispersively and advectively into Old River—the reason that conductivity is lower at OH4 (which is closer to the pumps) than at OBI (Figure 2.2.2-42A).

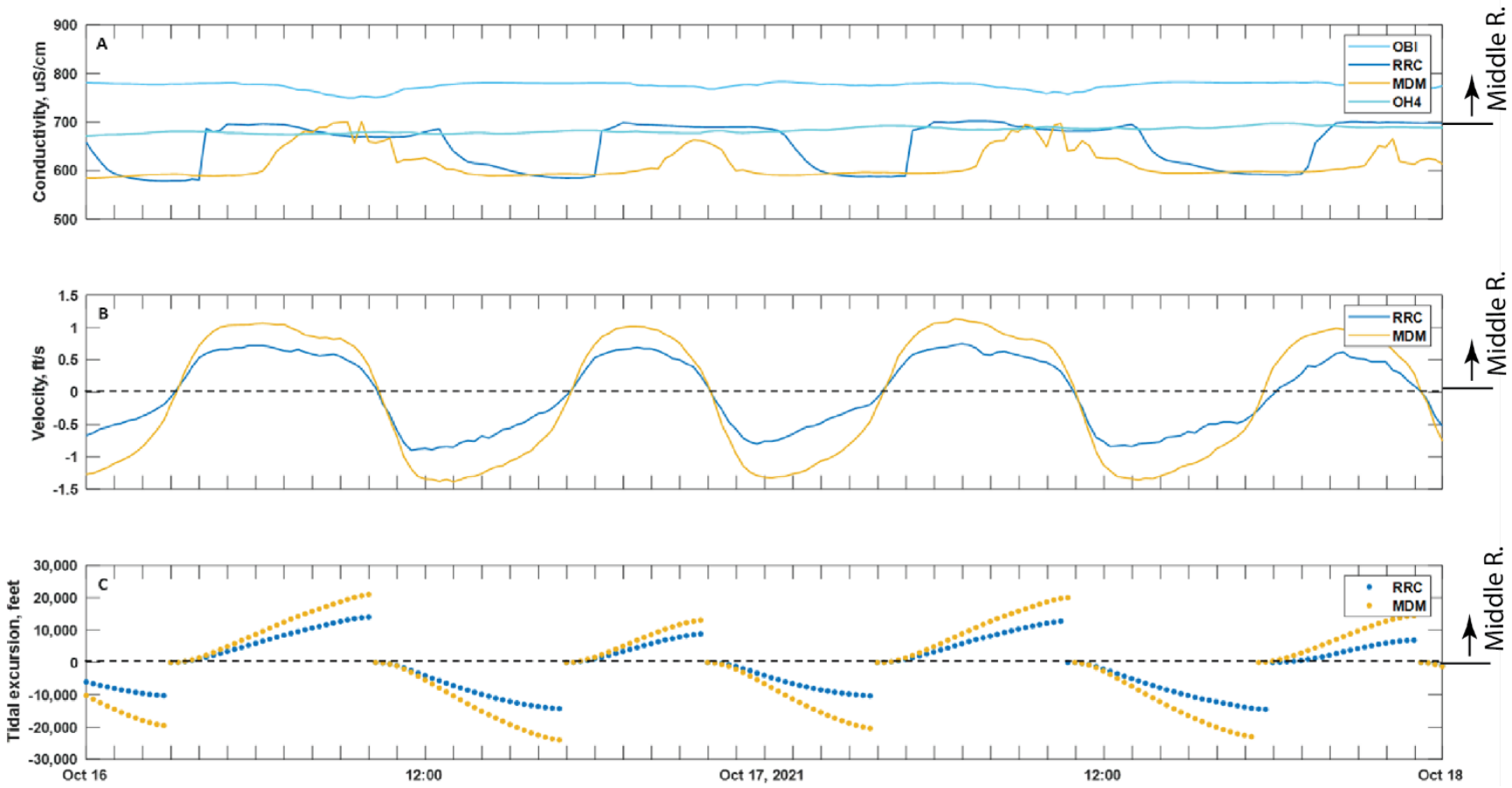

NOTES: µS/cm = microsiemens per centimeter; ft/s = feet per second; MDM = Middle River at Middle River; OBI = Old River at Bacon Island; OH4 = Old River at Highway 4; RRC = Railroad Cut. Data collection period: October 16–18, 2021. The y-axis interval in plot B is 7,300 feet, which is the distance between the RRC and MDM stations.

Figure 2.2.2-42 Time series plots: (A) Conductivity at Old River at Bacon Island, Railroad Cut, Middle River at Middle River, and Old River at Highway 4; (B) velocity at Railroad Cut south and Middle River at Middle River; and (C) tidal excursion distance at Railroad Cut and Middle River at Middle River.

In contrast, the LE ratio in the Woodward Canal was found to range from 0.2 to 0.8 during ebb tides and to be roughly 0.7 on flood tide (Figure 2.2.2-41B). Thus, in all cases, the channel length is longer than the tidal excursion (Figure 2.2.2-41), so dispersive transport through the Woodward Canal in either direction is likely minimal.

Advection: Transport via Net Flows

Net flows at Railroad Cut were found to range from nearly -700 cfs to 100 cfs (Figure 2.2.2-38B). These net flows were slightly higher than net flows in the Woodward Canal, which ranged from roughly -900 cfs to 0 cfs (Figure 2.2.2-39B).

Salt Transport

Conductivity at Railroad Cut and the Woodward Canal during the deployments of single salinity sensors (September 17, 2021, to February 3, 2022) averaged 500 microsiemens per centimeter (µS/cm) (**Figure 2.2.2-43**C). Railroad Cut and Woodward Canal conductivities look very similar at the tidally averaged time scale, with the tidal time-scale variability looking slightly different because of the difference in the LE ratios. Temporal variability was less at the Woodward Canal because the spatial gradient across the channel was less. Ultimately, because the tidal excursion was less than the channel length on both ebb and flood tides, conductivity in Old and Middle rivers gradually increased because of total net salt transport toward the pumps. However, net salt transport in Railroad Cut and the Woodward Canal was limited while the EDB was installed because salt transport through False River into Franks Tract was eliminated when the barrier was in place.

Conductivity in Middle River was found to increase as salt was transported from Old River through Railroad Cut and the Woodward Canal (Figure 2.2.2-43C), but total salt transport was driven by both the net flow and dispersive transport, which was minimal overall (Figure 2.2.2-38D and Figure 2.2.2-39D). Conductivity in Old and Middle rivers decreased simultaneously with increases in inflow from the Sacramento River because of storms or targeted management actions (e.g., releases from New Melones Reservoir into the San Joaquin River, opening of the DCC gates). However, when flow in the Sacramento River was less than 10,000 cfs, conductivity did not appear to decline significantly until increased flow was also observed in the San Joaquin River.

The declines in conductivity during deployment of the salinity sensors in Railroad Cut and the Woodward Canal began on October 29, 2021, after the region experienced a storm with record-breaking rainfall totals. Conductivity again began to decline on December 30, 2021, after another storm increased freshwater inflow into the system so that the effect of the EDB notch on salt flux in the Railroad Cut and Woodward Canal region was minimal.

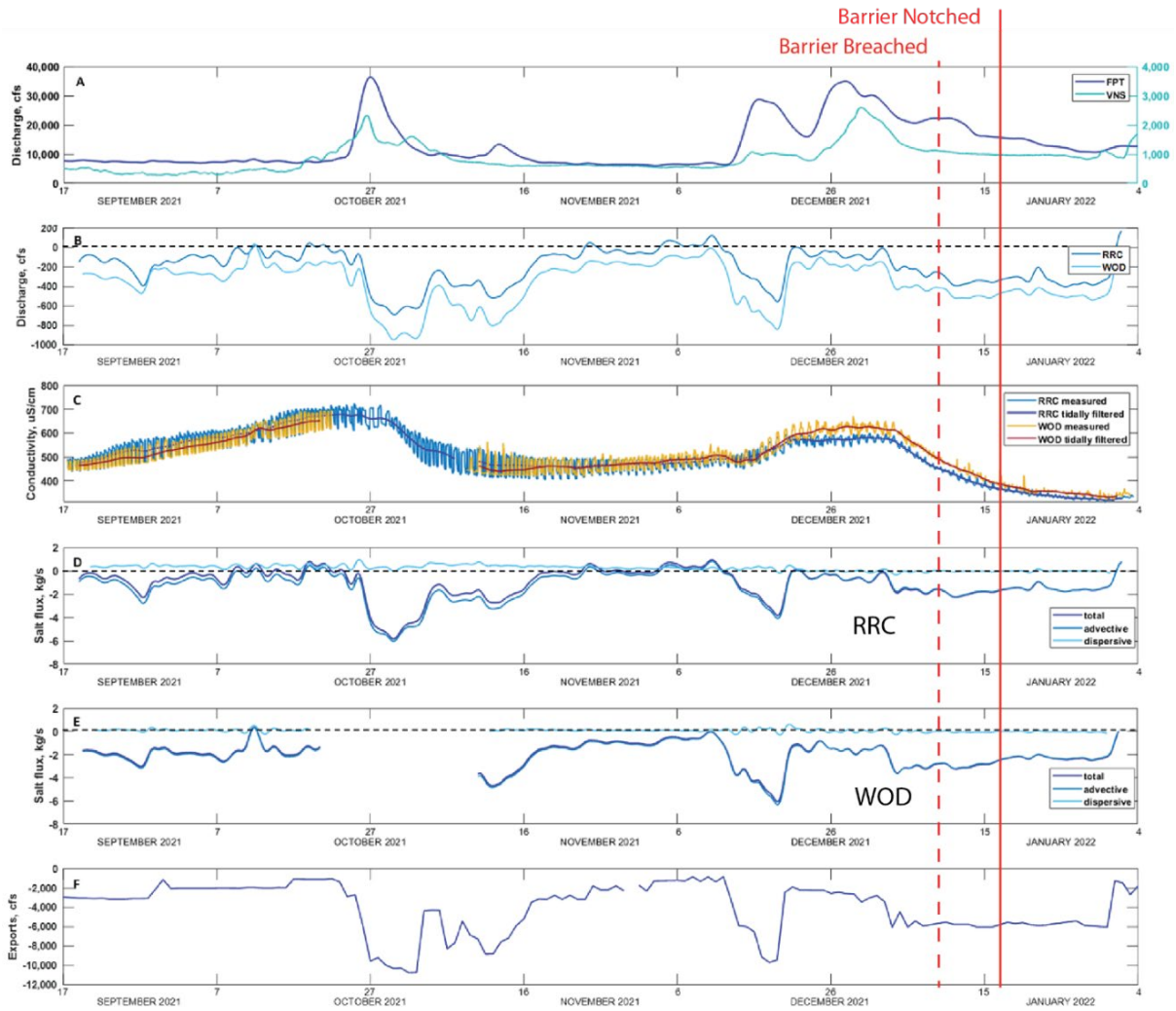

NOTES: µS/cm = microsiemens per centimeter; cfs = cubic feet per second; FPT = Sacramento River at Freeport; kg/s = kilograms per second; MDM = Middle River at Middle River; OBI = Old River at Bacon Island; OH4 = Old River at Highway 4; RRC = Railroad Cut; VNS = San Joaquin River at Vernalis; WOD = Woodward Canal. Data collection period: September 2021–January 2022.

Figure 2.2.2-43 Time series plots: (A) Tide-filtered discharge at the Sacramento River at Freeport and San Joaquin River at Vernalis (right y-axis) depicting timing and magnitude of fresh water into the Delta; (B) tide-filtered discharge in Railroad Cut and the Woodward Canal (RRC and WOD); (C) conductivity at RRC and WOD; and (D) and (E) total, advective, and dispersive salt flux in RRC and WOD, respectively.

This decline in conductivity was consistent with the timing of inflow from the San Joaquin River (December 30; Figure 2.2.2-43C). However, lower-conductivity water flowed into the Railroad Cut/Woodward Canal region from the Sacramento River. Because dispersive mixing is more limited in the Woodward Canal given its LE ratio, freshening was much slower there, and the Woodward Canal had the highest conductivity in the region after the freshwater inflow in late December.

Salt transport in Railroad Cut and the Woodward Canal was consistent with net flows.

For example, salt transport in both Railroad Cut and the Woodward Canal during the salinity sensor deployments was from Middle River toward Old River (Figure 2.2.2-38C and Figure 2.2.2-38D, Figure 2.2.2-39C and Figure 2.2.2-39D). Net salt flux during the deployments was slightly higher in the Woodward Canal (even with the 17-day data gap) because net flow is, and likely always will be, greater in the Woodward Canal than in Railroad Cut. Tidal salt flux at both Railroad Cut and the Woodward Canal decreased after the notch in the EDB was opened (Figure 2.2.2-38C and Figure 2.2.2-39C). This reduction in tidal flux coincided with freshwater inflows and a general decline in conductivity in the region, so any effect during the notch-open period beginning on January 7, 2022, is difficult to detect.

Finally, it may not be necessary to measure the total net flow from Middle River to Old River, depending on the level of accuracy desired. The quantity of fresh water (e.g., the net flow) that exchanges between Middle River and Old River through Railroad Cut and the Woodward Canal can be estimated by taking the difference between the net flow between HOL and OBI (Figure 2.2.2-33B) or between MDM and VCU (Figure 2.2.2-33C). This represents a verification, of sorts, that the estimates of net flow in Old and Middle rivers are consistent.

2.2.2.4 Hydrodynamics Effects of the West False River Drought Salinity Barrier Notch

Introduction

The EDB was initially scheduled for removal in November 2021, but continued drought conditions caused a delay in barrier removal. Given the delay, a temporary notch in the barrier was constructed in January 2022 to facilitate juvenile salmon out-migration through False River in the winter months. The notch was filled in April 2022.

As part of its environmental monitoring plan for the EDB, DWR is assessing the physical and biological effects of the barrier and the notch. For this project, the U.S. Geological Survey (USGS) assessed the near-field effects of the notch on hydrodynamics, by collecting velocity (hydrodynamic) data in February–March 2022 near the False River barrier (**Figure 2.2.2-44**). The goal of these measurements and analyses was to characterize the velocity fields downstream of the notch—to the east on a flood tide and to the west on an ebb tide—to document how the structure of the velocity field (location, magnitude, and direction of the currents) evolved over the course of a flood and ebb tide. A hypothesis was made that the notch would affect the structure of the velocity field by creating large-scale eddies that could provide refugia and increased opportunities for predatory fish.

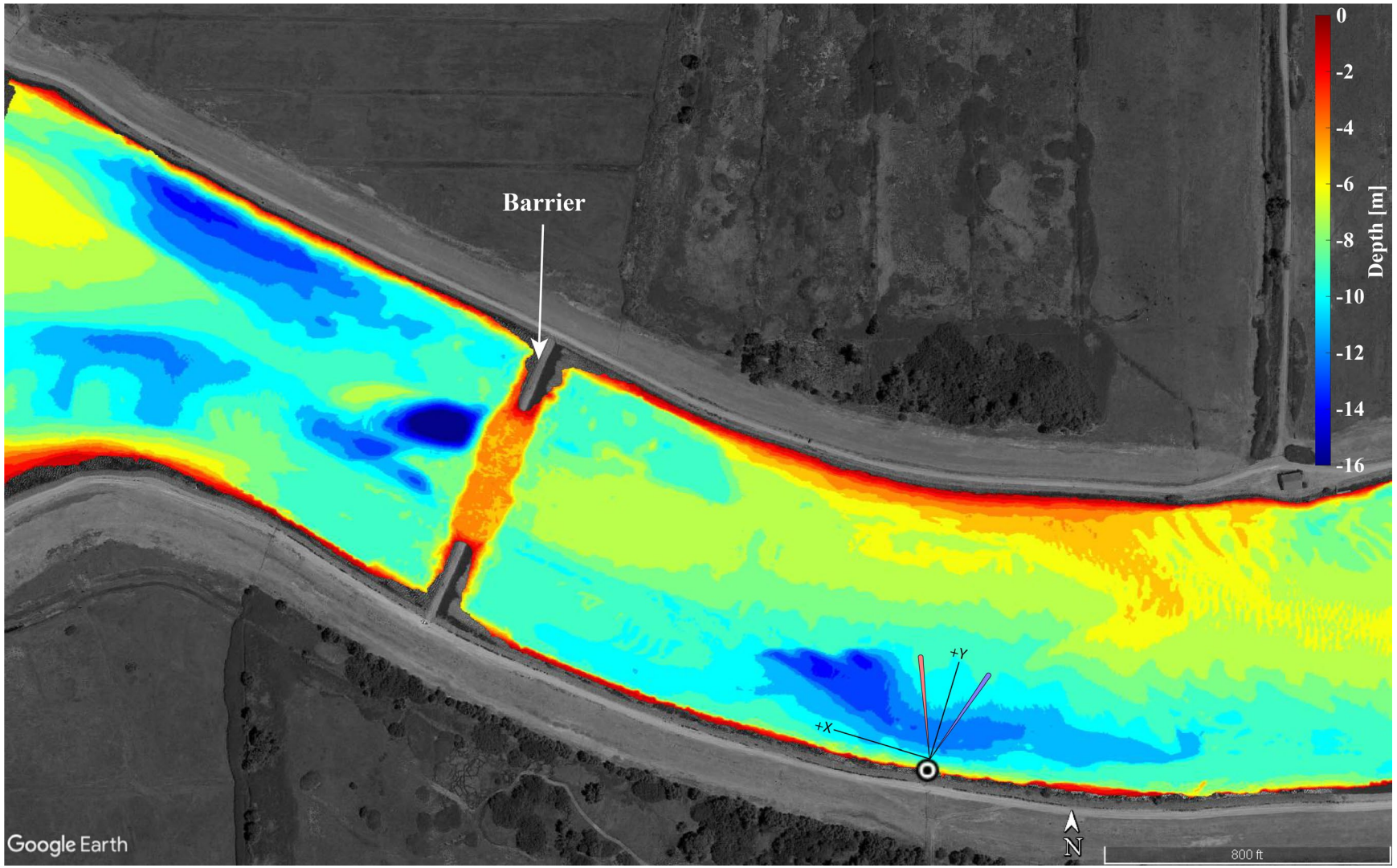

NOTE: The notch in the barrier is about half the width of the river (approximately 125 meters versus 250 meters); the notch is about 4–5 meters deep, more than half the river's depth (approximately 7 meters). The white dot shows the location of the side-looking acoustic Doppler current profiler, and the red and blue cones show the approximate sampling area of the beams. The instrument's coordinate system is also shown.

Figure 2.2.2-44 Bathymetric map of False River at the location of the study area.

To properly document the structure of the velocity field, the velocity measurements were converted into two-dimensional (2D) velocity maps. A more sophisticated 2D horizontal velocity interpolation was required for an accurate representation of the velocity field. Interpolation of 2D horizontal velocity fields in open channels is challenging because these flows are anisotropic; that is, the flow velocity at a given point will likely be more correlated with velocity upstream or downstream of a given location, following the velocity field streamlines, than with the velocities in the lateral direction. Therefore, a novel velocity interpolation technique was developed to create 2D horizontal velocity maps from discrete cross-sectional measurements.

The velocity maps were then used to estimate velocity magnitude and vorticity, and these were used as covariates in the fish predation analysis (see Section 2.3.3.4, "Predation Study"). Because the fish predation data did not overlap the periods that the velocity maps were generated, velocity maps were indexed to the periods of fish predation data during similar hydrodynamic conditions.

Interpolation of Spatial Data—General Methods

Interpolation of spatial data is well established in the literature. Some of the most widely used techniques are inverse distance weighting (IDW), spline fitting (or, more generally, polynomial fitting), kriging, and triangulation (Amidror 2002). Each technique has limitations and advantages depending on the input data (density, spacing, and accuracy) and the computational efficiency (Amidror 2002).

For example, IDW is one of the most commonly used techniques because it is easily implemented and computationally fast. IDW is a global method because it uses a prescribed number of points or a prescribed search radius, and it works well with high-density data (David et al. 2002) because the number of points within a search radius can be tuned to include only points near the interpolated point. However, for this application, the IDW method may inappropriately weight lower near-bank velocities the same as higher near-center-channel velocities because the weighting window is isotropic (i.e., equal in all directions).

Kriging, another popular data fitting technique, predicts a value at a given point as a weighted average based on a variogram function that describes the degree of spatial dependence of a stochastic process (Oliver and Webster 1990). Spline interpolation performed better than IDW for anisotropic processes (Sokolov and Rintoul 1999).

Triangular interpolation has the advantages of being local, computationally efficient, and usually more accurate than IDW (Amidror 2002). This technique is used extensively for unstructured mesh generation in

computational fluid dynamics because it can be adapted to more complex geometries and flow features (Weatherill 1992). Delaunay triangulation uses a set of non-overlapping convex polygons that avoid narrow angles and can better represent anisotropic data. For velocity data collected from multiple cross-sections, a Delaunay triangulation creates triangles that include upstream and downstream points.

Interpolation of Spatial Data—Fluid Dynamics Applications

To interpolate spatial data in hydrodynamic applications, the anisotropic nature of the flow field must be adequately represented, as demonstrated in the following studies, which helped guide development of the interpolation technique.

IDW interpolation was used to visualize flow dynamics in the lower Sacramento River (Dinehart and Burau 2005a). However, the limitations of this technique were noted by Dinehart and Burau (2005a), who also suggested that using an interpolation algorithm to account for velocity along streamlines would be more suitable.

Kriging can employ anisotropic model variograms that account for directional dependence (Rennie and Church 2010). Kriging provides spatial smoothing, similar to data averaging, and it has been used in acoustic Doppler current profiler (or ADCP) datasets from moving boats, with a high density of data points (Jamieson et al. 2011). In the studies conducted by both Rennie and Church (2010) and Jamieson et al. (2011), the aim of the project(s) was to estimate quantities related to scour and shear velocity, both of which can be difficult to ascertain from averaged data; therefore, kriging interpolation was employed from single transect data.

Tsubaki et al. (2012) developed a velocity interpolation technique with anisotropic gridding using ADCP data from a moving boat (high data density), which proved more accurate than kriging or IDW. With this method, anisotropic interpolation ellipses are defined with the semi-major axis four times the size of the semi-minor axis, in the flow direction. This method requires a high density of data. It also requires an initial isotropic interpolation to first define the flow direction for the anisotropic interpolation ellipses.

Andes and Cox (2017) developed a rectilinear IDW algorithm that uses a flow-oriented transformation, for interpolating bathymetric data. The rectilinear search neighborhood was defined upstream and downstream of the flow path lines (defined by the channel centerline). This method assumes that the flow direction is generally defined by the channel centerline.

For this analysis, an along-streamline interpolation algorithm was developed, where velocity between two cross-sections is interpolated along an estimate

of the streamline. The crux of this algorithm is determining the *location of the streamlines*, which is challenging because streamlines are dependent on the underlying velocity field, the very quantities to be estimated—a classic causality dilemma.

Methods

Data from ADCPs were used to characterize the velocity fields near the False River barrier notch. A stationary side-looking ADCP (SL-ADCP) was used to measure the velocity over a relatively small spatial scale (approximate 100-meter section of a 250-meter-wide river) but a longer temporal scale (approximately six weeks). Moving-boat ADCP (MB-ADCP) measurements were made at larger spatial scales (approximately 100,000 square meters [m^2]) to compute velocity maps, but over a relatively short time scale (multiple transects made over several hours on several days).

Acoustic Doppler Current Profiler Measurements

Side-Looking Acoustic Doppler Current Profiler

The SL-ADCP at False River is part of a longer term monitoring network (U.S. Geological Survey 2023a) that is located approximately 450 meters east of the False River barrier (Figure 2.2.2-44). Over a period of approximately five weeks (February 22–March 30, 2022) while the barrier was notched, the SL-ADCP was repositioned and reprogrammed to better characterize the distribution of near-bank lateral velocity (**Table 2.2.2-2**). Data were collected at one-minute intervals, with 60 ensembles averaged over the sampling interval. The SL-ADCP records data in instrument coordinates, e.g., coordinates relative to the orientation of the instrument. The x-velocity component is the velocity vector normal to the SL-ADCP heading, and the y-velocity component is the velocity along the SL-ADCP heading.

TABLE 2.2.2-2
PARAMETERS OF THE FALSE RIVER SIDE-LOOKING ACOUSTIC DOPPLER CURRENT PROFILER

Easting	Northing	Heading	Bin Size (meters)	Bins	Range (meters)
616936	4212808	10	2.5	34	85

SOURCE: Data compiled by U.S. Geological Survey in 2022

Individual bins (series of discrete measurement volumes extending from the instrument at the bank perpendicular to the flow) of the x- and y-components of one-minute velocity ($Xvel_B, Yvel_B$) from the SL-ADCP were bin-averaged ($Xvel, Yvel$) and time-averaged over 15 minutes ($Xvel_M, Yvel_M$) to remove large spatial and temporal fluctuations in the data. The bin- and time-averaged x-component of velocity ($Xvel_M$) was used as an index

velocity ($Ivel$). The average of the fluctuating components of $Xvel_M$,$Yvel_M$ (Vel_F) was used as an indicator of turbulence or unsteadiness of the flow, and Vel_F was calculated with the following equations:

$$Xvel' = Xvel_B - Xvel_M \quad (1)$$

$$Yvel' = Yvel_B - Yvel_M \quad (2)$$

$$Vel_F = \overline{Xvel' \cdot Yvel'} \quad (3)$$

Moving-Boat Acoustic Doppler Current Profiler

The MB-ADCP measurements were conducted, from multiple measurement vessels, on six days in March 2022—March 14, 15, 17, 23, 29, and 30—using standard USGS discharge techniques (Levesque and Oberg 2012). These measurements were conducted to characterize the velocity field generated by the tides passing through the notch in the False River barrier. To minimize turbulent fluctuations on the resultant velocity field, repeated surveys were performed along cross-sections (Dinehart and Burau 2005b). The repeated surveys were then averaged into one common cross-section.

MB-ADCP measurements conducted on March 14, 2022, were collected as reconnaissance data to provide a better sense of the spatial velocity patterns. Data from the SL-ADCP indicated that the scale of turbulence varied from small, short lengths and time scales to large slow-moving eddies; therefore, six repeated surveys (the number recommended by Dinehart and Burau [2005b]) might not be enough to minimize turbulent fluctuations. Because there is a trade-off between temporal and spatial resolution for interpolating velocity distributions, these early measurements were needed to estimate the time rate of change of the velocities to determine how many cross-sections could be measured over relatively steady conditions.

MB-ADCP measurements were collected on March 15, 2022, from 9:46 a.m. to 1:06 p.m. at six different cross-sections from three measurement vessels, and on March 17, 2022, from 11:20 a.m. to 2:25 p.m. at nine different cross-sections from three vessels. All measurements were collected over the course of a flood tide. Based on the data collected on March 15 and 17, the sampling strategy was changed. Instead of measuring different cross-sections with a single vessel, a single cross-section was measured continuously for the duration of the measurement period on that day. On March 23, 2022, measurements were collected at three different cross-sections on the west side of the barrier during an ebb tide from 8:08 a.m. to 11:26 a.m. On March 30, 2022, measurements were collected at four different cross-sections on the east side of the barrier during a flood tide from 10:00 a.m. to 12:24 p.m.

Data were then processed using the following steps:

1. ASCII files were exported from the data collection software (WinRiver) for use in the data processing platform Velocity Mapping Toolbox (VMT) (Parsons et al. 2013).
2. ASCII files were loaded into VMT and ship tracks (.kml files) were exported, to aid in grouping transects into separate cross-sections.
3. A batch file was generated based on transect groupings.
4. Transects were processed in VMT using the batch file.

Velocity Interpolation

Pre-processing

Sets of cross-sections were aggregated under relatively steady conditions (where the structure of the velocity field remained relatively stable over the aggregation period) to provide input for the velocity interpolation, which was completed using algorithms developed in Matlab (MathWorks 2022).

Interpolation between cross-sections was done using an along-streamline interpolation scheme. For each set of cross-sections (i.e., a single velocity map), a 5-meter by 5-meter grid was generated for a domain that included the cross-sections and the riverbanks. Riverbanks were drawn in Google Earth and converted to Matlab format. The coordinates of the cross-sections were extrapolated to the riverbanks, following the same orientation as the cross-sections. The u and v velocity components were extrapolated to the riverbanks, assuming that the sidewall boundary layer followed a 1/6 power law. The velocity magnitude (vector sum of u and v components) and direction were extrapolated separately. The velocity magnitude was extrapolated used for the 1/6 power law, and the velocity direction was linearly interpolated using the direction of the last measured point and a direction normal to the riverbank. The extrapolated velocity magnitude and direction were then converted to u and v components.

Along-Streamline Interpolation Algorithm

Generating accurate streamlines requires a velocity field, but an interpolated velocity field is the quantity that needs to be calculated. Therefore, the first step in this algorithm was to generate a "reasonable guess" of the streamlines.

In rivers, the thalweg (the lowest riverbed elevation) defines the principal flow direction. Based on the bathymetry (Figure 2.2.2-44), the western side of the West False River EDB shows two distinct deeper regions—one on the north bank and the other closer to the south bank—that might represent different flow pathways for the flood and ebb tides. There is also a deep scour hole, located near the barrier, that resulted from flow through the notch. At this location, and in tidal environments in general, the principal

flow direction may not be defined by the thalweg. Therefore, a relatively simplistic approach was used to define the initial set of streamlines that followed the shape of the river's centerline defined by the shape of the riverbanks. Initial streamlines were generated in curvilinear coordinates, based on the river's centerline, then converted back to Cartesian coordinates.

Velocities were interpolated along streamlines using an inverse distance weighting scheme,

$$U(x) = \frac{\sum_{i=0}^{N} w_i(x) u_i}{\sum_{i=0}^{N} w_i(x)} \quad (4)$$

$$w_i(x) = \frac{1}{d(x,x_i)^P} \quad (5)$$

where $U(x)$ is the interpolated velocity (u and v components are interpolated separately) at point x, w_i is the weighting parameter, and u_i is a known velocity at point x_i. The w_i is the inverse distance d from the interpolated point x and the known point x_i, which can be adjusted based on a power parameter P. Velocities at all points along a streamline were then interpolated onto the 5x5-meter grid to generate the initial velocity field.

Because the initial set of streamlines was likely inaccurate, an iterative process was performed to arrive at a final solution. Starting with a new set of streamlines generated from the initial velocity field, the velocity interpolation scheme was run again. This process was repeated until the solution converged. "Convergence" was defined as a minimal change in the median difference in the velocity field from iteration to iteration; that is, it was assumed that convergence was achieved when further iteration did not appreciably change the velocity field.

This was tested on a subset of interpolated velocity fields and it was determined that five iterations were suitable for convergence. Occasionally on subsequent iterations, the streamlines did not pass through all the 5x5 grid cells; therefore, an interpolated velocity could not be calculated in these cells. In these cases, the velocity from the previous iteration was used.

After interpolated velocity fields were computed, the vorticity was computed to quantitatively determine the location of shear zones and eddies. Vorticity ($\vec{\omega}$) describes the local rotation of a fluid that results from a spatial change in velocity magnitude or direction as follows:

$$\vec{\omega} = \nabla \times \vec{v} = \left(\frac{\partial v}{\partial x} - \frac{\partial u}{\partial y}\right)\hat{z} \quad (6)$$

where the curl of the 2D vector field ($\vec{v}$) is $\nabla \times \vec{v}$, with velocity components u and v at coordinate points x, y.

Velocity Interpolation Comparison

The iterative process of determining the velocity field and streamlines described above assumed that a reasonable estimate of the actual solution could be realized upon convergence. A calibration step was performed to determine the best fit to the measured data.

The velocity interpolation was tuned using the power parameter P. Values of 1, 2, and 4 were chosen for P. A value of 1 is equivalent to linear interpolation; the higher the value, the more the solution will be weighted toward the nearest points. A set of interpolated velocity maps was produced with both the second and third cross-sections removed (from the March 30, 2022, map; see Figure 2.2.2-51G later in this section). These maps were compared to the measured data at each cross-section. The root mean squared difference was used to determine which iteration and which value of P provided the best estimate of velocity at the second and third cross-sections.

Next, the along-streamline interpolation was compared to the IDW and triangulation methods, as these are easy to implement and are both common methods. For the IDW, a weighting parameter of 2 was established and the number of points to include was set to 10. For the triangulation interpolation, the scatteredInterpolant function (MathWorks 2022) in Matlab with a linear interpolation method was used. The scatteredInterpolant function uses a Delaunay triangulation (Amidror 2002) that draws triangles between measured cross-sections; thus, in a sense, this interpolation could be comparable to the initial streamline interpolation that follows streamlines along the channel centerline.

Indexing Velocity Maps

Interpolated velocity maps were produced over a single tidal phase for both flood and ebb tides; however, velocity maps were needed for periods that were not measured to compare with periods when fish predation sampling took place (**Table 2.2.2-3**). Velocity maps were indexed to a strength of tide (η_S) metric, defined as the difference in water level over a flood or ebb tide. Ideally, the velocity maps would have been indexed to the SL-ADCP, but there were samples of fish predation that occurred outside of the operational window of the SL-ADCP. Therefore, a linear regression was developed between η_S and the averaged (over a tidal phase; flood or ebb) index velocity ($\overline{Ivel}$).

Single sets of velocity maps were computed for both the flood and ebb tides, but these sets of velocity maps did not extend over the full tide. Therefore, the velocity maps had to be extrapolated to the end of tide. The maps were extrapolated from the last measured velocity map based on magnitude alone, assuming that the structure of the velocity field did not change. This assumption was made based on an examination of spatial plots of $Xvel_B$ and $Yvel_B$, which showed that from peak tide to the end of tide, the velocity

magnitudes changed while the directions of the velocities were more stable. Once a full set of velocity maps for each tide was computed and extrapolated, the period of each tidal phase (flood or ebb) was normalized from 0 to 1, with 0 indicating the beginning of the tide and 1 indicating the end of the tide, because the tides have different durations.

TABLE 2.2.2-3
DATE AND TIME OF VELOCITY MAPS AND TIDE AND VELOCITY CONDITIONS

Date	Time (PST)	Number of Velocity Maps	Number of Cross-Sections	Tide Condition	$Xvel_M$ (m/s)
March 15, 2022	12:30 p.m.	1	6	Flood	-1.05
March 17, 2022	1:51 p.m.	1	9	Flood	-1.12
March 23, 2022	8:08–11:26 a.m.	7	3	Ebb	0.17 to 0.37
March 30, 2022	10:00 a.m.–12:24 p.m.	9	4	Flood	-0.07 to (-1.31)

NOTES: m/s = meters per second; PST = Pacific Standard Time; $Xvel_M$ = 15-minute averaged velocity

SOURCE: Data compiled by U.S. Geological Survey in 2022

To index the velocity maps, two lookup tables were used: first, the normalized time in tide (t_N) from 0 to 1 for either a flood or ebb tide; and second, the η_S and associated $\overline{Ivel}$. For instance, a sample of fish predation that occurred on a flood tide halfway through the tide (t_N = 0.5) was registered to the flood velocity map that occurred closest to t_N = 0.5. Then, for the η_S for that fish, the predation sample was compared to the η_S when the velocity map was collected and the velocity map was scaled based on the ratio of the $\overline{Ivel}$, associated with each η_S. A major assumption in this indexing was that the structure of the velocity field would remain stable from tide to tide. The velocity map indexing and the assumptions in this method are addressed in more detail in the "Results" section below.

Results

Sideward-Looking Acoustic Doppler Current Profiler

Velocity data collected from the SL-ADCP show large spatial and temporal fluctuations on the flood tide (negative velocity; **Figure 2.2.2-45**). On peak flood tides, the 15-minute averaged velocity ($Xvel_M$, the cyan line in Figure 2.2.2-45A) was about three times as large as $Xvel_M$ on peak ebb tides. The $Yvel_M$ signal was similar to $Xvel_M$, where the largest magnitude and variations occurred on the flood tides (Figure 2.2.2-45B), which can also be seen in the velocity fluctuations (Figure 2.2.2-45C). The MB-ADCP measurements captured a representative range of the flood tide conditions but only a single set of ebb tide conditions.

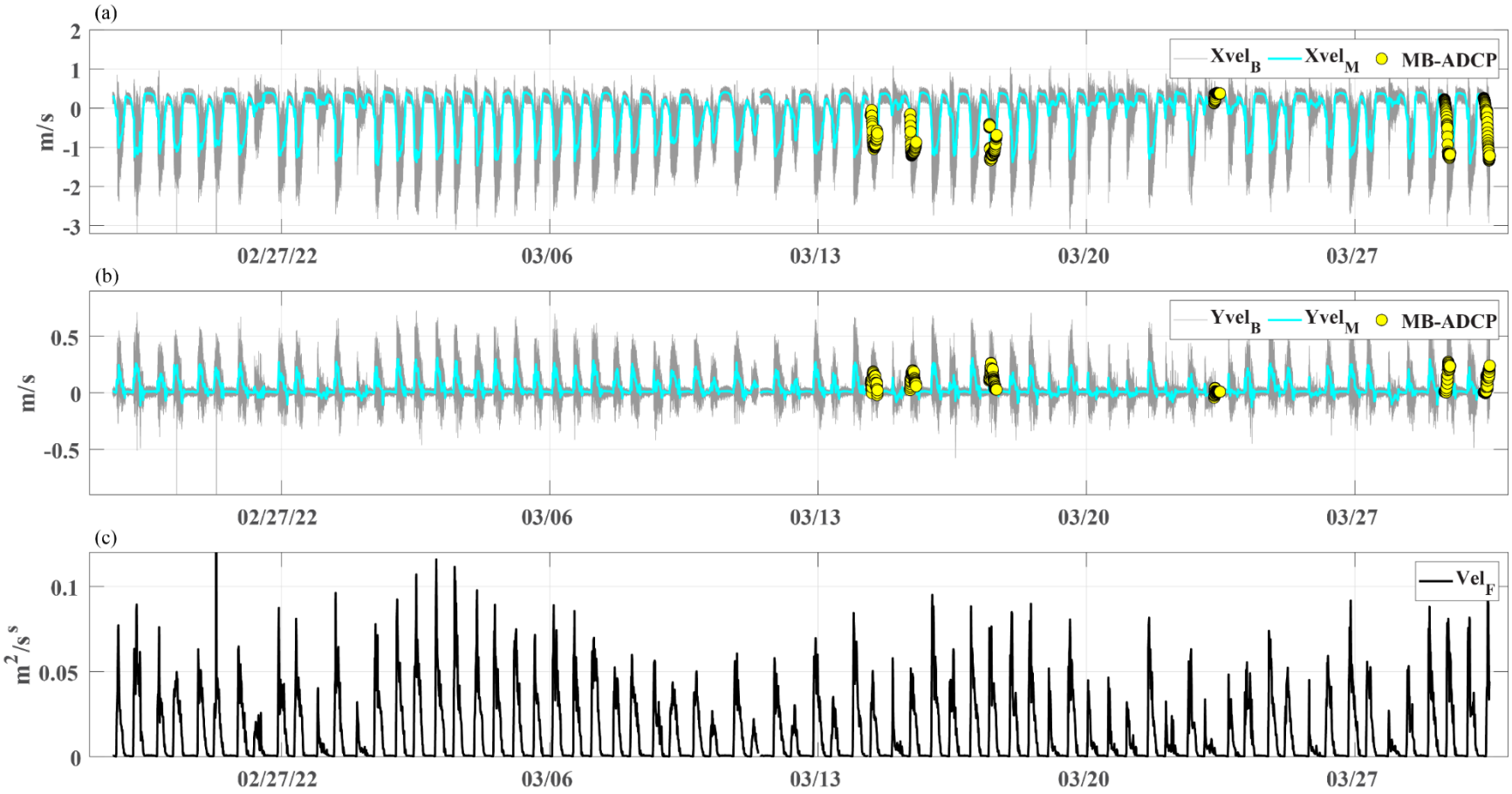

Notes: m/s = meters per second; m^2/s = square meters per second; Vel_F = average of spatial and temporal fluctuations
The gray dots (XvelB, YvelB) show single-bin one-minute data; the cyan lines (XvelM, YvelM) are the average of all bins and an average over 20 minutes; and the yellow circles (MB-ADCP) identify times when moving-boat acoustic Doppler current profiler measurements were collected.

Figure 2.2.2-45 Time series data from the side-looking acoustic Doppler current profiler of (a) x-velocity, (b) y-velocity, and (c) mean velocity fluctuations—February–March 2022.

Figure 2.2.2-46 is a representative example of spatial and temporal variation in velocity over several tides on March 14 and 15, 2022. On ebb tides, the single-bin data ($Xvel_B$ and $Yvel_B$, red lines in Figure 2.2.2-46A and B) show small temporal and spatial variation (approximately 0.2 meter per second [m/s] and 0.05 m/s) compared to the flood tide (greater than 1 m/s and greater than 0.5 m/s). The average of spatial and temporal fluctuations (Vel_F; Figure 2.2.2-46C) is several orders of magnitude larger on the flood tide, indicating large-scale turbulent features in the water. On the flood tide, water is constricted by the notch, which produces a turbulent jet that enters quiescent water, which results in higher magnitude velocity and increased turbulence (Fischer et al. 1979). The Vel_F signal, an indication of large-scale turbulence, increases quickly and peaks at the beginning of the flood tide, and then decreases steadily during the remaining flood tide. This indicates an adjustment period at the beginning of the flood as the spatial structure of the velocity field adjusts to flow through the notch.

The second flood tide shown in Figure 2.2.2-46—occurring just before the start of March 15—had a weak signal, where $Xvel_M$ was mostly positive or near zero, but there were still large velocity fluctuations. It is unclear exactly what occurred during this flood tide. SL-ADCP data quality indicators (signal strength and correlation, not shown) suggest that the data collected during this period were of good quality. Moreover, this trend was observed in 13 flood tides, or about 20 percent of the 70 flood tides measured, suggesting that this phenomenon was real and not a data collection malfunction. One possible explanation is that the jet from the notch did not travel far enough toward the bank to be captured by the SL-ADCP, which measured only about one-third of the width of the channel.

Performance of the Along-Streamline Velocity Interpolation Algorithm

The velocity interpolation algorithm was tuned using MB-ADCP data collected on March 30, 2022, because this dataset covered a range of conditions, and because it had larger spacing (approximately 200 meters) between cross-sections than data collected on other days. **Figure 2.2.2-47**A shows an example of the 5x5 meter grid generated between measured cross-section locations, with the cyan line showing the river centerline used to generate the initial set of streamlines depicted in Figure 2.2.2-47B. As shown, the initial set of streamlines does not necessarily follow the main flow, which moves toward the south bank.

Figure 2.2.2-48 shows a representative example of the streamlines and resulting along-streamline interpolation after the initial interpolation. In this example, several cross-sections show streamlines that do not simply move in an upstream-downstream direction, nor do they follow the along-stream direction defined by the initial set of streamlines; therefore, several iterations were necessary before the interpolation algorithm could reach a solution.

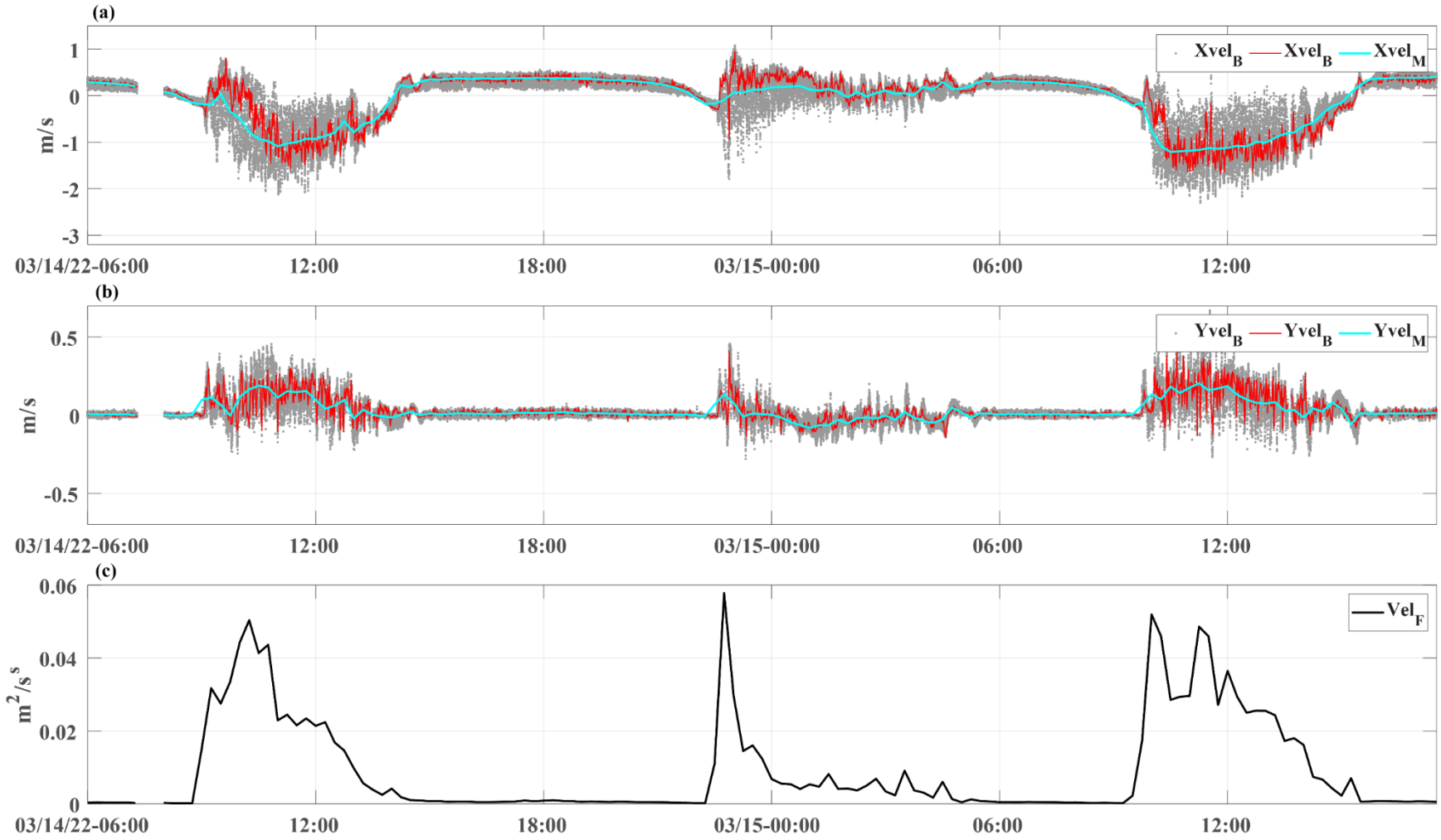

Notes: m/s = meters per second; m^2/s = square meters per second; Vel_F = average of spatial and temporal fluctuations
The gray dots (XvelB, YvelB) show all-bins one-minute data; the cyan lines (XvelM, YvelM) are the averages of all bins plus averaged over 20 minutes; and the red line shows single-bin data to illustrate temporal variation.

Figure 2.2.2-46 Time series data from the side-looking acoustic Doppler current profiler of (a) x-velocity, (b) y-velocity, and (c) mean velocity fluctuations—March 14–15, 2022.

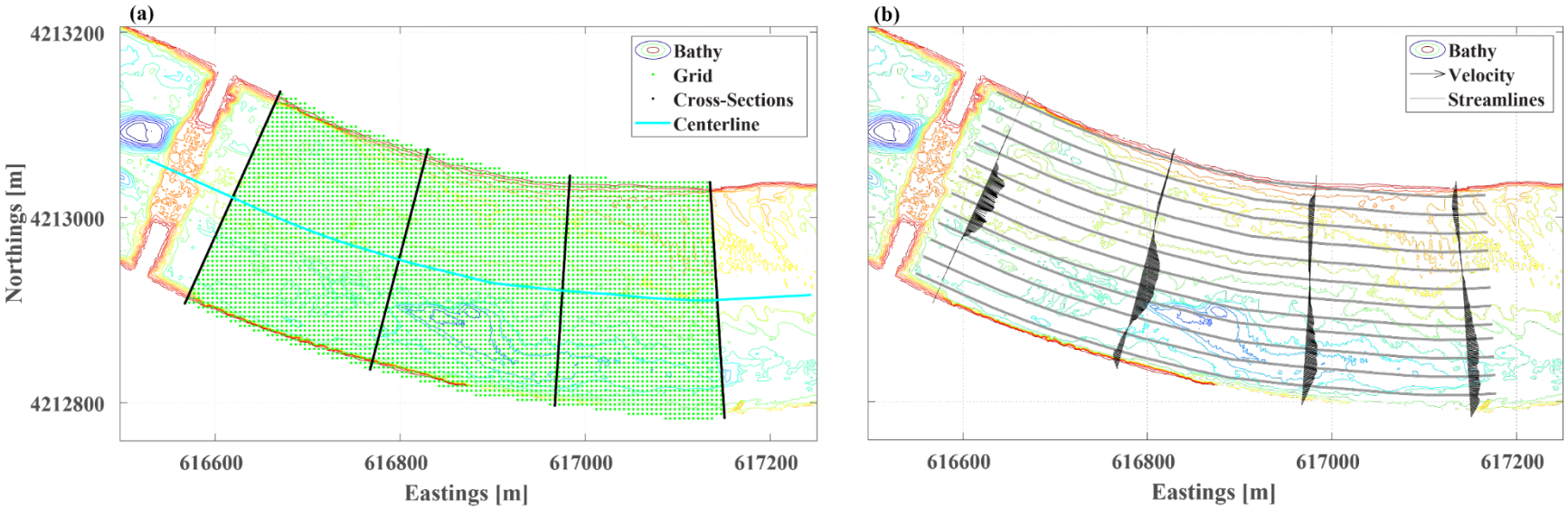

Note: In map (a), green dots = the 5x5 meter grid; black dots = cross-section locations; and cyan = the centerline for curvilinear coordinates. In map (b), black lines = velocity vectors (measured and extrapolated) and gray = initial streamlines used in first interpolation iteration.

Figure 2.2.2-47 Maps from March 30, 2022, data collection: (a) 5x5 meter grid, cross-section, and centerline used for curvilinear coordinates; and (b) velocity vectors (measured and extrapolated) and initial streamlines used in first interpolation iteration.

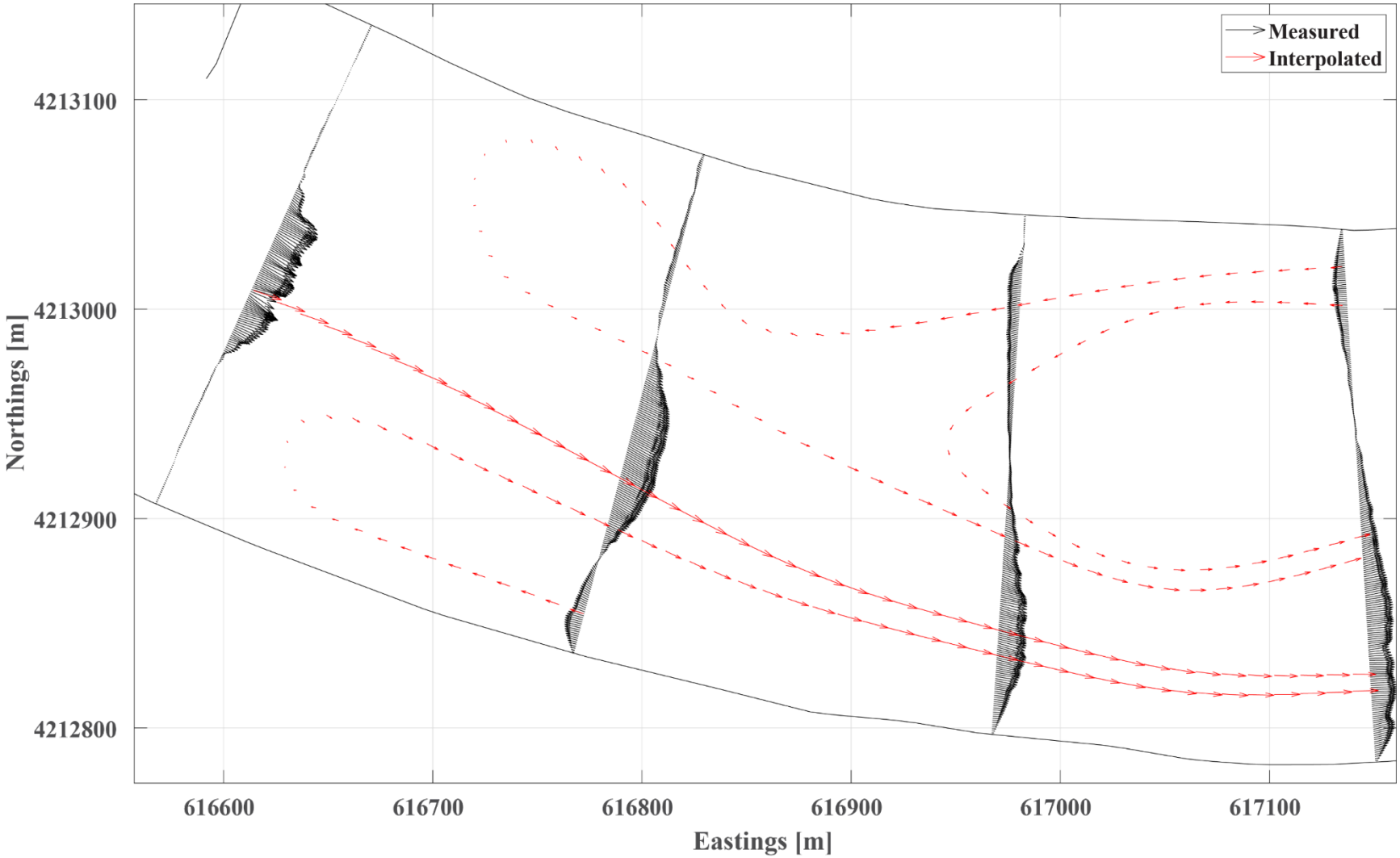

Figure 2.2.2-48 Velocity at measured cross-sections and examples of interpolated velocity along streamlines, March 30, 2022.

For the first few iterations of the velocity interpolation, changes in the structure of the velocity field were evident; however, the velocity field did not appreciably change after five additional iterations were performed (**Figure 2.2.2-49**). Moreover, the velocity interpolation appears to represent the salient features in the velocity field, with a jet that propagates through the notch and moves toward the south bank.

The power parameter (P) of 2 provided a better estimate of velocities in cross-sections 2 and 3 than P values of 1 or 4. Velocity interpolation methods were compared using the interpolated velocity fields generated on March 30, without the second and third cross-sections; overall, the along-streamline interpolation method performed better than the triangular or IDW interpolation methods, based on the root mean squared difference (**Figure 2.2.2-50**). In particular, the v component of velocity was significantly better when using the streamline method than when using the other methods; the root mean squared difference was about four times better in all cases. The u component of velocity with the streamline interpolation was about 20 percent better than with the triangulation method, and about twice as good as the IDW method with the second cross-section removed. The u component with the IDW method was about 33 percent better than with the streamline method with the third cross-section removed.

Although the root mean squared difference of the along-streamline interpolation was better, there was still a significant spread in the comparison of both components of velocity: **Figure 2.2.2-51** shows large velocity gradients between the cross-sections (1 and 3, and 2 and 4) and large spacing between these cross-sections (approximately 400 meters). For instance, at the third cross-section, the strong return flow near the northern bank is not captured in the interpolation (green lines in Figure 2.2.2-51) because this velocity structure was not represented in the data in the either the second or fourth cross-sections (Figure 2.2.2-51E through I). This illustrates the need to represent longitudinal changes in the velocity field with adequate spacing between cross-sections.

Therefore, based on transects with tighter spacing between cross-sections taken on March 15 and 17, it was determined that the four cross-sections measured on March 30 would adequately capture the main features of the velocity field. Because cross-sections 2 and 3 are not included in the interpolation, critical definition of the actual flow field is missing; thus, the results (without cross-section 2 or 3) are not expected to adequately represent the velocity field.

Although this comparison is not a rigorous validation of the along-streamline interpolation method, it does demonstrate that it is more accurate than the triangulation or IDW methods.

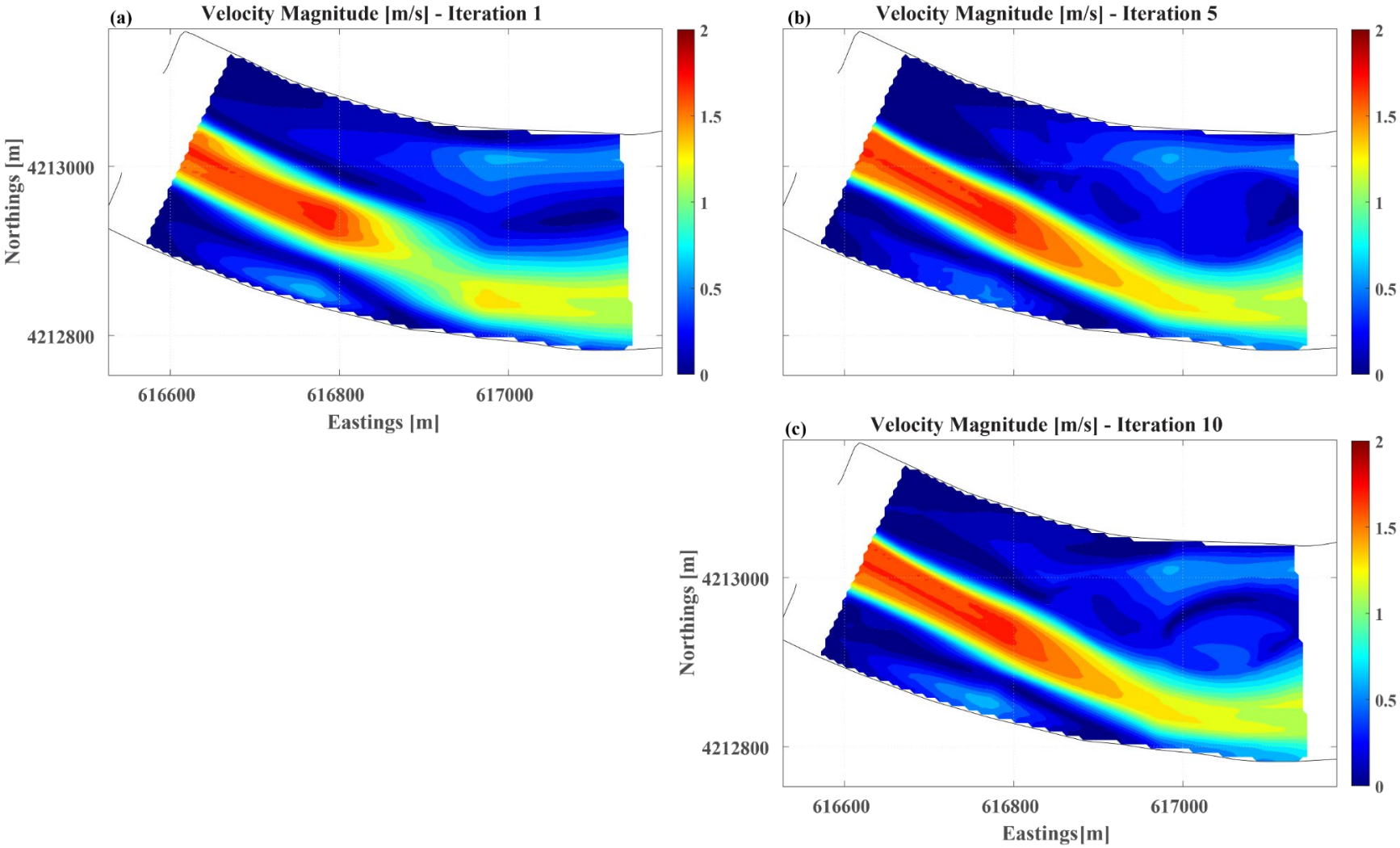

NOTE: Velocity map #12 is identified along with other flood tide indexed maps in Table 2.2.2-4 below.

Figure 2.2.2-49 Heat maps showing velocity magnitude from March 30, 2022 (velocity map #12) for iterations (a) 1, (b) 5, and (c) 10.

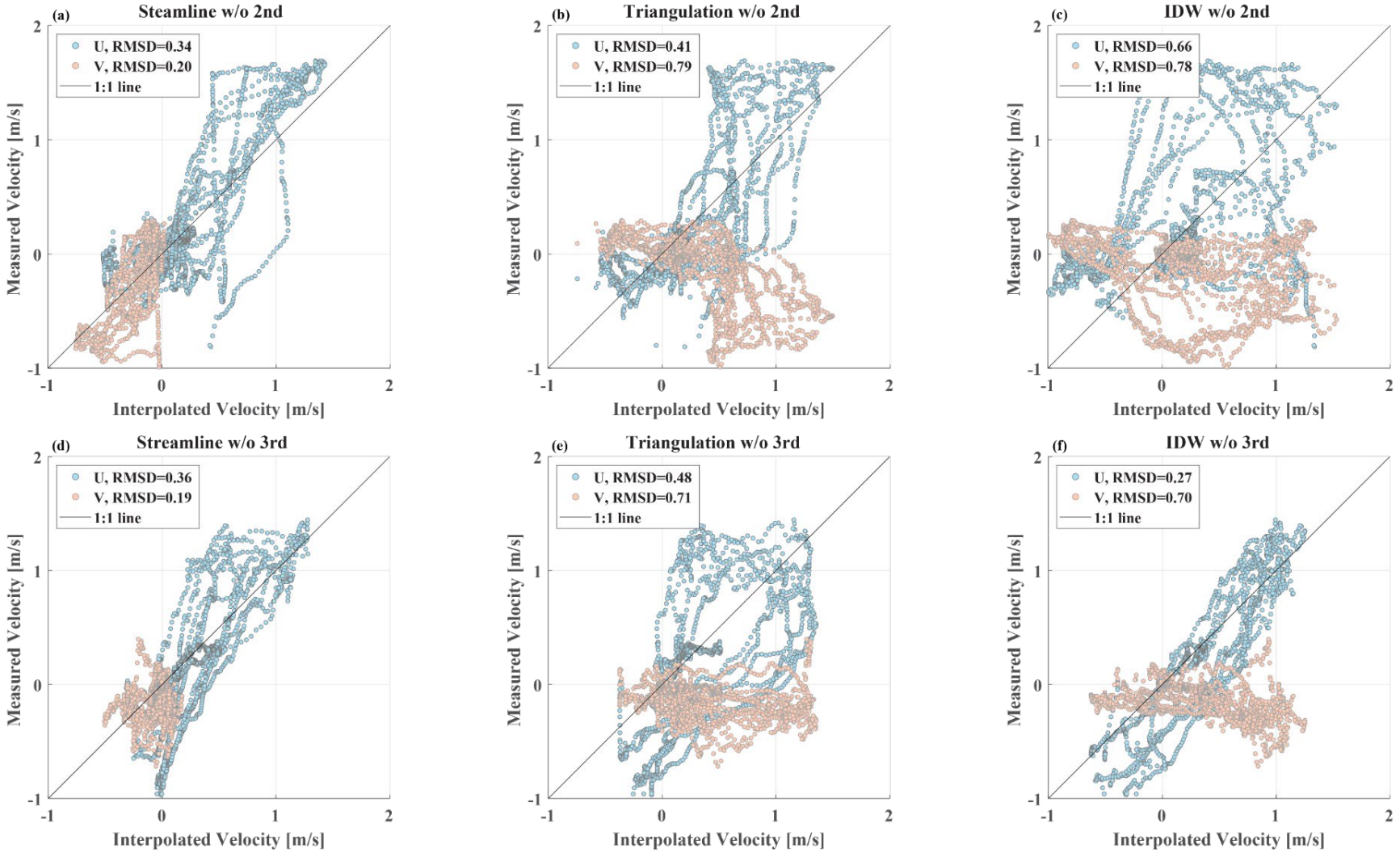

Note: m/s = meters per second; RMSD = root mean squared difference.
The top panels—(a), (b), and (c)—show a comparison of the streamline, triangulation, and inverse distance weighting methods at the second cross-section. The bottom panels—(d), (e), and (f)—show a comparison of the interpolation methods at the third cross-section.

Figure 2.2.2-50 X-Y scatter plots of measured velocity versus interpolated velocity.

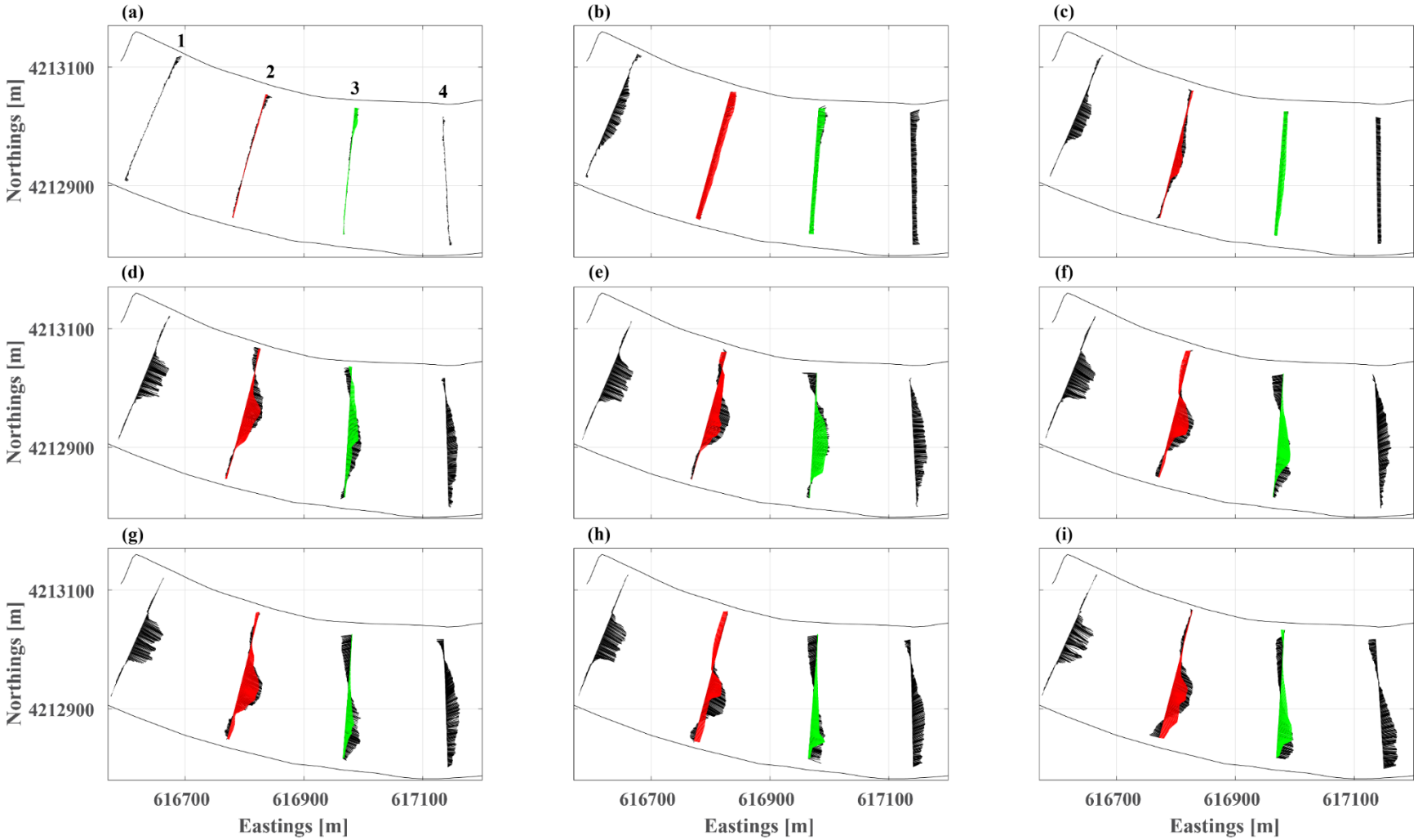

Figure 2.2.2-51 Velocity vector maps comparing measured velocity (black sticks) to interpolated velocity field, with second cross-section removed (red sticks) and third cross-section removed (green sticks).

Along-Streamline Velocity Interpolation

A total of 18 interpolated velocity fields were produced over a range of index velocities, from -1.31 to 0.37 (Table 2.2.2-3), covering most of the range of index velocities observed (-1.5 to 0.5). Additional transects collected on March 14, 15, and 17 were not used to produce velocity maps because they were not temporally close enough (i.e., the structure of the velocity field changed).

Smaller, spatial-scale velocity maps or cross-sections from other days under similar conditions could have been combined, but this did not improve the understanding of how the structure of the velocity field changed during a flood tide, because hydrodynamic conditions on March 14, 15, 17, and 30 were very similar, based on cross-sectional velocity and $Xvel_M$.

Figure 2.2.2-52 shows examples of the interpolated velocity field from March 30, 2022:

- Panel A, the velocity magnitude, shows the structure of the velocity field. A jet from the notch begins at the center of the channel but migrates to the southern bank while dissipating laterally.
- Panel B shows the resultant streamlines from the velocity field. A large eddy is centered near the western edge of the map.
- Panel C shows the vorticity or zone of highest shear near the edges of the velocity jet. The size of the large eddy on the western edge of the map is easy to identify.
- Panel D shows the normalized vorticity, the vorticity normalized by the velocity magnitude. This panel depicts the location of the center of eddies or null zones where adjacent flows are in opposition.

Interpolated velocity fields from March 15 and March 17, 2022 (**Figure 2.2.2-53**) cover similar extents and conditions (about the midpoint of the flood tide). Both show a strong jet (velocity of about 2 m/s) that is coming out of the notch and is directed toward the southern riverbank. The jet reaches the river bend about 450 meters downstream of the notch, where it begins to dissipate laterally. There is weaker flow on either side of the jet on the edge of the eddies that form on both the north and south sides of the jet. Farther downstream (beginning just before the river bend), there is a significant return flow (westerly direction, velocities of approximately 0.75 m/s) along the north against an easterly flow (velocities of approximately 1.25 m/s) along the southern bank.

Interpolated velocity fields from March 30, 2022 (**Figure 2.2.2-54**) show how the velocity field evolves from slack water to peak flood-tide velocities on the eastern side of the barrier:

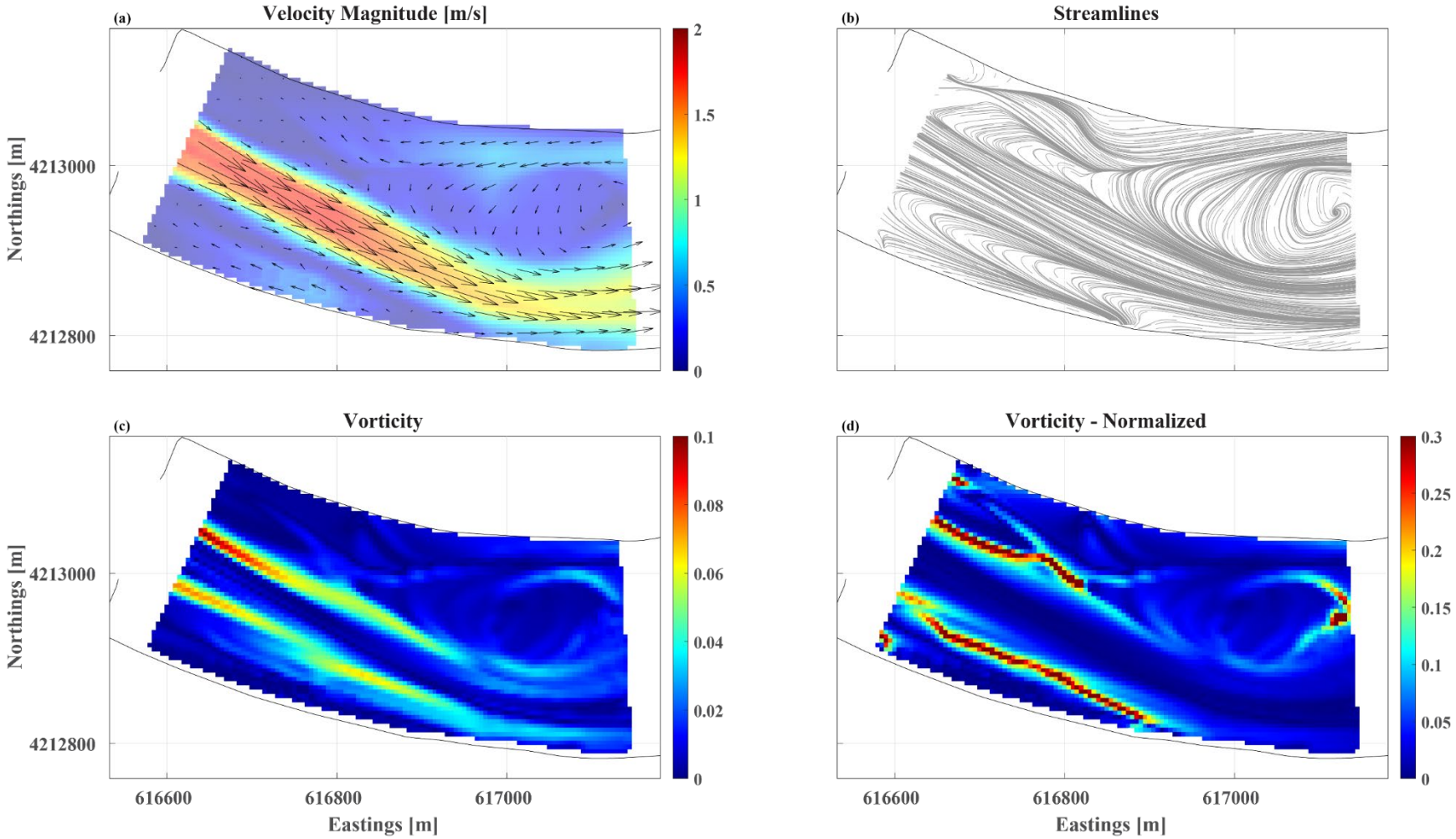

NOTE: m/s = meters per second.

Figure 2.2.2-52 Maps from March 30, 2022, data collection: (a) Velocity magnitude of final interpolated velocity field, (b) streamlines generated from velocity field, (c) vorticity of velocity field, and (d) vorticity as normalized by velocity magnitude.

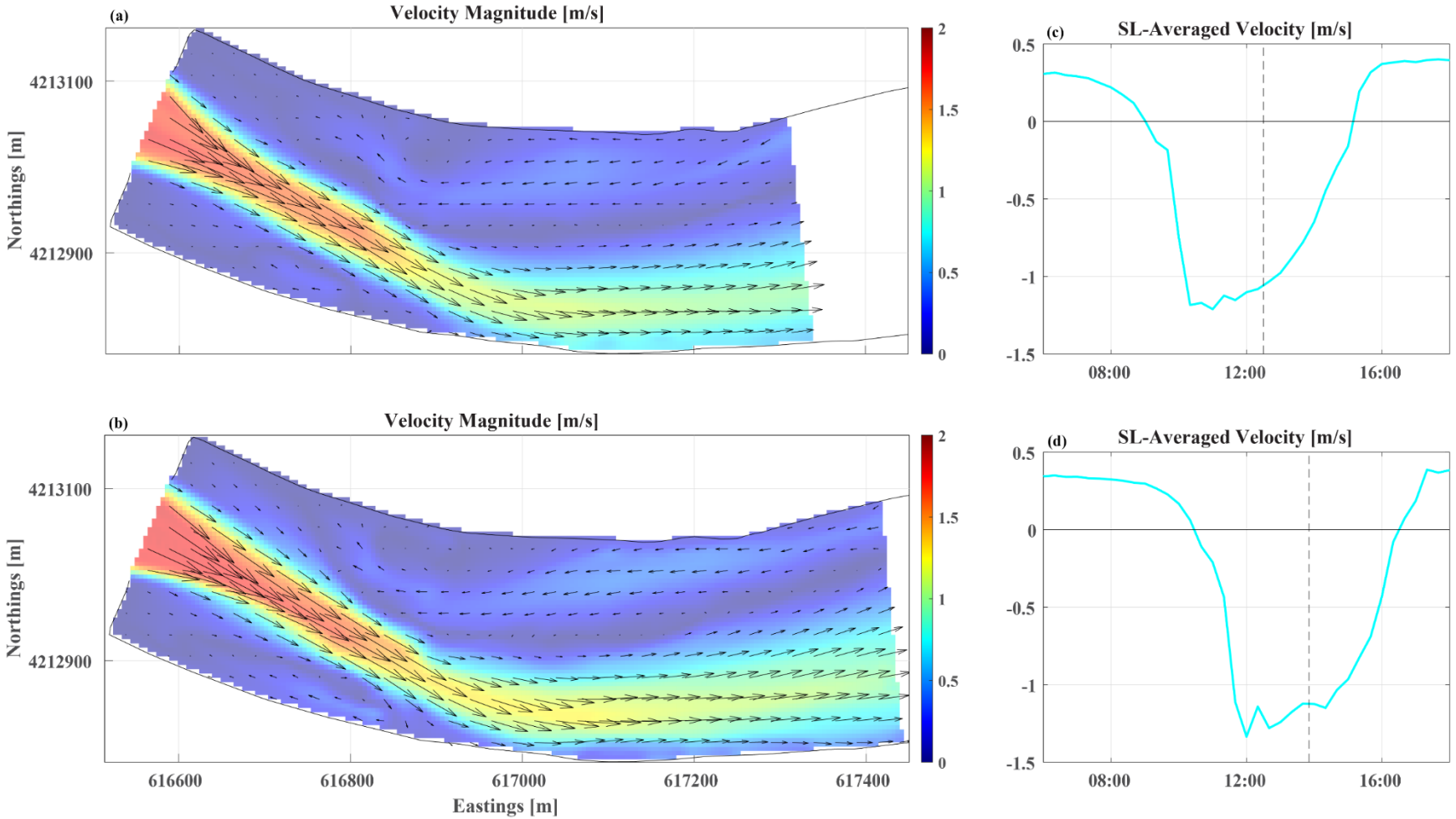

NOTES: m/s = meters per second; SL = side-looking.
Panels (a) and (b) show the velocity magnitude by color, with velocity vectors overlain on top; and panels (c) and (d) show a time series of the bin and 20-minute averaged velocity from the side-looking acoustic Doppler current profiler. The dashed vertical lines in panels (c) and (d) correspond to the time of the velocity maps in panels (a) and (b), respectively.

Figure 2.2.2-53 Maps of interpolated velocity fields from March 15, 2022 (top) and March 17, 2022 (bottom).

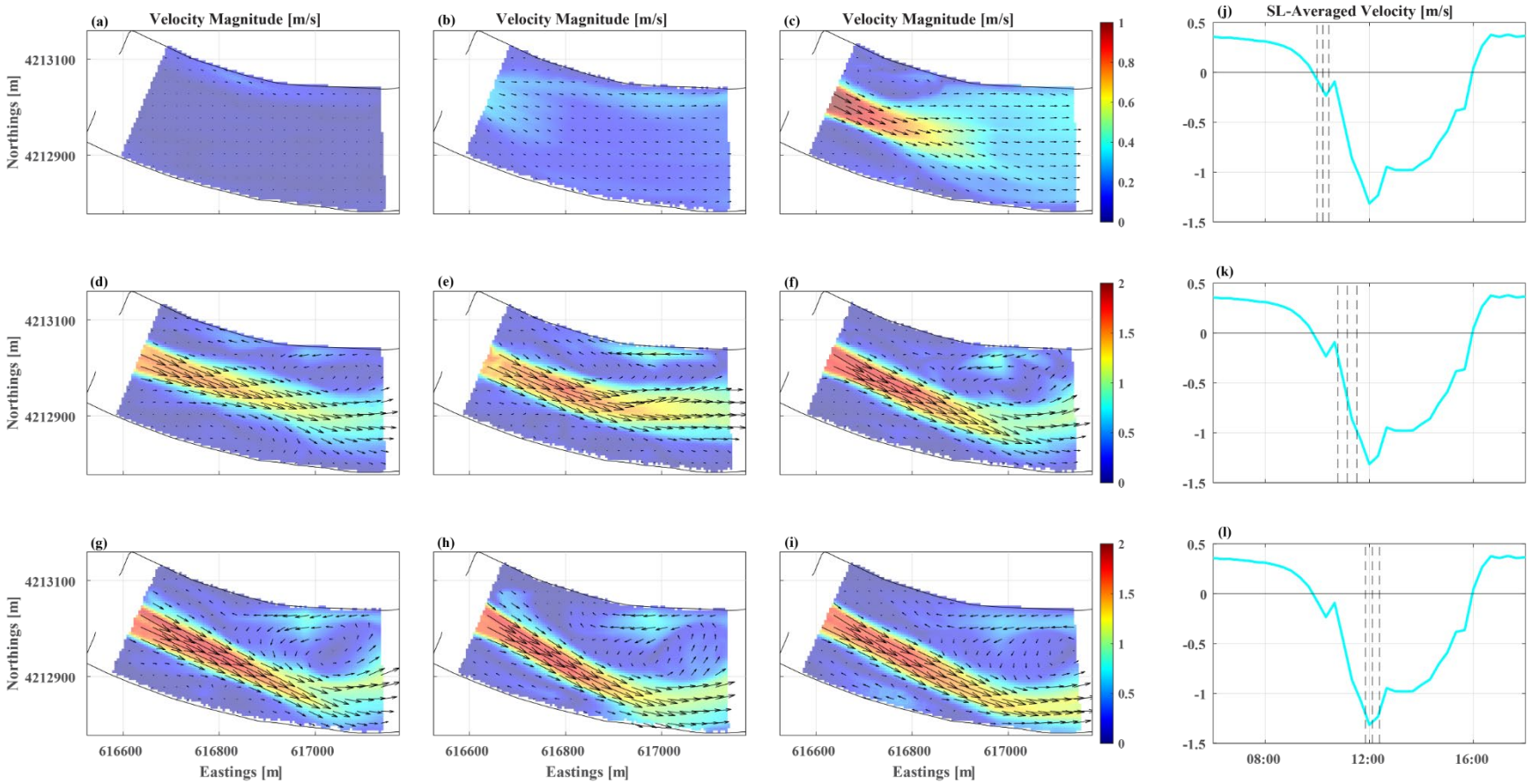

NOTES: m/s = meters per second; SL = side-looking.
For each row, the first three panels show the velocity magnitude by color; the corresponding colorbar is to the right of the third panel, with velocity vectors overlain on top. The fourth panel shows a time series of the bin and 20-minute averaged velocity from the side-looking acoustic Doppler current profiler; the dashed vertical lines correspond to the time of the three panels of velocity maps.

Figure 2.2.2-54 Maps of interpolated velocity field from March 30, 2022.

- At the start of the flood, velocities are weak (Panels A and B).
- By Panel C, a jet from the notch begins to develop. At first the jet is directed approximately normal to the angle of the barrier, and weaker velocities are observed on either side of the jet.
- A return flow along the northern bank is noticeable about one hour after the start of the flood (Panel E). The return flow begins to form a large eddy in the northeastern part of the map (Panel F), which coincides with the shift of the jet toward the southern bank.
- Over the course of the next hour (Panels G and H), the jet gradually shifts to the southern bank.
- By Panel I, the structure of the velocity field is closer to what was observed later in the flood tide, on March 15 and 17.

Interpolated velocity fields from March 23, 2022 (**Figure 2.2.2-55**) show how the velocity field evolves from slack to peak ebb-tide velocities on the western side of the barrier:

- Initially, higher magnitude velocities are observed on the southern bank (Panel A).
- The velocity jet from the notch is initially directed toward the center of the channel (Panels B and C).
- By the time the ebb velocities have reached a dynamic steady state, the structure of the velocity field remains consistent with flow directed toward the southern bank and a large eddy on the northwestern part of the map (Panels D–G).

Indexing Velocity Maps

Interpolated velocity maps from March 15, 17, and 30, 2022, were used to define 12 sets of velocity maps defining the evolution over the course of a flood tide on the eastern side of the barrier, while interpolated velocity maps on March 23 were used to define 12 sets of maps that estimate the velocity structure during ebb tides on the western side of the barrier. The lookup tables of *tN*, η_S, and $\overline{Ivel}$ were used to index velocity maps to periods when data were not collected, to be used in combination with fish predation sampling to determine whether velocity structure correlated with predation rates.

A value of t_N was assigned for each map based on the period of measurement relative to the total time of that tide. The first seven flood tide maps (**Figure 2.2.2-56**) were based on velocity maps collected on March 30, 2022, and covered t_N from 0 to 0.39 (**Table 2.2.2-4**). The eighth map was an average of the maps collected on March 15 and 17, 2022, because these covered a similar normalized time in tide (t_N from 0.39 to 0.70) and similar velocity conditions.

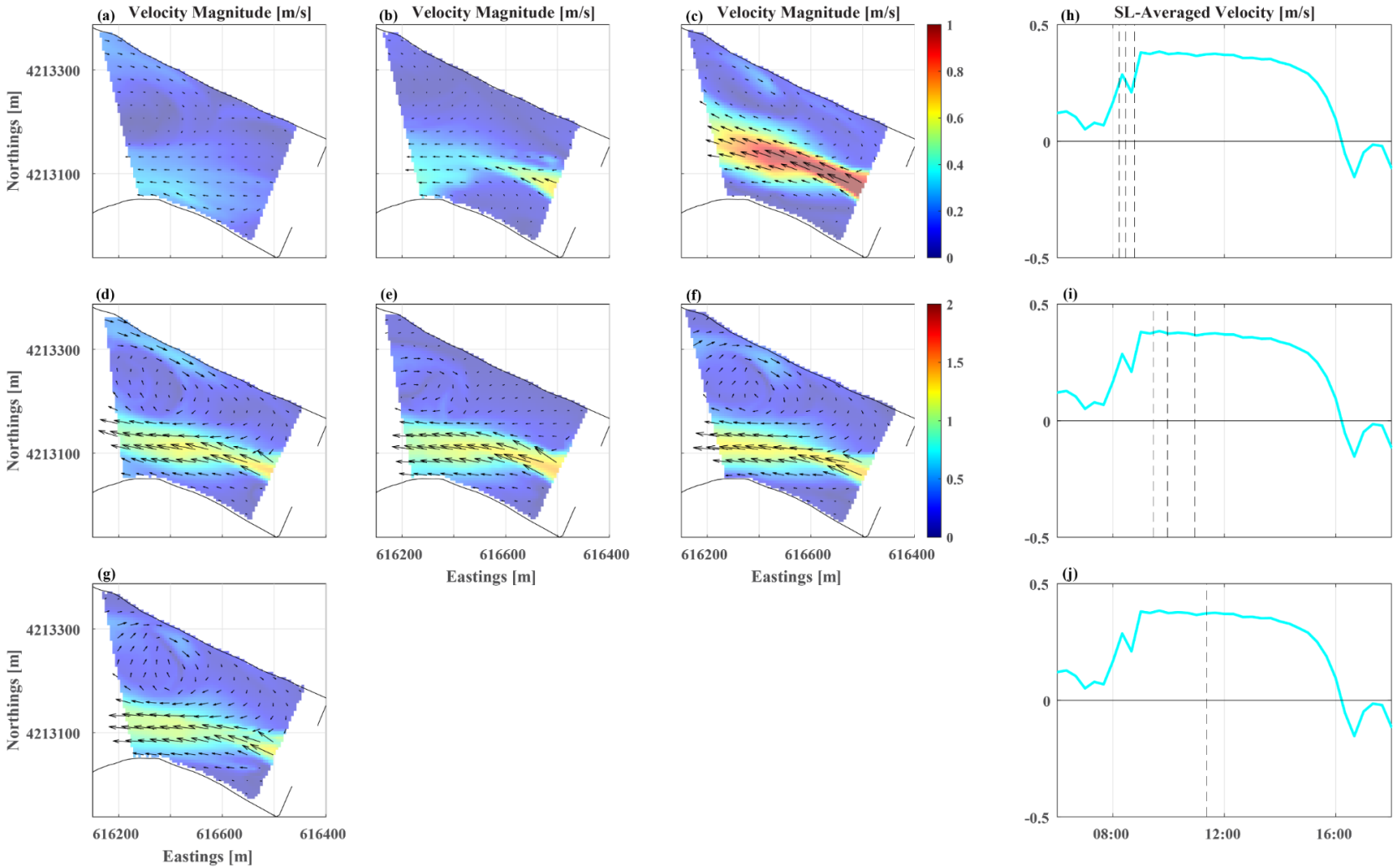

NOTES: m/s = meters per second; SL = side-looking.
For each row, the first three panels show the velocity magnitude by color; the corresponding colorbar is to the right of the third panel, with velocity vectors overlain on top. The fourth panel shows a time series of the bin and 20-minute averaged velocity from the side-looking acoustic Doppler current profiler; the dashed vertical lines correspond to the time of the three panels of velocity maps.

Figure 2.2.2-55 Maps of interpolated velocity field from March 23, 2022, on an ebb tide on the west side of the barrier.

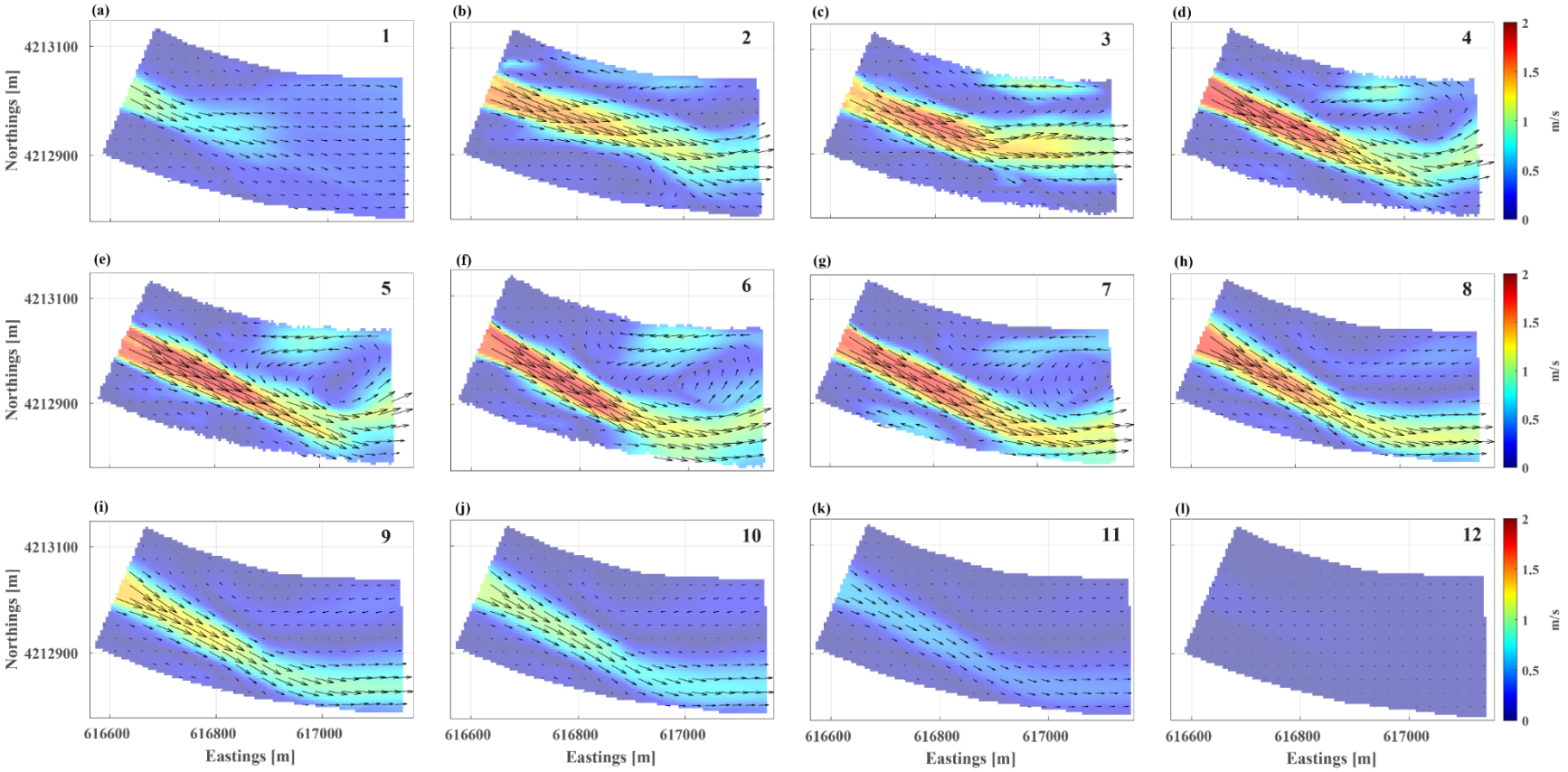

NOTES: m/s = meters per second.
The numbers in the upper right of each panel refer to the indexed velocity maps listed in Table 2.2.2-4 below.

Figure 2.2.2-56 Flood tide interpolated velocity maps.

TABLE 2.2.2-4
FLOOD TIDE INDEXED MAPS

Map Number	Date, Time (PST)	t_N Range	$Ivel$[c]	$Ivel$ Ratio
1	March 30, 2022, 10:17–10:36 a.m.	0.00 to 0.04	-0.18	–
2	March 30, 2022, 10:34–10:59 a.m.	0.04 to 0.13	-0.58	–
3	March 30, 2022, 10:58–11:22 a.m.	0.13 to 0.17	-1.03	–
4	March 30, 2022, 11:20–11:42 a.m.	0.17 to 0.26	-1.25	–
5	March 30, 2022, 11:39 a.m.–12:00 noon	0.26 to 0.30	-1.18	–
6	March 30, 2022, 11:58 a.m.–12:14 p.m.	0.30 to 0.35	-1.21	–
7	March 30, 2022, 12:14–12:33 p.m.	0.35 to 0.39	-1.20	–
8	March 15, 2022, 11:43 a.m.–1:24 p.m. March 17, 2022, 1:03–2:40 p.m.	0.39 to 0.70	-1.09	–
9[a]	–	0.70 to 0.78	-0.85	0.78
10[a]	–	0.78 to 0.85	-0.67	0.61
11[a]	–	0.85 to 0.93	-0.39	0.36
12[b]	–	0.93 to 1.00	-0.02	0.11

NOTES:
$Ivel$ = index velocity, averaged over the flood tide phase; PST = Pacific Standard Time; t_N = normalized time in tide

a. Indicates maps estimated from velocity map 8; $Ivel$ ratio based on ratio of $Ivel$ to $Ivel$ of velocity map 8.
b. Indicates map estimated from velocity map 1; $Ivel$ ratio based on ratio of $Ivel$ to $Ivel$ of velocity map 1.
c. Average $Ivel$ over the period of t_N.

SOURCE: Data compiled by U.S. Geological Survey in 2022

Four additional maps were estimated that covered a normalized time in tide (t_N) from 0.7 to 1. Maps 9–11 were based on Map 8 with the velocity magnitude of the map scaled down based on the $Ivel$ ratio (Table 2.2.2-4). Map 12 was based on the first map, with the velocity magnitude scaled down based on the $Ivel$ ratio.

For the ebb tide maps (**Figure 2.2.2-57**), the first six maps were based on maps collected on March 23, 2022, with a t_N from 0 to 0.43 (**Table 2.2.2-5**). The ebb tide maps were estimated in similar fashion to the flood tide maps. Maps 7–11 were based on Map 6, and Map 12 was based on the first map, where all maps were scaled using the $Ivel$ ratio.

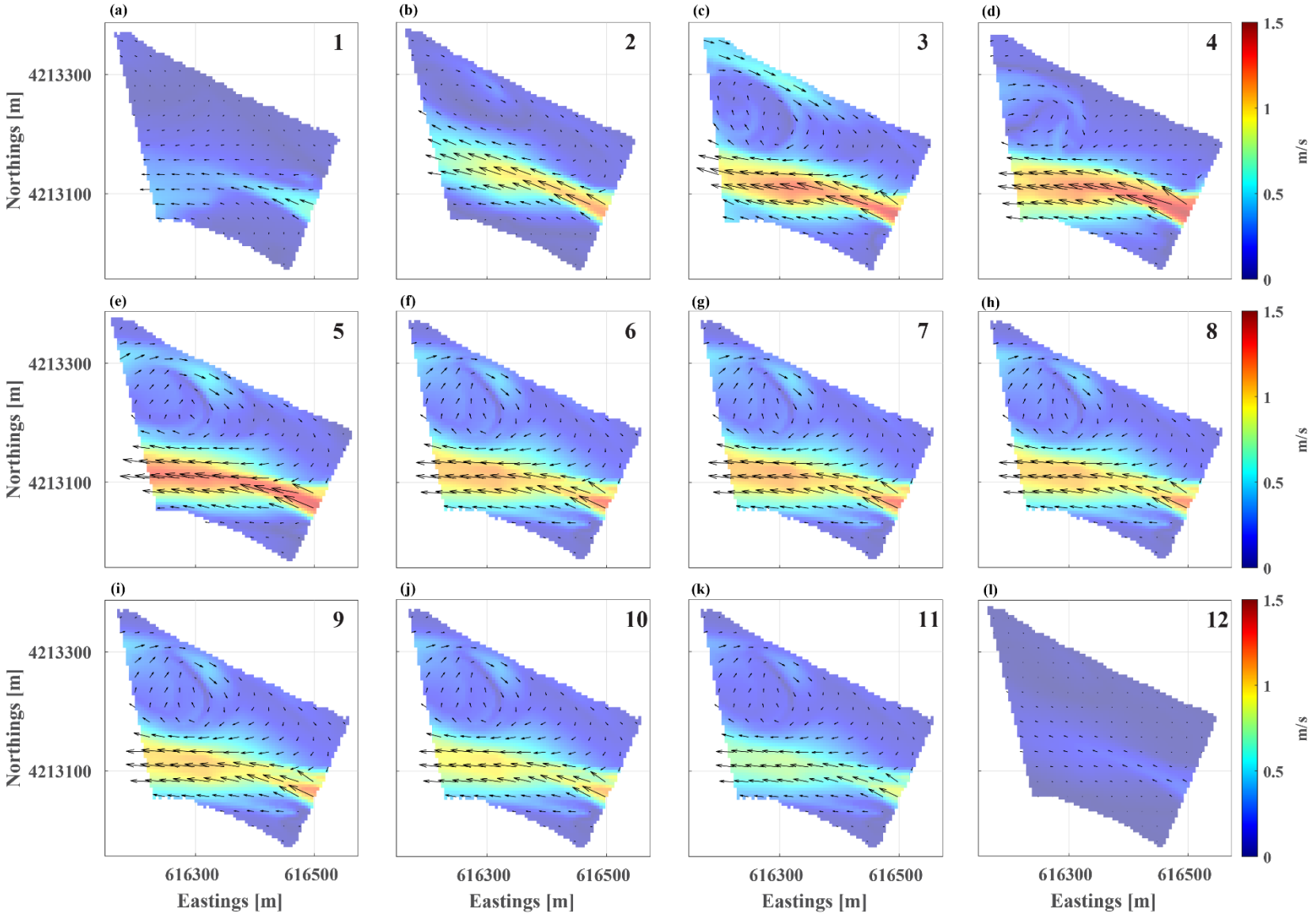

Notes: m/s = meters per second. The numbers in the upper right of each panel refer to the indexed velocity maps listed in Table 2.2.2-5 below.

Figure 2.2.2-57 Ebb tide interpolated velocity maps on the west side of the barrier.

TABLE 2.2.2-5
EBB TIDE INDEXED MAPS

Map Number	Date, Time (PST)	t_N Range	$Ivel^c$	$Ivel$ Ratio
1	March 23, 2022, 8:19–8:34 a.m.	0.00 to 0.03	0.30	
2	March 23, 2022, 8:33–9:02 a.m.	0.03 to 0.11	0.29	
3	March 23, 2022, 9:09–9:38 a.m.	0.11 to 0.18	0.38	
4	March 23, 2022, 9:38–10:10 a.m.	0.18 to 0.28	0.38	
5	March 23, 2022, 10:38–11:06 a.m.	0.28 to 0.34	0.37	
6	March 23, 2022, 11:07–11:40 a.m.	0.34 to 0.43	0.37	
7[a]	–	0.43 to 0.53	0.37	1.00
8[a]	–	0.53 to 0.62	0.36	0.97
9[a]	–	0.62 to 0.72	0.35	0.95
10[a]	–	0.72 to 0.81	0.32	0.87
11[a]	–	0.81 to 0.91	0.26	0.70
12[b]	–	0.91 to 1.00	0.08	0.27

NOTES: $Ivel$ = index velocity, averaged over the ebb tide phase; PST = Pacific Standard Time; t_N = normalized time in tide

a. Indicates maps estimated from velocity map 6; $Ivel$ ratio based on ratio of $Ivel$ to $Ivel$ of velocity map 6.
b. Indicates maps estimated from velocity map 1; $Ivel$ ratio based on ratio of $Ivel$ to $Ivel$ of velocity map 1.
c. Average $Ivel$ over the period of t_N.

SOURCE: Data compiled by U.S. Geological Survey in 2022

The next step, to index the velocity maps, was to scale the velocity magnitude of each map based on the velocity averaged over the tide ($\overline{Ivel}$). It was assumed that that the structure of the velocity map would remain constant, with increases or decreases relative to when the maps were collected where the magnitudes of the velocities would change proportionally with $\overline{Ivel}$. Not all predation samples (sample days 1–7, **Table 2.2.2-6**) were collected when the SL-ADCP was operational, and a linear regression between η_S and $\overline{Ivel}$ indicated that η_S was a good but not great predictor of $\overline{Ivel}$ (**Figure 2.2.2-58**; R2 = 0.82 for ebb tide and R2 = 0.60 for flood tide). As shown, the ebb tide velocities have a decreased range compared to the flood tide velocities because the SL-ADCP was on the east (opposite) side of the barrier, so the regression with $\overline{Ivel}$ may not reflect the true increase or decrease in velocity maps on the ebb tide. Nevertheless, η_S was used to determine the $\overline{Ivel}$ for each sampling period using a scaling factor that was calculated based on the ratio of $\overline{Ivel}$ for the velocity maps (red dots in Figure 2.2.2-58) and the $\overline{Ivel}$ for each sampling period (Table 2.2.2-6). This scaling factor was then applied to the velocity magnitude for the entire velocity map.

TABLE 2.2.2-6
PREDATION SAMPLING PERIODS WITH ASSOCIATED STRENGTH OF TIDE, INDEX VELOCITY, AND SCALING FACTOR

Sample Day	Tide	Date, Time (PST)	T_S	$Ivel$[a]	Scaling Factor
1	Ebb	January 24, 2022, 2:33–4:30 p.m.	-0.55	0.27	0.84
	Flood	January 24, 2022, 4:30–8:35 p.m.	0.34	-0.51	0.62
2	Ebb	January 25, 2022, 2:29–6:00 p.m.	-0.70	0.29	0.92
	Flood	January 25, 2022, 6:00–8:04 p.m.	0.35	-0.52	0.63
3	Ebb	January 26, 2022, 2:09–7:30 p.m.	-0.87	0.32	1.00
	Flood	January 26, 2022, 2:09–10:38 p.m.	0.44	-0.62	0.75
4	Ebb	January 27, 2022, 2:19–8:13 p.m.	-0.98	0.34	1.07
5	Ebb	January 28, 2022, 2:22–8:20 p.m.	-1.03	0.35	1.10
6	Flood	February 17, 2022, 2:45–5:15 p.m.	0.54	-0.72	0.88
	Ebb	February 17, 2022, 5:15–8:56 p.m.	-0.82	0.31	0.98
7	Flood	February 18, 2022, 3:02–6:00 p.m.	0.55	-0.73	0.89
	Ebb	February 18, 2022, 6:00–8:29 p.m.	-0.75	0.30	0.95
8	Ebb	February 22, 2022, 2:40–4:15 p.m.	-0.74	0.30	0.94
	Flood	February 22, 2022, 4:15–8:24 p.m.	0.36	-0.53	0.65
9	Ebb	February 23, 2022, 2:51–5:45 p.m.	-0.85	0.32	1.00
	Flood	February 23, 2022, 5:45–8:19 p.m.	0.43	-0.61	0.74
10	Ebb	February 24, 2022, 2:52–7:00 p.m.	-0.96	0.34	1.06
	Flood	February 24, 2022, 7:00–8:31 p.m.	0.55	-0.74	0.90
11	Flood	March 21, 2022, 3:30–8:00 p.m.	0.53	-0.71	0.86
	Ebb	March 21, 2022, 8:00–9:20 p.m.	-0.38	0.24	0.74
12	Flood	March 22, 2022, 3:29–9:07 p.m.	0.54	-0.72	0.87
13	Flood	March 23, 2022, 4:11–9:12 p.m.	0.53	-0.71	0.86
14	Ebb	March 24, 2022, 3:37–5:30 p.m.	-0.97	0.34	1.06
	Flood	March 24, 2022, 5:30–7:05 p.m.	0.61	-0.80	0.98
15	Ebb	March 25, 2022, 3:25–6:45 p.m.	-1.01	0.35	1.09
16	Flood	March 25, 2022, 6:45–9:25 p.m.	0.64	-0.83	1.01

NOTES: $Ivel$ = velocity averaged over the tide; PST = Pacific Standard Time; T_S = strength of tide

Green shaded sampling days overlap with the operational window of the side-looking acoustic Doppler current profiler; yellow shaded regions indicate sampling days where the structure of the velocity field may be different from the interpolation velocity maps.

SOURCE: Data compiled by U.S. Geological Survey in 2022

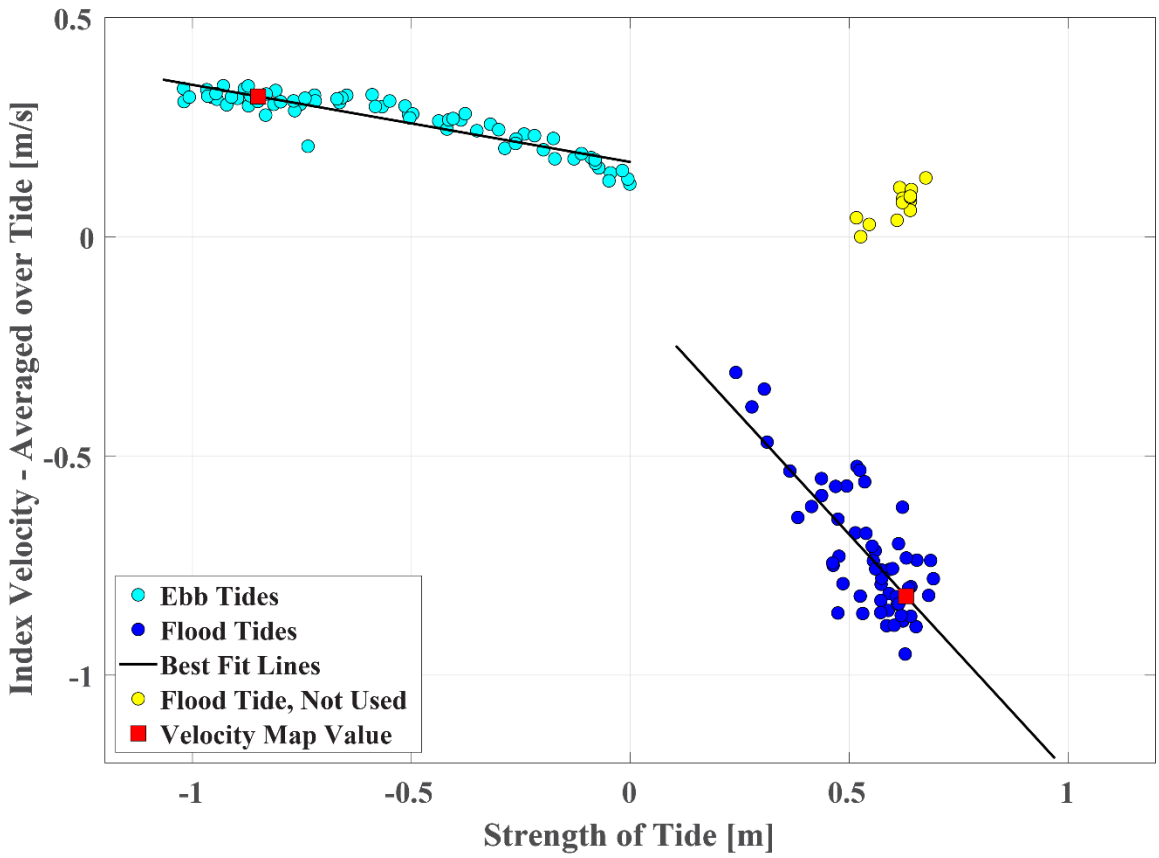

NOTES: m = meters; m/s = meters per second

Figure 2.2.2-58 X-Y plot of index velocity averaged over a tide versus strength of tide.

There is a high degree of uncertainty about how representative these maps are for all tidal conditions during the period when the barrier was notched. For example, the first source of uncertainty is variability in 15-minute averaged velocity ($Xvel_M$) between individual tides (**Figure 2.2.2-59**), which is particularly evident on the earlier part of the flood tide. The variability in $Xvel_M$ on ebb tides is less, but as stated above, the SL-ADCP does not reflect the magnitude of velocity on the west side of the barrier during ebb tides. An additional level of uncertainty exists for the indexed velocity maps outside of the SL-ADCP operational window (sample days 1–7; Table 2.2.2-6). The final source of uncertainty occurs on sampling days 13 and 16 (Table 2.2.2-6) where there is a weak or positive signal in $Xvel_M$, indicating that the velocity structure was likely different. By extension, indexed velocity maps on these days likely do not accurately represent the actual velocity fields.

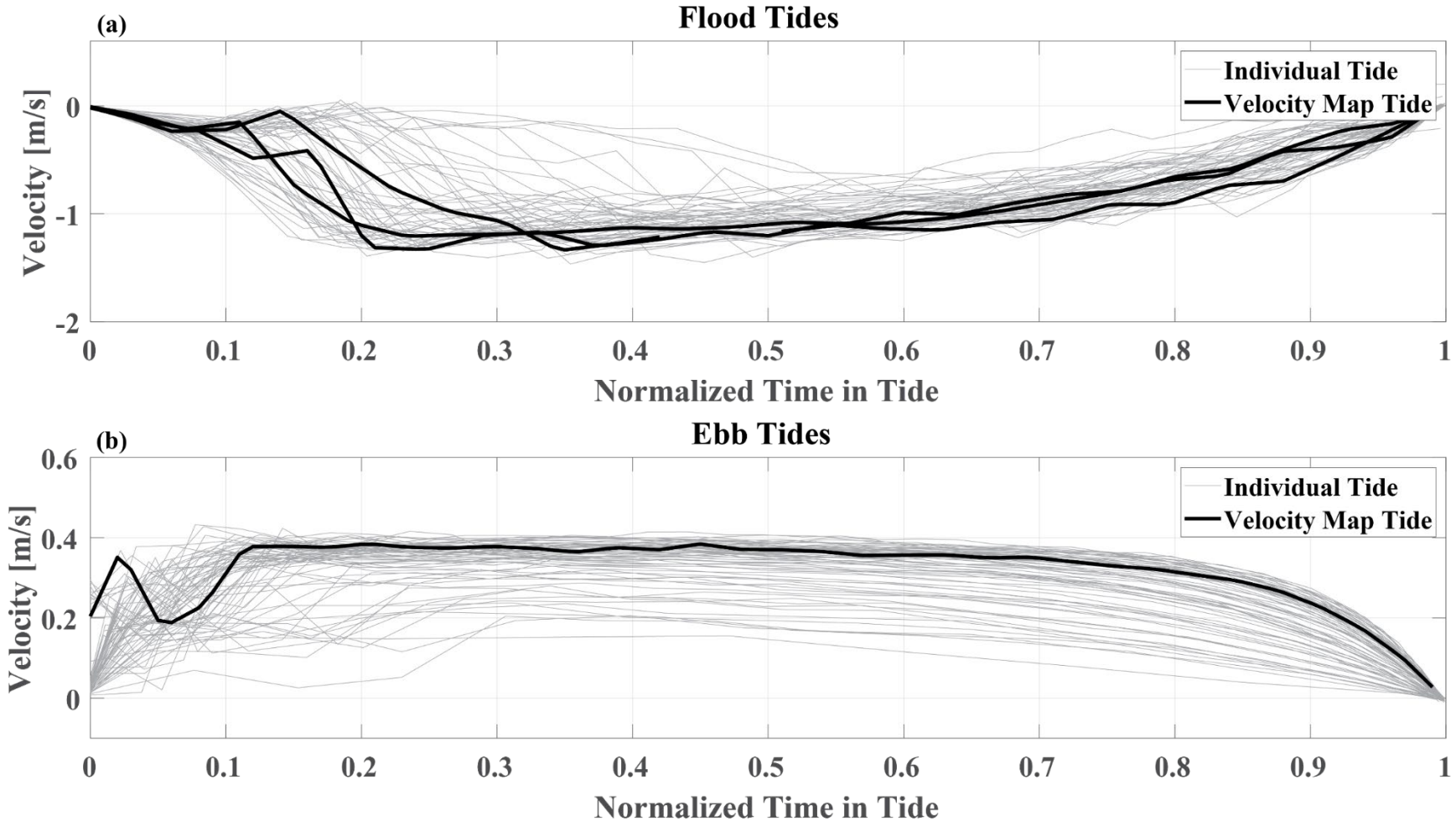

NOTE: m/s = meters per second

Figure 2.2.2-59 Index velocity as a function of normalized time in tide for each individual tide (gray lines), and the tides when the velocity maps were produced: (a) flood tides and (b) ebb tides.

Discussion

The interpolated velocity fields produced from MB-ADCP measurements show the evolution of velocity fields produced by the barrier notch on flood and ebb tides. On the flood tide (Figure 2.2.2-56), a strong jet propagated eastward, hundreds of meters downstream from the notch. As the flood increased, the jet migrated toward the southern bank, near the region of deeper water. The jet began to dissipate near the southern bank at the river bend, and a large eddy formed (on the scale of half the river width) on the northern bank. As the flood reached a more dynamic steady-state condition, during the latter part of the flood, the velocity structure was more constant (relative to the start of the flood), and the magnitude of velocities decreased. Velocity fluctuations were greatest at the beginning of the flood, which suggests more turbulence as the flow through the notch adjusts. Data from the SL-ADCP suggest that there could be variability in the structure of the velocity field from tide to tide.

A similar evolution of the velocity field was seen on the ebb tide (Figure 2.2.2-57). Initially a strong jet propagated from the notch; in this case, the jet migrated to the southern bank sooner in the tide than on the flood tide. A large eddy formed on the northern bank, covering about half of the river's width. The structure of the velocity field did not appreciably change over the course of the ebb tide. The spatial domain was not as large as the eastern side of the barrier, and the effect of the notch was observed 300–400 meters downstream of the notch. A velocity time series from SL-ADCP data, on the western side of the barrier, was not available; thus, it is difficult to assess whether there is variability in the structure of the velocity field from tide to tide.

Along-Streamline Velocity Interpolation

The along-streamline velocity interpolation is a novel method that produced better results than IDW or triangulation interpolation. This method therefore shows promise in representing large-scale flow features based on cross-sectional velocity measurements made in large domains (approximately 100,000 m^2).

Although this method proved to be superior to the other methods, improvements could be made based on mass conservation or changes to the sampling scheme. For instance, the along-streamline velocity interpolation method does not account for changes in bathymetry along a streamline, which can affect the velocity fields if mass is conserved along the streamline. Tsubaki et al. (2012) introduced a continuity correction in their interpolation to remove systematic errors. Using a continuity correction with datasets would have the potential to resolve gradients between cross-sections more accurately.

As was seen in the comparison of interpolated velocity fields with cross-sections 2 and 3 removed, some significant gradients may not be captured if spacing between cross-sections is greater than the scale of the intrinsic spatial gradients in the velocity field. This is evident with the stronger return flow at cross-section 3, compared to cross-sections 2 and 4 (Figure 2.2.2-51). An interpolation algorithm can only reproduce velocity structures that are represented in the native data. This is a problem more suited for numerical modeling, which solves the conservation of mass and momentum equations, and is outside the scope of an interpolation method.

Increasing the spacing between cross-sections or using a survey route that includes more of the unmeasured portion of the sample area can more accurately resolve more of the velocity field. In this case, there were a number of reconnaissance transects before placing multiple boats in the field to adequately capture the temporal evolution of the velocity fields down-current of the notch.

There are trade-offs in measurement time, area coverage, and data noise. For example, covering more area will involve longer measurement time, and using more repeated cross-sections will generate less data noise but involve longer measurement time. These trade-offs are less important in a riverine environment where discharges change at daily time scales, but they are more important in a tidal environment, where flows can change appreciably over short durations (i.e., less than 30 minutes).

Multiple transects can be averaged to remove turbulence time-scale motions and instrument noise to reveal 15-minute to hourly time-scale motions (Dinehart and Burau 2005b). A survey path without repeated transects (see Dinehart and Burau 2005a; Tsubaki et al. 2012) will have the advantage of increased coverage; however, such a path may sacrifice data accuracy because smaller scale turbulent motions and instrument noise cannot be averaged out. This is where a technique like kriging can be used to provide spatial smoothing (Jamieson et al. 2011). The along-stream velocity interpolation will likely work regardless of the survey techniques if the sampling design takes the inherent spatial and temporal scales into account.

To map the evolution of velocity over the flood and ebb tidal cycles (approximately six hours), continuous cross-sectional measurements were needed so that the number of cross-sections averaged could be limited to time scales sufficient to remove turbulent time scales but much shorter than the time scales of the processes of interest: in this case, tidal time-scale evolution of the jet/eddies created by the notch in the barrier. Using a survey path technique that covered more area, the measurement time would have been set by the time it took to complete a measurement circuit. This may have worked poorly for all conditions, particularly at the beginning of

the tide when conditions were changing rapidly. Either there were too few transects to average out the turbulence, or too many transects would poorly represent the tidally averaged motions of interest.

Another limitation of the along-streamline interpolation method was lack of a dataset to perform a more rigorous validation. Ideally, a validation dataset would include an independent measure of velocity. The set of cross-sections used for velocity interpolation was based on where the velocity gradients would likely be strongest, based on mapping performed on previous days, which left the validation method (removing cross-section) that likely underestimated the accuracy of the interpolation method.

2.3 Impacts

2.3.1 Bathymetry—Channel Bed Elevation

The Geomatics Branch of DWR's Division of Engineering mobilized to the West False River EDB site during 2021 and 2022 for field surveys involving inspections and assessments conducted both above and below water level. The initial survey was conducted before barrier construction, on May 17, 2021. During the next few weeks, multi-beam bathymetric data were collected at the site of the proposed barrier, at Bradford Island, and in a few of the waterways close to the site (**Figure 2.3.1-1**).

The bathymetric data were collected using two separate multi-beam–equipped vessels:

- A 23-foot North River Cathedral hull operating an R2Sonic system with a post-processed kinematic Position and Orientation System for Marine Vessels inertial measurement unit sensor.
- A 16-foot remote HydroCat operating dual-head T-50s with a submerged Position and Orientation System for Marine Vessels inertial measurement unit sensor.

Data for open-channel areas were collected using the North River setup; data for nearshore areas were collected using the remote HydroCat setup, with upper collection limits set to near the surface to maximize shoreline areas as much as possible. All data collected from this survey were processed and adjusted to the same survey control scheme that was used during the 2015 EDB project, to allow direct comparisons between the two projects.

A post–barrier construction survey was conducted on June 23, 2021, after in-water construction had been completed. The barrier remained in place until January 7, 2022, when it was breached. The barrier was subsequently modified into a notch barrier that was completed on January 18, 2022.

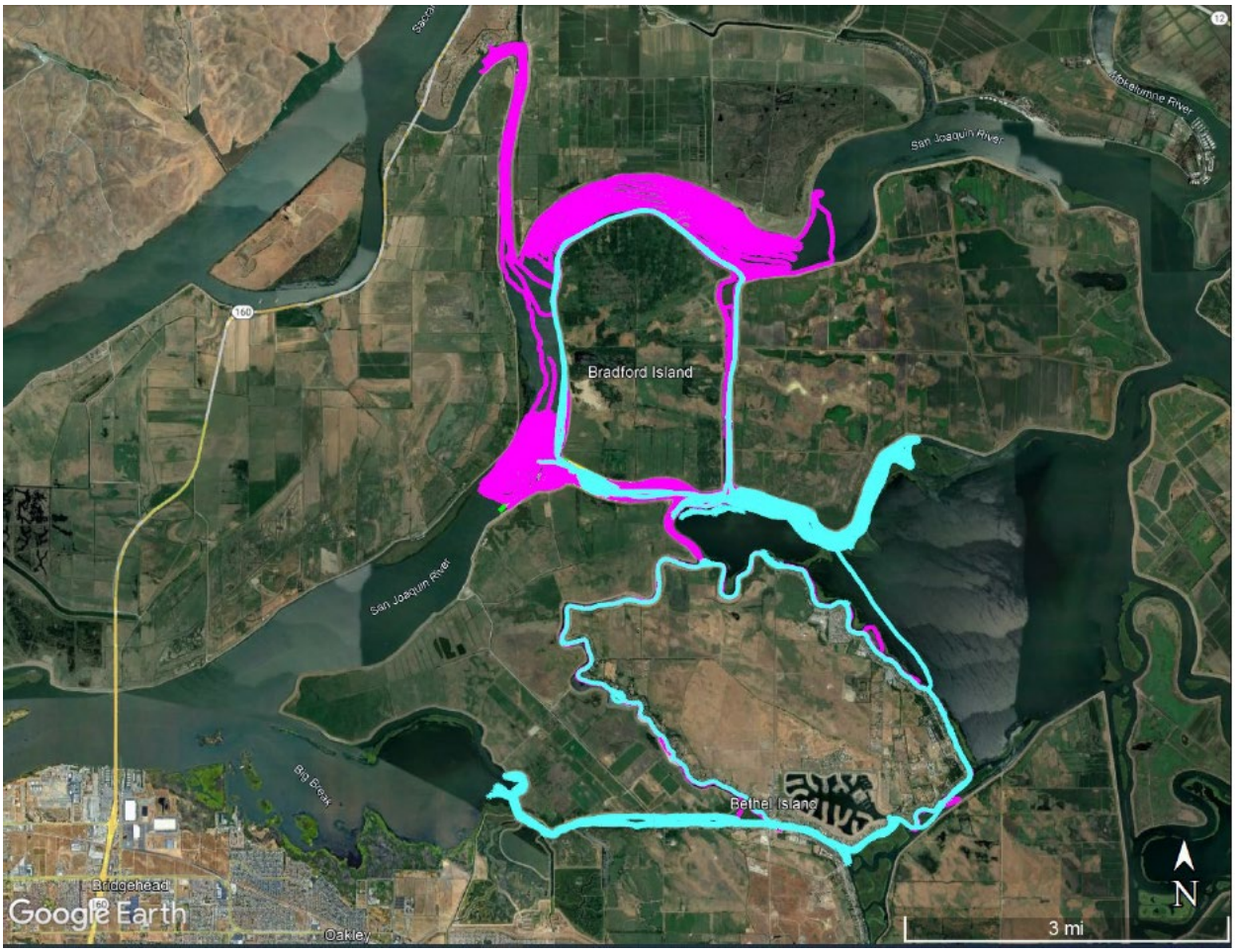

Figure 2.3.1-1 Bathymetry coverage areas.

A post–notch completion survey was conducted on January 20 and identified a 17-foot vertical depression on the downstream end of West False River near the notch area. Additional surveys were conducted on March 9, 17, and 23 to monitor the depression level, which deepened further to 30 feet by March 17, when it plateaued and stabilized.

In mid-April 2022, the notch was filled and the barrier was hydraulically closed again. Additional surveys were conducted on April 18–19 and June 6–8 to monitor the vertical depression and horizontal movement; the survey results confirmed that both the vertical depression and horizontal movement had halted. Bathymetric surveys conducted during 2015, 2021, and 2022 drought barrier activities are summarized in **Table 2.3.1-1**. For more details of the bathymetric surveys conducted during the 2021–2022 drought period, see **Appendix D** of this report.

The notched barrier configuration resulted in a scour hole; DWR implemented monitoring efforts to track the hole. Through biweekly monitoring of the scour hole area via mapping surveys, along with the use of existing levee

inclinometer units, DWR determined that the scour hole did not pose any threat to either the barrier's effectiveness or the nearby levees.

TABLE 2.3.1-1
SUMMARY OF 2015, 2021, AND 2022 BATHYMETRIC SURVEYS

Bathymetric Survey Date		Vessel Used in Survey Mission
2015	April 8	N/A; mission collected by North Central Regional Office
	November 23	N/A; mission collected by North Central Regional Office
2021	May 17	Seaflor Systems Hydrocat-150 catamaran
	June 23	North River Cathedral hull
2022	January 20	North River Cathedral hull
	March 9	North River Cathedral hull
	March 17	North River Cathedral hull
	March 23	North River Cathedral hull
	April 18–19	North River Cathedral hull
	June 6–8	North River Cathedral hull

NOTE: N/A = not applicable

SOURCE: Data compiled by California Department of Water Resources in 2023

2.3.2 Salinity, Water Quality, and Harmful Algal Blooms

2.3.2.1 Salinity Intrusion Pathway

Staff from DWR's North Central Region Office examined the effectiveness of the 2021–2022 EDB at preventing salt intrusion into the Central Delta. As defined for the purposes of this section, salinity data collected in the "Central Delta" were organized into three subregions (as depicted in **Figure 2.3.2-1**):

- *Sacramento River Region*, covering the northwest portion of the Central Delta from the confluence of the Sacramento and San Joaquin rivers, up the Sacramento River to the Rio Vista Bridge.
- *San Joaquin River Region*, covering the middle third of the Central Delta from the southern edge of Sherman Island upstream along the San Joaquin River to the northern end of Mandeville Island.
- *Interior Delta Region*, covering the southeast portion of the Central Delta from False River east of the barrier upstream to Clifton Court Forebay.

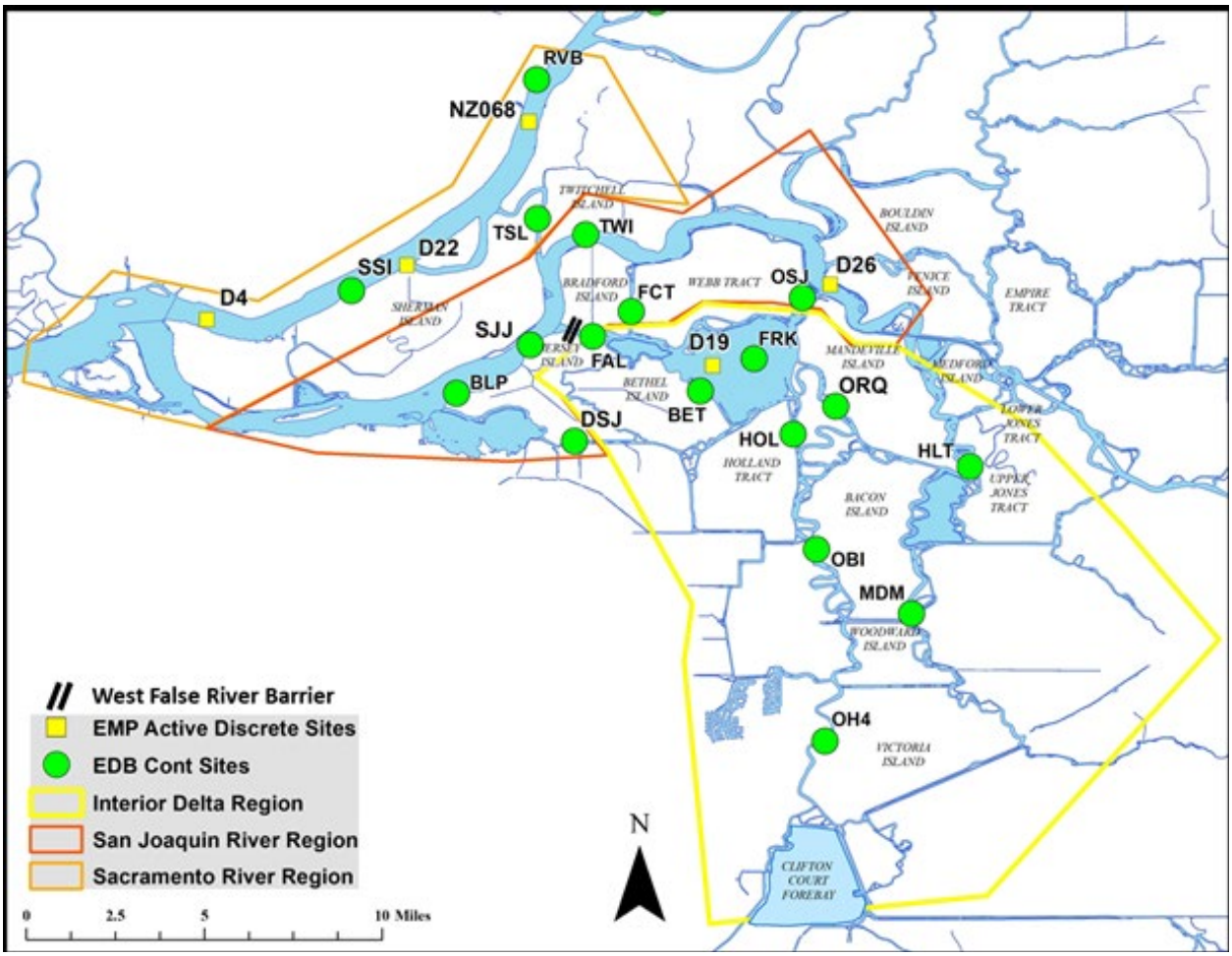

NOTES: Cont = continuous; EDB = emergency drought barrier; EMP = Environmental Monitoring Program

Figure 2.3.2-1 Regional view of all reported continuous and discrete water quality stations.

Salinity patterns were examined along the pathway of salinity propagation: the waterways that run southeast from False River through Franks Tract and Holland Cut into Old River, the route of salinity intrusion observed in previous years (**Figure 2.3.2-2**). Preventing salinity intrusion into the Central Delta channels that lead to the SWP and CVP pumping intakes is critical to maintaining the freshwater supply for urban, agricultural, and beneficial environmental uses.

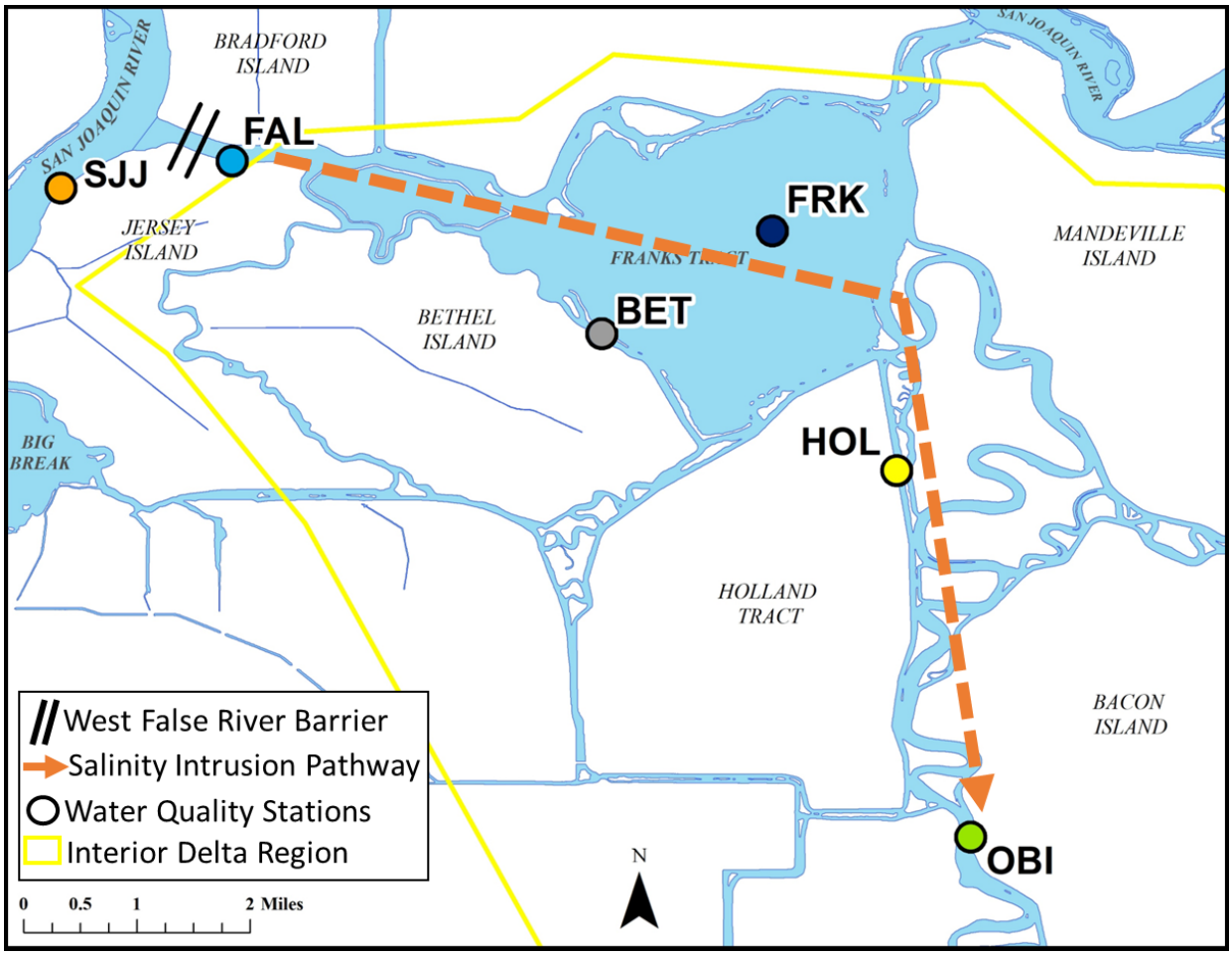

NOTE: Station abbreviations: BET = Bethel Island at Piper Slough; FAL = False River near Oakley; FRK = Franks Tract Mid Tract; HOL = Holland Cut near Bethel Island; OBI = Old River at Bacon Island; SJJ = San Joaquin River at Jersey Point.

Figure 2.3.2-2 Water quality monitoring stations in the Interior Delta Region along the salinity intrusion pathway.

Continuous specific-conductance data were collected at stations along the salinity intrusion pathway from April to December and were compared between the following years:

- 2020, a Dry water year when no barrier was installed.
- 2021, a Critically Dry water year when the barrier in False River was installed for the first time since 2015.
- 2022, a water year preliminarily classified as Critically Dry, and the second consecutive year that the barrier installed in 2021 was in place.

Daily-average specific conductance—used here as a surrogate for salinity—tracked closely at False River near Oakley (FAL) and San Joaquin River at Jersey Point (SJJ) in 2020, with measurements at FAL registering a few hundred microsiemens per centimeter, or µS/cm, lower than those at SJJ (**Figure 2.3.2-3**). Looking systematically upstream (arrayed from top to

bottom in Figure 2.3.2-3), the same pattern of specific conductance can be seen, though diminishing at each next upstream station into the Central Delta. As daily-average specific conductance at SJJ reached 2,400 µS/cm at the end of August 2020, specific conductance at Holland Cut near Bethel Island (HOL) peaked several days later at 1,100 µS/cm, or about 45 percent of the salinity measurements at SJJ.

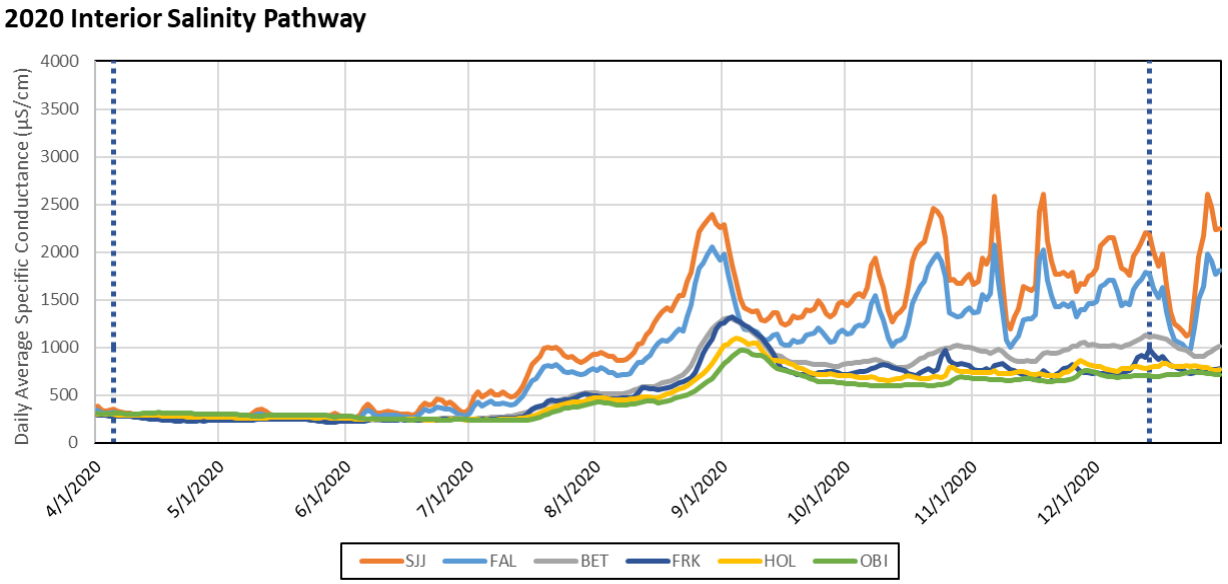

NOTES: µS/cm = microsiemens per centimeter. Station abbreviations: BET = Bethel Island at Piper Slough; FAL = False River near Oakley; FRK = Franks Tract Mid Tract; HOL = Holland Cut near Bethel Island; OBI = Old River at Bacon Island; SJJ = San Joaquin River at Jersey Point.

Figure 2.3.2-3 2020 daily-average specific conductance in the Interior Delta Region along the salinity intrusion pathway.

Conditions were even drier in 2021 than in 2020, which led salinity to rise more precipitously and earlier in the year. In response, DWR initiated construction on an EDB in West False River on June 3, 2021, achieving hydraulic closure of False River on June 18 and finishing construction of the barrier on June 24. Before construction of the 2021–2022 EDB was completed, patterns of specific conductance at stations along the interior pathway tracked in step with SJJ: Specific conductance at FAL was still only a few hundred µS/cm lower, and the specific conductance signal diminished at each station farther into the Central Delta (**Figure 2.3.2-4**).

Upon completion of the West False River barrier, the same patterns in specific conductance were greatly reduced at upstream stations. In late June 2021, when daily-average specific conductance at SJJ reached 2,650 µS/cm, the reading at FAL was more than 1,000 µS/cm lower, at 1,380 µS/cm. Specific conductance at interior stations such as HOL and Old River at Bacon Island (OBI) remained below 1,000 µS/cm through the end of the calendar year, peaking at about 880 µS/cm and 780 µS/cm, respectively, even as SJJ

specific conductance reached 3,300 µS/cm in early October. Thus, salinity levels at HOL were about 25 percent of SJJ measurements.

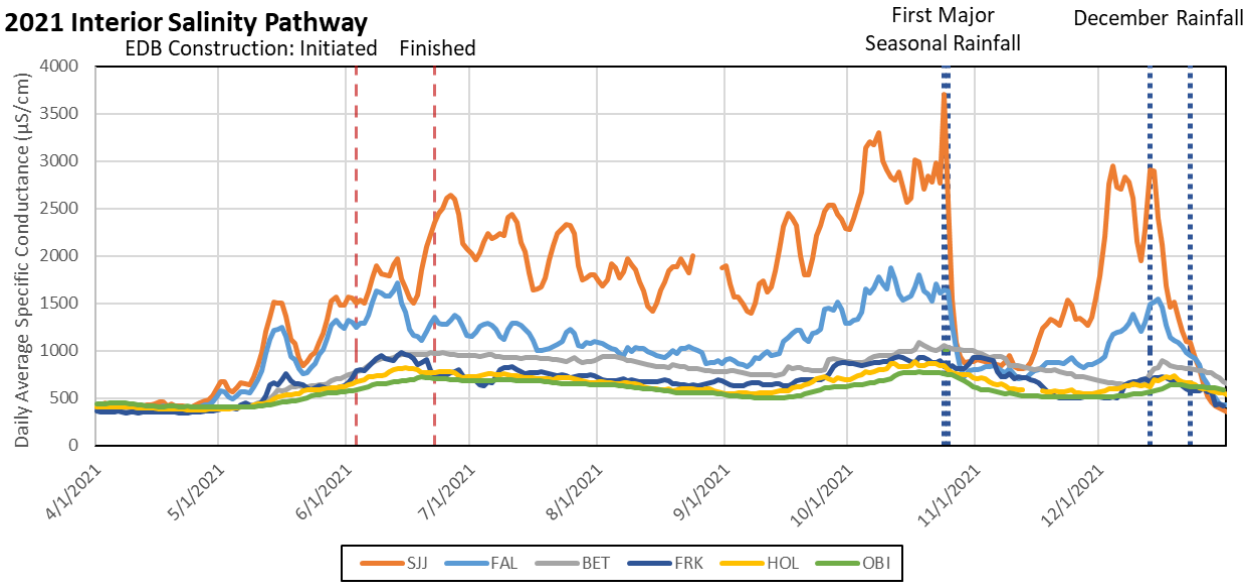

NOTES: µS/cm = microsiemens per centimeter; EDB = emergency drought barrier. Station abbreviations: BET = Bethel Island at Piper Slough; FAL = False River near Oakley; FRK = Franks Tract Mid Tract; HOL = Holland Cut near Bethel Island; OBI = Old River at Bacon Island; SJJ = San Joaquin River at Jersey Point.

Figure 2.3.2-4 2021 daily-average specific conductance in the Interior Delta Region along the salinity intrusion pathway.

In late October 2021 an extreme-rainfall event occurred, adding more than 5 inches of rain locally (and a good deal more in the foothills and high country) in a 24-hour period. Figure 2.3.2-3, Figure 2.3.2-4, and **Figure 2.3.2-5** show rainfall events of more than 0.5 inch per day at the Stockton Fire Station as vertical dotted blue lines. The larger rainfall events led to precipitous drops in daily-average specific conductance and helped to keep late-fall/early-winter salinity levels lower in the Delta from 2020 through 2022.

From January 7 to April 13, 2022, the EDB was notched to allow the hydraulic movement of water through False River during the seasonal low-salinity period. Specific conductance at SJJ reached nearly 2,900 µS/cm at the beginning of October, while at FAL it reached nearly 1,400 µS/cm, or about 48 percent of the SJJ salinity signal. Once barrier removal was initiated on October 15, 2022, the salinity patterns between SJJ and FAL grew more similar; by November 23, 2022, the date when barrier removal was completed, salinity at FAL was 80 percent of SJJ salinity. Whereas installation of the 2021–2022 EDB caused a decreased response in upstream salinity patterns compared to SJJ in 2021, the barrier removal in 2022 increased the upstream salinity response. This included increases in salinity at all upstream stations—FAL, BET, FRK, HOL, and OBI—in 2022 after the barrier removal.

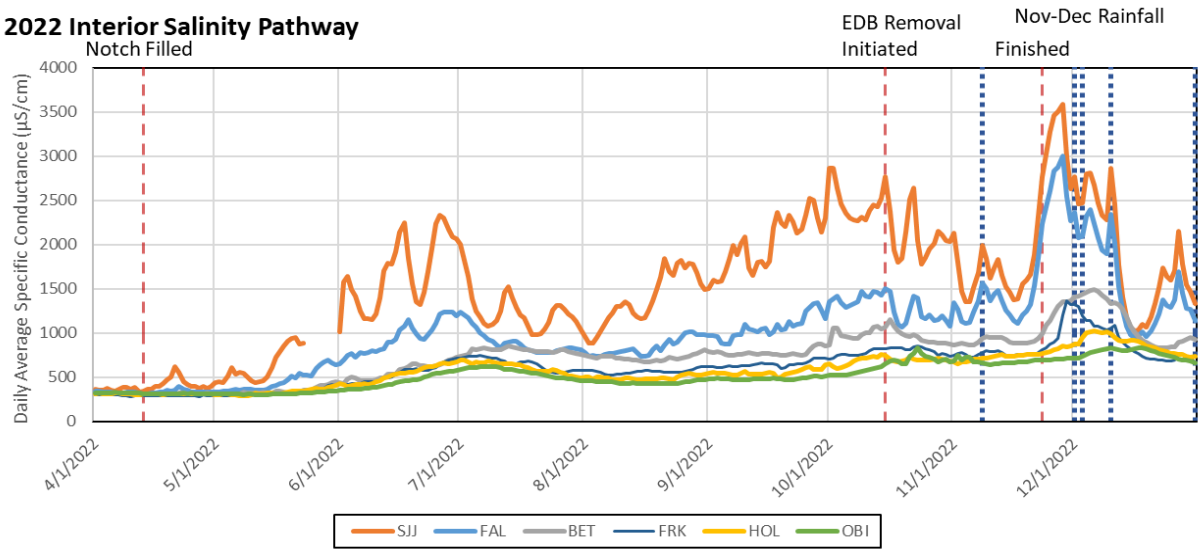

NOTES: µS/cm = microsiemens per centimeter; EDB = emergency drought barrier. Station abbreviations: BET = Bethel Island at Piper Slough; FAL = False River near Oakley; FRK = Franks Tract Mid Tract; HOL = Holland Cut near Bethel Island; OBI = Old River at Bacon Island; SJJ = San Joaquin River at Jersey Point.

Figure 2.3.2-5 2022 daily-average specific conductance in the Interior Delta Region along the salinity intrusion pathway.

2.3.2.2 Salinity Patterns near Franks Tract

An additional factor that limited the rate at which fresher water reached the Central Delta with the EDB installed in 2021 was the reduced lateral mixing of channel water from the east into the flooded island of Franks Tract. Stations in or near Franks Tract that show the lack of mixing are identified in **Figure 2.3.2-6** and plotted in **Figure 2.3.2-7**. The salinity levels better equilibrate in 2021 between Old River at Quimby Island (ORQ) and Old River at Franks Tract near Terminous (OSJ) than in non-EDB years, primarily because of increased tidal excursions past OSJ from the San Joaquin River (Figure 2.3.2-7). Salinity levels at HOL become more strongly associated with those at Franks Tract Mid Tract (FRK) and do not equilibrate with the lower salinity water in OSJ and ORQ.

Highlighting this event is important: It was observed in 2015 and has implications for the water quality eventually observed farther south into the Central Delta. This lack of east-to-west water source mixing in Franks Tract has been linked to the higher regional levels of submerged aquatic vegetation (SAV) that can block water movement and exchange.

This circumstance was not as evident in 2022 (Figure 2.3.2-7), as salinity trends and concentrations were similar between FRK, HOL, OSJ, and ORQ (shown in Figure 2.3.2-6), especially toward the end of the EDB installation period. This was likely a result of a second year of extreme drought conditions, with limited freshwater outflow and elevated salinity in the San Joaquin River.

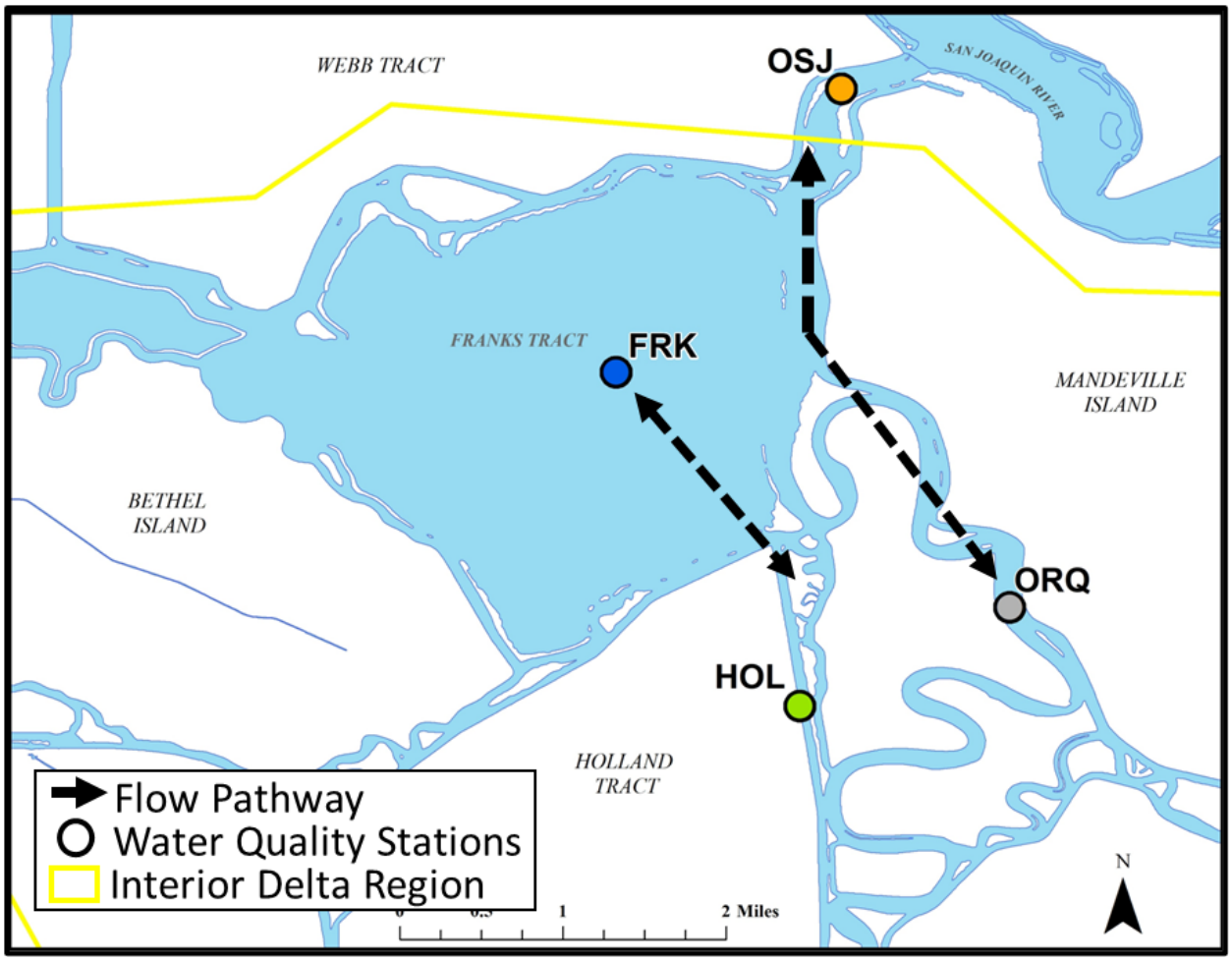

NOTE: Station abbreviations: FRK = Franks Tract Mid Tract; HOL = Holland Cut near Bethel Island; ORQ = Old River at Quimby Island; OSJ = Old River at Franks Tract near Terminous.

Figure 2.3.2-6 Pairs of stations around Franks Tract that equilibrate in salinity.

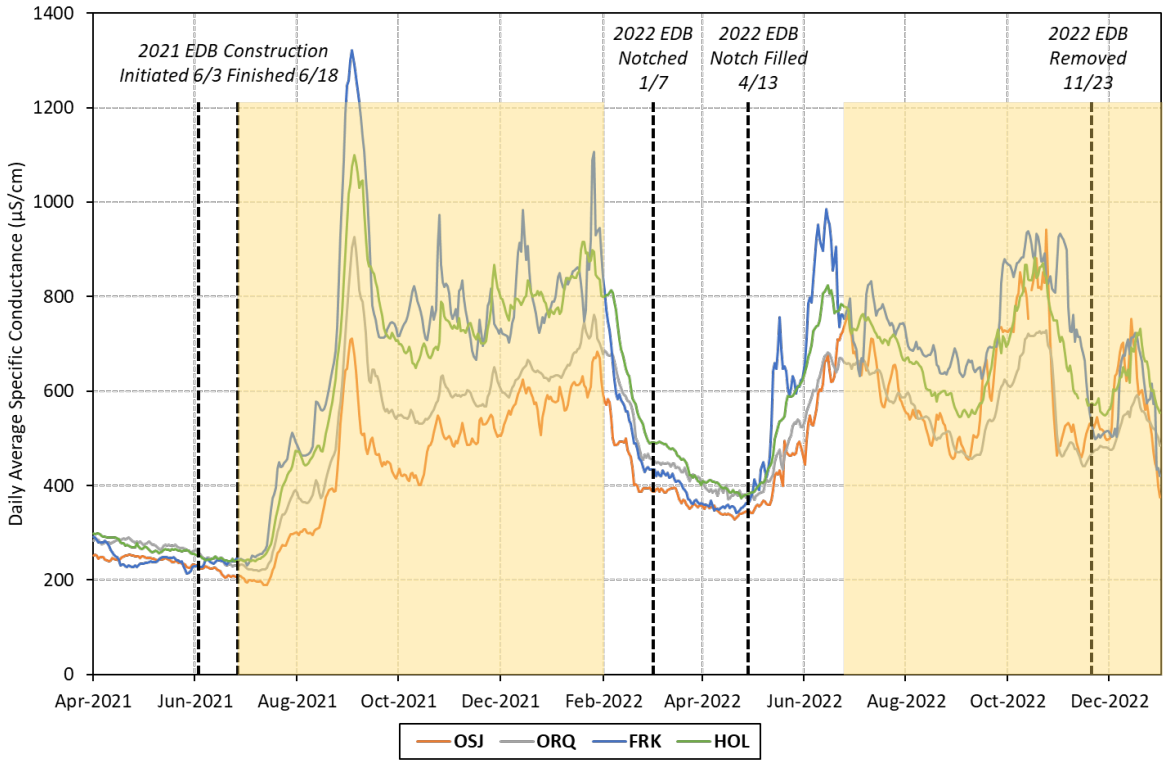

NOTES: µS/cm = microsiemens per centimeter; EDB = emergency drought barrier. Station abbreviations: FRK = Franks Tract Mid Tract; HOL = Holland Cut near Bethel Island; ORQ = Old River at Quimby Island; OSJ = Old River at Franks Tract near Terminous. Yellow-shaded area = period of July–October during equilibrated salinity levels between sites.

Figure 2.3.2-7 Daily-average specific conductivity data for stations on the eastern side of Franks Tract.

2.3.2.3 Old and Middle River Lateral Mixing

The lateral exchange of the fresher Middle River water with water in Old River also affected the rate at which fresher water reached the Central Delta during the EDB installation in 2021. The map in **Figure 2.3.2-8** shows stations in and along Old and Middle rivers and **Figure 2.3.2-9** plots levels of specific conductance. Salinity levels between Old and Middle rivers become more similar in June–October 2021, during the EDB installation period, than in 2020 (Figure 2.3.2-9). This trend was also observed in 2015. It suggests less influence from Middle River's freshening of Old River, possibly because the drought resulted in reduced cross-channel tidal mixing and/or lower water export flows in Old and Middle rivers.

In 2022, salinity levels between Old and Middle rivers (Figure 2.3.2-8) maintained the same trend as in 2021, with both rivers having a more similar salinity level throughout the EDB notch and installation period (Figure 2.3.2-9). This suggests the phenomenon of more cross-channel tidal mixing between Old River and Middle River, with higher dispersive flux of fresher (lower salinity water) in Middle River toward Old River during EDB installation periods.

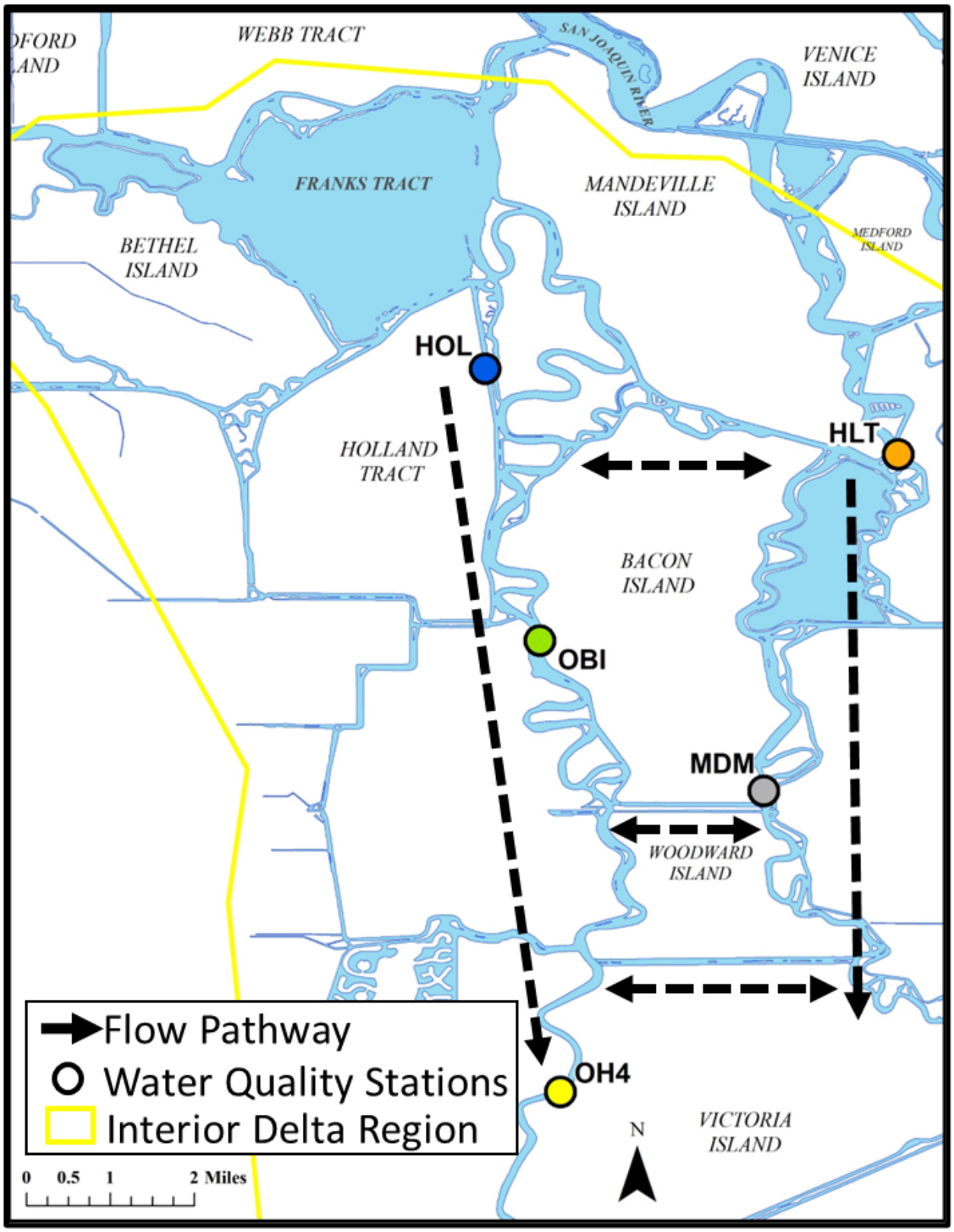

NOTES: Station abbreviations: HLT = Middle River near Holt; HOL = Holland Cut near Bethel Island; MDM = Middle River at Middle River; OBI = Old River at Bacon Island; OH4 = Old River at Highway 4.

Figure 2.3.2-8 Stations used to examine Old River and Middle River mixing.

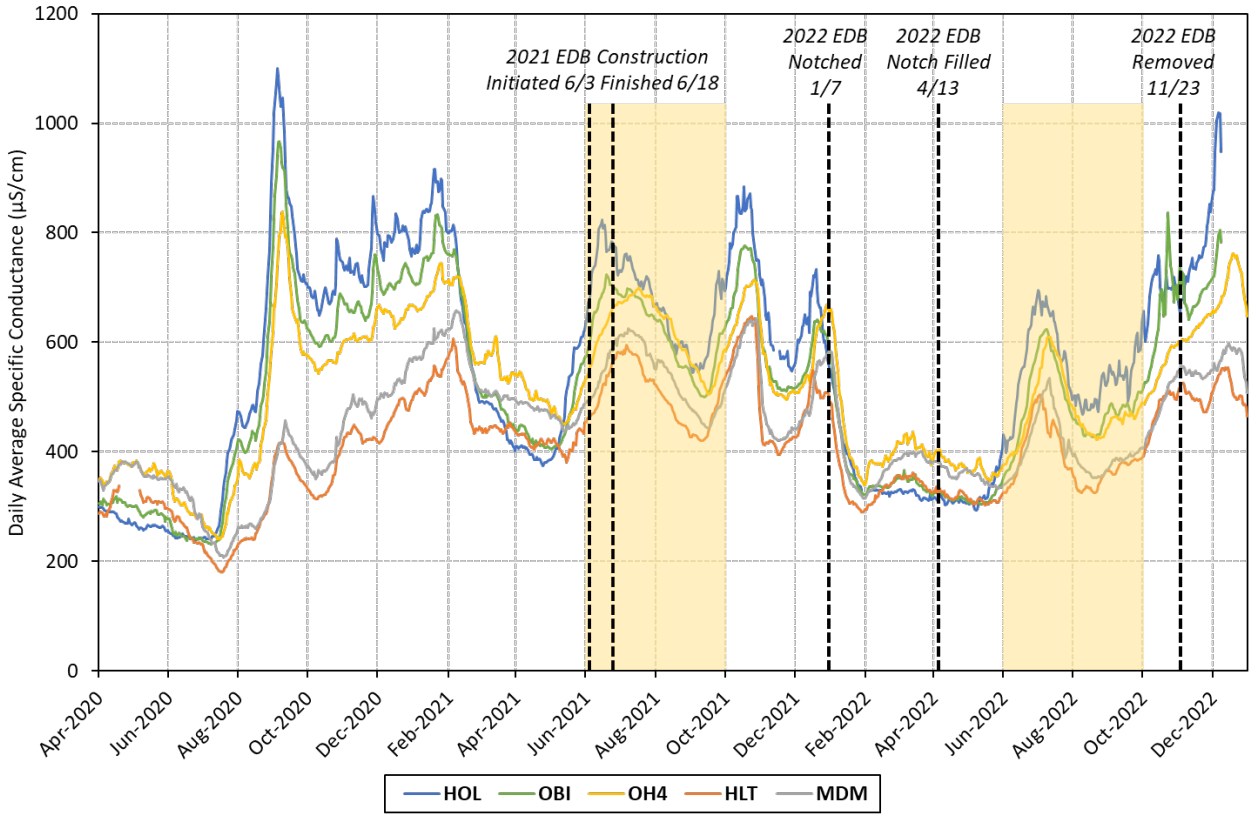

NOTES: µS/cm = microsiemens per centimeter; EDB = emergency drought barrier. Station abbreviations: HLT = Middle River near Holt; HOL = Holland Cut near Bethel Island; MDM = Middle River at Middle River; OBI = Old River at Bacon Island; OH4 = Old River at Highway 4. Yellow-shaded areas = June–October periods with differing salinity patterns in Old and Middle rivers.

Figure 2.3.2-9 Daily-average specific conductance data for stations along Old and Middle rivers.

2.3.2.4 2021–2022 Salinity Compared to Previous Water Years

HOL was used as the representative station for specific conductance in the Central Delta to compare salinity across the previous eight water years. This station was chosen because HOL is the first station along the salinity intrusion pathway at the entrance to the freshwater corridors of Old and Middle rivers, through which water flows to the State and federal pumping facilities. HOL was also chosen because of its legacy status as a key station used to examine the efficacy of the 2015 West False River barrier in previous DWR reports, produced in 2017 and 2019 (California Department of Water Resources 2019).

Figure 2.3.2-10 depicts daily-average specific conductance at HOL during the nine most recent water years. The figure shows 2015 and 2021 as dashed lines to denote that the EDB was installed in those years. The color-matched vertical dashed lines show the dates on which the barrier was first installed during each associated water year, or, in the case of WY 2022, the day when the barrier notch was hydraulically closed.

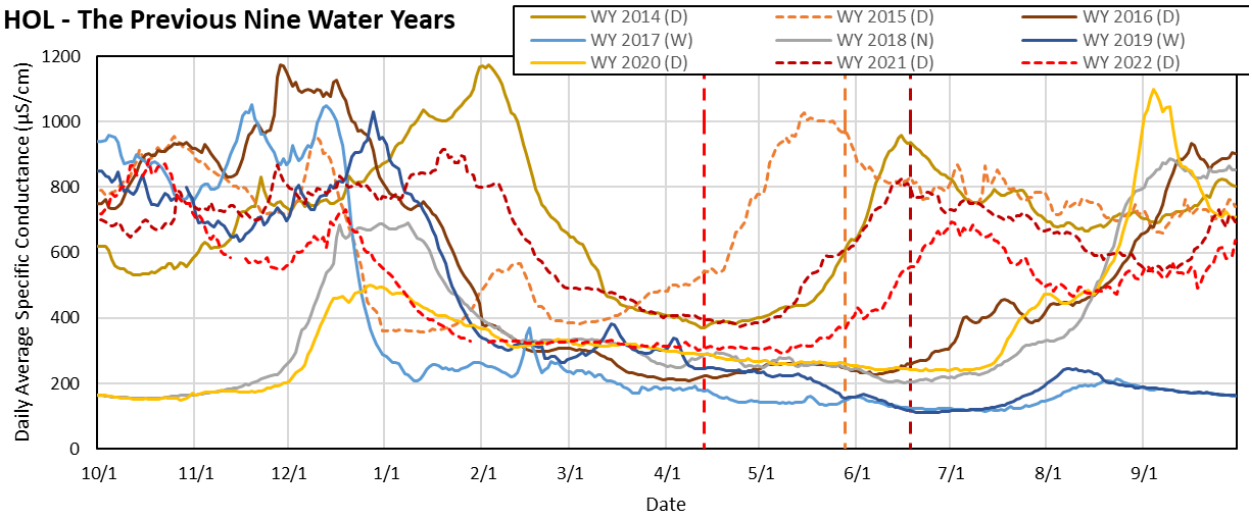

NOTES: µS/cm = microsiemens per centimeter; WY = Water Year. Water year abbreviations: D = Dry, N = Normal, W = Wet.

Figure 2.3.2-10 Daily-average specific conductance at Holland Cut near Bethel Island station during the nine preceding water years.

A water year begins on October 1 of the previous year and runs through September 30 of the named water year; for example, WY 2021 began October 1, 2020, and ran through September 30, 2021. Each water year has been classified by water year type, based on the unimpaired runoff that occurs in the Sacramento Valley and San Joaquin Valley watersheds going back to 1906 and 1901, respectively. The graphs in this section use warmer colors to show Dry water years, which include Critically Dry, Dry, and any combination of Dry and Below Normal designations between the two indices. Normal water years, which include all combinations of Above Normal and Below Normal across the two watershed indices, are shown in gray. Wet years, graphed in colder colors, include all Wet years and combinations of Wet and Above Normal designations between the two indices.

At the beginning of both WY 2021 and WY 2022—as at the start of five of the eight other most recent water years (including two Wet years, 2017 and 2019)—daily-average specific conductance at HOL was already elevated. Daily-average specific conductance dropped 400–600 µS/cm at HOL during the winter months (before February 1) for each previous water year except WY 2021 and WY 2014. In 2014, salinity climbed even higher than in any of the seven other most recent water years, reaching nearly 1,200 µS/cm in early February before decreasing gradually over the next few months. Most of the previous water years achieved a seasonally low salinity around June or July, with only the Wet years (2017 and 2019) staying at or below about 250 µS/cm through the end of the water year. WYs 2016, 2018, and 2020 experienced a late-summer to early-fall increase in salinity levels that was attributable to the absence of adequate rainfall, snowmelt, or released supply to help keep levels lower.

WY 2015 saw a decrease in salinity at HOL in the early winter, similar to WY 2017 (see the dashed orange and solid dark blue lines in Figure 2.3.2-10 for WY 2015 and WY 2017, respectively) and reminiscent of a typical Wet year (blue line in **Figure 2.3.2-11**). However, unlike most other water years, including most other designated Dry water years, salinity began to rise much earlier in 2015, climbing almost 600 µS/cm over 1½ months and reaching a yearly high in May of just over 1,000 µS/cm (Figure 2.3.2-10). In 2015, DWR installed the West False River EDB, achieving hydraulic closure of False River on May 28, 2015. Salinity levels declined gradually—about 300 µS/cm over the next four months—to drop below 700 µS/cm in early September before climbing slowly and reaching about 750 µS/cm by the end of WY 2015 (Figure 2.3.2-10).

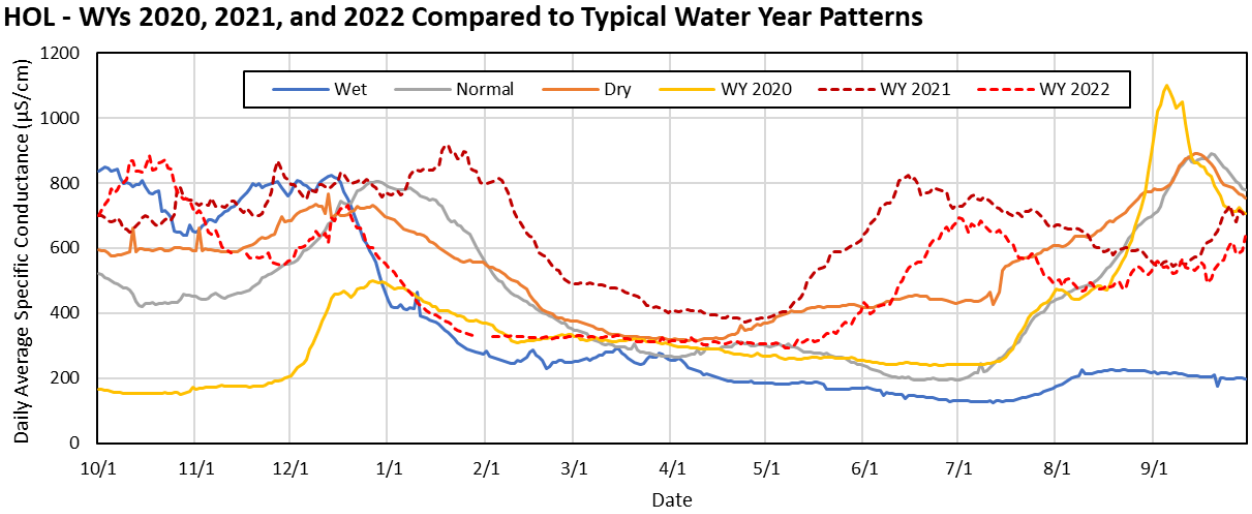

NOTES: µS/cm = microsiemens per centimeter; WY = water year. The chart compares daily-average specific conductance in WYs 2020, 2021, and 2022 to averages for a given day combined within water year type since the station's installation in 2005–2019.

Figure 2.3.2-11 Comparison of daily-average specific conductance at Holland Cut near Bethel Island station in Water Years 2020, 2021, and 2022 to typical water year patterns.

In WY 2021, salinity at HOL stayed above 800 µS/cm until early February, when it finally began to gradually decrease (Figure 2.3.2-10), similar to a pattern for a typical Normal or Dry year at HOL, though occurring about a month later than average (Figure 2.3.2-11). Unlike WY 2015, salinity in WY 2021 reached its lowest levels later in the year—around the beginning of May—before climbing sharply over the next 1½ months. Salinity then reached a seasonal high of just over 800 µS/cm in June, somewhat lower than the salinity peaks around the same time seen in WYs 2014 and 2015 (Figure 2.3.2-10).

In 2021, DWR again installed the West False River EDB, achieving hydraulic closure of False River on June 18, 2021. As in WY 2015, upon installation of the barrier in False River, salinity levels began to decrease gradually,

dropping to about 550 µS/cm by early September, and then climbed again and reached about 700 µS/cm by the end of WY 2021 (Figure 2.3.2-10).

In WY 2022, salinity at HOL peaked at about 900 µS/cm in mid-October, then began to decrease slightly. The salinity level climbed again to a smaller peak in mid-December before decreasing slightly later than the seasonal salinity drop in WY 2015, and not quite as sharply or by as much (Figure 2.3.2-10). Salinity at HOL reached its lowest levels later in WY 2022 than in WY 2015 or WY 2021—around mid-May—before climbing over the next 1½ months. In early July, salinity reached a seasonal high of about 700 µS/cm, which was a lower peak salinity and one that occurred later in the season than in WYs 2014, 2015, and 2021 (Figure 2.3.2-10).

In 2022, DWR filled the notch in the West False River EDB, achieving hydraulic closure of False River on April 13, 2022. Unlike WYs 2015 and 2021, salinity levels were already very low when False River was sealed in WY 2022, which likely helped keep salinity levels lower later into the year (Figure 2.3.2-10).

2.3.2.5 Methods

DWR and USGS water quality monitoring stations collected continuous real-time data at 15-minute intervals by deploying YSI EXO2 sondes (at a depth of 1 meter) for the following constituents:

- Water temperature (degrees Celsius [°C]).
- Dissolved oxygen (DO) (mg/L).
- Specific conductance (µS/cm).
- Turbidity (formazin nephelometric units [FNU]).
- Chlorophyll (micrograms per liter [µg/L]).

YSI EXO2 sondes are approximately 2 feet long and 3½ inches in diameter. They are completely submersible and self-contained, operating on a minimum of 6 volts of battery power from four D-cell alkaline batteries. Deployment data are logged in each sonde's internal memory. For detailed information on YSI multiparameter sondes, visit http://www.ysi.com/exo2.

Staff members regularly performed the following three procedures to check that sondes were operating properly and measuring accurately, and to validate the data:

- Daily data checks via the California Data Exchange Center and/or the Campbell Scientific LoggerNet and Real-Time Monitoring and Control software applications.

- A comparison between the field data measured by the YSI EXO2 sondes during each monthly site visit and the data collected by the station sondes at the closest 15-minute time interval.
- A post-deployment accuracy check, which involved checking sensors in the field before and after cleaning (checking for bio-fouling sensor errors) and checking sensors versus laboratory standards (checking for sensor drift errors) to establish a total sensor error.

The accuracy of sonde probes deployed in the field can be negatively affected by probe malfunction, drift away from initial calibration, and/or fouling caused by biological growth on the probe's reading surface (Wagner et al. 2006). DWR and USGS staff performed the post-deployment accuracy check by using the following procedures before cleaning the sonde probes during each monthly station visit:

- Before being cleaned, recently deployed YSI EXO2 sonde probes were placed in a bucket of ambient station water with a secondary verified, clean, lab-calibrated YSI EXO2 sonde, and values for all sensors were recorded and compared.
- Deployed YSI EXO2 sonde probes were cleaned, then were again placed in a bucket of ambient station water with a secondary verified, clean, lab-calibrated YSI EXO2 sonde, and values for all sensors were recorded and compared. Note: Some stations also collect sensor measurements for chlorophyll, pH, and fluorescent dissolved organic matter (fDOM); see Table 2 of the *2021 Emergency Drought Salinity Barrier Project Monitoring Plan*, May 2021 (California Department of Water Resources 2021).
- Deployed YSI EXO2 sondes and sensors were then brought back to the laboratory and were checked against fresh calibration standards with known values, and those values were recorded.
- Sensor values were given a final accuracy rating, using the total error from combined biofouling and sensor drift comparisons for each constituent. Sensor values were rated as either excellent, good, fair, or poor according to the USGS technical report *Guidelines and Standard Procedures for Continuous Water-Quality Monitors: Station Operation, Record Computation, and Data Reporting* (Wagner et al. 2006).

The applied ratings obtained during the accuracy check indicate the quality, accuracy, and reliability of the data collected by the sondes in the field. In addition to conducting the post-deployment accuracy check, DWR and USGS staff compared the water temperature, specific conductance, DO, and turbidity data measured in the field by the verified, lab-calibrated YSI EXO2 sonde to the deployed sonde data that were closest in time. While taking field measurements, DWR and USGS staff made every attempt to collect the

field readings at the same depth at which the sonde probes were measuring (1 meter) and as close to the sonde pipe as possible. Because field instruments are calibrated regularly, a large difference between the sonde and field readings could indicate inaccuracy of sonde data during the deployment period. DWR and USGS staff compared the field and sonde readings and the ratings applied from the post-deployment accuracy check when assessing data quality and entering the continuous data into the database.

In addition to continuous water quality monitoring, discrete water quality samples were collected at several co-located sites (FAL, BET, HOL, FCT, OSJ, Threemile Slough at San Joaquin River [TSL], and Sacramento River near Sherman Island [SSI]) as outlined in the 2021 EDB Monitoring Plan. Data were also acquired from the long-term and routine DWR Environmental Monitoring Program (EMP) stations: D19, D26, D22, D4, and NZ068. Several water quality constituents were analyzed in those discrete samples collected in 2021 and prior years, but this discussion focuses on constituents: chlorophyll *a* (chl *a*), dissolved nitrate + nitrite, dissolved ammonia, dissolved orthophosphate, total suspended solids (TSS), dissolved chloride, and dissolved bromide.

Measuring chl *a* is a common means of determining the amount of algal growth and biomass in a waterbody. Concentrations vary based on available nutrients, light, hydrodynamic conditions, and other associated environmental conditions. Nitrate + nitrite, ammonia, and orthophosphate were investigated because these forms of nutrients are the most available biological sources of algal growth and assimilation. TSS is a measure of the organic and inorganic particulates in the waterbody, contributing to the determination of water clarity as an important factor for algal production. Chloride and bromide were investigated further, as they are important anions that can provide a measure of the increase in salts in a waterbody resulting from seawater intrusion, surface water runoff, and/or groundwater contributions. Chloride concentrations are also outlined in State Water Board Water Right Decision 1641 and standards must be met in the Delta for maintaining water quality objectives for municipal and industrial beneficial uses (State Water Resources Control Board 2000).

DWR staff collected samples for all constituents at a depth of 1 meter using a Van Dorn water sampler. Water samples from each site were filtered in the laboratory in preparation for the quantification of nutrients and chl *a*. Nutrient samples were filtered through 0.45-micron (µm) filters (Millipore HATF04700), which were then immediately frozen at -20°C. Ambient nutrient concentrations were analyzed using various analysis methods established by the U.S. Environmental Protection Agency (EPA) and American Public Health Association: NO_2+NO_3 (Standard Method 4500-NO3-F Modified), NH_4 (EPA 350.1), and PO_4 (EPA 365.1). Concentrations of chl *a*

were acquired by extracting pigments on glass-fiber filters (47 µm Millipore) with 90 percent aqueous acetone and using spectrophotometry (Standard Method 10200H) (American Public Health Association et al. 2017). TSS concentrations were acquired using EPA Method 160.2. The analyte determination for April–November as outlined in the report (n = 7–13 per site) was conducted at the DWR Bryte Laboratory in West Sacramento.

Data from 2015 (the prior EDB installation year) and 2021 were further grouped into regions based on geography and proximity to the major tributary for trend analysis. The three regions and associated stations consist of Sacramento River (D4, SSI/D11A, D22, and NZ068), San Joaquin River (FCT, D26, and OSJ), and Interior Delta (FAL, FRK, BET, and HOL). Data from 2021 and 2015 were compared to data from previous Dry water years (2014 and 2020) and Wet water years (2017 and 2019) to investigate water quality differences both by water year and by EDB installation year.

Figure 2.3.2-1 shows a regional map of all continuous and discrete water quality sites. The sites were grouped into three regions:

- *Sacramento River Region*, covering the northwest portion of the Central Delta from the confluence of the Sacramento and San Joaquin rivers, up the Sacramento River to the Rio Vista Bridge.
- *San Joaquin River Region*, covering the middle third of the Central Delta from the southern edge of Sherman Island upstream along the San Joaquin River to the northern end of Mandeville Island.
- *Interior Delta Region*, covering the southeast portion of the Central Delta from False River east of the barrier upstream to Clifton Court Forebay.

2.3.2.6 Salinity Measurements

Real-time specific conductance data were collected at the SSI, TSL, and Sacramento River at Rio Vista Bridge (RVB) stations to examine regional salinity trends along the Sacramento River (**Figure 2.3.2-12**).

The three stations along the Sacramento River showed similar salinity patterns. Salinity levels at the more upstream stations, TSL and RVB, showed a slight lag and were heavily diminished relative to SSI: at TSL, about 25–35 percent of salinity downstream at SSI; and at RVB, about 50 percent of TSL salinity (**Figure 2.3.2-13**).

Salinity along the Sacramento River climbed steadily beginning in late April 2021, reaching a high at SSI of nearly 8,000 µS/cm in late June before gradually decreasing and then fluctuating between about 4,000 and 6,000 µS/cm in August and September.

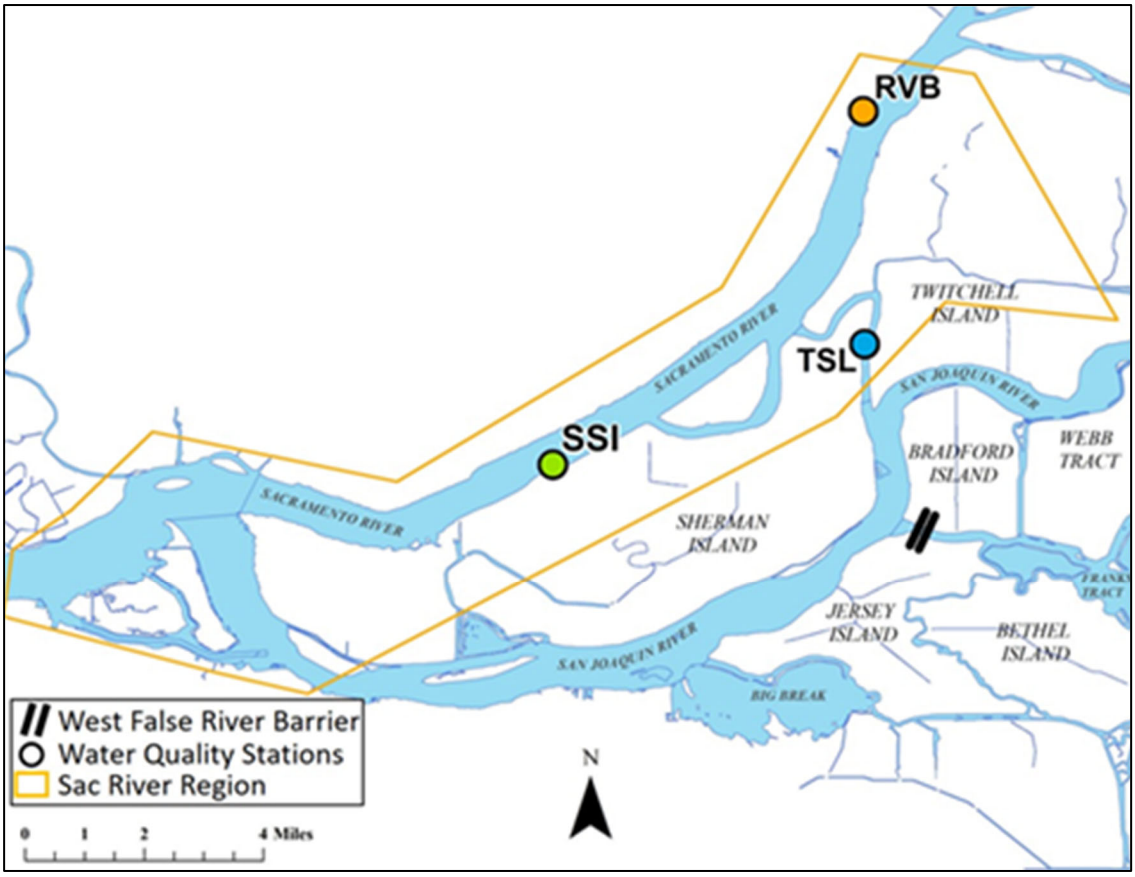

NOTE: Station abbreviations: RVB = Sacramento River at Rio Vista Bridge; SSI = Sacramento River near Sherman Island; TSL = Threemile Slough at San Joaquin River.

Figure 2.3.2-12 Water quality monitoring stations along the Sacramento River.

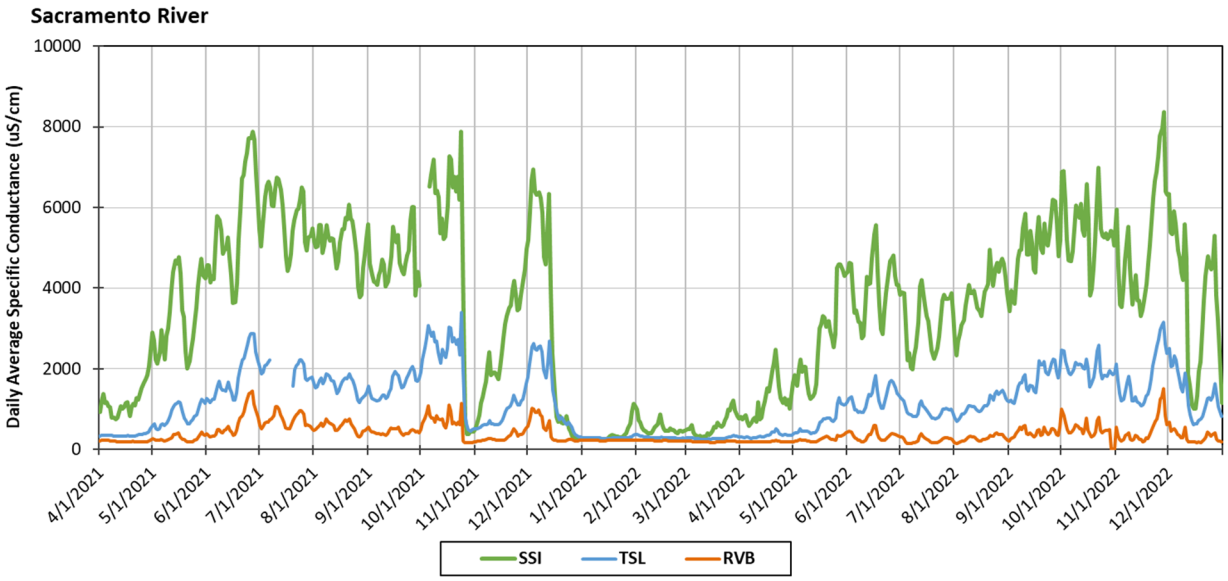

NOTES: µS/cm = microsiemens per centimeter. Station abbreviations: RVB = Sacramento River at Rio Vista Bridge; SSI = Sacramento River near Sherman Island; TSL = Threemile Slough at San Joaquin River.

Figure 2.3.2-13 Daily-average specific conductance along the Sacramento River.

Salinity then began to climb again, once more reaching nearly 8,000 µS/cm in late October 2021, when an exceptional rain event caused specific conductance along the Sacramento River to fall sharply to just a few hundred µS/cm. Salinity again increased quickly at SSI and increased more gradually at the upstream stations TSL and RVB before decreasing as a result of December rainfall (Figure 2.3.2-13). Salinity values stayed below 1,000 µS/cm at all stations until April 2022, when they began to creep up again, although salinity reached generally lower levels during the first half of the year than what was seen in 2021. Values again hit a period of valleys in November and December as a result of rainfall.

Data from six stations along the San Joaquin River were used to examine regional salinity trends in 2021 and 2022. From downstream to upstream, these stations are San Joaquin River at Blind Point (BLP), San Joaquin River at Jersey Point (SJJ), Dutch Slough at Jersey Island (DSJ), San Joaquin River at Twitchell Island (TWI), Fisherman's Cut (FCT), and Old River at Franks Tract near Terminous (OSJ) (**Figure 2.3.2-14**).

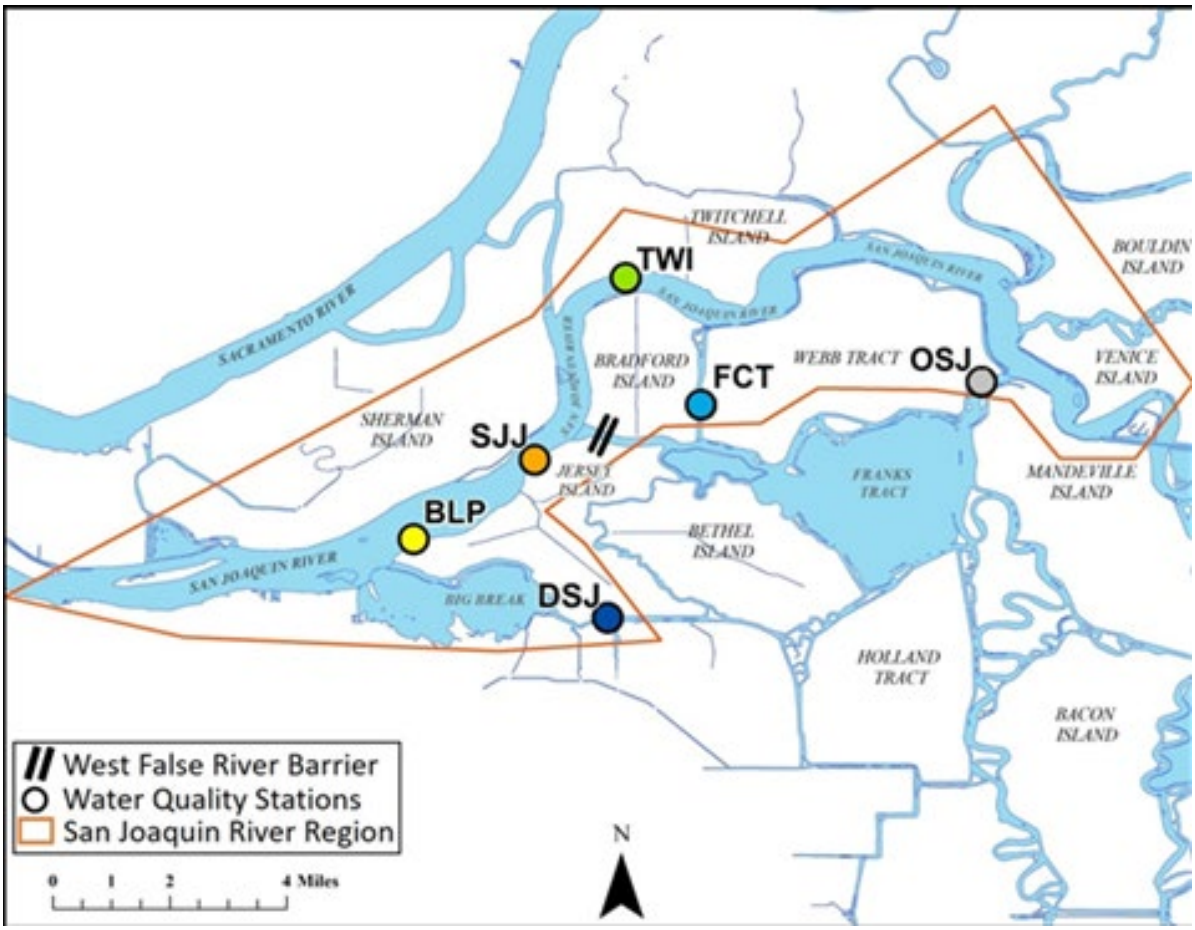

NOTE: Station abbreviations: BLP = San Joaquin River at Blind Point; DSJ = Dutch Slough at Jersey Island; FCT = Fisherman's Cut; OSJ = Old River at Franks Tract near Terminous; SJJ = San Joaquin River at Jersey Point; TWI = San Joaquin River at Twitchell Island.

Figure 2.3.2-14 Water quality monitoring stations along the San Joaquin River.

Daily-average specific conductance measurements along the San Joaquin River showed a pattern largely resembling the measurements along the Sacramento River. If overlaid along the Sacramento River salinity graph (Figure 2.3.2-13), BLP and SJJ would fit nicely between the graphs of SSI and TSL, with TWI falling in step just below TSL. DSJ was the exception in this region: It did not follow the pattern observed at the other San Joaquin Region stations. This finding can be at least partially explained by the fact that DSJ has an entirely separate hydraulic connection to the Interior Delta Region running east along Jersey Island and then Bethel Island (Figure 2.3.2-1 and Figure 2.3.2-14).

As with the Sacramento River Region stations, salinity along the San Joaquin River (**Figure 2.3.2-15**) rose in late April 2021, climbed to reach a seasonal high in late June, decreased slightly, and then rose again. Salinity likely would have continued to increase without the exceptional rainfall that occurred at the end of October 2021, which caused salinity to drop precipitously. Salinity then began to rise again in late November and early December and dropped again after several more rainfall events in December. Salinity then stayed below 500 µS/cm at all stations until April 2022, when values began to climb again, reaching highs similar to those observed in 2021. However, July and August saw a drop in EC in the San Joaquin River before climbing gradually during the fall months. As in the Sacramento River (Figure 2.3.2-13), rainfall in November and December 2022 caused salinity levels to drop, peak, and drop again.

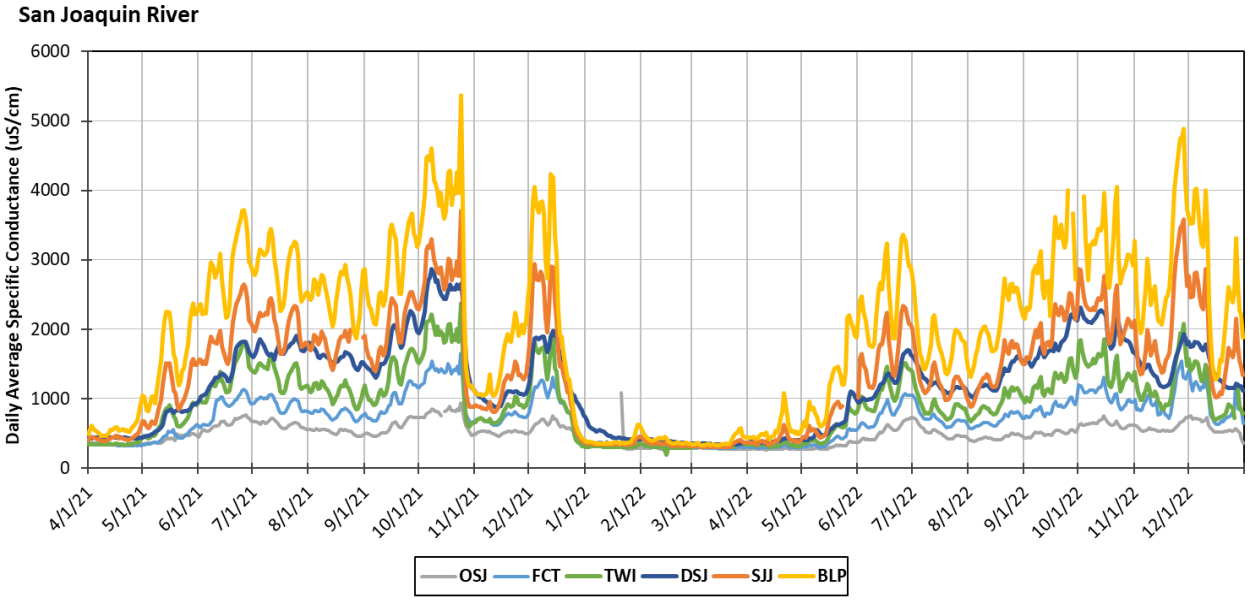

NOTES: µS/cm = microsiemens per centimeter. Station abbreviations: BLP = San Joaquin River at Blind Point; DSJ = Dutch Slough at Jersey Island; FCT = Fisherman's Cut; OSJ = Old River at Franks Tract near Terminous; SJJ = San Joaquin River at Jersey Point; TWI = San Joaquin River at Twitchell Island.

Figure 2.3.2-15 Daily-average specific conductance along the San Joaquin River.

2.3.2.7 Water Temperature

Daily-average water temperatures followed a generally similar pattern across each region (**Figure 2.3.2-16**). In 2021, water temperatures rose gradually from April to June, peaked in July, then gradually dropped in August and September. This drop was interrupted by a brief period of increasing water temperatures in October before the downward trend continued. In 2022, water temperatures climbed gradually, peaked in early September, and then fell more suddenly, dropping below 15°C at the beginning of November, almost half a month earlier than in 2021.

Water temperatures appeared to reach slightly higher levels in the Interior Delta Region than in the other two regions. Each station in the Interior Delta Region met or exceeded 24°C by July of each year, and the most interior stations—HOL and OBI—experienced the highest temperatures. The San Joaquin River Region stations also recorded water temperatures that exceeded 24°C in June and July, although they did not reach levels quite as high as the stations in the Interior Delta Region. Stations in the Sacramento River Region had slightly lower water temperatures than observed at most stations in the Interior Delta and San Joaquin River regions. These regional differences are likely caused by a combination of factors: differences in channel morphology near the stations, temperature of source-water inputs, and access to cooling air currents determined by channel orientation, levee height, and/or amount of open water adjacent to the stations.

2.3.2.8 Turbidity

The increase in turbidity at Franks Tract Mid Tract (FRK) coincided with a large increase in flow at OSJ beginning in early June 2021 (Figure 2.3.2-1), which may have helped stir sediment; however, high wind speeds occurred exactly as turbidity spikes were recorded at FRK on June 21 and December 13, 2021, which also may have been a factor (**Figure 2.3.2-17**). Turbidity also noticeably increased around the time of the rain events in late October and mid-December 2021. This turbidity was most visible at the Sacramento River at Rio Vista Bridge (RVB) station, exceeding that recorded at SSI (which normally has higher turbidity than RVB) or TSL (which normally has turbidity levels similar to or slightly higher than those at RVB).

In the first half of 2022, DSJ showed several peaks in turbidity that initially appeared to roughly coincide with the notching of the West False River barrier; however, a review of DSJ turbidity data from spring 2021 (before April) and spring 2020 showed a similar series of turbidity peaks. These peaks likely resulted from seasonal high flows or the die-off of submerged aquatic vegetation, or SAV, that had helped to anchor sediments in place along Dutch Slough, or some combination of these two factors.

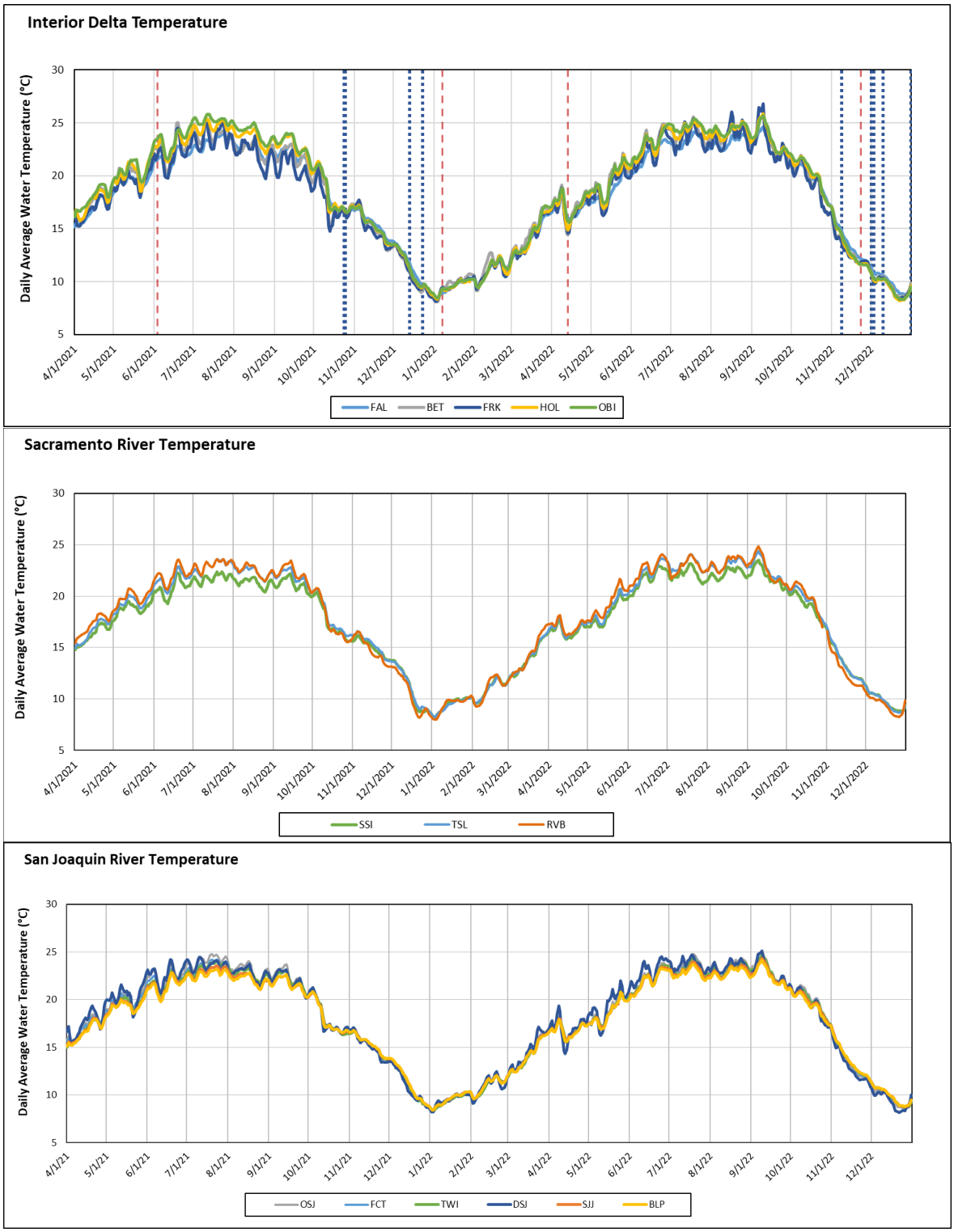

NOTES: °C = degrees Celsius. Station abbreviations: BET = Bethel Island at Piper Slough; BLP = San Joaquin River at Blind Point; DSJ = Dutch Slough at Jersey Island; FAL = False River near Oakley; FCT = Fisherman's Cut; FRK = Franks Tract Mid Tract; HOL = Holland Cut near Bethel Island; OBI = Old River at Bacon Island; OSJ = Old River at Franks Tract near Terminous; RVB = Sacramento River at Rio Vista Bridge; SJJ = San Joaquin River at Jersey Point; SSI = Sacramento River near Sherman Island; TSL = Threemile Slough at San Joaquin River; TWI = San Joaquin River at Twitchell Island.

Figure 2.3.2-16 Daily-average water temperature across Central Delta regions, April 1, 2021, to December 31, 2022.

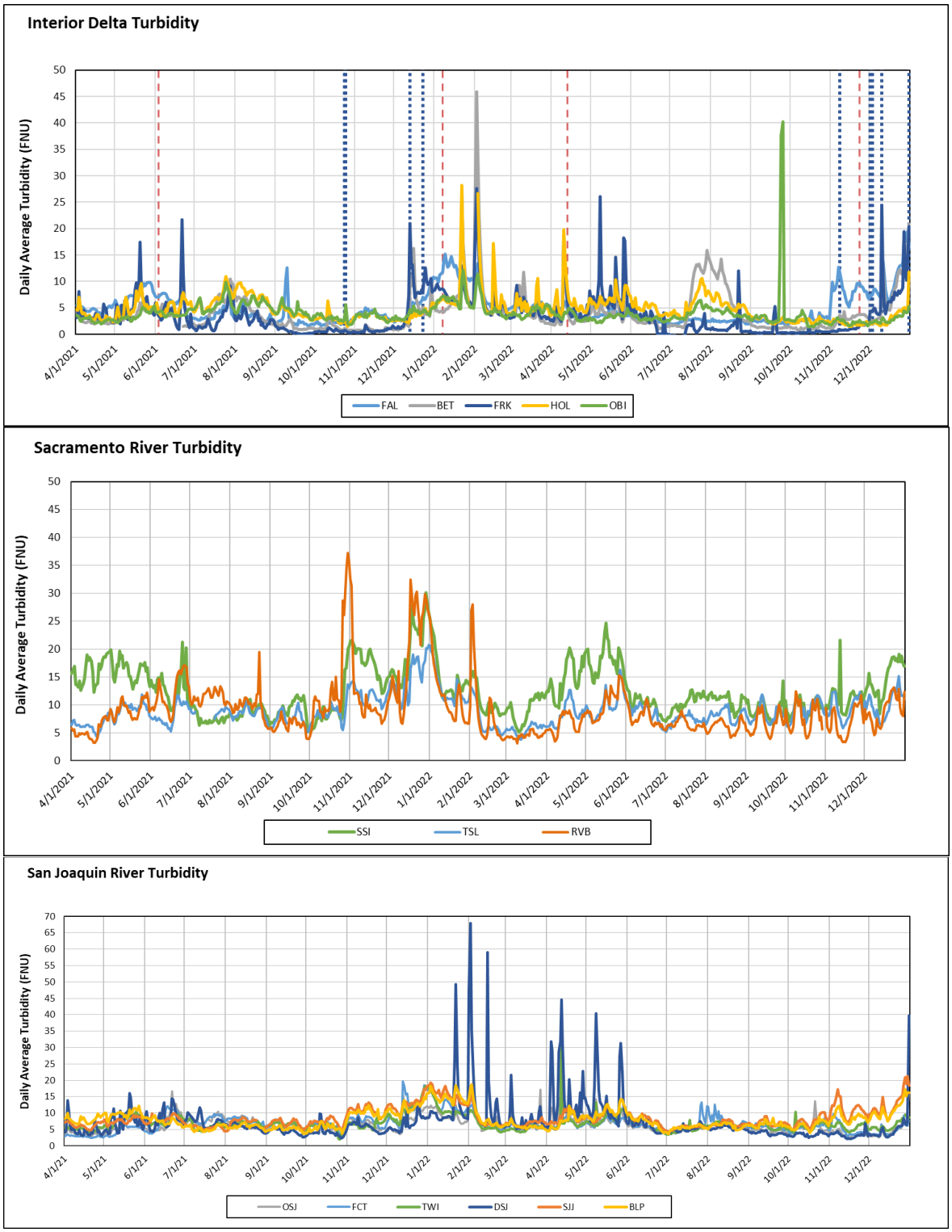

NOTES: FNU = formazin nephelometric units. Station abbreviations: BET = Bethel Island at Piper Slough; BLP = San Joaquin River at Blind Point; DSJ = Dutch Slough at Jersey Island; FAL = False River near Oakley; FCT = Fisherman's Cut; FRK = Franks Tract Mid Tract; HOL = Holland Cut near Bethel Island; OBI = Old River at Bacon Island; OSJ = Old River at Franks Tract near Terminous; RVB = Sacramento River at Rio Vista Bridge; SJJ = San Joaquin River at Jersey Point; SSI = Sacramento River near Sherman Island; TSL = Threemile Slough at San Joaquin River; TWI = San Joaquin River at Twitchell Island.

Figure 2.3.2-17 Daily-average turbidity across Central Delta regions, April 1, 2021, to December 31, 2022.

Dissolved Oxygen

Daily-average DO levels mostly showed a U-shaped pattern over each year across all regions because of the inverse relationship between water temperature and DO saturation in water (**Figure 2.3.2-18**). The notable exception was at FRK, where a large increase in DO levels began in July in both 2021 and 2022. Spikes exceeded 15 mg/L, indicating substantial growth of aquatic plants or algae in Franks Tract. A review of historical FRK DO data revealed that these seasonal peaks are not isolated to years with the West False River barrier in place, but in fact show up from late summer to early fall every year. However, the DO increases at FRK did appear comparatively diminished during the wettest year on record, 2017.

A noticeable drop in DO levels was also observed at many stations at the end of October 2021 (Figure 2.3.2-18)—most visible in the Sacramento River regional graph—and coincided with the major rain event during the last week of October.

2.3.2.1 Chlorophyll Fluorescence

Overall, daily median values for chlorophyll fluorescence were low at all sites across the Central Delta from April through December in 2020–2022, except for a few periods of elevated values at some stations (**Figure 2.3.2-19**). Most of the time, values were below 5 µg/L; however, in a few instances, daily medians increased to values exceeding 10 µg/L for about one week, most notably at OSJ in 2020 and 2021, Middle River near Holt (HLT) and Middle River at Middle River (MDM) in 2020, HLT in 2021, and FRK in 2022.

The increases in chlorophyll fluorescence in 2021 at both OSJ and HLT occurred in mid-May, which was before work on the barrier began. There appeared to be a much smaller increase in daily medians once barrier installation was complete in August 2021 at a few stations: SJJ, TWI, and FAL. A much larger increase in chlorophyll fluorescence values occurred at some stations within the San Joaquin and Interior Delta regions during a similar time of year in August 2020, but not in August 2022.

The most obvious increase in chlorophyll fluorescence occurred at FRK in spring 2022, when it increased sharply and remained elevated for about six weeks after the filling of the barrier notch in April 2022. However, discrete sampling in Franks Tract in July and August 2022 measured chlorophyll above 100 µg/L (see Section 2.3.2.4, "Harmful Algal Blooms," and **Appendix E**, "Remote Sensing Verification"). A cyanobacterial bloom occurred in Franks Tract in summer 2022 but was not detected by the FRK sensor.

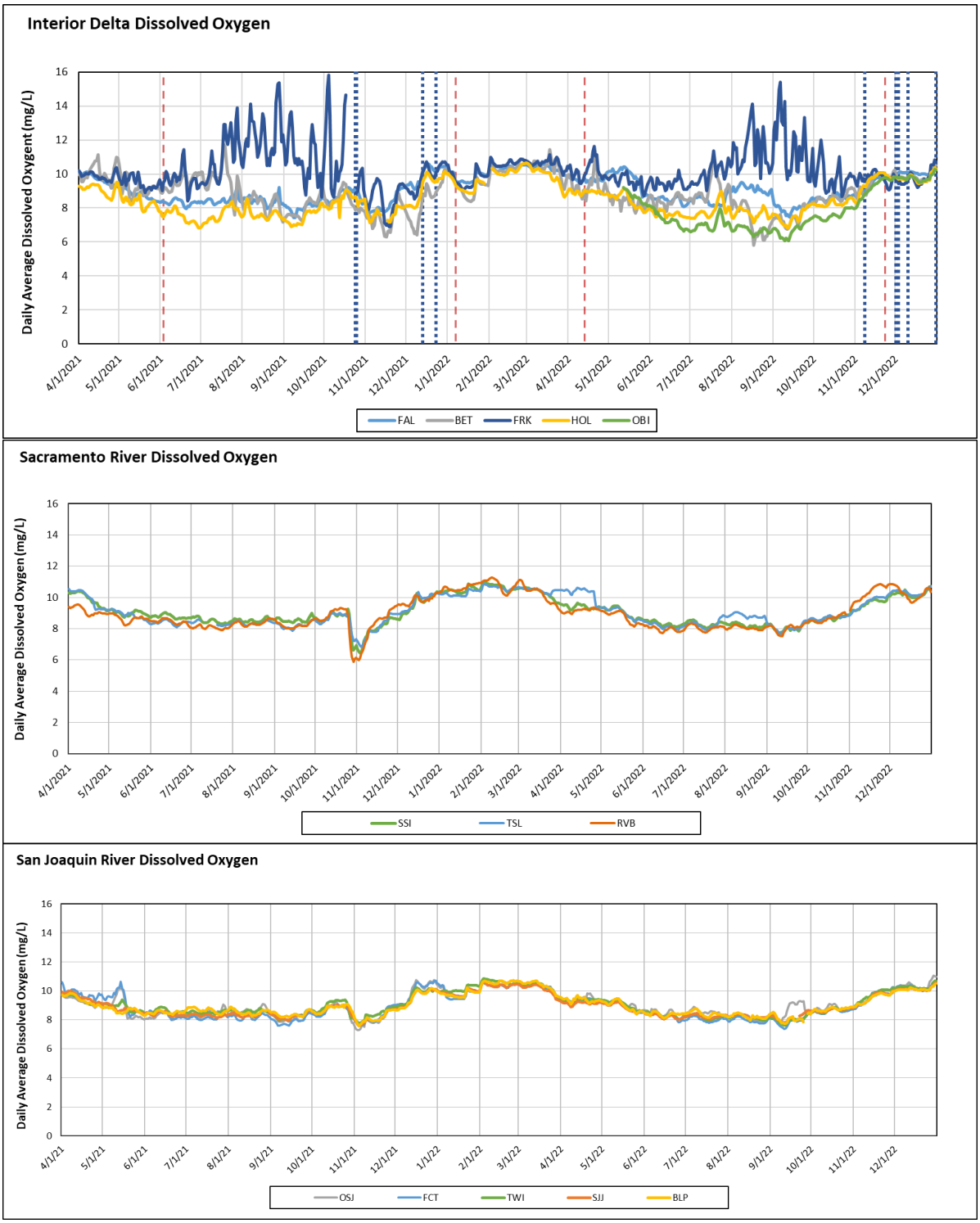

NOTES: mg/L = milligrams per liter. Station abbreviations: BET = Bethel Island at Piper Slough; BLP = San Joaquin River at Blind Point; DSJ = Dutch Slough at Jersey Island; FAL = False River near Oakley; FCT = Fisherman's Cut; FRK = Franks Tract Mid Tract; HOL = Holland Cut near Bethel Island; OBI = Old River at Bacon Island; OSJ = Old River at Franks Tract near Terminous; RVB = Sacramento River at Rio Vista Bridge; SJJ = San Joaquin River at Jersey Point; SSI = Sacramento River near Sherman Island; TSL = Threemile Slough at San Joaquin River; TWI = San Joaquin River at Twitchell Island.

Figure 2.3.2-18 Daily-average dissolved oxygen levels across Central Delta regions, April 1, 2021, to December 31, 2022.

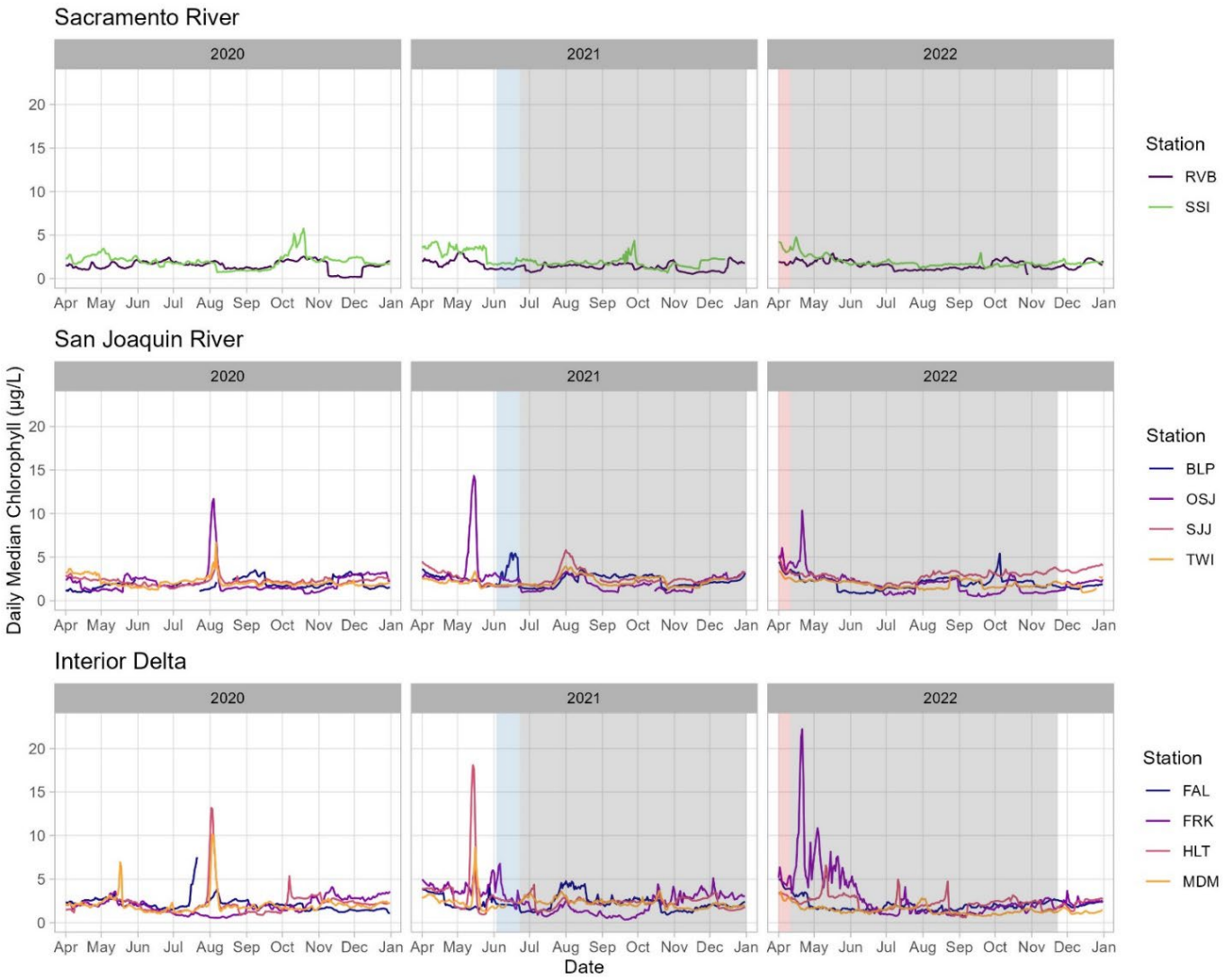

NOTES: µg/L = micrograms per liter. Light blue shading = emergency drought barrier under construction; brick red shading = barrier notched; gray shading = barrier complete and in place. Station abbreviations: BLP = San Joaquin River at Blind Point; FAL = False River near Oakley; FRK = Franks Tract Mid Tract; HLT = Middle River near Holt; MDM = Middle River at Middle River; OSJ = Old River at Franks Tract near Terminous; RVB = Sacramento River at Rio Vista Bridge; SJJ = San Joaquin River at Jersey Point; SSI = Sacramento River near Sherman Island; TWI = San Joaquin River at Twitchell Island.

Figure 2.3.2-19 Daily median values for continuous chlorophyll fluorescence in the Sacramento River, San Joaquin River, and Interior Delta regions, April–December 2020–2022.

Overall, daily median values of chlorophyll fluorescence in the San Joaquin and Interior Delta regions were slightly higher in 2021 than in 2020 and 2022; however, the increase in the overall median was very modest, at about 1 µg/L (**Figure 2.3.2-20**). Chlorophyll fluorescence values in the Sacramento River Region were almost identical in 2020–2022.

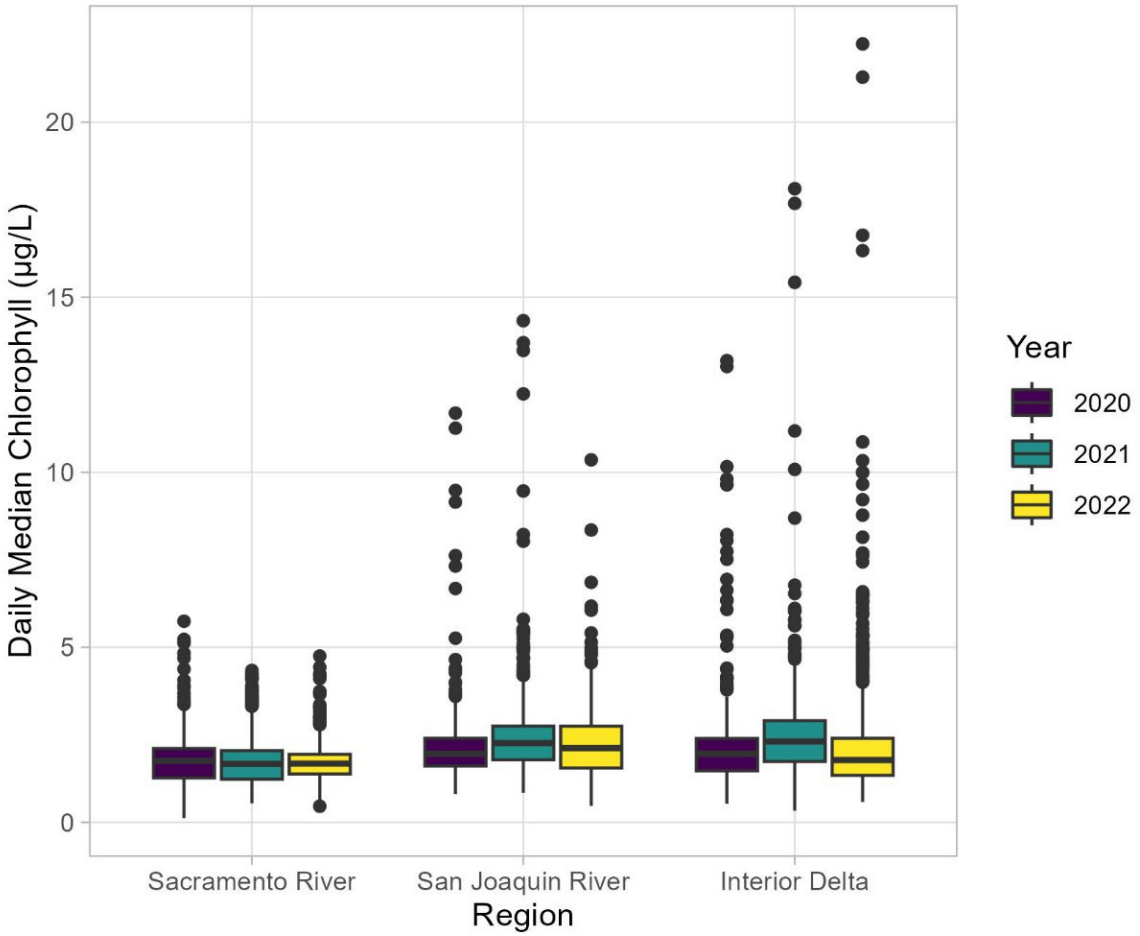

NOTE: µg/L = micrograms per liter.

Figure 2.3.2-20 Boxplots of daily median values of continuous chlorophyll fluorescence for each region, by year (April–December).

2.3.2.2 Chlorophyll-*a* and Nutrients

Table 2.3.2-1 shows water quality sampling sites in the Interior Delta, San Joaquin River, and Sacramento River regions and their respective locations.

TABLE 2.3.2-1
DISCRETE WATER QUALITY SAMPLING SITES, REGIONS, AND GEOGRAPHIC COORDINATES (WGS84)

Station Name	Station Code	Region	Latitude	Longitude
False River near Oakley	FAL	Interior Delta	38.05546	-121.66712
Bethel Island at Piper Slough	BET	Interior Delta	38.03335	-121.61984
Holland Cut near Bethel Island	HOL	Interior Delta	38.01584	-121.58214
Franks Tract near Russo's Landing	D19	Interior Delta	38.04376	-121.61480
Fisherman's Cut	FCT	San Joaquin River	38.06560	-121.64792
Old River at Franks Tract near Terminous	OSJ	San Joaquin River	38.07125	-121.57837
San Joaquin River at Twitchell Island	D16	San Joaquin River	38.09690	-121.66910
San Joaquin River at Potato Point	D26	San Joaquin River	38.07664	-121.56690
Threemile Slough at San Joaquin River	TSL	Sacramento River	38.10330	-121.68610
Sacramento River near Rio Vista	NZ068	Sacramento River	38.14272	-121.68950
Sacramento River at Emmaton	D22	Sacramento River	38.08453	-121.73910
Sacramento River near Sherman Island	SSI/D11A	Sacramento River	38.07410	-121.76174
Sacramento River above Point Sacramento	D4	Sacramento River	38.06248	-121.82050

NOTE: WGS84 = World Geodetic System 1984

Interior Delta Region

To characterize concentrations of chl *a*, nutrients, TSS, chloride, and bromide in the Interior Delta Region, four active sampling locations were investigated from April to December in 2015 and 2021 and from January to December in 2022 (**Figure 2.3.2-21**). These sampling locations included three co-located continuous monitoring locations that were sampled a minimum of once per month: FAL, BET, and HOL (2015: n=11–12 per site; 2021: n=7 per site; 2022: n=9–11 per site). In addition, DWR EMP monthly discrete monitoring station D19 was investigated to obtain data on ambient conditions in Franks Tract (2015 and 2021: n=8; 2022: n=12).

Chl *a* concentrations were low at all sites in the Interior Delta Region in 2021, ranging from 0.71 to 2.94 $\mu g/L^{-1}$ in April–May before installation of the EDB at West False River and in June just after EDB closure (**Figure 2.3.2-22**A). This differed from the prior EDB installation year, 2015, when chl *a* concentrations were high ($\geq$10 $\mu g/L^{-1}$) just before EDB closure, with notably elevated concentrations measuring more than 40 $\mu g/L^{-1}$ at sites FAL and HOL. However, chl *a* concentrations did increase considerably at all sites in July and August 2021 after EDB closure; concentrations peaked at all sites in August, ranging from 15 to 20 $\mu g/L^{-1}$, and the highest concentration was measured at HOL at 23 $\mu g/L^{-1}$.

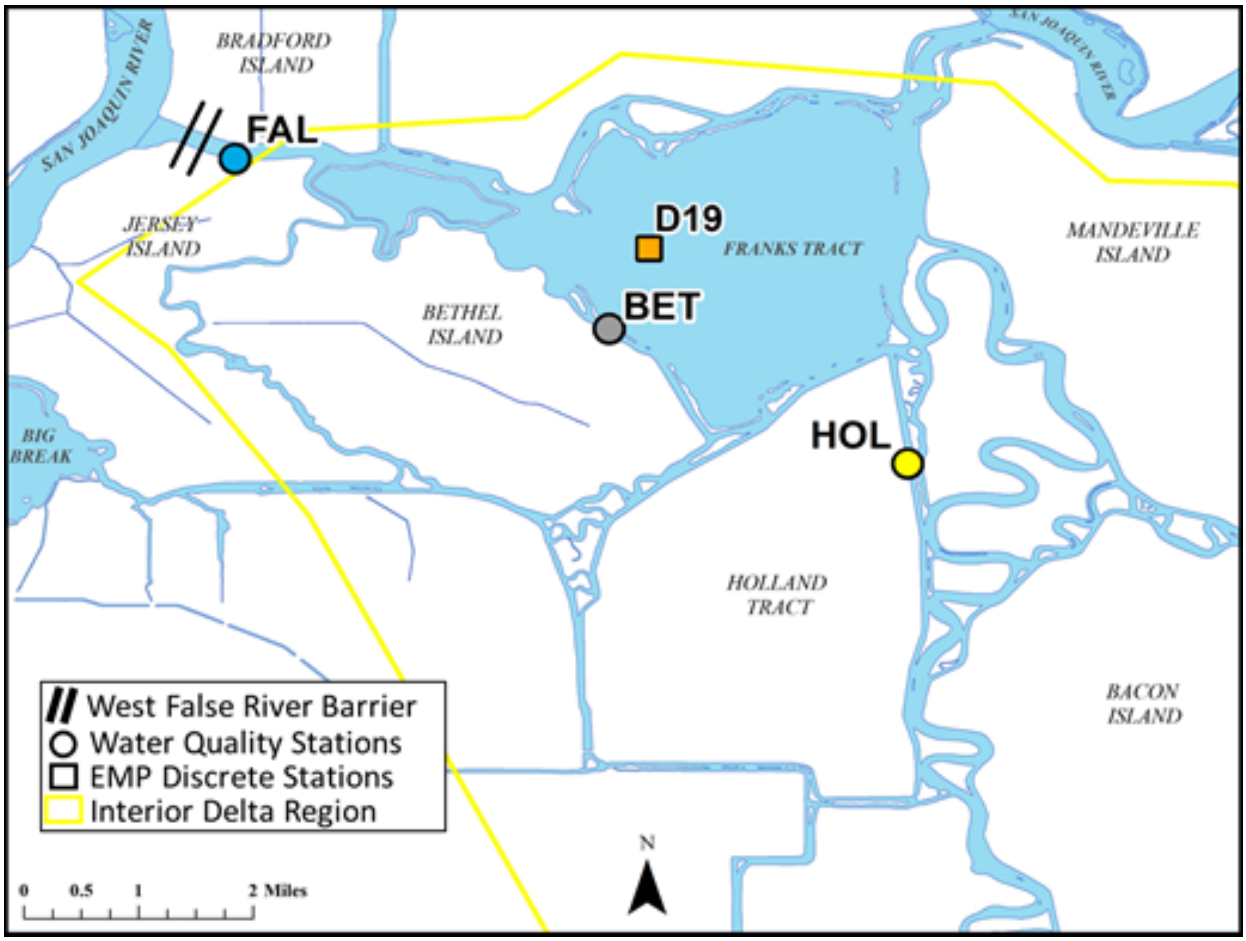

NOTES: EMP = Environmental Monitoring Program. Station abbreviations: BET = Bethel Island; D19 = Franks Tract near Russo's Landing; FAL = False River near Oakley; HOL = Holland Cut near Bethel Island.

Figure 2.3.2-21 Discrete water quality sampling sites in the Interior Delta Region.

In 2022, chl *a* concentrations were low at all sites during the notched EDB period, with a peak at site D19 of 9.21 µg/L^{-1} shortly after the EDB closure. After EDB installation, chl *a* concentrations remained low at all sites shown in Figure 2.3.2-22 until July 26 at site BET, where a large, isolated cyanobacteria bloom was observed at the southeast end of Franks Tract, with a peak concentration of 91 µg/L^{-1}. There was also an increase in the chl *a* concentration at site HOL of 6.54 µg/L^{-1} on August 23.

Nutrient concentrations at all sites in the Interior Delta Region were low both before and after EDB closure in 2021 (**Figure 2.3.2-23**G–J). Nitrate + nitrite concentrations were highest in April–June at sites FAL and D19 (Figure 2.3.2-23G), ranging from 0.164 to 0.473 mg/L^{-1}; however, the concentrations were decreasing leading up to EDB closure, reaching near or below the DWR Bryte Laboratory's reporting limit of 0.05 mg/L^{-1} at all sites in August. This low point in nitrate + nitrite concentrations aligned with peak chl *a* concentrations at all Interior Delta Region sites in 2021, suggesting that there was high algal uptake (Figure 2.3.2-23A and B).

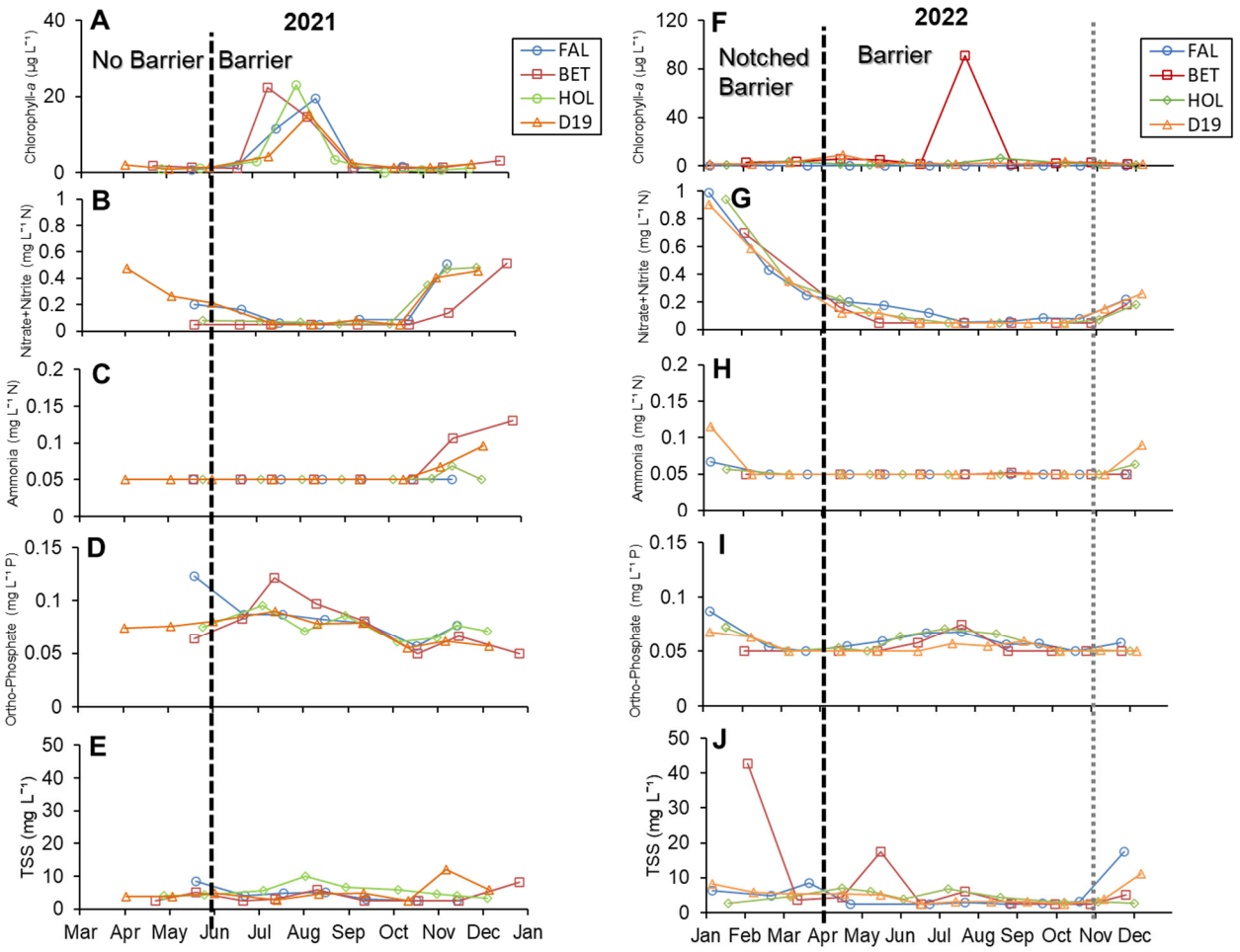

NOTES: µg/L = micrograms per liter; mg/L = milligrams per liter; TSS = total suspended solids. Station abbreviations: BET = Bethel Island at Piper Slough; D19 = Franks Tract near Russo's Landing; FAL = False River near Oakley; HOL = Holland Cut near Bethel Island. Black dashed line = emergency drought barrier (EDB) closure period; gray dotted line = EDB breach period. DWR Bryte Laboratory reporting limits for 2021 and 2022 were 0.05 mg/L⁻¹.

Figure 2.3.2-22 Discrete concentrations of chlorophyll *a,* dissolved nitrate + nitrite, dissolved ammonia, dissolved orthophosphate, and total suspended solids in the Interior Delta Region, by site, April–December 2021 and January–December 2022.

To compare 2021 conditions to 2015 conditions: The nitrate + nitrite concentrations in the Interior Delta Region were much lower in 2021 (Figure 2.3.2-23B and G), but the ammonia and orthophosphate concentrations were similar after EDB closure in both years (Figure 2.3.2-23C and H and Figure 2.3.2-23D and I, respectively). The TSS concentrations in 2021 observed minimal change, averaging 5 mg/L⁻¹ throughout April–November (Figure 2.3.2-23E and J). TSS concentrations were similar in 2015–2021 during the post–EDB closure period, but there were much higher TSS concentrations pre-EDB in 2015 (Figure 2.3.2-23E and J).

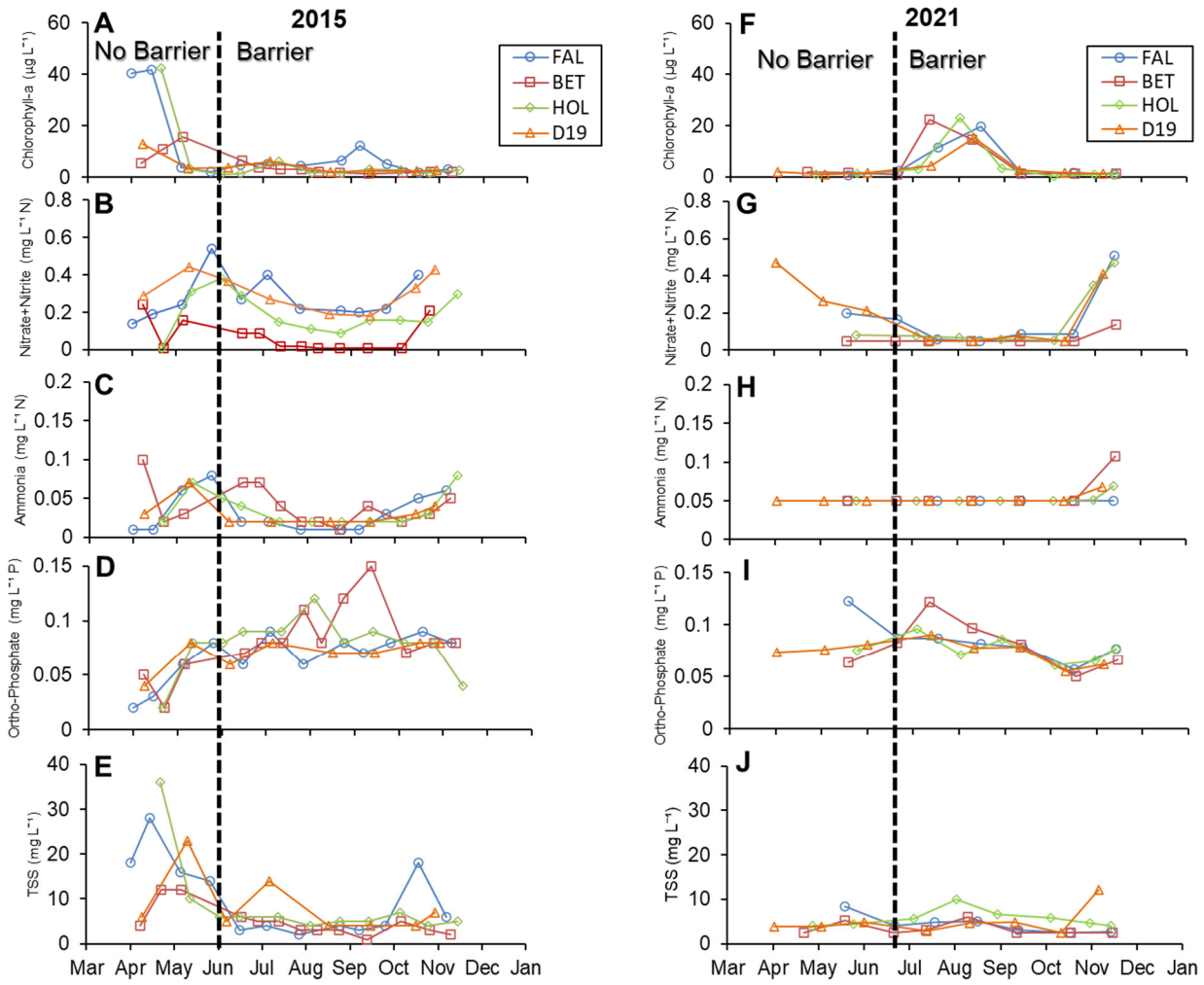

NOTES: µg/L = micrograms per liter; mg/L = milligrams per liter; TSS = total suspended solids. Station abbreviations: BET = Bethel Island; D19 = Franks Tract near Russo's Landing; FAL = False River near Oakley; HOL = Holland Cut near Bethel Island.

Figure 2.3.2-23 Discrete concentrations of chlorophyll *a,* dissolved nitrate + nitrite, dissolved ammonia, dissolved orthophosphate, and total suspended solids in the Interior Delta Region, by site, April–December 2015 and 2021.

In 2022, nutrient concentrations at all sites in the Interior Delta Region were similar to 2021 nutrient concentrations, during both the EDB notch and EDB closure periods, and some 2022 nutrient concentrations were lower than 2021 concentrations (Figure 2.3.2-22):

- Nitrate + nitrite concentrations were highest earlier in the year—January through April 2022—at all sites, ranging from 0.123 to 0.989 mg/L^{-1}. However, during EDB closure, concentrations remained below the DWR Bryte Laboratory's reporting limit of 0.05 mg/L^{-1} at all sites, except at site FAL in July–August. The low nitrate + nitrate concentrations did align

with the peak chl *a* concentrations measured at BET in July and at HOL in August, suggesting algal uptake (Figure 2.3.2-22F and G).

- As in 2021, ammonia concentrations remained low, and at the reporting limit of 0.05 mg/L^{-1}, at all sites throughout the EDB closure period (Figure 2.3.2-22C and H).
- Orthophosphate concentrations were lower in 2022 than in 2021 and were measured at or near the reporting limit of 0.05 mg/L^{-1} at all sites (Figure 2.3.2-22D and I).
- TSS concentrations in 2022 changed only minimally and were similar to 2021 concentrations, averaging near 5 mg/L^{-1} throughout January–December (Figure 2.3.2-22E and J). TSS concentrations were elevated on a few occasions at BET in the winter and spring; this may have been a result of elevated winds in Franks Tract.

In 2021, chloride concentrations in the Interior Delta Region were lowest in April and May before the EDB closure, ranging from 43 to 204 mg/L^{-1} across all sites, and increased to 66–375 mg/L^{-1} from June through November after the barrier closure (**Figure 2.3.2-24**A). Bromide concentrations followed trends similar to those of chloride concentrations, ranging from 0.13 to 0.65 mg/L^{-1} in April and May and increasing to a range of 0.25 to 1.22 mg/L^{-1} in June–November after the EDB closure. The highest concentrations of chloride and bromide were measured at the sites located the farthest to the west—FAL, D19, and BET—which are nearest the channels connecting to the San Joaquin River at Fisherman's Cut and Dutch Slough (Table 2.3.2-1 and Figure 2.3.2-24A and B).

To compare 2015 conditions to 2021 conditions: Chloride and bromide concentrations in the Interior Delta Region were lower in 2021, but concentrations became elevated again in fall 2021 as outflows remained low and salinity intrusion increased in the San Joaquin River.

In 2022, chloride concentrations were low during the notch and EDB installation period, but concentrations began to increase at all stations starting in June (Figure 2.3.2-24C). The notch allowed chloride concentrations in the Interior Delta Region to remain lower in 2022 than in 2021. The highest chloride concentrations were measured at sites FAL and BET after EDB removal, at 726 mg/L^{-1} and 350 mg/L^{-1}, respectively (Figure 2.3.2-24C). Bromide concentrations mirrored the chloride trends, with the highest concentrations occurring in June after closure of the EDB and peaking in December after EDB removal (Figure 2.3.2-24B and D).

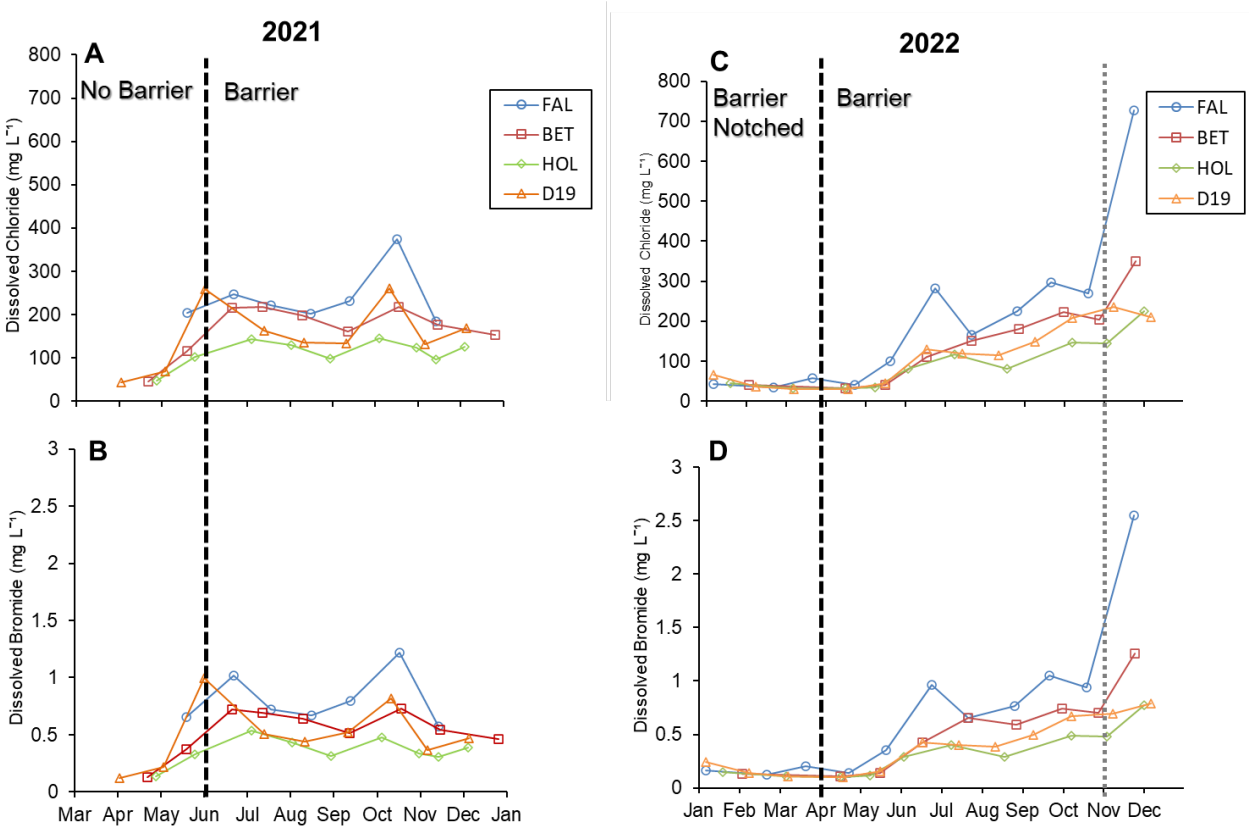

NOTES: mg/L = milligrams per liter. Station abbreviations: BET = Bethel Island; D19 = Franks Tract near Russo's Landing; FAL = False River near Oakley; HOL = Holland Cut near Bethel Island.
Black dashed line = emergency drought barrier (EDB) closure period; dotted gray line = EDB breach period.

Figure 2.3.2-24 Discrete concentrations of dissolved chloride and bromide in the Interior Delta Region, by site, April–December 2021 and January–December 2022.

San Joaquin River Region

To characterize the concentrations of chl *a*, nutrients, TSS, chloride, and bromide in the San Joaquin River Region, three active sampling locations were investigated from April to December in 2015 and 2021 and four were investigated from April to December in 2022 (**Figure 2.3.2-25**). These sampling locations included two co-located continuous monitoring locations that were sampled a minimum of once per month: FCT and OSJ (2015: n=11–12 per site; 2021: n=7 per site; 2022: n=10–11 per site). In addition, DWR EMP monthly discrete monitoring stations D26 and D16 were investigated to provide data on ambient conditions in the lower San Joaquin River (2015 and 2021: n=8, except site D26 dissolved bromide n=3 in 2021; sites D26 and D16 n=12 in 2022). D16 was sampled only in 2022 and not in the previous sampling years, 2015 and 2021.

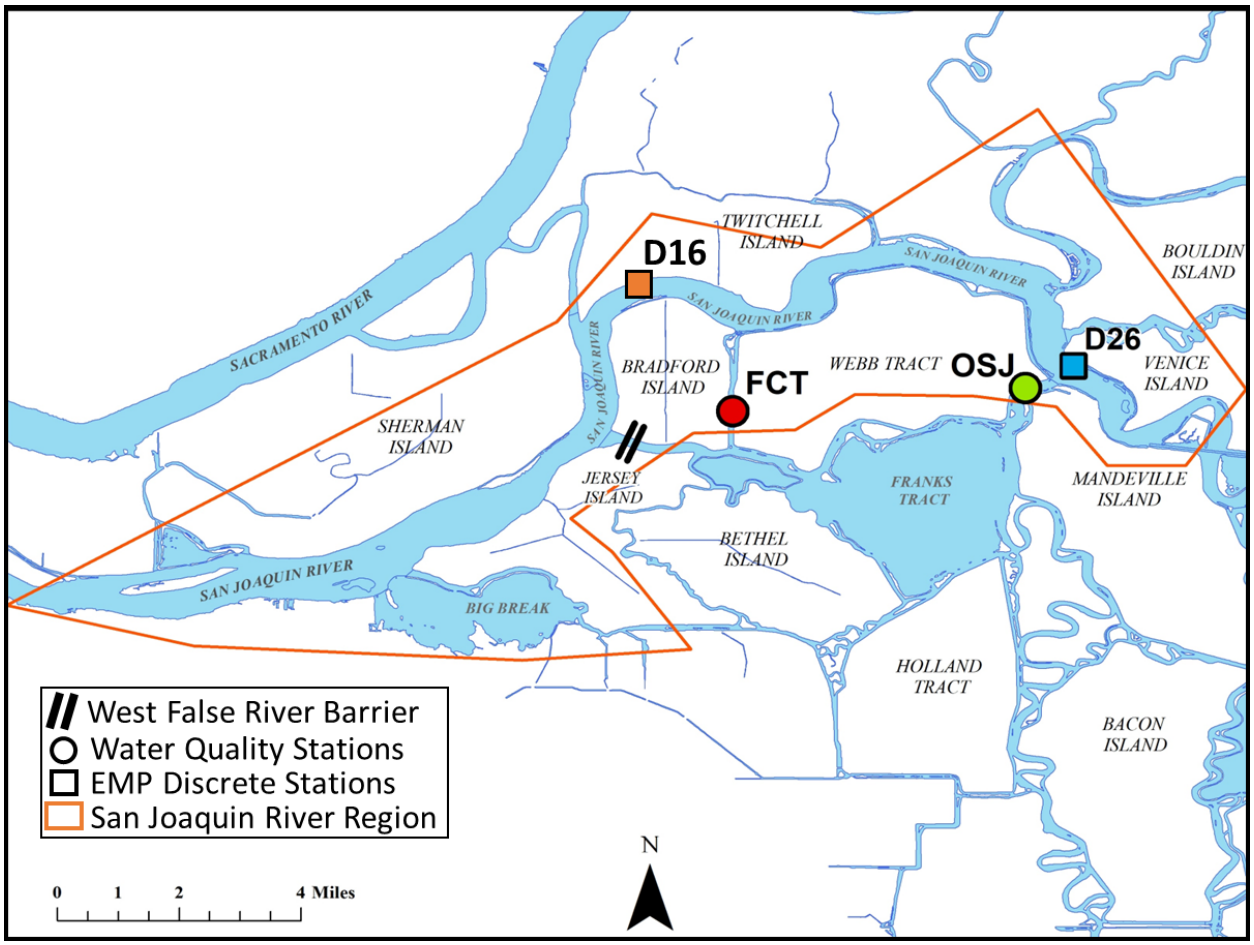

NOTES: EMP = Environmental Monitoring Program. Station abbreviations: D16 = San Joaquin River at Twitchell Island; D26 = San Joaquin River at Potato Point; FCT = Fisherman's Cut; OSJ = Old River at Franks Tract near Terminous.

Figure 2.3.2-25 Discrete water quality sampling sites in the San Joaquin River Region.

Similar to conditions in the Interior Delta Region, chl *a* concentrations were low at all sites in the San Joaquin River Region in 2021, ranging from 0.95 to 3.43 µg/L^{-1} in April–June before installation of the EDB and just after EDB closure at West False River (**Figure 2.3.2-26**F). This differed from the prior EDB installation year, 2015, when chl *a* concentrations were high (≥10 µg/L^{-1}) just before EDB closure, with notably elevated concentrations measuring more than 30 µg/L^{-1} across sites (Figure 2.3.2-26A) and a peak chlorophyll concentration of 83 µg/L^{-1} at FCT. However, chl *a* concentrations did increase at all sites in July and August 2021 after EDB closure; concentrations peaked at all sites in August, ranging from 10 to 30 µg/L^{-1}, and the highest concentration was measured at OSJ at 32 µg/L^{-1}.

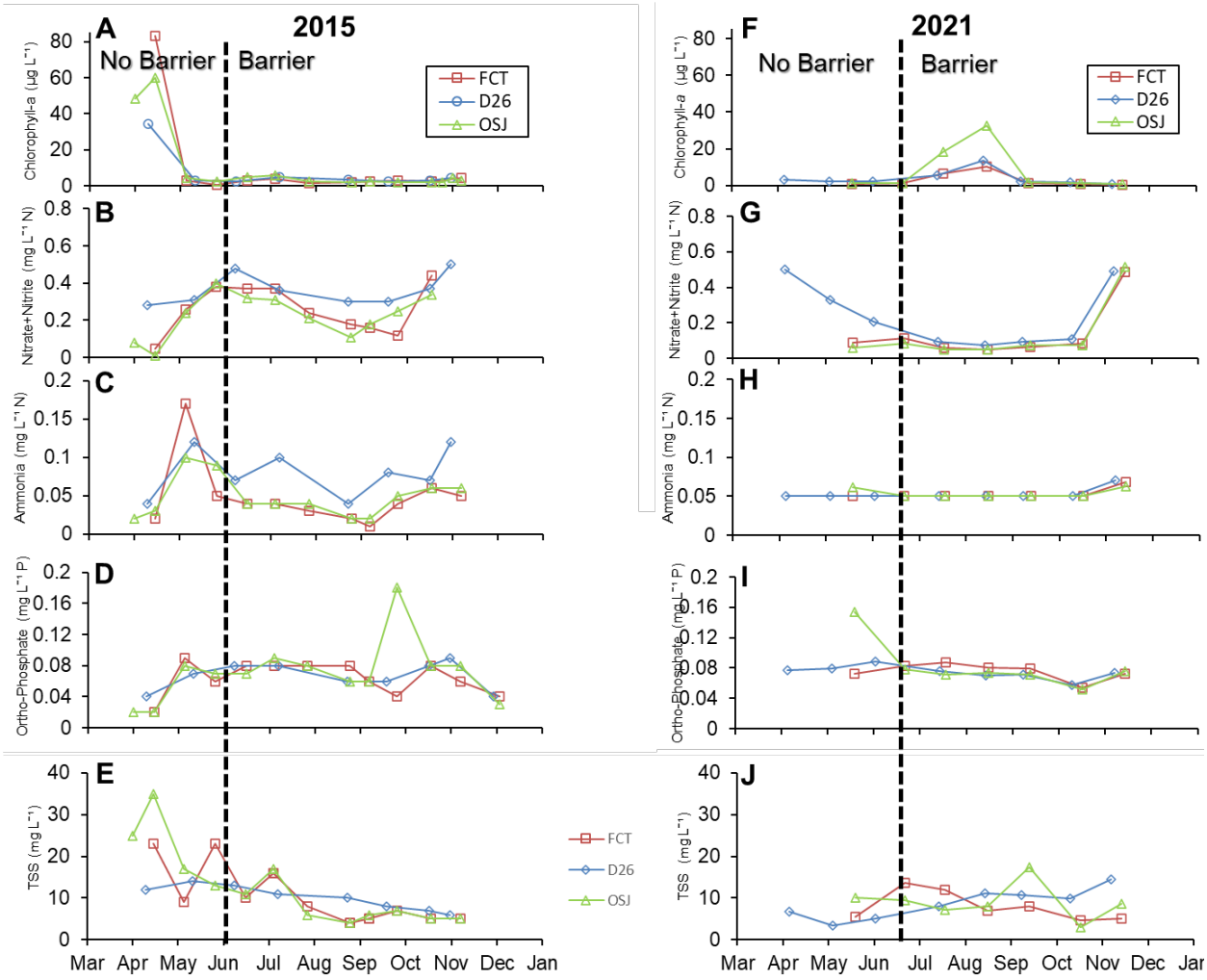

NOTES: µg/L = micrograms per liter; mg/L = milligrams per liter; TSS = total suspended solids. Station abbreviations: D26 = San Joaquin River at Potato Point; FCT = Fisherman's Cut; OSJ = Old River at Franks Tract near Terminous.

Black dashed line = emergency drought barrier (EDB) closure period. DWR Bryte Laboratory reporting limits for 2021 and 2022 were 0.05 mg/L^{-1} for nitrate + nitrite and ammonia.

Figure 2.3.2-26 Discrete concentrations of chlorophyll *a,* dissolved nitrate + nitrite, dissolved ammonia, dissolved orthophosphate, and total suspended solids in the San Joaquin River Region, by site, April–December 2015 and 2021.

In 2022, much like 2021, chl *a* concentrations were low at all sites in the San Joaquin River Region, ranging from 0.5 to 3.96 µg/L^{-1} from January through April before the complete EDB closure (**Figure 2.3.2-27**A and F). Chl *a* concentrations in 2022 remained low at all sites throughout the EDB installation period and peaked at 7.95 µg/L^{-1} at site D26 on October 14 (Figure 2.3.2-27F).

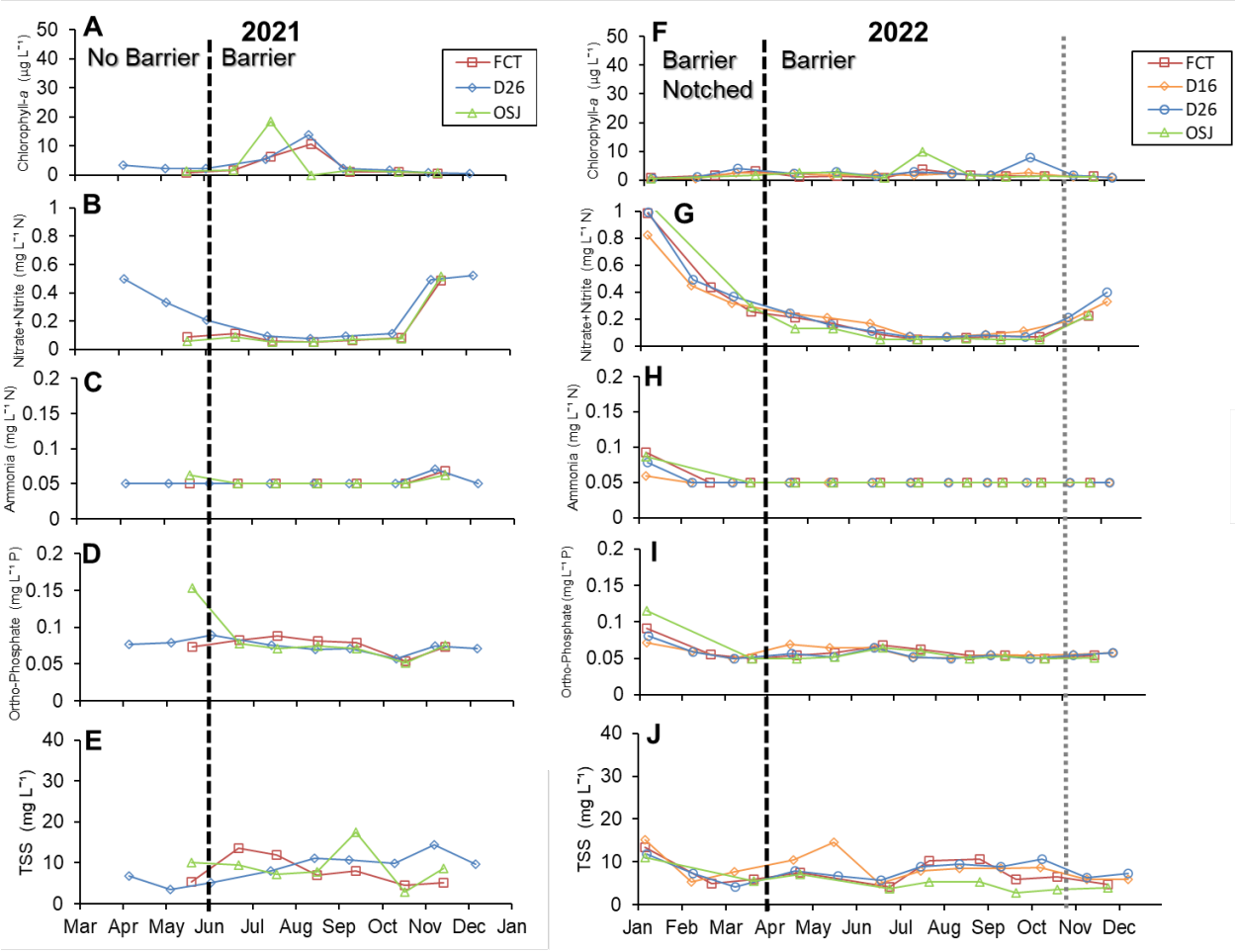

NOTES: µg/L = micrograms per liter; mg/L = milligrams per liter; TSS = total suspended solids. Station abbreviations: D16 = San Joaquin River at Twitchell Island; D26 = San Joaquin River at Potato Point; FCT = Fisherman's Cut; OSJ = Old River at Franks Tract near Terminous.
Black dashed line = emergency drought barrier (EDB) closure period; dotted gray line = EDB breach period. DWR Bryte Laboratory reporting limits for 2021 and 2022 were 0.05 mg/L^{-1} for nitrate + nitrite and ammonia.

Figure 2.3.2-27 Discrete concentrations of chlorophyll *a*, dissolved nitrate + nitrite, dissolved ammonia, dissolved orthophosphate, and total suspended solids in the San Joaquin River Region, by site, April–December 2021 and January–December 2022.

Nutrient concentrations at all sites in the San Joaquin River Region were low both before and after EDB closure in 2021 (Figure 2.3.2-26G, H, I, and J). Nitrate + nitrite concentrations were highest in April–June at site D26 (Figure 2.3.2-26G), ranging from 0.21 to 0.50 mg/L^{-1}; however, concentrations were decreasing leading up to EDB closure, reaching near or below the DWR Bryte Laboratory's reporting limit of 0.05 mg/L^{-1} at all sites in August. This low point in nitrate + nitrite concentrations aligned with peak chl *a* concentrations at all sites in the San Joaquin River and Interior Delta regions in 2021, suggesting high algal uptake (Figure 2.3.2-26F and G).

To compare 2021 conditions to 2015 conditions: The nitrate + nitrite, ammonia, and orthophosphate concentrations in the San Joaquin River Region were much lower in 2021 (Figure 2.3.2-26B and G, Figure 2.3.2-26C and H, and Figure 2.3.2-26D and I, respectively). TSS concentrations in 2021 observed minimal change, averaging 9 mg/L^{-1} throughout April–November (Figure 2.3.2-26J). TSS concentrations were similar in 2015 to 2021 during the post–EDB closure period, but as in the Interior Delta Region, pre-EDB TSS concentrations were much higher in 2015 (Figure 2.3.2-26J).

In 2022, trends for nutrient concentrations in the San Joaquin River Region were similar to those for the Interior Delta Region, with similarly low concentrations relative to 2021 during both the EDB notch and closure periods (Figure 2.3.2-27):

- Nitrate + nitrite concentrations were highest from January through May 2022 at all sites, ranging from 0.126 to 1.07 mg/L^{-1}. However, as in 2021, concentrations decreased leading up to closure of the EDB notch and were near or below the DWR Bryte Laboratory's reporting limit of 0.05 mg/L^{-1} at sites OSJ and FCT in July and August (Figure 2.3.2-27B and G). There was not a strong relationship between nutrients and peak chl *a* in the San Joaquin River in 2022, as chl *a* concentrations remained low for much of the year (Figure 2.3.2-27F and G).
- Ammonia and orthophosphate concentrations remained low throughout the EDB notch and closure periods in 2022 and were often at or near the DWR Bryte Laboratory's reporting limit of 0.05 mg/L^{-1} (Figure 2.3.2-27H and I).
- TSS concentrations remained primarily unchanged throughout the EDB notch and closure periods, but the TSS concentration did elevate at site D16 in 2022 after the full closure of the barrier, peaking at 14.5 mg/L^{-1} on May 20 (Figure 2.3.2-27E and J).

In 2021, chloride concentrations in the San Joaquin River Region were lowest in April and May before the EDB closure, ranging from 33 to 84 mg/L^{-1} across all sites, and increased to 66–294 mg/L^{-1} from June through November after the barrier closure (**Figure 2.3.2-28**A). Bromide concentrations followed trends similar to those of chloride concentrations, ranging from 0.10 to 0.61 mg/L^{-1} in April and May and increasing to a range of 0.24 to 1.0 mg/L^{-1} in June–November after the EDB closure. The highest concentrations of chloride and bromide were measured at FCT and OSJ, the sites located the farthest to the west and closest to the EDB (Figure 2.3.2-25 and Figure 2.3.2-28A and B).

To compare 2015 conditions to 2021 conditions: Chloride and bromide concentrations in the San Joaquin River Region were lower in 2021, but as in

the Interior Delta Region, concentrations became elevated again in fall 2021 as outflows remained low and salinity intrusion increased in the San Joaquin River.

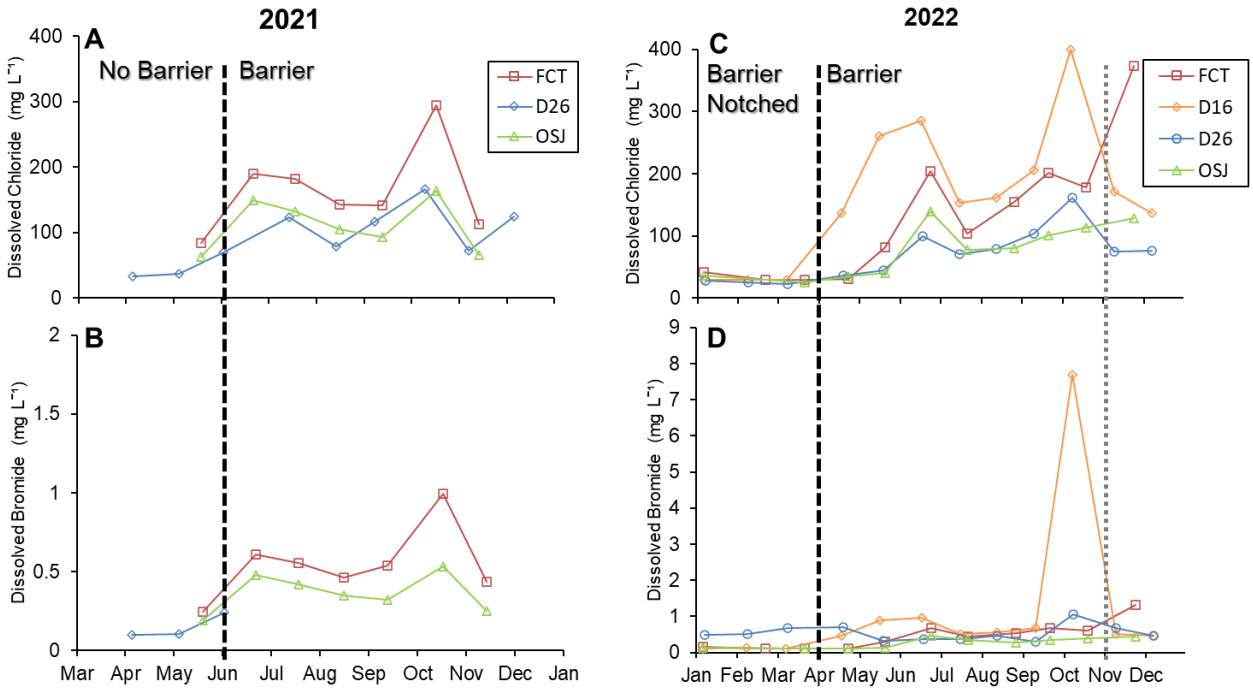

NOTES: mg/L = milligrams per liter. Station abbreviations: D16 = San Joaquin River at Twitchell Island; D26 = San Joaquin River at Potato Point; FCT = Fisherman's Cut; OSJ = Old River at Franks Tract near Terminous.
Black dashed line = emergency drought barrier (EDB) closure period; gray dotted line = EDB breach period.

Figure 2.3.2-28 Discrete concentrations of dissolved chloride and bromide in the San Joaquin River Region, by site, April–December 2021 and January–December 2022.

In 2022, chloride concentrations were low from January through April before the EDB notch closure, but concentrations increased rapidly at site D16 in May–October during the EDB installation period (Figure 2.3.2-28C). Chloride concentration trends at other San Joaquin River Region sites remained similar to those seen in 2021, with lower concentrations measured at FCT in 2022. Bromide concentrations followed data patterns similar to those for chloride. However, at D16—the station located the farthest to the east—there was a notable peak in the bromide concentration, which reached 7.7 mg/L^{-1} on October 13, just before the breach of the EDB (Figure 2.3.2-28D).

Sacramento River Region

To characterize concentrations of chl *a*, nutrients, TSS, chloride, and bromide in the Sacramento River Region, five active sampling locations were investigated from April to December in 2015 and 2021 and four were investigated from April to December in 2022 (**Figure 2.3.2-29**). These sampling locations included two co-located continuous monitoring locations that were sampled a

minimum of once per month: SSI and TSL (2015: n=11 at site TSL only; 2021: n=6–7 per site; 2022: n=12 per site; SSI was not sampled in 2022). In addition, DWR EMP monthly discrete monitoring stations D4, D22, and NZ068 were investigated to provide data on ambient conditions in the lower Sacramento River (2015: n=8 at site D4 only; 2021: n=8; 2022: n=12).

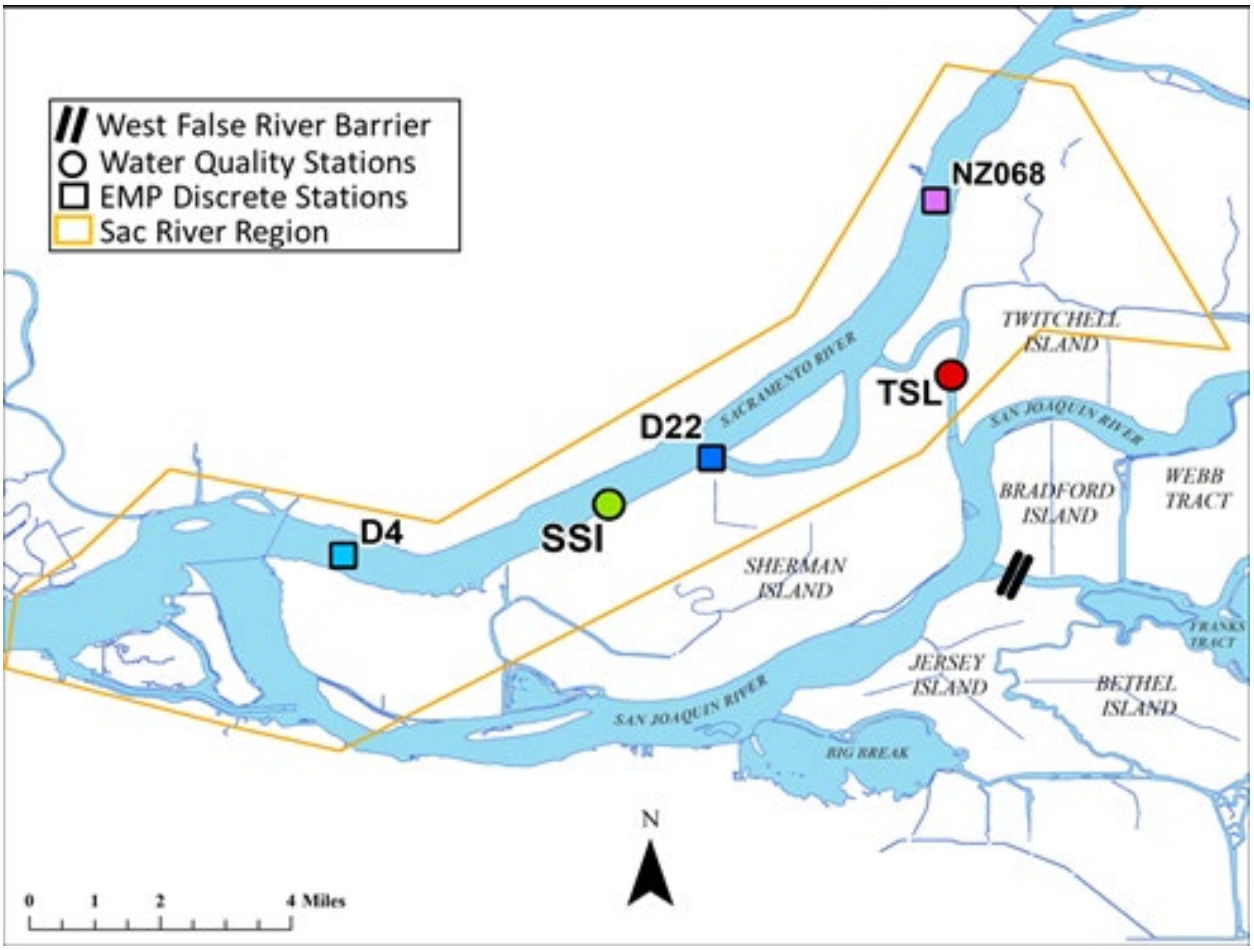

NOTES: EMP = Environmental Monitoring Program. Station abbreviations: D4 = Sacramento River above Point Sacramento; D22 = Sacramento River at Emmaton; SSI = Sacramento River near Sherman Island; TSL = Threemile Slough at San Joaquin River.

Figure 2.3.2-29 Discrete water quality sampling sites in the Sacramento River Region.

Chl *a* concentrations were low at all sites in the Sacramento River Region in 2021. Concentrations were highest in April, ranging from 5.12 to 12.07 µg/L^{-1} across all sites (**Figure 2.3.2-30**F). The highest concentration was measured at D4, closest to the Sacramento River–San Joaquin River confluence (Figure 2.3.2-29). Chl *a* concentrations averaged 2.32 µg/L^{-1} from May through November across all sites both before and after EDB closure. As at the sites in the Interior Delta and San Joaquin River regions, there was an increase in chlorophyll concentrations at TSL in 2021 after EDB closure, with a peak concentration of 8.49 µg/L^{-1} in August

(Figure 2.3.2-30F). In comparison to 2015, the Sacramento River Region's chl *a* level was like the 2021 level throughout the EDB closure period, remaining less than 3 µg/L^{-1} across sites from May through November before and after EDB closure (Figure 2.3.2-30A and F).

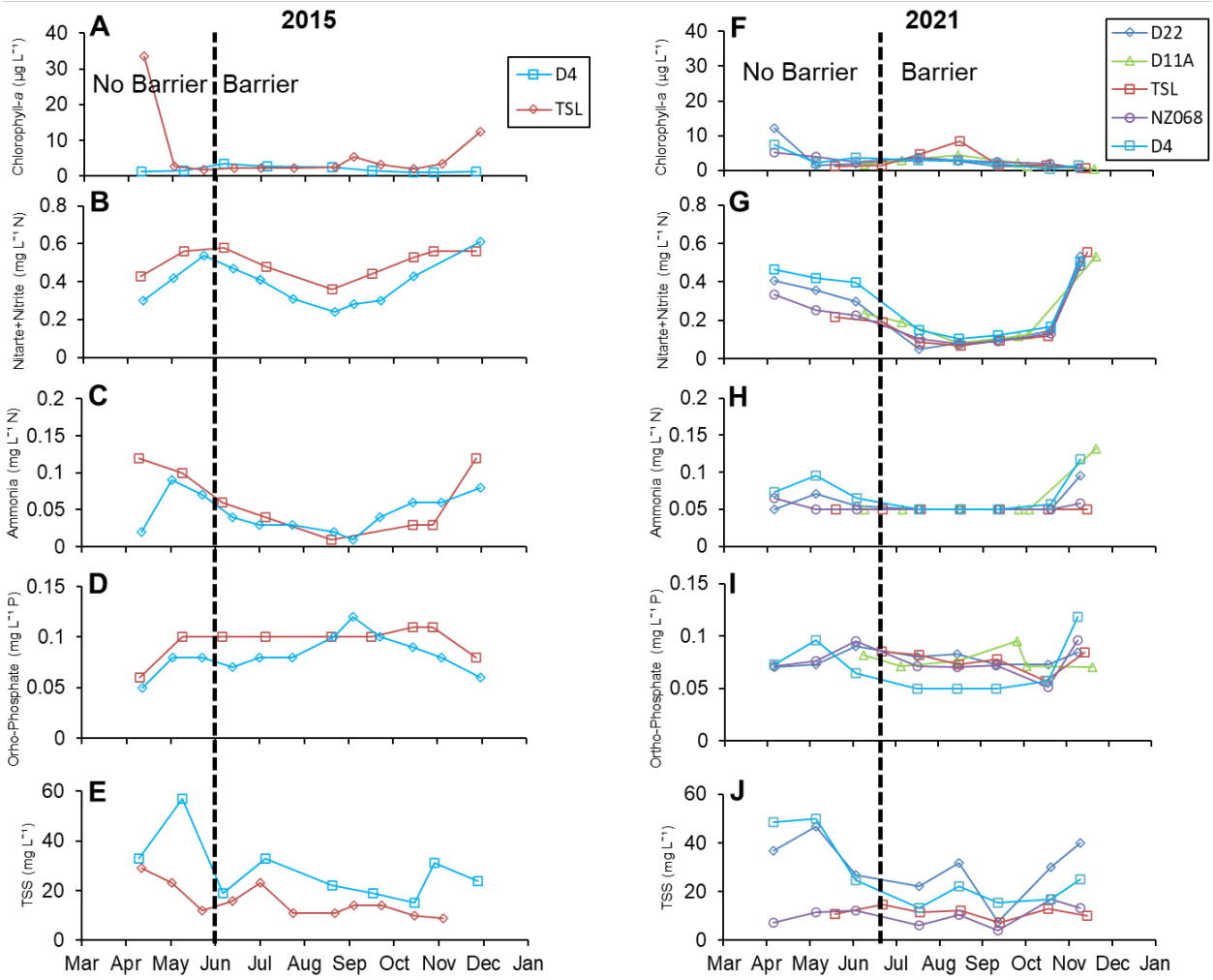

NOTES: µg/L = micrograms per liter; mg/L = milligrams per liter; TSS = total dissolved solids. Station abbreviations: D4 = Sacramento River above Point Sacramento; D11A = Sacramento River near Sherman Island; D22 = Sacramento River at Emmaton; NZ068 = Sacramento River near Rio Vista; TSL = Threemile Slough at San Joaquin River.

Black dashed line = emergency drought barrier (EDB) closure period. DWR Bryte Laboratory reporting limits for 2021 and 2022 were 0.05 mg/L^{-1}. Discrete sampling at D11A/SSI did not occur after April 2022, so data are not included.

Figure 2.3.2-30 Discrete concentrations of chlorophyll *a*, dissolved nitrate + nitrite, dissolved ammonia, dissolved orthophosphate, and total suspended solids in the Sacramento River Region, by site, April–December 2015 and 2021.

In 2022, much like 2021, chl *a* concentrations were low at all sites in the Sacramento River Region (**Figure 2.3.2-31**A and F). Chl *a* was highest in March (5.83 µg/L^{-1}) and April (5.3 µg/L^{-1}), at stations D4 and D22, respectively (Figure 2.3.2-31F). Chl *a* concentrations averaged 1.8 µg/L^{-1}

from January through December across all sites both before and after EDB notching and closure.

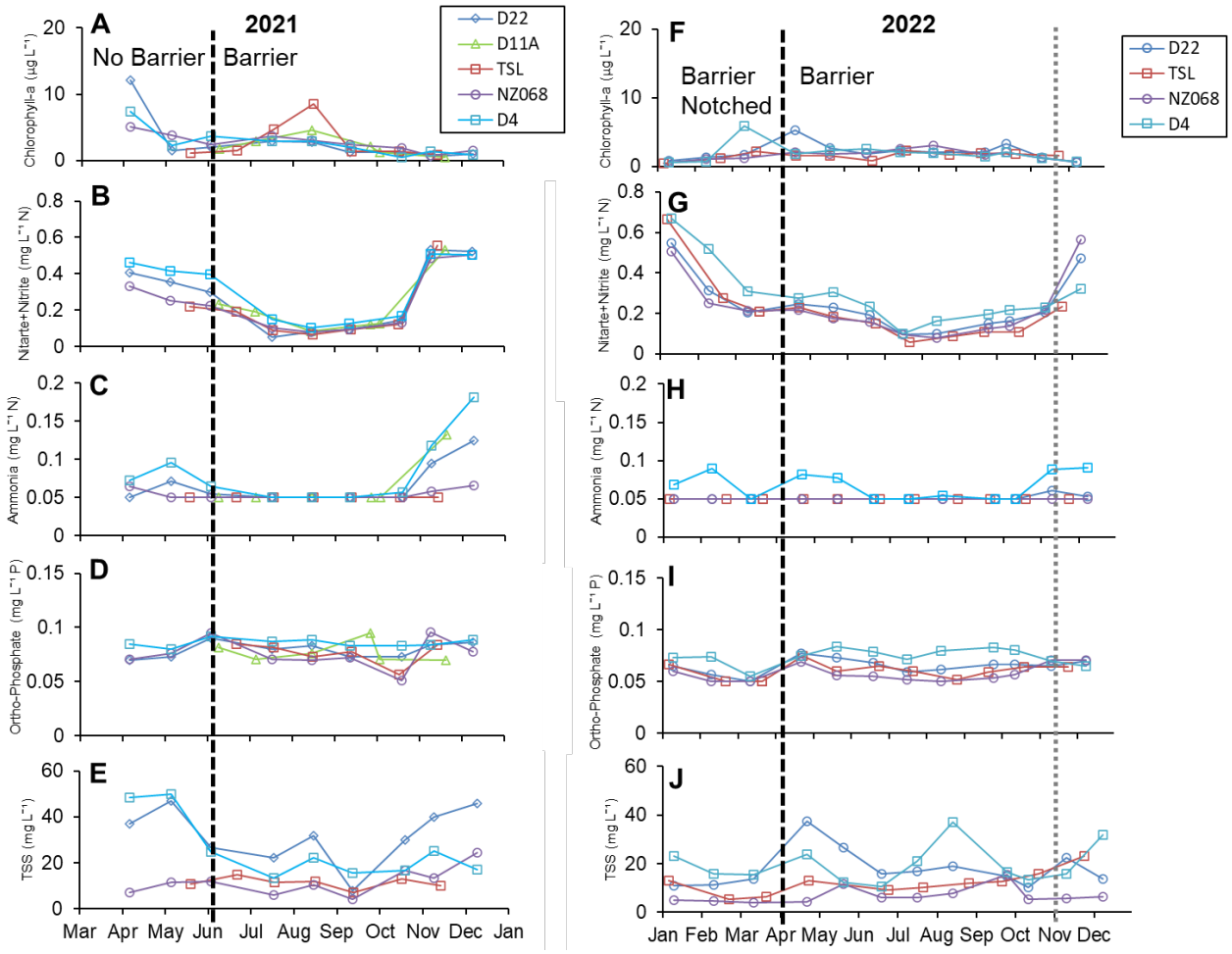

NOTES: µg/L = micrograms per liter; mg/L = milligrams per liter; TSS = total dissolved solids. Station abbreviations: D4 = Sacramento River above Point Sacramento; D11A = Sacramento River near Sherman Island; D22 = Sacramento River at Emmaton; NZ068 = Sacramento River near Rio Vista; TSL = Threemile Slough at San Joaquin River.
Black dashed line = emergency drought barrier (EDB) closure periods; gray dotted line = EDB breach period. DWR Bryte Laboratory reporting limits for 2021 and 2022 were 0.05 mg/L⁻¹. Discrete sampling at D11A/SSI did not occur after April 2022, so data are not included.

Figure 2.3.2-31 Discrete concentrations of chlorophyll *a,* dissolved nitrate + nitrite, dissolved ammonia, dissolved orthophosphate, and total suspended solids in the Sacramento River Region, by site, April–December 2021 and January–December 2022.

Nitrate + nitrite concentrations were highest in April–June across all sites (Figure 2.3.2-30G), ranging from 0.191 to 0.464 mg/L⁻¹; however, the concentrations were decreasing leading up to the EDB closure. Ammonia and orthophosphate concentrations were low throughout April–December 2021 and were decreasing leading up to EDB closure (Figure 2.3.2-30H and I).

To compare 2021 conditions to 2015 conditions: Nitrate + nitrite concentrations in the Sacramento River Region were higher in 2015, but ammonia and orthophosphate concentrations were equivalent to 2021 concentrations (Figure 2.3.2-30B and G, Figure 2.3.2-30C and H, and Figure 2.3.2-30D and I). TSS concentrations in 2021 were highest in April and May—before the EDB closure—at D22 and D4, the sites closest to the Sacramento River–San Joaquin River confluence, ranging from 36.9 to 50 mg/L^{-1} (Figure 2.3.2-30J). TSS concentrations were similar at sites D4 and TSL in 2015 and 2021 during both the pre- and post–EDB closure periods (Figure 2.3.2-30E and J).

In 2022, nutrient concentrations in the Sacramento River Region exhibited the following trends relative to 2021 concentrations:

- Nitrate + nitrite concentrations in 2022 were like 2021 concentrations. The highest concentrations occurred in April–June across all sites (Figure 2.3.2-31G), ranging from 0.15 to 0.669 mg/L^{-1}, then receded leading up to the closure of the EDB.
- Ammonia and orthophosphate concentrations were low throughout 2022, with ammonia concentrations often near or below the DWR Bryte Laboratory's reporting limit of 0.05 mg/L^{-1}.
- TSS concentrations were similar between 2021 and 2022, with a few elevated concentrations at D22 (37.3 mg/L^{-1} on April 25) and D4 (36.9 mg/L^{-1} on August 18).

In 2021, chloride concentrations in the Sacramento River Region were lowest in April and May before closure of the EDB, ranging from 409 to 2,760 mg/L^{-1} at downstream sites D4 and D22, and increased to 650–3,700 mg/L^{-1} from June through November after EDB closure (**Figure 2.3.2-32**A). Chloride concentrations averaged 50 mg/L^{-1} farther upriver at site NZ068 before EDB closure (Figure 2.3.2-32A). Bromide concentrations followed trends like those of chloride concentrations, increasing from April through November both before and after closure of the EDB. The highest concentrations of chloride and bromide were measured at the sites located the farthest to the west—D4 and D22—which are near the Sacramento River–San Joaquin River confluence (Figure 2.3.2-29 and Figure 2.3.2-32B and D).

To compare 2015 conditions to 2021 conditions: Chloride and bromide concentrations in the Sacramento River Region (though limited by sampling) were lower in 2021, but as in the Interior Delta and San Joaquin River regions, concentrations became elevated in fall 2021 as outflows remained low and salinity intrusion increased in the lower Sacramento River.

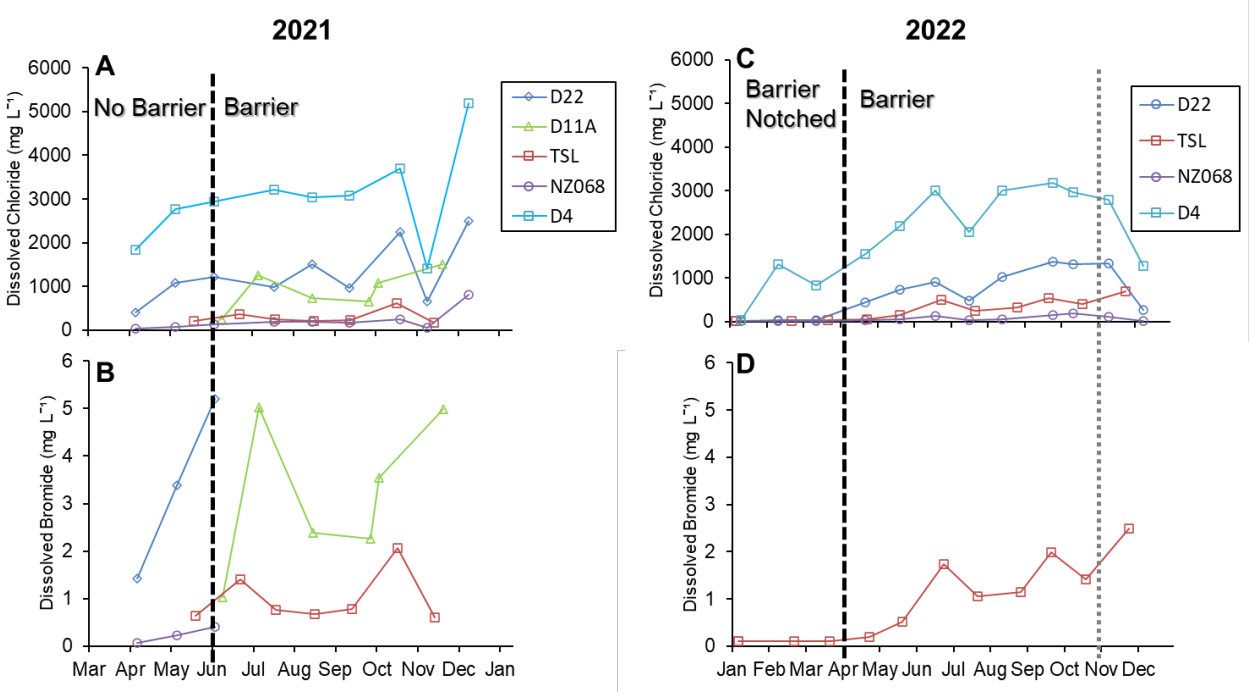

NOTES: mg/L = milligrams per liter. Station abbreviations: D4 = Sacramento River above Point Sacramento; D11A = Sacramento River near Sherman Island; D22 = Sacramento River at Emmaton; NZ068 = Sacramento River near Rio Vista; TSL = Threemile Slough at San Joaquin River.
Black dashed line = emergency drought barrier (EDB) closure period; dotted gray line = EDB breach period. Dissolved bromide was not analyzed at sites D22, D11A/SSI, D4, and NZ068 in 2022. D11A/SSI water samples were also not analyzed for dissolved chloride concentrations.

Figure 2.3.2-32 Sacramento River discrete concentrations of dissolved chloride and bromide, by site, April–December 2021 and January–December 2022.

In 2022, chloride concentrations were lowest in January–April during the EDB notch period, ranging from 13.7 to 1,540 mg/L^{-1}, and increased to 271–3,180 mg/L^{-1} at the farthest downstream sites D4 and D22 from May through December after EDB closure (Figure 2.3.2-32C). The chloride concentration averaged 14.7 mg/L^{-1} upriver at site NZ068 before the EDB closure and peaked at 181 mg/L^{-1} on October 17 after the closure (Figure 2.3.2-32C). Bromide concentrations were lowest in January–April and slowly increased at site TSL throughout the EDB closure period (Figure 2.3.2-32D).

As shown in **Figure 2.3.2-33**, summer (June–August) chl *a* concentrations at both D19 (Franks Tract) and D26 (San Joaquin River) were higher in 2021 than in 2015, and higher than in Dry and Wet water years; however, fall (September–November) concentrations were lower than in these other years. Nitrate + nitrite concentrations were lower in summer and fall 2021 than in other years; this was likely because of the presence and uptake of higher algal biomass, as seen in the DWR report on HABs published in 2021 (Hartman et al. 2021).

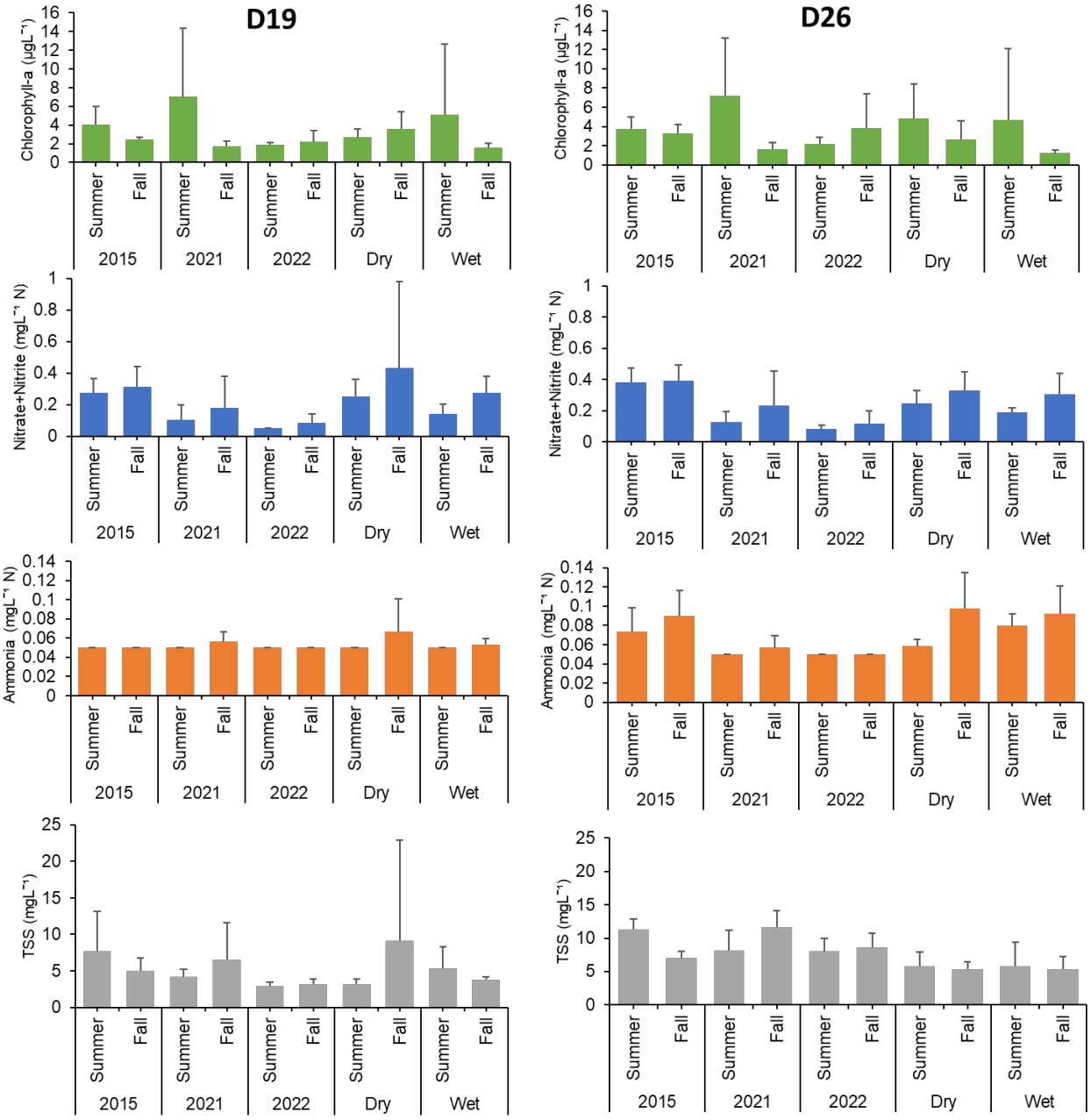

NOTES: µg/L = micrograms per liter; mg/L = milligrams per liter; TSS = total dissolved solids.
Error bars represent standard deviation for each dataset.

Figure 2.3.2-33 Average chlorophyll *a*, nitrate + nitrite, ammonia, and total suspended solids at sites D19 and D26 for summer and fall 2015, 2021, and 2022, and for Dry water years (2014, 2018, and 2020) and Wet water years (2017 and 2019).

Ammonia concentrations at D19 were similar across years and seasons, averaging at or near the DWR Bryte Laboratory's reporting limit of 0.05 mg/L^{-1}. D26 ammonia concentrations were lower in 2021. This was also likely attributable to the higher algal biomass and subsequent uptake

during the summer months, although the upgrade to the Sacramento Wastewater Treatment Plant (reducing ammonium inputs) may have also played a role (Sacramento Regional County Sanitation District 2021). At D19, TSS concentrations in 2021 followed patterns like those of other years, but TSS concentrations were higher in the San Joaquin River at D26, possibly related to higher levels of organic material from the summer algal bloom.

D19 and D26 had lower summer chl *a* concentrations in 2022 than in 2015, 2021, and previous Dry and Wet water years. Fall chl *a* concentrations were also low, especially at D19 (Figure 2.3.2-33). Nitrate + nitrite and ammonia concentrations were also lower in both summer and fall than in all other years analyzed, suggesting that the low nitrogen concentration may have contributed to limited algal growth at both sites (Figure 2.3.2-33). TSS at D19 was lower in both seasons than in other comparative years but was elevated at D26, much like the other EDB installation years.

2.3.2.3 North Delta Mapping to Document Conditions in the Absence of North Delta Drought Salinity Barriers

Introduction

The Sacramento River delivers most of the fresh water that flows into the Delta (Monsen et al. 2007). During drought years, lower flows from the Sacramento River contribute to the challenges of maintaining water quality in the Delta. The Delta Cross Channel and Georgiana Slough facilitate the delivery of fresh water from the Sacramento River into the Central Delta, where water flows south toward the State and federal export facilities, which then pump the water out of the Delta to meet drinking and irrigation water needs.

However, upstream of these features, some Sacramento River water is naturally routed through three distributaries: Sutter, Miner, and Steamboat sloughs (**Figure 2.3.2-34**). These sloughs deposit Sacramento River water into the Cache Slough Complex, where the water flows either landward toward the North Delta export pumps or seaward out to the lower Sacramento River.

The water that enters Sutter, Miner, and Steamboat sloughs has less effect on maintaining water quality in the Central Delta than water that remains in the Sacramento River. Therefore, if the volume of water flowing down these sloughs were to be reduced during drought conditions, more fresh water could be delivered down the mainstem of the Sacramento River, the Delta Cross Channel, and Georgiana Slough to help reduce the intrusion of high-salinity water into the Central and South Delta. Management actions have not been undertaken to date to constrain flow through the North Delta sloughs.

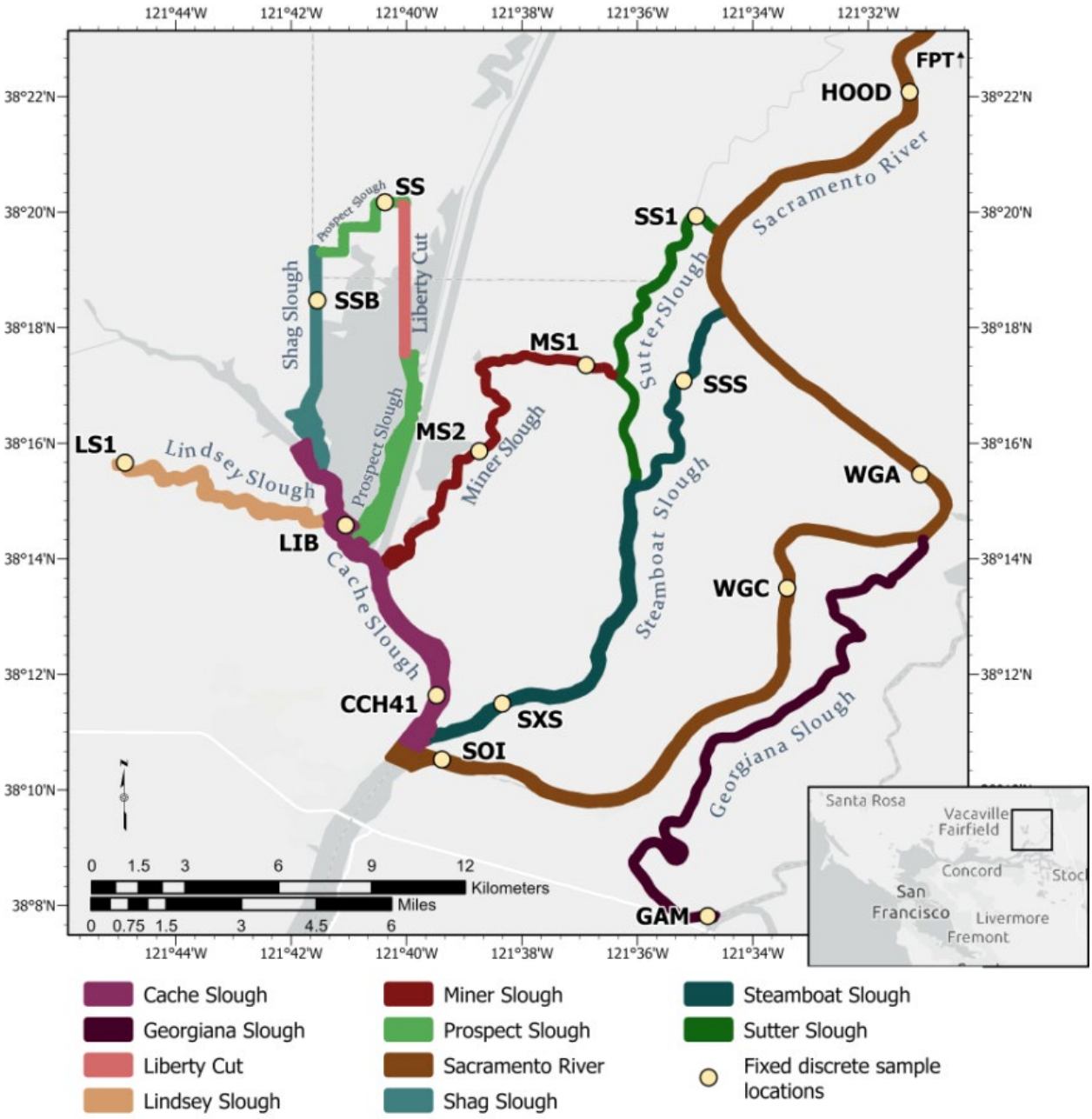

NOTE: For site information, see Table 2.3.2-3. Site FPT is located approximately 13 kilometers upstream of the HOOD site.

Figure 2.3.2-34 Locations of mapping region and fixed stations.

In anticipation of recurring future droughts, USGS collected water quality, nutrient, and phytoplankton data in the Sacramento River, the North Delta distributaries (Miner, Steamboat, Sutter, and Georgiana sloughs), and the Cache Slough Complex to document conditions during a Critically Dry water year in the absence of North Delta drought salinity barriers. Collecting data before management actions occur in this region will improve researchers' ability to interpret and analyze the impacts of future management actions, should they occur.

Methods

Data were collected as part of four-day Delta-wide mapping surveys conducted by USGS scientists in May, July, and October 2022. DWR leveraged these USGS surveys and supported USGS to extend data collection into Miner, Sutter, Steamboat, Georgiana, and Lindsey sloughs and to add measurements of stable water isotopes on select dates. Data used in this section are available from the USGS ScienceBase repository (www.ScienceBase.gov/catalog; O'Donnell et al. 2023).

The North Delta data used for this report (Figure 2.3.2-34) were collected on May 16 and 19, July 18 and 21, and October 18 and 20, 2022. Because of the large mapping area, data for the sections of the Sacramento River north of the mouth of Georgiana Slough were collected on a different day than the remaining data. Data collection included high-resolution, boat-based water quality mapping and discrete samples. The survey area included Miner, Steamboat, Sutter, Georgiana, Lindsey, Cache, Prospect, and Shag sloughs; Liberty Cut; and the Sacramento River (Figure 2.3.2-34).

For this report, these channels are grouped into two regions: (1) Cache Slough Complex and (2) Sacramento River and distributaries (SR&D). The Cache Slough Complex includes Cache, Lindsey, Prospect, and Shag sloughs and Liberty Cut. The SR&D includes the Sacramento River and four distributaries: Miner, Steamboat, Sutter, and Georgiana sloughs.

Sampling and Analysis

Underway High-Resolution Water Sampling and Onboard Analyses

Surveys were conducted using USGS Research Vessel *George Aiken*, equipped with the in situ continuous monitoring sensors listed in **Table 2.3.2-2**. The surveys followed the approach described by Downing et al. (2016), Fichot et al. (2016), and Stumpner et al. (2020). Detailed methods are described by Bergamaschi et al. (2020).

As the boat traveled at speeds up to 30 miles per hour (13 m/s), sample water was continuously pumped onboard using a pickup tube mounted at a fixed depth of approximately 1 meter below the surface. Water was routed through a 178 µm in-line strainer to remove large debris. Sample water was split into separate flow paths as described below and flows for each flow path were continuously monitored using a sight gauge.

The flow paths directed water to the following:

(1) A flow-through system consisting of the following equipment:

- A thermosalinograph that recorded temperature, salinity, and conductance (Sea-Bird Scientific SB45, Bellevue, Washington).

- A fluorometer that measured in situ chlorophyll fluorescence (fCHL) and fDOM (Sea-Bird Scientific WETstar, Philomath, Oregon).
- A beam transmissometer that recorded transmittance and attenuation (Sea-Bird Scientific model C-Star transmissometer, Philomath, Oregon).
- A nitrate (NO_3) analyzer (Submersible Ultraviolet Nitrate Analyzer [SUNA]; Sea-Bird Scientific, Bellevue, Washington).

(2) A multi-parameter water quality sonde (YSI EXO2; Xylem Inc., Rye Brook, New York) equipped with sensors to measure temperature, specific conductance, turbidity, pH, DO, fDOM, and fCHL.

(3) A fluorometer (FluoroProbe, bbe Moldaenke GmbH, Schwentinental, Germany), that measures total in situ fCHL and the fCHL of four phytoplankton groups: diatoms, chlorophytes, cyanobacteria, and cryptophytes.

TABLE 2.3.2-2
HIGH-RESOLUTION PARAMETERS COLLECTED ON THE R/V *GEORGE AIKEN*

Instrument	Parameter
YSI EXO2	Temperature, salinity, specific conductance, turbidity, dissolved oxygen, pH, fCHL, fDOM
WETstar	fCHL, fDOM
WETlabs C-star	Light transmission and attenuation
Thermosalinograph	Temperature and salinity
Onboard Ammonium Analyzer (TL-2800) (Timberline Instruments)	Ammonium
Submersible Ultraviolet Nitrate Analyzer	Nitrate
FluoroProbe	fCHL, phytoplankton taxonomy
Stable Water Isotope (^2H and ^{18}O) analyzer (A0217 and L2130-i (Picarro Inc.)	Stable isotopes δ^2H and $\delta^{18}O$ *(July survey only)*

NOTES: fCHL = chlorophyll fluorescence; fDOM = fluorescent dissolved organic matter; R/V = Research Vessel; YSI = Yellow Springs Instruments

SOURCE: Data compiled by U.S. Geological Survey in 2022

A second manifold was set up to provide 0.2 µm filtered water via an open-split interface at atmospheric pressure to the onboard ammonium (NH_4) analyzer (TL-2800; Timberline Instruments [Timberline], Boulder, Colorado) (Richardson et al. 2023) and stable water isotope (^2H and ^{18}O) analyzer (A0217 and L2130-i, Picarro Inc., Sunnyvale, California). The ammonium analyzer was run in continuous mode with frequent periodic introduction of deionized organic-free water. Standard solutions were applied to continuously assess instrument performance and correct for baseline drift

during the day. Full standard curves were run at the beginning and end of each day, and partial curves were run throughout the day.

The Picarro continuous water stable isotope (^{2}H and ^{18}O) instrument is a cavity ring-down spectrometer (Downing et al. 2016). Before fieldwork was conducted, three secondary standards and one tertiary standard were run on the Picarro instrument; the secondary standards are sold as a set by Picarro (part number C0356). The tertiary standard is Kona Deep bottled water (https://konadeep.com). Each standard was run for approximately 20 minutes or until stable, and the last two minutes of data were used to calculate an average standard value. The tertiary standard was taken into the field and analyzed on the Picarro instrument at the start and end of each sampling and approximately every four hours over the course of the field day. Sample splits of the tertiary standard were submitted to the USGS Reston Stable Isotope Laboratory (RSIL) (https://www.usgs.gov/labs/reston-stable-isotope-laboratory) for determination of $\delta^{2}H$ and $\delta^{18}O$ values. Water isotope data were collected with the Picarro instrument only during the July survey (July 18 and 21, 2022).

All instrumentation was cleaned, and calibrations were checked before each use, following the manufacturer's recommendation or as described above. Data for most instruments were recorded at a one-second frequency on a single data logger (CR6, Campbell Scientific, Logan, Utah) together with a time stamp and boat position obtained from a high-resolution Global Positioning System (GPS) receiver (16X-HVS, Garmin, Olathe, Kansas). The FluoroProbe logged data internally and to the host software every one to two seconds. The ammonium analyzer was connected to a stand-alone computer and collected data through its native software. The isotopic water sampler collected and logged data through its native software to an internal computer. All data were displayed in real time, so the scientists on board could respond when they observed changes relevant to study objectives or noted any issues with flow or instrument performance.

Discrete Water Sampling and Laboratory Analyses

Discrete water samples were collected either while the boat was underway or, for more extensive sampling requirements, while it was stopped on site. Filtered samples were collected while the boat was underway by passing water from the pickup tube through a 0.2 µm filter into a sample bottle.

At designated sampling sites (Figure 2.3.2-34, **Table 2.3.2-3**), the 0.2 µm filtered flow path was used to collect samples for analysis of ammonium (NH_4), nitrate (NO_3), nitrate and nitrite (NO_3 + NO_2), orthophosphate (PO_4), dissolved organic nitrogen, total dissolved phosphorus, dissolved organic carbon (DOC), total dissolved nitrogen (TDN), and water-stable isotopes (^{2}H and ^{18}O) (**Table 2.3.2-4**). Additionally, unfiltered samples were collected

from a depth of approximately 1 meter using a submersible pump for analysis of chl *a* concentration, pheophytin concentration, and phytoplankton enumeration (species identification, biovolume, and counts). Samples for phytoplankton enumeration were fixed immediately with Lugol's iodine solution (5 percent) and stored chilled. Additional samples for water-stable isotope analysis were collected on July 18 while the boat was underway at sites approximately 2 miles from one another.

TABLE 2.3.2-3
DISCRETE SAMPLING LOCATIONS IN THE NORTH DELTA

Station Abbrev.	Location	NWIS Site ID	NWIS Site Name	Latitude (decimal degrees)	Longitude (decimal degrees)
CCH41	Cache Slough	11455385	Cache Slough AB Ryer Island Ferry Nr Rio Vista Ca	38.19395556	-121.6580028
LIB	Cache Slough	11455315	Cache Slough A S Liberty Island Nr Rio Vista Ca	38.2430111	-121.684286
GAM	Georgiana Slough	380749121344701	Georgiana Slough A Tyler Island Rd Nr Isleton Ca	38.13028056	-121.5797
LS1	Lindsey Slough	381540121445301	Delta Rmp Yolo-003	38.26105	-121.748
MS1	Miner Slough	381721121365301	Miner Slough A Holland Rd Nr Paintersville Ca	38.28918889	-121.6148
MS2	Miner Slough	381552121384401	Miner Slough A Hwy 84 Nr Walker Landing Ca	38.26436667	-121.645675
FPT	Sacramento River	11447650	Sacramento R A Freeport Ca	38.45601954	-121.5013437
HOOD	Sacramento River	382205121311300	Sacramento R A Hood Ca	38.3679666	-121.5213432
SOI	Sacramento River	381031121392301	Sacramento R Nr Isleton Ca	38.1754222	-121.6564333
WGA	Sacramento River	11447890	Sacramento R Ab Delta Cross Channel Ca	38.25769218	-121.5182865
WGC	Sacramento River	381330121332401	Delta Rmp Sacr-028	38.22488056	-121.556725
SSB	Shag Slough	11455276	Shag Slough A Liberty Island Nr Courtland Ca	38.3078583	-121.6924278
SS	Prospect Slough	382010121402301	Liberty Island A Upper Stair Step Nr Five Points C	38.33616667	-121.672925
SSS	Steamboat Slough	11447850	Steamboat Slough Nr Walnut Grove Ca	38.2847222	-121.5866667
SXS	Steamboat Slough	381129121382101	Steamboat Slough Nr Isleton Ca	38.19153889	-121.63905
SS1	Sutter Slough	381956121345901	Delta Rmp Sacr-029	38.33215556	-121.5829306

NOTES: Abbrev. = abbreviation; Delta = Sacramento–San Joaquin Delta; ID = identification; NWIS = National Water Information System

SOURCE: Data compiled by U.S. Geological Survey in 2022

TABLE 2.3.2-4
DISCRETELY SAMPLED PARAMETERS COLLECTED IN THE NORTH DELTA

Discrete Parameters	
Nitrate (NO_3) and nitrite (NO_2)	Chlorophyll-*a* and phaeophytin
Ammonium (NH_4)	Dissolved organic carbon (DOC) and optics
Dissolved organic nitrogen (DON, by calculation)	Stable isotopes ^{2}H and ^{18}O *(July survey only)*
Total dissolved nitrogen (TDN)	Phytoplankton enumeration
Orthophosphate (SRP, PO_4)	Picophytoplankton enumeration
Total dissolved phosphorus (TDP)	

NOTES: Delta = Sacramento–San Joaquin Delta

SOURCE: Data compiled by U.S. Geological Survey in 2022

Most samples were stored on wet ice in the dark during transit to the laboratory, where they were stored at 2°C. DOC samples were preserved to less than pH 2 with high-purity sulfuric acid the day after collection and stored at 2°C. Samples for pigment analysis were filtered within 24 hours of collection and immediately frozen (-80°C). Total chl *a* samples were filtered through a 0.7 µm nominal-pore-size glass fiber filter (Advantec MFS, Inc., Dublin, California).

Chilled nutrient samples were shipped to the Chesapeake Biological Laboratory (Solomons, Maryland) for analysis. Frozen chl *a* filters were shipped to the USGS National Water Quality Laboratory (Denver, Colorado). Picophytoplankton and phytoplankton enumeration samples were shipped to BSA Environmental Services, Inc. (Beachwood, Ohio). Samples for water-stable isotope analysis were shipped to the USGS Reston Stable Isotope Lab.

Concentrations of nutrients were determined colorimetrically using an automated discrete photometric analyzer. Concentration of nitrogen as nitrite (NO_2-N) was determined by colorimetric analysis after diazotization with sulfanilamide (U.S. Environmental Protection Agency 1993a). For nitrate plus nitrite (NO_3-N + NO_2-N), samples were analyzed using enzymatic reduction (ASTM International 2014). If results were below the reporting limit, they were re-run using cadmium reduction (U.S. Environmental Protection Agency 1993a), which has a lower reporting limit. Concentration of ammonium as nitrogen (NH_4-N) was determined by colorimetric analysis after reaction with alkaline phenol-hypochlorite (American Public Health Association et al. 2017). Orthophosphate as phosphorus (PO_4-P; also referred to as "soluble reactive phosphorus," SRP) was determined by colorimetric analysis after reaction with NH_4 molybdate and reduction with ascorbic acid (U.S. Environmental Protection Agency 1993b). Total dissolved nitrogen (TDN) and total dissolved phosphorus were

determined by alkaline persulfate digestion (U.S. Environmental Protection Agency 1993a, 1993b). Chl *a* and phaeophytin concentrations were determined according to EPA Method 445.0 (Arar and Collins 1997).

Phytoplankton enumeration was completed by BSA Environmental Services in accordance with American Public Health Association Standard Method 10200 (Standard Methods 2023). This method focuses on counting and identifying microplankton (20–200 µm) and nanoplankton (2–20 µm). Briefly, phytoplankton were enumerated to the lowest possible taxonomic level using membrane-filtered slides, as described by McNabb (1960), and counted using a Leica DMLB compound microscope.

Water isotope samples (^{18}O and ^{2}H) were analyzed at the USGS RSIL using a dual-inlet isotope-ratio mass spectrometer according to RSIL Lab Code 489 for ^{18}O and Lab Code 1574 for ^{2}H (Révész and Coplen 2008a, 2008b). Final water isotope values ($\delta^{2}H$, $\delta^{18}O$) were expressed relative to the Vienna Standard Mean Ocean Water-Standard Light Antarctic Precipitation scale in per mil (‰).

Data Processing

High-Resolution Data

Timberline data were processed by first correcting for baseline drift and then using a regression model of voltage response to standard concentrations. Picarro data were corrected to discrete sample data by calculating the mean difference of paired discrete samples with Picarro data and adjusting all Picarro data by this value. Final water isotope values ($\delta^{2}H$, $\delta^{18}O$) were expressed relative to the Vienna Standard Mean Ocean Water-Standard Light Antarctic Precipitation scale in per mil (‰).

Data from onboard continuous instruments not directly logged to the flow-through data collection system were merged based on time stamp to the nearest second after the differential travel times for each instrument's flow path were estimated. The time differential arises from flow lag introduced by filtering and the specifics of each instrument's operation. All data, except those collected by the Timberline and Picarro instruments, were processed using pandas software library (0.220; McKinney 2010) in Python (3.7.3; Van Rossum and Drake 2009) to remove periods of compromised data (e.g., flow blockages, bubbles), to apply instrument corrections and unit conversions, and to apply a centered 20-second median filter to the time series.

Final NO_3 values were obtained by regressing each day's SUNA instrument response against NO_3 concentrations obtained from laboratory measurements of discrete samples collected over the course of the day (**Table 2.3.2-5**). Continuous DOC concentrations were developed by regressing onboard fDOM data against laboratory-determined DOC

concentrations measured in discrete samples, according to the methods of Snyder et al. (2018). These data are reported as estDOC. Data exceeding three times the standard deviation of the residuals were judged to be an outlier and were not included in the regression.

TABLE 2.3.2-5
SUBMERSIBLE ULTRAVIOLET NITRATE ANALYZER NITRATE BIAS CORRECTION REGRESSIONS WITH DISCRETE NITRATE SAMPLES—NORTH DELTA

Parameter	Month	Regression Equation
NO_3	May	1.00*SUNA – 4.56
NO_3	July	0.98*SUNA – 4.99
NO_3	October	0.71*SUNA + 1.33

NOTES: Delta = Sacramento–San Joaquin Delta; NO_3 = nitrate; SUNA = Submersible Ultraviolet Nitrate Analyzer

SOURCE: Data compiled by U.S. Geological Survey in 2022.

Finally, for each mapping survey (May, July, and October 2022), the high-resolution 20-second median data were binned into polygons the width of the channel and approximately 0.1 mile in length, and the mean value of all points within each polygon was calculated.

Water Age

Water age was calculated using the methods detailed in Downing et al. (2016) and Skrzypek et al. (2015) and a custom R script. The calculation of water age requires five parameters (**Table 2.3.2-6**): sample isotope data ($\delta_{\mathbf{L}}$), source water isotope data ($\delta_{\mathbf{P}}$), rainfall isotope data ($\delta_{\mathbf{R}}$), atmospheric temperature (T), and relative humidity (h). These parameters are first used to calculate the evaporation-to-inflow (E:I) ratio, a dimensionless parameter that describes the fraction of inflowing water that is lost to evaporation (Mayr et al. 2007; Skrzypek et al. 2015):

$$E{:}I = (\delta_L - \delta_P) / ((\delta^* - \delta_L) \times m) \qquad (7)$$

where δ^* is the limiting isotopic composition and *m* is a calculation factor, and these two parameters are derived from the five input parameters.

Source water ($\delta_{\mathbf{P}}$) values were obtained from the discrete sample collected at Site 13 in the Sacramento River near the entrance to Sutter Slough or from the Picarro data collected at the mouth of Sutter Slough (latitude = 38.30387, longitude = -121.5766). Isotope values of rain ($\delta_{\mathbf{R}}$) were estimated using the Online Isotopes in Precipitation Calculator (https://wateriso.utah.edu/waterisotopes/pages/data_access/oipc.html) (Welker 2000; Bowen et al. 2005), using coordinates from the center of Liberty Island (latitude = 38.2699, longitude = -121.679, elevation = 5.5 meters).

TABLE 2.3.2-6
INPUT PARAMETERS USED TO CALCULATE WATER AGE

Parameter	Definition	Value
δ_L	Sample water isotopes (‰)	Field data: δ^2H and $\delta^{18}O$
δ_P	Source water isotopes (‰)	Discrete samples δ^2H = -79.03, $\delta^{18}O$ = -11.18 Picarro samples δ^2H = -78.92, $\delta^{18}O$ = -10.95
δ_R	Rainfall isotopes (‰)	δ^2H = -32, $\delta^{18}O$ = -3.8
T	Temperature (°C)	24.474
h	Relative humidity	0.473
Depth	Depth (cm)	300
ET_o	Evapotranspiration (cm day^{-1})	0.82148

NOTES: ‰ = per mil; °C = degrees Celsius; cm = centimeters

SOURCE: Data compiled by U.S. Geological Survey in 2022

Next, water age was calculated from E:I:

$$\text{water age (days)} = E{:}I \times (\text{Depth}/ET_o) \qquad (8)$$

Temperature, relative humidity, and evapotranspiration data were obtained from the Twitchell Island station in the California Irrigation Management Information System (www.cimis.water.ca.gov). The values input into the model were derived by calculating the mean of each parameter over the 60 days before the sampling date. Evapotranspiration rates were multiplied by 1.1 to correct for evaporation over water (Jensen 2010). A water depth of 300 centimeters was used as an estimate of mean depth in the region.

Results and Discussion

Water Quality

Water quality trends across the North Delta were examined by binning data by specific river reach and using violin plots to visualize differences between the 10 defined channels (e.g., **Figure 2.3.2-35**) and by plotting the data spatially on maps (e.g., **Figure 2.3.2-36**).

Because the Cache Slough Complex is strongly tidal and does not receive large volumes of water from upland sources (unless the Yolo Bypass is flooding), this region's hydrodynamics are dominated by landward flow, resulting in longer water residence times (Downing et al. 2016; Stumpner et al. 2020). Longer water residence times mean more time for abiotic processes such as evapotranspiration and temperature changes, and for biogeochemical processes such as nutrient cycling and phytoplankton growth (Fackrell et al. 2021).

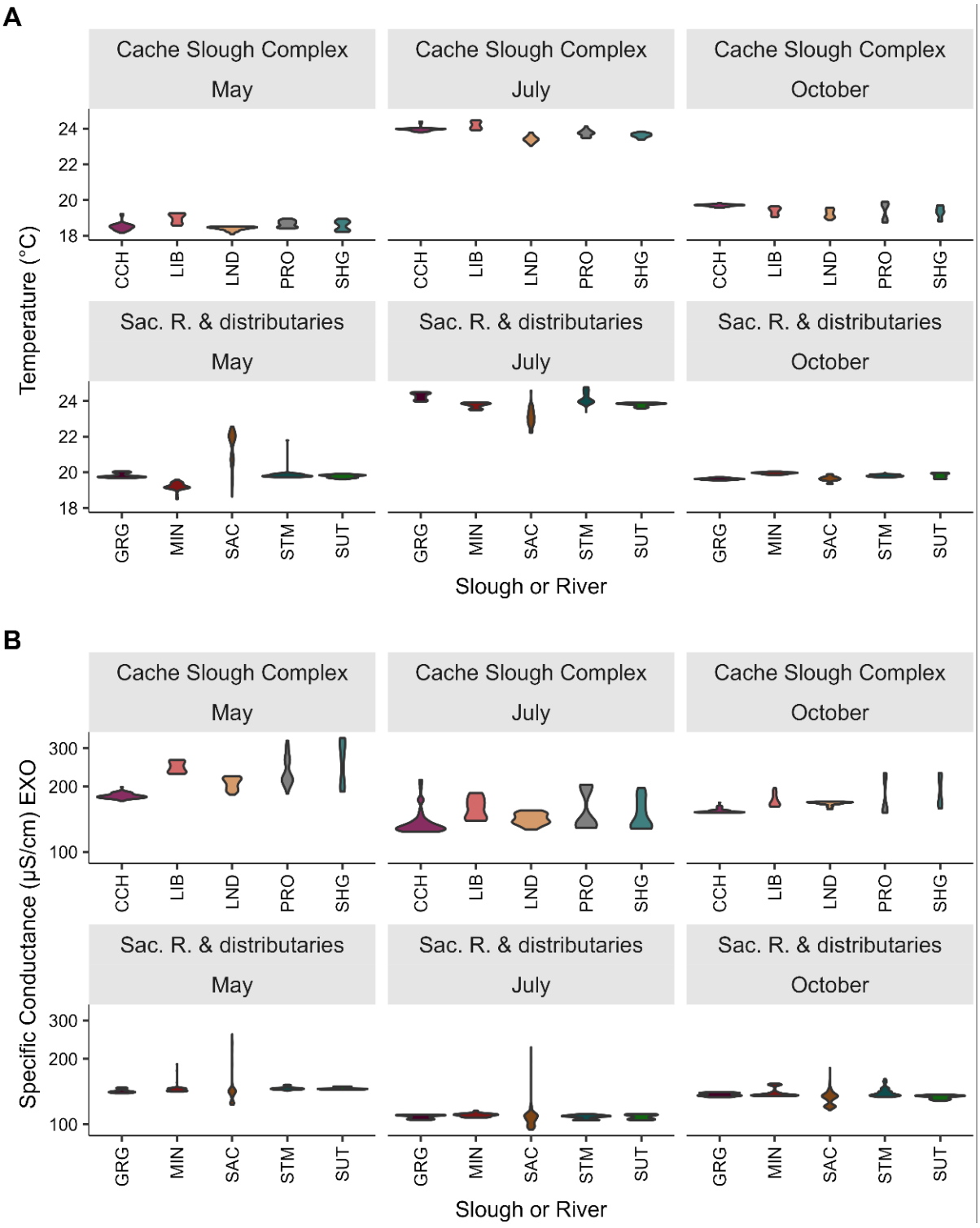

Notes: CCH = Cache Slough, GRG = Georgiana Slough, LIB = Liberty Cut, LND = Lindsey Slough, MIN = Miners Slough, PRO = Prospect Slough, SAC = Sacramento River, SHG = Shag Slough, STM = Steamboat Slough, SUT = Sutter Slough. Both temperature and specific conductance were detected by Yellow Springs Instruments EXO2 sondes. Specific conductance is scaled with a $\log_{10}$ axis.

Figure 2.3.2-35 High-resolution continuous (A) temperature and (B) specific conductance, from mapping surveys conducted in May, July, and October 2022.

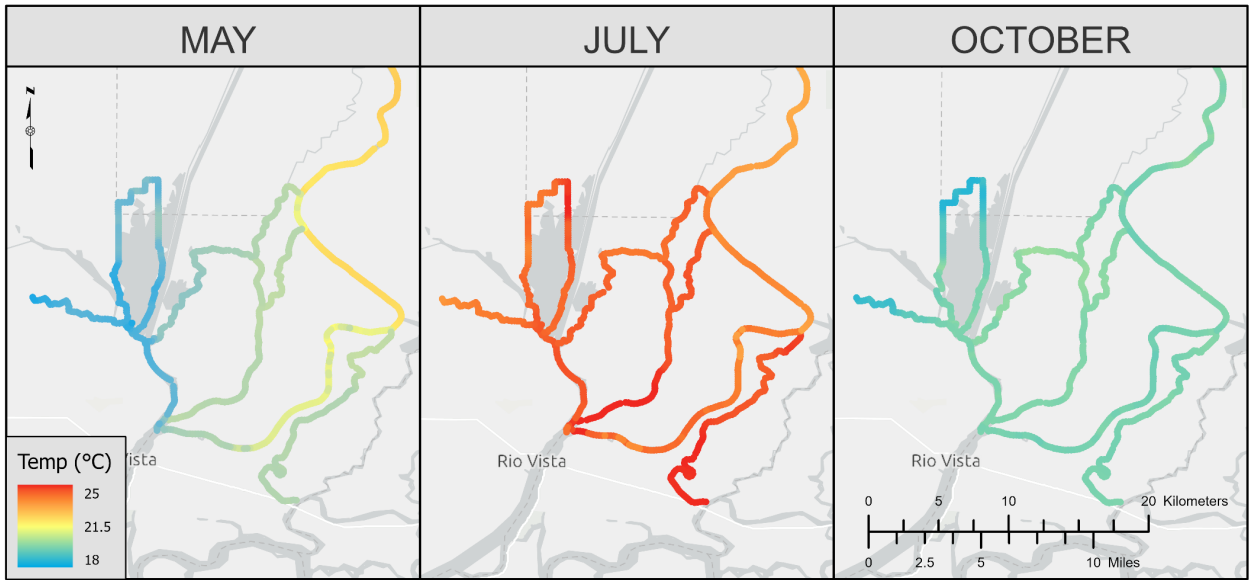

NOTES: °C = degrees Celsius; YSI = Yellow Springs Instruments.

Figure 2.3.2-36 Temperatures in the North Delta, from high-resolution mapping surveys conducted using YSI EXO2 sondes in May, July, and October 2022.

Therefore, in this analysis, water quality conditions in the Cache Slough Complex were expected to differ substantially from those in the SR&D. (For this reason, in some of the figures in this section, these two regions are separated into sub-panels to group similar channels together.)

The results of the water quality analysis show some variation among parameter values in a given month, caused by mapping different channels at different times of day or times in the tidal cycle, or on different days. Small variations within the three-to-four-day period of a given survey month are difficult to attribute to actual consistent differences between sites, rather than to short-term daily or weekly temporal variation in water quality entering these regions. This primarily affects comparisons between the Sacramento River north of Georgiana Slough and other channels, because this portion of the Sacramento River was usually mapped on a different day, while the other channels were all mapped on the same day.

In the May and October surveys, average temperatures in the SR&D ranged from about 19°C to 22°C (Figure 2.3.2-35A and Figure 2.3.2-36). The highest temperatures were measured on May 19 in the mainstem of the Sacramento River, reflecting increasing temperatures over the four-day survey period (U.S. Geological Survey 2022). Average temperatures in the SR&D were higher in July than in May and October, ranging from about 23°C to 24.5°C. Average May temperatures in the Cache Slough Complex were between about 18.5°C and 19°C, slightly cooler than temperatures in the

SR&D. In July and October, temperatures were similar between the Cache Slough Complex and the SR&D.

Specific conductance was lower in July (94–226 µS/cm) than in May and October (123–334 µS/cm), and was higher in the Cache Slough Complex—particularly the northern portion—than in the SR&D (Figure 2.3.2-35B, **Figure 2.3.2-37**), reflecting the longer residence times in this region.

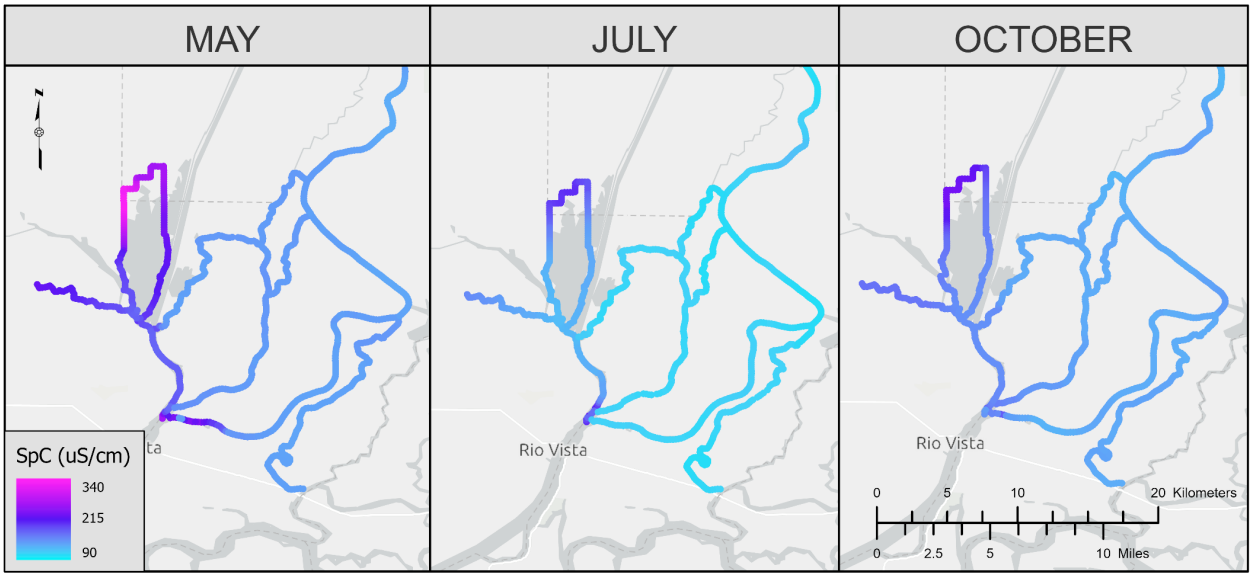

NOTES: µS/cm = microsiemens per centimeter; SpC = specific conductance; YSI = Yellow Springs Instruments

Figure 2.3.2-37 Specific conductance in the North Delta, from high-resolution mapping surveys conducted using YSI EXO2 sondes in May, July, and October 2022.

In the SR&D, specific conductance exceeded 200 µS/cm only in the lower portion of the Sacramento River where it mixes in tidally with Cache Slough (Figure 2.3.2-37).

During the mapping surveys, nitrate in the SR&D ranged from 4.5 to 16 micromoles (µM) per liter (**Figure 2.3.2-38**A and **Figure 2.3.2-39**). In each survey, nitrate concentrations were more variable in the mainstem of the Sacramento River than in the distributaries; this primarily reflects variability in riverine effluent concentrations, which result from hourly changes in both river and effluent flows (Kraus et al. 2017a). Nitrate concentrations decreased as water transited through all four distributaries (Miner, Sutter, Steamboat, and Georgiana sloughs), with lower concentrations at the distributaries' southern terminuses (Figure 2.3.2-39). This decrease with travel reflects biological uptake of nitrate and tidal mixing with downstream waters toward the ends of the distributary channels.

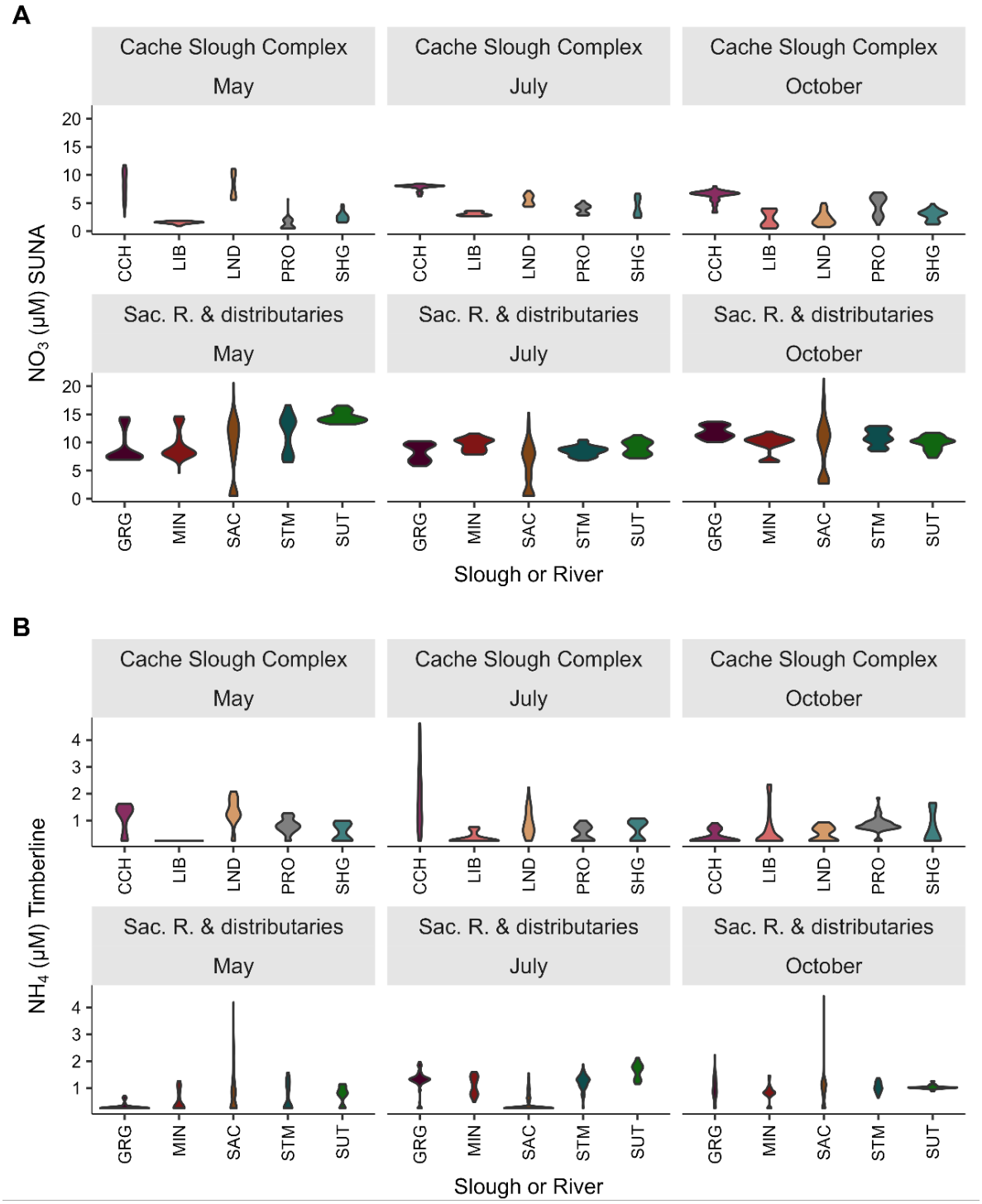

NOTES: µM = micromoles per liter; CCH = Cache Slough; GRG = Georgiana Slough; LIB = Liberty Cut; LND = Lindsey Slough; MIN = Miners Slough; NH_4 = ammonium; NO_3 = nitrate; PRO = Prospect Slough; SAC = Sacramento River; SHG = Shag Slough; STM = Steamboat Slough; SUNA = Submersible Ultraviolet Nitrate Analyzer; SUT = Sutter Slough. Plot set A depicts nitrate and plot set B depicts ammonium, both observed in the Cache Slough Complex and North Delta Complex per slough during May, July, and October 2022. Nitrate was detected by Sea-Bird Scientific's SUNA and ammonium was detected by Timberline Instruments' onboard ammonium analyzer.

Figure 2.3.2-38 High-resolution continuous (A) nitrate and (B) ammonium detected during mapping surveys in May, July, and October 2022.

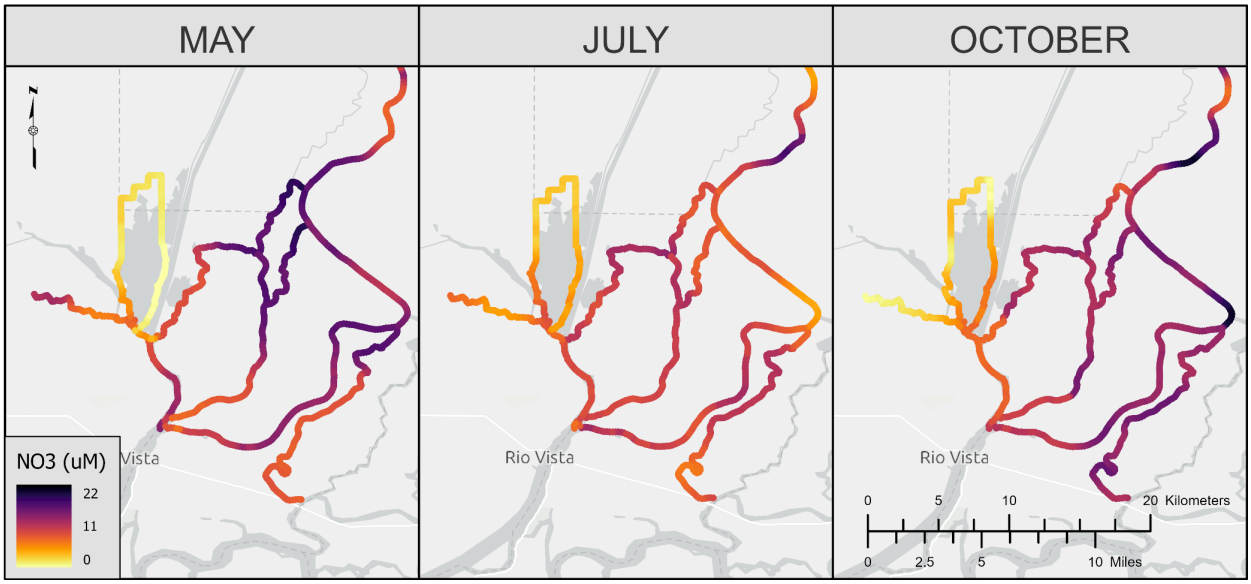

NOTES: µM = micromoles per liter; NO_3 = nitrate.

Figure 2.3.2-39 Nitrate in the North Delta, from high-resolution mapping surveys conducted using the Submersible Ultraviolet Nitrate Analyzer in May, July, and October 2022.

In the Cache Slough Complex, the northern areas had the lowest nitrate concentration on all three dates, along with Lindsey Slough in October (Figure 2.3.2-39). Concentrations of dissolved inorganic nitrogen are often low in these long-residence-time areas in the Cache Slough Complex because of the biological uptake of dissolved inorganic nitrogen (Stumpner et al. 2020). Ammonium concentrations across the study region were generally below 2 µM (Figure 2.3.2-38 and **Figure 2.3.2-40**).

Nitrogen delivered to the North Delta decreased in 2021 when the Sacramento Regional Wastewater Treatment Plant completed upgrades that reduced concentrations of dissolved inorganic nitrogen (ammonium and nitrate) in effluent discharged into the Sacramento River (https://www.regionalsan.com/echowater-project). Before the upgrade, there were strong gradients in both ammonium and nitrate concentrations in the SR&D (Kraus et al. 2017b; Fackrell et al. 2021). In 2011 and 2012, ammonium concentrations in Miner and Steamboat sloughs were approximately 20 µM (Fackrell et al. 2021), but during this 2022 study, they did not exceed 3 µM (Figure 2.3.2-38). In contrast, nitrate concentrations in this region remained fairly constant, at approximately 10 µM, both before the Sacramento Regional Wastewater Treatment Plant upgrade (Fackrell et al. 2021) and after the upgrade (Figure 2.3.2-38). The few instances when ammonium concentrations exceeded 2 µM are likely the result of short-term changes in effluent nutrient concentrations and/or higher ratios of effluent to riverine flow (Figure 2.3.2-38B and Figure 2.3.2-40).

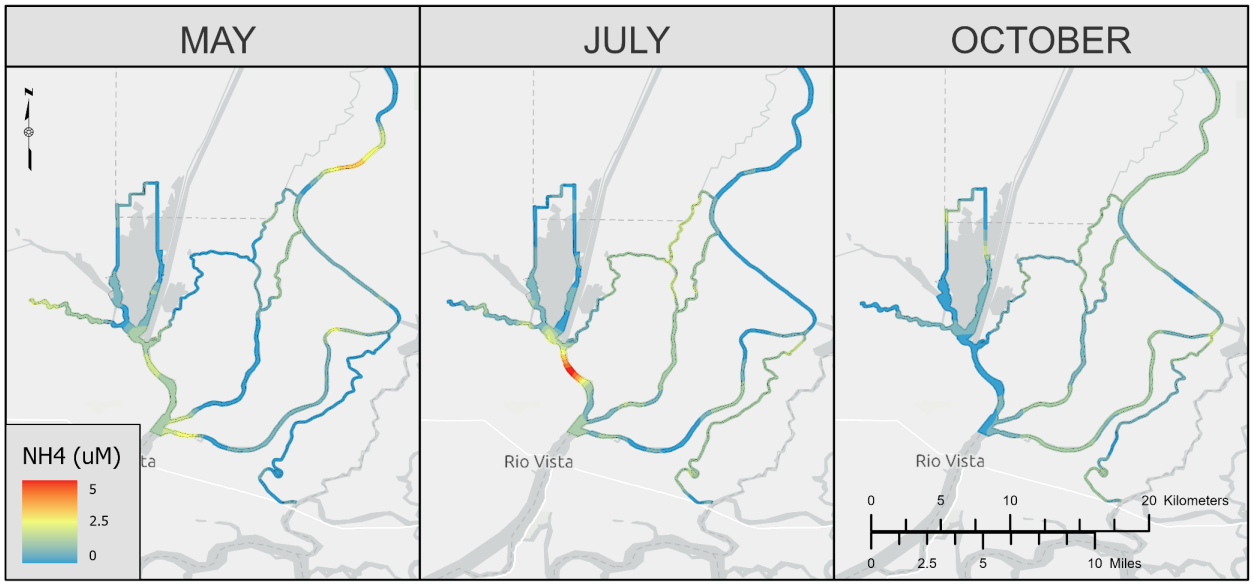

NOTES: µM = micromoles per liter; NH_4 = ammonium.

Figure 2.3.2-40 Ammonium in the North Delta, from high-resolution mapping surveys conducted by Timberline Instruments in May, July, and October 2022.

During the three surveys, in situ fCHL concentrations reported by the YSI EXO2 were predominantly below 2 µg/L, except in the SR&D in May. In the distributaries, the YSI EXO2 measured fCHL concentrations from 2 to 8 µg/L (**Figure 2.3.2-41**A and **Figure 2.3.2-42**) and the FluoroProbe

Measured fCHL concentrations ranging from 4 to 15 µg/L (**Figure 2.3.2-43** and **Figure 2.3.2-44**). The EXO2 and FluoroProbe results differ because of the respective instruments' different sensor configurations and manufacturer calibration coefficients. Different sensors are known to produce different fCHL estimates (Foster et al. 2022). For this dataset, when fCHL data were compared with discrete samples analyzed in the laboratory, the EXO2 concentrations were closer to discrete concentrations than the FluoroProbe (**Figure 2.3.2-45**). The overall range of fCHL values is relatively low, and no high-biomass phytoplankton blooms were measured during any of these 2022 mapping surveys.

High-resolution DOC concentrations were estimated by regressing continuous fDOM sensor data with laboratory-analyzed DOC concentrations (Bergamaschi et al. 2020). DOC concentrations were higher in the Cache Slough Complex (2 to 3.5 milligrams carbon per liter [mg-C/L]) than in the SR&D (less than 2 mg-C/L) (Figure 2.3.2-41 and **Figure 2.3.2-46**). The northern areas of the Cache Slough Complex had the highest DOC concentrations (Figure 2.3.2-46), likely because of the longer residence times and connectivity to shallow wetland habitats.

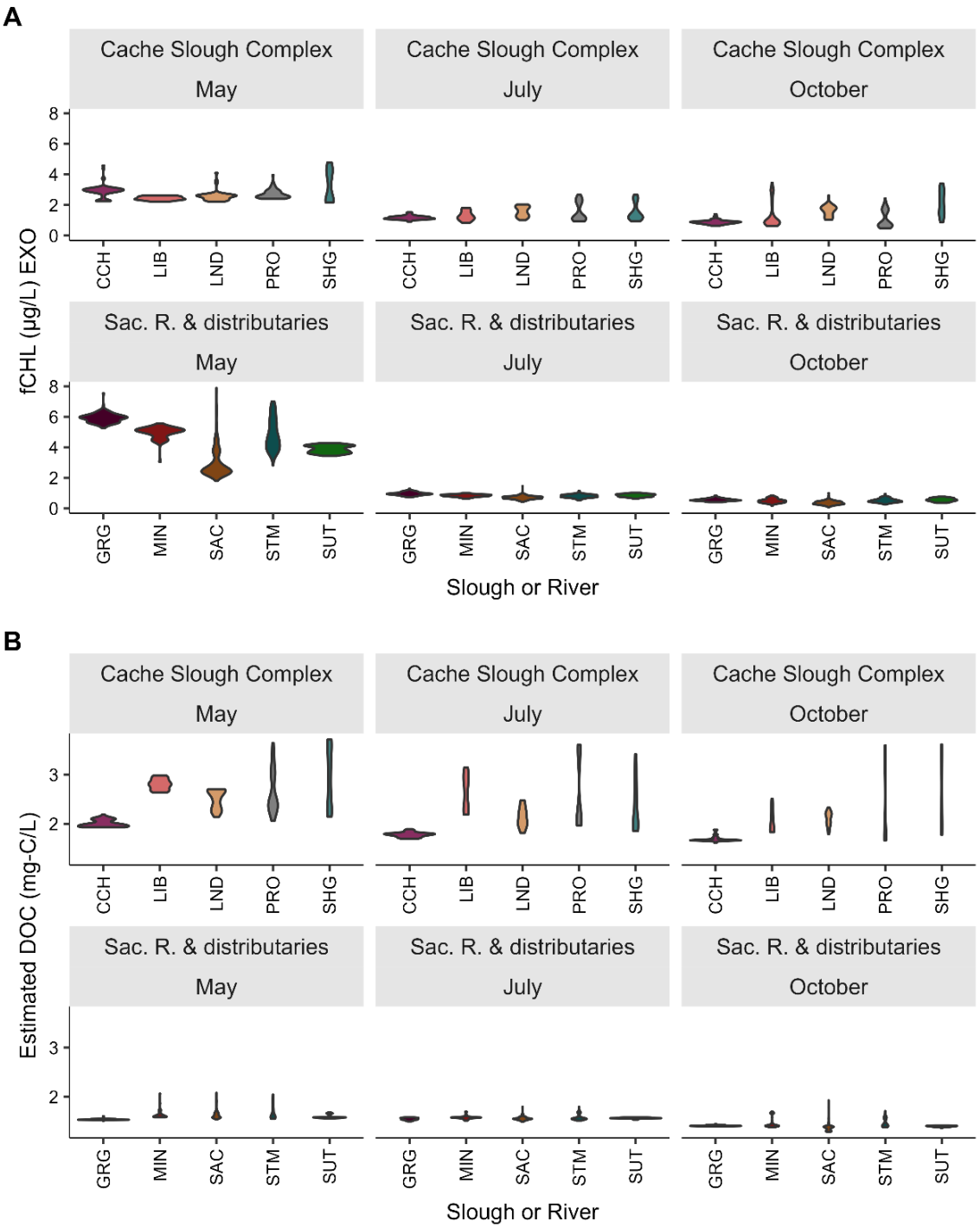

NOTES: µg/L = micrograms per liter; CCH = Cache Slough; DOC = dissolved organic carbon; fCHL = chlorophyll fluorescence; GRG = Georgiana Slough; LIB = Liberty Cut; LND = Lindsey Slough; mg-C/L = milligrams carbon per liter; MIN = Miners Slough; PRO = Prospect Slough; SAC = Sacramento River; SHG = Shag Slough; STM = Steamboat Slough; SUT = Sutter Slough.

Plot set A depicts chlorophyll and plot set B depicts estimated dissolved organic carbon, both as observed in the Cache Slough Complex and North Delta Complex per slough during May, July, and October 2022 and collected by Yellow Springs Instruments EXO2 sondes.

Figure 2.3.2-41 Comparison of high-resolution continuous data for (A) in situ chlorophyll fluorescence and (B) estimated dissolved organic carbon concentrations, collected during mapping surveys in May, July, and October 2022.

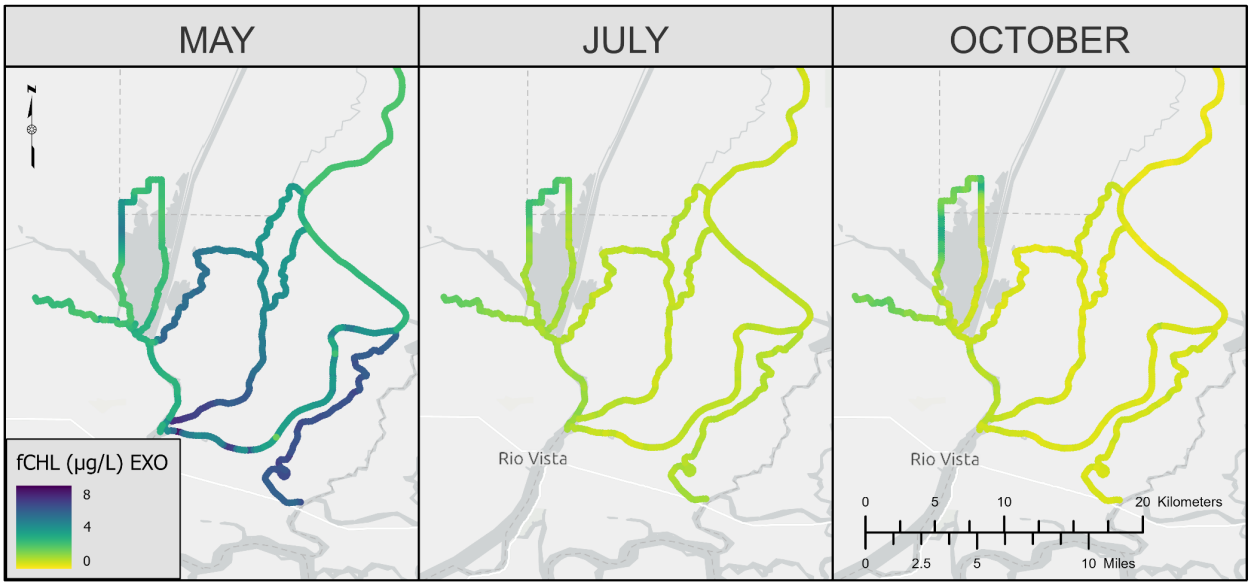

NOTES: µg/L = micrograms per liter; EXO = Yellow Springs Instruments (YSI) EXO2 sonde; fCHL = chlorophyll fluorescence

Figure 2.3.2-42 In situ chlorophyll fluorescence in the North Delta, from high-resolution mapping surveys conducted using YSI EXO2 sondes in May, July, and October 2022.

Sources of dissolved organic matter to the Delta include terrestrial material transported into the system through overland and subsurface flows; wastewater treatment plant effluent; exudates from aquatic vegetation, phytoplankton, and bacteria; and likely most importantly, decomposition of detrital material. DOC is a constituent of concern with respect to drinking water because it reacts to form disinfection byproducts.

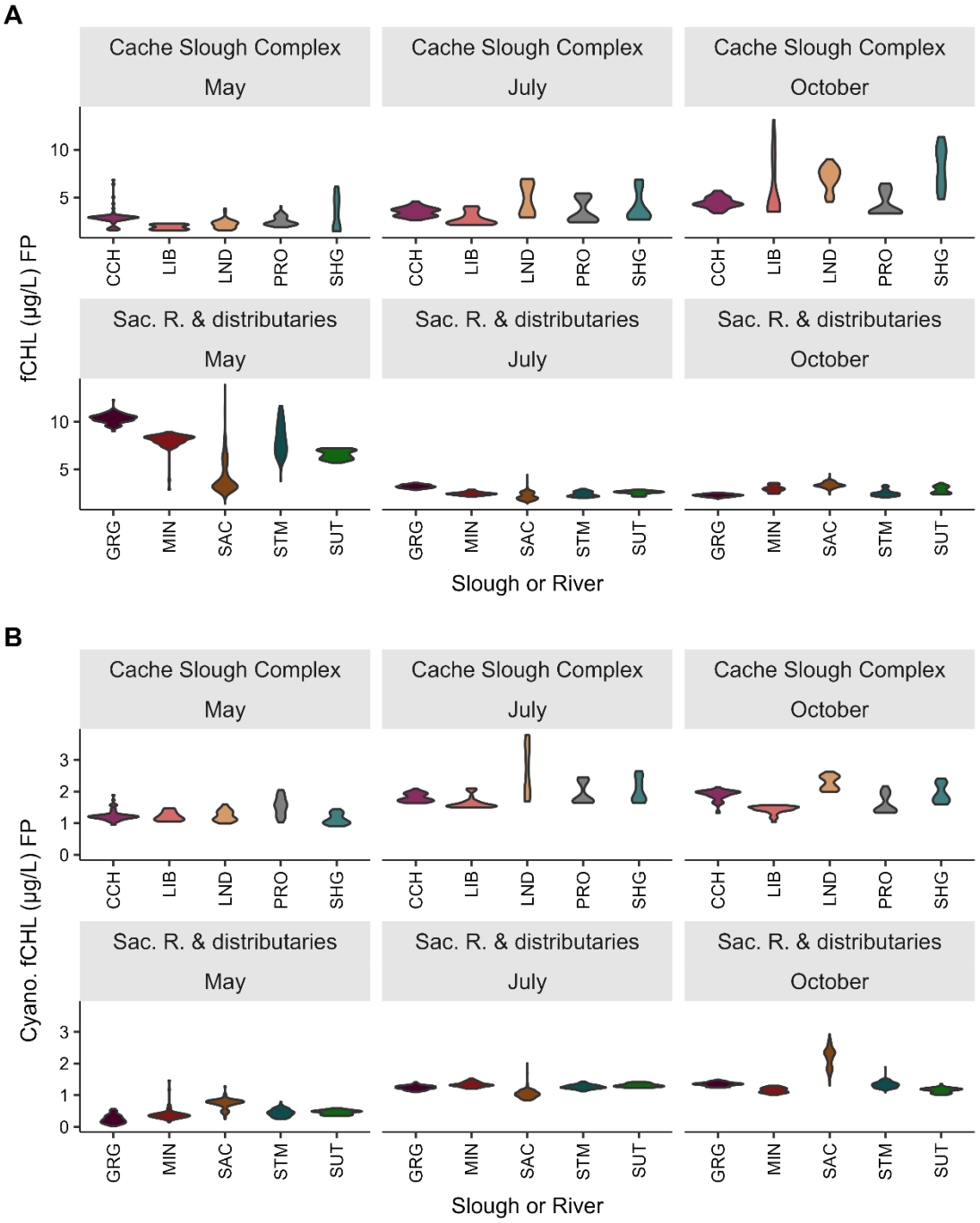

NOTES: µg/L = micrograms per liter; CCH = Cache Slough; Cyano. = cyanobacterial; DOC = dissolved organic carbon; fCHL = chlorophyll fluorescence; FP = FluoroProbe; GRG = Georgiana Slough; LIB = Liberty Cut; LND = Lindsey Slough; mg-C/L = milligrams carbon per liter; MIN = Miners Slough; PRO = Prospect Slough; SAC = Sacramento River; SHG = Shag Slough; STM = Steamboat Slough; SUT = Sutter Slough.
Plot set A depicts chlorophyll fluorescence and plot set B depicts cyanobacterial chlorophyll fluorescence, both as observed in the Cache Slough Complex and North Delta Complex per slough during May, July, and October 2022 and collected by the FluoroProbe.

Figure 2.3.2-43 Comparison of high-resolution continuous data for (A) total in situ chlorophyll fluorescence and (B) cyanobacterial in situ chlorophyll fluorescence, collected during mapping surveys in May, July, and October 2022.

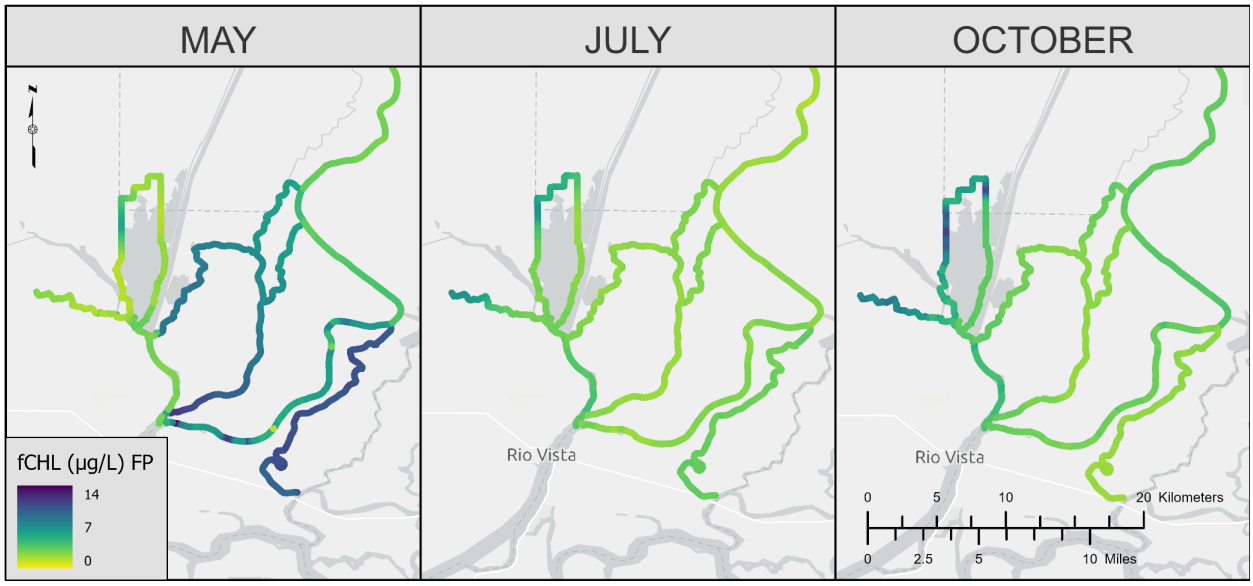

NOTES: µg/L = micrograms per liter; fCHL = chlorophyll fluorescence; FP = FluoroProbe

Figure 2.3.2-44 In situ total chlorophyll fluorescence in the North Delta, mapped by the FluoroProbe during high-resolution surveys in May, July, and October 2022.

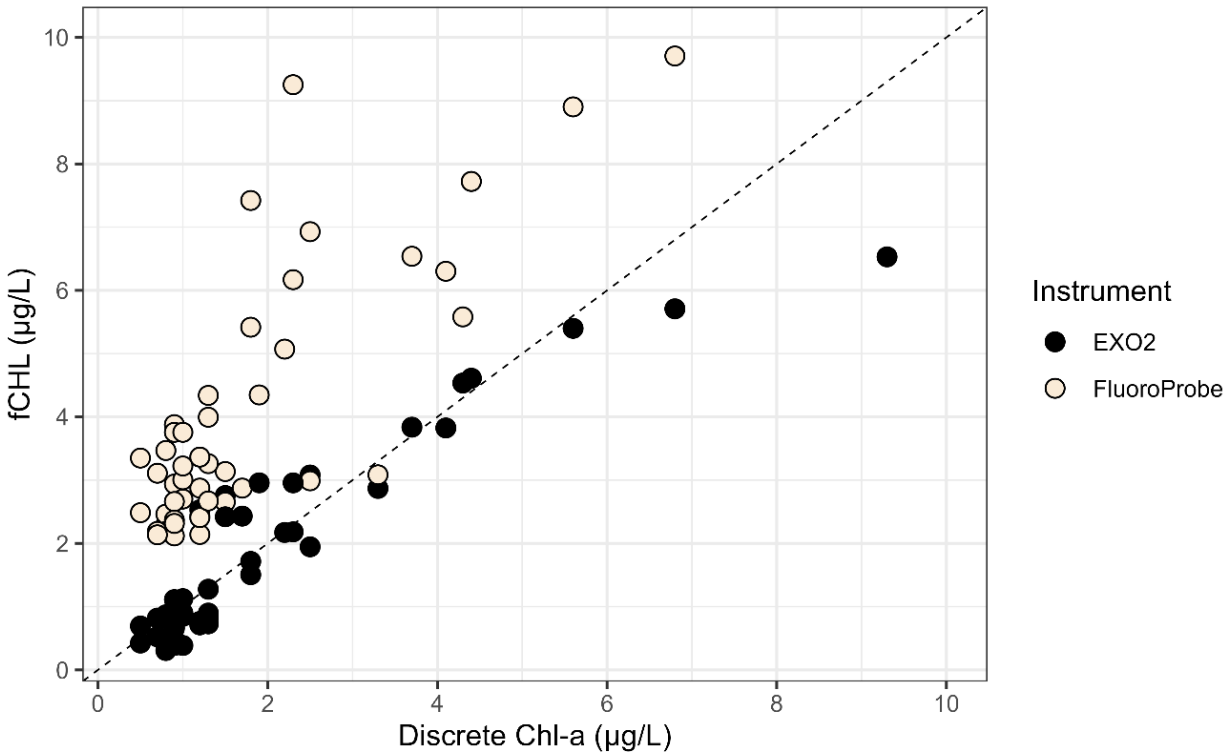

NOTES: µg/L = micrograms per liter; Chl-a = chlorophyll *a*; EXO2 = Yellow Springs Instruments (YSI) EXO2 sonde; fCHL = chlorophyll fluorescence

Figure 2.3.2-45 Comparison of discrete chlorophyll *a* concentrations with in situ chlorophyll fluorescence concentrations measured by the YSI EXO2 and FluoroProbe.

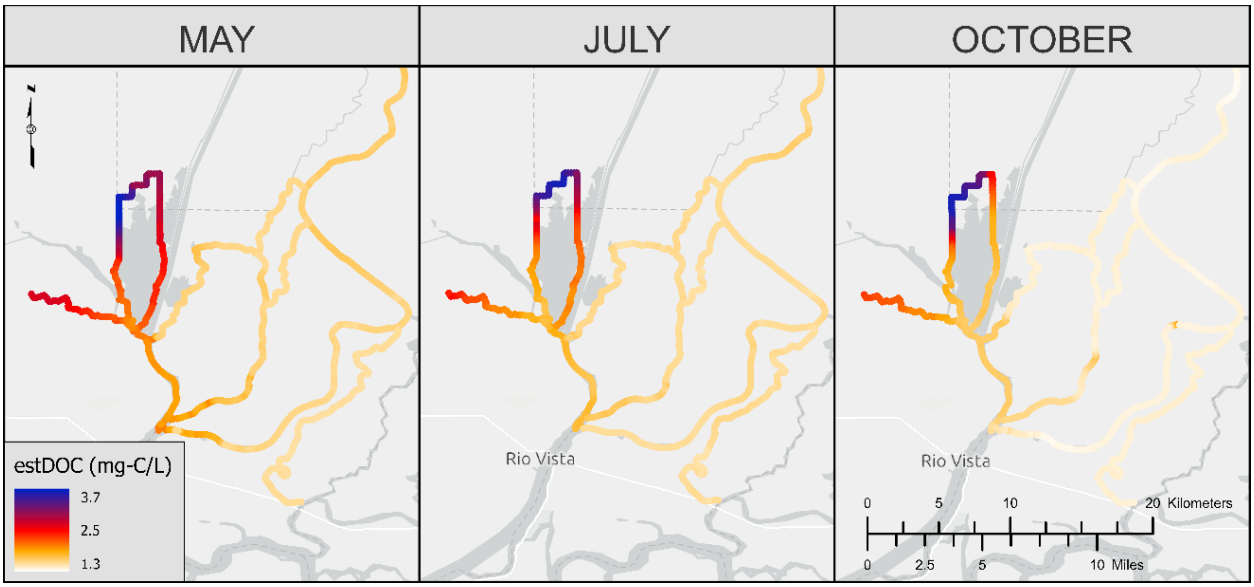

NOTES: estDOC = estimated dissolved organic carbon; mg-C/L = milligrams carbon per liter

Figure 2.3.2-46 Estimated dissolved organic carbon in the North Delta, mapped during high-resolution surveys in May, July, and October 2022.

As summarized below, discrete samples collected during the mapping surveys showed patterns similar to those shown in the continuous high-resolution data (**Figure 2.3.2-47**). For site locations, see Figure 2.3.2-34 and Table 2.3.2-3.

- Chlorophyll concentrations in the SR&D were highest in May (approximately 0.005–0.010 mg/L), but otherwise were below 0.005 mg/L.
- DOC concentrations were less than 5 mg/L in all samples. The highest concentrations were observed across all three survey months at Shag Slough at Liberty Island near Courtland (SSB), Liberty Island at Upper Stair Step near Five Points (SS), and Delta Rmp Yolo-003 (LS1)—areas of the Cache Slough Complex with longer water residence times.
- Concentrations of soluble reactive phosphorus (SRP; PO_4) were always below 1.5 µM in the SR&D but exceeded 2.5 µM at sites SSB, SS, and LS1 in the Cache Slough Complex. The higher SRP concentrations at these sites are likely the result of longer residence time and the accrual of SRP during decomposition, similar to the accrual of DOC at these sites.
- Nitrite and nitrate (NO_2 + NO_3) concentrations were higher in the SR&D than in the Cache Slouch Complex.
- Ammonium (NH_4) concentrations were low across the region, at less than 2 µM.

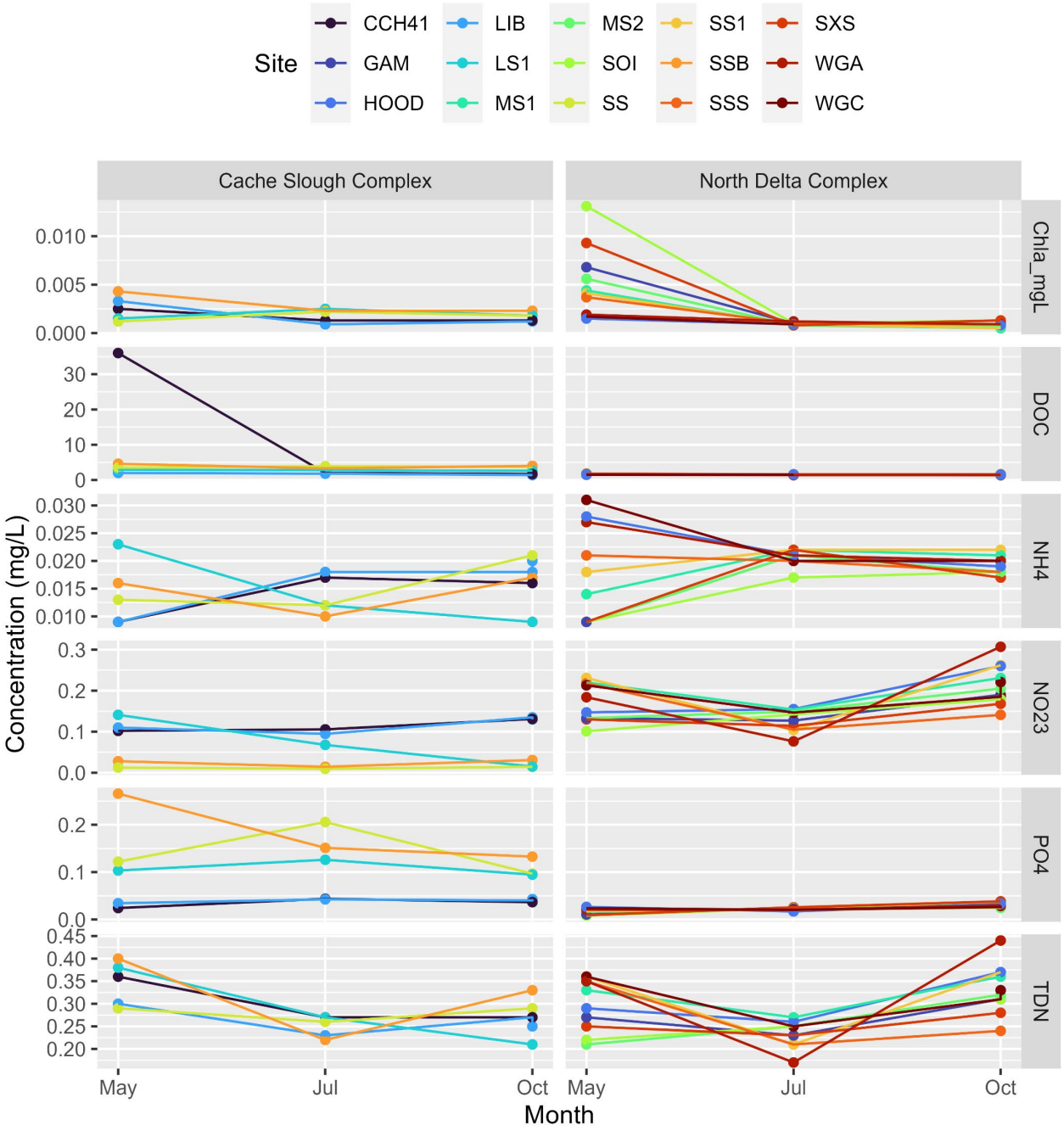

NOTES: Chla_mgL = chlorophyll *a,* milligrams per liter; DOC = dissolved organic carbon; mg/L = milligrams per liter; NH_4 = ammonium (NH_4); NO23 = nitrite and nitrate (NO_2 + NO_3); PO4 = soluble reactive phosphorus (PO_4); TDN = total dissolved nitrogen. For site locations, see Figure 2.3.2-34 and Table 2.3.2-3.

Figure 2.3.2-47 Concentrations of water quality parameters from discrete samples collected at fixed stations during mapping surveys in May, July, and October 2022.

Phytoplankton Community

Microscopy was conducted to enumerate phytoplankton in the discrete samples. The results showed that the phytoplankton community was numerically dominated by cyanobacteria, but because these organisms are

small, biovolume was dominated by Bacillariophyta (diatoms; **Figure 2.3.2-48**). As was observed with the in situ fCHL (Figure 2.3.2-41 through Figure 2.3.2-44) and discrete chl *a* concentrations (Figure 2.3.2-47), phytoplankton were most abundant in May, with more than 20,000 cells per milliliter at seven of the 15 sites (Figure 2.3.2-48). Abundances then decreased to fewer than 20,000 cells per mL in the July and October samples at most sites. The exceptions were Steamboat Slough near Isleton (SXS), Cache Slough at South Liberty Island near Rio Vista (LIB), and Sacramento River above Delta Cross Channel (WGA) (Figure 2.3.2-34, Table 2.3.2-3), where abundances were 20,000–40,000 cells per mL.

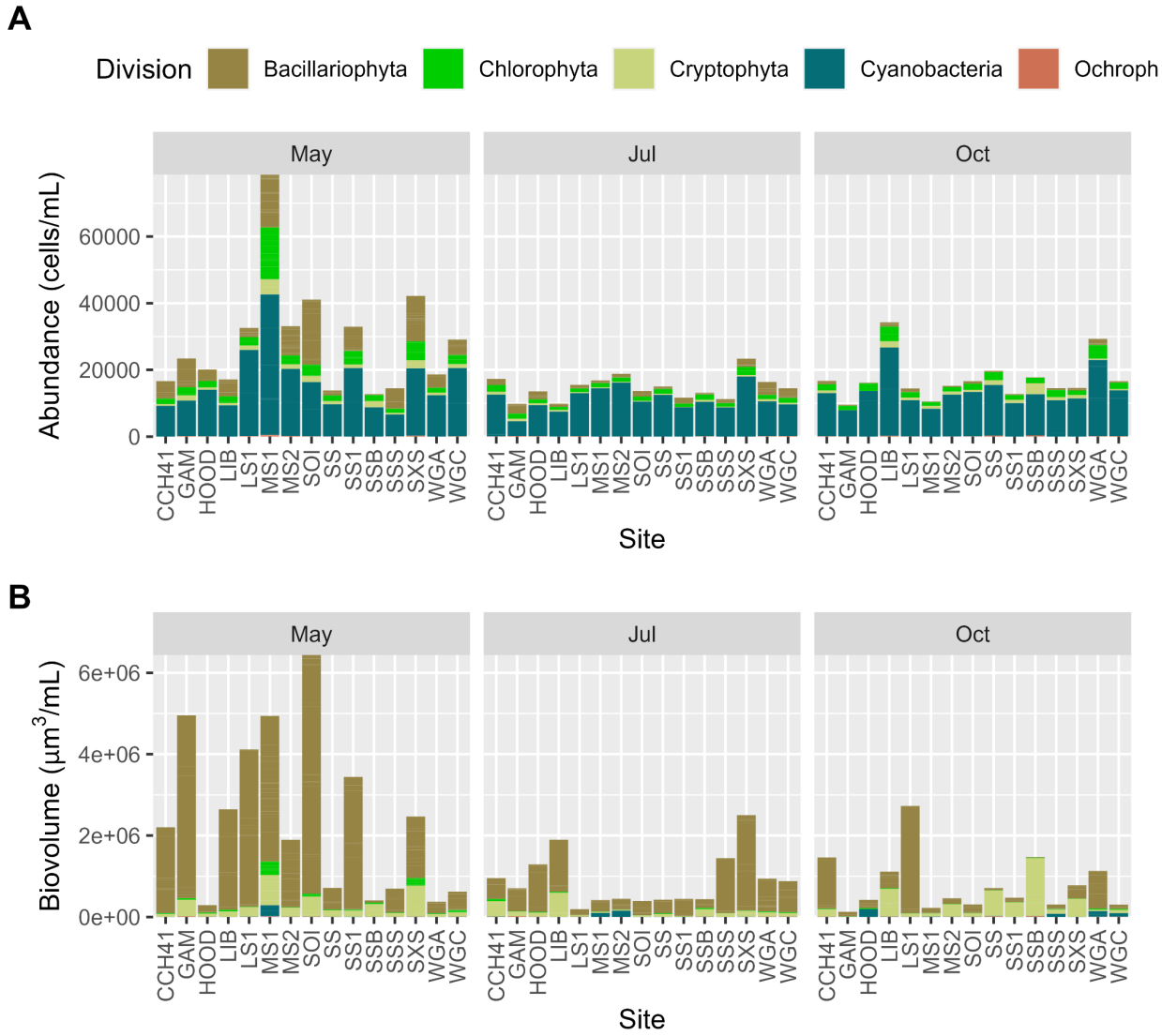

NOTES: µm^3/mL = cubic microns per milliliter; cells/mL = cells per milliliter.
For site locations, see Figure 2.3.2-34 and Table 2.3.2-3.

Figure 2.3.2-48 (A) Abundance and (B) biovolume of the five phytoplankton divisions determined by phytoplankton enumeration of discrete samples collected in the North Delta in May, July, and October 2022.

The phytoplankton community was numerically dominated by the cyanobacterial genus *Eucapsis*, a nontoxic picocyanobacterium (**Figure 2.3.2-49**). However, potentially toxigenic cyanobacterial genera were detected as minor members (Figure 2.3.2-49). For example:

- The cyanobacterial genus *Cuspidothrix* composed 26 percent and 36 percent, respectively, of the relative cell abundance at Miner Slough at Holland Road near Paintersville (MS1) and Miner Slough at Highway 84 near Walker Landing (MS2) in July.
- *Dolichospermum* composed 19 percent of the relative cell abundance at Sacramento River at Hood (HOOD) in October.
- *Aphanizomenon* composed 15 percent at Sacramento River Mile 28 near Walnut Grove (WGC) in October.
- *Microcystis* composed 3 percent at site Cache Slough above Ryer Island Ferry near Rio Vista (CCH41) in July.

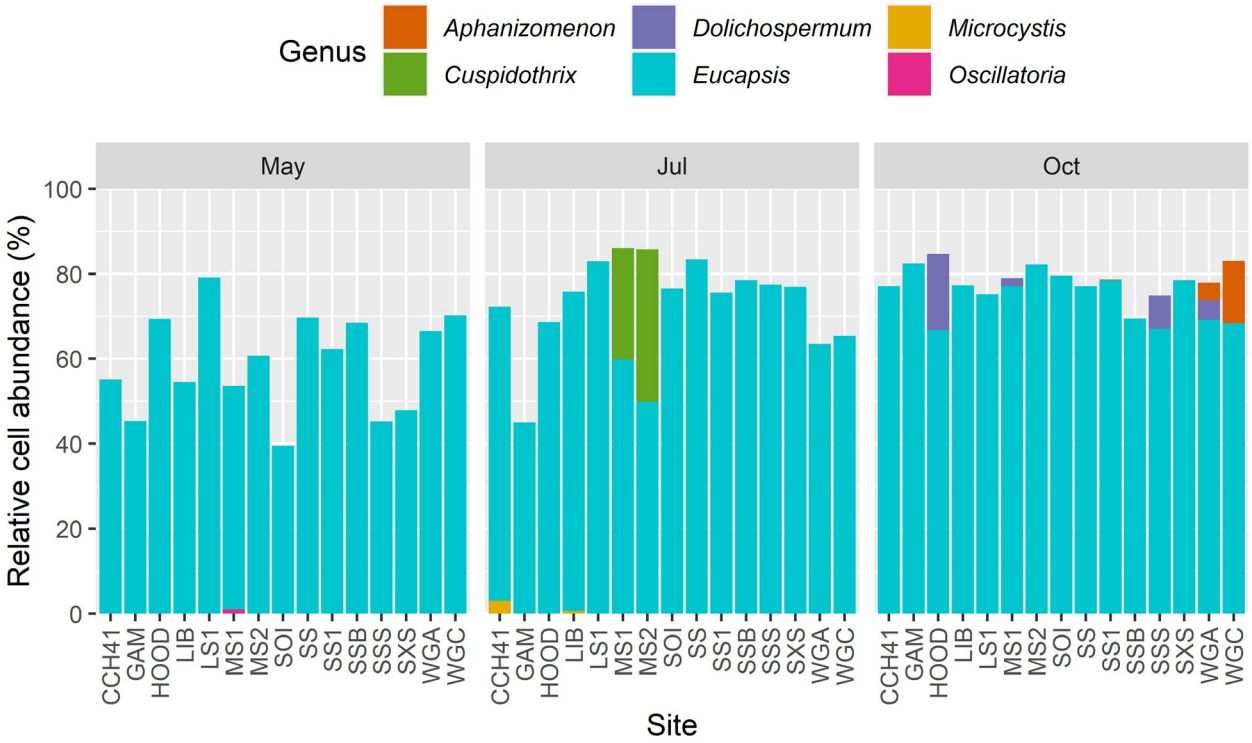

NOTE: For site locations, see Figure 2.3.2-34 and Table 2.3.2-3.

Figure 2.3.2-49 Relative abundance (% of total community) of six cyanobacterial genera across sites in the North Delta, as determined by phytoplankton enumeration of discrete samples in May, July, and October 2022.

Water Age

"Water age" is defined as the average amount of time a parcel of water remains in an arbitrarily defined region of interest. Water age can also sometimes be referred to as "residence time," although definitions of these terms can vary (Monsen et al. 2002). As water ages, it gives time for phytoplankton biomass to potentially increase. Water age was calculated in the SR&D on July 18, 2022, from calculations of water-stable isotopes using discrete sample data (**Figure 2.3.2-50**) and Picarro instrument data (**Figure 2.3.2-51**). There were gaps in the Picarro data for both Steamboat Slough and Miner Slough; because air bubble contamination occurred during the field surveys, no water age data were available for some portions of these sloughs (Figure 2.3.2-51).

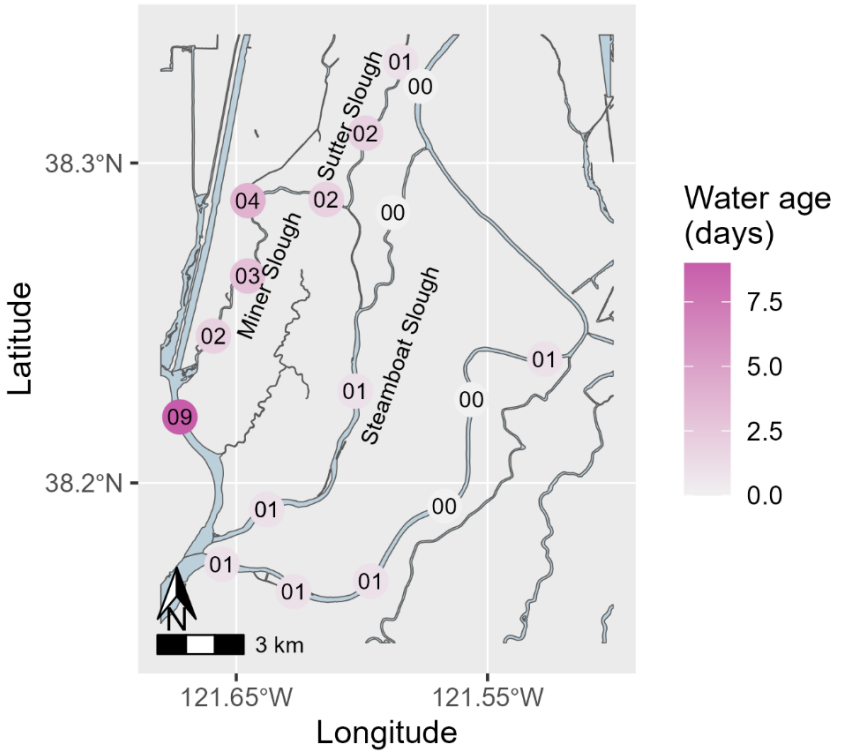

SOURCE: Data compiled by U.S. Geological Survey in 2022

Figure 2.3.2-50 Water age estimates derived from hydrogen- and oxygen-stable isotopes values from discrete water samples collected on July 18, 2022.

The two datasets showed similar trends, and although calculated values differed, the ranges of water ages were similar (discrete: 0–9 days, Picarro: -4 to 4 days). The data showed that it took longer for water to flow down Sutter Slough and Miner Slough than down Steamboat Slough. For Miner Slough, calculated water age from discrete samples was 2–4 days and water age from Picarro data was 0–4 days. Picarro instrument data showed water

age increasing at the southern terminus of Miner Slough, likely because the water was mixing with older water from Cache Slough.

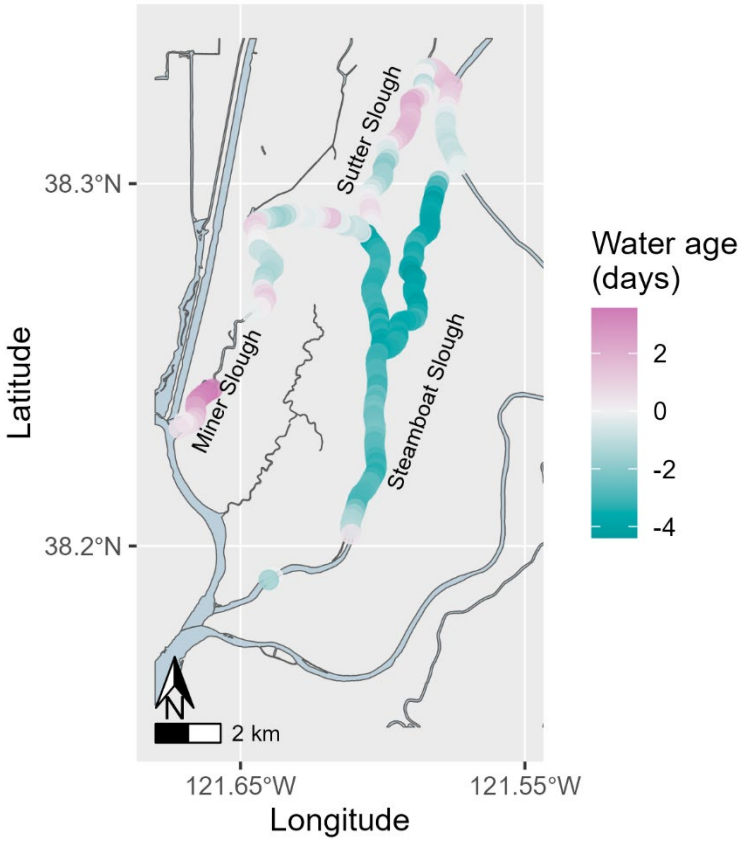

SOURCE: Data compiled by U.S. Geological Survey in 2022

Figure 2.3.2-51 Water age estimates derived from hydrogen- and oxygen-stable isotope data collected on July 18, 2022.

In Steamboat Slough, calculated water age from discrete samples was 0–1 day (Figure 2.3.2-50) and water age from Picarro data was 0 to -4 days (Figure 2.3.2-51). The Picarro instrument data show negative age values because water in Steamboat Slough has less of the ^{2}H and ^{18}O isotopes than the source water in the Sacramento River. This result could have arisen if source waters had changed over time. However, because this pattern was not observed in the discrete data, it could also be a result of measurement imprecision in the Picarro data and in the offset applied to the Picarro data to calibrate it with the discrete samples. The water age values in the distributaries are short and may be approaching the limits of what can be resolved with water-stable isotope data, given the assumptions required for the calculation and the hourly to daily changes in source water entering the Sacramento River.

Although the absolute age values for the Picarro and discrete data differ, the qualitative pattern in Steamboat Slough does not show water age increasing

in the slough and suggests travel times of a day or two to transit this slough. If barriers are placed in Miner and Steamboat sloughs in the future, water residence times in these channels—which would become dead-end sloughs—would likely increase on the order of weeks. In that case, using water-stable isotopes to estimate water age along the channels will identify much longer water ages than the ages estimated in this study without barriers.

Conclusions

North Delta water quality conditions during droughts need to be understood before any drought-related management actions are taken, to better predict how such actions—like installing barriers in Steamboat and Miner sloughs—are likely to alter baseline conditions.

Data collected in the Sacramento River and its distributaries (Sutter, Miner, Steamboat, and Georgiana sloughs) in May, July, and October 2022 showed that water quality in these channels is similar. This finding is not surprising because the distributaries all receive Sacramento River source water. Differences in water quality in these river reaches are likely predominantly caused by different water travel times on the order of only a day or two, which affects the extent of abiotic and biotic processes (Fackrell et al. 2021). Placing rock barriers in these distributary sloughs would dramatically affect water residence time and water exchange there, thus affecting water temperature, salinity, and nutrient cycling along with phytoplankton growth and community composition. The results of USGS data collection efforts in the North Delta indicate that if drought barriers were placed in Steamboat Slough or Miner Slough, or both, the effects of those barriers could be identified by using the Sacramento River mainstem and/or Georgiana Slough as "controls."

Data collected in the Cache Slough Complex (Cache Slough, Liberty Cut, and Lindsey, Prospect, and Shag sloughs) showed more variation among the channels than data collected in the SR&D, with different patterns for different parameters. The Cache Slough Complex is shallower than the SR&D, is more connected to wetland habitat, and has been colonized by more invasive aquatic vegetation. However, one of the primary drivers of water quality patterns and trends in the Cache Slough Complex is water residence time, which are long (20–50 days) in the complex's western and northern reaches (Downing et al. 2016; Gross et al. 2019; Stumpner et al. 2020). For example, these studies showed that longer water residence times are associated with higher specific conductance by evapotranspiration, loss of ammonium by nitrification, and loss of ammonium and nitrate to uptake by biota in the Cache Slough Complex.

One management concern is that reducing Sacramento River flows to the Cache Slough Complex via Steamboat and Miner sloughs not only would degrade water quality for drinking water and irrigation, but also would

increase the potential for cyanobacterial harmful algal blooms (cyanoHABs) in these sloughs. Installing barriers in these two sloughs would increase residence time, decrease mixing, and increase temperatures; these conditions generally favor cyanobacteria over other phytoplankton taxa (Huisman et al. 2018) and could result in increased cyanobacterial biomass. Cyanobacterial blooms are a potential concern during droughts because they purportedly benefit from longer water residence times and higher temperatures. To date, however, higher cyanobacterial biomass has been documented only in the Central and South Delta (Lehman et al. 2013, 2022; Berg and Sutula 2015), and no cyanobacterial blooms were observed in the Cache Slough Complex or the SR&D during this study.

Based on FluoroProbe data collected for this study, the higher chlorophyll concentrations in May (Figure 2.3.2-47) were not associated with higher cyanobacterial fCHL concentrations (Figure 2.3.2-48). Phytoplankton enumeration of discrete samples showed that cyanobacterial biomass was dominated by the non-toxigenic picocyanobacterium *Eucapsis* (Figure 2.3.2-49). Potentially toxigenic *Microcystis*, *Cuspidothrix*, and *Dolichospermum* were observed in discrete samples collected in July and October 2022, but they remained minor members of the phytoplankton community (Figure 2.3.2-49) and never formed any blooms. Potentially toxigenic *Dolichospermum* and *Aphanizomenon* have been detected in the Sacramento River since the 1960s (Greenberg 1964; Britton 1977), but they have never been documented to accumulate nuisance-level biomass in this region of the Delta. In contrast, nontoxic picophytoplankton such as *Eucapsis* have previously been found to compose a large fraction of the chl *a* biomass in Cache Slough Complex channels with longer residence time (Stumpner et al. 2020).

The possibility exists that reducing flows down Sacramento River distributaries by installing drought barriers, thereby reducing nutrient inputs to the Cache Slough Complex, would result in nutrient-limiting conditions that could slow the growth of phytoplankton. Reducing potentially toxic cyanobacteria may be desirable, but limiting nutrients would adversely affect phytoplankton that are beneficial for the food web.

High concentrations of dissolved organic matter and salts negatively affect the use of water for drinking or irrigation. The Cache Slough Complex is a source or sink for different dissolved constituents, depending on the season (Lehman et al. 2010). The net-landward flows up Lindsey and Barker sloughs in summer mean that changes to water quality parameters in the Cache Slough Complex will move up the channels toward the export pumps. The Barker Slough Pumping Plant is at the terminus of Lindsey Slough in the Cache Slough Complex. DOC concentrations in Lindsey Slough during mapping surveys ranged between 2 and 3 mg-C/L (Figure 2.3.2-41 and

Figure 2.3.2-47). Salinity in the Cache Slough Complex remained low, with specific conductivity less than 500 µS/cm, but increased toward the end of each channel (e.g., Lindsey and Shag sloughs; Figure 2.3.2-37 and Figure 2.3.2-47). Future management actions in the North Delta will need to consider potential impacts on water quality conditions at export pumps in Lindsey and Barker sloughs.

The results of this study provide baseline information about water quality conditions in the North Delta during drought conditions, without barriers placed in Miner and Steamboat sloughs. Water quality conditions in the Sacramento River and its distributaries were found to be similar; thus, if future management actions would affect only some of these channels, the other unaffected channels could be used as a control to separate the effects of the action from stochastic environmental variation.

However, water quality conditions in the Cache Slough Complex are more variable, and thus it will be more challenging to identify the impacts of drought management actions on this region. This effort will be further complicated by wetland restoration efforts in this region (e.g., Lookout Slough, Lower Yolo Ranch, Yolo Flyway Farms) that will affect hydrodynamics and biogeochemistry. Collecting data and identifying potential comparable control sites before management actions or extreme hydrologic situations will make it easier to separate the effects of management actions from environmental conditions during years involving specific management actions.

2.3.2.4 Harmful Algal Blooms

Introduction

The first EDB in Franks Tract was installed during a drought period in May 2015 and remained in West False River for seven months before being removed during October and November 2015. Before the 2015 installation, researchers generated several hypotheses about how the EDB would influence the hydrology and food web of Franks Tract. Kimmerer et al. (2019) hypothesized that the EDB would increase phytoplankton abundance in Franks Tract. In particular, they hypothesized that the amount of *Microcystis*, a genus capable of forming toxin-producing cyanoHABs, would also increase as a result of the EDB. However, sampling and monitoring conducted in September–November 2015 to test these hypotheses found no evidence of an increase of phytoplankton or *Microcystis* as a result of the EDB (Kimmerer et al. 2019).

After 2015, an EDB was not installed in West False River again until 2021, when California was experiencing another multiyear drought. In June 2021, an EDB was placed in the same location in West False River as the 2015 EDB.

Surprisingly, in July 2021, satellite remote sensing algorithms indicated that cyanobacterial biomass in Franks Tract was increasing (**Figure 2.3.2-52**) (Hartman et al. 2022). (See **Appendix E** for details about remote sensing algorithms and their performance in Franks Tract.) However, because no additional monitoring for phytoplankton or cyanoHABs was planned during the 2021 EDB deployment, collection of water samples during the 2021 bloom was limited. Hartman et al. (2022) used data from long-term monitoring programs, continuous sonde data, and satellite remote sensing to analyze the potential impact of the EDB on the bloom in 2021. They concluded that the EDB may have contributed to the 2021 bloom in Franks Tract but did not contribute to elevated cyanobacterial biomass elsewhere in the Delta (Hartman et al. 2022).

A full discussion on harmful algal blooms is provided in the *Report on the Impact of the Temporary Urgency Change Petition and Emergency Drought Barrier on Harmful Algal Blooms and Aquatic Weeds in the Delta* (Hartman et al. 2022) and the update of that report for 2022 (U.S. Bureau of Reclamation and California Department of Water Resources 2023) (**Appendix F**).

In brief, during 2021, high concentrations of cyanobacteria, chiefly *Microcystis* but also *Dolichospermum* and *Aphanizomenon*, were observed on the eastern side of Franks Tract in late July and August (Figure 2.3.2-52). This bloom may have been exacerbated by the reduced flow from the EDB. Low levels of cyanotoxins were detected in Franks Tract (maximum of 0.63 µg/L microcystin, below the level where a warning would be issued). However, cyanotoxin sampling was infrequent, so levels may have been higher during other time periods.

During 2022, another bloom occurred in Franks Tract, although the distribution and the community composition of cyanobacteria were different. This bloom was centered in the southern end of Franks Tract, rather than the east (**Figure 2.3.2-53**), and it was dominated by *Dolichospermum* rather than *Microcystis*. Regular toxin testing was conducted in and around Franks Tract, and toxin levels remained below the detection limit throughout the summer.

Because of the conditions seen during 2021, additional monitoring was initiated during 2022. The results of this monitoring are described below.

Blooms form when growth rates exceed loss rates and environmental conditions allow for a high carrying capacity of phytoplankton biomass. If growth rates exceed loss rates for a long enough time, sufficient biomass may accrue to form a bloom.

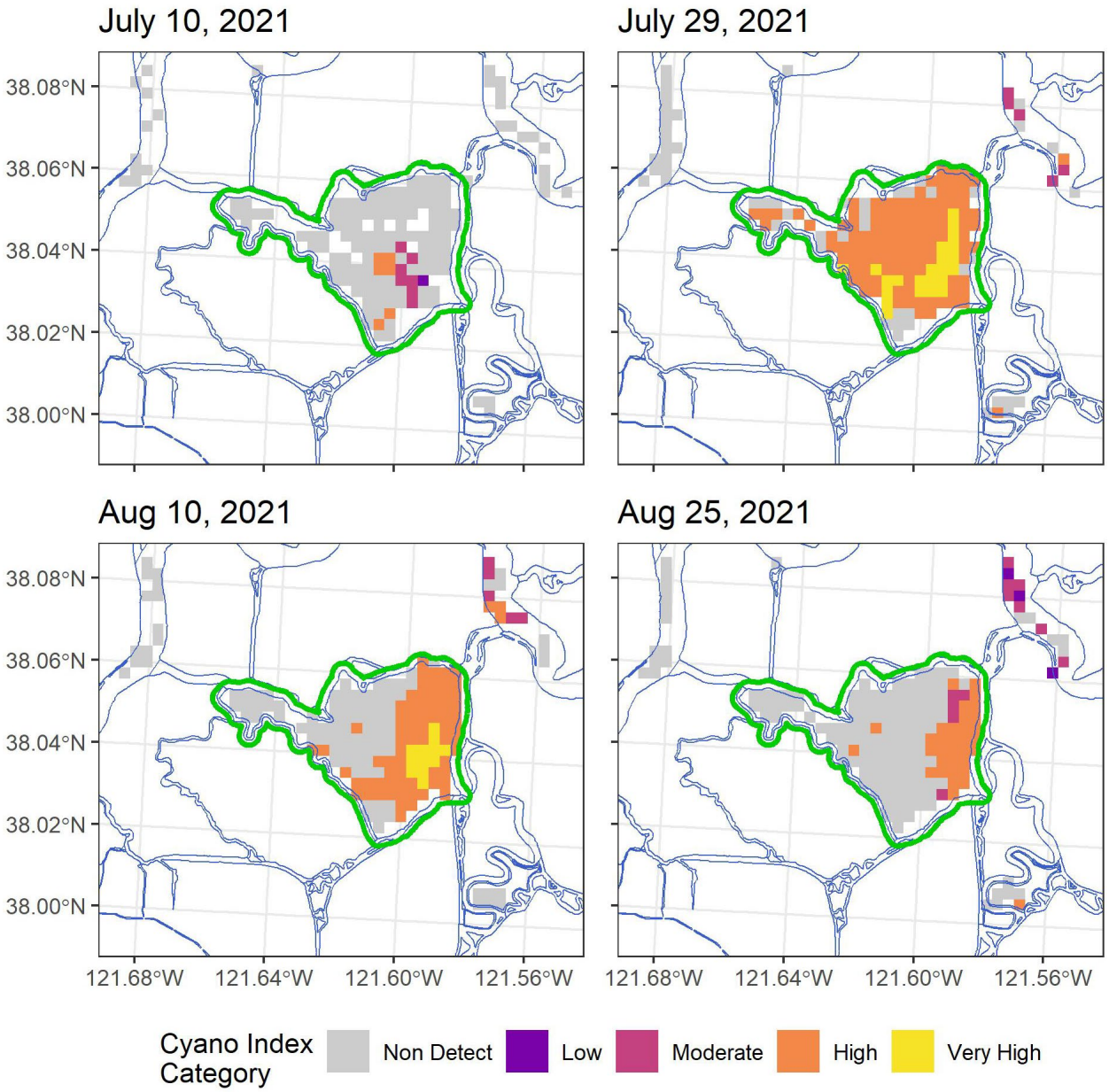

NOTE: The summer 2021 cyanobacteria bloom in Franks Tract is highlighted in green.

Figure 2.3.2-52 Cyanobacteria Index categories at the beginning, peak, and end of the cyanobacteria bloom in Franks Tract during summer 2021.

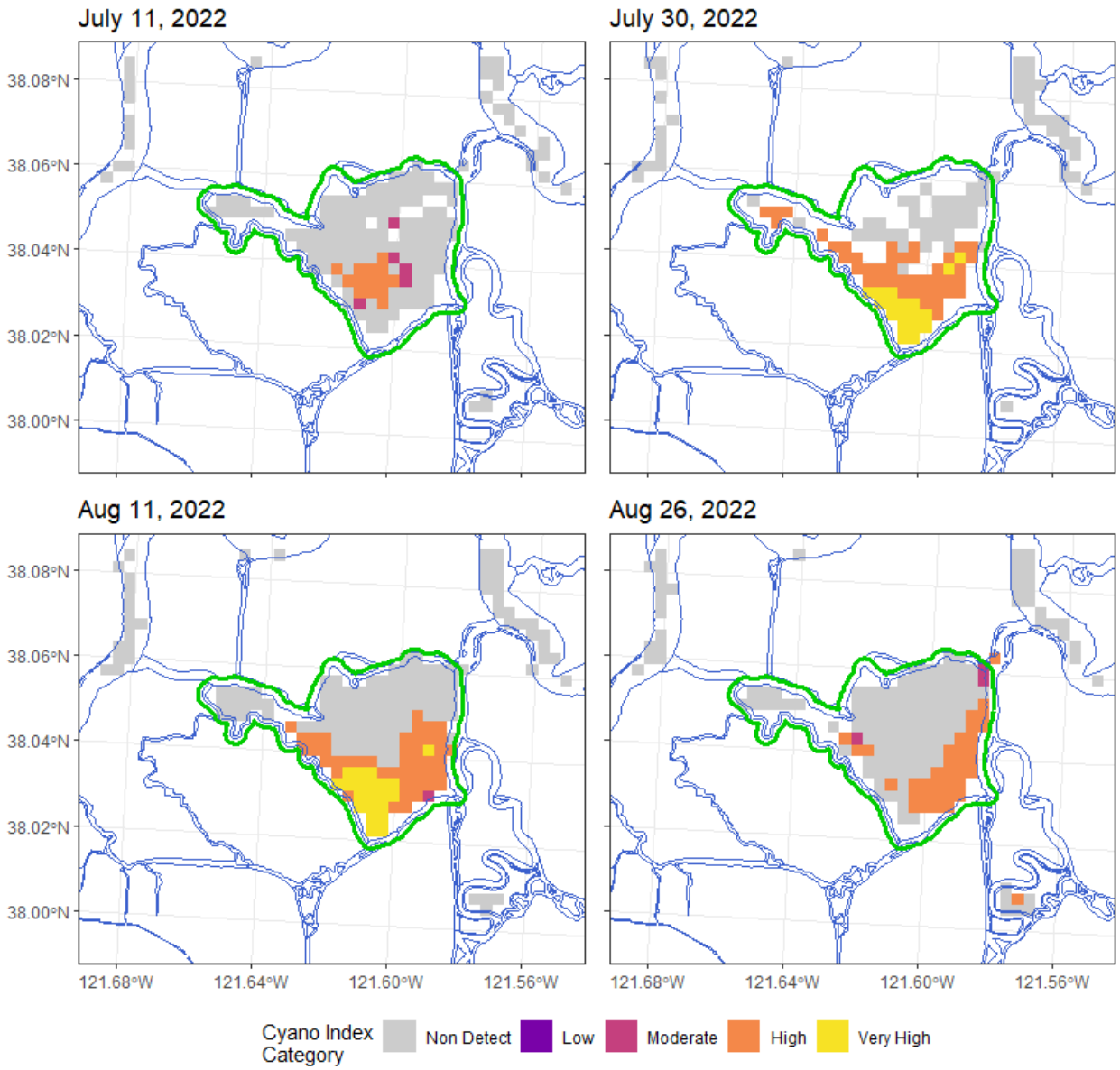

NOTE: The summer 2022 cyanobacteria bloom in Franks Tract is highlighted in green.

Figure 2.3.2-53 Remote sensing Cyanobacterial Index categories at the beginning, peak, and end of the cyanobacteria bloom in Franks Tract during summer 2022.

Ultimately, bloom formation depends on the presence of an organism containing a set of traits that enable it to grow well in an environment so that growth exceeds losses, with enough resources to support high biomass and enough time to use those resources and increase biomass. There is no strict definition of a cyanobacterial bloom. This report's definition of bloom conditions is based on the World Health Organization's recreational Alert

Level 1 criteria: chl *a* concentrations exceeding 20 µg/L and a phytoplankton community dominated by cyanobacteria (World Health Organization 2021).

The effect of the EDB on water age in Franks Tract is one of the primary hypothesized mechanisms for how the EDB could contribute to cyanobacterial blooms. As stated in Section 2.3.2.3, "North Delta Mapping to Document Conditions in the Absence of North Delta Drought Salinity Barriers," water age is defined as the average amount of time a parcel of water remains in an arbitrarily defined region of interest.

Water age can be spatially heterogeneous within a region and does not need to be averaged over the entire region of interest. The age of the water exerts some control over the amount of phytoplankton biomass that can be present during a bloom, and water age has been found to be an important variable in understanding or predicting cyanobacterial biomass in regulated rivers (Romo et al. 2013; Lehman et al. 2022; Nietch et al. 2022). Because cyanobacterial cells grow more slowly than many other types of phytoplankton, they need more time to accrue a large amount of biomass. Therefore, if water moves quickly through a region (young water age), there may not be enough time for cyanobacteria to reach bloom conditions, even if other environmental conditions (such as nutrients or temperature) are optimal for growth.

In summer 2022, scientists at the USGS California Water Science Center used boat-based, high-resolution water quality mapping and discrete sampling approaches to measure spatial variability in water quality, nutrients, and phytoplankton in Franks Tract and Mildred Island. The primary objectives of the project were to (1) study phytoplankton community composition and water quality data in Franks Tract; (2) calculate water age in Franks Tract; and (3) describe factors that may contribute to cyanobacterial blooms in Franks Tract, particularly as they relate to installation of the EDB. Mildred Island was surveyed to provide a comparison open-water site located in the Central Delta that was minimally affected by installation of the EDB.

Methods

Data were collected by boat in Franks Tract and Mildred Island on four dates in summer 2022 when the EDB was installed in West False River: June 7, June 21, July 27, and August 9, 2022. Additional surveys, conducted to collect a reduced set of parameters for calculating water age, took place on October 12 and November 30, 2022. The November 30 survey occurred after the EDB was removed from Franks Tract. Transects were established in each flooded island: three at Franks Tract (FT1, FT2, FT3) and two at Mildred Island (MI1, MI2) (**Figure 2.3.2-54**). High-resolution continuous data were

collected along each transect and discrete data were collected at predetermined stations along the transects (e.g., FT1-1, FT1-2).

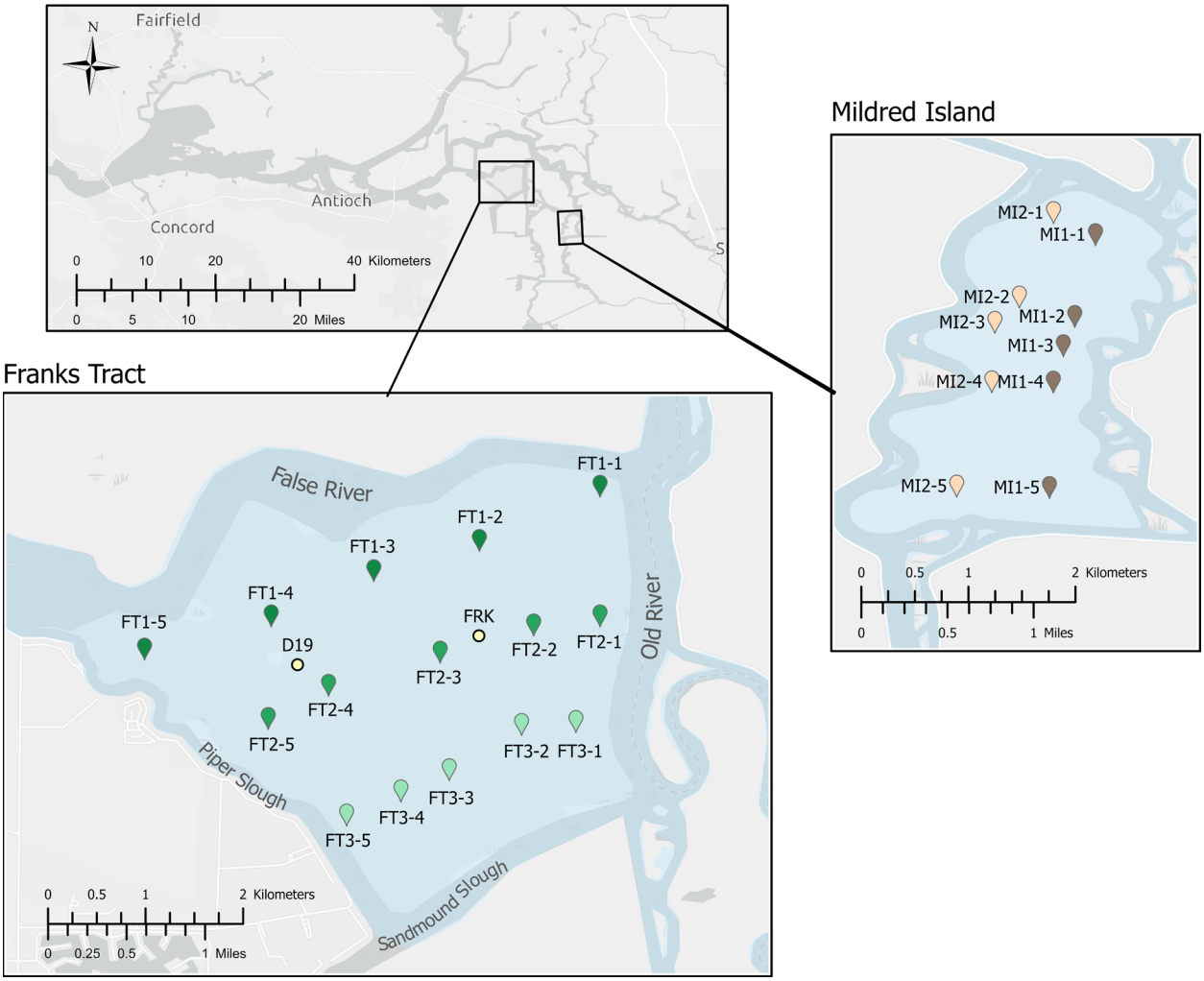

NOTE: DWR sites D19 (Franks Tract near Russo's Landing) and FRK (Franks Tract Mid Tract) are shown in white.
SOURCE: U.S. Geological Survey 2023b

Figure 2.3.2-54 Overview of Franks Tract and Mildred Island depicting USGS discrete sample locations and DWR sites D19 and FRK.

To rapidly characterize water quality conditions in both Franks Tract and Mildred Island, the boat first traveled along each transect without stopping to collect discrete samples. This approach enabled USGS California Water Science Center scientists to collect high-resolution data across each island within approximately 20 minutes so that the water quality changes attributable to tidal advection and dispersion would be minimal. After the initial survey, the boat returned to each transect and began collecting data at each discrete sampling location. The flow-through system collected data throughout the sampling day, even during the collection of discrete samples.

Data collection took approximately 30–45 minutes per transect. Data were collected near high slack tide on June 7 and 21 and November 30, near low slack tide on July 27 and August 9, and between the slack tides on October 12, 2022 (**Figure 2.3.2-55**). Because of the presence of dense amounts of SAV biomass and the low tides on July 27, high-resolution data could not be collected along part of transect FT2 and all of transect FT3 on that day.

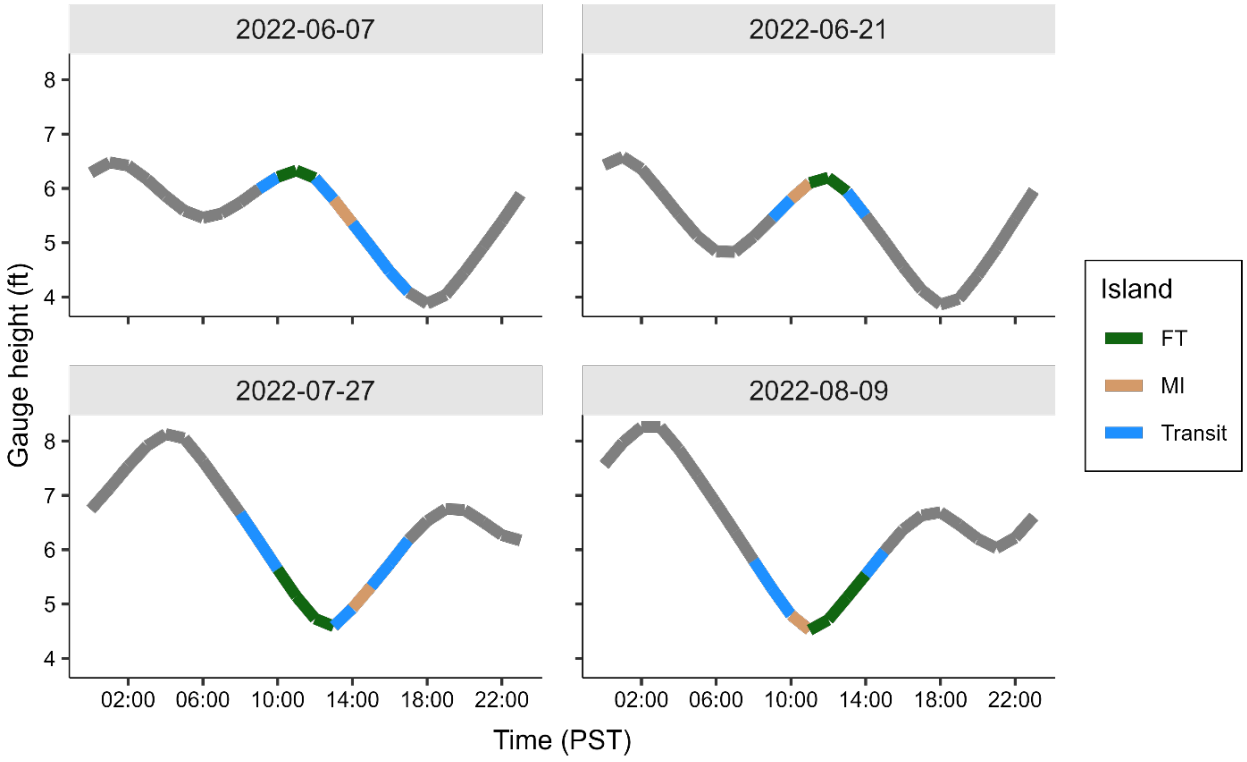

NOTE: These graphs show tide heights at the Old River at Franks Tract near Terminous station (OSJ; National Water Information System ID: 11313452). The color of the line shows times when data were collected in Franks Tract (FT) and Mildred Island (MI), and when transiting between islands occurred. The gray line shows times when no data collection occurred.

SOURCE: Data compiled by U.S. Geological Survey in 2022

Figure 2.3.2-55 Tide heights at the Old River at Franks Tract near Terminous station on each sampling day.

Underway High-Resolution Water Sampling and Onboard Analyses

Details about the collection of high-resolution water sampling data and onboard analyses are provided under "Methods" in Section 2.3.2.3, "North Delta Mapping to Document Conditions in the Absence of North Delta Drought Salinity Barriers," of this report. All high-resolution parameters listed in Table 2.3.2-2 were included except the onboard continuous ammonium flow-through analyzer (Timberline instrument).

Discrete Water Sampling and Laboratory Analyses

Discrete water samples were collected at 15 sites in Franks Tract and 10 sites in Mildred Island (Figure 2.3.2-54 and **Table 2.3.2-7**). **Table 2.3.2-8**

shows the number of samples collected for each parameter at each discrete sampling location. See the methods portion of Section 2.3.2.3 of this report for a discussion of sample collection methods for the discrete water samples analyzed for ammonium, nitrate and nitrite, orthophosphate, dissolved organic nitrogen, total dissolved phosphorus, DOC, TDN, water-stable isotopes, chl *a*, pheophytin, and phytoplankton enumeration.

TABLE 2.3.2-7
DISCRETE SAMPLING LOCATIONS IN FRANKS TRACT AND MILDRED ISLAND

Station Abbrev.	Island	NWIS Site ID	NWIS Site Name	Latitude (decimal degrees)	Longitude (decimal degrees)
FT1-1	Franks Tract	380333121351301	Franks Tract Site 0.1 Nr Bethel Island Ca	38.05916667	-121.5869444
FT1-2	Franks Tract	380315121355301	Franks Tract Site 0.2 Nr Bethel Island Ca	38.05416667	-121.5980556
FT1-3	Franks Tract	380305121362801	Franks Tract Site 0.3 Nr Bethel Island Ca	38.05138889	-121.6077778
FT1-4	Franks Tract	380250121370201	Franks Tract Site 0.4 Nr Bethel Island Ca	38.0472222	-121.6172222
FT1-5	Franks Tract	380239121374401	Franks Tract Site 0.5 Nr Bethel Island Ca	38.04416667	-121.6288889
FT2-1	Franks Tract	380250121351301	Franks Tract Site 1.1 Nr Bethel Island Ca	38.0472222	-121.5869444
FT2-2	Franks Tract	380247121353501	Franks Tract Site 1.2 Nr Bethel Island Ca	38.04638889	-121.5930556
FT2-3	Franks Tract	380238121360601	Franks Tract Site 1.3 Nr Bethel Island Ca	38.04388889	-121.6016667
FT2-4	Franks Tract	380227121364301	Franks Tract Site 1.4 Nr Bethel Island Ca	38.0408333	-121.6119444
FT2-5	Franks Tract	380216121370301	Franks Tract Site 1.5 Nr Bethel Island Ca	38.03777778	-121.6175
FT3-1	Franks Tract	380215121352101	Franks Tract Site 2.1 Nr Bethel Island Ca	38.0375	-121.5891667
FT3-2	Franks Tract	380214121353901	Franks Tract Site 2.2 Nr Bethel Island Ca	38.0372222	-121.5941667
FT3-3	Franks Tract	380159121360301	Franks Tract Site 2.3 Nr Bethel Island Ca	38.03305556	-121.6008333
FT3-4	Franks Tract	380152121361901	Franks Tract Site 2.4 Nr Bethel Island Ca	38.0311111	-121.6052778
FT3-5	Franks Tract	380144121363701	Franks Tract Site 2.5 Nr Bethel Island Ca	38.02888889	-121.6102778
MI1-1	Mildred Island	375944121310401	Mildred Island Site 1.1 Nr Orwood Ca	37.99555556	-121.5177778
MI1-2	Mildred Island	375919121310901	Mildred Island Site 1.2 Nr Orwood Ca	37.9886111	-121.5191667
MI1-3	Mildred Island	375910121311201	Mildred Island Site 1.5 Nr Orwood Ca	37.9861111	-121.52
MI1-4	Mildred Island	375918121310901	Mildred Island Site 1.3 Nr Orwood Ca	37.98302	-121.52068

Station Abbrev.	Island	NWIS Site ID	NWIS Site Name	Latitude (decimal degrees)	Longitude (decimal degrees)
MI1-5	Mildred Island	375827121311401	Mildred Island Site 1.4 Nr Orwood Ca	37.97416667	-121.5205556
MI2-1	Mildred Island	375950121311701	Mildred Island Site 2.1 Nr Orwood Ca	37.9972222	-121.5213889
MI2-2	Mildred Island	375924121312601	Mildred Island Site 2.2 Nr Orwood Ca	37.99	-121.5238889
MI2-3	Mildred Island	375916121313301	Mildred Island Site 2.5 Nr Orwood Ca	37.98777778	-121.5258333
MI2-4	Mildred Island	375858121313301	Mildred Island Site 2.3 Nr Orwood Ca	37.98277778	-121.5258333
MI2-5	Mildred Island	375826121314201	Mildred Island Site 2.4 Nr Orwood Ca	37.97388889	-121.5283333
GOX	N/A	380904121353601	Georgiana Slough A Oxbow Marina Drive Nr Isleton	38.0904	-121.353601
NMR	N/A	380837121333401	N Mokelumne R A Tyler Island Rd Nr Isleton CA	38.0037	-121.333401

NOTES: Abbrev. = abbreviation; ID = identification; N/A = not applicable; NWIS = National Water Information System

SOURCE: Data compiled by U.S. Geological Survey in 2022

TABLE 2.3.2-8
DISCRETELY SAMPLED PARAMETERS COLLECTED IN FRANKS TRACT AND MILDRED ISLAND

Discrete Parameters	
Nitrate (NO_3-N) and nitrite (NO_2-N)	Chlorophyll *a* and phaeophytin
Ammonium (NH_4-N)	Dissolved organic carbon and optics
Dissolved organic nitrogen (DON, by calculation)	Stable isotopes δ^2H and $\delta^{18}O$
Total dissolved nitrogen (TDN)	Phytoplankton enumeration
Soluble reactive phosphorus (orthophosphate, PO_4-P)	Total particulate nitrogen and carbon (TPCN)
Total dissolved phosphorus (TDP)	Total phosphorus

SOURCE: Data compiled by U.S. Geological Survey in 2022

For this study, discrete samples were analyzed at the USGS National Water Quality Laboratory:

- Concentrations of nitrogen as nitrite (NO_2-N) and as nitrate plus nitrite (NO_3-N + NO_2-N) were determined by colorimetric analysis (Fishman 1993; Patton and Kryskalla 2011).
- Ammonium as nitrogen (NH_4-N) was determined by colorimetric analysis after reaction with salicylate-hypochlorite (Fishman 1993).
- Total dissolved nitrogen (TDN) was determined by alkaline persulfate digestion (Patton and Kryskalla 2003).
- Orthophosphate as phosphorous (PO_4-P; also referred to as "soluble reactive phosphorus") was determined by colorimetric analysis after

reaction with NH_4 molybdate and reduction with ascorbic acid (Patton and Truitt 1992).

- Concentrations of chl *a* and phaeophytin were determined according to EPA Method 445.0 (Arar and Collins 1997); 0.7 µm filtered samples were extracted using sonication.

In addition to the parameters listed above, samples were analyzed for total particulate carbon and nitrogen (TPCN) and total phosphorus (Table 2.3.2-8). The TPCN samples were filtered within 24 hours of collection through pre-weighed 25-millimeter (mm) 0.7 µm combusted glass fiber filters and immediately frozen at -80°C. Frozen TPCN samples were shipped to the USGS National Water Quality Laboratory for analysis. The filters were dried and the mass of collected particles on the filter calculated, then the particulate carbon and nitrogen on the filter were combusted at high temperature and measured using an elemental analyzer (Zimmerman et al. 1997). Total phosphorus was determined by alkaline persulfate digestion (U.S. Environmental Protection Agency 1993b). Molar ratios for dissolved inorganic nitrogen (DIN) and dissolved inorganic phosphorus (DIP) were calculated using the following equation:

(TDN (mg-N/L) / 14) / (PO_4 (mg-P/L) / 31)

Molar ratios for total nitrogen (TN) and total phosphorus (TP) were calculated as follows:

((TDN + PN (mg-N/L)) / 14) / (TP (mg-P/L) / 31)

Water Age

Stable water isotopes, ^{2}H and ^{18}O, were collected for calculating water age. Samples were collected on June 7, June 21, July 27, August 9, October 12, and November 30, 2022. Water age was calculated using the methods detailed by Downing et al. (2016) and Skrzypek et al. (2015) using a custom R script. Details of the method are provided in Section 2.3.2.3, and specific parameters for used for these calculations are listed in **Table 2.3.2-9**. Source water (δ_P) values were obtained by calculating the mean of all discrete samples collected at the GOX and NMR sites in Georgiana Slough and North Fork Mokelumne River, respectively. Isotope values of rain (δ_R) were estimated using the Online Isotopes in Precipitation Calculator (https://wateriso.utah.edu/waterisotopes/pages/data_access/oipc.html; Welker 2000; Bowen et al. 2005), using coordinates within Franks Tract (latitude = 38.0426, longitude = -121.604, elevation = 1.22 meters).

To assess changes in residence time and temperature, 3D simulations were carried out using the Bay-Delta SCHISM 3D circulation model (Ateljevich et al. 2014), an application of the Semi-implicit Cross-scale Hydroscience

Integrated System Model (Zhang and Baptista 2008; Zhang et al. 2016). The model was run during the same time periods that field data were collected. Mean water age was used as a surrogate for residence time, evaluated using the Constituent oriented Age and Residence Time (CART) concept (Deleersnijder et al. 2001) using the formulation described by Delhez et al. (2014). This method uses pairs of supplementary tracer transport equations to evolve the mean age of water at each point in the domain. Relative to methods based on particle tracking, CART naturally accommodates multiple pathways of travel and dispersion and is an economical tool for evaluating spatial patterns. In this case, age is defined relative to the moment of last contact with the San Joaquin River. This same approach was used in Hartman et al. (2022) to model water age in Franks Tract in 2021.

TABLE 2.3.2-9
INPUT PARAMETERS USED TO CALCULATE WATER AGE

Date	$\delta_P{}^2H$ (‰)	$\delta_P{}^{18}O$ (‰)	$\delta_R{}^2H$ (‰)	$\delta_R{}^{18}O$ (‰)	T (°C)	h	ET_o (cm day^{-1})	Depth (cm)
June 7, 2022	-78.518	-10.851	-26	-4	17.777	0.541	0.658	200
June 21, 2022	-78.518	-10.851	-26	-4	19.688	0.503	0.741	200
July 27, 2022	-78.518	-10.851	-32	-3.8	22.604	0.474	0.834	200
August 9, 2022	-78.518	-10.851	-24.5	-3.15	22.939	0.489	0.83	200
October 12, 2022	-78.518	-10.851	-32	-5.1	23.383	0.541	0.602	200
November 30, 2022	-78.518	-10.851	-46	-6.8	14.900	0.643	0.291	200

NOTES: °C = degrees Celsius; δP = source water isotopes; δR = rainwater isotopes; cm = centimeters; Et_O = evapotranspiration; h = relative humidity; T = temperature

The outflowing water parameter, δL, comes from discrete or picaro samples and is not shown in this table.

Quantitative results within Franks Tract are sensitive to assumptions regarding the vegetation field. Vegetation was included using the method of Zhang et al. (2019), which was originally tested in Franks Tract using spatial patterns of vegetation inferred from hyperspectral imagery from 2015 (Ustin et al. 2016). The modeled vegetation has many effects (e.g., wave suppression, biogeochemical competition, shading), but the dominant consequences for circulation are assumed to be drag within the canopy and turbulence production caused by shear at the top of the canopy (Figure 2.3.2-55). The resulting velocities are stratified and tidally asymmetric (because of surging structured flow over the canopy during high tide), while also producing constituent concentrations that are more homogenous (because of regular turbulent mixing).

To evaluate the impact of submerged aquatic vegetation, or SAV, new parameters were used for SAV canopy height and the SAV drag coefficient. In the original calibration, the canopy height was allowed to reach from bed to

0.25 meter NAVD88, or was 0.25 meter, whichever was bigger. In the revised model, the canopy height was shortened to -0.1 meter NAVD88 or 0.25 meter, whichever was bigger. The original drag coefficient, 1.13, was reduced to 0.28.

Data Analyses

Details about data processing are provided in Section 2.3.2.3, "North Delta Mapping to Document Conditions in the Absence of North Delta Drought Salinity Barriers." Briefly, data from onboard continuous instruments that were not directly logged to the flow-through data collection system were merged based on time stamp, to the nearest second. All data directly logged to the flow-through data collection system were processed to remove periods of compromised data (e.g., flow blockages, bubbles), to apply instrument corrections and unit conversions, and to apply a centered 20-second median filter to the time series. Final nitrate values were obtained by regressing on each day the instrument's response against nitrate concentrations obtained from laboratory measurements of discrete samples collected through the course of the day (**Table 2.3.2-10**). High-resolution and discrete sample data collected as part of this study are publicly available (Bouma-Gregson et al. 2023a; U.S. Geological Survey 2023b).

TABLE 2.3.2-10
SUBMERSIBLE ULTRAVIOLET NITRATE ANALYZER NITRATE BIAS CORRECTION REGRESSIONS WITH DISCRETE NITRATE SAMPLES—FRANKS TRACT AND MILDRED ISLAND

Parameter	Date	Regression Equation
NO_3	June 7, 2022	0.862*SUNA - 2.606
NO_3	June 21, 2022	0.983*SUNA-3.780
NO_3	July 27, 2022	0.851*SUNA - 2.007
NO_3	August 9, 2022	0.769*SUNA - 1.134
NO_3	October 12, 2022	0.998*SUNA - 2.982
NO_3	November 30, 2022	0.858*SUNA - 4.188

NOTES: NO_3 = nitrate; SUNA = Submersible Ultraviolet Nitrate Analyzer

SOURCE: Data compiled by U.S. Geological Survey in 2022

Results

In 2022 when the EDB was in place, a cyanobacterial bloom occurred in Franks Tract in July and August. The bloom began between June 21, when chlorophyll concentrations were still less than 10 µg/L, and July 27, when chlorophyll concentrations exceeded 50 µg/L. The most abundant organism at sites with the highest chlorophyll concentrations was the cyanobacterial genus *Dolichospermum*.

Chlorophyll

During the first two surveys, on June 7 and 21, 2022, average discrete chlorophyll concentrations along each of the three Franks Tract transects were less than 5 µg/L (**Figure 2.3.2-56**A), within the typical range of summer concentrations for the Central Delta (Jabusch et al. 2018).

By the July 27 survey, chlorophyll concentrations had increased to bloom conditions; average concentrations along transects FT1, FT2, and FT3 were 15, 22, and 117 µg/L, respectively. Chlorophyll levels remained elevated during the August 9 survey; concentrations along transects FT1, FT2, and FT3 were 13, 23, and 72 µg/L, respectively (Figure 2.3.2-56A). The highest discrete chlorophyll concentration measured was 205 µg/L, at station FT3-5 on July 27.

Meanwhile, at Mildred Island, discrete chlorophyll concentrations never exceeded 8 µg/L at any site during all four surveys (Figure 2.3.2-56).

The high-resolution in situ chlorophyll fluorescence (fCHL) instruments also measured the phytoplankton bloom in Franks Tract. Both the FluoroProbe and YSI EXO2 sensors measured higher fCHL concentrations in July and August (**Figure 2.3.2-57**, **Figure 2.3.2-58**, and **Figure 2.3.2-59**). The fCHL concentrations were highest in the western and southern areas of Franks Tract on July 27 and August 9 (Figure 2.3.2-57). The discrete samples had the same pattern in July and August, during which the highest chlorophyll concentration for each transect was measured at the westernmost stations (stations FT1-5, FT2-5, and FT3-5). The one exception was the August concentration along transect FT3, where station FT3-4 had a slightly higher discrete chlorophyll concentration (100 µg/L) than station FT3-5 (92 µg/L) (Figure 2.3.2-56A).

The EXO2 and FluoroProbe results differ because of the respective instruments' different sensor configurations and manufacturer calibration coefficients (Figure 2.3.2-58). Different sensors are known to produce different fCHL estimates (Foster et al. 2022), but in this dataset, the relative differences and spatial patterns are both temporally and spatially consistent between the EXO2 and FluoroProbe sensors.

Phytoplankton Community

Phytoplankton enumeration by microscopy confirmed that the phytoplankton bloom observed in July and August 2022 was formed by cyanobacteria. During the two June sampling events, phytoplankton abundance in Franks Tract was mostly below 30,000 cells/mL (**Figure 2.3.2-60**) and biovolume was dominated by Bacillariophytes (diatoms) and Cryptophytes (**Figure 2.3.2-61**). In July and August, cell abundance exceeded 100,000 cells/mL at some sites (Figure 2.3.2-60) and the biovolume became dominated by potentially toxigenic cyanobacteria (ptox) (*Aphanizomenon*, *Dolichospermum*, *Microcystis*, and *Planktothrix*) (Figure 2.3.2-61).

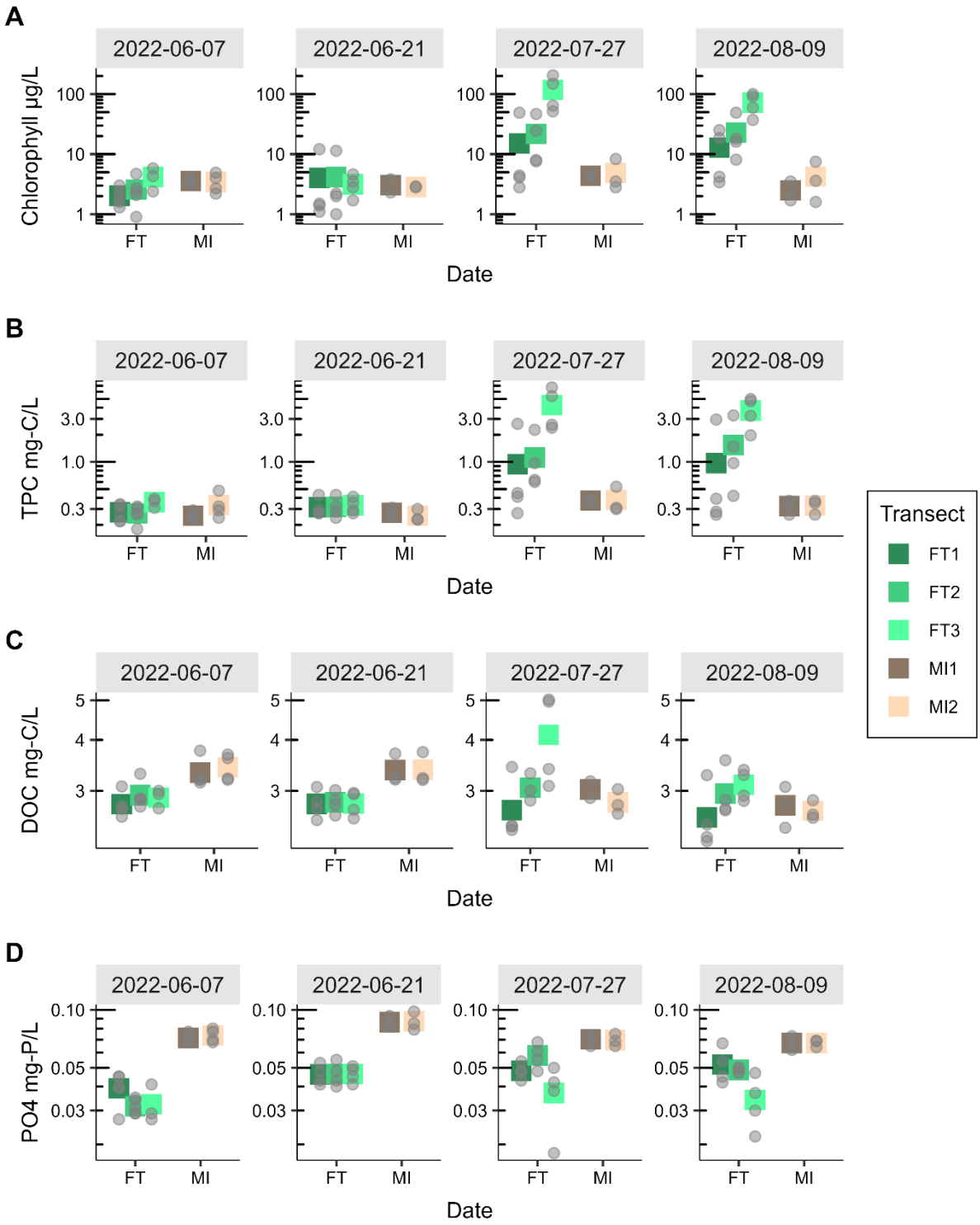

NOTES: DOC = dissolved organic carbon; FT = Franks Tract; mg-C/L = milligrams carbon per liter; mg-P/L = milligrams phosphorus per liter; MI = Mildred Island; PO_4 = orthophosphate; TPC = total particulate carbon. Colored boxes show the mean concentration of discrete samples collected from each transect. The gray points show the values of each discrete sample collected within each transect.

Source: Data compiled by U.S. Geological Survey in 2022

Figure 2.3.2-56 Chlorophyll *a*, total particulate carbon, dissolved organic carbon, and soluble reactive phosphorus, as measured in discrete samples from Franks Tract and Mildred Island.

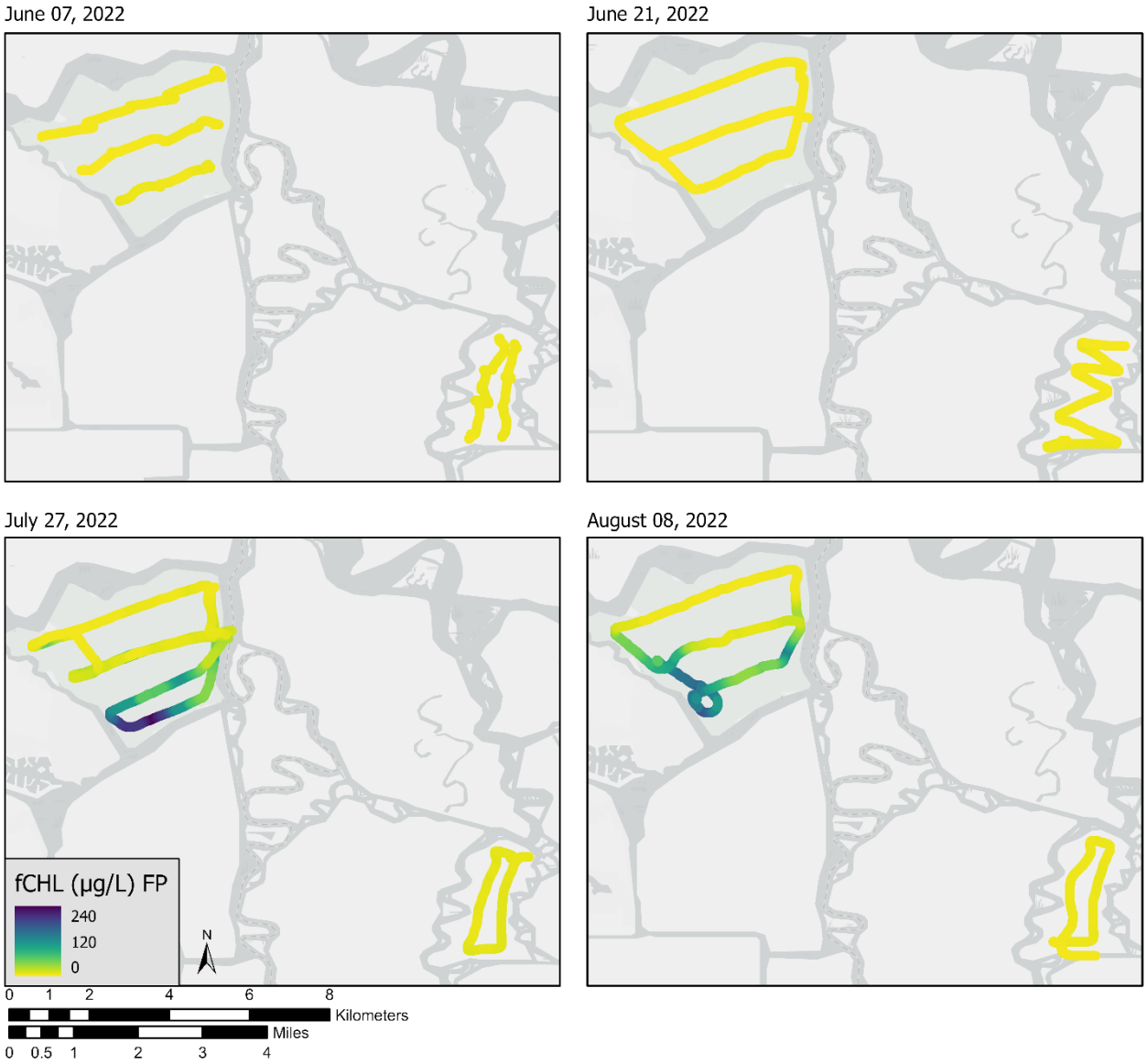

NOTES: µg/L = micrograms per liter; fCHL = chlorophyll fluorescence; FP = FluoroProbe

Source: Data compiled by U.S. Geological Survey in 2022

Figure 2.3.2-57 FluoroProbe measurements of in situ chlorophyll fluorescence in Franks Tract and Mildred Island, 2022.

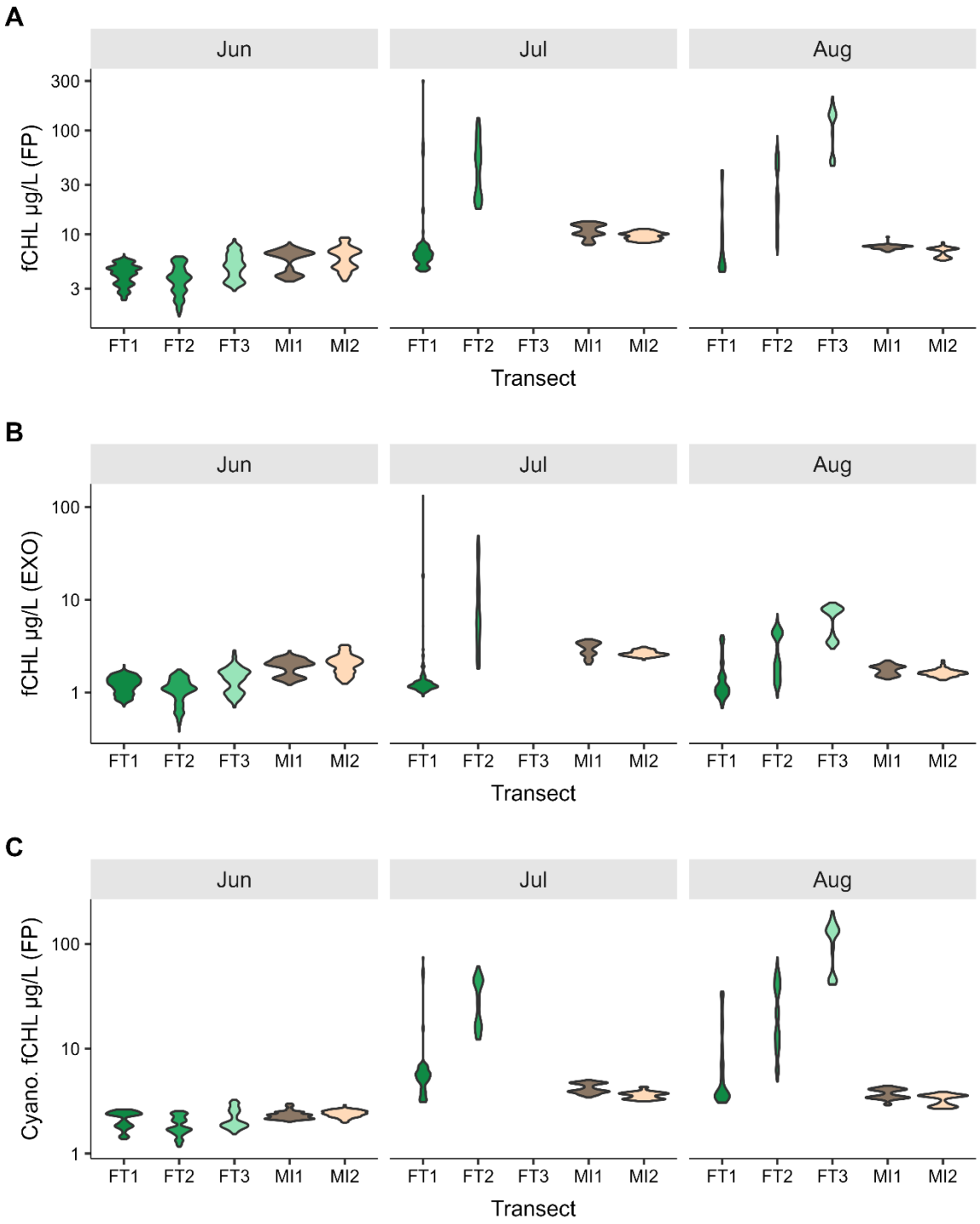

NOTES: µg/L = micrograms per liter; Cyano. = cyanobacterial; EXO = Yellow Springs Instruments (YSI) EXO2 sonde; fCHL = chlorophyll fluorescence; FP = FluoroProbe.
Comparisons: Plot set A—chlorophyll detected by the FluoroProbe between transects in Franks Tract and Mildred Island; plot set B—chlorophyll detected by the YSI EXO2 between transects in Franks Tract and Mildred Island; plot set C—cyanobacterial chlorophyll detected by the FluoroProbe between transects in Franks Tract and Mildred Island.

Source: Data compiled by U.S. Geological Survey in 2022

Figure 2.3.2-58 Comparison of high-resolution data for chlorophyll per transect during mapping of Franks Tract and Mildred Island, June, July, and August 2022.

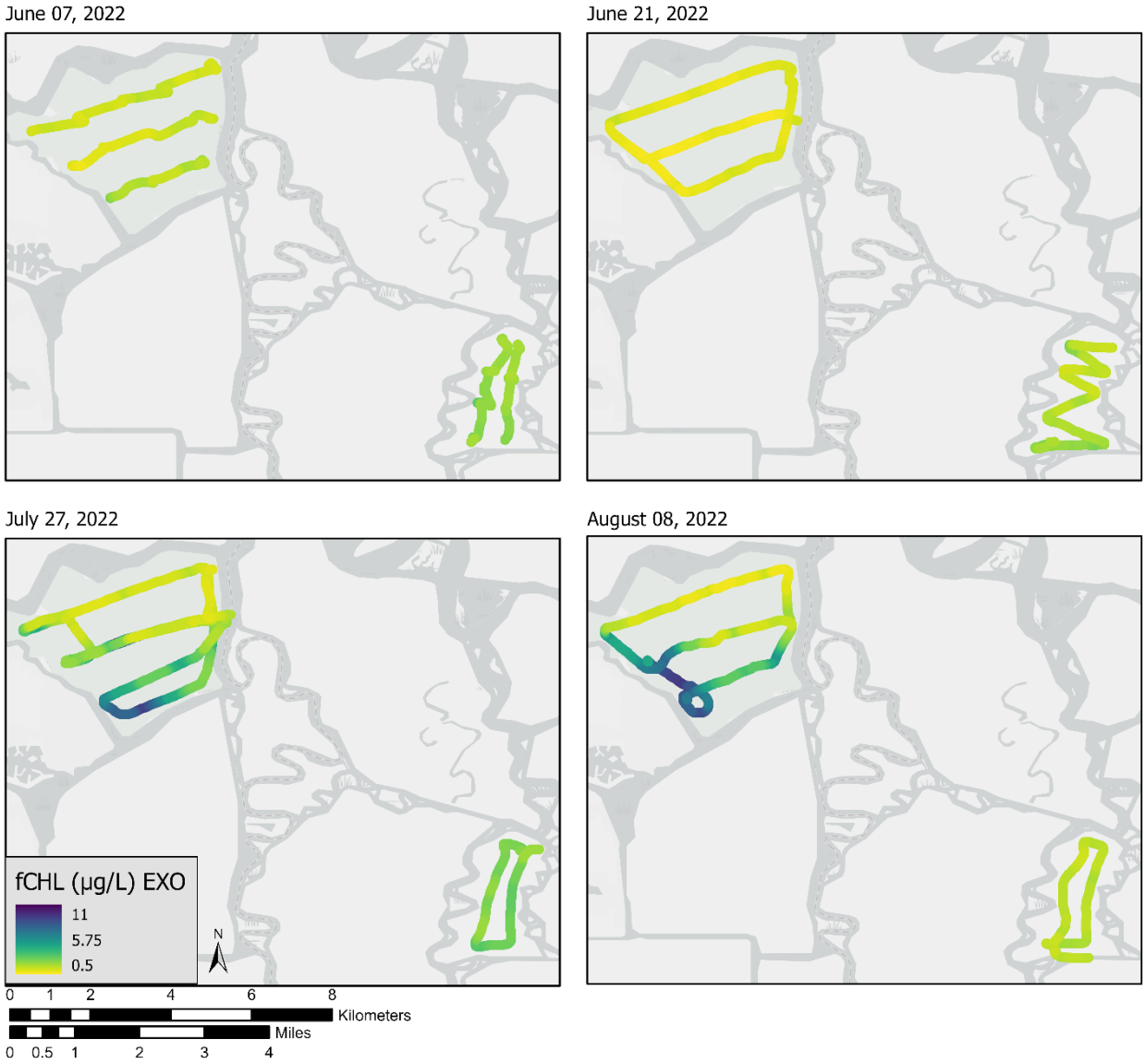

NOTES: µg/L = micrograms per liter; EXO = Yellow Springs Instruments EXO2 sonde; fCHL = chlorophyll fluorescence
Source: Data compiled by U.S. Geological Survey in 2022

Figure 2.3.2-59 YSI EXO2 measurements of chlorophyll fluorescence in Franks Tract and Mildred Island, 2022.

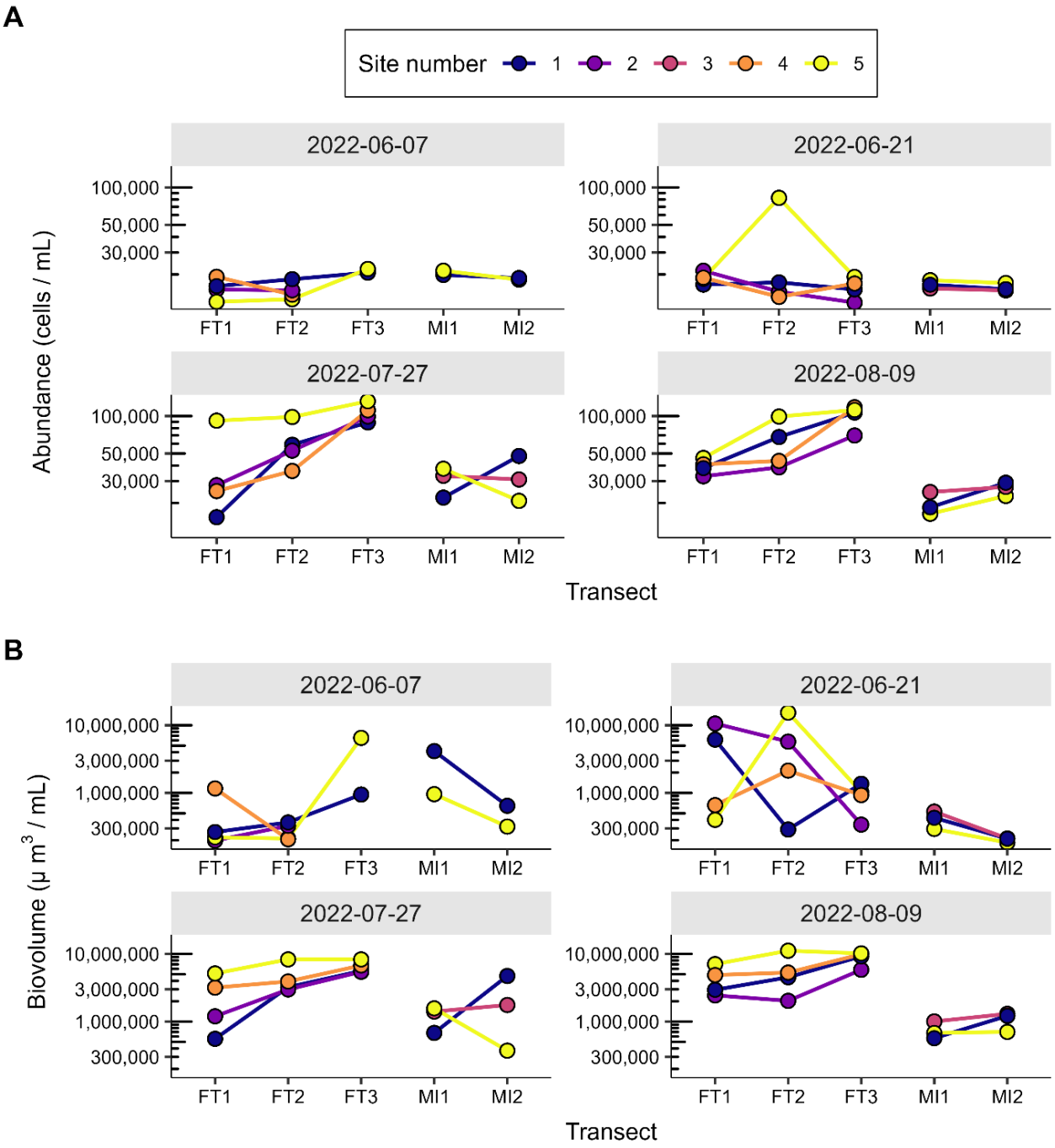

NOTES: μm^3/mL = cubic microns per milliliter; cells/mL = cells per milliliter.

Source: Data compiled by U.S. Geological Survey in 2022.

Figure 2.3.2-60 Abundance and biovolume of the total phytoplankton community in Franks Tract and Mildred Island, June, July, and August 2022.

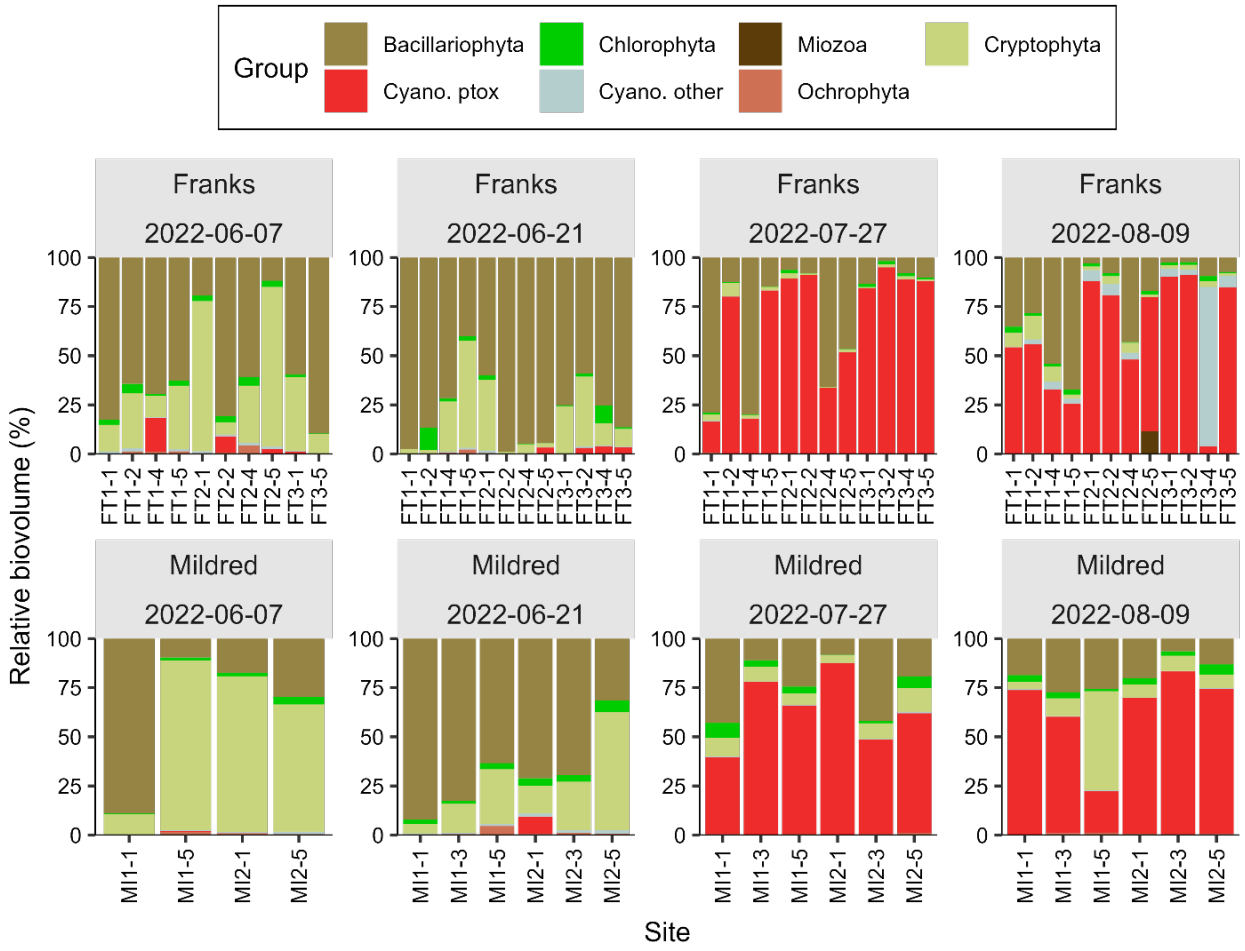

NOTE: Cyano. ptox = potentially toxigenic cyanobacterial taxa

SOURCE: Data compiled by U.S. Geological Survey in 2022

Figure 2.3.2-61 Relative biovolume of the phytoplankton community in Franks Tract and Mildred Island, June, July, and August 2022.

High-resolution mapping data also measured cyanobacterial fCHL concentrations exceeding 200 µg/L during the July and August mapping surveys (**Figure 2.3.2-62**).

In Mildred Island, cell abundance remained at fewer than 50,000 cells/mL through June, July, and August (Figure 2.3.2-60); however, as in Franks Tract, in July and August the phytoplankton community shifted toward a greater proportion of potentially toxigenic cyanobacteria (Figure 2.3.2-61). The magnitude of this shift was not as large in Mildred Island as in Franks Tract, with potentially toxigenic taxa accounting for up to 60 percent of the biovolume in Mildred Island but up to 80 percent of the biovolume in Franks Tract (Figure 2.3.2-61).

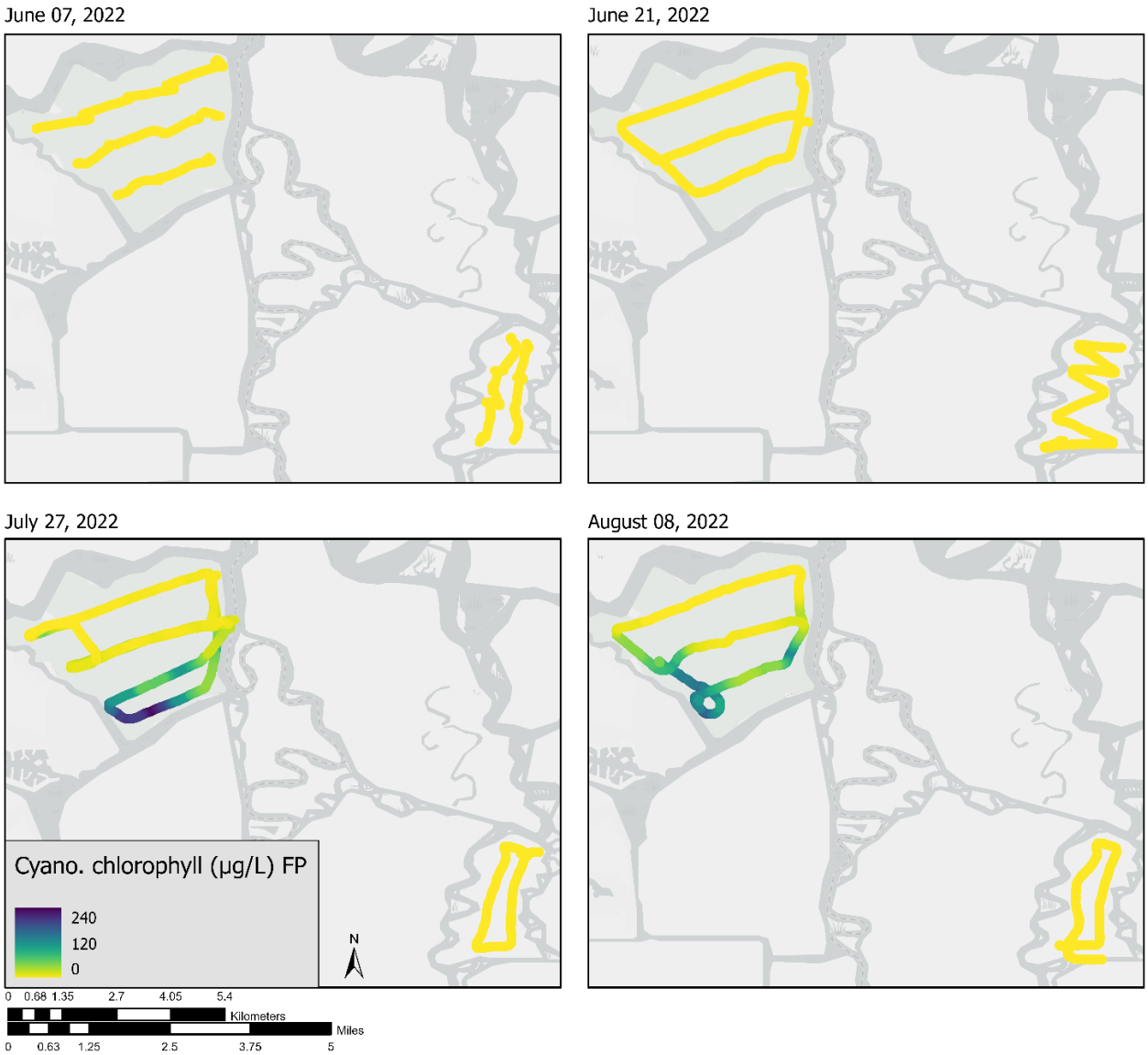

NOTES: µg/L = micrograms per liter; Cyano. = cyanobacterial; FP = FluoroProbe
Source: Data compiled by U.S. Geological Survey in 2022

Figure 2.3.2-62 FluoroProbe measurements of cyanobacterial chlorophyll in Franks Tract and Mildred Island, 2022.

The most abundant potentially toxigenic taxa in Franks Tract were *Dolichospermum*, followed by *Aphanizomenon*, *Planktothrix*, and *Microcystis* (**Figure 2.3.2-63** and **Figure 2.3.2-64**). Once *Dolichospermum* concentrations exceeded 10,000 cells/mL, there was a positive relationship between *Dolichospermum* abundance and overall chlorophyll concentration (Figure 2.3.2-63). All these potentially toxigenic taxa, except *Planktothrix*, were also observed in Mildred Island. *Aphanizomenon* and *Microcystis* had similar cellular abundances at Mildred Island and Franks Tract, but maximum *Dolichospermum* abundances were about 10 times higher in Franks Tract than

in Mildred Island (Figure 2.3.2-64). *Microcystis* was detected at Franks Tract and Mildred Island less frequently than *Dolichospermum* or *Aphanizomenon*. *Microcystis* was not observed in any of the June samples and was observed in only two of the three Franks Tract transects in July and August.

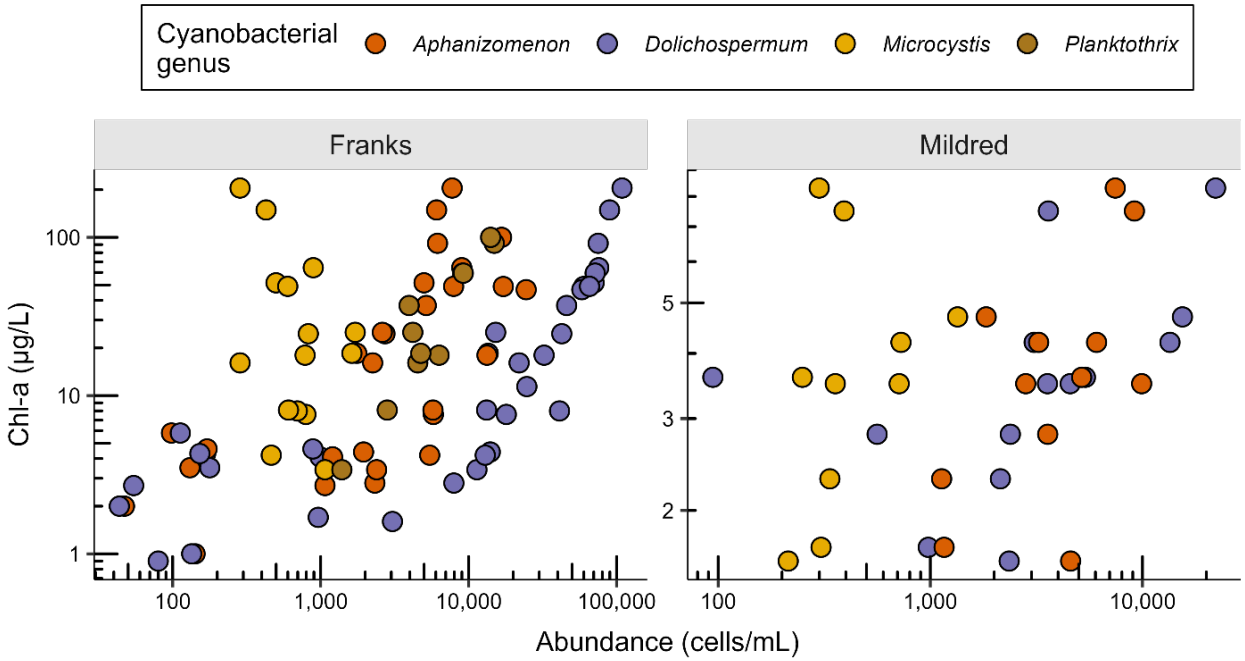

NOTES: µg/L = micrograms per liter; cells/ML = cells per milliliter; Chl-a = chlorophyll *a*

Source: Data compiled by U.S. Geological Survey in 2022

Figure 2.3.2-63 Relationship between abundance of potentially toxigenic cyanobacterial genera and discrete chlorophyll *a* concentration.

Analyzing the phytoplankton community's composition with non-metric multidimensional scaling shows that the July 27 and August 9 samples from Franks Tract transects 2 and 3 are most different from the other samples collected (**Figure 2.3.2-65**). Although the abundance of all the potentially toxigenic taxa is strongly associated with the first non-metric multidimensional scaling axis, the association is strongest for *Dolichospermum*.

Before 2022, most documented cyanobacterial blooms in the Delta were dominated by *Microcystis* or *Aphanizomenon*, not *Dolichospermum*. During 2004–2008 and 2014–2018, *Dolichospermum* was a minor member of the phytoplankton community and was consistently outnumbered by *Microcystis* cells in the Delta (Lehman et al. 2013, 2017, 2021). From June to October 2011, however, *Dolichospermum* was present more frequently than *Microcystis* at DWR EMP station D19 in Franks Tract (Mioni et al. 2011) (Figure 2.3.2-51). In 2011, *Dolichospermum* was observed at station D19 in July, August, and September, with abundances ranging from 3,042 to 14,621 cells/mL.

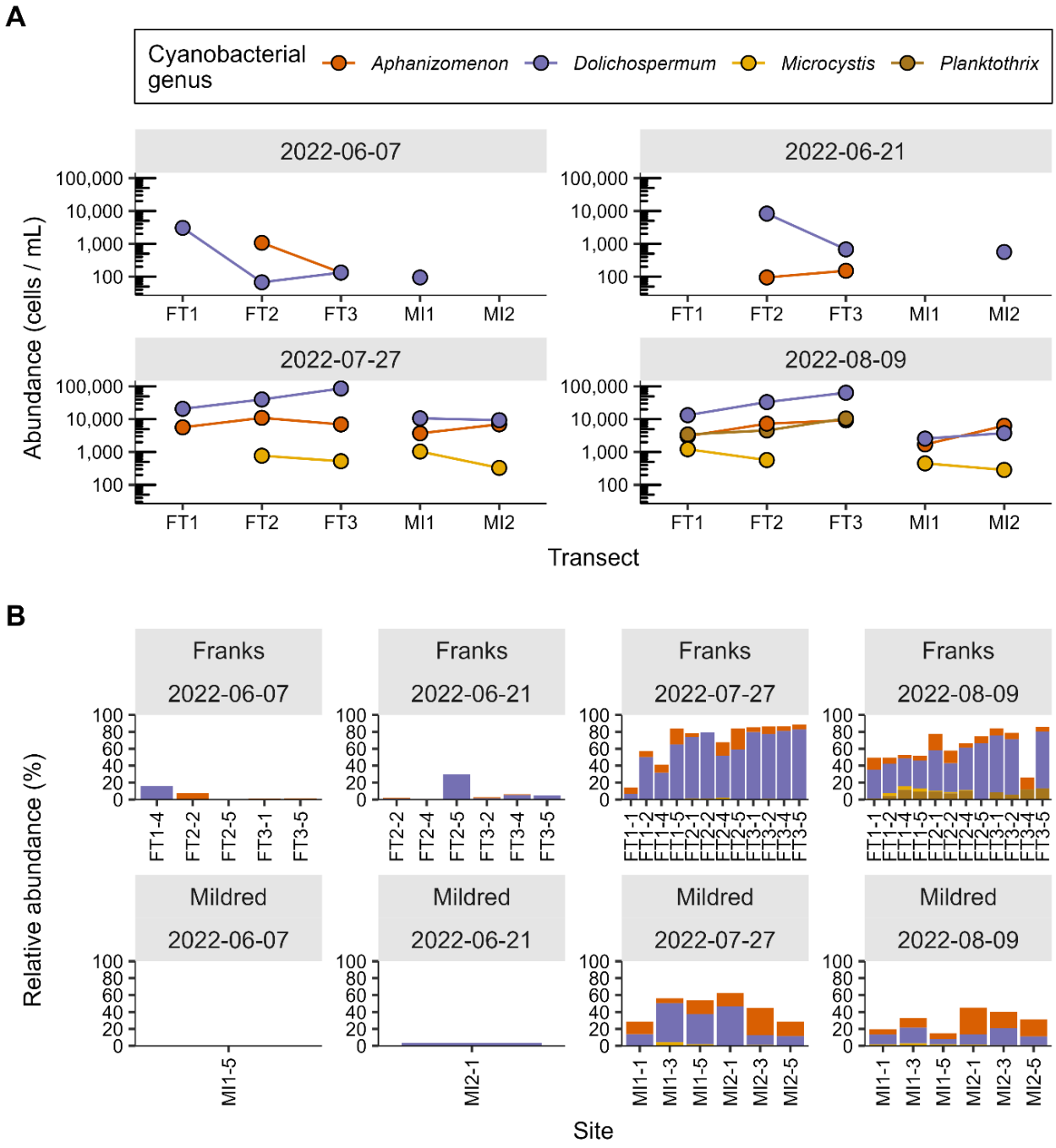

Source: Data compiled by U.S. Geological Survey in 2022

Figure 2.3.2-64 Abundance and relative cell abundance of potentially toxigenic cyanobacterial genera present across Franks Tract and Mildred Island sampling transects in 2022.

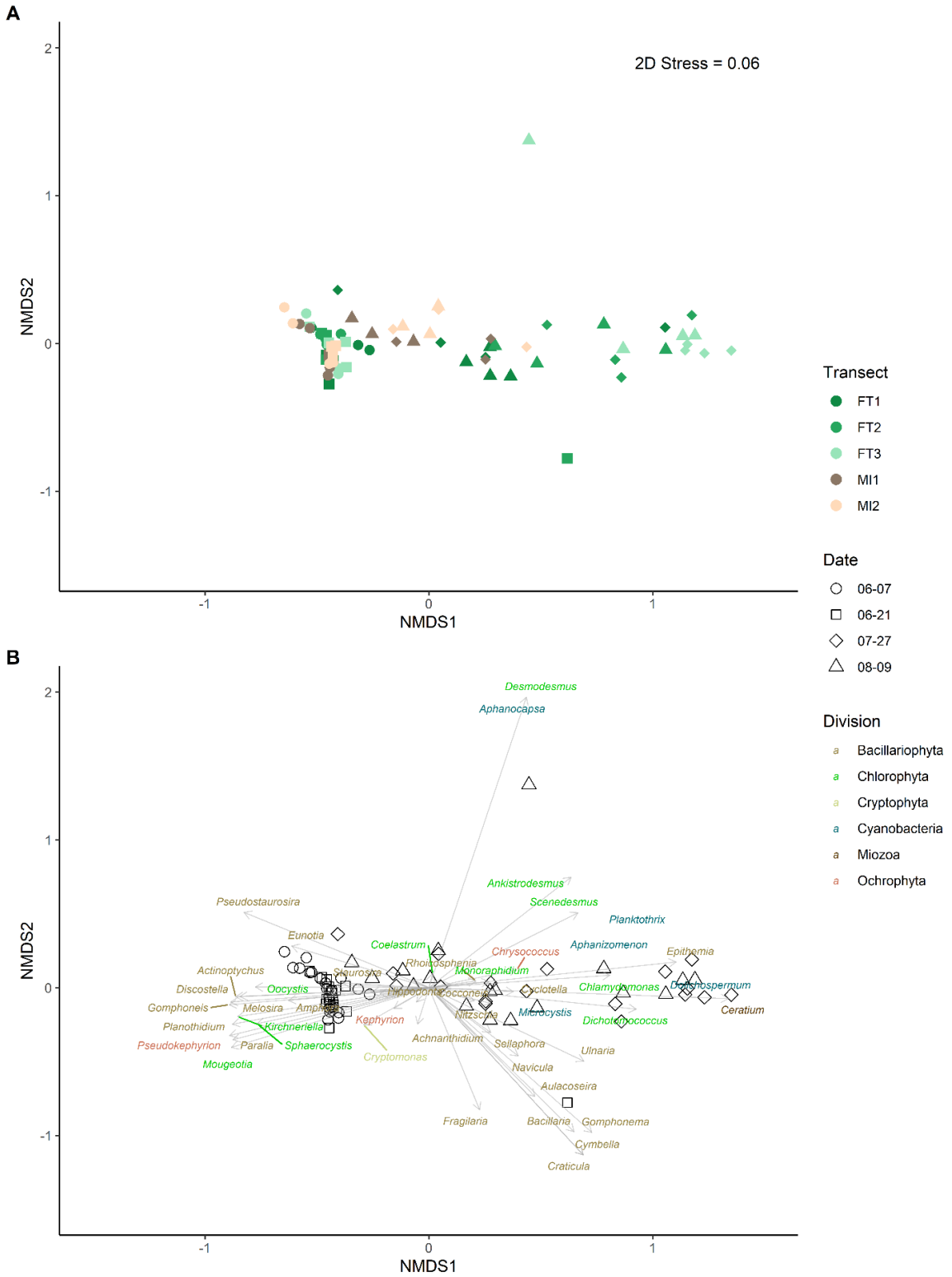

NOTE: Plot A highlights the differences between the five transects in Franks Tract (shown in shades of green) and Mildred Island (shown in shades of brown) in June, July, and August 2022 (shape). Plot B includes species scores of the genera present, color-coded by their respective division. Final 2D stress score was 0.06.

SOURCE: Data compiled by U.S. Geological Survey in 2022

Figure 2.3.2-65 Non-metric multidimensional scaling ordination plot of phytoplankton cell abundance based on Bray-Curtis distances.

Microcystis was observed only in July, but at 82,131 cells/mL, which made *Microcystis* about six times more abundant than *Dolichospermum* on that date (14,621 cells/mL of *Dolichospermum*). *Aphanizomenon* is frequently observed across the Delta, and it was even the most dominant in the Central Delta in 2011 (EMP stations D16, D19, D26, and D28A; Mioni et al. 2011). After *Microcystis*, *Aphanizomenon* is often the next most abundant potentially toxigenic cyanobacteria (Lehman et al. 2021).

Water Quality

Similar to chlorophyll concentrations, temperature and specific conductance were highest in the western and southern areas of Franks Tract in June, July, and August 2022. In July and August, temperature was highest in the southwestern area of Franks Tract (**Figure 2.3.2-66**). Similar to temperature, specific conductance in July and August was higher along the western area of Franks Tract (**Figure 2.3.2-67**). Temperatures in July and August 2022 were approximately 2°C higher in Mildred Island than in Franks Tract (**Figure 2.3.2-68**D); however, conductance was higher in Franks Tract than in Mildred Island (400–800 µS/cm versus less than 450 µS/cm; Figure 2.3.2-68C).

Nitrate concentrations were also higher in the southwestern section of Franks Tract on July 27 and August 9 (**Figure 2.3.2-69** and **Figure 2.3.2-70**). This pattern was particularly distinct on July 27, when some of the highest high-resolution SUNA nitrate concentrations were measured (Figure 2.3.2-70), although higher nitrate concentrations also extend along the eastern edge of Franks Tract on this date. In August, the nitrate concentration along transect FT3 (mean = 0.04, max = 0.06 mg-N/L) was double the concentration along transects FT2 (mean = 0.02, max= 0.04 mg-N/L) and FT1 (mean = 0.01, max = 0.03 mg-N/L).

Nitrate concentrations were generally higher in June. The average high-resolution SUNA nitrate concentrations in June across the two Mildred Island transects were 0.14 and 0.16 milligrams nitrogen per liter (mg-N/L), while the averages of the three Franks Tract transects were all below 0.06 mg-N/L. In July and August, SUNA nitrate concentrations were below 0.05 mg-N/L across Franks Tract and Mildred Island. However, nitrate concentrations increased along transect FT3 in August, and this pattern was seen in both continuous and discrete samples (Figure 2.3.2-69 and **Figure 2.3.2-71**A, respectively).

Nitrate + nitrite concentrations from discrete samples were highest at about 0.15 mg-N/L in Mildred Island during the two sampling events in June, and then decreased to below 0.05 mg-N/L at all sites in July and August (Figure 2.3.2-71A). In Franks Tract, the maximum nitrate + nitrite and ammonium concentrations never exceeded 0.1 mg-N/L, while in June the

maximum values of nitrate + nitrite in Mildred Island were 0.21 mg-N/L. Ammonium concentrations were at the detection limit (0.02 mg-N/L) at most sites. The highest ammonium concentrations were measured along transect FT3 on July 27, reaching a maximum of 0.09 mg-N/L.

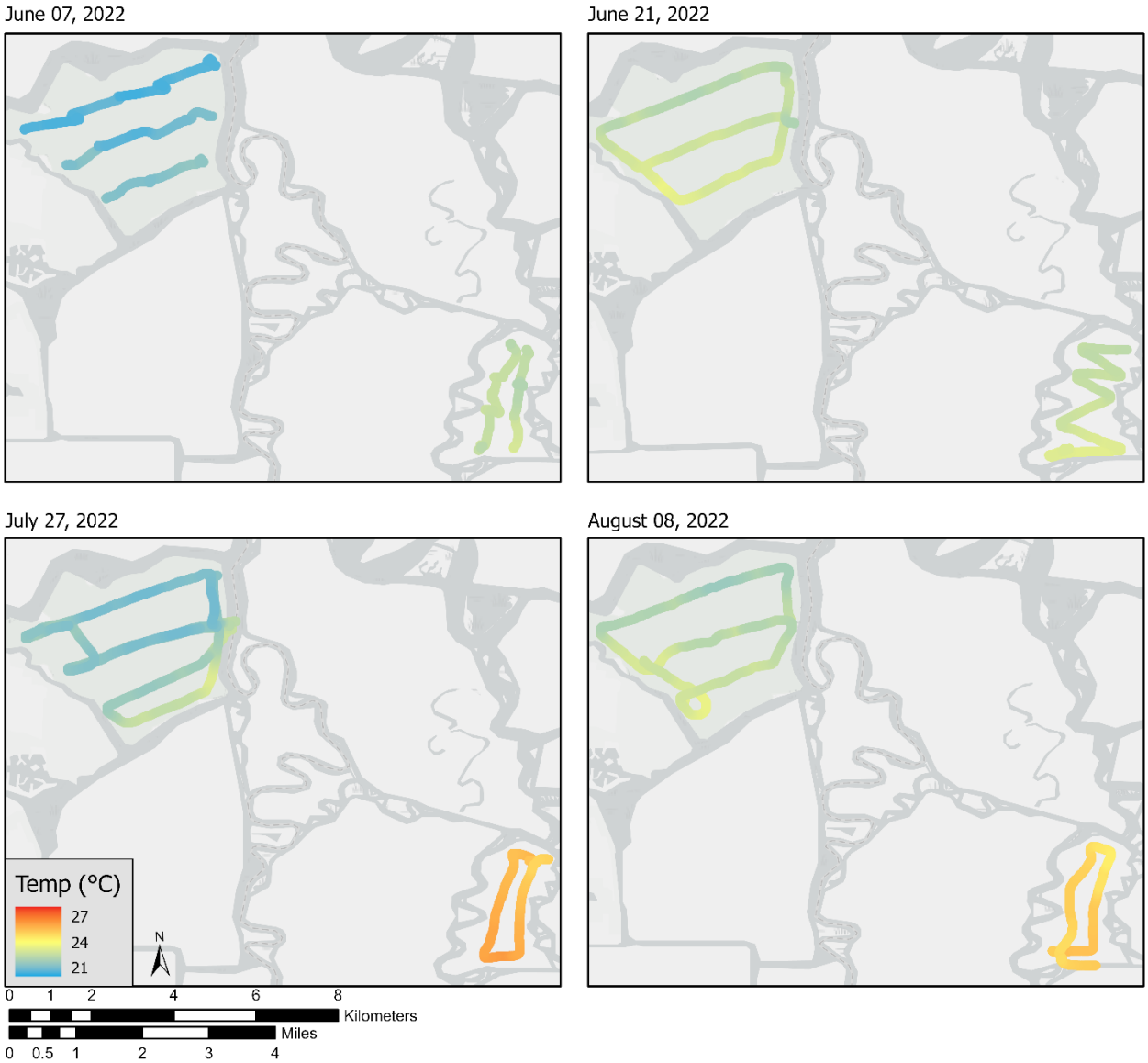

NOTE: °C = degrees Celsius

Figure 2.3.2-66 YSI EXO2 measurements of temperature in Franks Tract and Mildred Island, 2022.

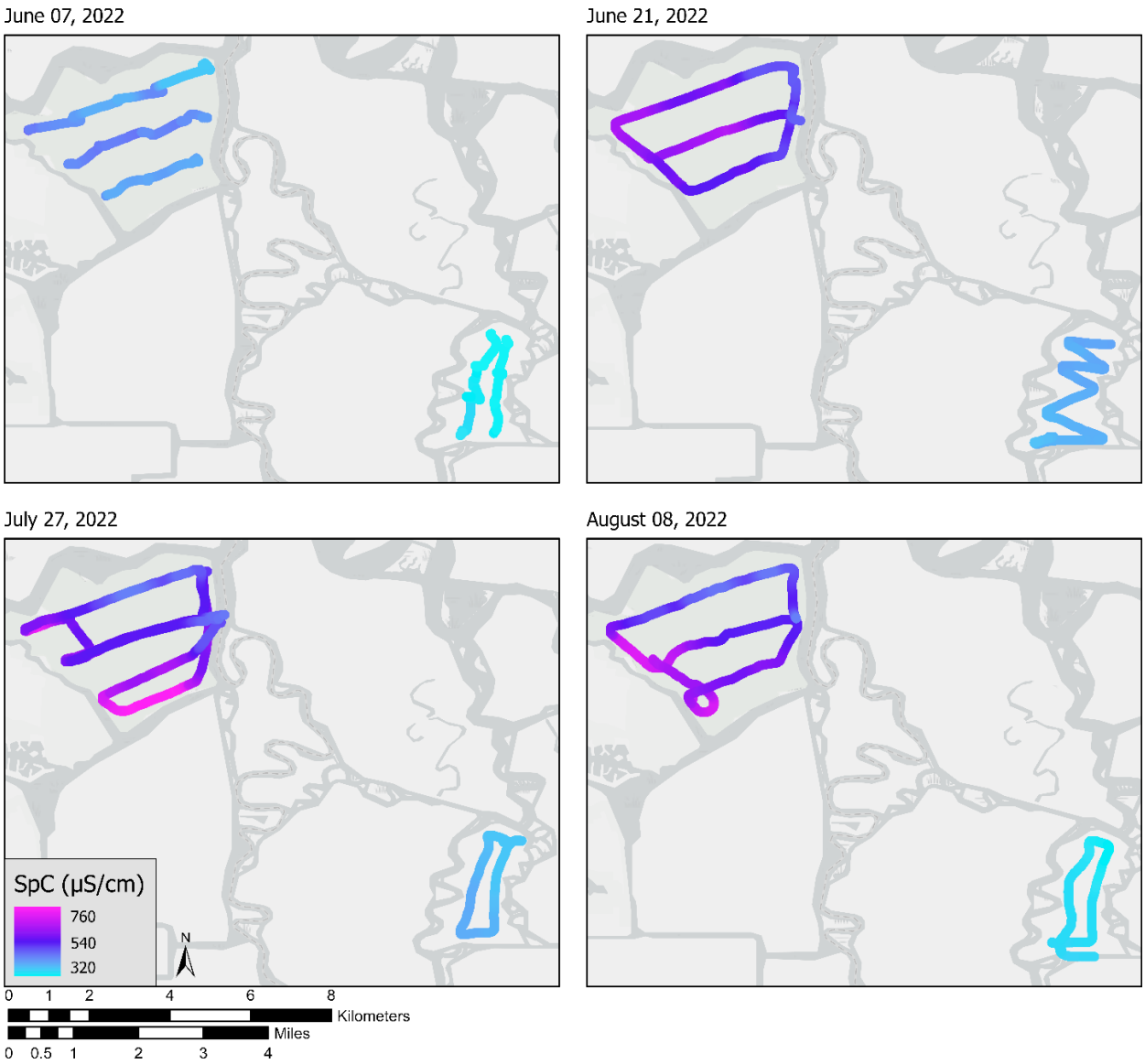

NOTES: µS/cm = microsiemens per centimeter; SpC = specific conductance

Figure 2.3.2-67 YSI EXO2 measurements of specific conductance in Franks Tract and Mildred Island, 2022.

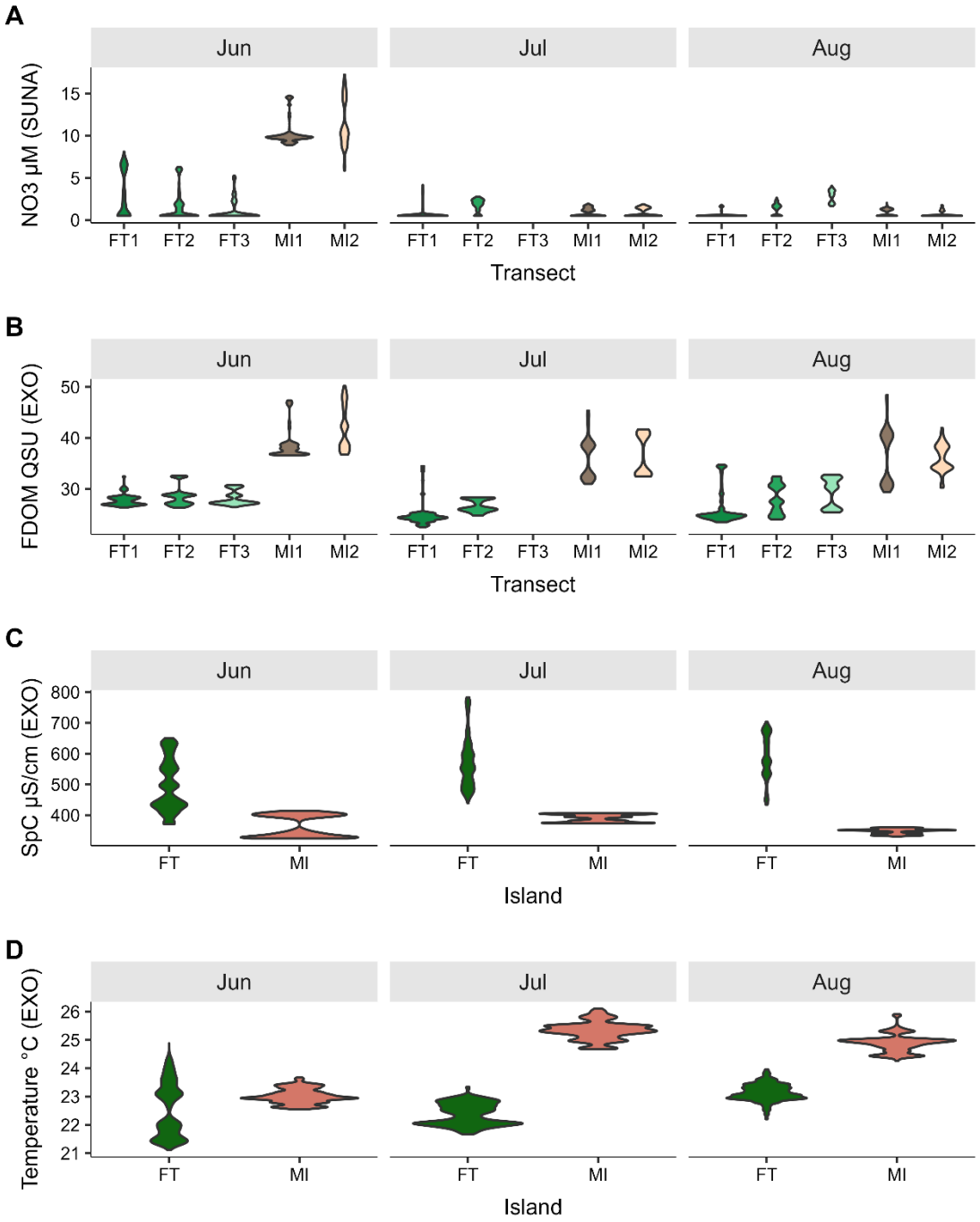

NOTES: °C = degrees Celsius; µM = micromoles per liter; µS/cm = microsiemens per centimeter; EXO = Yellow Springs Instruments EXO2 sonde; fDOM = fluorescent dissolved organic matter; FT = Franks Tract; MI = Mildred Island; NO_3 = nitrate; SpC = specific conductance; SUNA = Submersible Ultraviolet Nitrate Analyzer.
(A) Nitrate (mg/L) detected by SUNA. (B) Fluorescent dissolved organic matter (quinine sulfate units, QSU) detected by EXO. (C) Specific conductance detected by EXO. (D) Temperature detected by EXO.

Source: Data compiled by U.S. Geological Survey in 2022

Figure 2.3.2-68 Comparisons of high-resolution water quality parameters observed during mapping of Franks Tract and Mildred Island during June, July, and August 2022.

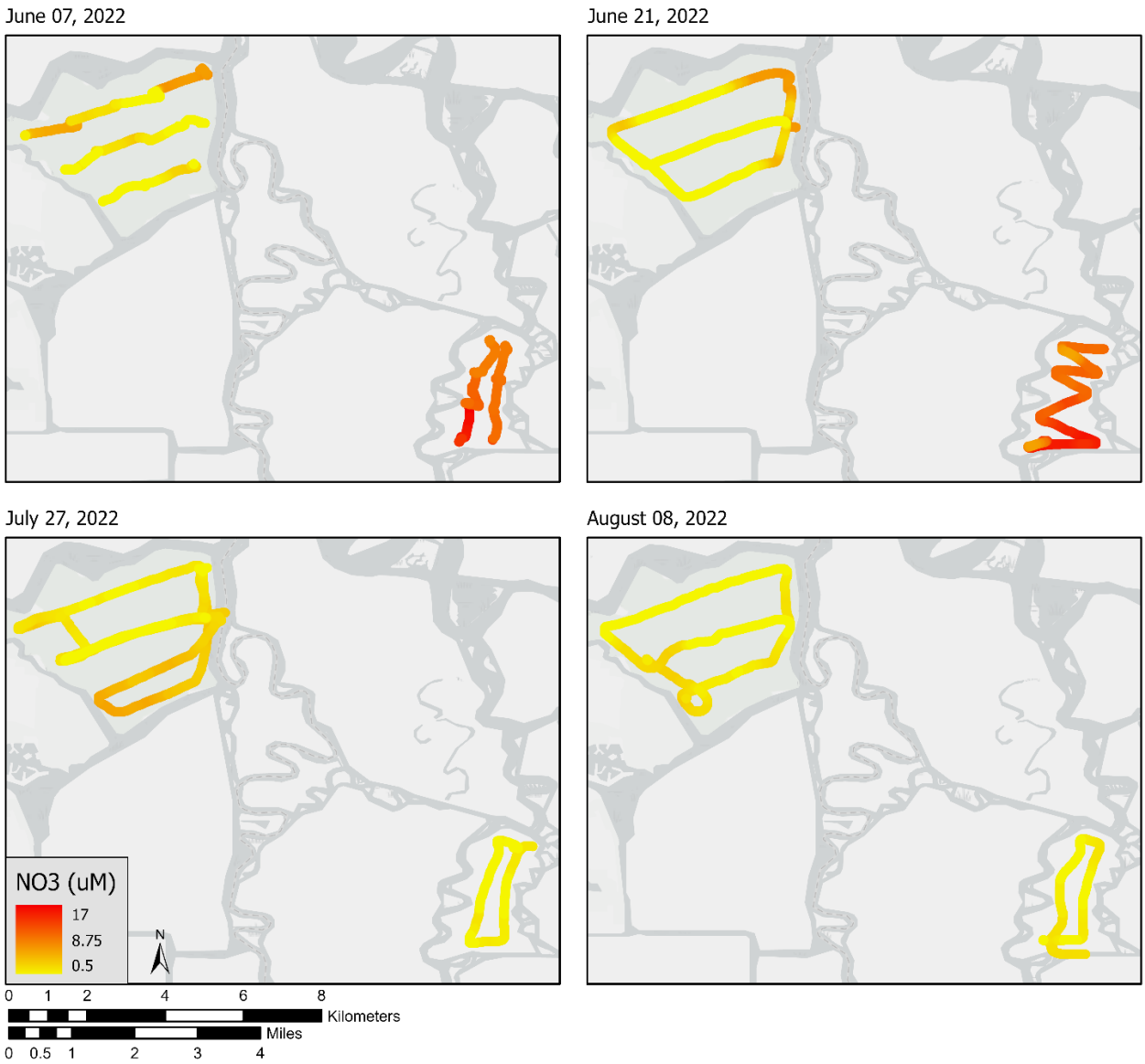

NOTES: µM = micromoles per liter; NO_3 = nitrate

Figure 2.3.2-69 Submersible Ultraviolet Nitrate Analyzer measurements of nitrate in Franks Tract and Mildred Island, 2022.

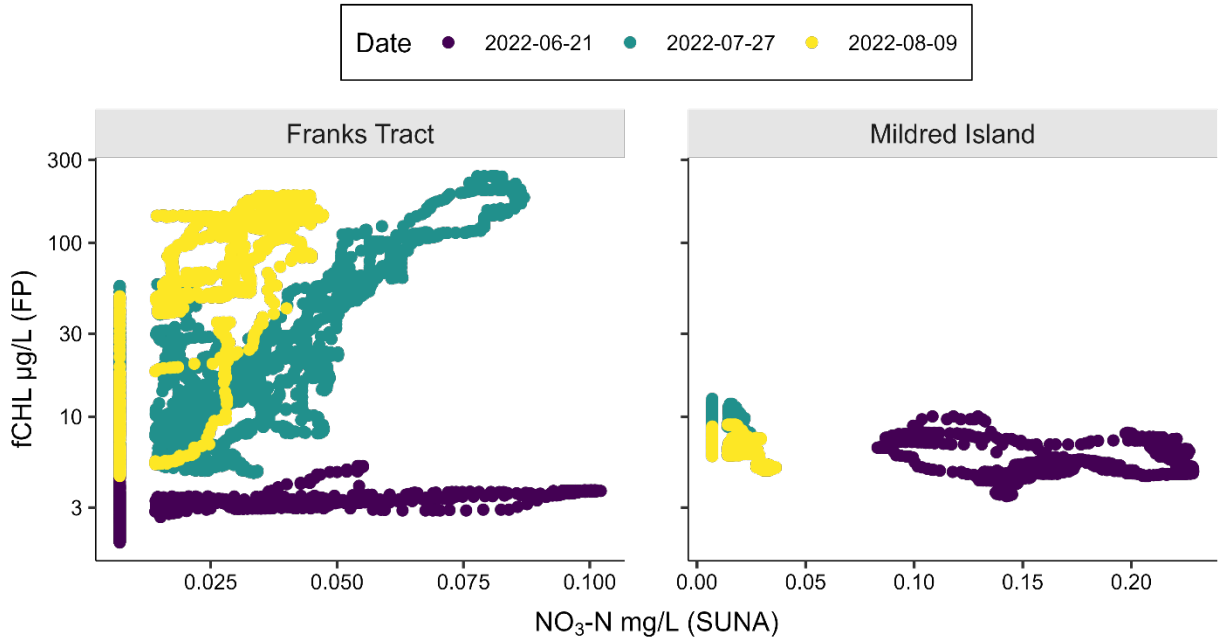

NOTES: µg/L = micrograms per liter; fCHL = chlorophyll fluorescence; FP = FluoroProbe; mg/L = milligrams per liter; NO_3-N = nitrate nitrogen; SUNA = Submersible Ultraviolet Nitrate Analyzer

Figure 2.3.2-70 Relationship between high-resolution chlorophyll from the FluoroProbe and Submersible Ultraviolet Nitrate Analyzer nitrate concentrations.

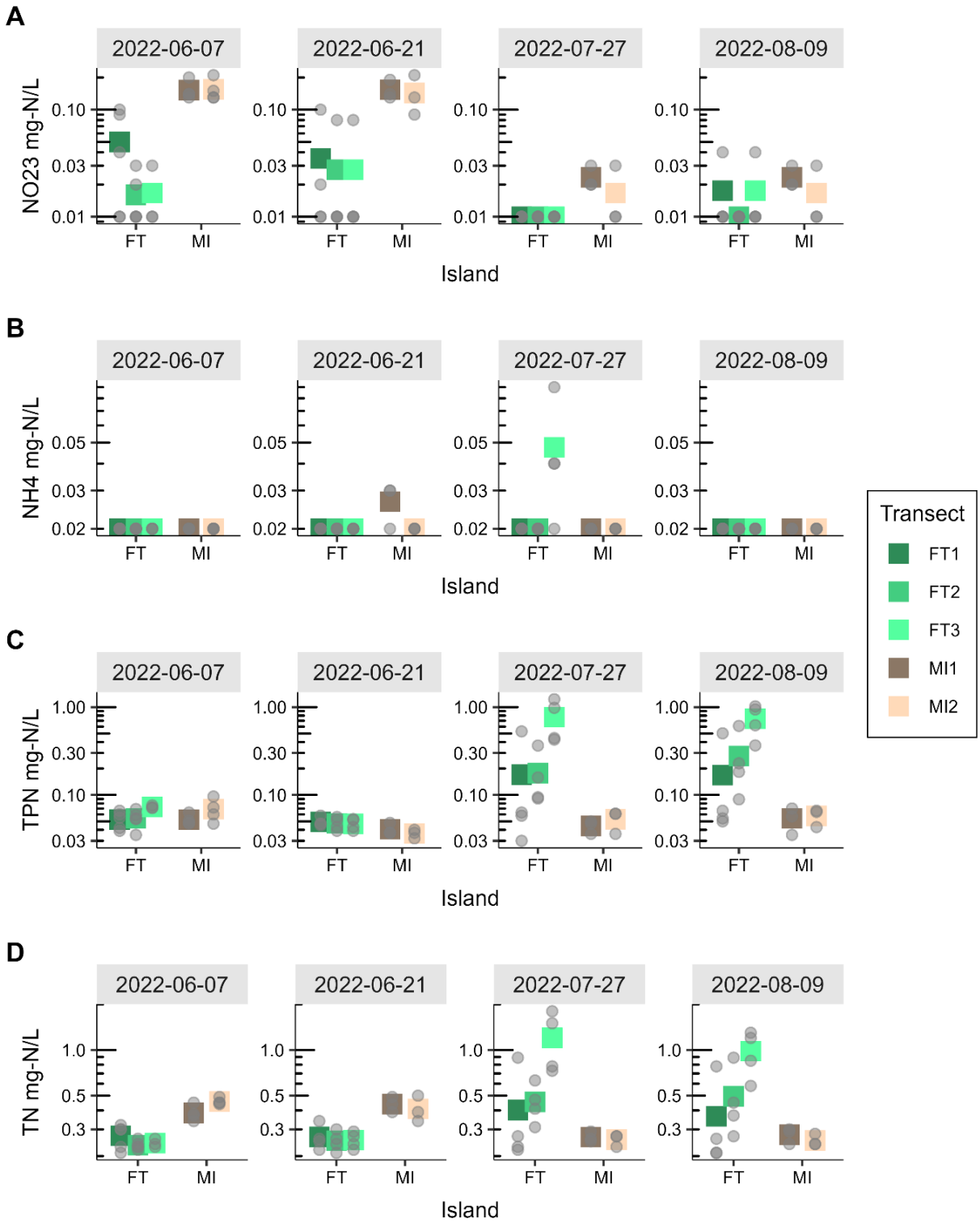

NOTES: FT = Franks Tract; MI = Mildred Island.
Colored boxes show the mean concentration of discrete samples collected from each transect. The gray points show the values of each discrete sample.

SOURCE: Data compiled by U.S. Geological Survey in 2022

Figure 2.3.2-71 Nitrogen forms measured in discrete samples collected from Franks Tract and Mildred Island.

While dissolved inorganic nitrogen concentrations remained low, total particulate nitrogen in Franks Tract increased up to tenfold in July and August compared to June (Figure 2.3.2-69C). In June, the average particulate nitrogen concentration across the three Franks Tract transects ranged from 0.047 to 0.073 mg-N/L. In July and August, the average concentration tripled along transect FT1, to 0.17 mg-N/L, but increased approximately tenfold along transect FT3, to 0.7 mg-N/L (Figure 2.3.2-69C). By contrast, the average concentration of total particulate nitrogen along the Mildred Island transects ranged from 0.04 to 0.07 mg-N/L across all sampling dates. The highest chlorophyll concentrations occurred at the locations of some of the lowest nitrate + nitrite and ammonium concentrations (**Figure 2.3.2-72**A and B). This is likely because phytoplankton uptake drew down dissolved inorganic nitrogen at a faster rate than it could be replaced. Concentrations of both total particulate nitrogen and chl a increased in July and August (Figure 2.3.2-56 and Figure 2.3.2-71), providing evidence for the hypothesis that nitrate and ammonium were being incorporated into new phytoplankton biomass.

Unlike nitrogen, which had notably different concentrations between June and July, orthophosphate concentrations were relatively stable throughout the sampling dates (Figure 2.3.2-72D). The average orthophosphate concentration along the Franks Tract transects ranged from 0.03 to 0.06 milligrams phosphorus per liter (mg-P/L). The southern transect, FT3, had slightly lower average PO_4 concentrations, with averages of 0.03 mg-P/L compared to 0.04 to 0.05 mg-P/L for transects FT1 and FT2. Orthophosphate concentrations were higher in Mildred Island, with averages ranging from 0.07 to 0.09 mg-P/L.

The ratios of nitrogen and phosphorus concentrations can provide information about how phytoplankton are using nutrients and which nutrients may be limiting to phytoplankton growth (Reynolds 1999; Chorus and Spijkerman 2021). The ratio of total nitrogen to total phosphorus (TN:TP) represents the overall nutrient pool of a waterbody but does not represent what is bioavailable. The ratio of dissolved inorganic nitrogen to dissolved inorganic phosphorus (DIN:DIP) represents what is available to phytoplankton for uptake and new growth. Low ratios (less than 9–20) indicate that nitrogen may become limiting first, and high ratios (greater than 20–50) indicate that phosphorus may become limiting first (Downing and McCauley 1992; Scott et al. 2013; Dolman et al. 2015; Chorus and Spijkerman 2021). However, nutrient limitation cannot be determined by ratios alone. If nutrients are replete and at concentrations that are not limiting to phytoplankton, then nutrients are not limiting even if ratios are high or low. Proposed values for phosphorus and nitrogen uptake limitation from the literature are approximately 0.01 mg-P/L and 0.1 mg-N/L (Chorus and Spijkerman 2021). Both nutrient concentrations and ratios need to be considered when evaluating nutrient limitation.

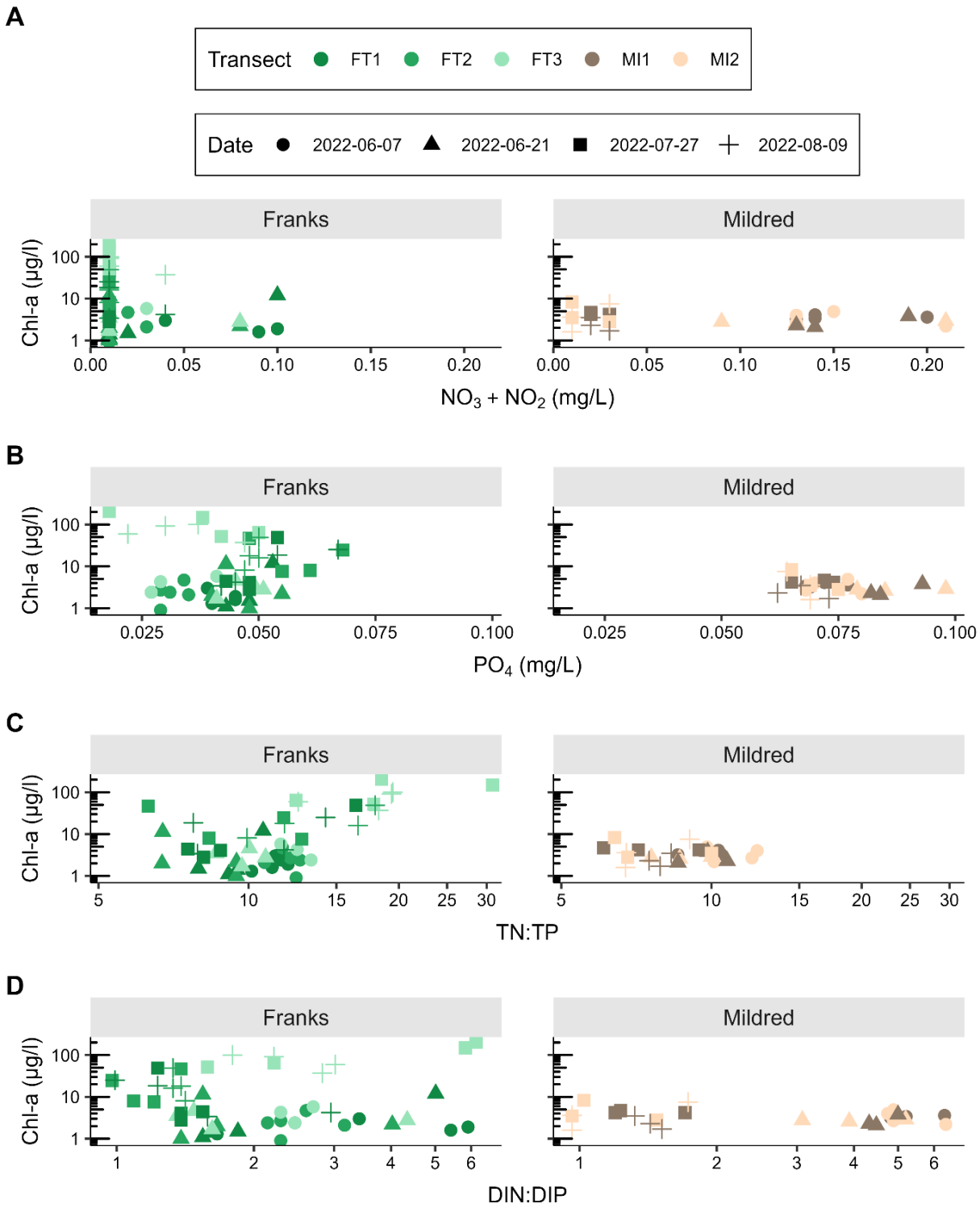

Notes: µg/L = micrograms per liter; Chl-a = chlorophyll *a*; mg/L = milligrams per liter.
(A) Nitrate and nitrite (NO_3 + NO_2). (B) Soluble reactive phosphorus (PO_4). (C) Molar ratio of total nitrogen to total phosphorus (TN:TP) scaled on a $\log_{10}$ x-axis. (D) Molar ratio of dissolved inorganic nitrogen (NO_3 + NO_2 + NH_4) to dissolved inorganic phosphorus (SRP, PO_4) (DIN:DIP) scaled on a $\log_{10}$ x-axis.

Source: Data compiled by U.S. Geological Survey in 2022

Figure 2.3.2-72 Relationship between discrete chlorophyll *a* concentrations and nutrient concentrations or ratios.

Molar ratios of TN:TP mostly ranged from 6 to 14 in Franks Tract and Mildred Island (Figure 2.3.2-72C and D). Only at station FT1-5 and stations along transects FT2 and FT3 during July and August did these ratios increase above 14, with a maximum value of 31 on July 27 at station FT3-4 (Figure 2.3.2-72C). In Franks Tract, discrete chlorophyll concentrations were above 50 µg/L across the entire range of TN:TP ratios; however, the highest chlorophyll concentrations occurred when TN:TP was greater than 15 (Figure 2.3.2-72C), suggesting that new inputs of nitrogen supported the bloom. The DIN:DIP ratio ranged from 0.9 to 6.4 in both Franks Tract and Mildred Island (Figure 2.3.2-72D). DIN:DIP decreased between June and July and August, not exceeding 4.1 in Franks Tract and 2 in Mildred Island after the June sampling.

Both the low concentrations of dissolved inorganic nitrogen (less than 0.1 mg-N/L) and low DIN:DIP ratios (less than 9) in Franks Tract suggest that nitrogen would become limiting to phytoplankton growth before phosphorus. Nitrogen limitation can be alleviated by nitrogen fixation, and the ability of *Dolichospermum* to fix nitrogen is one of the distinguishing traits differentiating *Microcystis* from *Dolichospermum*. This trait may have contributed to the dominance of *Dolichospermum* in Franks Tract. However, nitrogen fixation is energetically costly, requiring high amounts of light to provide energy to support the fixation process (De Tezanos Pinto and Litchman 2010; Marcarelli et al. 2022), and often results in lower growth rates when cyanobacteria fix nitrogen (Osburn et al. 2021). The shallow depth and low turbidity in Franks Tract would deliver more photons for the energetically costly task of fixing nitrogen than deeper or more turbid regions of the Delta. The dominance of a diazotrophic organism, *Dolichospermum*, in the Franks Tract bloom points to a potential role of nutrients in selecting *Dolichospermum* over *Microcystis*, which has dominated most other reported cyanobacterial blooms in the Delta.

Beyond diazotrophy, other traits distinguish *Dolichospermum* from *Microcystis*. *Dolichospermum* has a lower optimal growth temperature than *Microcystis* (Robarts and Zohary 1987). Analyzing samples collected in the Delta during the 2014 drought, Lehman et al. (2017) found that *Microcystis* was more strongly correlated with higher temperature than *Dolichospermum*. Across the United States, *Microcystis* abundances were found to be more sensitive to temperatures than *Dolichospermum* abundances (Rigosi et al. 2014). In Europe, *Dolichospermum* abundance is associated with lower concentrations of total nitrogen and total phosphorus than *Microcystis* abundance (Dolman et al. 2012). While *Microcystis* is often associated with high phosphorus concentrations, it also is very effective at acquiring phosphorus when concentrations decrease in the environment. During a bloom, inorganic phosphorus often becomes depleted, and *Microcystis* species' high affinity for phosphorus has been proposed as a mechanism

contributing to the succession of *Microcystis* over other cyanobacterial taxa (Gobler et al. 2016). Phosphorus concentrations are usually well above the concentration that could begin to limit phytoplankton uptake, approximately 0.01 mg-P/L (Jassby et al. 2008; Jabusch et al. 2018). The consistently non-limiting concentrations of dissolved orthophosphate in Franks Tract may not have given *Microcystis* a competitive advantage over *Dolichospermum* for acquiring phosphorus.

Nitrogen Resources to Support a Bloom

Although factors like light, temperature, hydrodynamics, and water residence time can affect phytoplankton abundance, nutrient availability is considered a major control of bloom formation in estuaries. It has generally been assumed that the Delta is nutrient replete (Jassby et al. 2002; Lopez et al. 2006; Dahm et al. 2016), but this study did not find nutrient concentrations to be present in excess.

Concentrations of dissolved inorganic nitrogen (NO_3 + NO_2 + NH_4) were less than 0.1 mg-N/L. Concentrations between 0.1 and 0.13 mg-N/L have been proposed as the threshold for instantaneous nitrogen limitation for phytoplankton (Reynolds 1999; Chorus and Spijkerman 2021). Therefore, phytoplankton, including cyanobacteria, may have already been straining to acquire sufficient nitrogen for growth in June, before the bloom began. Inorganic nitrogen concentrations near 0.1 mg-N/L were also measured in 2021 in Franks Tract (Hartman et al. 2022). These low nitrogen concentrations contrast with the average dissolved inorganic nitrogen concentration of 0.48 mg-N/L measured by Lopez et al. (2006) in Franks Tract, Mildred Island, and the Central Delta in 2001 and 2002. Although the Delta is generally considered nutrient replete (Jassby et al. 2002; Lopez et al. 2006), this study and Loken et al. (2022) observed potential nutrient limitation of phytoplankton.

Total nitrogen at sites along transects FT2 and FT3 more than tripled from June through August 2022 (Figure 2.3.2-55), suggesting some loading of nitrogen into the water column to account for this increase. Potential sources include (1) nitrogen fixation by cyanobacteria (*Dolichospermum* or *Aphanizomenon*), (2) fluxes of remineralized nitrogen from benthic sediments and detritus, (3) loadings from water originating in Sandmound Slough and Piper Slough and then transported into Franks Tract with the tides, (4) fluxes from aquatic vegetation, and (5) atmospheric deposition.

Nitrogen fixation is an energetically demanding process for cyanobacteria, and cyanobacterial taxa capable of fixing nitrogen do not always do so (De Tezanos Pinto and Litchman 2010; Marcarelli et al. 2022). No data were collected to confirm whether cyanobacteria in Franks Tract were fixing nitrogen. Nitrogen fixation usually occurs when nitrogen concentrations have

decreased, especially ammonium and urea, which have been shown to repress nitrogen fixation rates. Assuming that *Dolichospermum* cells fixed approximately 150 femtomols of nitrogen per cell per day (Klawonn et al. 2016; Kramer et al. 2022), 50,000 cells per mL could have fixed 0.07 mg-N/L day^{-1} of nitrogen over the course of 10 hours of daylight per day. This rate is faster than the increase in total particulate nitrogen observed in Franks Tract. On June 21, total particulate nitrogen was approximately 0.25 mg-N/L (Figure 2.3.2-55) and increased to 0.4 to 1 mg-N/L on July 27, which is a rate of 0.001 to 0.027 mg-N/L day^{-1}. Future measurements of nitrogen fixation during cyanobacterial blooms would confirm the role of diazotrophy in supplying nitrogen for cyanobacteria.

Nitrogen fluxing out of the sediments could be another potential nitrogen source that could have supported the bloom. Nitrogen fluxes from lab-incubated benthic cores were measured in Franks Tract by Cornwell et al. (2014) during September and March in 2011 and 2012. The results indicated that the benthic zone was a sink for nitrate. Ammonium patterns were not consistent, with Franks Tract being a ammonium source in September but an ammonium sink in March. Based on the range of measurements made by Cornwell et al. (2014), a flux of 100 µM NH_4-N/m^2 $hour^{-1}$ and water column depth of 2 meters convert into 0.017 mg NH_4-N/L day^{-1} efflux from the sediments into the water column. This is less than the maximum rate of increase in total particulate nitrogen (0.027 mg-N/L day^{-1}). Some of the ammonium effluxing out of the sediment would be rapidly converted to nitrate through nitrification, and Cornwell et al. (2014) found that nitrate fluxed into the sediment at rates of 100–200 µM NO_3-N/m^2 $hour^{-1}$, which would then be unavailable to phytoplankton for growth. More studies are needed to understand whether cyanobacteria are using nitrogen fluxing out of the sediments.

Nutrients could also have been delivered into Franks Tract from surrounding waterways. Sandmound and Piper sloughs have an inlet in the southwestern corner of Franks Tract. Importation of nitrogen into Franks Tract from this region could explain why total nitrogen increased only in the southern and western portions of Franks Tract and not the northern and eastern portions. If high nitrogen loading was occurring from Old River or False River, total nitrogen would be expected to increase at the northern and eastern sites, but this did not occur. Additional nutrient fluxes from aquatic vegetation or atmospheric vegetation could also contribute to nitrogen concentrations in Franks Tract. Atmospheric deposition is estimated to contribute approximately 14 percent of the total nitrogen in the San Joaquin River at Vernalis (Saleh and Domagalski 2021), but the summer contribution to Franks Tract is unknown. The contribution of nutrients from aquatic vegetation over the summer season is also unknown.

Water Age

Previous predictions of water age by the SCHISM hydrodynamic model as reported by Hartman et al. (2022) showed a sharp east-west water age gradient in Franks Tract (**Figure 2.3.2-73**). The youngest water was predicted to be present in the northeastern region (i.e., around site FT1-1) near the opening with Old River because water exchange with the San Joaquin River occurs through Old River when the drought barrier is installed. However, even with the barrier in place, water still travels through Fisherman's Cut, then False River, and enters Franks Tract near site FT1-4 (Figure 2.3.2-54); thus, the hydrodynamic models show a decrease in water age near the western opening with False River (Figure 2.3.2-73). The modeled water-age results from Hartman et al. (2022) were derived from a date in 2021 that had different hydrologic conditions from the dates in 2022 when field samples were collected. Therefore, for this report, the SCHISM model, using the same parameters as used by Hartman et al. (2022) and revised parameters, was run for the dates and approximate time of day when water-stable isotope field samples were collected (**Figure 2.3.2-74**).

The stable isotope water-age calculations are displayed relative to the northeastern sampling site (FT1-1), where age was set to zero. As a supplement to the sampling conducted in June, July, and August 2022, sampling occurred on two additional days—October 12 and November 30—to calculate water age, but parameters related to nutrients and phytoplankton were not collected on these days. Water age calculated with the discrete samples ranged from -2 days to 13 days (**Figure 2.3.2-75**), and water age calculated with the in situ Picarro data ranged from -4 days to 11 days (**Figure 2.3.2-76**). Negative water age occurred when stable isotope values were less negative than the values at site FT1-1. Water ages within Franks Tract were youngest on November 30, after the mid-November removal of the EDB.

The stable isotope water-age calculations are a function of evapotranspiration, which changes seasonally (Table 2.3.2-9). The dimensionless ratio of evaporation to inflow (E:I) is used to calculate water age and can be used to evaluate patterns of water age, albeit without units. As with water age, the E:I ratios are highest—indicating older water—along transect FT3, the southernmost transect (**Figure 2.3.2-77**). The average E:I ratios were less than 0.03 during the November 30 sampling, less than half the average in most other months. The decrease in E:I in the November data was a larger magnitude (Figure 2.3.2-77) than the decrease in water age in November (Figure 2.3.2-75). Water age in November did not decrease as much as E:I because the lower evapotranspiration rate in November increased water age, offsetting the effect of the lower E:I to decrease water age.

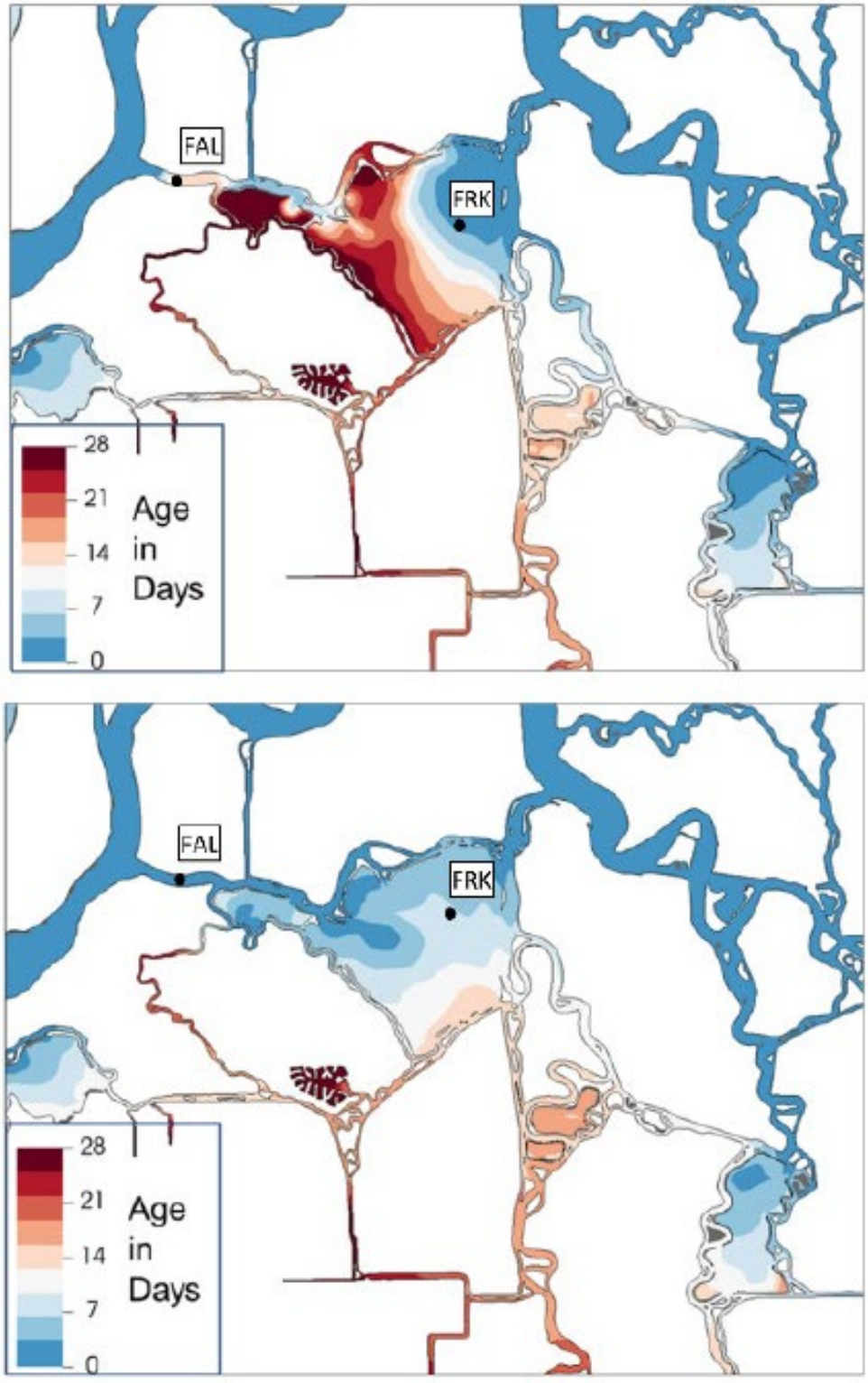

NOTES: (TOP PANEL) Water age (days since last contact with the San Joaquin River) in Franks Tract without the emergency drought barrier. (BOTTOM PANEL) Water age with the barrier.

SOURCE: Hartman et al. 2021

Figure 2.3.2-73 DWR hydrodynamic modeling results showing water age in Franks Tract without and with the emergency drought barrier.

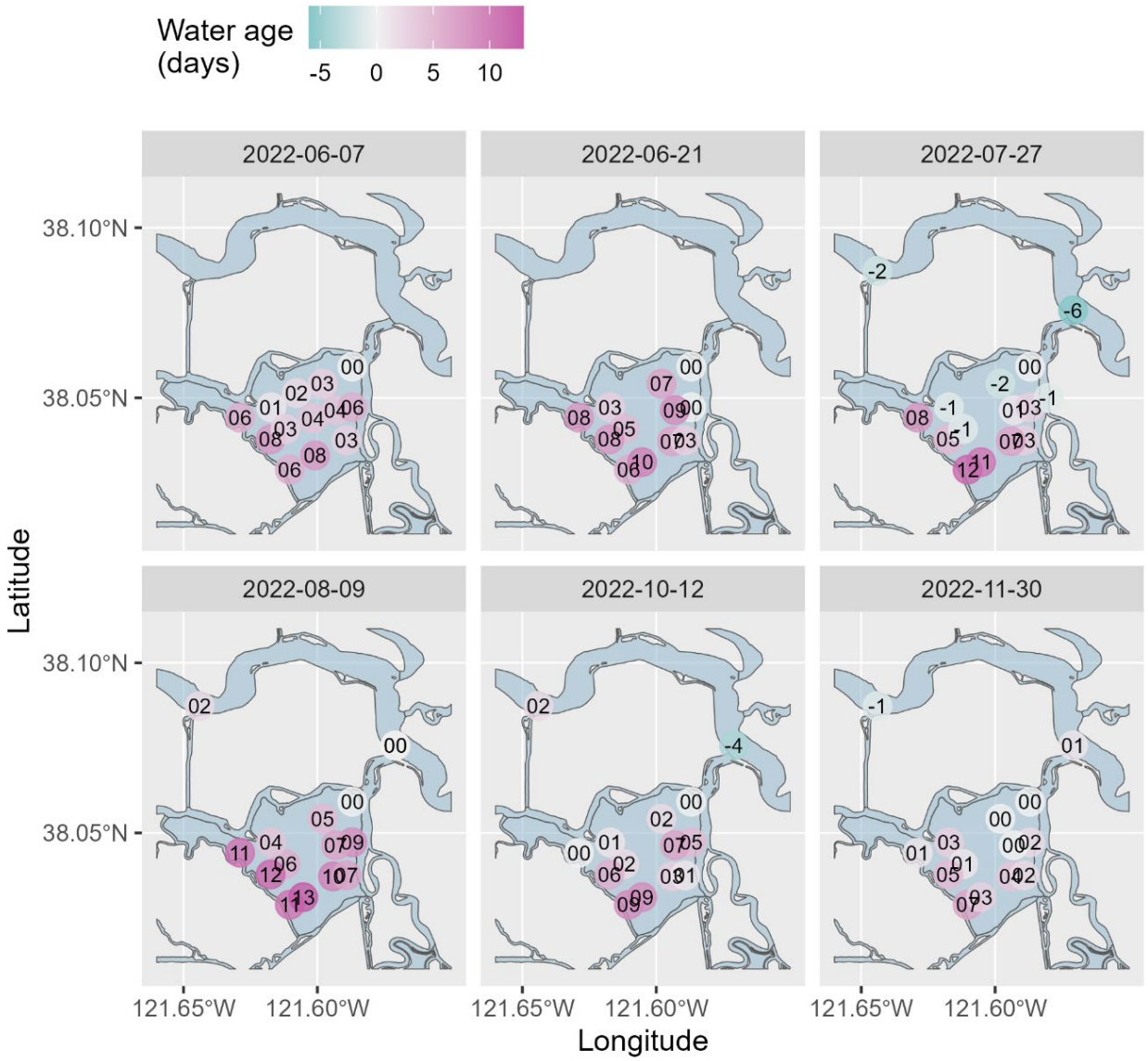

Figure 2.3.2-74 Water age estimated from stable isotope values in discrete samples.

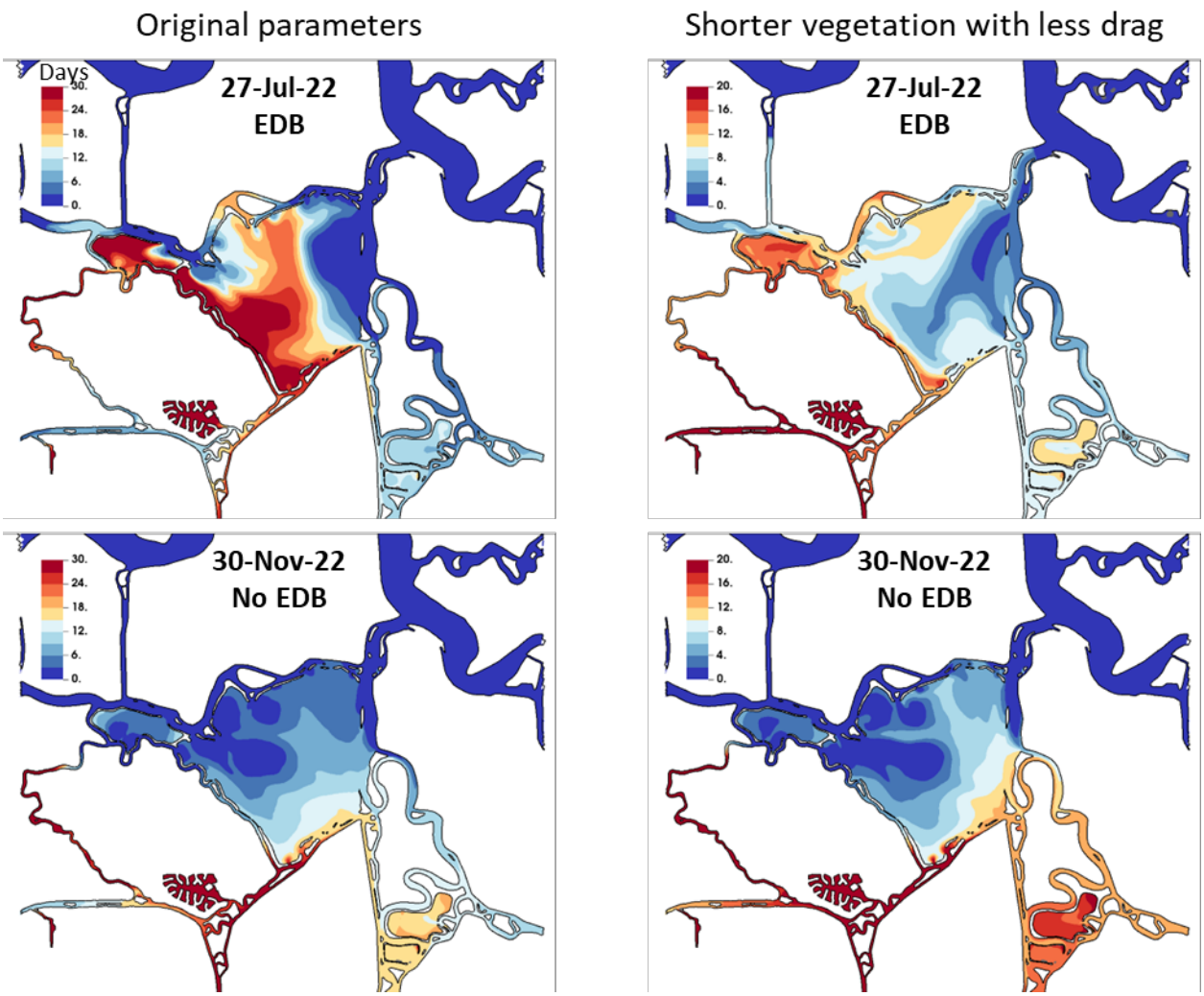

NOTES: (LEFT COLUMN) Age with original parameters used in Hartman et al. (2022); (RIGHT COLUMN) Age with revised parameters to decrease the submerged aquatic vegetation (SAV) canopy height and lower the SAV drag coefficient.
The color scales are different in the left and right columns.
SOURCE: Data compiled by California Department of Water Resources in 2023.

Figure 2.3.2-75 Hydrodynamic model (SCHISM 3D) of water age (days) for July 27 and November 30, 2022.

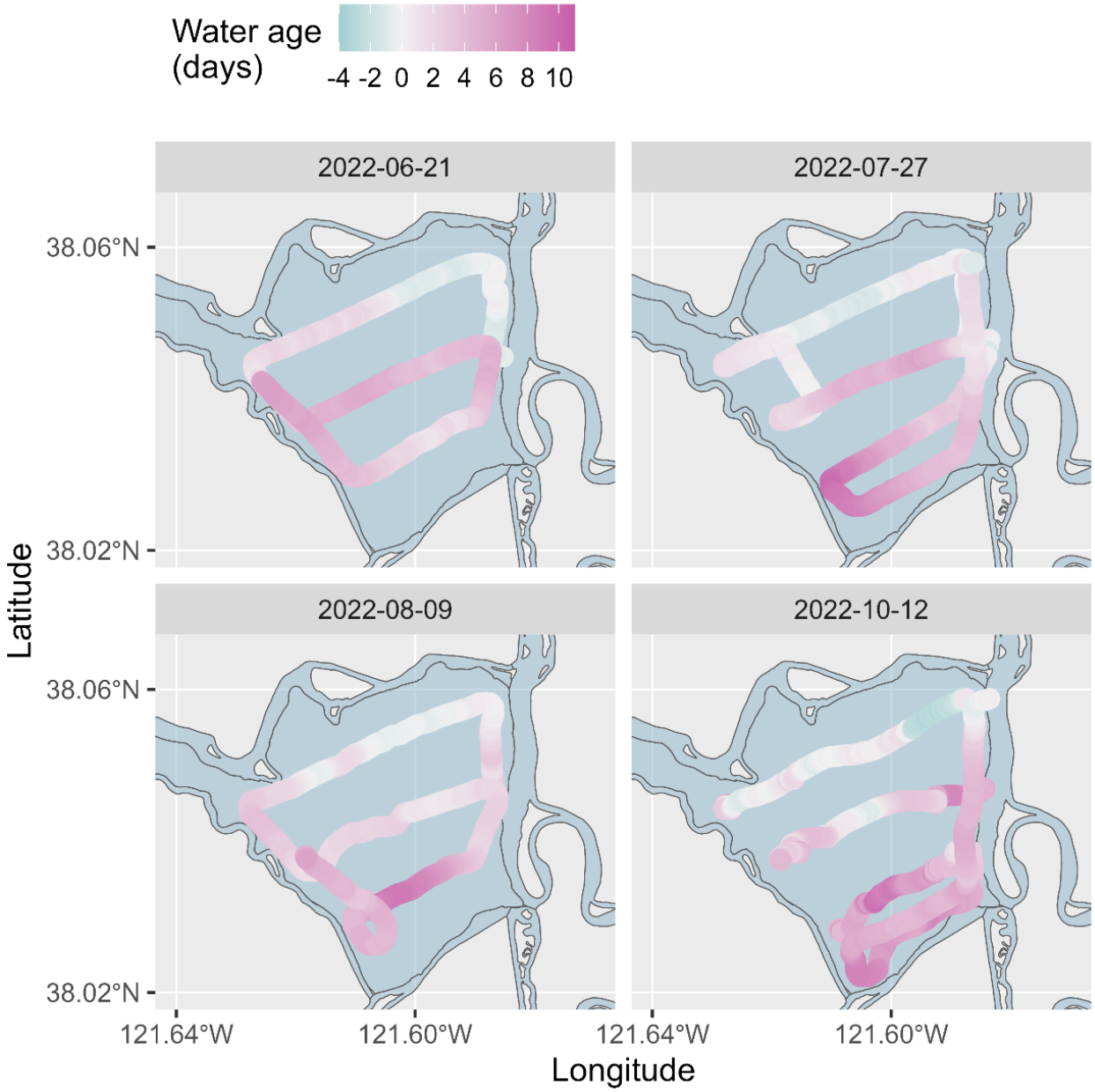

Figure 2.3.2-76 Water age estimated from stable isotope values in high-resolution data (Picarro).

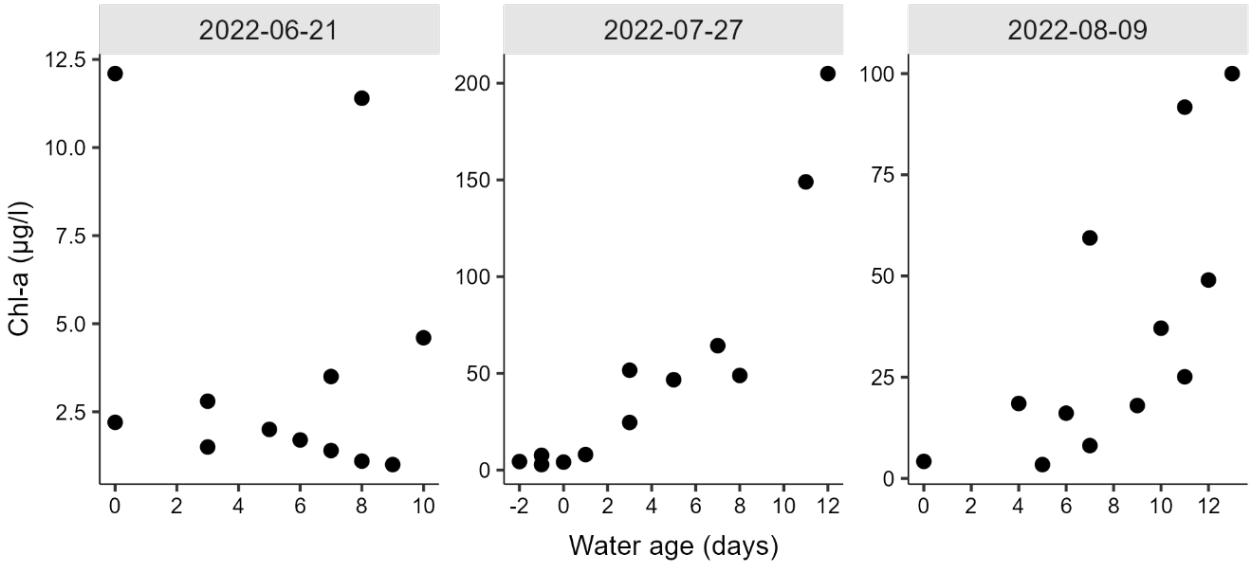

NOTES: µg/L = micrograms per liter; Chl-a = chlorophyll *a*

Figure 2.3.2-77 Relationship between water age and chlorophyll *a* concentration in discrete samples from Franks Tract.

If cyanobacteria are in the exponential growth phase, a few additional days can result in markedly higher biomass. As hypothesized, during the bloom in July and August, higher phytoplankton biomass was found at sites with older water (**Figure 2.3.2-78**). This was in contrast to June, before the bloom occurred, when chlorophyll was mostly below 5 µg/L and there was no relation with water age. Multiple parameters—salinity, temperature, and nitrate—spatially correlate with water age, so it is difficult to identify the primary factor driving the rise in biomass (Figure 2.3.2-59, Figure 2.3.2-60, Figure 2.3.2-61, and Figure 2.3.2-62).

Water age estimated from stable isotopes was younger than water age predicted by the original hydrodynamic model parameterization (Figure 2.3.2-74). Even with this variation, some spatial patterns emerged in the stable isotope data that can be compared to the model predictions.

Similar to the modeled water age, the oldest water was found along the western and southern periphery of Franks Tract (Figure 2.3.2-74 and Figure 2.3.2-76). At site FT1-4, near the opening with False River, in June, July, and August, the water was five to nine days younger than at site FT1-5, farther to the east. This pattern is consistent with the model predictions showing younger water near the opening with False River (Figure 2.3.2-75). The pattern changed during the October and November sampling, however, when the difference in water age between sites FT1-4 and FT1-5 was only one day. In November, the change was expected because the barrier had been removed and exchange with False River was expected to increase. However, the similarity in the October values could have resulted from

differential flow patterns as SAV biomass increased throughout the summer and fall, or from unexpected hydrodynamics or measurement errors. The frequent exchange of water flowing through the eastern opening with Old River and the western opening with False River appears to exchange more frequently and extensively with the northern and central regions of Franks Tract, leaving older water along the periphery.

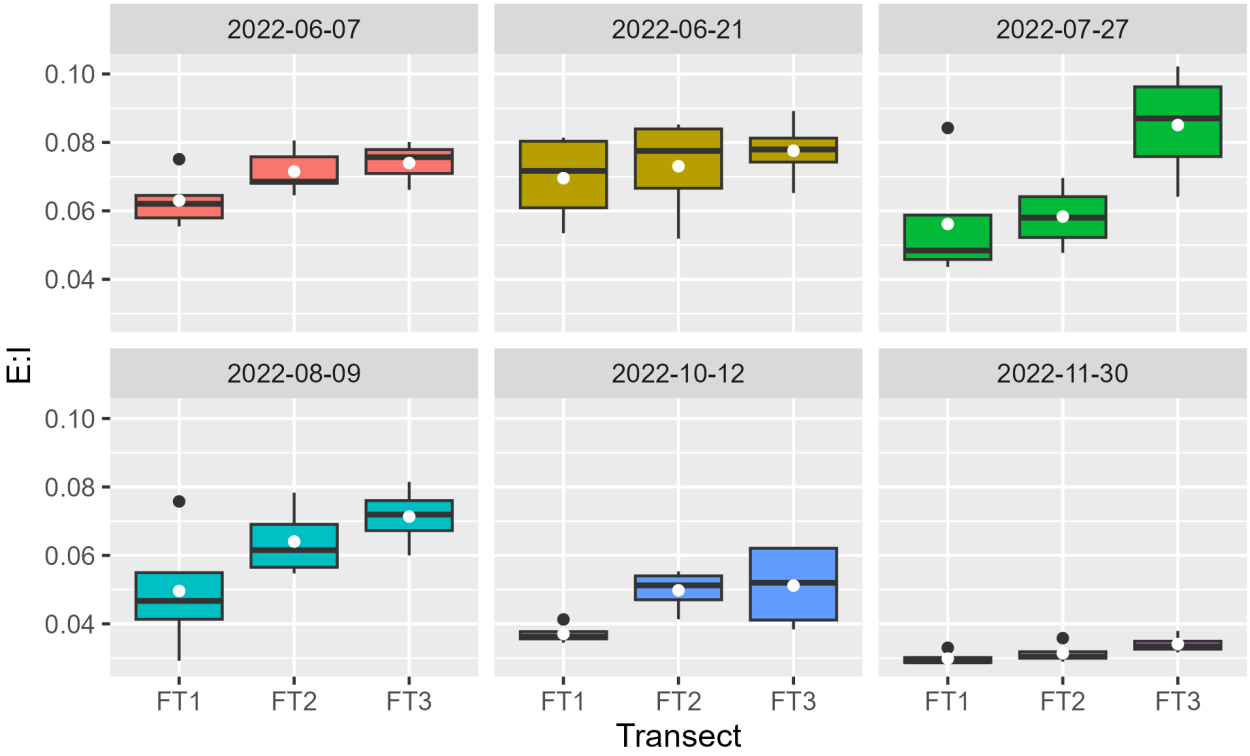

NOTES: E:I = evaporation-to-inflow ratio.
The white point indicates the mean of each set of samples.

Figure 2.3.2-78 Evaporation-to-inflow ratios calculated from discrete samples collected along the three transects in Franks Tract.

The original hydrodynamic model's parameters predicted older water in the southeastern region of Franks Tract (Figure 2.3.2-75). Franks Tract water exchanges with old water in Holland Cut through this opening; during slack tides, water age in this region increases when old water is pulled into Franks Tract from Holland Cut. The July and August samples were collected at low tide (Figure 2.3.2-55), and water ages at southeastern sites FT3-1 and FT3-2 were similar to water ages at southeastern sites FT3-4 and FT3-5.

The model results with original parameters show a similar pattern of water age on July 27, 2022 (Figure 2.3.2-75), compared with the estimates from different days in 2021 presented in Hartman et al. (2022) (Figure 2.3.2-73). When the SAV canopy height and drag coefficients were reduced in the revised model version, the modeled water age in western Franks Tract

decreased from approximately 30 days to approximately 20 days (Figure 2.3.2-75). The age estimates generated by the revised hydrodynamic model with shorter SAV and less drag are closer to the relative ages estimated by the stable isotope method; the spatial pattern of age also changes in the revised model (Figure 2.3.2-75 and Figure 2.3.2-74).

In the re-parametrized model, younger water from Old River penetrates farther into the western side of Franks Tract, reducing the strong east-west gradient in water age. The revised model also shows water from False River entering Franks Tract from the northwest. Older water remains close to the northern, western, and southern edges of Franks Tract, forming a horseshoe shape of older water. The horseshoe shape of old water contrasts with the original model results, which produced more resistance from SAV that prevented water from Old River from penetrating western Franks Tract. Based on patterns in the stable isotope water age, the old water from Holland Cut may travel farther northward than predicted by the hydrodynamic model. The stable isotope water ages at sites FT2-1 and FT2-2 were older (five to nine days; Figure 2.3.2-74) than the values predicted by the original model (less than five days; Figure 2.3.2-75). The revised model shows approximately eight-day-old water on the eastern side of Franks Tract, which better matches the spatial pattern for stable isotope water age. On November 30, 2022, after the EDB had been removed, the reduced SAV height and drag had little effect on modeled water age.

The modeling of vegetation interaction in the revised hydrodynamic model produced a more realistic circulation pattern and produced contrasts in velocity above and below the canopy that tally with measurements by Lucas and Stewart (2005). Including SAV also tends to lead to a more accurate tidal distribution between False River (FAL), Old River (OSJ), and Holland Cut (HOL).

However, several aspects of the vegetation field can be specified only approximately. The model requires stem density, stem width, canopy height, and a drag coefficient. Stem density is derived based on binned Normalized Density Vegetation Index remote sensing values. The method produces a realistic spatial pattern of density that agrees well with both imagery and local samples. However, it is not well determined in absolute terms and tends to vary from image to image, an uncertainty that is absorbed in part by the choice of drag coefficient. A more sensitive and consequential parameter for modeling age is canopy height. Reducing canopy height allows flow over the top of the canopy that more rapidly transmits water changes and nutrients to remote areas.

One of the desired outcomes of the sampling program was to compare the patterns observed during modeling and improve characterization of the

canopy, including the effective drag and height of vegetation. Until now, modeling simulations have indicated that a steep east-west gradient in water age develops when the EDB is in place and the jet inflow at False River is fed only by Fisherman's Cut. Under this weakened tidal forcing when the EDB is in place, the role of vegetation in modulating circulation becomes more important, and the western part of the Franks Tract becomes more isolated. Longtime scales of response at the Franks Tract (FRK) and Bethel Island at Piper Slough (BET) continuous monitoring stations have tended to support this result.

Discussion

A cyanobacterial phytoplankton bloom occurred in Franks Tract in July and August 2022. The bloom began between June 21, when the chlorophyll concentration was still less than 10 µg/L, and July 27, when the chlorophyll concentration was more than 50 µg/L. The most abundant organism at sites with the highest chlorophyll concentrations was the cyanobacterial genus *Dolichospermum*. Blooms form when growth rates exceed loss rates and environmental conditions have a high carrying capacity for phytoplankton biomass. If growth rates exceed loss rates for a long enough time, sufficient biomass may accrue to form a bloom. Ultimately, bloom formation depends on having an organism with a set of traits that enable it to succeed in an environment, enough resources to support high biomass, and enough time to use those resources and increase biomass.

Cyanobacterial Bloom Composition and Traits

Most other documented cyanobacterial blooms in the Delta have been dominated by *Microcystis* or *Aphanizomenon*, not *Dolichospermum*. During 2004–2008 and 2014–2018, *Dolichospermum* was a minor member of the phytoplankton community and was outnumbered by *Microcystis* cells in the Delta (Lehman et al. 2013, 2017, 2021). In 2011, however, *Dolichospermum* was present more frequently from June to October than *Microcystis* at the DWR EMP's D19 station in Franks Tract (Mioni et al. 2011) (Figure 2.3.2-54). *Dolichospermum* was observed in July, August, and September with abundances ranging from 3,042 to 14,600 cells/mL, while *Microcystis* was identified only in July, at an abundance of 82,131 cells/mL compared to 14,621 cells/mL for *Dolichospermum*. *Aphanizomenon* is observed frequently across the Delta and was even the most dominant in 2011 (Mioni et al. 2011). After *Microcystis*, *Aphanizomenon* is often the next most abundant potentially toxigenic cyanobacteria (Lehman et al. 2021).

Because *Dolichospermum*, *Aphanizomenon*, and *Microcystis* were all co-occurring, the environmental conditions may have been more favorable for *Dolichospermum*, enabling it to accrue more biomass than the other taxa. The ability of *Dolichospermum* to fix nitrogen is one of the most

distinguishing traits differentiating *Microcystis* from *Dolichospermum*. Dissolved inorganic nitrogen ratios were low in Franks Tract, and the DIN:DIP ratio suggests that nitrogen would become limiting before phosphorus. Nitrogen fixation is energetically costly (De Tezanos Pinto and Litchman 2010; Marcarelli et al. 2022) and often results in lower growth rates (Osburn et al. 2021); therefore, *Dolichospermum* may not have actually been fixing nitrogen in Franks Tract. However, the shallow depth and low turbidity in Franks Tract represent a more favorable underwater light field, providing photons for the energetically costly task of fixing nitrogen, than deeper or more turbid regions of the Delta. The dominance of a diazotrophic organism, *Dolichospermum*, in the Franks Tract bloom points to a potential role of nutrients in selecting *Dolichospermum* over *Microcystis*, which has dominated most other reported cyanobacterial blooms.

Beyond diazotrophy, other traits distinguish *Dolichospermum* and *Microcystis*. *Dolichospermum* has a lower optimal growth temperature than *Microcystis* (Robarts and Zohary 1987). Analyzing samples collected in the Delta during the 2014 drought, Lehman et al. (2017) found that *Microcystis* was more strongly correlated with temperature than *Dolichospermum*. Across the United States, *Microcystis* abundances were found to be more sensitive to temperatures than *Dolichospermum* abundances (Rigosi et al. 2014). In Europe, *Dolichospermum* abundance is associated with lower total nitrogen and total phosphorus concentrations than *Microcystis* (Dolman et al. 2012). While *Microcystis* is often associated with high phosphorus concentrations, it also is very effective at acquiring phosphorus when concentrations decrease in the environment. During a bloom, inorganic phosphorus often becomes depleted, and the high affinity for phosphorus has been proposed as a mechanism contributing to the succession of *Microcystis* over other cyanobacterial taxa (Gobler et al. 2016). Phosphorus is rarely limiting in the Delta, and the stable dissolved inorganic phosphorus in Franks Tract may not have given *Microcystis* a competitive advantage over *Dolichospermum* for acquiring phosphorus.

Environmental Resources to Support a Bloom

The amount of biomass that can accrue during a bloom is limited by the concentration of resources available in the environment in addition to any consistent loading that occurs. The Delta is considered nutrient replete and light is usually the next factor, after nutrients, limiting phytoplankton growth in estuarine systems. However, there were not excessive inorganic nutrients in Franks Tract in June 2022. Dissolved inorganic nitrogen (NO_3 + NO_2 + NH_4) concentrations were less than 0.1 mg/L, and concentrations between 0.1 and 0.13 mg/L have been proposed as the threshold for instantaneous nitrogen limitation for phytoplankton (Reynolds 1999; Chorus and Spijkerman 2021). Therefore, cyanobacteria may have already been straining to acquire sufficient nitrogen for growth in June, before the bloom

began. Inorganic nitrogen concentrations near 0.1 mg/L were also measured in 2021 in Franks Tract (Hartman et al. 2022). These low nitrogen concentrations are in contrast to the average dissolved inorganic nitrogen concentration of 0.476 mg/L measured by Lopez et al. (2006) around Franks Tract. While the Delta is generally considered nutrient replete (Jassby et al. 2002; Lopez et al. 2006), potential nutrient limitation of phytoplankton was observed in this study and also been observed by Loken et al. (2022).

Total nitrogen at sites along transects FT2 and FT3 more than tripled from June through August (Figure 2.3.2-71), suggesting some loading of nitrogen into the water column to account for this increase. Potential sources include (1) nitrogen fixation by cyanobacteria (*Dolichospermum* or *Aphanizomenon*), (2) fluxes of remineralized nitrogen from benthic sediments and detritus, (3) loadings from water originating in Mound Slough and Piper Slough and then transported into Franks Tract with the tides, (4) fluxes from aquatic vegetation, and (5) atmospheric deposition.

Nitrogen fixation is an energetically demanding process for cyanobacteria. and cyanobacterial taxa capable of fixing nitrogen do not always do so. No data were collected to confirm whether cyanobacteria in Franks Tract were fixing nitrogen. Nitrogen fixation usually occurs when nitrogen concentrations have decreased, especially ammonium and urea, which have been shown to repress nitrogen fixation rates. Assuming that *Dolichospermum* cells fixed approximately 150 femtomols of nitrogen per cell per day (Klawonn et al. 2016; Kramer et al. 2022), 50,000 cells per mL could have fixed 0.07 mg of nitrogen over the course of 10 hours of daylight per day. This rate is faster than the increase in total particulate nitrogen observed in Franks Tract. On June 21, total particulate nitrogen was approximately 0.25 mg-N L^{-1} (Figure 2.3.2-71) and increased to 0.4 to 1 mg-N L^{-1} on July 27, an increase of 0.001 to 0.027 mg-N L^{-1} day^{-1}. Future measurements of nitrogen fixation during cyanobacterial blooms would confirm the role of diazotrophy in supplying nitrogen for cyanobacteria.

Fluxes of nitrogen from benthic cores were measured in Franks Tract by Cornwell et al. (2014) during September and March. The benthic zone was a sink for nitrate, but it was a source for ammonium in September but not March. Based on their range of measurements, using an estimate of 100 µM NH_4-N m^{-2} h^{-1} and a 2-meter water column depth converts into 0.017 mg NH_4-N L^{-1} day^{-1} effluxing from the sediments into the water column. This is the same order of magnitude as the increase in total particulate nitrogen observed in Franks Tract. On June 21, total particulate nitrogen was approximately 0.25 mg-N L^{-1} (Figure 2.3.2-71) and increased to 0.4 to 1 mg-N L^{-1} on July 27, an increase of 0.001 to 0.027 mg-N L^{-1} day^{-1}. However, some of the NH_4 effluxing out of the sediment would be converted to NO_3 through nitrification, and Cornwell et al. (2014) found that NO_3 fluxed into

the sediment at rates of 100–200 µM NO_3-N m^{-2} h^{-1}, which would then be unavailable to phytoplankton for growth.

Uptake of ammonium from the sediments must be fast because there is no increase in ammonium or total nitrogen concentrations at some of the transect FT1 sites and at Mildred Island across the sampling dates (Figure 2.3.2-71). If ammonium was consistently loading from the sediments and was not used by phytoplankton or other organisms, water column concentrations of ammonium and nitrate would be expected to increase, but this was not observed in the data (Figure 2.3.2-71). Therefore, if phytoplankton are using nitrogen fluxing from the sediments, then phytoplankton population growth supported by benthic ammonium is balanced by losses, due to grazing or sedimentation, which keeps the overall biomass steady.

Nutrients could also have been delivered into Franks Tract from surrounding waterways. Mound and Piper sloughs have an inlet in the southwestern corner of Franks Tract. Nitrogen from this region could explain why total nitrogen increased only in the southern and western areas of Franks Tract, and not the northern and eastern areas. If high nitrogen loading was occurring from Old River or False River, it would be expected that total nitrogen would increase in the northern and eastern areas, which did not occur. Additional nutrient fluxes from aquatic vegetation or atmospheric vegetation could also contribute to nitrogen concentrations in Franks Tract. Atmospheric deposition is estimated to contribute approximately 14 percent of the total nitrogen in the San Joaquin River at Vernalis (Saleh and Domagalski 2021), but the summer contribution to Franks Tract is unknown. The contribution of nutrients from aquatic vegetation over the summer season is also unknown.

Water Age

As hypothesized, higher phytoplankton biomass was found at sites with older water. Multiple other parameters correlate with water age, so it is difficult to identify the primary factor driving the rise in biomass. Salinity, temperature, and nitrate all had spatial patterns that were similar to water age (Figure 2.3.2-66, Figure 2.3.2-67, Figure 2.3.2-69, and Figure 2.3.2-70). If cyanobacteria are in the exponential growth phase, a few additional days can result in markedly higher biomass.

2.3.3 Fish and Wildlife

2.3.3.1 Fish Community

The drought of 2020–2022 was predicted to cause an overall decline in pelagic fishes (including longfin smelt and delta smelt) and an increase in invasive littoral fishes (Mahardja et al. 2021). The 2021–2022 EDB caused

an increase in salinity in the Sacramento River and a slight increase in X2; however, this was not expected to have a significant effect on the distribution or abundance of pelagic fish beyond the impact of the drought itself. The EDB may cause local increases in the number of predatory fishes (striped bass and black bass) immediately around the barrier or notched barrier and an increase in centrarchids and other vegetation specialists in the area around Franks Tract (Conrad et al. 2016).

Methods

The response of the fish community to the EDB in West False River was assessed by comparing fish catch during CDFW's Summer Townet Survey and surveys by the U.S. Fish and Wildlife Service's Delta Juvenile Fish Monitoring Program in years with the EDB present to fish catch in years without the barrier. In addition, the number of fish salvaged at the State and federal fish rescue facilities was compared for years with and without the barrier.

For the analysis of the Summer Townet Survey, catch data were obtained from the CDFW FTP site: https://filelib.wildlife.ca.gov/Public/TownetFallMidwaterTrawl/TNS%20MS%20Access%20Data/TNS%20data/

The Delta Juvenile Fish Monitoring Program's beach seine data were obtained from the program's data publication on the Environmental Data Initiative (Interagency Ecological Program et al. 2022): https://doi.org/10.6073/pasta/57b6c257edd72691702f9731d5fe4172

A subset of the datasets was established including only surveys from 2014 through 2022 and only stations within the regions shown in **Figure 2.3.3-1**.

With these data, a Bayesian generalized linear model was used with a zero-inflated negative binomial distribution to model the total catch of fish and invertebrates using the following formula:

Catch ~ Year * Region + (1|Station) + offset(Volume)

Analyses were performed using the function `brm` from the R package `brms` (Bürkner 2018).

To test for differences in community composition between region and year, the relative percent composition was calculated for each species, and a permutational multivariate analysis of variance was performed using the function `adonis` from the R package `vegan` (Oksanen et al. 2020) using the following formula:

Catch ~ Year * Region + block(Station)

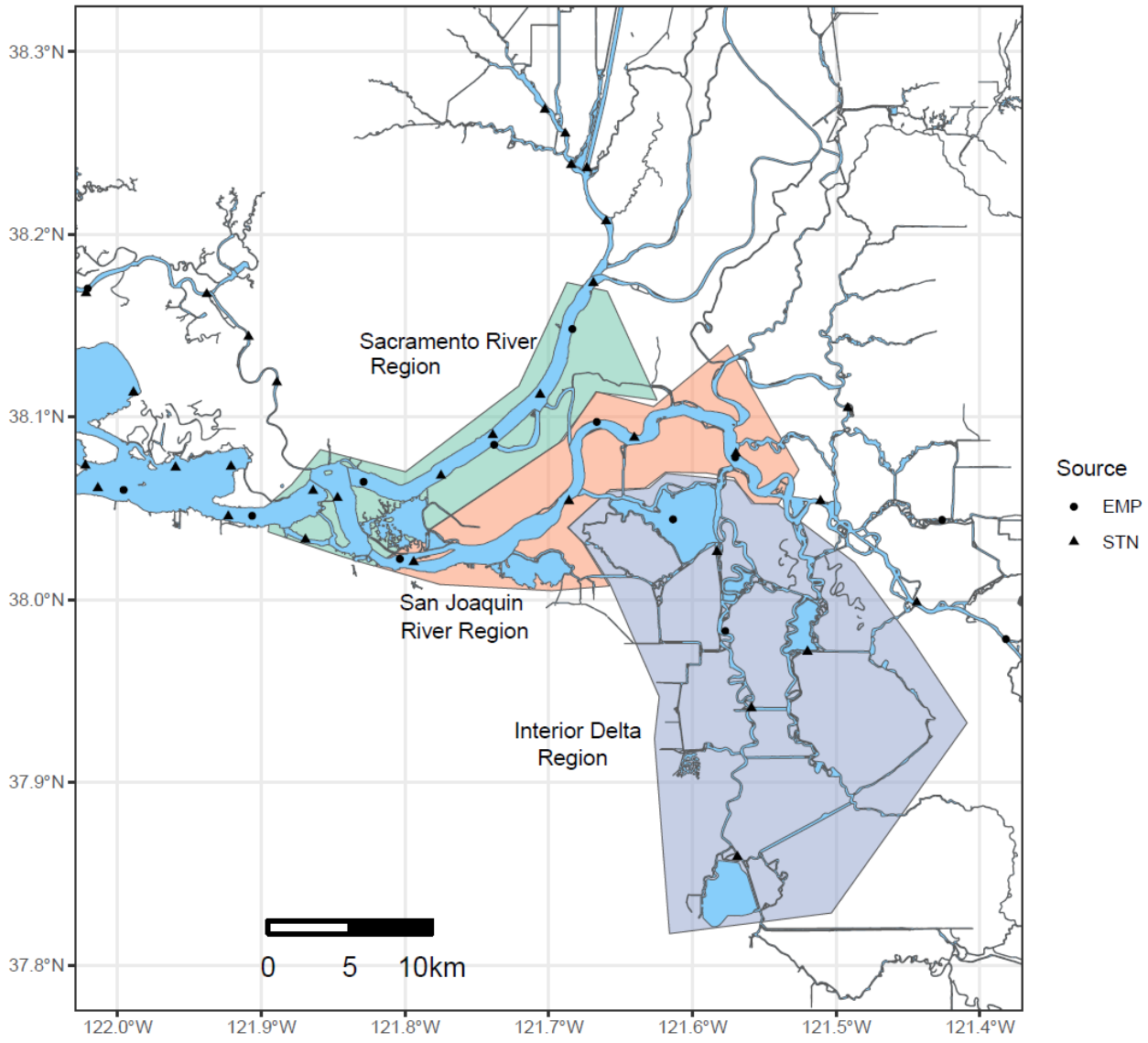

NOTES: DJFMP = Delta Juvenile Fish Monitoring Program; mm = millimeter

Figure 2.3.3-1 Locations of fish surveys in the Central Delta.

Should the modeling analyses show a significant impact of year, or a significant interaction between region and year, with a similar response in years with a barrier in place (2015, 2021, 2022), the results would indicate that the barrier had an impact on fish abundance and/or community composition.

For the analysis of fish salvage data, the salvage database was downloaded from the CDFW website: https://filelib.wildlife.ca.gov/Public/salvage/

The total catch for each year from 2014–2022 was calculated for all listed fish species: Chinook salmon (*Oncorhynchus tshawytscha*), delta smelt (*Hypomesus transpacificus*), longfin smelt (*Spirinchus thaleichthys*), green

sturgeon (*Acipenser medirostris*), and steelhead (*Oncorhynchus mykiss*). The resulting data were graphed to visually inspect trends in salvage; however, catches of listed fishes were too erratic to model statistically.

Results

Summer Townet

In all years, Summer Townet catch was highest in the Sacramento River Region; some fish were caught in the San Joaquin River Region, but fish catches in the Interior Delta Region were very low (**Figure 2.3.3-2**, **Figure 2.3.3-3**, and **Table 2.3.3-1**). Catch in the Sacramento River Region was higher during barrier years (2015, 2021, and 2022) than during dry, non-barrier years or wet years. This response appears to have been driven partially by an increase in the catch of the jellyfish *Maeotius*, which is a brackish-water specialist, although catch of juvenile gobies also increased in the Sacramento River Region during barrier years. The EDB and associated salinity intrusion farther up the Sacramento River may have facilitated the dispersal of these species farther upstream than normal.

The permutational multivariate analysis of variance on the relative abundance of species caught by the Summer Townet between Central Delta regions and years found significant differences between both regions and years, although neither factor explained more than 8 percent of the variance (**Table 2.3.3-2**). Catch in the San Joaquin River and Interior Delta regions was often very small and highly variable, with many trawls catching no fish at all, so generalizations are difficult to make. Differences between years were easier to see: 2014, 2015, 2017, and 2021 had greater proportions of *Maeotias*, 2016 and 2017 had greater proportions of Siberian prawns, and 2016, 2017, and 2020 had more catfish (**Figure 2.3.3-4**).

When looking just at listed fish species, no salmon, sturgeon, or smelt were caught in the Interior Delta Region or San Joaquin River Region from 2014 through 2022 (**Figure 2.3.3-5**). A few delta smelt were caught in the Sacramento River Region during 2014–2017 and a few longfin smelt were caught in 2014 and 2020–2022. None of these patterns appear associated with the EDB.

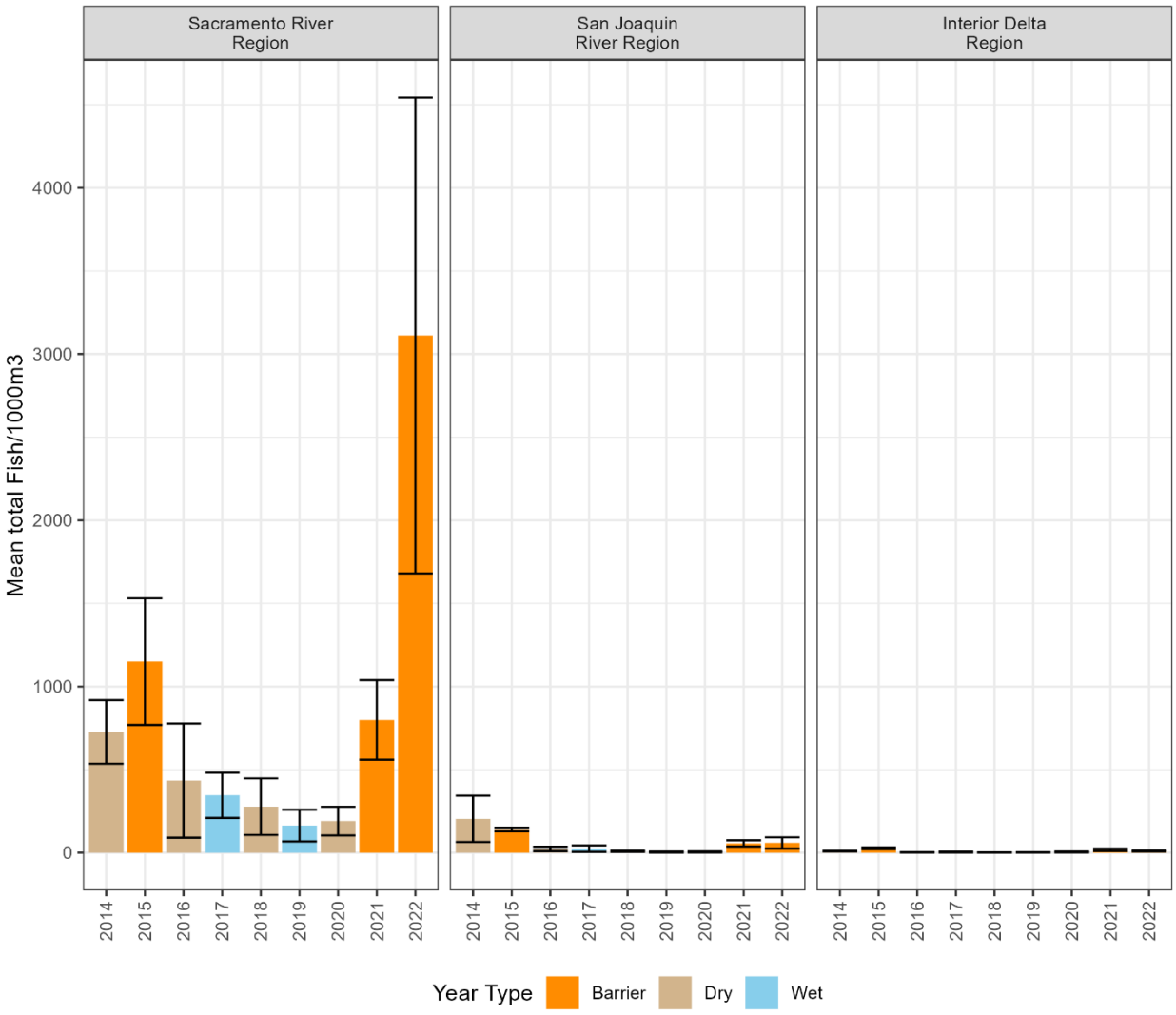

NOTE: m^3 = cubic meters

Figure 2.3.3-2 Average fish catch per unit of fishing effort (±1 standard error) collected in the Summer Townet Survey, by Central Delta region and year.

TABLE 2.3.3-1
COEFFICIENTS OF BAYESIAN ZERO-INFLATED NEGATIVE BINOMIAL MODEL OF SUMMER TOWNET CATCH

Model Term	Estimate	Est. Error	Lower 95% CI	Upper 95% CI	Rhat
Intercept (Interior Delta, 2014)	0.532	0.581	-0.581	1.674	1.001
Sacramento	4.420	0.733	2.956	5.885	1.001
San Joaquin	2.560	0.805	0.994	4.163	1.001
2015	1.065	0.471	0.138	2.002	1.002
2016	-1.538	0.570	-2.674	-0.449	1.002
2017	-1.027	0.550	-2.144	0.041	1.002
2018	-2.198	0.654	-3.524	-0.994	1.001
2019	-1.628	0.571	-2.760	-0.516	1.001
2020	-0.899	0.528	-1.956	0.121	1.002
2021	0.614	0.473	-0.316	1.525	1.001
2022	0.110	0.478	-0.854	1.035	1.002
Sacramento:2015	-0.961	0.593	-2.133	0.215	1.002
San Joaquin:2015	-0.858	0.624	-2.093	0.320	1.001
Sacramento:2016	-0.095	0.682	-1.396	1.279	1.003
San Joaquin:2016	-0.574	0.731	-2.020	0.855	1.001
Sacramento:2017	-0.098	0.661	-1.386	1.240	1.003
San Joaquin:2017	-1.164	0.701	-2.515	0.222	1.002
Sacramento:2018	0.674	0.750	-0.709	2.182	1.001
San Joaquin:2018	-0.416	0.798	-1.947	1.171	1.003
Sacramento:2019	-0.731	0.682	-2.058	0.634	1.002
San Joaquin:2019	-1.734	0.762	-3.228	-0.241	1.001
Sacramento:2020	-0.927	0.652	-2.183	0.331	1.003
San Joaquin:2020	-2.765	0.710	-4.149	-1.326	1.002
Sacramento:2021	-0.894	0.591	-1.999	0.278	1.001
San Joaquin:2021	-1.541	0.635	-2.798	-0.265	1.001
Sacramento:2022	1.010	0.597	-0.174	2.197	1.002
San Joaquin:2022	-1.206	0.642	-2.469	0.048	1.001

NOTES: CI = confidence interval; Est. = estimated; Rhat = potential scale reduction statistic (Gelman-Rubin statistic)

SOURCE: Data collected by California Department of Fish and Wildlife; modeling conducted by California Department of Water Resources in 2023.

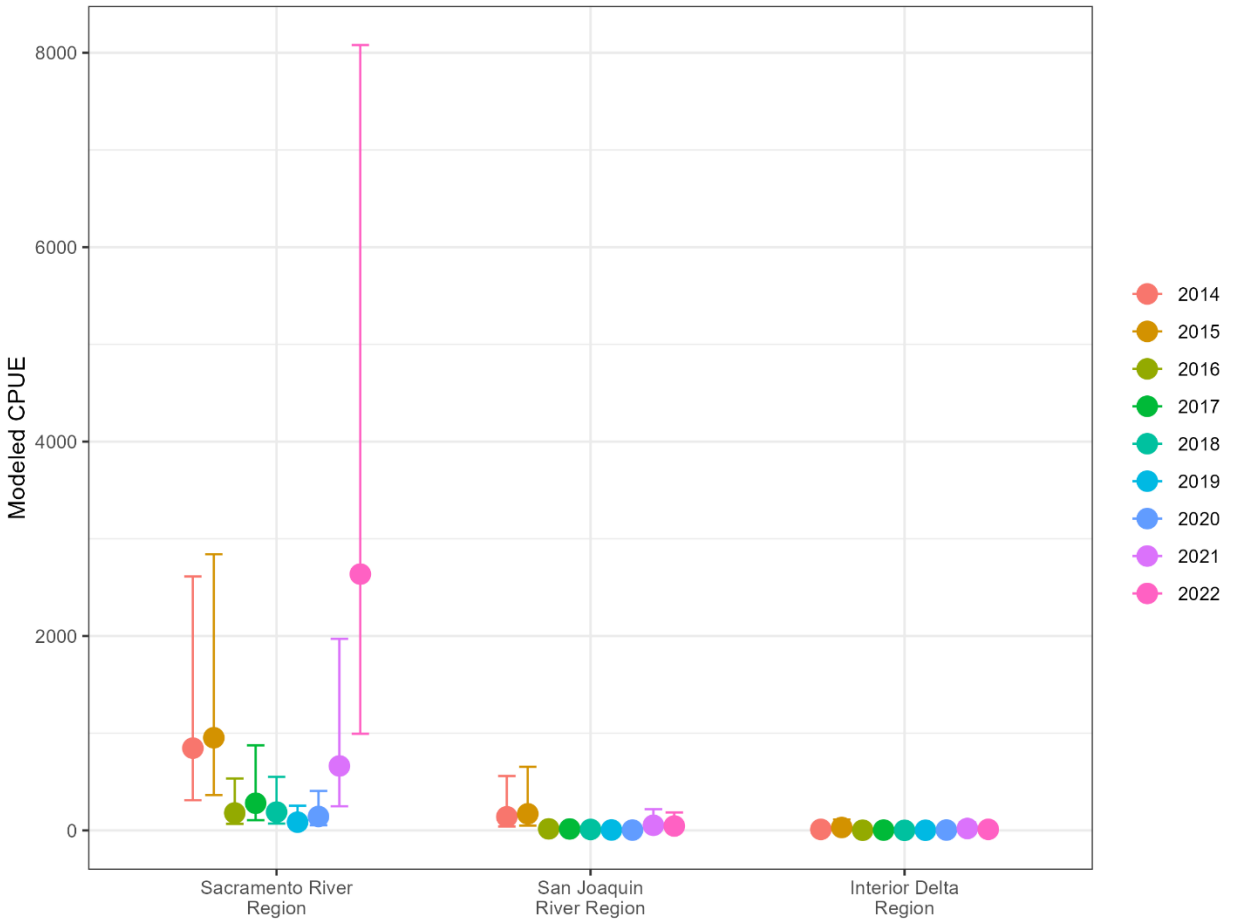

NOTE: CPUE = catch per unit effort

Figure 2.3.3-3 Conditional effects plot from zero-inflated negative binomial Bayesian model of total fish catch per unit of fishing effort, by season and Central Delta region.

TABLE 2.3.3-2
RESULTS OF PERMUTATIONAL MULTIVARIATE ANALYSIS OF VARIANCE ON SUMMER TOWNET DATA, 2014–2021

	Degrees of Freedom (Df)	Sums of Squares (SumsOfSqs)	F-statistic (F.Model)	Coefficient of Determination (R2)	P-value (Pr(>F))
Year	8	12.616	6.154	0.081	0.001
Region	2	9.148	17.849	0.058	0.001
Year*Region	16	10.478	2.555	0.067	
Residuals	482	123.510		0.793	
Total	508	155.752		1.000	

SOURCE: Data collected by California Department of Fish and Wildlife; modeling conducted by California Department of Water Resources in 2023.

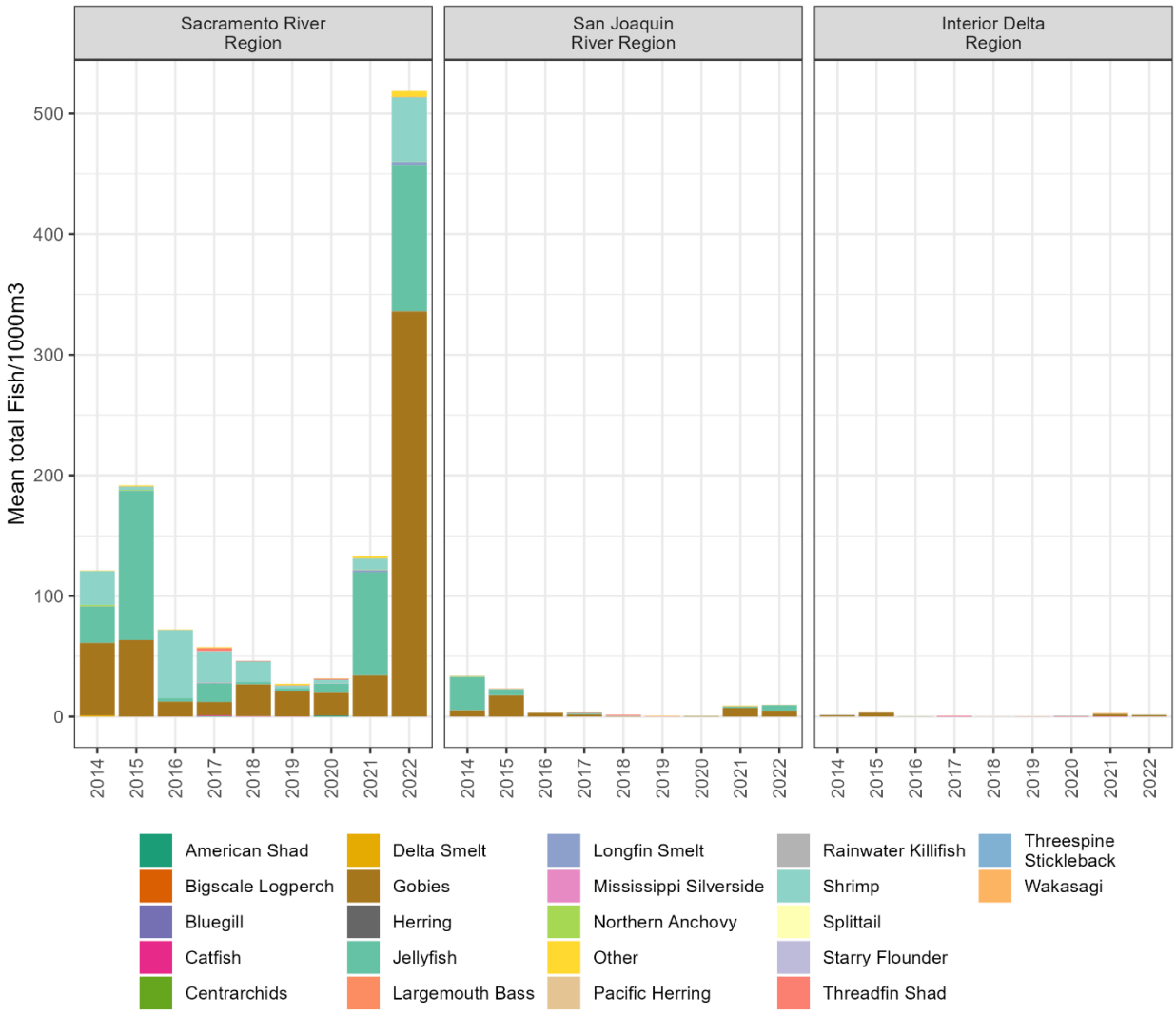

NOTE: m^3 = cubic meters

Figure 2.3.3-4 Community composition of townet samples collected in each Central Delta region and year.

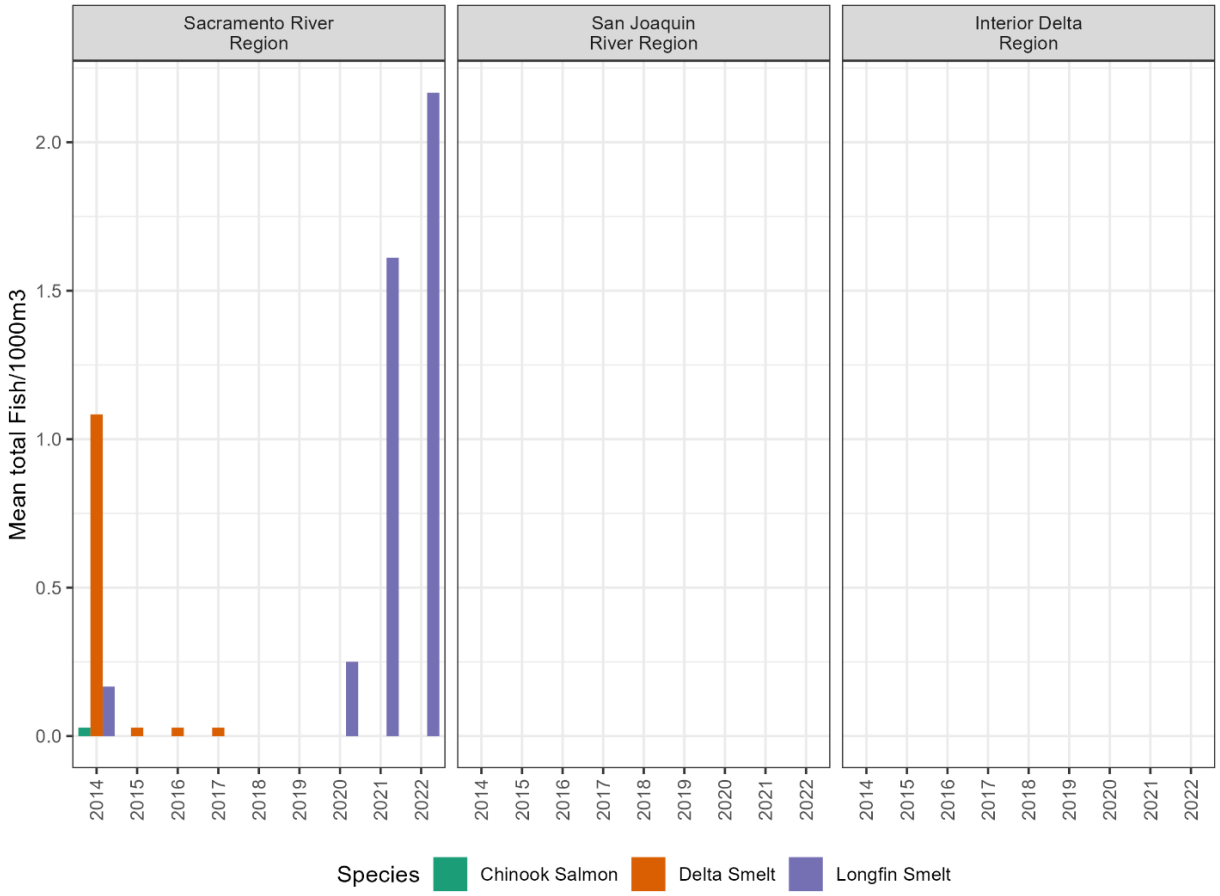

NOTES: m^3 = cubic meters
No green sturgeon or steelhead were caught during the Summer Townet survey during this time period.

Figure 2.3.3-5 Catch of special-status species during the Summer Townet survey, by year and Central Delta region.

Delta Juvenile Fish Monitoring Program

The beach seine data, which target littoral fishes rather than pelagic fishes, showed higher catch per unit effort in most samples than the pelagic surveys. During many years, average catch per unit of fishing effort was highest in the San Joaquin River Region rather than in the Sacramento River Region, but the Interior Delta Region still had relatively low catch (**Figure 2.3.3-6**, **Figure 2.3.3-7**, and **Table 2.3.3-3**). Mississippi silversides (*Menidia audens*) was the most frequently caught species in all regions and years; western mosquitofish (*Gambusia affinis)* and threadfin shad (*Dorosoma petenense*) were the second and third most abundant species caught.

The permutational multivariate analysis of variance on community composition found that there was a significant difference in community composition between regions, years, and interaction of Central Delta region and year; however, none of these three terms explained more than 8 percent of the variance (**Table 2.3.3-4**).

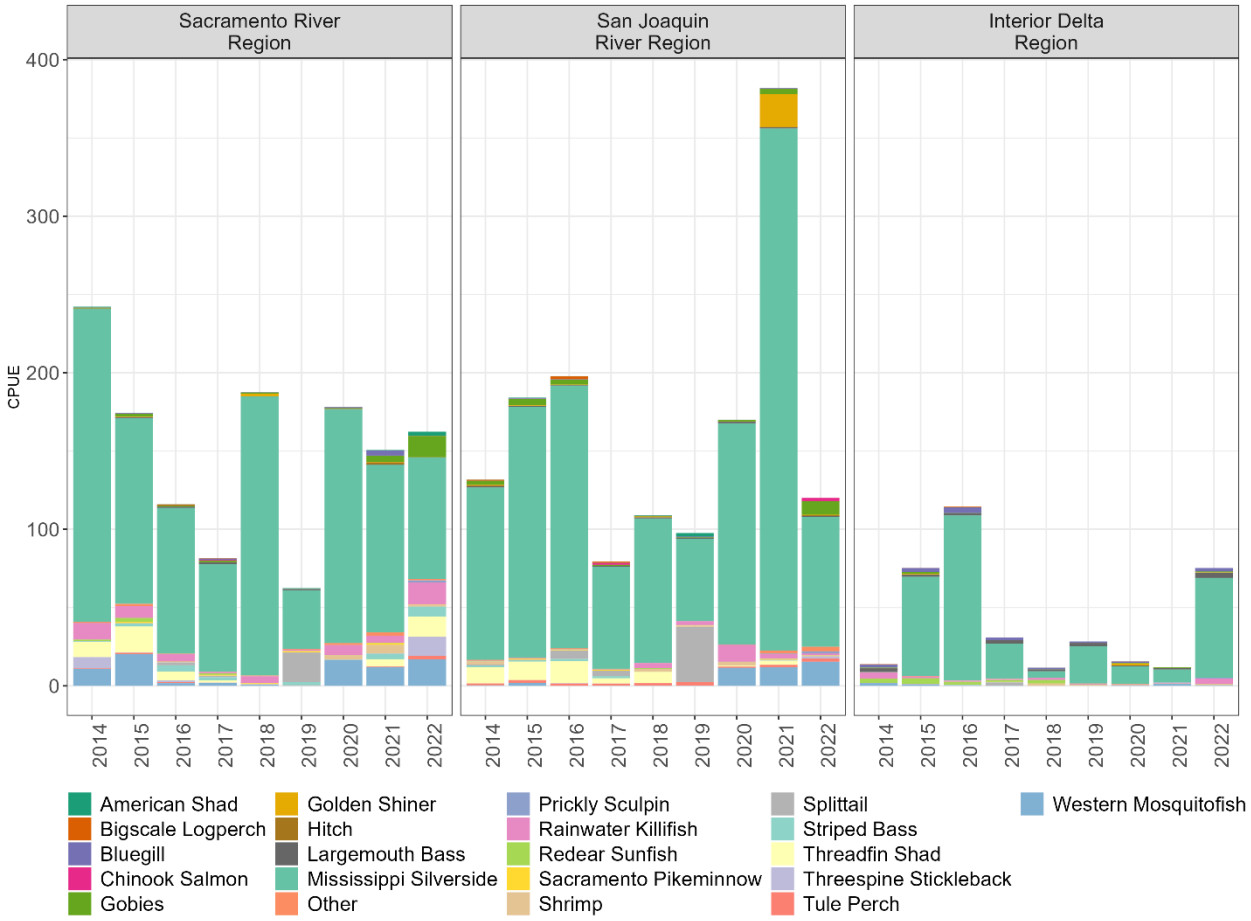

NOTE: CPUE = catch per unit effort

Figure 2.3.3-6 Delta Juvenile Fish Monitoring Program community composition, by Central Delta region and year.

Some notable differences between regions were the higher relative abundance of redear sunfish (*Lepomis microlophus*) and bluegill (*L. macrochirus*) in the Interior Delta Region; the higher relative abundance of threadfin shad and western mosquitofish in the Sacramento River Region; and the relatively high abundance of threadfin shad and Sacramento splittail (*Pogonichthys macrolepidotus*) in the San Joaquin River Region. Notable differences between years include higher abundances of splittail in 2016, 2017, and 2019; higher abundances of western mosquitofish in 2014, 2015, 2020, and 2022; an unusually high catch of golden shiners in 2021; and an unusually high catch of gobies in 2022.

Listed fish species were rarely caught in beach seines, although a few delta smelt were caught in 2014 and 2015 (**Figure 2.3.3-8**). Chinook salmon were caught occasionally in the Sacramento River and San Joaquin River regions, especially during 2017, but were never caught in the Interior Delta Region (Figure 2.3.3-8).

TABLE 2.3.3-3
COEFFICIENTS OF BAYESIAN ZERO-INFLATED NEGATIVE BINOMIAL MODEL OF DELTA JUVENILE FISH MONITORING PROGRAM BEACH SEINE

Model Term	Estimate	Est. Error	Lower 95% CI	Upper 95% CI	Rhat
Intercept (Interior Delta, 2014)	3.018	0.541	1.943	4.085	1.002
Sacramento	2.126	0.908	0.269	3.886	1.003
San Joaquin	1.187	0.864	-0.584	2.906	1.000
2015	1.349	0.386	0.612	2.114	1.001
2016	1.275	0.409	0.471	2.067	1.001
2017	0.026	0.377	-0.732	0.761	1.000
2018	-1.063	0.422	-1.903	-0.220	1.000
2019	0.402	0.420	-0.418	1.238	1.001
2020	0.246	0.756	-1.058	1.913	1.001
2021	-1.117	0.676	-2.341	0.318	1.001
2022	1.172	0.474	0.265	2.147	1.000
Sacramento:2015	-1.608	0.528	-2.662	-0.571	1.001
San Joaquin:2015	-0.914	0.468	-1.861	-0.008	1.001
Sacramento:2016	-1.702	0.551	-2.780	-0.627	1.000
San Joaquin:2016	0.187	0.504	-0.801	1.185	1.000
Sacramento:2017	-1.034	0.515	-2.010	-0.024	1.000
San Joaquin:2017	-0.300	0.465	-1.173	0.627	1.000
Sacramento:2018	0.497	0.559	-0.612	1.556	1.001
San Joaquin:2018	1.161	0.512	0.155	2.174	1.000
Sacramento:2019	-1.030	0.580	-2.200	0.092	1.000
San Joaquin:2019	-0.307	0.507	-1.307	0.692	1.000
Sacramento:2020	-0.289	1.017	-2.387	1.655	1.000
San Joaquin:2020	0.442	0.862	-1.446	2.015	1.002
Sacramento:2021	0.894	0.786	-0.807	2.351	1.000
San Joaquin:2021	3.544	0.762	1.971	4.979	1.001
Sacramento:2022	-1.059	0.639	-2.259	0.174	1.000
San Joaquin:2022	-0.233	0.603	-1.418	0.955	1.002

NOTES: CI = confidence interval; Est. = estimated; Rhat = potential scale reduction statistic (Gelman-Rubin statistic)

SOURCE: Data collected by U.S. Fish and Wildlife Service; model conducted by California Department of Water Resources in 2023

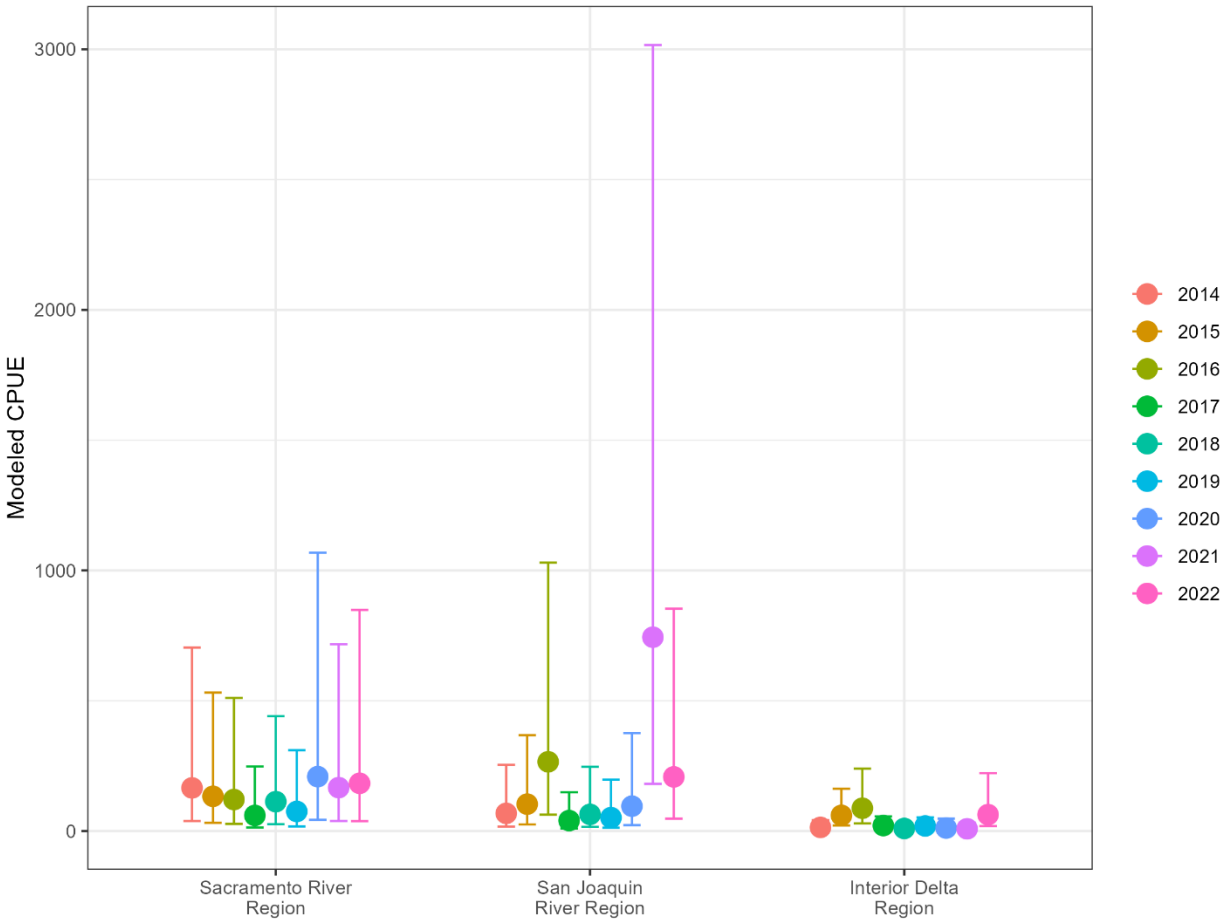

NOTE: CPUE = catch per unit effort

Figure 2.3.3-7 Conditional effects plot of the Bayesian model of total fish catch in the Delta Juvenile Fish Monitoring Program's beach seines interaction of year and Central Delta region.

TABLE 2.3.3-4
RESULTS OF PERMUTATIONAL MULTIVARIATE ANALYSIS OF VARIANCE OF BEACH SEINE COMMUNITIES

Model Term	Degrees of Freedom	Sums of Squares	F-statistic	Coefficient of Determination (R2)	P-value
Year	8	2.785	4.718	0.0373	0.001
Regions	2	5.502	37.289	0.0737	0.001
Year: Regions	16	2.685	2.275	0.0359	0.001
Residuals	863	63.670		0.853	
Total	889	74.642		1.000	

SOURCE: Data collected by U.S. Fish and Wildlife Service; modeling conducted by California Department of Water Resources in 2023.

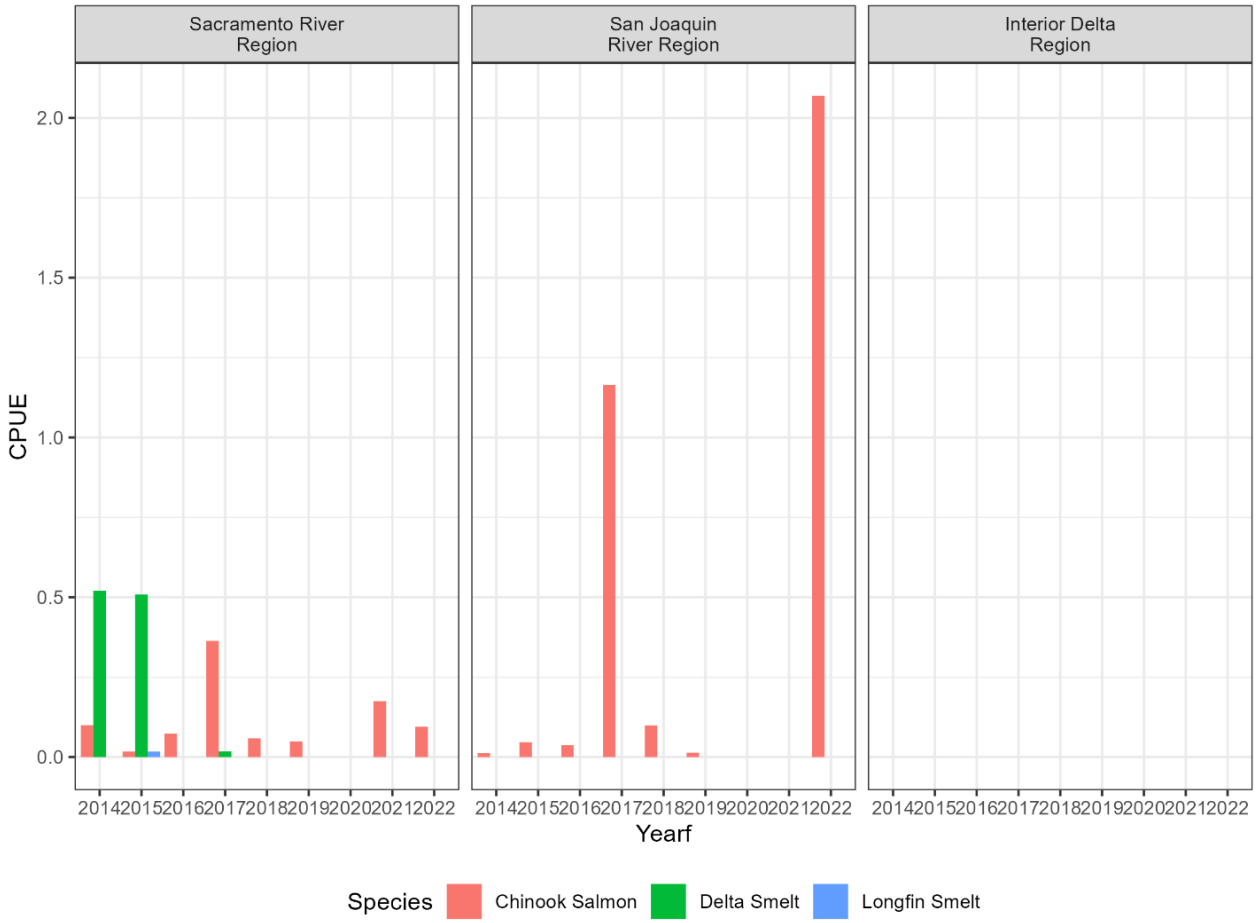

NOTES: CPUE = catch per unit effort
No green sturgeon or steelhead were caught during this time period.

Figure 2.3.3-8 Catch of Chinook salmon, delta smelt, and longfin smelt in the Delta Juvenile Fish Monitoring Program beach seine by region and year.

One of the hypotheses about the effect of the barrier on fish communities was that there would be an increase in centrarchids in the Interior Delta, because fish in this family tend to associate with slower moving water and vegetation. Although the Delta Juvenile Fish Monitoring Program beach seine surveys do not include a site within Franks Tract itself, sites in the Interior Delta Region had a lower abundance of centrarchids in 2021 than in previous years (**Table 2.3.3-5**, **Figure 2.3.3-9**, and **Figure 2.3.3-10**). In contrast, the Sacramento River Region saw the highest catch per unit of fishing effort of centrarchids seen in that region, mostly bluegill (Figure 2.3.3-9). In 2022, the trend reversed, with the Sacramento River Region having one of the lowest abundances of centrarchids and the Interior Delta Region having the highest centrarchid abundance since 2017, with particularly high abundance of largemouth bass.

TABLE 2.3.3-5
COEFFICIENTS OF BAYESIAN ZERO-INFLATED NEGATIVE BINOMIAL MODEL OF DELTA JUVENILE FISH MONITORING PROGRAM BEACH SEINE CENTRARCHID CATCH

Model Term	Estimate	Est. Error	Lower 95% CI	Upper 95% CI	Rhat
Intercept (2014, Interior Delta)	2.083	0.615	0.886	3.290	1.002
Sacramento	-3.086	1.083	-5.328	-1.030	1.004
San Joaquin	-2.363	1.033	-4.518	-0.350	1.002
2015	0.107	0.354	-0.594	0.813	1.002
2016	-0.319	0.361	-1.011	0.368	1.000
2017	-0.515	0.350	-1.206	0.175	1.001
2018	-0.763	0.387	-1.515	-0.001	1.001
2019	-0.686	0.378	-1.422	0.045	1.001
2020	-1.489	0.669	-2.755	-0.074	1.001
2021	-1.698	0.623	-2.879	-0.438	1.001
2022	-0.160	0.517	-1.134	0.897	1.000
Sacramento:2015	0.926	0.592	-0.263	2.095	1.001
San Joaquin:2015	-0.040	0.484	-0.976	0.909	1.001
Sacramento:2016	1.100	0.678	-0.201	2.392	1.001
San Joaquin:2016	0.070	0.491	-0.914	1.044	1.000
Sacramento:2017	2.455	0.605	1.282	3.635	1.000
San Joaquin:2017	0.700	0.472	-0.208	1.642	1.000
Sacramento:2018	0.262	0.744	-1.239	1.681	1.002
San Joaquin:2018	1.181	0.514	0.156	2.183	1.000
Sacramento:2019	2.899	0.705	1.519	4.275	1.001
San Joaquin:2019	1.136	0.510	0.133	2.135	1.002
Sacramento:2020	2.256	1.120	0.063	4.380	1.001
San Joaquin:2020	1.836	0.788	0.259	3.358	1.001
Sacramento:2021	4.542	0.825	2.883	6.146	1.001
San Joaquin:2021	1.993	0.715	0.557	3.350	1.001
Sacramento:2022	-0.671	1.051	-2.696	1.449	1.000
San Joaquin:2022	0.024	0.683	-1.362	1.333	1.000

NOTES: CI = confidence interval; Est. = estimated; Rhat = potential scale reduction statistic (Gelman-Rubin statistic)

SOURCE: Data collected by U.S. Fish and Wildlife Service; modeling conducted by California Department of Water Resources in 2023.

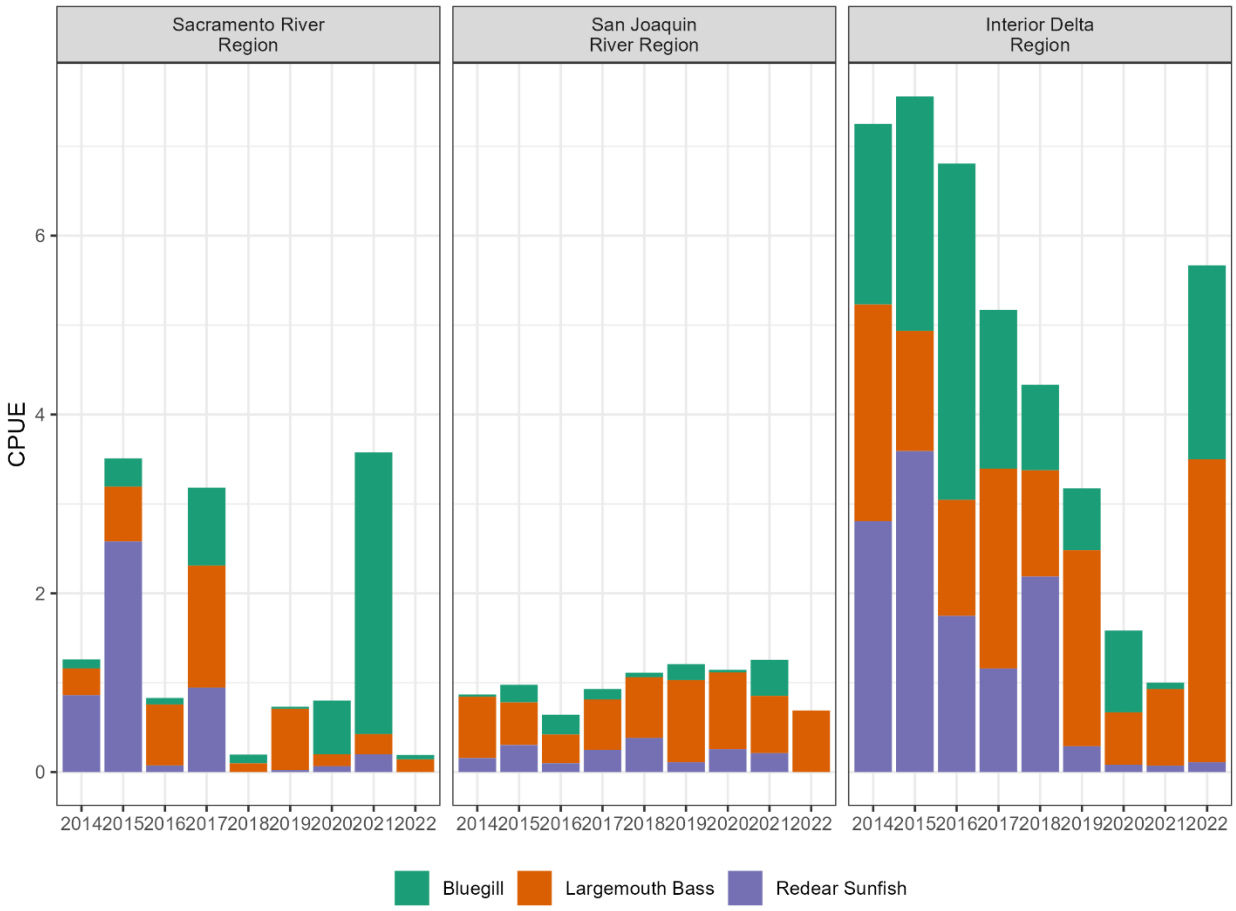

NOTE: CPUE = catch per unit effort

Figure 2.3.3-9 Graph of Delta Juvenile Fish Monitoring Program beach seine catch in the family Centrarchidae.

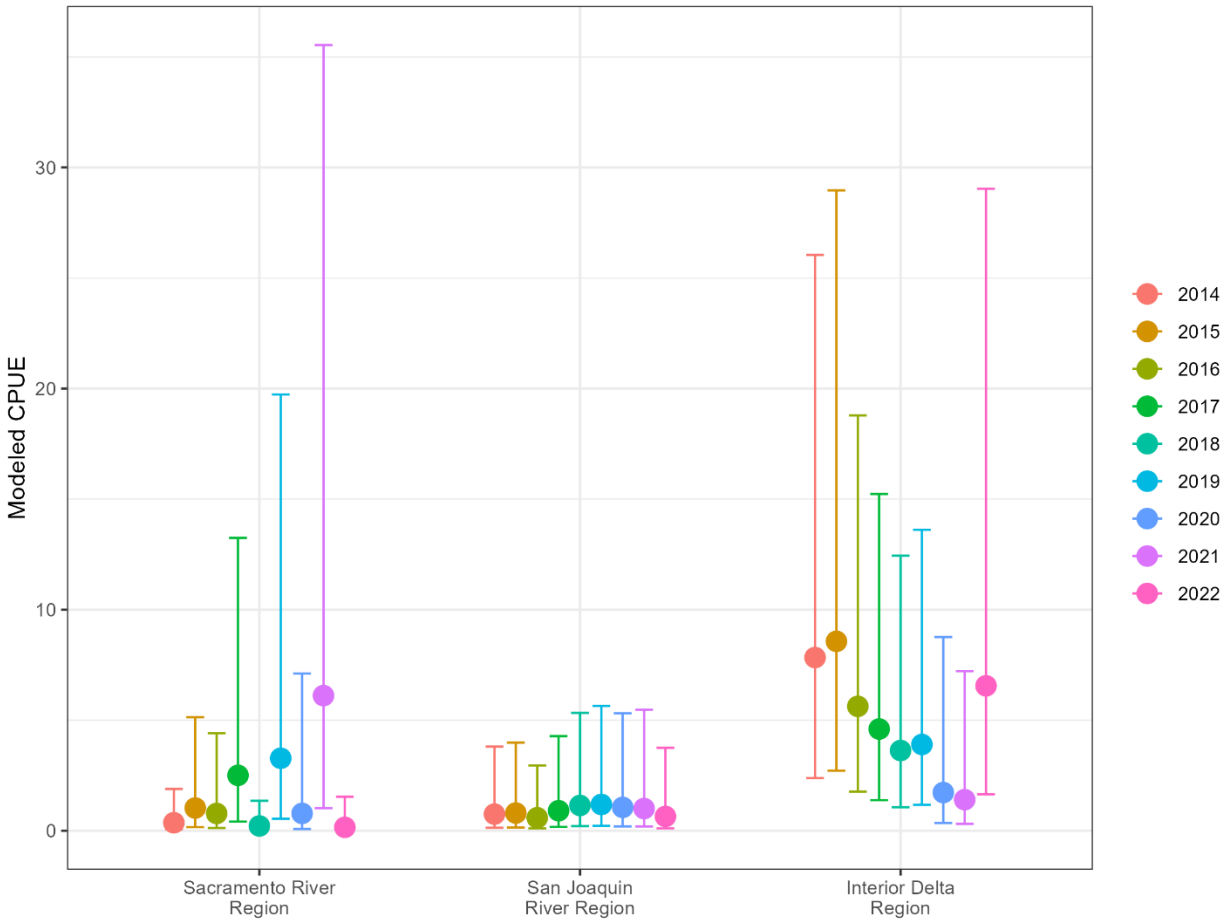

NOTE: CPUE = catch per unit effort

Figure 2.3.3-10 Conditional effects plot of the Bayesian model of total Centrarchid catch in the Delta Juvenile Fish Monitoring Program's beach seines interaction of year and Central Delta region.

Salvage

From May 2021 through November 2022 (the period when the 2021–2022 EDB was in place), salvage totaled 482 juvenile Chinook salmon, one delta smelt, 2,387 longfin smelt, and 168 rainbow/steelhead trout. No green sturgeon were caught. In 2015, the other "barrier year," four Chinook salmon and no other listed fishes were caught when the barrier was in place. Catch of delta smelt was too sporadic to statistically test for differences between years, particularly in recent years, and the salvaged delta smelt in 2022 were from an experimental release of cultured fish. High salvage of longfin smelt in the spring of 2020 and 2022 tracks the estuary-wide increase in the population of these fish. Other efforts are underway to model Chinook salmon salvage, so they will not be discussed further here. However, when looking at the data graphically, catch of Chinook salmon was lower in years with the barrier in place (**Figure 2.3.3-11**).

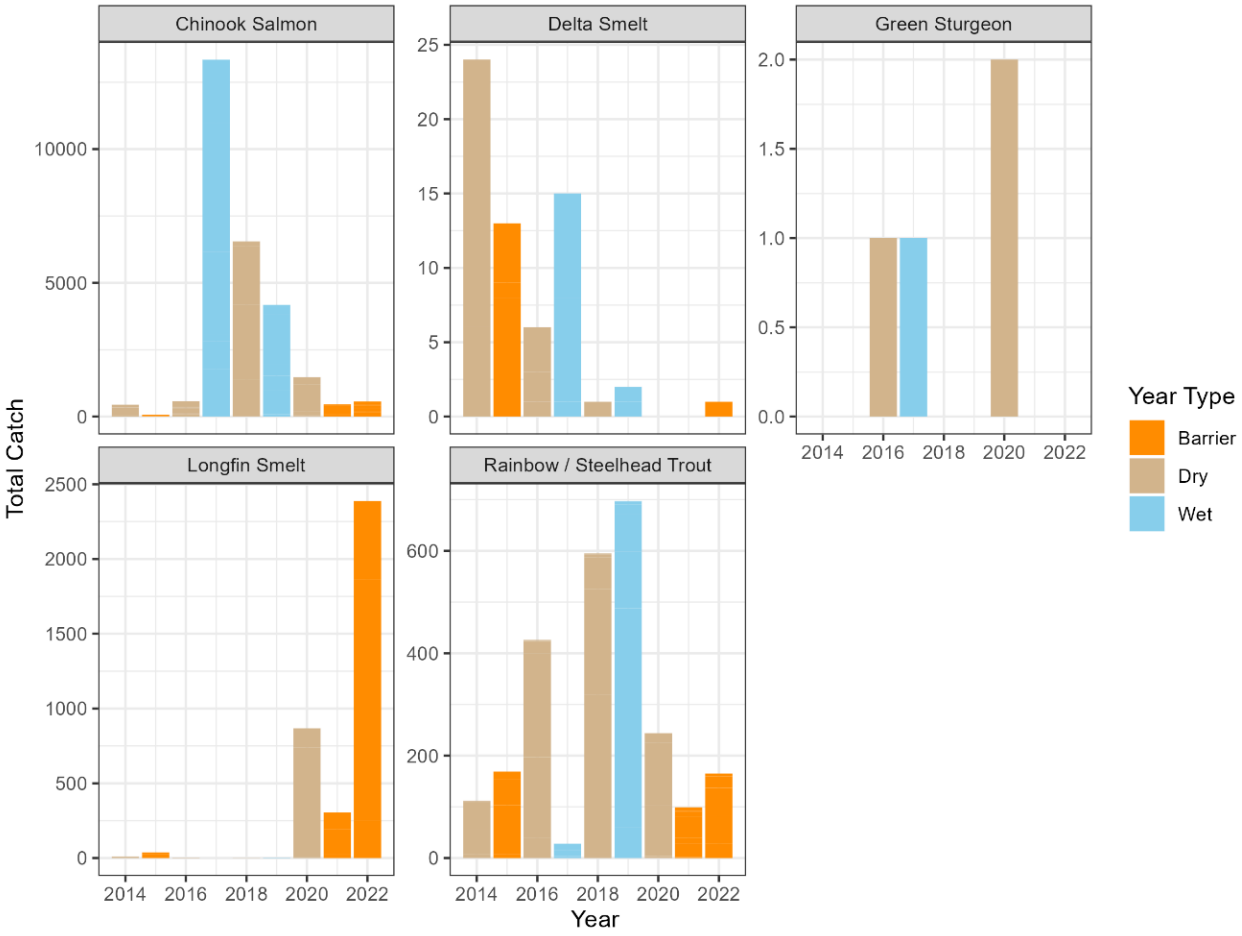

Figure 2.3.3-11 Total catch of listed fish species collected at the State and federal fish salvage facilities, by calendar year.

Discussion

The clearest effect of the West False River EDB on fish communities was higher total catch, higher catch of jellyfish, and higher catch of gobies in the Sacramento River in the Summer Townet Survey during years when the barrier was in place. The increase in catch of gobies and jellyfish in all three barrier years gives strong evidence that the EDB was at least partially responsible for this trend. Other similarities between 2015, 2021, and 2022, such as the extreme conditions, could have been driving this relationship; however, the increase in catch was not as dramatic in other dry years, such as 2014, 2016, and 2020. Changes in jellyfish distributions during drought were also seen by Hartman et al. (in prep.), who found that the center of distribution of *Maeotias marginata* (the most common jellyfish in brackish water) shifts upstream into the Sacramento Region during drier years.

No clear patterns in the littoral fish community that could be attributed to the barrier were apparent (Figure 2.3.3-6), although several patterns can be

tied to the drought in general. Total fish catch was higher across all regions during dry years, possibly driven by the high catch of Mississippi silversides, which are known to increase with droughts (Mahardja et al. 2016). Mahardja et al. (2021) found that littoral fish had higher resistance to multiyear droughts, so higher catch in drier years may be attributable to increases in other pelagic fish across the board. The Delta Juvenile Fish Monitoring Program's beach seines did not exhibit any clear similarities between 2015, 2021, and 2022, but splittail catch was particularly high in the wet years of 2017 and 2019. Splittail spawn in floodplains, so young-of-year splittail catch shows a strong relationship with wet years, particularly with inundation of the Yolo Bypass and Cosumnes River floodplains (Moyle et al. 2004).

2.3.3.2 Zooplankton

Researchers predicted a decline in zooplankton abundance in downstream regions during the drought, which would reduce the availability of this critical source of food for fishes. The 2021–2022 EDB was not expected to significantly affect the abundance of zooplankton beyond any changes caused by the drought itself, although it may reduce the import of freshwater zooplankton from the Delta into Suisun Bay (as seen in Kimmerer et al. 2019). Local increases in zooplankton density in the Central Delta may result if local phytoplankton blooms occur and these blooms consist of beneficial phytoplankton (Barros et al. in prep).

Methods

Zooplankton were monitored primarily using four existing Interagency Ecological Program surveys: the CDFW 20-mm Survey, the Summer Townet Survey and Fall Midwater Trawl (described above), and the EMP (see Figure 2.3.3-6).

Zooplankton sampling by the Summer Townet Survey and Fall Midwater Trawl are described in the previous section. The EMP conducts monthly water quality, phytoplankton, and zooplankton sampling throughout the upper estuary at 17 stations. At each station, the CDFW Zooplankton Survey (part of the EMP) collects a 10-minute stepped oblique trawl using the same zooplankton sled used by the Fall Midwater Trawl (see above). Additionally, the EMP collects microzooplankton using a vertically integrated pump sample (see Barros [2022] for full details). Two of these stations are not fixed, but instead follow the salinity field and sample at locations where the bottom's specific conductance reaches 2,000 µS/cm and 6,000 µS/cm, respectively.

All three surveys have similar zooplankton processing methods (see Kayfetz et al. [2020] for full details). Samples are concentrated in the laboratory by pouring them through a sieve screened with 150 µm mesh wire and reconstituted to organism densities of 200–400/mL. The sample is stirred to

distribute the animals homogeneously and a 1 mL subsample is extracted with an automatic pipette and placed in a Sedgewick-Rafter cell (slide). All animals on a slide are identified and counted under a compound microscope to the lowest possible taxonomic classification. This procedure is repeated until 6 percent of the sample (consisting of five to 20 slides) is analyzed.

Data from the three surveys were combined using the zooper package in R (Bashevkin et al. 2022). This package combines datasets by standardizing variable names and accounting for differences in taxonomic resolution. The EMP used only mesozooplankton data (150 µm net) and removed any taxa not quantitatively sampled by this mesh size. The analysis involved comparing total zooplankton catch per unit effort per sample. It used a linear mixed model on the log-transformed catch per unit effort versus year (as a factor), region, and the interaction of year and region, with sampling station as a random effect (package lme4, function lmer; Bates et al. 2022). To compare community composition between regions, the analysis used a permutational multivariate analysis of variance (package vegan, function adonis; Oksanen et al. 2020) with the same predictor variables.

Results

Overall, mean zooplankton catch per unit effort was highest in all years in the Interior Delta Region, and within this region, zooplankton abundance was highest in dry years, with no difference between barrier years and other dry years (**Figure 2.3.3-12** and **Table 2.3.3-6**). In the San Joaquin River Region, there were no differences between years. In the Sacramento River Region, zooplankton abundance was significantly higher in wet years than in dry years. Abundance was slightly lower in 2015 than in other dry years, but there was no difference between 2021 and 2020.

TABLE 2.3.3-6
RESULTS OF LINEAR MIXED MODEL OF LOG-TRANSFORMED TOTAL ZOOPLANKTON CATCH PER UNIT EFFORT VERSUS YEAR, REGION, AND THE INTERACTION OF YEAR AND REGION

Model Term	Chisq	Df	Pr(>Chisq)
(Intercept)	464.38	1	<0.0001
Year	93.32	7	<0.0001
Region	1.21	2	0.5453
Year* Region	143.11	14	<0.0001

NOTE: A post-hoc Tukey's range test was performed and results are shown as letters in Figure 2.3.3-12.

SOURCE: Data collected by California Department of Fish and Wildlife; modeling performed by California Department of Water Resources in 2023.

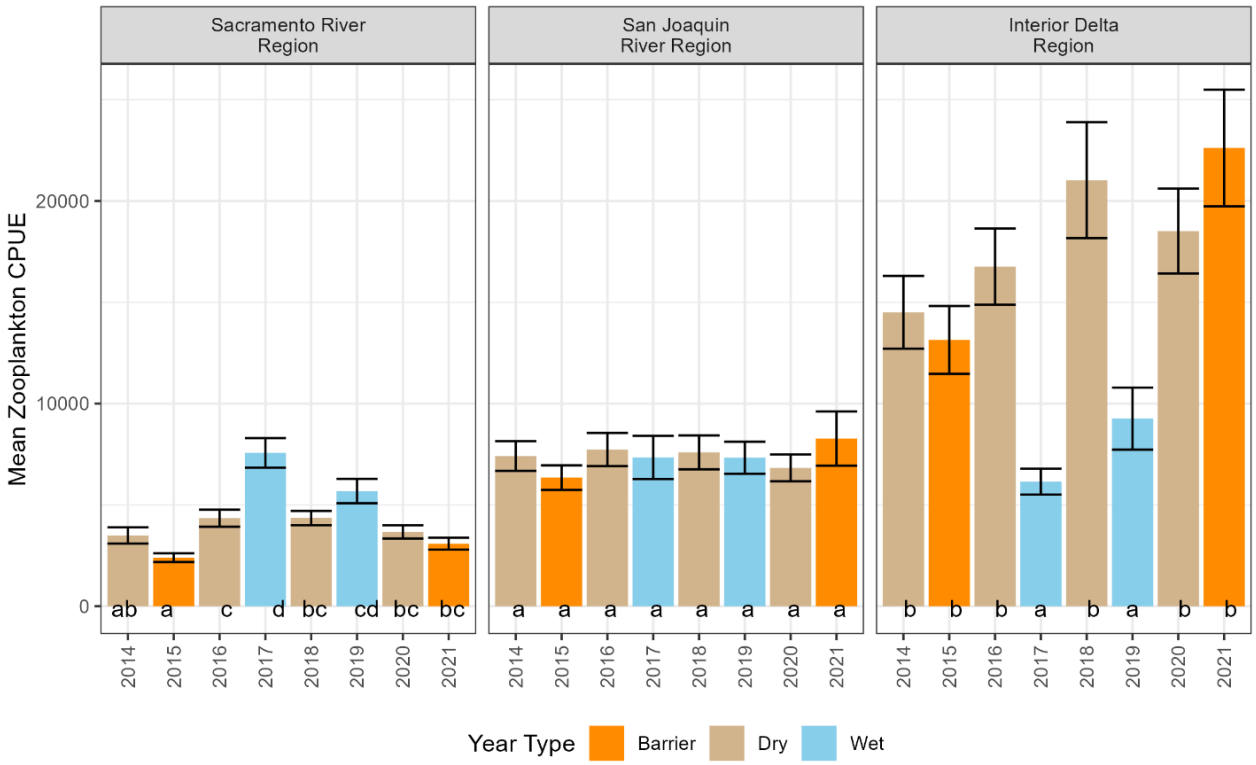

NOTES: CPUE = catch per unit effort

Letters below the bars indicate years in which catch per unit effort was not significantly different (within a given region).

Figure 2.3.3-12 Total zooplankton catch per unit effort (+/- one standard error) between Central Delta regions and years.

Community composition also varied between years and between Central Delta regions (**Figure 2.3.3-13**), although this was a very small proportion of the variance (**Table 2.3.3-7**). The Interior Delta Region had more cladocera (*Daphnia*, *Bosmina*, *Diaphanasoma*, and other Cladocera) than the other regions, particularly in dry years. The Sacramento River Region had more *Acartiella* and barnacle nauplii than the other regions, particularly during dry years. However, *Pseudodiaptomus* dominated the zooplankton communities in all years and regions.

Discussion

The EDB did not appear to affect zooplankton abundance and community composition. There were consistent trends between wet and dry years: abundances were higher in wetter years (2017, 2019) in the Sacramento River Region and in drier years in the Interior Delta Region. However, in dry years, abundances were similar between barrier years and non-barrier years. Zooplankton abundance in the Sacramento River Region was lower in 2015 than in some dry years but did not differ significantly from 2014 conditions, so it is difficult to know whether this decline was attributable to the barrier.

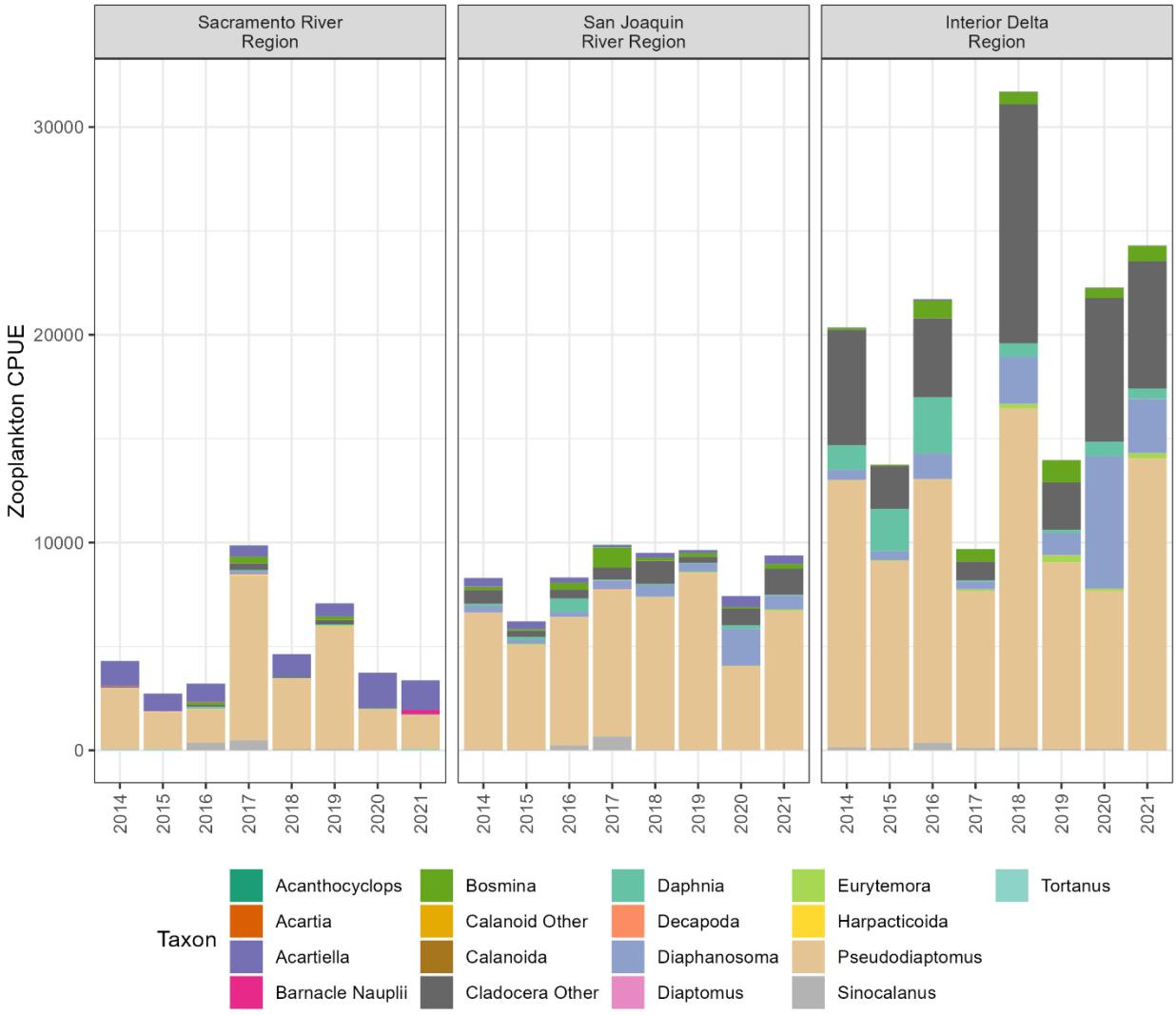

NOTE: CPUE = catch per unit effort.

Figure 2.3.3-13 Community composition of zooplankton by Central Delta region and year.

TABLE 2.3.3-7
RESULTS OF A PERMUTATIONAL MULTIVARIATE ANALYSIS OF VARIANCE OF ZOOPLANKTON COMMUNITY COMPOSITION, 2015–2021

Model Term	Df	SumOfSqs	R2	F	Pr(>F)
Region	2	41.2	0.03461	73.5485	0.001
Year	7	57.08	0.04795	29.1174	0.001
Region*Year	14	31.31	0.0263	7.9859	0.001
Residual	3788	1060.85	0.89114		
Total	3811	1190.44	1		

SOURCE: Data collected by California Department of Fish and Wildlife; modeling performed by California Department of Water Resources in 2023.

The extremely dry conditions and changes to salinity compliance points along the Sacramento River meant that salinity in the Sacramento River Region was higher during 2015 and 2021 than during other dry years (see Section 2.3.2, "Salinity, Water Quality, and Harmful Algal Blooms"). This may explain why higher numbers of the brackish-water *Acartia* sp. and barnacle nauplii, and fewer of the dominant copepod *Pseudodiaptomus forbesi*, were found in the Sacramento River Region. *P. forbesi* has its highest abundance in fresh water, and its abundance in the brackish water is negatively correlated to freshwater flow.

These results are similar to the findings of Barros et al. (in prep.) that *P. forbesi* decreased in the region around the Sacramento–San Joaquin River confluence and increased in the South-Central Delta during droughts. Kimmerer et al. (2019) predicted lower subsidies of *P. forbesi* copepodites from freshwater areas to downstream regions, but they did not find significantly lower abundances when looking at the long-term monitoring surveys. This may have been the case because decreased abundance in the Sacramento River Region was offset by increased abundance in the Interior Delta Region (Figure 2.3.3-12).

2.3.3.3 Aquatic Weeds

Franks Tract, on the eastern side of the EDB, has been inundated with submerged aquatic vegetation, or SAV, for the past several years. To assess the impact of the barrier, aquatic vegetation was monitored across the Delta using hyperspectral imagery. Imagery has been collected over all or most of the Delta annually since 2014; additional surveys were conducted in 2004 and 2008. Imagery was collected in July 2021 and July 2022.

SAV within Franks Tract has also been monitored annually using rake surveys conducted by the California Department of Parks and Recreation, Division of Boating and Waterways, in collaboration with SePRO Corporation, Carmel, Indiana. These data are summarized in the *Report on the Impact of the Temporary Urgency Change Petition and Emergency Drought Barrier on Harmful Algal Blooms and Aquatic Weeds in the Delta* (Hartman et al. 2022) and the update of that report for 2022 (U.S. Bureau of Reclamation and California Department of Water Resources 2023).

In brief, the hyperspectral imagery from 2021 indicated that the changes to currents within Franks Tract resulting from the barrier altered the distribution of SAV within Franks Tract but did not change total SAV coverage (**Figure 2.3.3-14**). Increased velocities on the eastern side of Franks Tract cleared a large part of the tract that had weeds in it during 2017–2020, but the center of the tract near False River filled in with weeds to a greater extent than previously. In 2022, hyperspectral imagery showed a decrease in area of SAV, particularly in the southern area of Franks Tract (Figure 2.3.3-14).

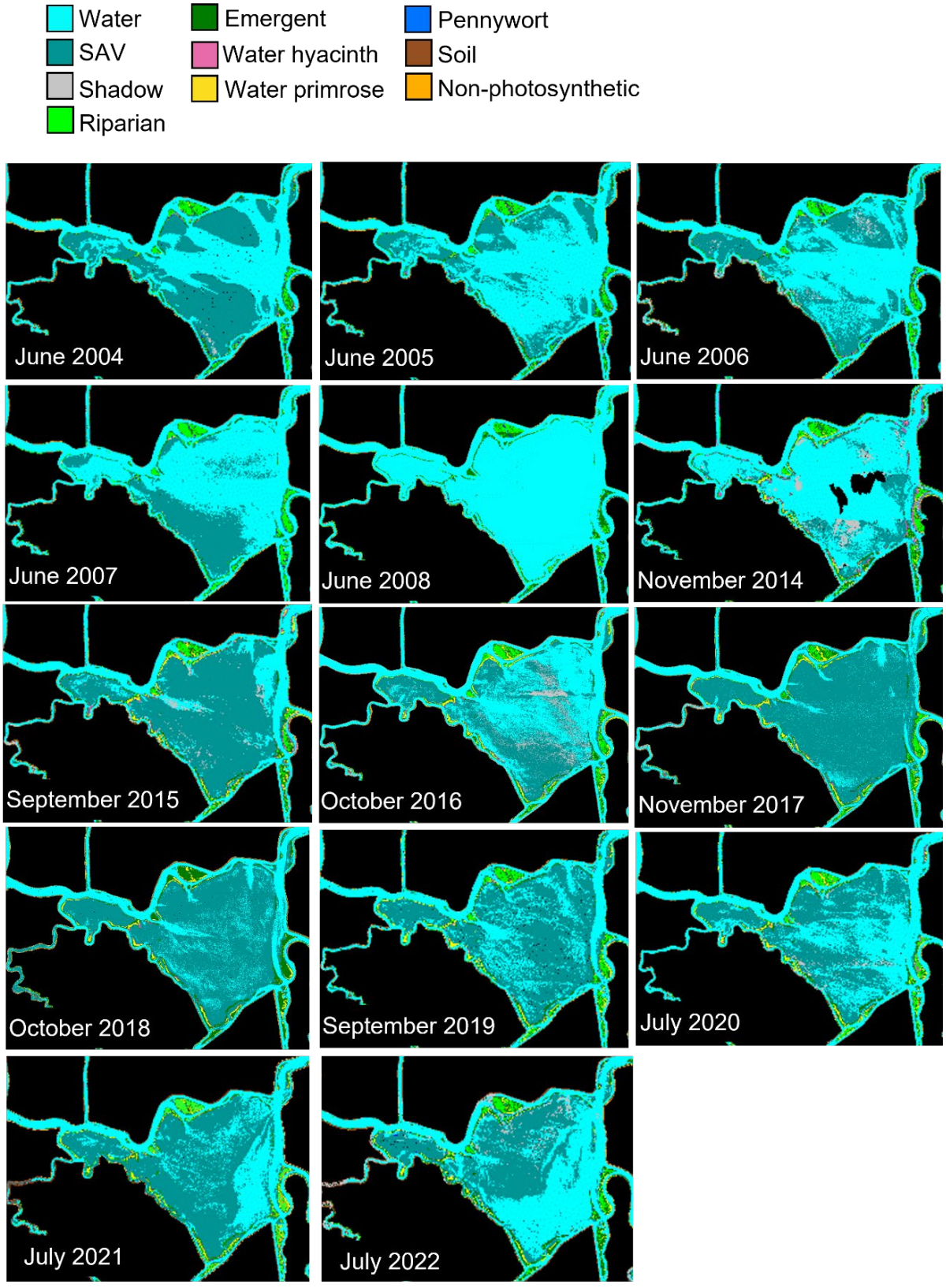

NOTE: SAV = submerged aquatic vegetation.

Figure 2.3.3-14 Time series of hyperspectral imagery for Franks Tract.

Encroachment of weeds into the center of Franks Tract was first identified during the 2015 barrier installation (Kimmerer et al. 2019). There was also a Delta-wide increase in aquatic weeds in 2015 that did not reverse in the ensuing wetter years, and it is unclear whether this regime shift was influenced by the 2012–2016 drought (Hartman et al. 2022).

2.3.3.4 Predation Study

Objectives

The purpose of the EDB Predation Study (EDBPS) was to assess impacts of the EDB on the predation rate of juvenile salmonids. The EDBPS study addressed the following conservation measure from the 2021 EDB Biological Assessment:

> To address the uncertainty associated with potential predation effects from the retained barrier rock, DWR will conduct a study using predation event recorders or other appropriate technology to examine the evidence for areas along the barrier with relatively high predation and, should any such areas be identified, the feasibility of structural modifications to address any predation concerns noted will be evaluated. In the event that embankment rock is retained, through a subsequent permit action, DWR will expand this analysis to continue during the period when the embankment rock is retained within the channel.

The EDBPS had the following objectives:

(1) Determine the effects of construction, presence, and notching of the EDB on the juvenile salmon predation rate relative to other environmental variables.

(2) Examine the influence of the EDB on predation rate through time.

(3) Examine the influence of the EDB on the movement and survival of acoustically tagged salmonids from other studies.

The following sections provide an overview of the study design, methods, approach, analysis, and results. Details of the study are available in **Appendix G** of this report.

Predation Study Design

The EDBPS was conducted at the site of the EDB in False River. The study reach extended 500 meters east and 500 meters west of the barrier and included the entire width of the channel (**Figure 2.3.3-15**). The study used drifting predation loggers to measure where and when predation events occurred. The drifting predation loggers were designed and constructed

based on the National Marine Fisheries Service's predation-event recorders (PERs) (Demetras et al. 2016). Each PER was equipped with a GPS transponder and a magnetic timer. A tethered golden shiner was attached to each PER as a surrogate bait species for Chinook salmon.

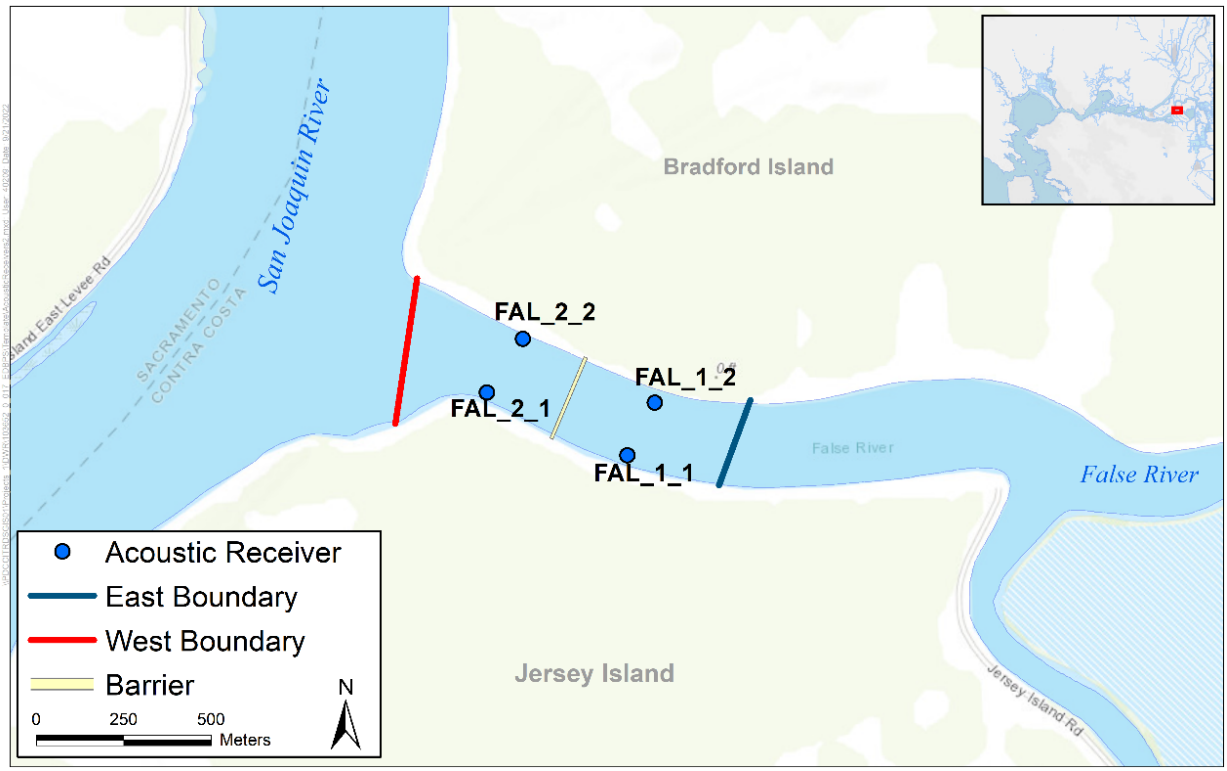

Figure 2.3.3-15 Emergency Drought Barrier Predation Study site, including study reach boundaries and locations of acoustic receivers.

Sampling occurred at the study site from three hours before sunset until three hours after sunset, to target a total of 600 minutes of cumulative float time on each sampling day. Sampling was conducted during three periods: before, during, and after construction of the EDB.

Before and during construction of the EDB, PERs were deployed across the width of False River 500 meters up-current of the barrier. The PERs were allowed to drift to 500 meters down-current of the barrier, or to drift for one hour if the current was insufficient for the PERs to drift the entire 500 meters.

After construction of the EDB, PERs were deployed simultaneously on the east and west sides of the barrier. Depending on prevailing current and winds, PERs were allowed to drift either from the EDB to 500 meters away, or from 500 meters away toward the barrier, or for one hour within 500 meters of the barrier. If a PER intersected the EDB's buoy line and became stuck, crews manually guided the PER under the buoy line to enable it to continue to drift.

PERs were manually retrieved one by one. Upon retrieval, the status of the predation-triggered time and golden shiner was recorded. If triggered, the timer was reset and the golden shiner replaced before subsequent deployments. A "predation event" was defined as having occurred when the timer was triggered and the fish was missing.

Statistical Approach

To evaluate effects of the EDB on predation risk, a Cox proportional-hazards regression model was used. This model evaluates the effects of spatial and temporal parameters during each construction period. The response variable, "predation," is a Boolean value, which may occur at a single point in time for a trial (the trigger time), and after which the trial ends. The predictor variables are a mix of linear parameters and categorical values.

A full model selection scheme was used to determine which covariates most strongly influenced predation risk. Because the study was intended to evaluate the effects of the barrier's presence and the spatial extent of those effects, the model comparisons always included the effects of "barrier period" and "distance to barrier" and iterated through all combinations of other covariates. The Akaike information criterion (AIC) was used to determine the best model with the lowest AIC score (Burnham and Anderson 2002).

As discussed below, the following predictor variables, which were hypothesized to affect predation risk, were included as covariates in the Cox model:

- Barrier period.
- Temporally and spatially varying covariates—distance to barrier, distance to shore, and speed of predation event.
- Temporally varying covariates—illuminance and time to night.
- Spatially varying covariates—bottom roughness and SAV.
- Point covariates—starting position and water quality.
- Tidal phase.

Barrier Period

Barrier period was used in all models to examine how the EDB's various construction phases affected predation risk. Barrier period is a categorical variable with six levels that correspond to time periods throughout the study (**Table 2.3.3-8**).

TABLE 2.3.3-8
BARRIER PERIOD, TIMELINE OF BARRIER CONSTRUCTION AND PRESENCE, AND EMERGENCY DROUGHT BARRIER PREDATION STUDY SAMPLING

Period	Dates	Barrier Status	Sampling Days
Preconstruction	May 22, 2021–May 27, 2021	No barrier	6
Construction	June 3, 2021–June 17, 2021	Partially constructed barrier	11
Postconstruction	June 18, 2021–August 3, 2021	Barrier in place	10
Pre-notch	November 15, 2021–December 10, 2021	Barrier in place	10
Notched	January 18, 2022–March 25, 2022	Notched barrier	15
Post-notch	April 25, 2022–June 24, 2022	Barrier in place	14

Temporally and Spatially Varying Covariates

Temporally and spatially varying covariates were estimated for all records within a PER deployment, representing a unique value for each status record in the model.

- *Distance to Barrier:* The great circle distance (in meters), accounting for the curvature of the earth, was calculated from each GPS location to the nearest point on the barrier from a KMZ Google Earth file R package *Geosphere* (Hijmans 2016).
- *Distance to Shore:* The great circle distance (in meters) was calculated from each GPS location to the nearest point on shore from the National Hydrography Dataset's subbasin-level data.
- *Speed of Predation Event Recorder Movement:* For each status record, PER speed was calculated as the change in the great circle distance (in meters) over the prior 60 seconds (in m/s).

Temporally Varying Covariates

These covariates were recorded continuously during each sampling day and did not vary with PER location.

- *Illuminance:* Illuminance was measured using a light meter (units: kilolux) anchored to the east side of the barrier at a depth of roughly 1 meter. The model used direct light meter values except when the light meter was shaded. For these shaded time periods, the light meter values were ignored and illuminance was instead estimated from a smoothed locally estimated scatterplot smoothing or LOESS model predicting light values over time. Each status record used the ping nearest in time to the record time.

- *Time to Night:* For each status record, time to night was calculated as minutes until the sun was 18 degrees below the horizon (astronomical twilight), using the R package *suncalc* (Thieurmel and Elmarhraoui 2019).

Spatially Varying Covariates

These covariates vary over spatial coordinates and link to all GPS ping locations of a PER deployment.

- *Bottom Roughness:* The closest bottom roughness beneath each PER was reported for each status record. The terrain roughness index (Riley et al. 1999) was calculated from hydrographic survey data provided by DWR using the QGIS terrain roughness index tool. This value represents the variability of the river's bottom surface by evaluating the depth differences of neighboring survey points.
- *Submerged Aquatic Vegetation:* The presence of SAV was evaluated using the mosaiced and georeferenced photos from the drone survey nearest to the deployment date.

Point Covariates

These covariates were measured only once for each PER deployment session.

- *Starting Position:* This was a categorical variable. PERs started on either the east or the west side of the barrier location, whether or not the barrier was installed.
- *Water Quality:* An onboard YSI EXO2 or the nearby California Data Exchange Center station FAL was used to measure water temperature (°C), salinity (parts per thousand), and turbidity (NTU) at the start of each deployment session near the location of the first PER deployed.

Tidal Phase

As a categorical variable, tidal phase was categorized in the field by the direction of flow at the beginning of PER deployment. Currents were categorized as follows: moving east to west, an "ebb"; moving west to east, "flood tide"; with little movement after an ebb, "low slack"; and with little movement after a flood, "high slack."

Acoustic Telemetry of Tagged Salmonids

Acoustic Telemetry Barrier Arrays

Juvenile Salmonid Acoustic Telemetry System (JSATS) arrays were deployed to monitor the survival, passage, and behavior of juvenile salmonids at the EDB. Two arrays of two Advanced Telemetry Systems acoustic receivers—the SR3001 *Trident* and SR3000 *Trident*—were deployed, one on each side of the barrier location (Figure 2.3.3-15). The receivers were moored to the river bottom using a weighted frame and were located approximately

0.7 meter above the river bottom. Receiver deployment was completed on December 10, 2021, and most receivers were retrieved on March 9, 2022. A single receiver (FAL_2_1) was unretrievable, as it had been tangled in a buoy line. Upon retrieval, a large rock—presumably from the barrier—was found on top of the frame. Redeployment of the receivers was also completed on March 9, 2022, with an average downtime of 14 minutes. FAL_2_1 was replaced with a new receiver when it was found to be unrecoverable. The second receiver deployment lasted until June 29, 2022.

Central Valley Coordinated Acoustic Telemetry Array

An array of coordinated acoustic receivers is currently maintained in the Central Valley along the Sacramento and San Joaquin rivers and in the Delta. Each November, detection data for the previous water year are processed and uploaded to the federal JSATS telemetry repository in the National Oceanic and Atmospheric Administration's ERDDAP database. Thus, no processed data were available for WY 2022 from arrays associated with the West False River barrier during the writing of this report. However, some preliminary detection data were available from another ERDDAP database, CalFishTrack. These data have undergone minimal processing to remove multi-path detections (transmission reflections) and false positives. More information on this processing is available on the CalFishTrack website (https://oceanview.pfeg.noaa.gov/CalFishTrack/).

Tagged Salmonid Releases

No tagged juvenile salmonids were released specifically to study the effects of the EDB, although several concurrent studies released fish that were expected to be detectable by the receivers deployed for this study. As described above, the federal JSATS telemetry repository is updated only once annually, in November, after quality assurance/quality control (QA/QC) is conducted by database administrator Arnold Ammann. Therefore, fish metadata for this analysis were retrieved directly from Arnold Ammann and represent metadata delivered to him through August 2022.

In total, 8,809 salmonids from 14 different studies were released during the study period. No tagged fish were released within 150 days before receiver deployments. Released salmonids were a mix of five races/species: 1,236 California Central Valley steelhead, 4,374 fall-run Chinook salmon, 1,770 winter-run Chinook salmon, 1,120 spring-run Chinook salmon, and 309 wild-caught Chinook salmon.

Analysis of Detection Data

Optimal Blanking Period

Identifying when a fish functionally leaves a site versus when it goes undetected within or near the site is an important step in assessing delay

and site fidelity. Methods adapted from Capello et al. (2015) were used to quantitatively identify an optimal blanking period that groups detections of a single individual occurring at a single receiver site within the blanking period.

A range of maximum blanking periods (MBPs), from three seconds to 50 minutes at intervals of three seconds, was used on detection records to create datasets of continuous detection events (CDEs) (referred to as "Continuous Residence Time" in Capello et al. [2015]), one dataset per MBP. A CDE represents a continuous period of time when an individual is estimated to be present at an acoustic receiver despite not being detected.

The duration of each CDE created within each MBP dataset was then compared to a range of times (t), from three seconds to 28 hours. Next, the proportion of CDEs lasting longer than time (t) was calculated; this is considered "survivorship." A survivorship curve was created for each CDE dataset, with t on the x axis.

The survivorship curves for each MBP were then compared pairwise with the curve of the next larger MBP by calculating the sum of squared residuals, or SSR. These were then renormalized (a process referred to here as "rSSR") based on the number of CDEs created for each dataset. Convergence, which occurs when increasing the MBP no longer affects the number of CDEs created, was then assessed by examining a plot of the log(rSSR) as a function of MBP. A threshold was set at 1 percent of the full rSSR range to identify when convergence was sufficient to select an optimal MBP. This optimal MBP was then used to create a final set of CDEs, which was used for the remaining analyses.

Predator-like Behavior

After CDEs were created, the events were examined for movements or behaviors that were considered predator-like. This involved identifying tag codes that either (1) were detected at Benicia before being detected at the barrier; (2) were first detected passing the barrier, then were detected at Benicia, then returned to the barrier; or (3) were detected across the barrier appearing to move against the tide or during slack tides. Although it is impossible to positively identify whether a JSATS tag is no longer within a living fish, especially given the tendency of some steelhead to exhibit predator-like behavior, these tags were removed from the analysis.

Time in Vicinity

Time in vicinity of the barrier was evaluated at two scales: Time in Vicinity at the visit scale (TIV), defined as total time elapsed during a single visit to a receiver, allowing multiple visits per receiver per individual; and Total Time in Vicinity at the individual scale (TTIV), defined as the sum of the total time spent in the vicinity of all barrier receivers per individual.

TIV for a visit was calculated using the CDEs created above, from the first time they were detected at either barrier array (east or west) to the last continuous time they were detected at the same array. When a period of time longer than the optimal MBP (defined above) was reached before another CDE began at the opposite array, then the visit ended at the end of the last CDE, and a new visit began when they returned or when they were detected on the opposite array. For the individual scale, the total amount of time a fish spent within the barrier site (i.e., TTIV) was calculated, summing the duration of all CDEs at the barrier site. Given the low numbers of detections, no statistical analysis was possible for TIV or TTIV to examine the impact of barrier period on time in vicinity.

Travel Time to Benicia

It is hypothesized that the barrier would affect travel times for migrating salmonids, particularly during the full-barrier periods. To assess this impact, travel times were calculated from the barrier to the receivers at Benicia. Travel time was calculated as the difference in time between the last detection on any receiver at the barrier site to the first detection on any receiver in the Benicia arrays (east and west).

Detections in the Vicinity

Of the 8,809 fish within the metadata, only 43 fish matching the list of tags were recorded at the EDB receivers. Therefore, to examine the migration patterns of tagged fish adjacent to the EDB, the field staff also evaluated detection data for the five arrays closest to the EDB array: Sacramento River below Georgiana Slough, Benicia East, Benicia West, Holland Cut, and Old River near Quimby.

Assumptions and Limitations

The design and implementation of the EDBPS encountered several limitations, each of which provided an opportunity to learn. The limitations encountered are described here to minimize their occurrence in the future, or to prevent them to the extent possible.

Emergency Timeline

The planning phase of the EDBPS was unavoidably truncated, given the emergency nature of the study. This short timeline limited the amount of time available to design and fully evaluate the PERs and their components (e.g., GPS units) and the field and data collection processes. As a result, some of the methods for and design of the PERs were revised after the study had begun, and some data loss occurred.

Among the problems encountered were malfunctioning GPS units. During the first months of the study, several units would power down without warning,

resulting in the loss of data because there was no way to track the locations of the PERs. After several attempts to troubleshoot this problem, some of which resulted in more lost data, GPS transponder units were replaced with GPS data loggers. Two lessons were learned as a result: (1) If something cannot be fixed, try a new product; and (2) starting the QA/QC process early, while a study is ongoing, limits the extent of data loss by addressing the problem quickly after the problem arises.

Another problem encountered was the high variability in pull strength of the magnets used on the PERs. Detailed calibration was required to identify which magnets were not within the range of acceptable pull strength and to eliminate them from the study. Furthermore, the cavity in which the magnet sat on the bottom of the PER was modified by filing down the edges, so that if a predator pulled from the side, it would require a similar pull strength to release the magnet as if it were pulled from directly below. Future studies that include the use of PERs should perform this calibration before field deployment to avoid inconsistent triggering of predation events.

Prey Surrogate

Because the study's planning phase was less than two weeks, ordering juvenile Chinook salmon from a hatchery for the study—typically a several-month-long process—was not feasible. As a result, a surrogate prey species was needed. Using a surrogate for this study would involve using an untested assumption: that predatory fish would have similar prey selectivity for both the surrogate species and juvenile Chinook salmon. The following criteria were chosen for this surrogate species:

- Same general size, shape, and swimming ability and speed as juvenile Chinook salmon.
- Readily available for year-round purchase at local bait shops.
- Robust to warm, tidal conditions.

"Jumbo-sized" golden shiners generally met these requirements. Occasionally, the jumbo-sized fish were smaller than expected, which caused some fish to fall off the leaders, resulting in missing data. The field crew discovered that there was some variation among bait shops and through time in what was considered "jumbo-sized"; this required that the crew inspect the fish before purchase. If fish were too small or too large, fish in a different size category were purchased.

Bait Availability

Despite the field crew's best efforts to ensure that golden shiners would be available year-round, several occasions arose when the fish were not available at a regional scale. In the middle of the study, the crew discovered

that there was only one supplier for all bait shops in the Delta region. The supplier had had a large mortality event at its facility and was unable to deliver the usual supply to all bait shops.

Dozens of phone calls to bait shops were made to locate golden shiners as far away as Yuba City, California, and Reno, Nevada. Regular communication with the bait shops was necessary, and ultimately, the study was able to continue despite the shortages. Only one sampling week was postponed, for one week, because of a lack of bait availability. A staff member needed to be ready and willing to travel a substantial distance to obtain bait fish.

Sampling Outside of the Target Species' Temporal Window

Aside from October and November, to allow sufficient sampling of each barrier condition, this study was conducted year-round even though juvenile Chinook salmon are typically present in the western Delta only in the winter and spring months. Therefore, for many months of the study, the results are not representative of juvenile Chinook salmon predation risk, which limits the study's predictive power. For example, water temperatures during the summer and fall were likely too warm for Chinook salmon to tolerate.

Influence of Barrier Construction and Presence on Sampling

The construction and presence of the EDB forced fieldwork modifications during the study. For safety reasons during the barrier construction period, field crews avoided active work areas and deployed the PERs in a manner intended to prevent them from floating into work areas. If PERs floated into work areas, they could not be retrieved until after the site was safe to navigate.

During full barrier installation, the study design changed because the east and west sides of the EDB were isolated from each other. As a result, two field crews released PERs, one on either side of the barrier. Each side had a different strategy for PER deployment, which was dependent on wind direction. Typically, the crew on one side of the barrier released PERs away from the barrier upwind, and the PERs floated downwind into the barrier (or to shore). The crew on the other side released PERs upwind at the barrier, and the PERs floated downwind away from the barrier.

Predator Identification

Ideally, an understanding of the predation risk for juvenile Chinook salmon would include species identification of the fish that preyed upon the tethered fish. However, because the water was highly turbid and sampling frequently occurred late in the day and into the night, GoPro cameras could not be added to the PERs to observe the predation event and identify the predatory species. However, anecdotal hook-and-line sampling in the area suggested that small striped bass were the predominant predatory fish. Future studies

may include a hook and line or other sampling component to estimate the relative abundance of various predatory fish species, or light or acoustics may be employed to capture the predation event on camera without altering fish behavior.

Light Surveys

Construction activities occurred 24 hours per day and involved illumination by artificial light, which might have affected nighttime predation risk. For this study, pilot surveys were conducted to map light on sampling dates during the 2021 construction period (June 9, 14, 16, and 17) and one sampling date during the postconstruction period (July 26). The pilot surveys used a LI-COR LI 1500 light sensor logger and LI-193 spherical quantum sensor. The surveys involved three components:

- Dusk sampling, 30 minutes before and 30 minutes after sunset, to compare natural light levels with artificial illumination after sunset.
- Sampling at five depths (2–6 feet) to assess attenuation.
- Mobile transects after sunset to map levels of artificial light.

Dusk and mobile sampling were conducted with the light meter immediately below the water surface. Attenuation sampling was used to develop a relationship between depth and light to adjust the dusk and mobile values to the approximate depth of tethered fish on the PERs. The attenuation relationship indicated that light levels at the depth of tethered fish were approximately 14 percent of the light levels at the surface.

The primary conclusion from the pilot mobile light surveys was that artificial light from construction was highly local and highly variable. Mobile surveys would have to have been conducted multiple times during every night of PER sampling to fully characterize the spatial patterns. Such repeated surveys were not feasible because the mobile surveys were almost as time- and labor-intensive as the PER sampling and required a dedicated boat. As an alternative, from November 2021 through June 2022, stationary light surveys were conducted by deploying the same light meter used in the mobile surveys at a fixed location on the east side of the barrier during each day's PER sampling. The light meter was placed roughly 1 meter below the water surface to match the depth of tethered fish on the PERs. The results of the fixed light sampling were deemed unusable in the survival model because of the limited collection period.

Light surveys have the potential to explain predation risk if sufficient spatial and temporal coverage is achieved. An alternative approach for future work is to deploy a grid of fixed light meters throughout the study site that collect data continuously. Determining an appropriate sampling regime will include tradeoffs between spatial versus temporal coverage of light data,

labor costs versus equipment costs, and overall spatiotemporal coverage versus total costs.

Study Results

Predation Risk Results

During the 13-month study, 621 predation events occurred over 6,500 PER deployments on 66 sampling days, with a total soak time of 4,387.9 hours (**Table 2.3.3-9**). Effort was unequal between each period, as fewer days were available for deployments during the preconstruction and construction periods. Fewer and shorter deployments occurred when the barrier was not closed, as higher flows carried PERs out of the study region more quickly and more time was necessary to recover drifting units.

TABLE 2.3.3-9
SAMPLING EFFORT BY PERIOD WITHIN THE STUDY AREA
(WITHIN 500 METERS OF THE BARRIER LOCATION)

Period (Barrier Status)	Date Range	Sampling Days	Deploy-ments	Soak Time (hours)	Predation Events	Records per Deployment [mean (SD)]
Preconstruction (open)	May 22–27, 2021	6	379	211.8	24	33.7 (13.9)
Construction (partially open)	June 7–17, 2021	11	823	448.2	57	31.9 (19.6)
Postconstruction (closed)	July 12–August 3, 2021	10	1,198	946.3	120	47.8 (18.1)
Pre-notch (closed)	November 15–December 10, 2021	10	1,213	979.0	161	48.4 (18.2)
Notch (notched)	January 24–March 25, 2022	15	1,351	668.6	31	29.5 (13.2)
Post-notch (closed)	April 25–June 24, 2022	14	1,536	1,134.0	228	44.4 (17.8)
All Periods		66	6,500	4,387.9	621	40.5 (18.9)

NOTE: SD = standard deviation

SOURCE: Data compiled by Environmental Science Associates in 2022

A Cox model was selected, using a full model selection approach utilizing AIC, that evaluated eight numeric and three categorical parameters to predict predation risk over time.

The most parsimonious model with the lowest AIC included the following parameters: period, distance from barrier, distance from shore, salinity, movement speed, temperature, time to night, turbidity, bottom roughness,

and interaction of period and distance from barrier (**Table 2.3.3-10**). All numeric parameters except distance to barrier were evaluated as penalized splines to predict nonlinear trends. All parameters selected in the most parsimonious model were included in the top five models, except turbidity, which was in four of the top five models.

TABLE 2.3.3-10
SURVIVAL MODELS WITHIN LESS THAN 4 Δ-AIC SCORES OF THE MOST PARSIMONIOUS MODEL

Formula	AIC
Period, distance from barrier, distance from shore,† salinity,† speed,† temperature,† time to night,† turbidity,† bottom roughness,† and interaction of period and distance from barrier	12092.33
Period, distance from barrier, distance from shore,† salinity,† speed,† start position, temperature,† time to night,† turbidity,† bottom roughness,† and interaction of period and distance from barrier	12093.93
Period, distance from barrier, distance from shore,† salinity,† speed,† temperature,† tidal stage, time to night,† turbidity,† bottom roughness,† and interaction of period and distance from barrier	12094.65
Period, distance from barrier, distance from shore,† salinity,† speed,† temperature,† time to night,† bottom roughness,† and interaction of period and distance from barrier	12095.13
Period, distance from barrier, distance from shore,† salinity,† speed,† start position, temperature,† tidal stage, time to night,† turbidity,† bottom roughness,† and interaction of period and distance from barrier	12096.3

NOTES: AIC = Akaike's Information Criterion; † = nonlinear term

SOURCE: Data compiled by Environmental Science Associates in 2022

In the selected model, higher predation risk is predicted during the pre-notch, notch, and post-notch periods, and risk increases nearer to the shore. Predation risk is predicted to increase as salinity increases, water temperature increases, and as time approaches night. There were no significant relationships ($p < 0.05$) between predation risk and distance from barrier, PER speed, turbidity, bottom roughness, or the interaction of period and distance from barrier.

Summary of Detailed Predation Risk Analysis

The EDBPS examined whether the EDB on West False River influenced predation over time through key phases of construction and notching and relative to several environmental variables. The study found that in the selected model, distance from the barrier did not increase predation risk; however, an interaction between study periods after construction (pre-notch, notch, and post-notch) and distance from barrier suggests the existence of a zone of influence that increases predation risk within 150 meters of the barrier. One management implication of this finding is that postconstruction monitoring was critical to revealing the lag in the barrier's predation effects, which may have been attributable to the time needed for resident predatory fishes like black bass to establish their hunting territory.

The study also found that notching the barrier to allow fish passage during the juvenile salmon migration period resulted in the lowest observed predation rate. However, the notch period was also associated with the lowest water temperatures and lowest salinities, likely in response to increased Delta outflows relative to other periods. In the modeling space, where the effects of individual covariates are held constant to evaluate the effects of each covariate on its own, predation risk was higher during the notch period than during earlier periods. Eddies around the barrier appeared to be associated with the location of most predation events during the notch period.

An important caveat of the study findings is that this study occurred across only a single calendar year. Additional effort would be needed to examine how relationships may vary under a wider range of environmental and operating conditions.

During the notch period, a large reduction in predation rate was observed that had not been evident in the predicted predation hazard ratio. More rapid transit speeds past the barrier were observed; intuitively, these are expected to be related to lower time of exposure to predators associated with the barrier structure. However, the barrier's hydrodynamic influence on adjacent eddy formations may have expanded the zone of influence, paradoxically creating a larger predation zone for predators to take advantage of PERs entrained in eddy vortices. Furthermore, the hazard model could account for seasonally autocorrelated temperature effects in which predation rates increased in response to elevated metabolic energy demands (Rice et al. 1983; Hartman and Brandt 1995). These effects likely increased predation rates near the barrier during other periods when the barrier was in place.

Comparing the predation rate observed in this study with other recent investigations in the Delta is warranted: Such a comparison would put observed predation risk at the barrier into context with predation risk in the adjacent region. The predation rates and modeled predation risk were slightly lower than reported by other PER studies in the Delta. However, this study is unique because it focused on major hydrologic changes occurring over a year in a single reach within the Delta. In addition, prior PER studies used hatchery-reared Chinook salmon, which were unavailable for this study.

This study's overall predation rate, 9.6 percent of deployments, is slightly lower than that of other studies in the region. The first trials of PERs in the Delta deployed 216 PERs, with a 15.3 percent predation rate (Demetras et al. 2016). Michel et al. (2020) describe similar results, with reported PER predation rates of 15.7 percent of deployments, and with predation risk correlating with higher temperatures and peaking soon after sunset. In their shallower study sites, rougher bottom surfaces correlated with increased

risk, as did proximity to predators. A study by Nelson et al. (2021) investigated the effect of artificial lights on predation rates; the study found that predation rates increased in the presence of artificial lighting at night, especially after dark, with predation rates of 0–30 percent of light-binned deployments.

Summary of Acoustic Telemetry Results

Of the 6,883 and 976 salmonids tagged in winter/spring 2021–2022 in the Sacramento and San Joaquin river basins, respectively, 43 tags were detected at the receivers at the barrier. Tags that did not exhibit predator-like behavior (35 of the 43 tags) spent short amounts of time at the barrier receivers, averaging 15 minutes when the barrier was open and 1.3 hours when the barrier was fully closed.

Although total tag numbers were small, the tags arrived at the barrier receivers across the entire range of the salmonid emigration season (December through June), covering all barrier operation periods. Because of the lack of receiver coverage immediately east and west of the barrier, this study resulted in only limited understanding of the routes of tagged salmonids as they approach West False River, and of how routes may vary seasonally and under different barrier conditions. Incorporating a more comprehensive receiver array in the region would enable future studies to better identify the baseline movement patterns of salmonids and determine how barrier installation may affect them. In particular, adding acoustic receivers at the other Franks Tract entry points would provide a comprehensive look at entrainment into the Central Delta and effects of the barrier on that entrainment.

Also, a focused effort of tagging and releases near the barrier site would increase sample size. Such an effort may allow for the statistical analysis of factors such as delays in transit caused by the barrier, or for the evaluation of the extent to which the barrier reduces entrainment into Franks Tract.

Management Implications

Distance to the barrier had a more pronounced effect on predation risk in the latter five months of the study, which may suggest that predators' colonization of the EDB over time led to increased predation risk. If this is the case, this study's estimates of predation risk are likely to be low, and the degree of the underestimated risk could be evaluated by periodically conducting field trials at given periods throughout the duration of barrier presence. On the other hand, if the EDB is to be removed or notched on an annual basis, the estimates are more likely to accurately reflect predation risk, because this study was carried out over the course of several months and encompassed various degrees of barrier construction and deconstruction.

Predation rate was lower when the barrier was notched, but predation risk was paradoxically elevated. Closer inspection revealed that lower predation rates during the notch period were attributable to lower water temperatures, lower salinity caused by high outflows, and a distance-to-barrier effect from higher PER speeds and the resulting reduction in exposure to the barrier. The relationship between predation risk and distance to barrier during the notch period appears to result from flow dynamics that create eddies that can entrain passing salmon. More analysis is needed regarding the ways in which flow velocity and vorticity changes around the shoulders of the notch may have increased the risk of predation.

There was evidence that near-field exposure of tethered fish to within 150 meters of the EDB resulted in increased predation risk, and tagged salmonids did become exposed to the barrier; however, far-field impacts of the barrier on movement and survival of salmonids are uncertain. As evidenced by changes in the salinity field, tidal dynamics suggest that the influence of ebb tides via the San Joaquin River may have been stronger with the EDB in place. Furthermore, juvenile salmon outmigrating down the Sacramento River and entering the San Joaquin River via Threemile Slough, Georgiana Slough, or the Delta Cross Channel are not likely to be entrained east into West False River when the barrier is in place because the relative influence of flood tides is muted.

Franks Tract and the Central Delta have long been known to be poor habitat for outmigrating juvenile salmon because of the high abundance of warmwater invasive predators that reside there. This study did not evaluate the effectiveness of the EDB at preventing juvenile salmon from entering the Central Delta, but the EDB may be an effective conservation tool in the future if it results in increased cumulative survival to ocean entry.

This page intentionally left blank

CHAPTER 3
Conclusions and Lessons Learned

3.1 Summary of Effectiveness and Impacts

The 2021–2022 EDB effectively reduced the salinity of water entering the Central Delta and the Old/Middle River corridor in 2021, although it had at best a modest influence on salinity at the State Water Project (SWP) and Central Valley Project (CVP) pumps. This salinity reduction was achieved by altering tidal dispersion patterns so that less saline water was pumped through Franks Tract into the South Delta. The cost of this change in dispersion patterns was higher tidal energy on the Sacramento and San Joaquin rivers, which caused enough salinity to intrude near San Andreas Landing—a Water Right Decision 1641 compliance point on the San Joaquin River.

Models suggest that there are advantages to using flow-based management when water supply allows: Residence time is lower, the amount of carriage water is lower, and water quality improvement is broader, extending to San Andreas Landing, Jersey Point, most of Middle River, and the export sites. These improvements require both sufficient through-flow (3,500–4,000 cubic feet per second of exports) and sufficient outflow. The benefits of the EDB in medium-flow conditions should be evaluated, as the barrier is a significant engineering project that requires a lengthy planning and implementation process and variations in flow should be expected.

The strongest impact of the 2021–2022 EDB on flow occurred within Franks Tract itself, where water age increased significantly on the western side and decreased slightly on the eastern side. Similar to the response to the 2015 barrier, velocity increased greatly through Fisherman's Cut and Old River at Franks Tract while decreasing at Holland Cut and Quimby Island.

Changes to flow within Franks Tract may have contributed to the large cyanobacteria bloom in July and August 2021, which was dominated by *Microcystis*. Although toxin levels were relatively low at the time, sampling was insufficient to fully record the bloom. This also coincided with increases in chlorophyll and pH, a decrease in nitrogen, and highly variable levels of dissolved oxygen (DO), which could have had further impacts on the food web.

A second bloom occurred in 2022 and extensive monitoring was in place to track the bloom. This bloom was dominated by *Dolichospermum* rather than by *Microcystis*; no toxins were reported, although the high variability of DO and pH could have had additional ecological impacts.

During the EDB construction period, no harm to any special-status species was observed and all water quality parameters remained within acceptable levels. There was no evidence of increased rates of predation on pelagic fishes before and after construction of the barrier. There was some evidence of increased abundance of the jellyfish *Maeotias* and juvenile Tridentiger gobies in the Sacramento River during years when the barrier was in place.

The assessment of the hydrodynamic effects of the EDB notch reached the following conclusions:

- Velocity measurements were made to map temporal and spatial changes in the velocity field hundreds of meters downstream of the notch, either on the east side during a flood tide or on the west side during an ebb tide. The high-energy environment (high velocity magnitude and turbulent fluctuations) proved to be challenging for fieldwork, but after several days of reconnaissance, the measurements were successful.
- A novel two-dimensional velocity interpolation was developed, an along-streamline interpolation algorithm that showed better results than traditional methods such as inverse distance weighting and triangulation. This interpolation algorithm was used to produce velocity maps over an ebb tide and a flood tide. The algorithm documented velocity magnitudes up to 3 meters per second, about three times higher than pre-EDB velocity magnitudes. These velocity maps allow the extraction of different quantities (velocity magnitude, streamlines, and vorticity), which is useful for the analysis of spatial data.
- Combining velocity maps and the associated velocity magnitude and vorticity with biological data (i.e., predation sampling) could be a powerful tool for assessing the biological effects of structures that significantly alter velocity fields in the Delta and elsewhere. The pilot analysis shows promise in interpreting spatial patterns of fish predation (see Section 2.3.3.4, "Predation Study").

3.2 Recommendations for the Future

Overall, the 2021–2022 EDB achieved its objective of reducing salinity in the Central Delta while preserving upstream storage. The 2021 installation represented the second time in seven years that drought conditions required an emergency barrier at the West False River location. Therefore, planning for

the installation of a drought barrier on a non-emergency basis would be very beneficial to regional water management. These plans are already underway.

Coverage by the acoustic fish tracking receivers and the numbers of tagged juvenile salmonids detected near the barrier were both limited. As a result, the juvenile salmonid tracking study provided a minimal understanding of the routes of tagged salmonids as they approach West False River, and of how routes may vary seasonally and under different barrier conditions. Even though thousands of tagged juvenile salmonids were released in the upper watershed, only a few were detected in the focused study area. Additional fish passage data in the region could help better understand passage in the region. DWR may consider deploying receivers near the barrier and using detections of fish tagged from other studies to the extent possible to increase sample sizes and better understand fish passage in the region.

The hydrodynamics analyses described in Section 2.2.2, "Effect of the Emergency Drought Barrier on Hydrodynamics and Salt Transport," demonstrated the along-stream interpolation algorithm produced better results than other interpolation methods. However, another independent measure of velocity could have been taken for a more rigorous calibration.

3.3 Lessons Learned

Implementation of the 2021–2022 EDB resulted in the following lessons learned:

- **Enhancing coordination prior to a decision to install the EDB, to the extent possible, would increase the chances that the barrier could be built when needed.** The hydrologic conditions that necessitated the need to install the EDB is complex. Improving coordination among other DWR groups (e.g., hydrologic forecasting, reservoir operators, other drought-related programs) would help to inform a future decision regarding the timing of installation of the EDB at West False River and allow more time to prepare.
- **The Drought Barrier Program should continue its planning efforts and secure environmental permits for future installations of the West False River EDB regardless of hydrologic conditions.** Given the cyclical nature of drought in California, it is highly likely that the EDB will need to be installed again. DWR is working to obtain environmental permits using the normal process and timelines to allow up to two installations over the next 10 years, if needed. An environmental impact report and environmental impact statement are being prepared to provide compliance under the California Environmental Quality Act (CEQA) and National Environmental Policy Act. For previous installations of the EDB, the requirement for CEQA compliance was suspended as a result of the

Governor's drought proclamations because the need for the barrier was deemed an emergency. DWR is working toward having permits ready ("on the shelf") so that permit coverage will be in place before DWR needs to install the EDB in the future.

- **Advance mitigation for future EDB installations should be identified and developed or purchased.** Compensatory mitigation for delta smelt and salmonids is scarce and was not available to fully mitigate impacts of the 2021–2022 EDB, thus requiring the development of an alternative mitigation strategy that has proven to be very expensive. To avoid future mitigation challenges associated with additional barrier installations, DWR should work with the California Department of Fish and Wildlife, National Marine Fisheries Service, and U.S. Fish and Wildlife Service to identify and implement advance mitigation if funding is available.
- **DWR would consider information available at the time of potential notch placement to decide whether a notch should be placed**. Notching the EDB between January and March 2022 allowed for fish and boat passage, but it also resulted in a large scour hole at the bottom of the channel near the barrier's location. DWR plans to evaluate information available at the time of potential notch placement to determine whether a notch should be placed in the future because keeping West False River closed may help prevent fish from entering the Central Delta, where their mortality is known to be higher. Additionally, boats could detour around the barrier, using Fisherman's Cut or Taylor Slough to access West False River.
- **Ample time should be provided to complete project closeout activities.** Barrier removal activities were completed in November 2022, although some activities remain outstanding. Project closeout activities include submitting the post-effects report to the fishery agencies; because the 2021–2022 EDB was installed under an emergency, Section 7 consultation is being handled after the fact. Additionally, the Drought Barrier Program is still working to fulfill the mitigation requirements to offset project impacts, which will extend several years, and to recover up to $8.6 million through an established Financial Assistance Agreement with the U.S. Bureau of Reclamation for EDB removal costs.

CHAPTER 4
References

Amidror I. 2002. "Scattered Data Interpolation Methods for Electronic Imaging Systems: A Survey." Journal of Electronic Imaging Volume 11 (Issue 2): Pages 157–176. Viewed online at: https://doi.org/10.1117/1.1455013.

Andes LC, Cox AL. 2017. "Rectilinear Inverse Distance Weighting Methodology for Bathymetric Cross-Section Interpolation along the Mississippi River." Journal of Hydrologic Engineering Volume 22 (Issue 7): 04017014. Viewed online at: https://doi.org/10.1061/(ASCE)HE.1943-5584.0001514.

Arar EJ, Collins GB. 1997. *Method 445.0: In Vitro Determination of Chlorophyll a and Pheophytin a in Marine and Freshwater Algae by Fluorescence.* Washington, DC: U.S. Environmental Protection Agency, Office of Research and Development, National Exposure Research Laboratory. [Government Report.] Viewed online at: https://cfpub.epa.gov/si/si_public_record_report.cfm? Lab=NERL&dirEntryId=309417.

ASTM International. 2014. ASTM Standard D7781-14: *Standard Test Method for Nitrite-Nitrate in Water by Nitrate Reductase*. West Conshohocken (PA).

Ateljevich E, Nam K, Zhang Y, Wang R, Shu Q. 2014. "Bay-Delta SELFE Calibration Overview." In: *Methodology for Flow and Salinity Estimates in the Sacramento–San Joaquin Delta and Suisun Marsh*, Chapter 7*.* 35th Annual Progress Report to the State Water Resources Control Board. June 2017. Sacramento (CA): Bay-Delta Office. Delta Modeling Section, California Department of Water Resources. [Government Report.]

Barros A, Hartman R, Bashevkin S, Burdi C. In prep. *Years of Drought and Salt: Decreasing Flows Determine the Distribution of Zooplankton Resources in the Estuary.* Draft manuscript.

Barros AE. 2022. Interagency Ecological Program Zooplankton Study ver 11. Environmental Data Initiative. Viewed online at: https://doi.org/10.6073/pasta/51bfce9bc26011095d8b99b3a2aee1b8. Accessed April 27, 2023.

Bashevkin SM, Hartman R, Thomas M, Barros A, Burdi CE, Hennessy A, Tempel T, Kayfetz K. 2022. "Five Decades (1972–2020) of Zooplankton Monitoring in the Upper San Francisco Estuary." PLOS ONE Volume 17 (Issue 3): e0265402. Viewed online at: https://doi.org/10.1371/journal.pone.0265402. Accessed May 17, 2022.

Bates D, Maechler M, Bolker B, Walker S. 2022. Lme4: Linear Mixed-Effects Models using 'Eigen' and S4. 1.1-30 ed.: The Comprehensive R Archive Network (CRAN). Viewed online at: https://cran.r-project.org/web/packages/lme4/index.html. Accessed July 8, 2022.

Berg M, Sutula M. 2015. *Factors Affecting Growth of Cyanobacteria with Special Emphasis on the Sacramento-San Joaquin Delta*. Costa Mesa (CA): Southern California Coastal Water Research Project. Viewed online at: https://ftp.sccwrp.org/pub/download/DOCUMENTS/TechnicalReports/869_FactorsAffectGrowthOfCyanobacteria-1.pdf.

Bergamaschi BA, Kraus TEC, Downing B. 2020. "Assessing Spatial Variability of Nutrients and Related Water Quality Constituents in the California Sacramento–San Joaquin Delta at the Landscape Scale: High Resolution Mapping Surveys." U.S. Geological Survey. [Government Data Release.] Viewed online at: https://doi.org/10.5066/P9FQEUAL. Last updated: May 4, 2020.

Bouma-Gregson K, O'Donnell K, Uebner MQ, Sturgeon CL, Cone KM, Jaegge AC, Brinkman JD, Bergamaschi BA, Kraus TEC. 2023a. *Water Quality, Nutrient, and Phytoplankton Data from Franks Tract, Mildred Island, and Neighboring Channels in the California Sacramento–San Joaquin Delta: 2022 and 2023 High-Resolution Mapping Surveys*. U.S. Geological Survey. [Government Data Release.] Viewed online at: https://doi.org/10.5066/P9TDMWDH.

Bowen GJ, Wassenaar LI, Hobson KA. 2005. "Global Application of Stable Hydrogen and Oxygen Isotopes to Wildlife Forensics." Oecologia Volume 143: Pages 337–348. Viewed online at: https://doi.org/10.1007/s00442-004-1813-y.

Britton LJ. 1977. "Periphyton and Phytoplankton in the Sacramento River, California, May 1972 to April 1973." U.S. Geological Survey Journal of Research Volume 5 (Issue 5): Pages 547–559.

Bürkner P-C. 2018. "Advanced Bayesian Multilevel Modeling with the R Package brms." The R Journal Volume 10: Pages 395–411.

Burnham KP, Anderson DR. 2002. *Model Selection and Multimodel Inference: A Practical Information-Theoretic Approach*. Second edition. New York (NY): Springer.

California Data Exchange Center. 2021. Department of Water Resources California Cooperative Snow Surveys: Chronological Reconstructed Sacramento and San Joaquin Valley Water Year Hydrologic Classification Indices. California Department of Water Resources. Viewed online at: https://cdec.water.ca.gov/reportapp/javareports?name=WSIHIST.

California Department of Water Resources. 1995. *Sacramento–San Joaquin Delta Atlas.* Reprinted July 1995. Viewed online at: www.waterboards.ca.gov/waterrights/water_issues/programs/bay_delta/california_waterfix/exhibits/exhibit3/rdeir_sdeis_comments/RECIRC_2646_ATT%203.pdf.

———. 2019. *Efficacy Report—2015 Emergency Drought Barrier Project*. West Sacramento (CA): California Department of Water Resources, Bay-Delta Office.

———. 2020. "Water Year 2020: Summary Information." Sept. 2020. [Government Handout.]

———. 2021. *2021 Emergency Drought Salinity Barrier Project Monitoring Plan.* May 2021.

Capello M, Robert M, Soria M, Potin G, Itano D, Holland K, Deneubourg J-L. 2015. "A Methodological Framework to Estimate the Site Fidelity of Tagged Animals Using Passive Acoustic Telemetry." PloS ONE 10(8): E0134002. Viewed online at: https://doi.org/10.1371/journal.pone.0134002.

Chorus I, Spijkerman E. 2021. "What Colin Reynolds Could Tell Us About Nutrient Limitation, N:P Ratios and Eutrophication Control." Hydrobiologia Volume 848: Pages 95–111. Viewed online at: https://doi.org/10.1007/s10750-020-04377-w.

Conrad JL, Bibian AJ, Weinersmith KL, De Carion D, Young MJ, Crain P, Hestir EL, Santos MJ, Sih A. 2016. "Novel Species Interactions in a Highly Modified Estuary: Association of Largemouth Bass with Brazilian Waterweed *Egeria densa*." Transactions of the American Fisheries Society Volume 145: Pages 249–263. Viewed online at: https://doi.org/10.1080/00028487.2015.1114521. Accessed Jan. 3, 2023.

Cornwell JC, Glibert PM, Owens MS. 2014. "Nutrient Fluxes from Sediments in the San Francisco Bay Delta." Estuaries and Coasts Volume 37: Pages 1120–1133. Viewed online at: https://doi.org/10.1007/s12237-013-9755-4.

Dahm CN, Parker AE, Adelson AE, Christman MA, Bergamaschi BA. 2016. "Nutrient Dynamics of the Delta: Effects on Primary Producers." San Francisco Estuary and Watershed Science Volume 14 (Issue 4). Viewed online at: https://doi.org/10.15447/sfews.2016v14iss4art4. Accessed Jan. 6, 2023.

David L, Esnault A, Calluaud D. 2002. *Comparison of Interpolation Techniques for 2D and 3D Velocimetry.* Eleventh International Symposium on Application of Laser Techniques to Fluid Mechanics, Lisbon, Portugal. July 2002. Page 8.

De Tezanos Pinto P, Litchman E. 2010. "Interactive Effects of N:P Ratios and Light on Nitrogen-Fixer Abundance." Oikos Volume 119: Pages 567–575. Viewed online at: https://doi.org/10.1111/j.1600-0706.2009.17924.x.

Deleersnijder E, Campin J-M, Delhez EJM. 2001. "The Concept of Age in Marine Modelling: I. Theory and Preliminary Model Results." Journal of Marine Systems Volume 28 (Issues 3–4, 2001): Pages 229–267. Viewed online at: https://doi.org/10.1016/S0924-7963(01)00026-4.

Delhez EJM, de Brye B, Debrauwere A, Deleersnijder E. 2014. "Residence Time vs. Influence Time." Journal of Marine Systems Volume 132: Pages 185–195.

Demetras NJ, Huff DD, Michel C, Smith JM, Cutter GR, Hayes SA, Lindley ST. 2016. "Development of Underwater Recorders to Quantify Predation of Juvenile Chinook Salmon (*Oncorhynchus tshawytscha*) in a River Environment." Fishery Bulletin Volume 114: Pages 179–185.

Dinehart RL, Burau JR. 2005a. "Repeated Surveys by Acoustic Doppler Current Profiler for Flow and Sediment Dynamics in a Tidal River." Journal of Hydrology Volume 314 (Issues 1–4): Pages 1–21. Viewed online at: https://doi.org/10.1016/j.jhydrol.2005.03.019.

———. 2005b. "Averaged Indicators of Secondary Flow in Repeated Acoustic Doppler Current Profiler Crossings of Bends." Water Resources Research Volume 41 (Issue 9). Viewed online at: https://doi.org/10.1029/2005WR004050.

Dolman AM, Rücker J, Pick FR, Fastner J, Rohrlack T, Mischke U, Wiedner C. 2012. "Cyanobacteria and Cyanotoxins: The Influence of Nitrogen Versus Phosphorus." PloS ONE Volume 7, e38757. Viewed online at: https://doi.org/10.1371/journal.pone.0038757.

Dolman AM, Wiedner C. 2015. "Predicting Phytoplankton Biomass and Estimating Critical N:P Ratios with Piecewise Models that Conform to Liebig's Law of the Minimum." Freshwater Biology Volume 60: Pages 686–697. Viewed online at: https://doi.org/10.1111/fwb.12518.

Downing BD, Bergamaschi BA, Kendall C, Kraus TEC, Dennis KJ, Carter JA, Von Dessonneck TS. 2016. "Using Continuous Underway Isotope Measurements to Map Water Residence Time in Hydrodynamically Complex Tidal Environments." Environmental Science & Technology Volume 50: Pages 13387–13396. Viewed online at: https://doi.org/10.1021/acs.est.6b05745.

Downing JA, McCauley E. 1992. "The Nitrogen:Phosphorus Relationship in Lakes." Limnology and Oceanography Volume 37: Pages 936–945. Viewed online at: https://doi.org/10.4319/lo.1992.37.5.0936.

Fackrell JK, Kraus TEC, Young MB, Kendall C, Peek S. 2021. "Stable Isotopes Provide Insight into Sources and Cycling of N Compounds in the Sacramento–San Joaquin Delta, California, USA." Science of The Total Environment Volume 816: 151592. Viewed online at: https://doi.org/10.1016/j.scitotenv.2021.151592.

Fichot CG, Downing BD, Bergamaschi BA, Windham-Myers L, Marvin-DiPasquale M, Thompson DR, Gierach MM. 2016. "High-Resolution Remote Sensing of Water Quality in the San Francisco Bay–Delta Estuary." Environmental Science & Technology Volume 50: Pages 573–583. Viewed online at: https://doi.org/10.1021/acs.est.5b03518.

Fischer HB, List JE, Koh CR, Imberger J, Brooks NH. 1979. *Mixing in Inland and Coastal Waters*. New York (NY): Elsevier.

Fishman MJ. 1993. *Methods of Analysis by the U.S. Geological Survey National Water Quality Laboratory—Determination of Inorganic and Organic Constituents in Water and Fluvial Sediments*. U.S. Geological Survey Open-File Report 93-125. 217 pp. [Government Report.] Viewed online at: https://doi.org/10.3133/ofr93125.

Foster GM, Graham JL, Bergamaschi BA, Carpenter KD, Downing BD, Pellerin BA, Rounds SA, Saraceno JF. 2022. "Field Techniques for the Determination of Algal Pigment Fluorescence in Environmental Waters—

Principles and Guidelines for Instrument and Sensor Selection, Operation, Quality Assurance, and Data Reporting." *U.S. Geological Survey Techniques and Methods*, Book 1, Chap. D10. 34 pp. [Government Report.] Viewed online at: https://doi.org/10.3133/tm1D10.

Gobler CJ, Burkholder JM, Davis TW, Harke MJ, Johengen T, Stow CA, Van de Waal DB. 2016. "The Dual Role of Nitrogen Supply in Controlling the Growth and Toxicity of Cyanobacterial Blooms." Harmful Algae Volume 54: Pages 87–97. Viewed online at: https://doi.org/10.1016/j.hal.2016.01.010.

Godin G. 1972. *The Analysis of the Tides*. Toronto (ON), Canada: University of Toronto Press. 264 pp.

Greenberg AE. 1964. "Plankton of the Sacramento River." Ecology Volume 45 (Issue 1): Pages 40–49. Viewed online at: https://doi.org/10.2307/1937105.

Gross E, Andrews S, Bergamaschi B, Downing B, Holleman R, Burdick S, Durand J. 2019. "The Use of Stable Isotope-Based Water Age to Evaluate a Hydrodynamic Model." Water Volume 11 (Issue 11): 2207. Viewed online at: https://doi.org/10.3390/w11112207.

Hartman KJ, Brandt SB. 1995. "Comparative Energetics and the Development of Bioenergetics Models for Sympatric Estuarine Piscivores." Canadian Journal of Fisheries and Aquatic Sciences Volume 52 (Issue 8): Pages 1647–1666.

Hartman R, Ateljevich E, Berg M, Bouma-Gregson K, Bosworth D, Rasmussen N, Flynn T, Pennington T. 2021. *Report on the Impact of the Emergency Drought Barrier on Harmful Algal Blooms and Aquatic Weeds in the Delta*. Sacramento (CA): California Department of Water Resources. 86 pp. [Government Report.]

Hartman R, Rasmussen N, Bosworth D, Berg M, Ateljevich E, Flynn T, Wolf B, Pennington T, Khanna S. 2022. *Temporary Urgency Change Petition of 2021 and Emergency Drought Salinity Barrier: Impact on Harmful Algal Blooms and Aquatic Weeds in the Delta.* Report to the State Water Resources Control Board. Sacramento (CA). [Government Report.] Viewed online at: www.waterboards.ca.gov/drought/tucp/docs/2022/2022-10-14-habs-weeds-report.pdf. Accessed Jan. 6, 2023.

Hartman R, Twardochleb L, Burdi C, Wells E. In prep. Amazing Graze: *Shifts in Distribution of Maeotias and Potamocorbula during Droughts*. Draft manuscript.

Hijmans RJ. 2016. geosphere: Spherical Trigonometry. R package Version 1.5-18. Viewed online at: https://CRAN.R-project.org/package=geosphere.

Huisman J, Codd GA, Paerl HW, Ibelings BW, Verspagen JMH, Visser PM. 2018. "Cyanobacterial Blooms." Nature Reviews Microbiology Volume 16: Pages 471–483. Viewed online at: https://doi.org/10.1038/s41579-018-0040-1.

Interagency Ecological Program, Speegle J, McKenzie R, Nanninga A, Holcombe E, Stagg J, Hagen J, Huber E, Steinhart G, Arrambide A. 2022. Interagency Ecological Program: Over Four Decades of Juvenile Fish Monitoring Data from the San Francisco Estuary, collected by the Delta Juvenile Fish Monitoring Program, 1976–2022 ver. 11. Environmental Data Initiative. Viewed online at: https://doi.org/10.6073/pasta/57b6c257edd72691702f9731d5fe4172. Accessed Feb. 14, 2023.

Jabusch TW, Trowbridge PR, Wong A, Heberger M. 2018. *Assessment of Nutrient Status and Trends in the Delta in 2001–2016: Effects of Drought on Ambient Concentrations and Trends*. Prepared for the Delta Regional Monitoring Program Technical Advisory Committee. SFEI Contribution No. 865. Richmond (CA): Aquatic Science Center. March 2018. Viewed online at: https://www.sfei.org/documents/delta-nutrient-status-2018.

Jamieson EC, Rennie CD, Jacobson RB, Townsend RD. 2011. "3-D Flow and Scour near a Submerged Wing Dike: ADCP Measurements on the Missouri River." Water Resources Research Volume 47 (Issue 7). Viewed online at: https://doi.org/10.1029/2010WR010043.

Jassby A. 2008. "Phytoplankton in the Upper San Francisco Estuary: Recent Biomass Trends, Their Causes and Their Trophic Significance." San Francisco Estuary and Watershed Science Volume 6 (Issue 1): Page 24. Viewed online at: https://doi.org/10.15447/sfews.2008v6iss1art2. Accessed Jan. 5, 2012.

Jassby AD, Cloern JE, Cole BE. 2002. "Annual Primary Production: Patterns and Mechanisms of Change in a Nutrient-Rich Tidal Ecosystem." Limnology and Oceanography Volume 47: Pages 698–712. Viewed online at: https://doi.org/10.4319/lo.2002.47.3.0698.

Jensen ME. 2010. "Estimating Evaporation from Water Surfaces." Presentation at CSU/ARS Evapotranspiration Workshop: Using the Best Science to Estimate Consumptive Use – CoAgMET, March 15, 2010, Fort Collins (CO). Viewed online at: https://coagmet.colostate.edu/ET_Workshop/ET_Jensen/ET_water_surf.pdf.

Kayfetz K, Bashevkin SM, Thomas M, Hartman R, Burdi CE, Hennessy A, Tempel T, Barros A. 2020. *Zooplankton Integrated Dataset Metadata Report.* IEP Technical Report 93. Sacramento (CA): California Department of Water Resources. [Government Report.] Viewed online at: https://deltacouncil.ca.gov/pdf/science-program/2020-11-09-iep-93-zooplankton-integrated-dataset-metadata.pdf. Accessed July 8, 2022.

Kimmerer W, Wilkerson F, Downing B, Dugdale R, Gross ES, Kayfetz K, Khanna S, Parker AE, Thompson J. 2019. "Effects of Drought and the Emergency Drought Barrier on the Ecosystem of the California Delta." San Francisco Estuary and Watershed Science Volume 17 (Issue 3). Viewed online at: https://doi.org/10.15447/sfews.2019v17iss3art2. Accessed Jan. 4, 2023.

Klawonn I, Nahar N, Walve J, Andersson B, Olofsson M, Svedén JB, Littmann S, Whitehouse MJ, Kuypers MMM, Ploug H. 2016. "Cell-Specific Nitrogen- and Carbon-Fixation of Cyanobacteria in a Temperate Marine System (Baltic Sea)." Environmental Microbiology Volume 18: Pages 4596–4609. Viewed online at: https://doi.org/10.1111/1462-2920.13557.

Kramer BJ, Jankowiak JG, Nanjappa D, Harke MJ, Gobler CJ. 2022. "Nitrogen and Phosphorus Significantly Alter Growth, Nitrogen Fixation, Anatoxin-a Content, and the Transcriptome of the bloom-Forming Cyanobacterium, *Dolichospermum*." Frontiers in Microbiology Volume 13: 955032. Viewed online at: https://doi.org/10.3389/fmicb.2022.955032.

Kraus TEC, O'Donnell K, Downing BD, Burau JR, Bergamaschi BA. 2017a. "Using Paired In Situ High Frequency Nitrate Measurements to Better Understand Controls on Nitrate Concentrations and Estimate Nitrification Rates in a Wastewater-Impacted River." Water Resources Research Volume 53 (Issue 10): Pages 8423–8442. Viewed online at: https://agupubs.onlinelibrary.wiley.com/doi/10.1002/2017WR020670.

Kraus TEC, Carpenter KD, Bergamaschi BA, Parker AE, Stumpner EB, Downing BD, Travis NM, Wilkerson FP, Kendall C, Mussen TD. 2017b. "A River-Scale Lagrangian Experiment Examining Controls on Phytoplankton Dynamics in the Presence and Absence of Treated

Wastewater Effluent High in Ammonium: Effluent Effects on River Phytoplankton." Limnology and Oceanography Volume 62: Pages 1234–1253. Viewed online at: https://doi.org/10.1002/lno.10497.

Lehman PW, Kurobe T, Huynh K, Lesmeister S, Teh SJ. 2021. "Covariance of Phytoplankton, Bacteria, and Zooplankton Communities within *Microcystis* Blooms in San Francisco Estuary." Frontiers in Microbiology Volume 12, 632264. Viewed online at: https://doi.org/10.3389/fmicb.2021.632264.

Lehman PW, Kurobe T, Lesmeister S, Baxa D, Tung A, Teh SJ. 2017. "Impacts of the 2014 Severe Drought on the *Microcystis* Bloom in San Francisco Estuary." Harmful Algae Volume 63: Pages 94–108. Viewed online at: https://doi.org/10.1016/j.hal.2017.01.011.

Lehman PW, Kurobe T, Teh SJ. 2022. "Impact of Extreme Wet and Dry Years on the Persistence of Microcystis Harmful Algal Blooms in San Francisco Estuary." Quaternary International Volume 621: Pages 16–25. Viewed online at: https://doi.org/10.1016/j.quaint.2019.12.003.

Lehman PW, Marr K, Boyer GL, Acuna S, Teh SJ. 2013. "Long-Term Trends and Causal Factors Associated with Microcystis Abundance and Toxicity in San Francisco Estuary and Implications for Climate Change Impacts." Hydrobiologia Volume 718 (Issue 1, November 1, 2013): Pages 141–158. Viewed online at: https://doi.org/10.1007/s10750-013-1612-8.

Lehman PW, Mayr S, Mecum L, Enright C. 2010. "The Freshwater Tidal Wetland Liberty Island, CA Was Both a Source and Sink of Inorganic and Organic Material to the San Francisco Estuary." Aquatic Ecology Volume 44 (Issue 2, June 1, 2010): Pages 359–372. Viewed online at: https://doi.org/10.1007/s10452-009-9295-y.

Levesque VA, Oberg KA. 2012. *Computing Discharge Using the Index Velocity Method*. U.S. Geological Survey Techniques and Methods 3-A23. 148 pp. [Government Report.] Viewed online at: https://pubs.usgs.gov/tm/3a23/.

Loken LC, Sadro S, Lenoch LEK, Stumpner PR, Dahlgren RA, Burau JR, Van Nieuwenhuyse EE. 2022. "Whole-Ecosystem Experiment Illustrates Short Timescale Hydrodynamic, Light, and Nutrient Control of Primary Production in a Terminal Slough." Estuaries and Coasts Volume 45: Pages 2428–2449. Viewed online at: https://doi.org/10.1007/s12237-022-01111-8.

Lopez CB, Cloern JE, Schraga TS, Little AJ, Lucas LV, Thompson JK, Burau JR. 2006. "Ecological Values of Shallow-Water Habitats: Implications for the Restoration of Disturbed Ecosystems." Ecosystems Volume 9: Pages 422–440. Viewed online at: https://doi.org/10.1007/s10021-005-0113-7.

Lucas LV, Stewart AR. 2005. *Transport, Transformation and Effects of Selenium and Carbon in the Delta of the Sacramento–San Joaquin Rivers: Implications for Ecosystem Restoration*. Final Report. Project No. ERP-01-C07. Sacramento (CA): California Bay Delta Authority. [Government Report.]

Mahardja B, Conrad JL, Lusher L, Schreier B. 2016. "Abundance Trends, Distribution, and Habitat Associations of the Invasive Mississippi Silverside (*Menidia audens*) in the Sacramento–San Joaquin Delta, California, USA." San Francisco Estuary and Watershed Science Volume 14 (Issue 1). Viewed online at: http://dx.doi.org/10.15447/sfews.2016v14iss1art2. Accessed Jan. 3, 2023.

Mahardja B, Tobias V, Khanna S, Mitchell L, Lehman P, Sommer T, Brown L, Culberson S, Conrad JL. 2021. "Resistance and Resilience of Pelagic and Littoral Fishes to Drought in the San Francisco Estuary." Ecological Applications Volume 31 (Issue 2): e02243. Viewed online at: https://dx.doi.org/10.1002%2Feap.2243. Accessed Jan. 3, 2023.

Marcarelli AM, Fulweiler RW, Scott JT. 2022. "Nitrogen Fixation: A Poorly Understood Process along the Freshwater-Marine Continuum." Limnology and Oceanography Letters Volume 7: Pages 1–10. Viewed online at: https://doi.org/10.1002/lol2.10220.

MathWorks Inc. 2022. scatteredInterpolant: Interpolate 2-D or 3-D scattered data. Viewed online at: https://www.mathworks.com/help/matlab/ref/scatteredinterpolant.html.

Mayr C, Lücke A, Stichler W, Trimborn P, Ercolano B, Oliva G, Ohlendorf C, Soto J, Fey M, Haberzettl T, et al. 2007. "Precipitation Origin and Evaporation of Lakes in Semi-arid Patagonia (Argentina) Inferred from Stable Isotopes (δ18O, δ2H)." Journal of Hydrology Volume 334: Pages 53–63. Viewed online at: https://doi.org/10.1016/j.jhydrol.2006.09.025.

McKinney W. 2010. "Data Structures for Statistical Computing in Python." In: van der Walt S, Millman J, editors. *Proceedings of the 9th Python in Science Conference*, pages 56–61. Viewed online at: https://doi.org/10.25080/Majora-92bf1922-00a.

McNabb CD. 1960. "Enumeration of Freshwater Phytoplankton Concentrated on the Membrane Filter." Limnology and Oceanography Volume 5: Pages 57–61. Viewed online at: https://doi.org/10.4319/lo.1960.5.1.0057.

Michel CJ, Henderson MJ, Loomis CM, Smith JM, Demetras NJ, Iglesias IS, Lehman BM, Huff DD. 2020. "Fish Predation on a Landscape Scale." Ecosphere Volume 11 (Issue 6): e03168. Viewed online at: https://doi.org/10.1002/ecs2.3168.

Mioni CE, Kudela K, Raphael M, Baxa DV. 2011. *Harmful Cyanobacteria Blooms and Their Toxins in Clear Lake and the Sacramento–San Joaquin Delta (California).* Rancho Cordova (CA): Central Valley Regional Water Quality Board. [Government Report.]

Monismith SG. 2016. "A Note on Delta Outflow." San Francisco Estuary and Watershed Science Volume 14 (Issue 3). Viewed online at: https://escholarship.org/uc/item/89k7b61m.

Monsen NE, Cloern JE, Burau JR. 2007. "Effects of Flow Diversions on Water and Habitat Quality: Examples from California's Highly Manipulated Sacramento–San Joaquin Delta." San Francisco Estuary & Watershed Science Volume 5 (Issue 3). Viewed online at: https://doi.org/10.15447/sfews.2007v5iss5art2.

Monsen NE, Cloern JE, Lucas LV, Monismith SG. 2002. "A Comment on the Use of Flushing Time, Residence Time, and Age as Transport Time Scales." Limnology and Oceanography Volume 47: Pages 1545–1553. Viewed online at: https://doi.org/10.4319/lo.2002.47.5.1545.

Moyle PB, Baxter RD, Sommer T, Foin TC, Matern SA. 2004. "Biology and Population Dynamics of the Sacramento Splittail (*Pogonichthys macrolepidotus*) in the San Francisco Estuary: A Review." San Francisco Estuary and Watershed Science Volume 2 (Issue 2): Pages 1–47. Viewed online at: https://doi.org/10.15447/sfews.2004v2iss2art3.

Nelson TR, Michel CJ, Gary MP, Lehman BM, Demetras NJ, Hammen JJ, Horn MJ. 2021. "Effects of Artificial Lighting at Night on Predator Density and Salmonid Predation." Transactions of the American Fisheries Society Volume 150 (Issue 2): Pages 147–159.

Newsom G. 2021. Proclamation of a State of Emergency. Sacramento (CA): Executive Department, State of California. May 10, 2021. 5 pp. Viewed online at: https://www.gov.ca.gov/wp-content/uploads/2021/05/5.10.2021-Drought-Proclamation.pdf.

Nietch CT, Gains-Germain L, Lazorchak J, Keely SP, Youngstrom G, Urichich EM, Astifan B, DaSilva A, Mayfield H. 2022. "Development of a Risk Characterization Tool for Harmful Cyanobacteria Blooms on the Ohio River." Water Volume 14 (Issue 4), 644. Viewed online at: https://doi.org/10.3390/w14040644.

O'Donnell K, Richardson ET, Soto Perez J, Sturgeon CL, Delascagigas A, Nakatsuka KK, Uebner MQ, Bergamaschi TR, Hansen JA, Bouma-Gregson K, Kraus TEC, Bergamaschi BA. 2023. *Assessing Spatial Variability of Nutrients, Phytoplankton and Related Water-Quality Constituents in the California Sacramento–San Joaquin Delta at the Landscape Scale: 2022 High-Resolution Mapping Surveys*. U.S. Geological Survey. [Government Data Release.] Viewed online at: https://doi.org/10.5066/P9QULEAT.

Oksanen J, Blanchet FG, Kindt R, Legendre P, Minchin PR, O'Hara RB, Simpson GL, Solymos P. 2020. Community Ecology Package "vegan." Version 2.5-7. Comprehensive R Archive Network (CRAN). Viewed online at: https://cran.r-project.org/web/packages/vegan/index.html. Accessed April 17, 2022.

Oliver MA, Webster R. 1990. "Kriging: A Method of Interpolation for Geographical Information Systems." International Journal of Geographical Information Systems Volume 4 (Issue 3): Pages 313–332. Viewed online at: https://doi.org/10.1080/02693799008941549.

Osburn FS, Wagner ND, Scott JT. 2021. "Biological Stoichiometry and Growth Dynamics of a Diazotrophic Cyanobacteria in Nitrogen Sufficient and Deficient Conditions." Harmful Algae Volume 103, 102011. Viewed online at: https://doi.org/10.1016/j.hal.2021.102011.

Parsons DR, Jackson PR, Czuba JA, Engel FL, Rhoads BL, Oberg KA, Best JL, Mueller DS, Johnson KK, Riley JD. 2013. "Velocity Mapping Toolbox (VMT)—A Processing and Visualization Suite for Moving-Vessel ADCP Measurements." Earth Surface Processes and Landforms Volume 38 (Issue 11): Pages 1244–1260. Viewed online at: https://doi.org/10.1002/esp.3367.

Patton CJ, Kryskalla JR. 2003. *Methods of Analysis by the U.S. Geological Survey National Water Quality Laboratory—Evaluation of Alkaline Persulfate Digestion as an Alternative to Kjeldahl Digestion for Determination of Total and Dissolved Nitrogen and Phosphorus in Water*. U.S. Geological Survey Water-Resources Investigations Report 2003-4174. 33 pp. [Government Report.] Viewed online at: https://doi.org/10.3133/wri034174.

———. 2011. *Colorimetric Determination of Nitrate plus Nitrite in Water by Enzymatic Reduction, Automated Discrete Analyzer Methods*. U.S. Geological Survey Techniques and Methods 5B-8. 34pp. [Government Report.] Viewed online at: https://doi.org/10.3133/tm5B8.

Patton CJ, Truitt EP. 1992. *Methods of Analysis by the U.S. Geological Survey National Water Quality Laboratory—Determination of the Total Phosphorus by a Kjeldahl Digestion Method and an Automated Colorimetric Finish that Includes Dialysis*. U.S. Geological Survey Open-File Report 92-146. 39 pp. [Government Report.] Viewed online at: https://doi.org/10.3133/ofr92146.

Rennie CD, Church M. 2010. "Mapping Spatial Distributions and Uncertainty of Water and Sediment Flux in a Large Gravel Bed River Reach Using an Acoustic Doppler Current Profiler." Journal of Geophysical Research Volume 115: F03035. Viewed online at: https://doi.org/10.1029/2009JF001556.

Révész K, Coplen T. 2008a. "Determination of the δ($^{18}O/^{16}O$) of Water: RSIL Lab Code 489." In: Révész K, Coplen T, editors. *Methods of the Reston Stable Isotope Laboratory.* U.S. Geological Survey Techniques and Methods, 10–C2. Chapter C2. 28 pp. Viewed online at: https://doi.org/10.3133/tm10C2.

———. 2008b. "Determination of the δ($^{2}H/^{1}H$) of Water: RSIL Lab Code 1574." In: Révész K, Coplen T, editors. *Methods of the Reston Stable Isotope Laboratory.* U.S. Geological Survey Techniques and Methods, 10–C1. Chapter C1. 27 pp. Viewed online at: https://doi.org/10.3133/tm10C1.

Reynolds CS. 1999. "Non-determinism to Probability, or N:P in the Community Ecology of Phytoplankton." Archiv für Hydrobiologie Volume 146 (Issue 1): Pages 23–35. Viewed online at: https://doi.org/10.1127/archiv-hydrobiol/146/1999/23.

Rice JA, Breck JE, Bartell SM, Kitchell JF. 1983. "Evaluating the Constraints of Temperature, Activity and Consumption on Growth of Largemouth Bass." Environmental Biology of Fishes Volume 9: Pages 263–275.

Richardson ET, Hansen AM, Kraus TEC, Downing BD, Forsberg D, Stillian J, O'Donnell K, Sturgeon CL, Bergamaschi BA. 2023. "A Novel Boat-Based Field Application of a High-Frequency Conductometric Ammonium Analyzer to Characterize Spatial Variation in Aquatic Ecosystems."

Limnology & Ocean Methods Volume 21: Pages 761–774. Viewed online at: https://doi.org/10.1002/lom3.10579.

Rigosi A, Carey CC, Ibelings BW, Brookes JD. 2014. "The Interaction between Climate Warming and Eutrophication to Promote Cyanobacteria is Dependent on Trophic State and Varies among Taxa." Limnology and Oceanography Volume 59: Pages 99–114. Viewed online at: https://doi.org/10.4319/lo.2014.59.1.0099.

Riley SJ, DeGloria SD, Elliot R. 1999. "Index that Quantifies Topographic Heterogeneity." Intermountain Journal of Sciences Volume 5 (Issues 1–4): Pages 23–27.

Robarts RD, Zohary T. 1987. "Temperature Effects on Photosynthetic Capacity, Respiration, and Growth Rates of Bloom-Forming Cyanobacteria." New Zealand Journal of Marine and Freshwater Research Volume 21: Pages 391–399. Viewed online at: https://doi.org/10.1080/00288330.1987.9516235.

Romo S, Soria J, Fernández F, Ouahid Y, Barón-Solá Á. 2013. "Water Residence Time and the Dynamics of Toxic Cyanobacteria." Freshwater Biology Volume 58: Pages 513–522. Viewed online at: https://doi.org/10.1111/j.1365-2427.2012.02734.x.

Ruhl CA, Simpson MR. 2005. *Computation of Discharge Using the Index-Velocity Method in Tidally Affected Areas*. U.S. Geological Survey Scientific Investigations Report 2005-5004. Prepared in cooperation with the Interagency Ecological Program. Sacramento (CA). [Government Report.] Viewed online at: https://doi.org/10.3133/sir20055004.

Sacramento Regional County Sanitation District. 2021. *Sacramento Regional County Sanitation District, Sacramento Regional Wastewater Treatment Plant: Progress Report, Method of Compliance Work Plan, and Schedule for Ammonia Effluent Limitations and Title 22 or Equivalent Disinfection Requirements*. Sacramento (CA).

Saleh D, Domagalski J. 2021. "Concentrations, Loads, and Associated Trends of Nutrients Entering the Sacramento–San Joaquin Delta, California." San Francisco Estuary & Watershed Science Volume 19 (Issue 4): Article 6. Viewed online at: https://doi.org/10.15447/sfews.2021v19iss4art6.

Scott JT, McCarthy MJ, Otten TG, Steffen MM, Baker BC, Grantz EM, et al. 2013. "Comment: An Alternative Interpretation of the Relationship

between TN:TP and Microcystins in Canadian Lakes." Canadian Journal of Fisheries and Aquatic Sciences Volume 70: Pages 1265–1268. Viewed online at: https://doi.org/10.1139/cjfas-2012-0490.

Simpson M, Bland R. 2000. "Methods for Accurate Estimation of Net Discharge in a Tidal Channel." IEEE Journal of Oceanic Engineering Volume 25 (Issue 4): Pages 437-445.

Skrzypek G, Mydłowski A, Dogramaci S, Hedley P, Gibson JJ, Grierson PF. 2015. "Estimation of Evaporative Loss Based on the Stable Isotope Composition of Water Using Hydrocalculator." Journal of Hydrology Volume 523: Pages 781–789. Viewed online at: https://doi.org/10.1016/j.jhydrol.2015.02.010.

Snyder L, Potter JD, McDowell WH. 2018. "An Evaluation of Nitrate, fDOM, and Turbidity Sensors in New Hampshire Streams." Water Resources Research Volume 54 (Issue 3): Pages 2466–2479. Viewed online at: https://doi.org/10.1002/2017WR020678.

Sokolov S, Rintoul SR. 1999. "Some Remarks on Interpolation of Nonstationary Oceanographic Fields." Journal of Atmospheric and Oceanic Technology Volume 16 (Issue 10): Pages 1434–1449. Viewed online at: https://doi.org/10.1175/1520-0426(1999)016<1434:SROION>2.0.CO;2.

Standard Methods. 2023. *Standard Methods for the Examination of Water and Wastewater*. Viewed online at: https://www.standardmethods.org. Accessed March 29, 2023.

State Water Resources Control Board. 2000. Revised Water Right Decision 1641. *In the Matter of Implementation of Water Quality Objectives for the San Francisco Bay/Sacramento–San Joaquin Delta Estuary; A Petition to Change Points of Diversion of the Central Valley Project and the State Water Project in the Southern Delta, and A Petition to Change Places of Use and Purposes of Use of the Central Valley Project*. Sacramento (CA). Dec. 29, 1999; revised in accordance with Order WR 2000-02, March 15, 2000. Viewed online at: www.waterboards.ca.gov/waterrights/board_decisions/adopted_orders/decisions/d1600_d1649/wrd1641_1999dec29.pdf.

———. 2021. *In the Matter of Specified License and Permits of the Department of Water Resources and U.S. Bureau of Reclamation for the State Water Project and Central Valley Project: Order Conditionally Approving a Petition for Temporary Urgency Changes to License and Permit Terms and Conditions Requiring Compliance with Delta Water*

Quality Objectives in Response to Drought Conditions. June 1, 2021. Viewed online at: www.waterboards.ca.gov/drought/tucp/.

Stumpner EB, Bergamaschi BA, Kraus TEC, Parker AE, Wilkerson FP, Downing BD, Dugdale RC, Murrell MC, Carpenter KD, Orlando JL, Kendall C. 2020. "Spatial Variability of Phytoplankton in a Shallow Tidal Freshwater System Reveals Complex Controls on Abundance and Community Structure." Science of The Total Environment Volume 700, 134392. Viewed online at: https://doi.org/10.1016/j.scitotenv.2019.134392.

Stumpner P, Burau JR, Forrest A. 2020. "A Lagrangian-to-Eulerian Metric to Identify Estuarine Pelagic Habitats." Estuaries and Coasts Volume 44: Pages 1231–1249. Viewed online at: https://doi.org/10.1007/s12237-020-00861-7.

Thieurmel B, Elmarhraoui A. 2019. suncalc: Compute Sun Position, Sunlight Phases, Moon Position and Lunar Phase. R package version 0.5.1. Viewed online at: https://CRAN.R-project.org/package=suncalc.

Tsubaki R, Kawahara Y, Muto Y, Fujita I. 2012. "New 3-D Flow Interpolation Method on Moving ADCP Data." Water Resources Research Volume 48 (Issue 5). Viewed online at: https://doi.org/10.1029/2011WR010867.

U.S. Bureau of Reclamation and California Department of Water Resources. 2023. *Temporary Urgency Change Petition of 2022 and Emergency Drought Salinity Barrier: Impact on Harmful Algal Blooms and Aquatic Vegetation in the Delta*. Sacramento (CA): U.S. Bureau of Reclamation. March 2023. 120 pp. + appendix.

U.S. Environmental Protection Agency. 1993a. *Method 353.2: Determination of Nitrate-Nitrite Nitrogen by Automated Colorimetry*. Environmental Monitoring Systems Lab.

———. 1993b. *Method 365.1: Determination of Phosphorus by Semi-Automated Colorimetry: Methods for Chemical Analysis of Water and Wastes.*

U.S. Geological Survey. 2022. Sacramento R a Freeport CA – 11447650, May 16, 2022–May 20, 2022: Temperature, Water, Degrees Celsius. Viewed online at: https://waterdata.usgs.gov/monitoring-location/11447650/#parameterCode=00010&timeSeriesId=15760&startDT=2022-05-16&endDT=2022-05-20.

———. 2023a. Gage data: False R NR Oakley CA – 11313440. Viewed online at: https://waterdata.usgs.gov/monitoring-location/11313440/#parameterCode=00065&period=P7D.

———. 2023b. National Water Information System. Viewed online at: https://doi.org/10.5066/F7P55KJN. Accessed June 10, 2023.

Ustin S, Khanna S, Bellvert J, Boyer JD, Shapiro K. 2016. *Impact of Drought on Submerged Aquatic Vegetation (SAV) and Floating Aquatic Vegetation (FAV) Using AVIRIS-NG Airborne Imagery.* California Department of Fish and Wildlife. [Government Report.]

Van Rossum G, Drake FL. 2009. *Python 3 Reference Manual*. Scotts Valley (CA): CreateSpace.

Wagner RJ, Boulger RW Jr., Oblinger CJ, Smith BA. 2006. *Guidelines and Standard Procedures for Continuous Water-Quality Monitors: Station Operation, Record Computation, and Data Reporting.* Techniques and Methods 1–D3. Reston (VA): US Geological Survey. 51 pp. + 8 attachments. [Government Report.] Viewed online at: http://pubs.water.usgs.gov/tm1d3.

Walters RA, Gartner JW. 1985. "Subtidal Sea Level and Current Variations in the Northern Reach of San Francisco Bay." Estuarine, Coastal and Shelf Science Volume 21: Pages 17–32.

Walters RA, Heston C. 1982. "Removing Tidal-Period Variations from Time-Series Data Using Low-Pass Digital Filters." Journal of Physical Oceanography Volume 12 (Issue 1): Pages 112–115.

Weatherill NP. 1992. "Delaunay Triangulation in Computational Fluid Dynamics." Computers & Mathematics with Applications Volume 24 (Issues 5–6): Pages 129–150. Viewed online at: https://doi.org/10.1016/0898-1221(92)90045-J.

Welker JM. 2000. "Isotopic (δ18O) Characteristics of Weekly Precipitation Collected across the USA: An Initial Analysis with Application to Water Source Studies." Hydrological Processes Volume 14: Pages 1449–1464. Viewed online at: https://doi.org/10.1002/1099-1085(20000615)14:8<1449::AID-HYP993>3.0.CO;2-7.

World Health Organization. 2021. *Guidelines on Recreational Water Quality. Volume 1: Coastal and Fresh Waters.* Geneva, Switzerland. Viewed online at: https://www.who.int/publications/i/item/9789240031302.

Zhang Y, Baptista AM. 2008. "SELFE: A Semi-implicit Eulerian-Lagrangian Finite-Element Model for Cross-Scale Ocean Circulation." Ocean Modelling Volume 21 (Issues 3–4): Pages 71–96.

Zhang Y, Ye F, Stanev EV, Grashorn S. 2016. "Seamless Cross-Scale Modeling with SCHISM." Ocean Modelling Volume 102: Pages 64–81.

Zhang YJ, Gerdts N, Ateljevich E, Nam K. 2019. "Simulating Vegetation Effects on Flows in 3D Using an Unstructured Grid Model: Model Development and Validation." Ocean Dynamics Volume 70: Pages 213–230 (2020). Viewed online at: https://doi.org/10.1007/s10236-019-01333-8.

Zimmerman CF, Keefe CW, Bashe J. 1997. *Method 440.0: Determination of Carbon and Nitrogen in Sediments and Particulates of Estuarine/Coastal Waters Using Elemental Analysis.* U.S. Environmental Protection Agency, Office of Research and Development, National Exposure Research Laboratory, Cincinnati (OH). [Government Report.] Viewed online at: https://cfpub.epa.gov/si/si_public_record_Report.cfm?Lab=NERL&dirEntryId=309418.